3D Seismic Characterisation of The Cantarell Field, Campeche Basin, Mexico

Valente Ricoy-Paramo

Submitted in partial fulfilment of the requirements for the degree of Ph.D.

Cardiff University

February 2005

ProQuest LLC
789 East Eisenhower Parkway
P.O. Box 1346
Ann Arbor, MI 48106-1346

This thesis is dedicated with all my heart to the memory of J. Ulises Ricoy Saldaña my father, my teacher, and my friend. It is also dedicated to Ana Laura, my wife, and Cecilia, my daughter, for their love and support through this endeavour.

DECLARATION

This work has not previously been accepted in substance for any degree and is not being concurrently submitted in candidature for any degree.

Signed Valerie Kinoy P. (candidate)

Date 22/06/05

STATEMENT 1

This thesis is the result of my own investigations, except where otherwise stated.
Other sources are acknowledged by footnotes giving explicit references. A bibliography is appended.

Signed Valerie Kinoy P. (candidate)

Date 22/06/05

STATEMENT 2

I hereby give consent for my thesis, if accepted, to be available for photocopying and for inter-library loan, and for the title and summary to be made available to outside organisations.

Signed Valerie Kinoy P. (candidate)

Date 22/06/05

Summary

A detailed 3D seismic investigation coupled with key well data of the Cantarell Field located in the southern Gulf of Mexico was undertaken with the view to developing a seismic-structural framework in order to address the geological features observed in the Cantarell Field.

The Cantarell Field hosts a world class petroleum system. The most productive reservoir of the giant Cantarell Field is a complex brecciated and fractured Upper Cretaceous carbonate system that has been interpreted as a response to subaerial exposure and karstification. The 3D seismic interpretation shows the Cantarell area to be intensely deformed by a complex array of thrusts, normal, reverse and strike-slip fault systems that uplifted the Mesozoic carbonate sequences. This work details the structural evolution and shows how the broader understanding of the structural history allows a re-examination of the reservoir model and in particular the development of key fracture sets, that are so critical for the production strategy deployed on the field.

From the regional interpretation of seismic lines coupled with key well data a depositional setting is interpreted to have evolved from a shallow ramp during the Jurassic to a scarp dominated platform margin at the end to the Cretaceous. During the Cenozoic the basin underwent significant subsidence and the sedimentation style switched from carbonate dominated to a siliciclastic dominated.

The structural interpretation allowed suggesting three main phases of structural deformation, which exhibit evidence of reactivation: (1) Jurassic to Early Cretaceous Early extension, (2) Mid Miocene to Pliocene compression, and (3) Pleistocene to recent mild extension.

From the spatial distribution of seismic facies assemblages, this work proposes a polyphase model for the origin of the Upper Cretaceous calcareous breccias: (1) Late Cretaceous sedimentary breccias occurring in a basinal setting as cyclic talus deposits in a carbonate-slope-apron system. (2) During the Neogene structural evolution the area resulted in a complex array of thrusts and fractures which resulted in the development of tectonic breccias occurring at various scales. (3) Subaerial to medium depth karstification related to the Neogene structural evolution of the area which resulted in a thrust controlled uplift of 1000 metres, affecting the breccias situated at the crest of the Akal block. This model has major implications for future field development and the understanding of the fractured reservoir system in this basin.

Acknowledgements

First I would like to say that this research would not have been possible without the support I received from many friends, family, the Instituto Mexicano del Petróleo and Pemex; whom I would like to show my appreciation below.

Professors Joe Cartwright and Paul Wright, I am deeply thanked for all of your support. I guess I have troubled and puzzled you with my project and my ideas. I appreciate very much your patience and your effort to scrutinise all the ideas as well as the outcome. I am also greatly indebted for the support I receive when I went through the difficult family times I had to endure.

The Instituto Mexicano del Petróleo provided a research fellowship, allowing this study to be completed. Pemex Exploración Producción, Activo Cantarell, is also thanked for providing the data and allowing it to be used, especially I would like to thank Enrique Ortuño Maldonado for going out of his way to make the data available.

Andy Horbury receives my deeply gratitude for all the guidance and the great geological experience of Mexico that he shared with me. Without his observations and ideas a great deal of this work would not have been possible.

All my appreciation to all my University peers who have provided with good times and with the scientific push. Thanks to Dorthe and Mads for all the good times we had on and off the bicycles, and for all the cups of coffee that some way or another I managed to drink, from the magnificent expresso machine. The best in town. Dorthe, many thanks for reading some of my ideas and helping me organizing them better. Jose and Mike, it was really good fun to share the office, I had my very good laughs. I am very grateful to Andy Robinson who received me and my wife when we first landed from Mexico. He gave us a very warm welcome and give me plenty of ideas on how to develop the thesis.

To all my family back home I thank you all for always being there for me, for providing me with all of you r support and affection. I thank you and appreciate very much all of time we have not spent together in the name of this thesis to be accomplished. Thanks to my mamá y papá for being my friends, my guidance, and my parents; for teaching me how to "meditate" and search for happiness and harmony. Thanks father for taking me to

my first geological field trip of my life, thanks for all of your love. Thanks to Ulises and Rebeca for being my best brother and sister. Thanks to Lila, Ramón, Lila pequeña, Miguel, Silvia. I appreciate very much all of the support and love that Cecy, Julio, Lalo, Cuca, and Lalo (mi querido suegro) have provided me.

With all my heart and love I thank my beloved wife Ana Laura who supported me throughout this endeavour. Without Ana Laura and her unconditional love this thesis would not be here. I thank you for tolerating my moods and my breccia and structural related explications that I repeated to you over and over. Cecilia, my wonderful and loved daughter I thank you for all the happiness and love you brought to my life.

Table of contents

Chapter 3
Seismic stratigraphy of the Cantarell area

Chapter 4
Structural geology of Cantarell

Chapter 5
Kinematics of the main phase of deformation

Chapter 6
Implications for the reservoir hosted in the Upper Cretaceous calcareous breccias of Cantarell

Chapter 7
Conclusions and future research

List of Figures

Appendices

A1. Well names and platforms of the Cantarell Field.

A2. Well logs loaded on the Geoframe system.

A3. Well synthetics

A4. Core photos evidencing the different lithologies and facies for the Upper Cretaceous, Mid-Cretaceous, Early Cretaceous, Tithonian and Kimmeridgian.

A5. Summary of well completion logs.

Enclosures

Enclosure 1. Seismic line oriented NW – SE, for detailed description, see Chapter 2.
Enclosure 2. Seismic line oriented SW-NE, for detailed description, see Chapter 2.
Enclosure 3. Seismic line oriented SW-NE, for detailed description, see Chapter 2.
Enclosure 4. Seismic line oriented SW-NE, for detailed description, see Chapter 2.
Enclosure 5. Seismic line oriented NW – SE, for detailed description, see Chapter 2.

For basemap showing locations of seismic lines see Figure 2.2.

Map Legend

Normal fault

Symbols employed in the various maps presented throughout this work.

Reverse fault

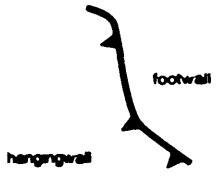

Thrust fault

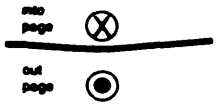

Thrust fault

strike and dip

Chapter 1

Introduction

1.1 Definition of PhD research

This PhD project uses 3D and 2D seismic data combined with key well data to improve our understanding of the fundamental processes involved in the geological evolution of the Cantarell Field. This will allow addressing the geological uniqueness of the Cantarell Field. The geological uniqueness includes: (1) a thick breccia deposit (up to 300 m) located at the Upper Cretaceous interval, which is the most important reservoir unit of the Field and the petroleum province located in the Campeche Basin, (2) the structural architecture, and (3) the internal plumbing system of the reservoir.

1.2 The Cantarell Field

The Cantarell Field is located approximately 80 km north of Ciudad del Carmen, Campeche, within the continental shelf of the Campeche Basin in the southern Gulf of Mexico (see Chapter 2 Figure 2.1). The Cantarell area is a geologically complex structure that resulted from three main phases of deformation (this PhD project). In this study it is divided into five structural blocks. Lithologically the Upper Mesozoic interval is made up almost entirely of carbonate rocks and the Cenozoic consists of a terrigenous-dominated succession with minor carbonate incursions. The Cantarell reservoir system is ranked as the second largest offshore field in the world (Morton, 2004).

Different geological processes have shaped and structured the current Cantarell area. This PhD thesis aims to unravel the tectonics that drove and shaped the current structure, whose morphology and dimensions are unique. The various geological processes associated with the structural deformation will be investigated, some of these include: faulting and fracturing, development of unconformable surfaces, structural syn-sedimentation architectures. Furthermore, the significance that these geological processes have on the porous reservoir network will be investigated.

1.3 Exploration and production history

During the mid 1970's, the discovery of oil seeps that Mr. Rudecindo Cantarell, a fisherman, reported to Pemex (the nationally owned petroleum company) resulted in further exploration of the Campeche Basin which eventually resulted in the discovery of the Cantarell field (Cantu-Chapa, 2001). Production was established in 1979 with the discovery well Akal-1. From well production and in place calculated volumes, the Cantarell field was considered as a giant (Santiago 1992). The initial production came from well Chac-1 that without stimulation produced 952 BOPD (Barrels of Oil per day) of 20° API oil. This well is located to the west of the study area (see Chapter 3, Figure 3.2). After well Chac-1, the Akal-1A well located at the crest of the structure produced 34,000 BOPD of 22° API oil. After this well, Akal-2 flowed without stimulation at a rate of 5,000 BOPD. The hydrocarbon production of these wells was derived from the Upper Cretaceous calcareous breccia interval.

The Cantarell Field went on stream production in June 1979. By 1980 the configuration was outlined by 18 producing wells and the structure was considered as a large complex anticline dissected by northwest striking faults and oil production was estimated at 600,000 BOPD. Production facilities, drilling platforms and pipe lines were being constructed by the mid 1980's. The maximum production rate per well during the initial stage of field development was 57,356 BOPD. This was reduced to 35,500 BOPD in 1982. With time the average well production declined to 21,645 BOPD during 1983. By 1994 Cantarell was producing 961,000 BOPD. Cumulative production during 1994 reached 5,273 MMBO (billion barrels of oil). Ultimate recoverable reserves were estimated at 8 billion bbl of oil during 1994. However, by year 2000 the cumulative production for Cantarell was approximately 7,861 billion bbl of oil (Aquino, 2003).

During June 1998, well C-418D was deepened which led to the discovery of a repeated section of Oligocene to Mid Cretaceous strata underlying Oxfordian sediments. This suggested the occurrence of a major thrust structure. Oil chemistry analysis revealed two types of heavy oil: 30° API and 22° API oils. Production tests confirmed hydrocarbon production of 5200 BOPD of 22° API oil and at 3,000 BPOD of 30° API oil. From 1998 to present further drilling of 8 well locations proposed for the footwall block confirmed the presence of a significant thrust structure.

1.4 Previous work

The geological information employed in this thesis relevant to the Cantarell area is derived from Pemex and IMP (Institute of Mexican Petroleum) internal reports, a masters thesis, and limited published literature (Sanchez, 1979; Meyerhoff, 1980; Viniegra-Osorio, 1981; Salvador, 1987; Buffler, 1991; Sawyer, 1991; Santiago, 1992; Angeles-Aquino, 1994; Gonzalez-G., 1994; Bally, 1995; Western-Atlas International, 1996; Limon, 1996; Ramirez-Cruz, 1996; Ortuno-Maldonado, 1999; Grajales-Nishimura, 2000; Angeles-Aquino, 2001; Meneses-Rocha, 2001; Pacheco-Gutierrez, 2002; Rivas 2002; Soriano, 2003).

Of these works, not all by any means refer in a direct way to the Cantarell area; instead many are found on a regional scale of investigation. This provides insights to some of the geological processes related to the area as whole. From a regional perspective, but making special reference to the Cantarell area, the work of Viniegra-Osorio (1981), appears to be the most comprehensive and also the most cited. In his paper he puts forward a geological model of southern Mexico based on geological observations derived from wells located in the region and supported with some fieldwork. The conceptual model suggests that the former Yucatan platform and parts of the Chiapas, Tabasco and Veracruz states formed a carbonate bank. An extensive bank-edge talus deposit is interpreted to the north, northwest, in a basinwards direction (Viniegra-Osorio, 1981).

Studies most relevant to the Cantarell field include: Western Atlas International (1996); Angeles-Aquino, (1994); Angeles-Aquino (2001); Grajales -Nishimura, (2000); Horbury, (2001); Pacheco-Gutierrez, (2002); Ortuno-M. (1999); Ortuno-Maldonado, (2001).

The study presented in Western Atlas International (1996) consists of a reservoir characterisation of the "Akal" reservoir which is hosted within the hangingwall block of the structure. This work was the first attempt to integrate geological, geophysical and engineering data. This resulted in a robust document that presents various examples of the above data, however it is considered that the initial attempt of integrating the data was not fully accomplished. Instead descriptions and isolated interpretations of the various types of data were provided.

Angeles-Aquino (1994), integrated well logs and key seismic lines together with previous studies, to put forward a model for the tectonic evolution and structural styles encountered in the Campeche Basin. Angeles-Aquino (2001) suggested a stratigraphic division for the Upper Jurassic for the Campeche shelf and proposed a depositional model of the area. The work is based from the analysis of 50 exploratory wells of the area.

Grajales-Nishimura (2000) proposed a model for the Upper Cretaceous calcareous breccias that occur within the Campeche Basin and surrounding areas. The main argument is that the calcareous breccias resulted from a massive collapse of the platform margin triggered by the Chicxulub meteorite impact. This work is based on stratigraphic and mineralogic analysis of Upper Cretaceous sections.

Horbury (2001) in an internal Pemex report, proposed an alternative geological model for the Cantarell area during the Cretaceous period. His work is mainly based from core data (fabric) and the correlation of Gamma Ray well logs within the field. Karstic textures were recognised, and from the correlation of well logs and their stratigraphic relationships, a karstic environmental setting was proposed for the Upper Cretaceous calcareous breccias.

A kinematic structural framework is suggested by Pacheco-Gutierrez (2002) that explains the occurrence and nature of the fracture network systems observed at core scale for the northeastern Campeche Basin. His work is based on the structural interpretation of some 2D seismic lines, and the interpretation of structural features observed in cores and the relationship between these.

Ortuno-Maldonado (1999) has presented a study in which he describes the spatial distribution of the Jurassic Tithonian interval throughout the Campeche Basin. The stratigraphic subdivision is based on well data (biostratigraphic, lithological and electrical perspective). He describes the oil characteristics in terms of API that have been produced in the different wells of the Cantarell area. Later Ortuno-Maldonado (2001), presents a well log description for the calcarenites identified in Eocene stratigraphic interval within the Cantarell area, specifically for the wells that penetrated the Akal reservoir.

Other works have studied the area from a regional scale (e.g. Salvador, 1987; Winker, 1988; Horbury, 2002; Ewing, 1991; Sawyer, 1991; Marton, 1999; Guzman-Vega, 1999; Meneses-Rocha, 2001).

1.5 Seismic interpretation in carbonate depositional settings

Identifying and understanding the impact and relevance of geological processes from a seismic perspective is of great importance. Previous authors (Mitchum, 1977; Vail, 1977) have developed various methodologies for seismic interpretation techniques that have enlightened and broadened the understanding of different geological processes observed from a seismic data.

It is important to mention and emphasize that most of the methodology and expertise on seismic data acquisition, data processing, and data interpretation has been developed mainly in siliciclastic environments, where the sand and clay have been transported by rivers, streams, wind, or waves, or have been mechanically reworked by other processes. In contrast, carbonates differ significantly in the sense that they are formed in place: organically grown, precipitated, or geochemically precipitated, as well as transported (Palaz, 1997).

The generation and precipitation of carbonate sediments requires specific environmental conditions. Carbonate production is responsive to: clear water with little or no silt input, specific water temperatures, nutrient supply, and water depth. Carbonate production occurs along slopes, platforms, and margins extending for hundreds of kilometres. Environments favourable for carbonate deposition can also be favourable for precipitation of thick evaporites (sulphates and salt), which present intrinsic seismic imaging and interpretation issues (e.g. Palaz, 1997; Marcuda, 1997, Borgomano, 2000).

Once generated, carbonate rocks are more susceptible to rapid diagenetic changes than clastic rocks. At times these diagenetic changes are radical, creating great variations of porosity and permeability from the original parent rock. Carbonates are able to maintain steep marginal slopes and wave-resistant structures which can shed significant amounts of debris onto and into the base-of-slope and basinwards (Marcuda, 1997).

From a seismic perspective carbonate rocks have greater velocities and densities than most siliciclastics. In addition associated anhydrite velocities may be faster. These faster velocities result in lower vertical and spatial seismic resolution in carbonate strata compared to siliciclastics of comparable thickness. This results in what is called the "resolution problem" (Palaz, 1997). When overlain by siliciclastics of lower velocities, the top of the carbonates are easily recognisable. However, when embedded in yet more carbonate stratigraphy, the reflectivity between formations is notoriously low, giving a transparent appearance.

To complicate matters further, with the rise and fall of sea level, carbonates are often exposed subaerially, where they undergo further diagenesis and karstification. Complicated networks of macroscopic pores are generated. These pores may be filled with gas, oil, water, or partially mineralised, which produces laterally back-scattering seismic noise, that results in poor seismic imaging (Marion, 1997).

In this PhD study, seismic data is employed to identify geological processes and investigate how these have influenced the Cantarell area. Understanding these geological processes will allow some of the many questions that surround the Canterell area to be addressed. Furthermore, the observations derived from this thesis can be applied to neighbouring analogous reservoirs. Some of the questions that can be addressed relate to the timing of deformation, hydrocarbon generation and migration, secondary recovery, formation evaluation, reservoir modelling, reservoir properties spatial distribution, and oil field development.

1.6 Aims and scope of thesis

The main aim of this thesis is to provide a detailed three-dimensional analysis of the structural and stratigraphic evolution of the Cantarell area based on 3D and 2D seismic data combined with key well data to provide a well constrained model for the Cantarell reservoir intervals against which numerical and geometric models can be tested in the future. Additionally to this main aim, secondary aims consist of:

1. To revise the current geological data base mainly stratigraphic and structural for the Cantarell area.

2. To provide a regional geological setting for the Campeche Basin with special emphasis on Cantarell and surrounding areas based on the integration and analysis of previous data and the interpretation of five regional seismic lines.

3. To review and discuss the current depositional models suggested for the Upper Cretaceous calcareous breccia in the light of new evidence provided from this study.

1.7 Data Base

The data employed in this study consists of a P-reflection Ocean Bottom Cable seismic cube, five 2D regional lines, and over 250 well boreholes with deviation surveys, wireline data, and some completion logs reports, core photos and lithologic descriptive reports. The data was provided by Pemex Exploracion y Produccion, Activo Cantarell. At the very late stages of the PhD project, a 3D seismic streamer survey was made available that provided better resolution of shallow sections than the OBC data. This data set was utilised to analyse the kinematics of the main phase of compression (see Chapter 5).

1.7.1 3D Seismic and 2D seismic data

The 3D Ocean Bottom Cable seismic cube is a two way time migrated data set whose amplitude is registered at 8 bit. The data have been processed with special filters and gain algorithms in order to illuminate the deeper stratigraphy and structural setting. Pemex did not provide any information concerning the processing procedure of the seismic data. The dominant average frequency for the Upper Mesozoic is 10 Hz and for the Cenozoic interval 20 Hz. Ocean bottom cable or also referred to as ocean bottom seismographs (OBC and OBS) data sets are deployed on the sea bed. These contain a digital recorder together with a high-precision clock unit to provide an accurate time base for the seismic recordings. Sea bed recording systems provide a better signal-to-noise ratio than hydrophones suspended in the water column and, in deep water, recording at the sea bed allows much better definition of shallow structures. In this type of survey the dominant frequency is typically in the range 10-50 Hz and travel times are known to about 10 sec.

The 2D data consists of five arbitrary lines that are composite lines of various 3D seismic cubes. Theses 2D lines were provided by Pemex (2000) as paper and digitised sections. Interpretation and description of these lines are presented in Chapter 2, Section 2.3.

1.7.2 Well Data

The Cantarell area has been drilled by over 260 wells. Most of these wells are located in the Thrust Block of the structure targeting the hangingwall. Twenty two platforms occur, from which most wells are projected on to the structure as both production and injection wells (Appendix 1). In Appendix 1 all the platforms and the wells allocated to each production or injection platform are listed. Not all of the wells were loaded on the Geoframe system for the current study. The criteria employed to determine the wells to be used in this study is detailed in Chapter 3, (see Figure 3.1).

The well data consists of: wireline data, biostratigraphic and lithostratigraphic reports in the form of well completion logs and core description reports. Not all wells contain the same data. Appendix 2 lists all of the available wireline data that were loaded on the Geoframe system. The amount of data is overwhelming. However, this was used in some cases to calibrate the seismic correlations.

Only seven wells contain check-shot data (C-3001, C-3068, C-1065D, C-99D, C-418D, C-6A, C-468 and Chac-2). These wells were considered as key in the calibration of the Top-Breccia-1 and Top-Tithonian seismic horizons (see Chapter 3, Section 3.3). Prior to beginning this thesis, during a visit to Pemex (2000), synthetics for wells C-3068, Chac-2, C-1065D, and C-6A were constructed to assess the correlation between the seismic and the well data. It was considered that a good correlation for the Top Cretaceous or Base Tertiary level, Tithonian and Kimmeridgian levels the stratigraphic markers showed a good correlation with the seismic data (Appendix 3).

The stratigraphic nomenclature employed in this study is derived from the Pemex nomenclature. This has been constructed from the correlation of biostratigraphic, lithostratigraphic and well log response analysis on a well to well basis (See Chapter 3, Section 3.3). However the lateral correlation of the stratigraphic markers that is best seen provided by the seismic data has been mainly omitted.

The core descriptions and the completion log reports provided by Pemex are of poor quality and do not provide a detailed description of all the lithological variation. However, the core photos presented in Appendix 4 are considered to be representative of the lithological variations (Appendix 4).

1.8 Thesis structure

This thesis combines detailed 3D and regional 2D seismic interpretation with a geological analysis of a comprehensive well database. The thesis is structured from a regional scale to the field scale, and is subdivided into seven chapters including the introduction.

Chapter 2 is divided into two parts. The first section presents a comprehensive literature review of the study area with a regional perspective. In the second part of the chapter, five 2D seismic regional lines are described and put into the defined regional context. The chapter concludes by presenting the basin margin architecture as seen from the 2D seismic lines combined with the regional geological context as provided by previous authors.

Chapter 3 presents a seismic stratigraphic framework for the Cantarell Field by describing the morphology and character of the seismic reflections observed within the Upper Mesozoic and Cenozoic successions. The relationships between seismic character and lithology within the structural framework are investigated. A geologic depositional setting is proposed for the various units of the proposed stratigraphic framework.

Chapter 4 presents a detailed interpretation of the structural framework for the Cantarell Field based on the analysis of structural maps and seismic sections from the 3D seismic volume. This interpretation allowed to suggest the structural evolution of the Cantarell Field.

Chapter 5 presents a kinematical model for the main compressional phase of deformation that resulted in the development of the significant thrust structure observed in the Cantarell area.

Chapter 6 presents a critical review of the previous models for the Upper Cretaceous calcareous breccias in the light of the seismic observations derived in this

thesis. An alternative model is suggested for the evolution of these Upper Cretaceous calcareous breccias, which includes a discussion of the effects the structural evolution had on the reservoir intervals.

Chapter 7 is a short conclusions chapter with suggestions for future work.

Chapter 2

Regional geological setting

2.1 Introduction

This chapter aims at describing the regional geological context and tectonic framework in which the Cantarell area is situated. The geological setting here provided is based on previous studies and the interpretation of five regional 2D seismic lines that traverse the Cantarell area and image the basin margin architecture. Subsequent chapters will focus on the Cantarell area itself.

The Cantarell complex is considered to be in the top ten largest oil fields in the world in terms of production. Morton (2004) reports the Cantarell area as the second largest oil field in the world. It is located 80 Km north of Ciudad del Carmen, Campeche, on the continental shelf in the south-eastern Gulf of Mexico. This area is referred to as the Campeche Basin, situated in the south-eastern Gulf of Mexico Basin (Figure 2.1). Within the Campeche Basin Tertiary and Mesozoic structural provinces overlap. These provinces consists from west to east: the Isthmian Saline Basin, the Comalcalco Basin, the Reforma-Akal Uplift, and the Macuspana Basin, all of which have onshore and offshore expressions and are the foreland signature of the Sierra de Chiapas (Meneses-Rocha, 2001 and Horbury, et al., 2002; Figure 2.2.). The Isthmian Saline, Comalcalco and Macuspana Basins are northeast oriented trends which are interpreted as Neogene depocentres (Meneses-Rocha, 2001). The offshore region is referred to as the Campeche Basin and this name will be referred to in this thesis (Figure 2.3). The Cantarell area is situated in the northernmost region of the Reforma-Akal Uplift. The Reforma-Akal Uplift is bounded to the east by the Macuspana Basin, to the west by the Comalcalco Basin, to the north-northeast by the Yucatan Platform and to the south – southwest by the Chiapas Massif (Meneses-Rocha, 2001). The Yucatan Platform is found within the foreland region of the Sierra de Chiapas that has remained structurally stable since the Early Cretaceous (Meneses-Rocha, 2001 and Pindell, 2000).

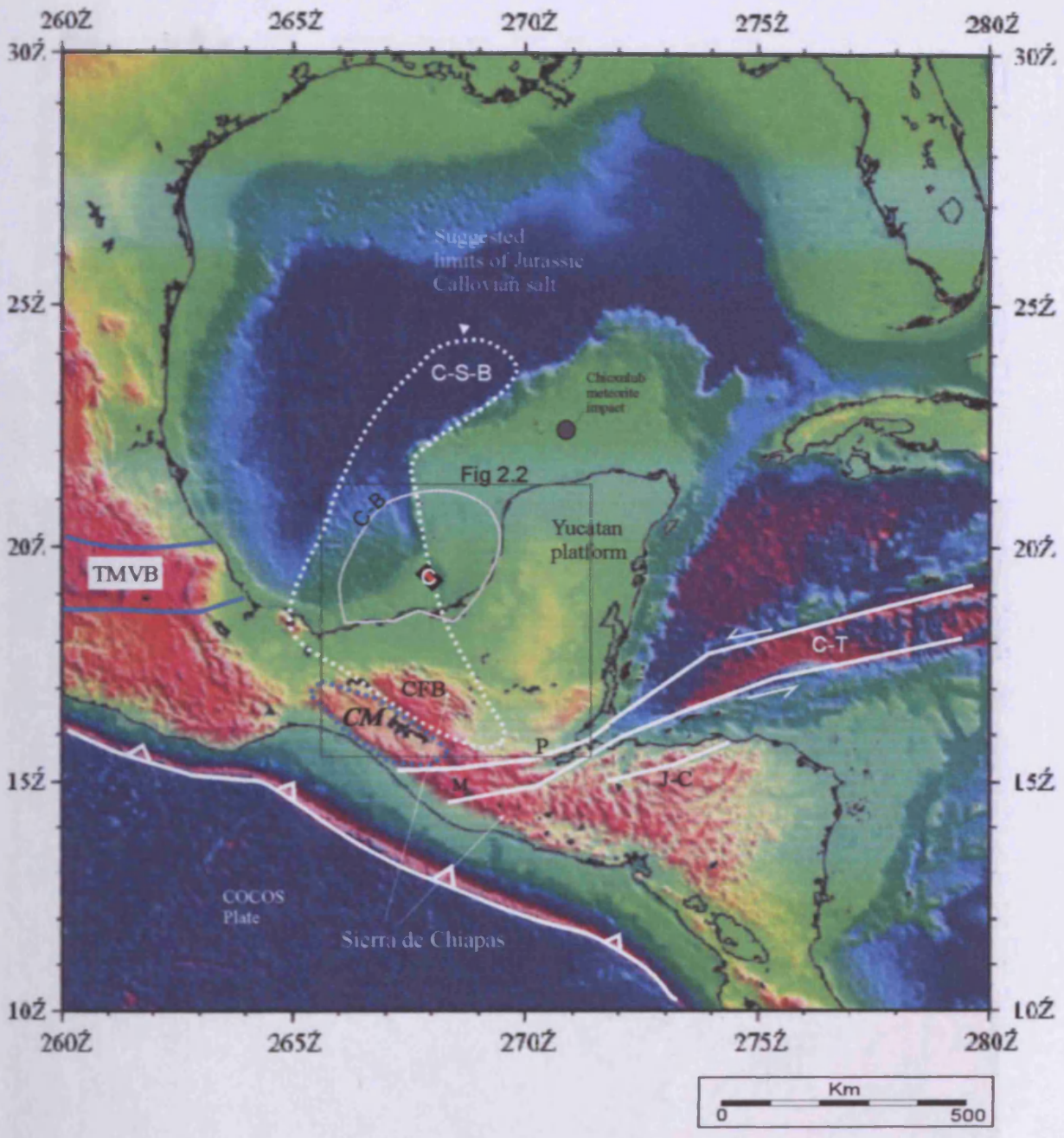

Figure 2.1
Present day map of the Gulf of Mexico, illustrating the key geological elements: (RAU) Reforma-Akal Uplift, (CM) Campeche massif, (P) Polochic strike-slip fault, (M) Motagua fault, (J-C) Jocotan-Chamelecon strike-slip fault, (C-T) Cayman Trough, (C-S-B) Campeche salt basin, (TMVB) Trans-Mexican Volcanic Belt, (C-B) Campeche Basin, (CFB) Chiapas Fold Belt. Figure 2.2 denotes the extent of the South-east Gulf of Mexico. Modified from Sedlock,1993; Meneses-Rocha, 2001, and Pindell, 2001. Digital bathymetric-relief map after provided by Mitchell, 2001.Approximately 38% of the Gulf is comprised by shallow and intertidal areas (< 20 m deep). Located in the southwestern quadrant, the Sigsbee Deep is the deepest region of the Gulf of Mexico and contains depths of up to 4,384 m. Mean (average) water depth of the Gulf is ~1,615 m (Turner, 1999) Mean (average) water depth of the Gulf is ~1,615 m (Turner, 1999). Located in continental Mexico, the Trans Mexican Volcanic Belt has an average altitude is at 2700 m above sea level oscillating from 2000 m to 5000 m above sea level. The Chiapas Massif has an altitude range of 1000 to 2300 m above sea level.

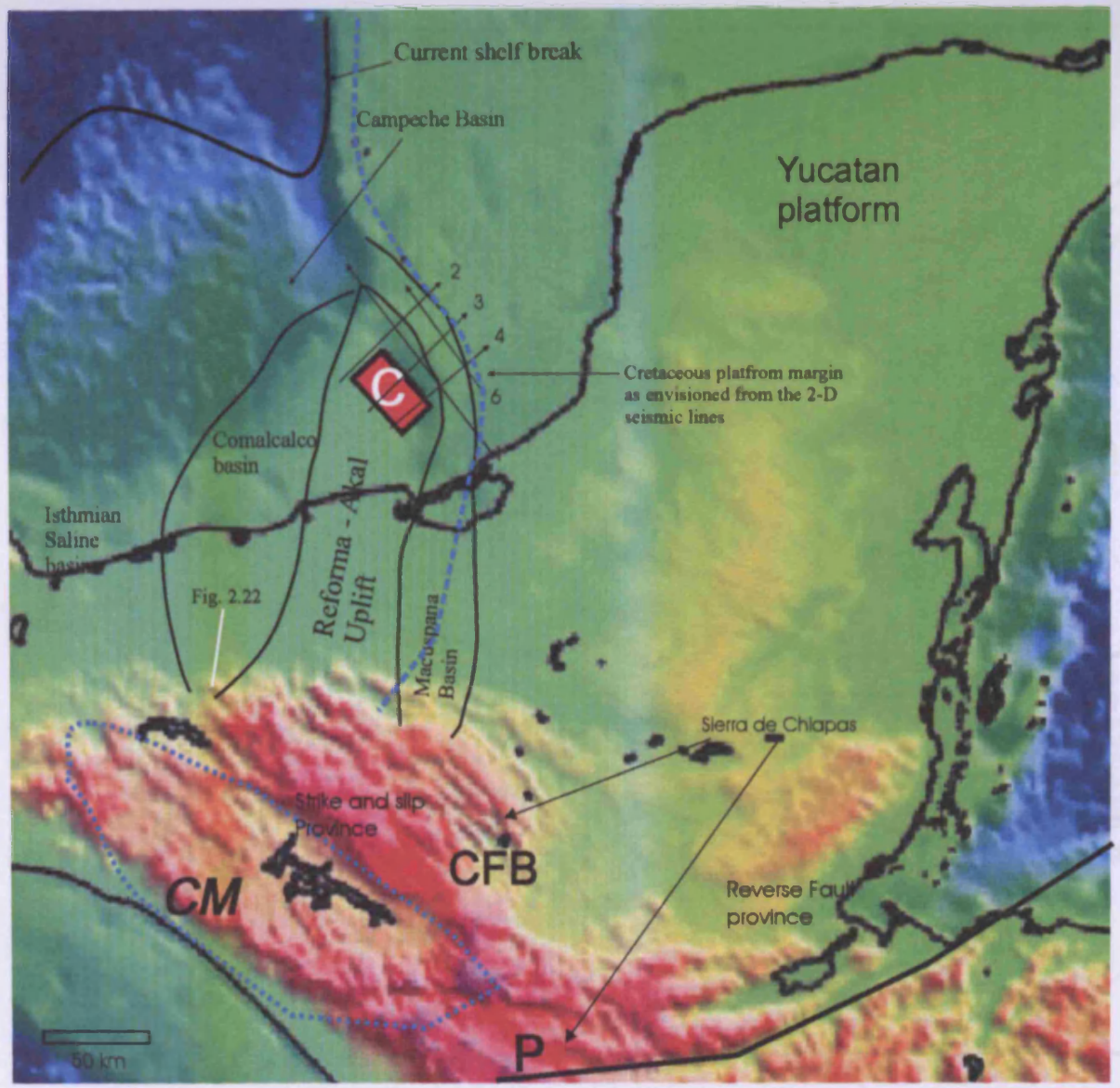

Figure 2.2
South eastern Gulf of Mexico, illustrating the different geological elements, the location of the Cantarell 3D survey, and the location of five 2D transects (Enclosures 1 to 5). Abbreviations: CM, Chiapas Massif; P, Polochic fault; CFB, Chiapas Fold Belt The different provinces: The Isthmian Saline Basin, the Comalcalco Basin, the Reforma-Akal Uplift, Macuspana Basin, are the foreland subsurface signature of the structural belt, Sierra de Chiapas, that has a significant surface expression.

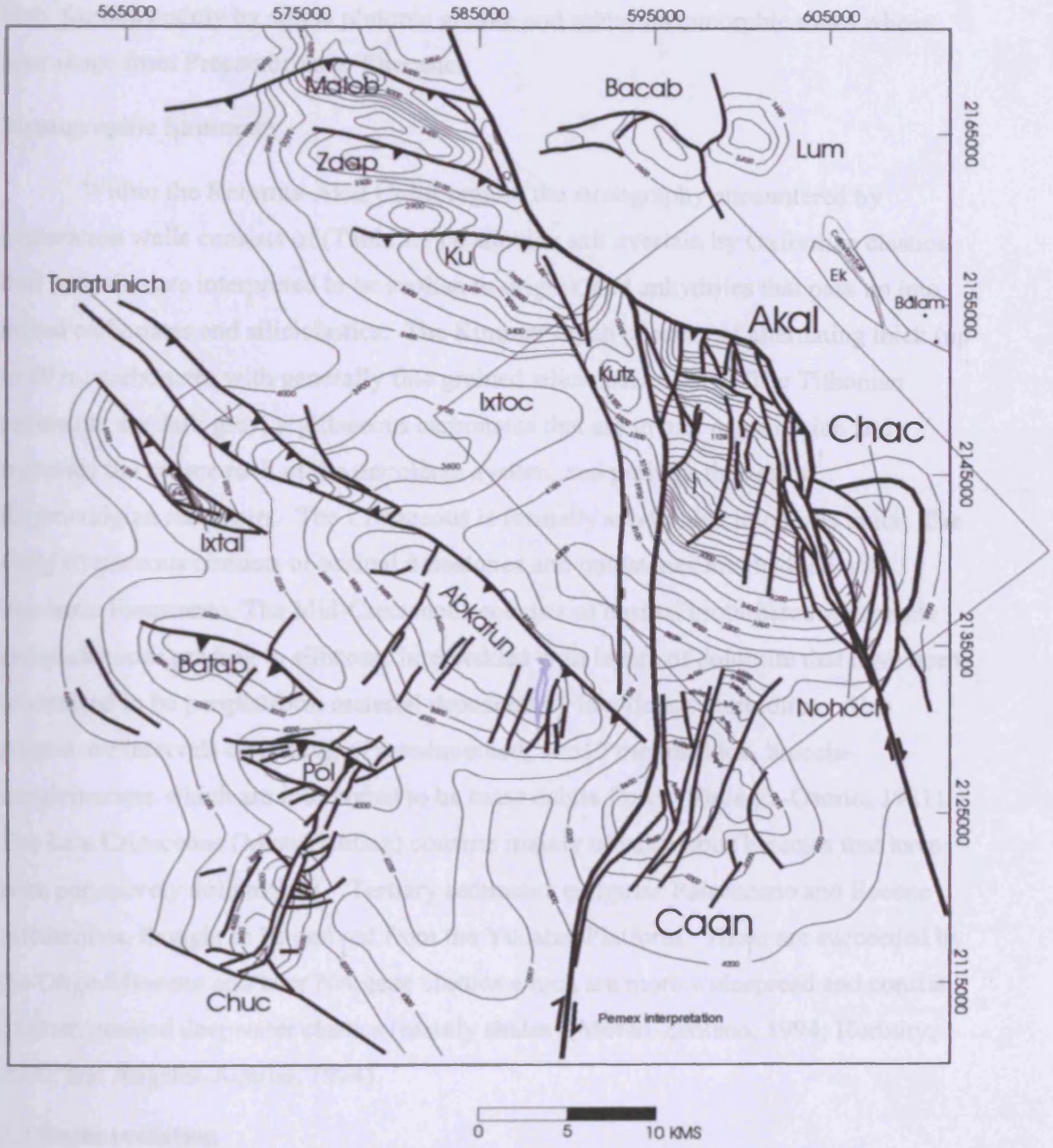

Figure 2.3
Structural map (in meters) for the top of the Late Cretaceous; structural top for the top Upper Cretaceous reservoirs; the different structures are the different producing fields. After Pemex, 1998. Note the layout and location of the 3D seismic survey used for this study.

The Sierra de Chiapas is a mountain chain extending parallel to the Pacific coastal plain from the Isthmus of Tehuantepec to the Mexico-Guatemala border. It is characterised by a rugged topography with altitudes from 38 to 3800 metres, which contains a massif body formed mainly by silicic plutonic granite and minor metamorphic rocks whose ages range from Precambrian to Pliocene.

Stratigraphic Summary

Within the Reforma-Akal Uplift region, the stratigraphy encountered by exploration wells consists of (Table 2.1) Callovian salt overlain by Oxfordian clastics (red beds that are interpreted to be aeolian in origin), and anhydrites that pass up into mixed carbonates and siliciclastics. The Kimmeridgian consists of alternating thick (up to 10 m) carbonates with generally fine grained siliciclastics (silt). The Tithonian sediments are dark grey, argillaceous carbonates that are in part organic-rich and represent the source rock of the petroleum system, and perhaps the seal to Kimmeridgian reservoirs. The Cretaceous is formally subdivided into three units. The Early Cretaceous consists of basinal dolostones and mudstones interbedded with bioclastic limestones. The Mid-Cretaceous consists of basinal bioturbated wackstone and packstones grading to siltstone, interbedded with layers of dolomite that have been interpreted to be periplatform material deposited by low-density turbidites. Also present are intervals consisting of resedimented, 5 to15 metres thick, breccia-conglomerates which are interpreted to be mass debris flows (Viniegra-Osorio, 1981). The Late Cretaceous (Maastrichtian) consists mainly of calcareous breccias that have been pervasively dolomitised. Tertiary sediments comprise Palaeocene and Eocene calcarenites, thought to be derived from the Yucatan Platform. These are succeeded by the Oligo-Miocene and later Neogene clastics which are more widespread and consist of finer, grained deepwater clastics (mainly shales) (Moran-Zenteno, 1994; Horbury, 2000; and Angeles-Aquino, 1994).

2.2 Basin evolution

This section presents the geological evolution of the Gulf of Mexico from the Late Mesozoic to Recent. Different tectonic models exist for the origin of the Gulf Basin (Buffler, 1985; Pindell, 1985; Sawyer, 1991). The tectonic framework presented here helps identify possible controlling factors for the location and evolution of the basin margin of the southeastern Gulf of Mexico. The following section illustrates the

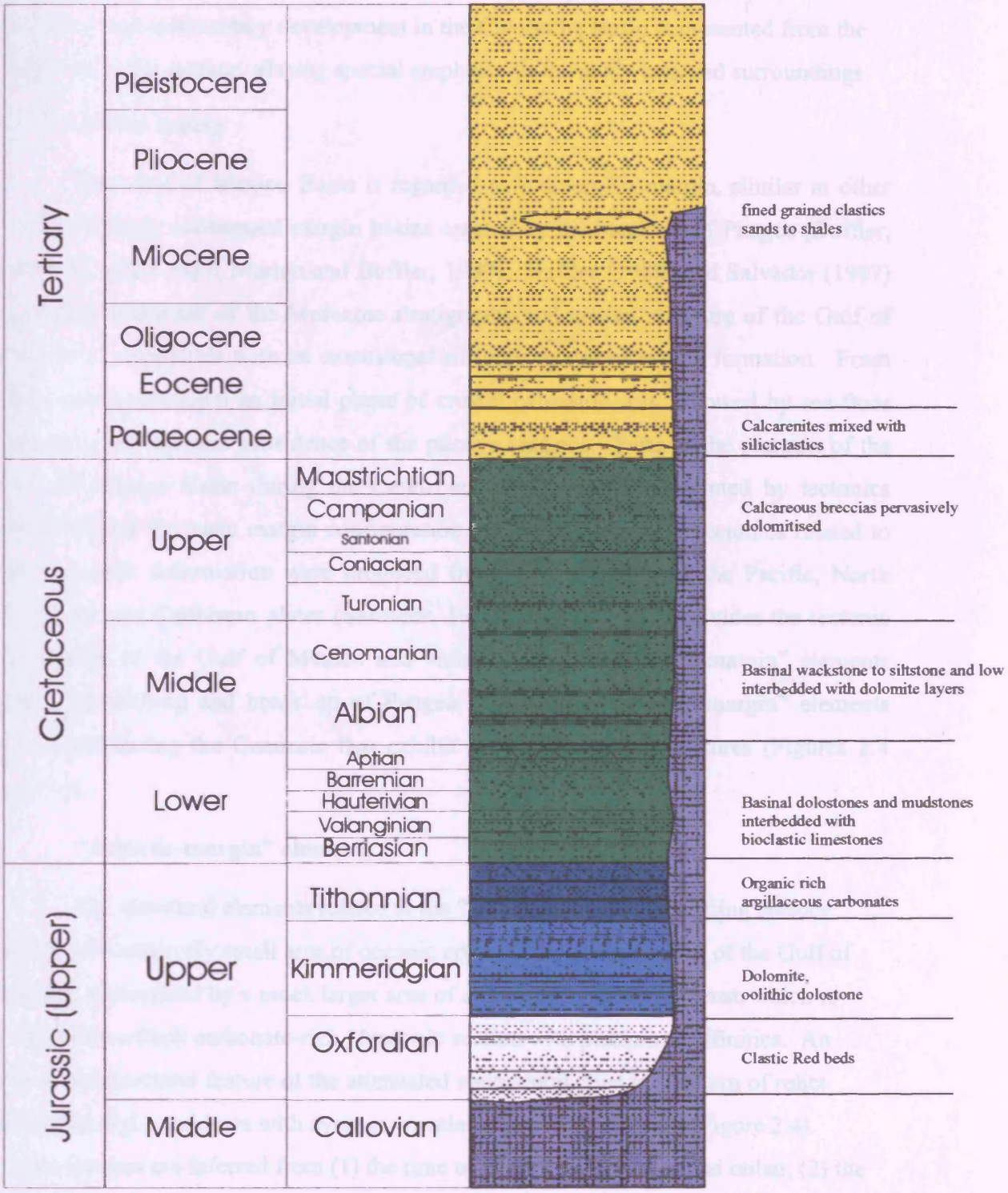

Table 2.1
Stratigraphic column for the Cantarell area.

tectonic setting of the Gulf of Mexico as collated from various authors (Buffler, 1985, 1991; Salvador, 1987; Winker, 1988; Faust, 1990). A summary of the geological evolution and sedimentary development in the Campeche Basin is presented from the basement to the surface, placing special emphasis on the study area and surroundings.

2.2.1 Tectonic setting

The Gulf of Mexico Basin is regarded as a divergent margin, similar to other circum-Atlantic continental margin basins created by the break up of Pangea (Buffler, 1985; Salvador 1987; Marton and Buffler, 1999). Buffler (1985) and Salvador (1987) suggested that most of the Mesozoic stratigraphy and crustal structure of the Gulf of Mexico is compatible with an extensional rift-drift model of crustal formation. From this conceptual model an initial phase of crustal extension was followed by sea-floor spreading and thermal subsidence of the passive margins. Parts of the margins of the Gulf of Mexico Basin during the Cenozoic were strongly overprinted by tectonics which altered the basin margin configuration (Winker, 1988). The tectonics related to the Cenozoic deformation were produced from the interaction of the Pacific, North American and Caribbean plates (Salvador, 1987). Winker (1988) divides the tectonic framework of the Gulf of Mexico and vicinity into the "Atlantic-margin" elements related to drifting and break up of Pangea, and into the "Pacific-margin" elements developed during the Cenozoic that exhibit convergent margin features (Figures 2.4 and 2.5).

"Atlantic-margin" elements

The structural elements related to the "Atlantic-margin" or drifting episode consist of a relatively small area of oceanic crust situated at the centre of the Gulf of Mexico, surrounded by a much larger area of attenuated continental crust, which is overlain by a thick carbonate-rich Mesozoic section with platformal affinities. An important structural feature of the attenuated continental crust is a pattern of relict basement highs and lows with average wavelengths of 100 -500 km (Figure 2.4). These features are inferred from (1) the time of initial transgression and onlap; (2) the distribution of Jurassic salt structures; (3) the relative thickness of Upper Jurassic marine deposits; and (4) the present depth to basement. These post-break-up features are also referred to as horst and graben topography, although the scale is about an order

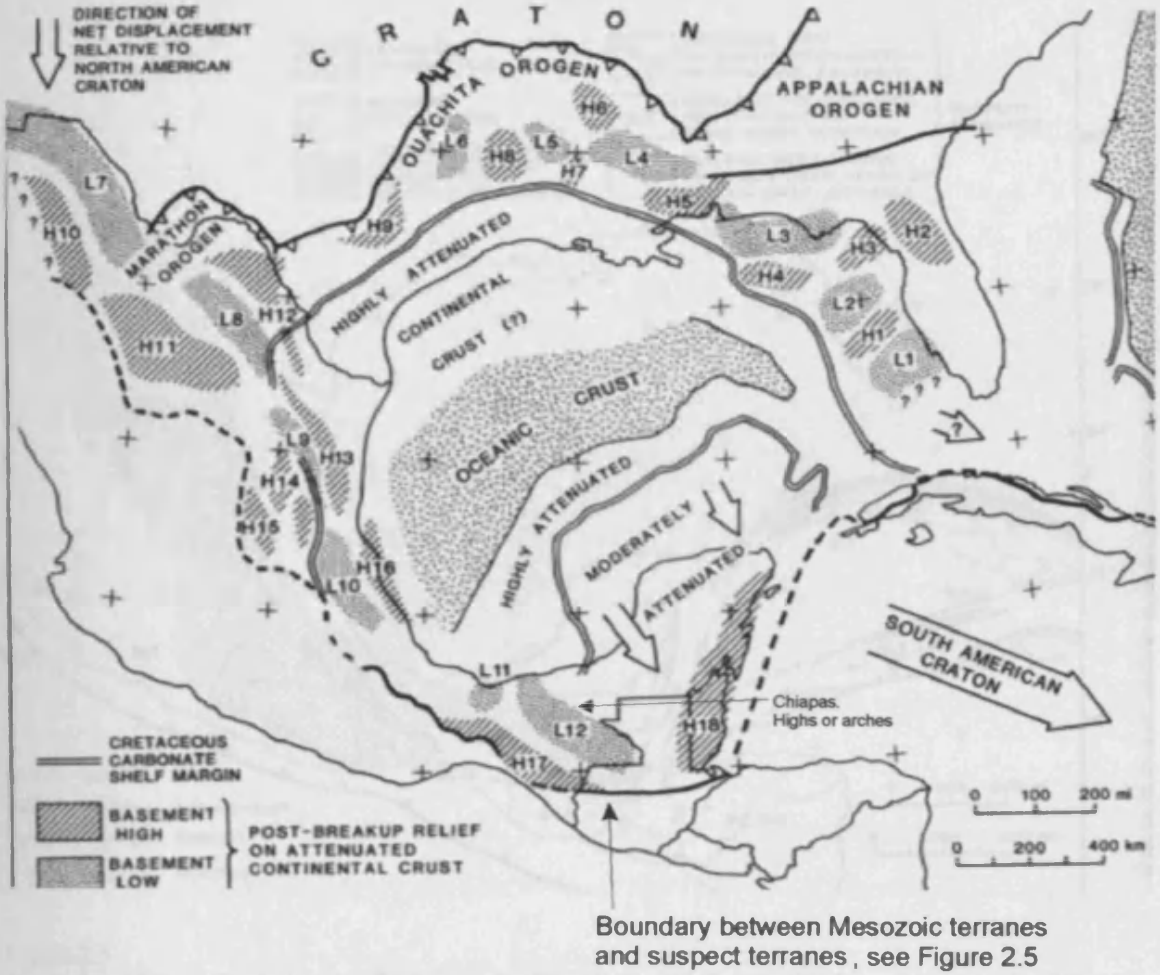

Figure 2.4
Gulf of Mexico tectonic elements for the Mesozoic circum-Gulf provinces related to the breakup of Pangea, and the opening of the Gulf of Mexico, illustrates the "Atlantic-Margin" tectonic terranes. Relict basement highs and lows are presented in shades and inferred from timing of transgression and onlap, differential thickness of pre-marine evaporites and Upper Jurassic sediments and present depth to basement. After Winker, 1988.

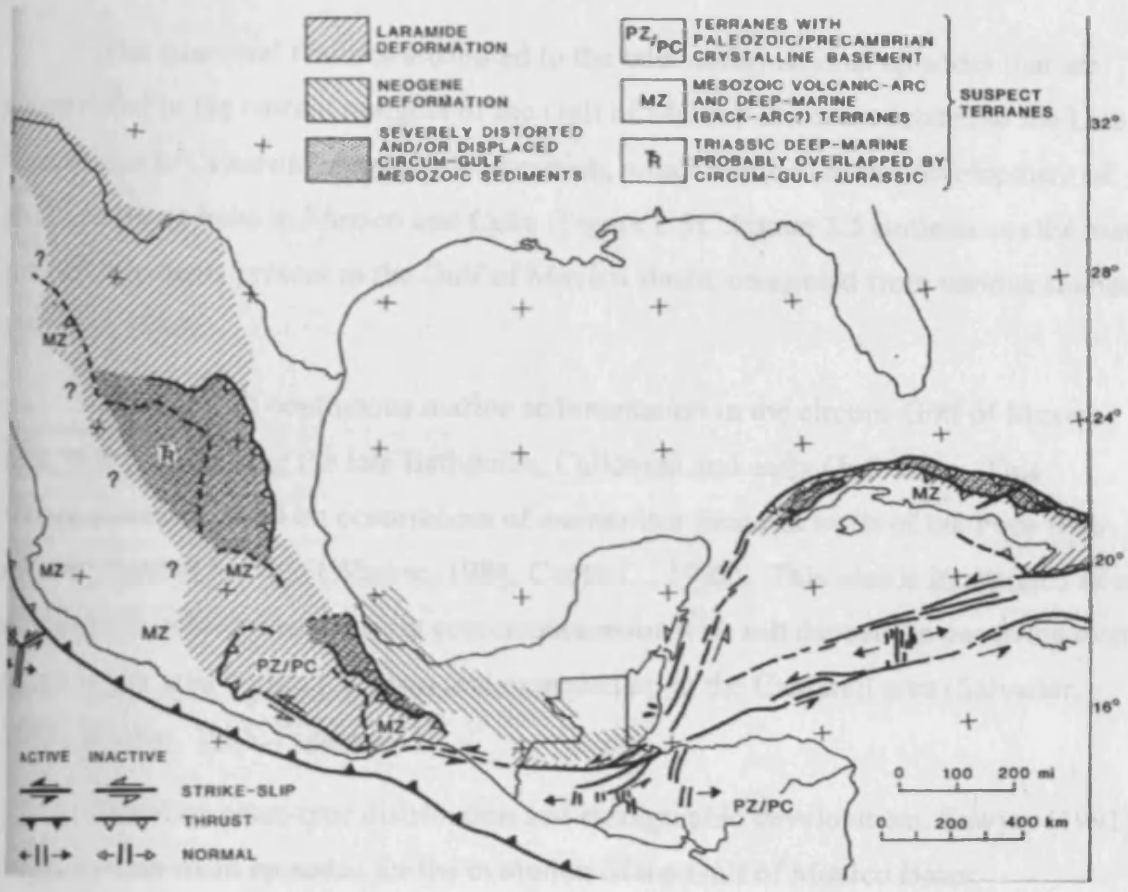

Figure 2.5
The Gulf of Mexico and vicinity illustrating the "Pacific-margin" tectonic element terranes (mainly convergent). After Winker, 1988.

of magnitude larger than typical horsts and grabens of the Basin-and-Range type (Winker, 1988).

"Pacific-margin" convergent elements

The structural features attributed to the later deformational episodes that are overprinted in the current margins of the Gulf of Mexico Basin are related to the Late Cretaceous to Cenozoic orogenic deformation, which resulted in the development of fold and thrust belts in Mexico and Cuba (Figure 2.5). Figure 2.5 summarises the main tectonic elements present in the Gulf of Mexico Basin, computed from various studies (Winker, 1988).

The onset of continuous marine sedimentation in the circum-Gulf of Mexico area took place during the late Bathonian, Callovian and early Oxfordian. This interpretation is based on occurrences of ammonites found in wells of the Poza Rica district, Central Mexico (Winker, 1988; Cantu-C., 1992). This area is interpreted as an embayment, which was possibly contemporaneous with salt deposition occurring over a much larger area within the basin that extended up to the Cantarell area (Salvador, 1987; Winker, 1988; Figure 2.1).

Based on crust-type distribution and stratigraphic development, Sawyer (1991) suggests four main episodes for the evolution of the Gulf of Mexico Basin:

(1) Late Triassic – Early Jurassic phase of early rifting;

(2) Middle Jurassic phase of rifting, crustal attenuation and formation of a broad area of transitional crust. During this time it is postulated that the Yucatan block began rotating out of the northern Gulf of Mexico basin in a northwest – southeast transtensional trend across Mexico and Florida (Pindell, 1985; Salvador, 1987; Winker, 1988; Buffler, 1991; Sawyer, 1991). There is general agreement on the concept that the Yucatan block has drifted southwards from the northern Gulf of Mexico, although the kinematic intepretations involved differ from author to author (Dewey, 1975; Pardo, 1975; Pindell, 1982). It is beyond the scope of this project to include these models. Therefore the concept that is agreed on is that the Yucatan block drifted southward during the Middle Jurassic and it reached its present position during the Early Cretaceous, as suggested by the presence of broad carbonate platforms with prominent rimmed margins (Pindell, 2000).

(3) Late Jurassic period of ocean crust formation in the deep central Gulf of Mexico. The area of oceanic crust became wider to the west as the Yucatan block continued to rotate in a counterclock direction, as suggested by Sawyer (1991).

(4) The Gulf of Mexico was certainly locked into its present configuration by Early Cretaceous time. Crustal subsidence rates were probably highest for oceanic crust, less for transitional and minimal for thick transitional or continental crust.

Although by the Early Cretaceous the Gulf of Mexico was locked into its present configuration, subsequent formation of the Caribbean region resulted in the deformation of the Sierra de Chiapas, and in turn modified the margin of the Gulf of Mexico in the southeast. Figures 2.6 A, B, C, D presents a series of tectonic evolutionary maps for the formation of the Gulf of Mexico and the Caribbean as suggested by Pindell (2000).

2.2.2 Basement distribution

In the study area of this thesis, the basement has not been encountered by any wells. The oldest rocks were encountered in the northern Yucatan Platform by wells that penetrated into Palaeozoic(?) metavolcanic rocks, quartzite and schists. Metamorphic rocks yielded radiometric dates of 420 to 410 Ma with an inferred metamorphic event at 330 and 290 +- Ma, as suggested by Dengo (1969) and Viniegra-Ososrio (1971), respectively.

In the study area, the basement is thought to be similar to those rocks found in wells Cobo 301, Quintana Roo-1, and Yucatan -1, and others found within the Yucatan Platform; and to the exposed rocks of the Chiapas and Mixtequita Massifs (Angeles-Aquino, 1994; Figure 2.7).

The crust of the Gulf of Mexico has been subdivided into four major types: oceanic, thin transitional, thick transitional and continental (Buffler, 1991). These divisions reflect the manner in which the crust was either generated or significantly modified during rifting of the Gulf of Mexico. The rationale behind these divisions is that continental crust appears around the periphery of the basin. The transitional crust is continental crust that was significantly extended and thinned, and probably in places intruded with magma during Middle and Late Jurassic rifting. The oceanic crust was formed under the deep Gulf of Mexico basin during the Late Jurassic (Buffler, 1985).

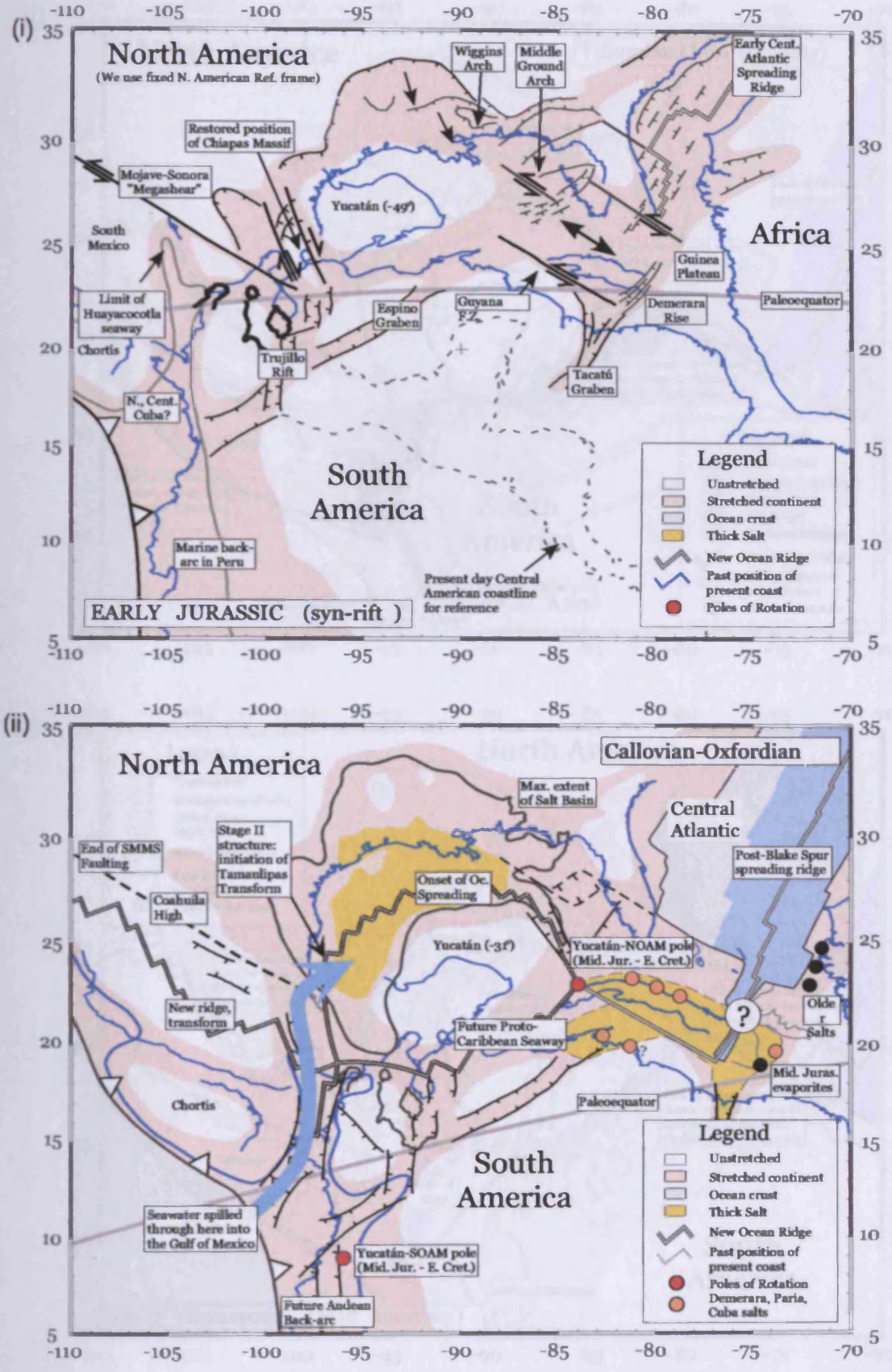

Figure 2.6 (A),
Tectonic evolutionary maps for the Gulf of Mexico and Caribbean sea representing (i) the Early Jurassic syn-rift episode and (ii) the Callovian-Oxfordian time. After Pindell, 2000.

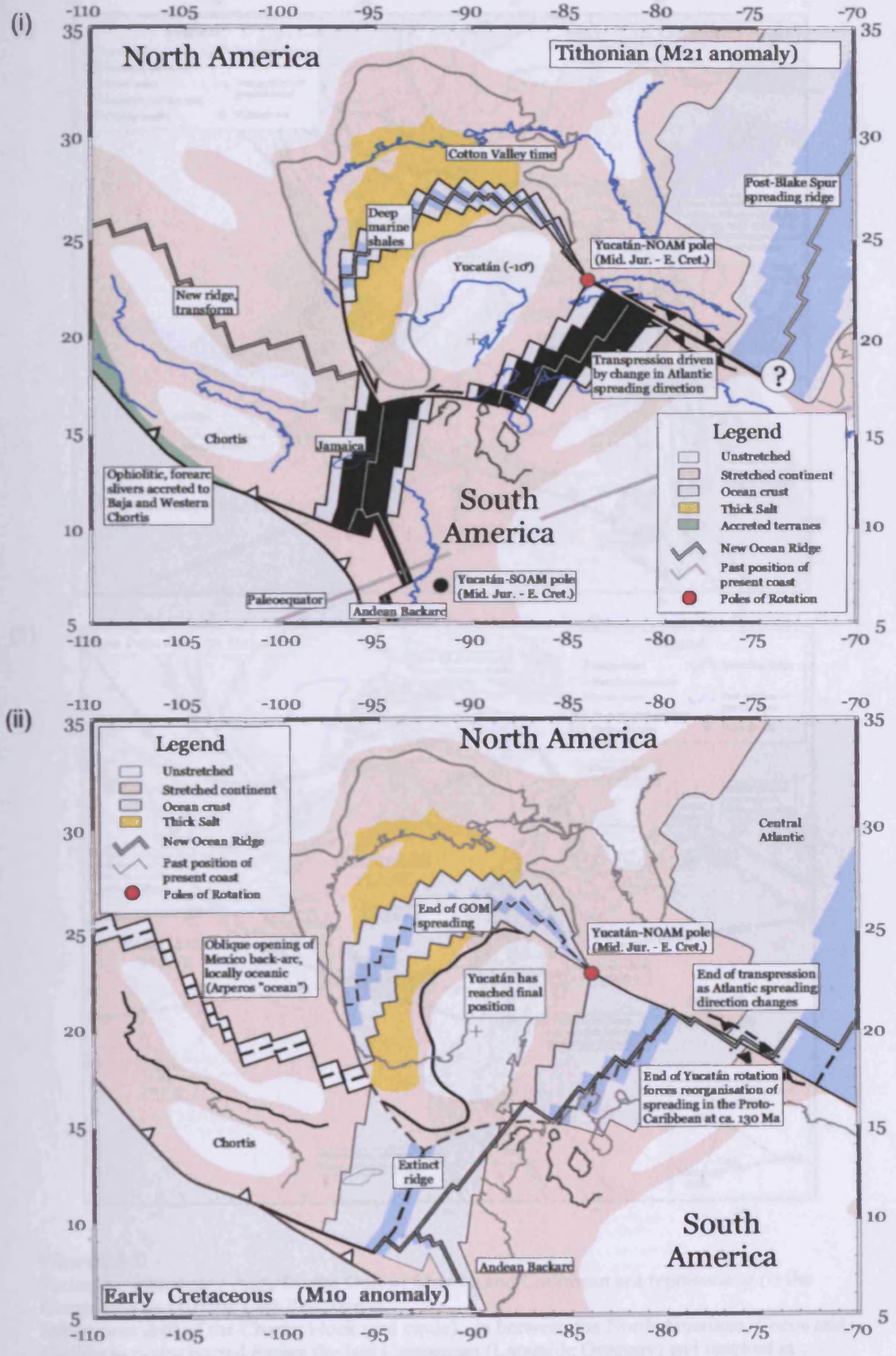

Figure 2.6 B
Tectonic evolutionary maps for the Gulf of Mexico and Caribbean sea representing (i) the Tithonian and (ii) Early Cretaceous time. Note the southward translation of the Yucatan block from Early Jurassic to Early Cretaceous (compare Figures 2.6A and 2.6B). After Pindell, 2000.

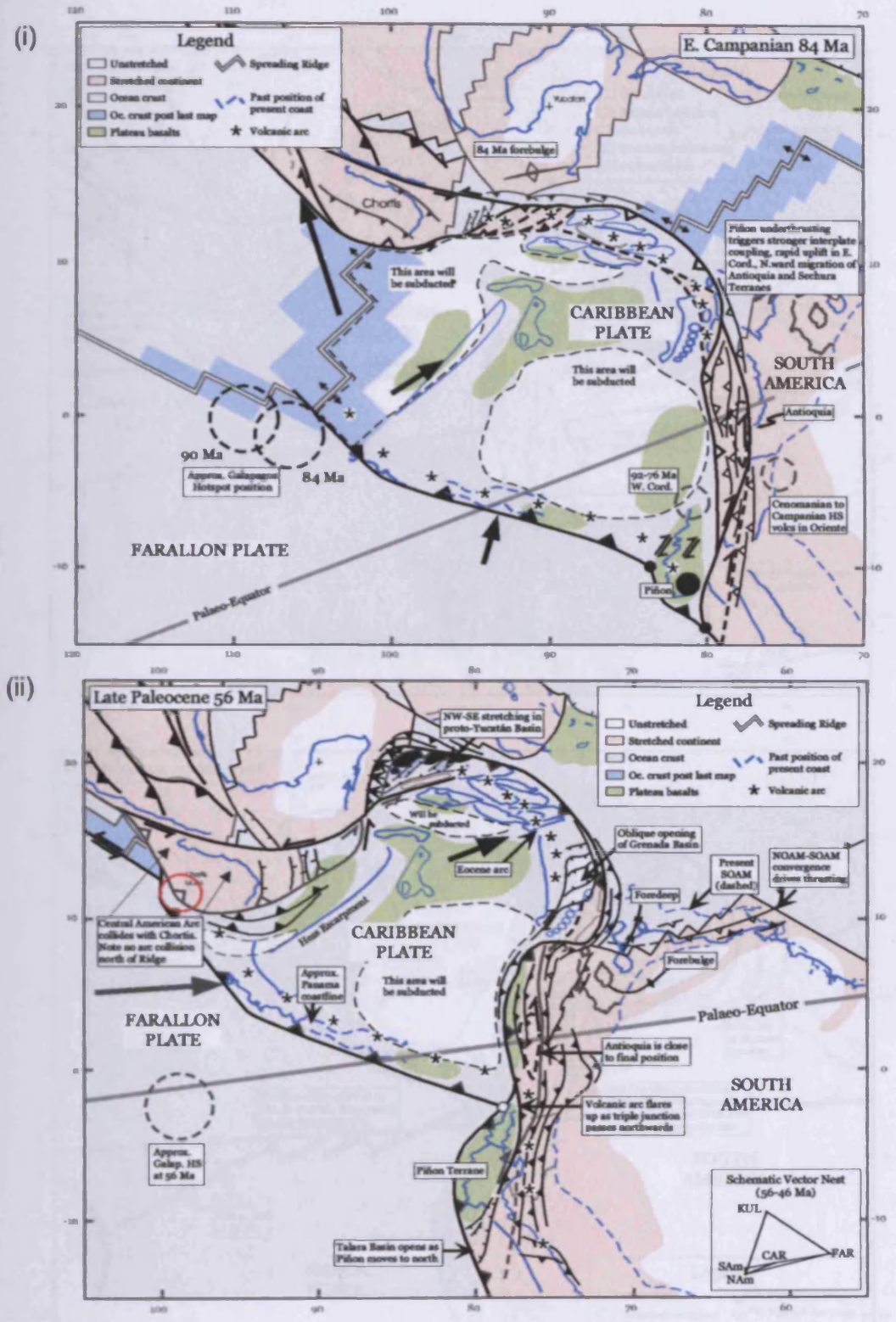

Figure 2.6 C
Tectonic evolutionary maps for the Gulf of Mexico and Caribbean sea representing (i) the Campanian and (ii) the Late Palaeocene.
Subsequent drift of the Chortis block (red circle), in between the North American, Cocos and Caribbean plates started during the late Campanian (Laramide Orogeny) and resulted in folding, faulting and uplifting of Cretaceous carbonates section which developed the complex thrust belt and large folds of the Sierra Madre Oriental (the southern region includes the Sierra de Chiapas). After Pindell, 2000.

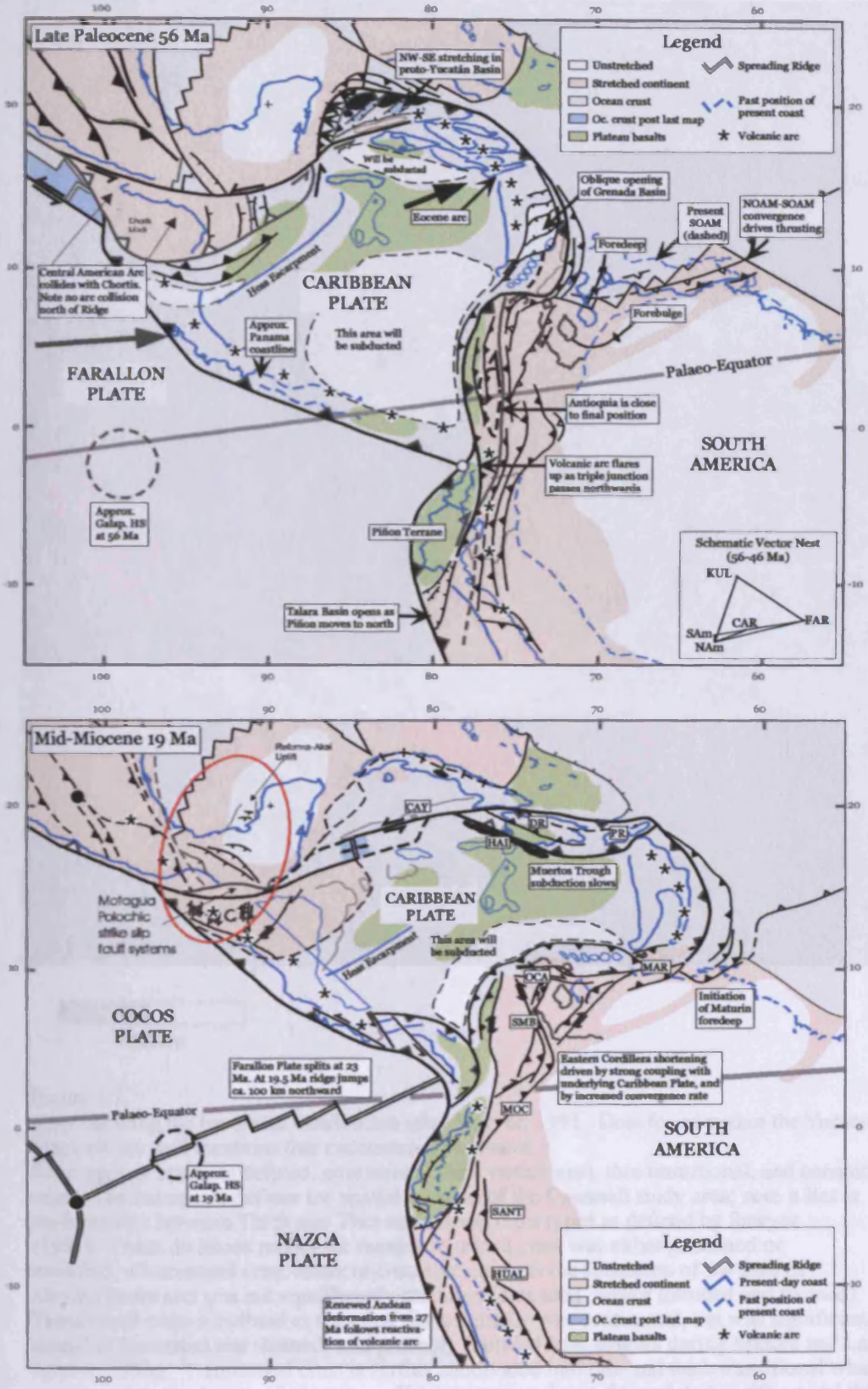

Figure 2.6 D
Tectonic evolutionary maps for the Gulf of Mexico and Caribbean sea representing (i) the Late Palaeocene, and (ii) the Mid-Miocene.
Note the eastward drift of the Chortis block (red circle) in between the North American, Cocos and Caribbean resulted in folding, faulting and uplift of Cretaceous carbonates section and developed the complex thrust belt and large folds of the Sierra Madre Oriental and along the Reforma-Akal Uplift. After Pindell, 2000.

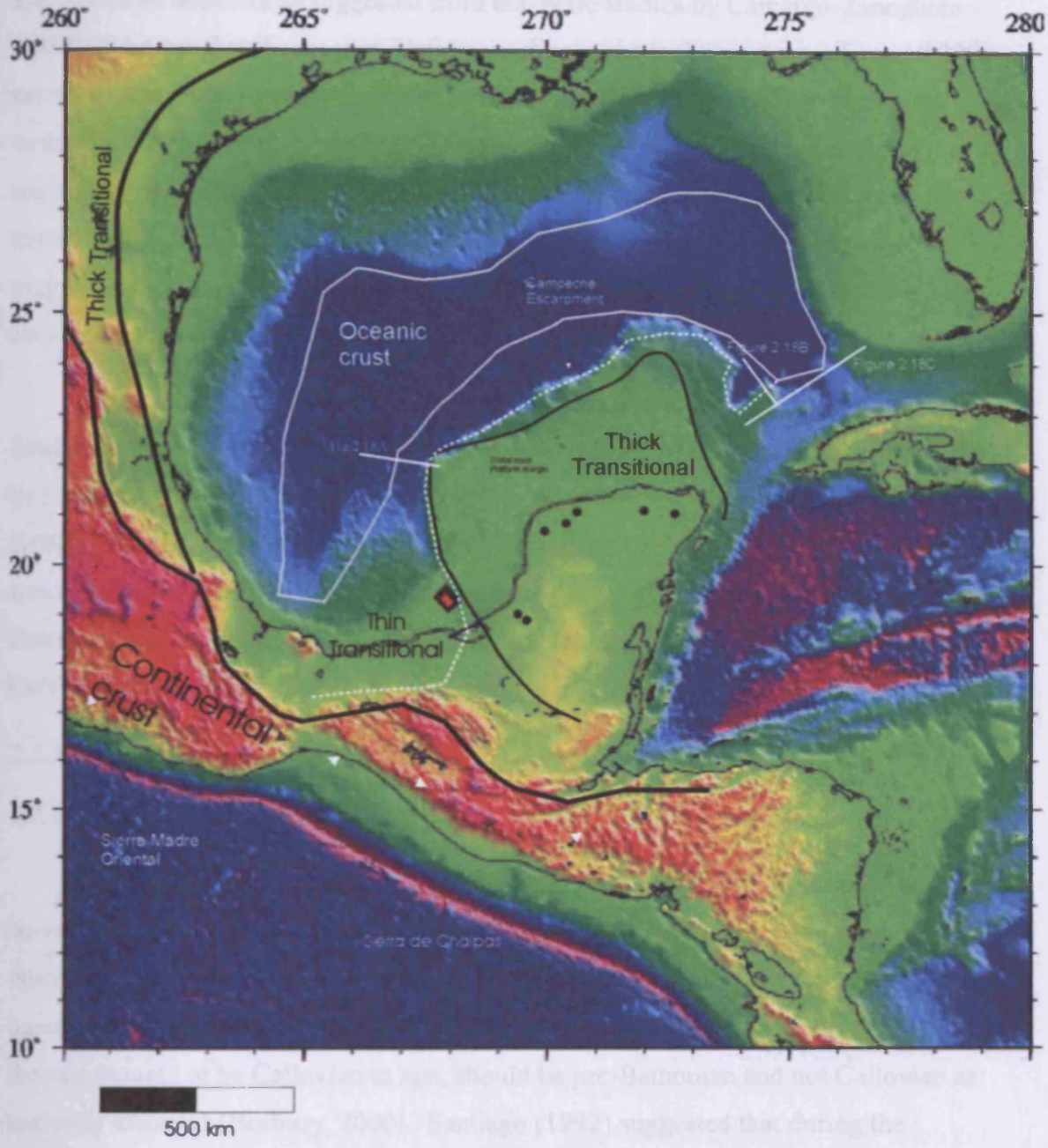

Figure 2.7
Map showing the basement distribution after Sawyer, 1991. Dots found within the Yucatan Platform are well locations that encountered basement.
Four types of crust are defined: continental, thick transitional, thin transitional, and oceanic crust. The red square defines the spatial location of the Cantarell study area; note it lies at the boundary between Thick and Thin transitional crust types as defined by Sawyer (1991). These divisions reflect the manner in which crust was either generated or modified. Continental crust refers to crust that predates the formation of the Gulf of Mexico Basin and was not significantly modified (extended and/or intruded and thinned). Transitional crust is defined as the crust that originally was continental, but was significantly modified (extended and thinned) and probably intruded with magma during Middle and Late Jurassic rifting. Transitional crust is further subdivided into thin and thick transitional which correspond to the degree of thinning. Thick transitional was thinned during rifting and thin transitional crust was dramatically thinned during rifting. Note the relationship between the location of the Cretaceous platform margin and are where the continental crust passes from thick to transitional.

The basement structure as suggested from magnetic studies by Camargo-Zanoguera (1980), indicates that the magnetic basement dips towards the southwest from 10,000 metres subsea at the western region of the Campeche Basin to 12,000 metres in the central part of the Basin. Sawyer (1991) proposed that the basement underlying the sedimentary sequence at the Campeche Basin consists of the boundary between transitional to thick crust towards the east and thin transitional crust basinwards. This suggestion is based on seismic observations, magnetic studies and well data that has encountered the basement.

In summary, it can be said that the study area is most likely underlain by the limit between "thin transitional" and "thick transitional" continental crust as suggested by Sawyer (1991), or within moderately attenuated crust as expressed by Winker (1988). The boundary between thin and thick continental crust corresponds to a major tectonic hinge zone in the basement. This boundary appears to be coincident with the distribution of the Early Cretaceous carbonate platform margin that rimmed the deep Gulf of Mexico during the Early Cretaceous (Figure 2.7).

2.2.3 Jurassic

2.2.3.1 Bathonian – Callovian

It is understood that the Gulf of Mexico is primarily a Late Jurassic basin, however dating of this event is imprecise. Cantu-C (1992) suggests that permanent open marine environments of the Gulf Coast were established by the Late Bathonian, based on the presence of *Wagnericeras*. Therefore the underlying evaporitic sequences, that are thought to be Callovian in age, should be pre-Bathonian and not Callovian as currently assumed (Horbury, 2000). Santiago (1992) suggested that during the Callovian and earliest Oxfordian, the advance of the sea became more predominant, thus giving rise to deposition of dolomites and anhydrites in the Chiapas-Tabasco Mesozoic basin. However, it is difficult to constrain the ages at this stratigraphic level due to the fact that most basins have no ammonite control. Ammonites first appeared in Kimmeridgian – Tithonian times (Perez-C., 1992), which makes precise correlation difficult (Salvador, 1987).

Angeles-Aquino (1994) and Salvador (1987) suggested that the oldest sedimentary succession found in the Campeche Basin consists of salt deposits identified as the Isthmian Salt, which are expected to be contemporaneous to the

Louann Salt of the northern Gulf of Mexico (Salvador, 1987). In the Campeche Basin, Angeles-Aquino (1994) proposed that the salt deposits cover the entire area as revealed by well and seismic data. The salt deposits vary in thickness from approximately 3,000 metres in the southwest to 160 metres in the northeast of the Campeche Basin, near the Cantarell area. Based on the distribution of salt among the Campeche Basin (Peterson, 1983) the Cantarell system should be underlain by a thick succession of salt, which thickens considerably underneath the Cantarell area wedging out against the Yucatan Platform (Figure 2.1).

García-Hernández (2000), reports from well Lum-1 at a depth of 5151 measure depth (MD), seven metres of a white translucent salt with anhydrite inclusions underlying Kimmeridgian deposits. It is suggested that the salt is distributed throughout the Campeche Basin in an irregular manner. This irregular distribution is attributed to variations in the original depositional configuration, the plastic nature of salt, and the tectonics that have affected the area after its deposition. Three stratigraphic and structural relationships have been identified for the salt deposits; concordant, abnormal injected through fault planes, and discordant as intrusive bodies (Figures 2.8 and 2.9).

There is general agreement that within the Campeche Basin evaporites were laid down during the Callovian (Salvador, 1987; Cantu-C., 1992; Gonzalez-G., 1994; Angeles –Aquino, 1994; Garcia-Hernandez, 2000). However, Cantu-C (1992) based on stratigraphic and sedimentary evidence, interprets that the evaporitic successions are Late Bathonian. It is beyond the scope of this study to explain the occurrence and timing of this evaporitic succession. In this work the evaporitic sequences will be considered as most probably Callovian in age. The areal distribution of the evaporites in the Campeche Basin and the role that they have played in the deformation structures is of great importance and still controversial. This will become clearer when further seismic and well data become available and by compiling and integrating current studies into a holistic basin study for the Campeche Basin.

2.2.3.2 Oxfordian

The sedimentary section for the Oxfordian stratigraphic succession throughout the Campeche Basin consists of sandstones, anhydrites, shales, limestones, including oolitic limestones which are referred to by Angeles-Aquino (1994) as the Ek-Balam

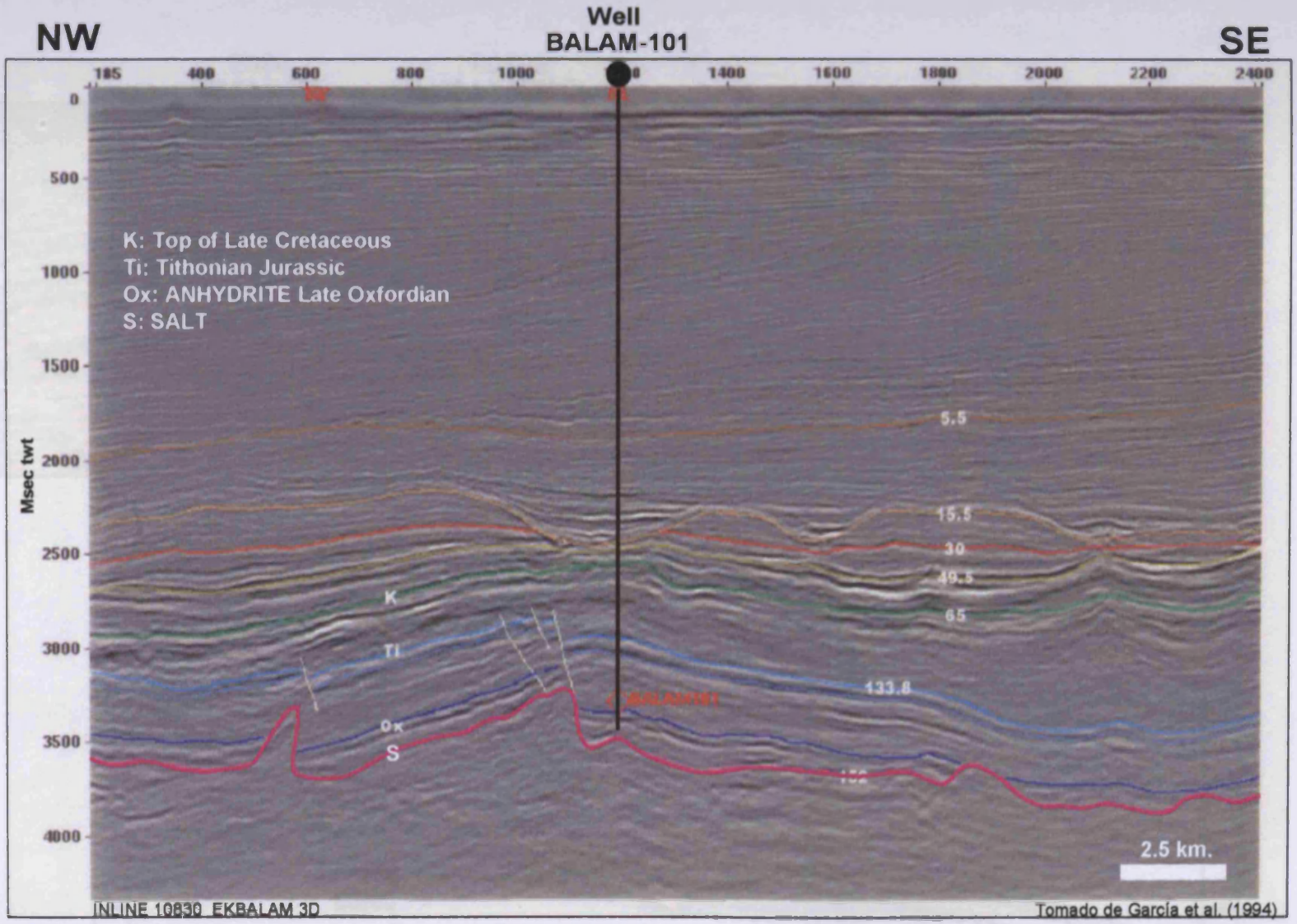

Figure 2.8

Seismic line through the Ek-Balam Field; note the top salt distribution as interpreted from the seismic appearance and the salt intrusions encountered in other wells of the field (Ek-63 and Ek-45), after Tomado de Garcia (1994) *in* García-Hernández, 2000.

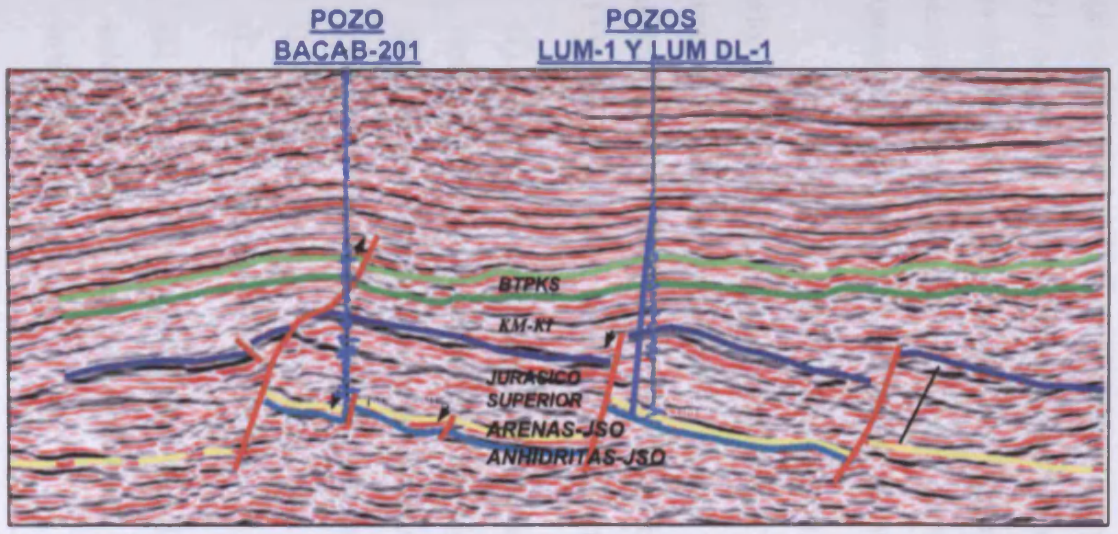

Figure 2.9
Seismic section and interpreted section from Bacab to Lum. Note the half graben topography of the Mesozoic successions. Salt underlies the Jurassic successions.
In well Lum-1 the salt appeared to conformably underlie the Jurassic Oxfordian sands. In well Bacab 201 the salt was encountered in the fault plane.
After Soriano, 1999 *in* Garcia-Hernandez, 2000.

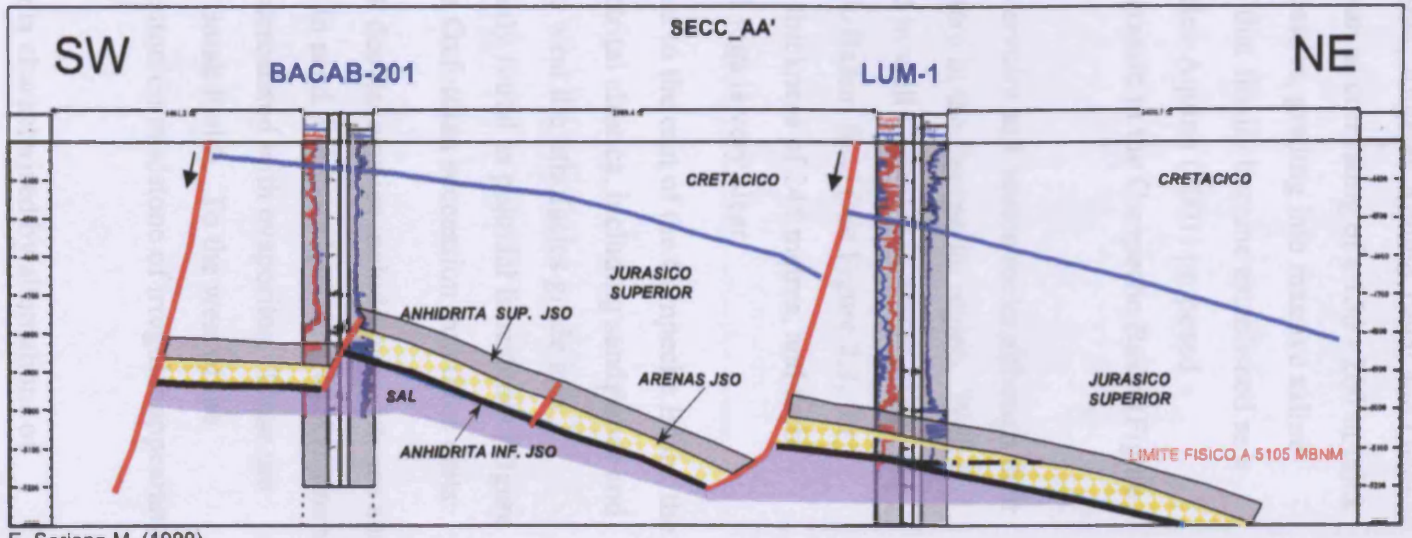

E. Soriano M. (1999)

Group. The top Oxfordian was established with the appearance of *Caucasella oxfordiana* (García-Hernández, 2000).

Previous authors (e.g. Gonzalez-G., 1994; Angeles-Aquino 1994; and Ortuno-Maldonado, 1999) described the base Oxfordian as consisting of a 150 - 200 m thick succession of aeolian and other redbed siliciclastics, grading into massive saline anhydrites, deposited within a restricted shelf that finally became established as a carbonate ramp with little clastic input. Angeles-Aquino (2001) proposed a stratigraphic division scheme for the Upper Jurassic in the Campeche Basin (Figure 2.10).

The Oxfordian rocks are important reservoirs and source rocks although their total thickness has not been penetrated anywhere in the Campeche region. Well C-2239 penetrated a gross thickness is 57 m and in well Caan-1 it is 440 m. The best development of this interval is found in the Ek-Balam field (see Figure 2.3, for location), where the sand bodies reach a total thickness of 245 metres, and their expression in the gamma-ray and density well logs is very clear.

Angeles-Aquino (2001) recognized that to the east of the Campeche Basin, the Oxfordian consists of a thick succession of detrital clastics, including sandstones and laminated bentonitic mudstones. Towards the west the lithofacies grade into carbonates with marine influence and are mainly found as peloidal limestones (Figure 2.11). Angeles-Aquino (2001) subdivides the Oxfordian succession into three units:

(1) A lower unit consisting of thin to thick detrital clastics including sandstones and laminated bentonitic mudstones; and clay to sand dominated peloidal wackestone to packstone, with quartz cements that are intercalated with evaporites. These are mainly encountered in the Ek-Balam and Batab Fields. To the west of the Campeche Basin this unit grades into a bentonitic mudstone of irregular appearance (Cantarell, Chac and Caan Fields).

(2) The middle member of the Oxfordian is characterised by alternations of calcareous sandstones, mudstones, and bentonitic shales. Salt intrusions are found in the Ek-Balam field.

(3) The upper member is characterised by sandy limestone that grades into calcareous sandstones with anhydrite. The top of the Oxfordian is marked by

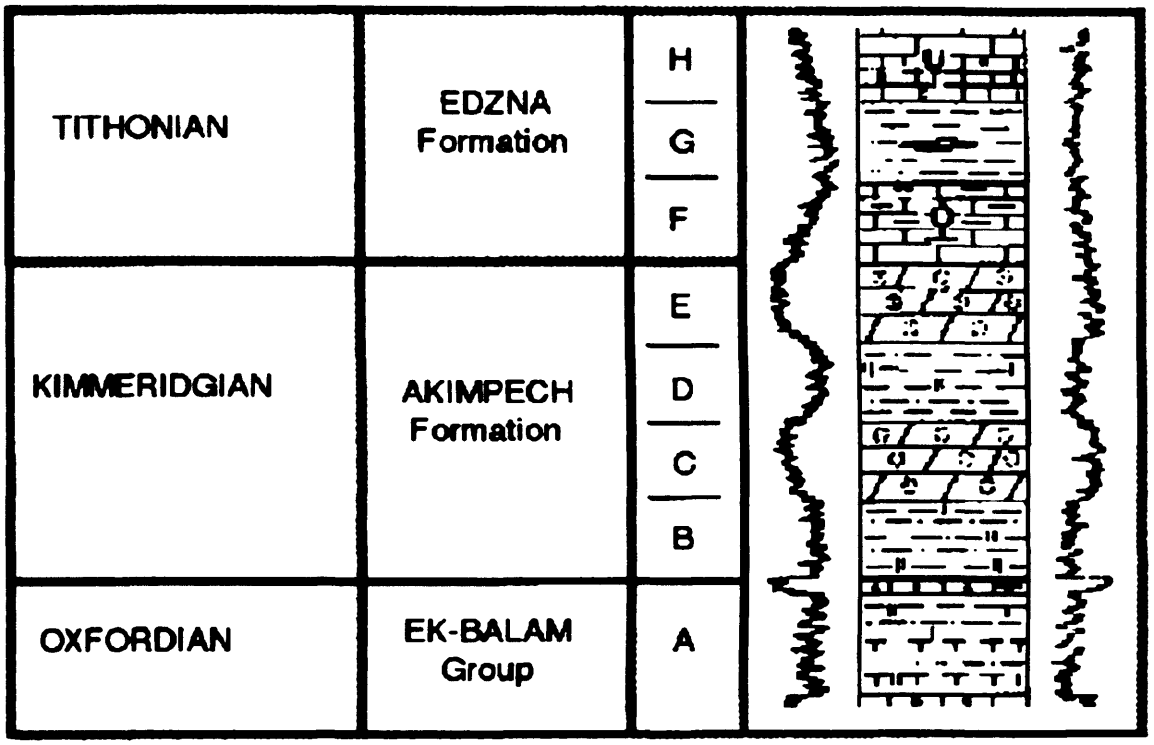

Figure 2.10
Stratigraphic division for the Upper Jurassic of the Campeche Basin, divided in eight different units: (A) sands, mudstone, and claystone; (B) terrigenous mudstone and claystone; (C) dolomitized limestone; (D) muds and algal sales; (E) oolitic dolomitized limestones; (F) clayey limestones with radiolarians; (G) calcareous shales with saccocoma; and (H) clayey limestones with presence of tintinides. After Angeles-Aquino, 2001

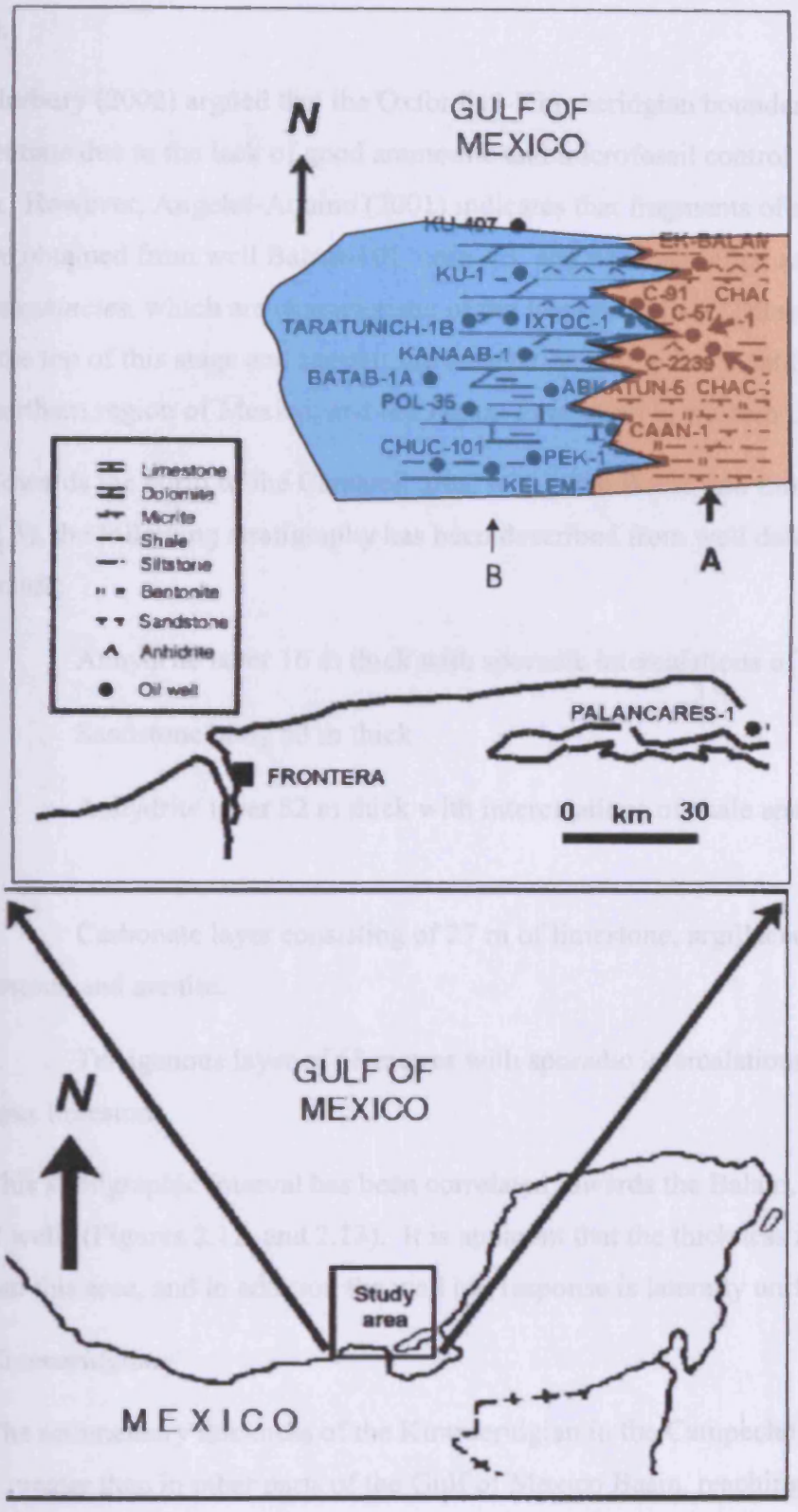

Figure 2.11
Areal distribution for the Oxfordian Jurassic terrigenous lithofacies with continental influence (A), The lithofacies grade into carbonates with a marine influence towards the west (B). After Angeles-Aquino, 2001.

anhydrite layers that range from 5 to 200 m thick (Chac-1 well, 4540 m; Bacab-21 well).

Horbury (2002) argued that the Oxfordian-Kimmeridgian boundary is difficult to differentiate due to the lack of good ammonite and microfossil control throughout the basin. However, Angeles-Aquino (2001) indicates that fragments of ammonites have been obtained from well Balam-101, core – 3, and were classified as *Ochetoceras* and *Discosphinctes,* which are characteristic of the late Oxfordian. These ammonites indicate the top of this stage and support the correlation with other localities in the central-northern region of Mexico, and the Jaguar Formation in western Cuba.

Towards the north of the Cantarell area, within the Bacab and Lum Fields, (Figure 2.3), the following stratigraphy has been described from well data from the base upwards:

- Anhydrite layer 16 m thick with sporadic intercalations of arenite.
- Sandstone body 53 m thick
- Anhydrite layer 82 m thick with intercalations of shale and calcareous shale.
- Carbonate layer consisting of 27 m of limestone, argillaceous limestone, with limestone and arenite.
- Terrigenous layer of 68 metres with sporadic intercalations of argillaceous limestone.

This stratigraphic interval has been correlated towards the Balam, Sam and Chacmol wells (Figures 2.12, and 2.13). It is apparent that the thickness is uniform throughout this area, and in addition the well log response is laterally uniform.

2.2.3.3 Kimmeridgian

The sedimentary thickness of the Kimmeridgian in the Campeche Basin is typically greater than in other parts of the Gulf of Mexico Basin, reaching 500-600 metres of section (Horbury, 2002). Angeles-Aquino (2001) designated the Kimmeridgian as the Akimpech Formation, consisting of carbonates and terrigenous rocks characterised by oolitic and partially dolomitized limestones, shales and

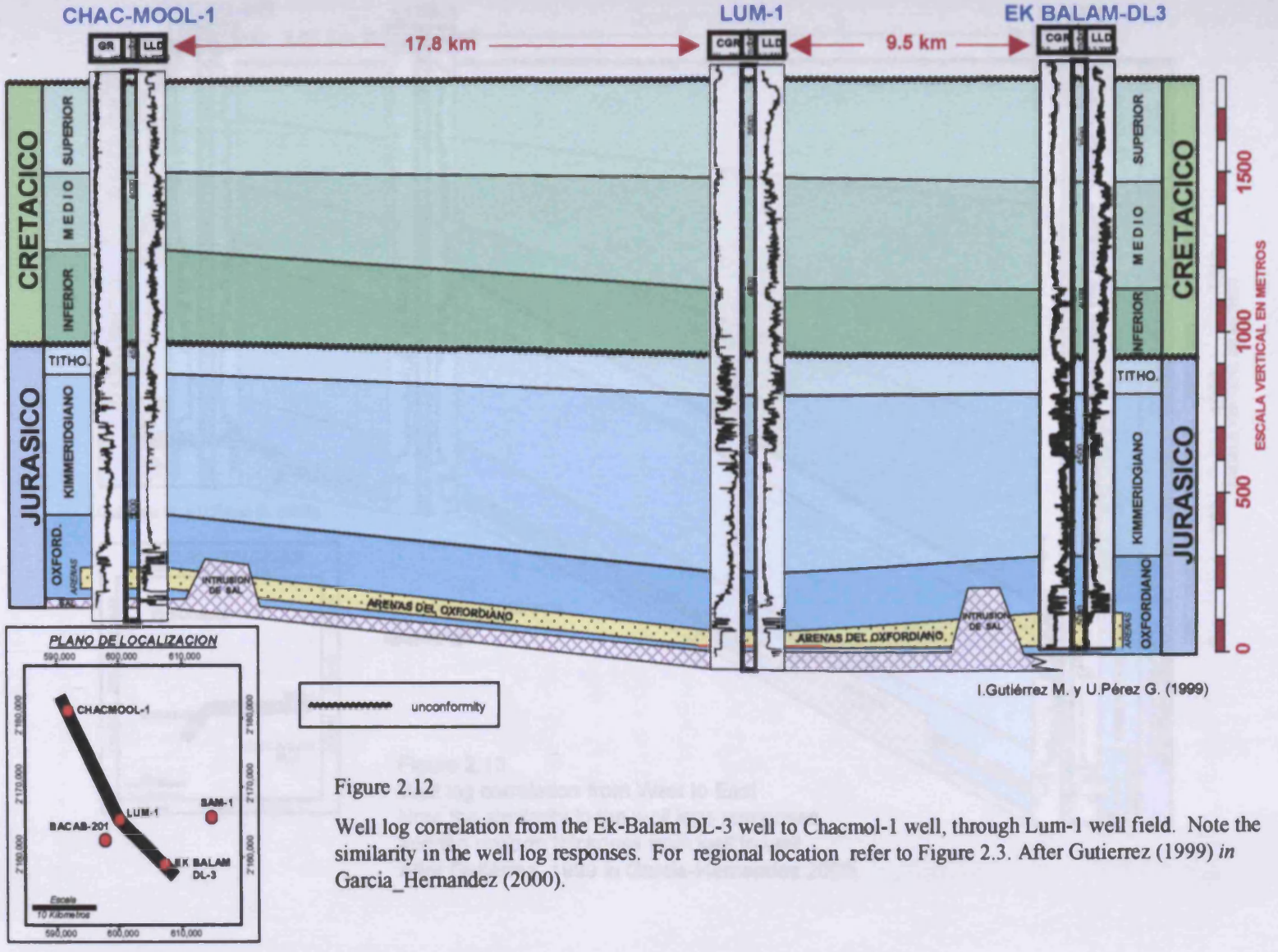

Figure 2.12

Well log correlation from the Ek-Balam DL-3 well to Chacmol-1 well, through Lum-1 well field. Note the similarity in the well log responses. For regional location refer to Figure 2.3. After Gutierrez (1999) *in* Garcia_Hernandez (2000).

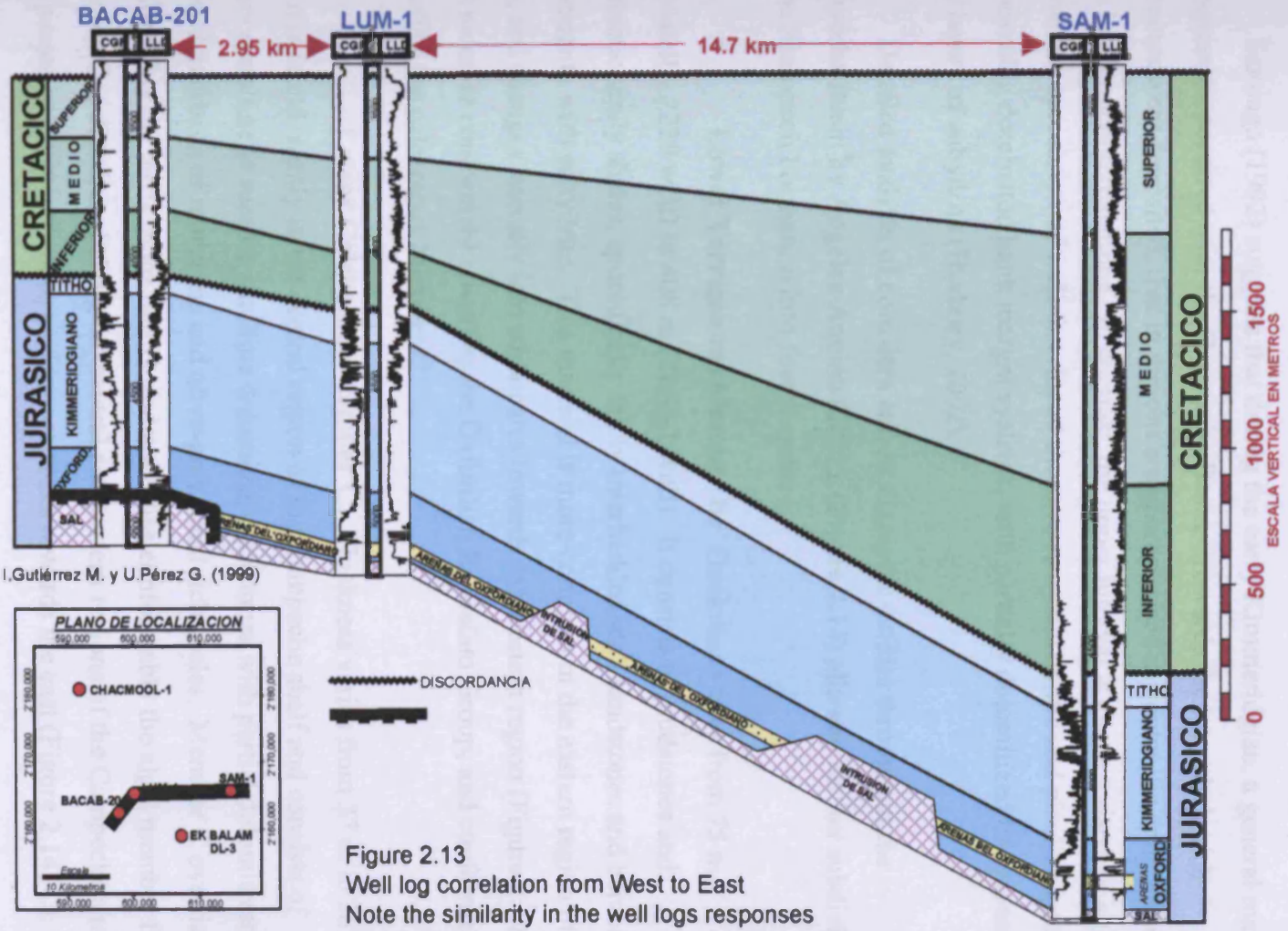

Figure 2.13
Well log correlation from West to East
Note the similarity in the well logs responses
and the uniform thickness from well to well.
After Gutiérrez, 1999 *in* Garcia-Hernandez 2000.

bentonitic mudstones. The *Akimpech Formation* is the most important reservoir rock of the Upper Jurassic of the Campeche Basin.

Santiago (1992) suggests that during the early Kimmeridgian, a general marine transgression occurred over the Campeche Basin. Towards the base shale rich sediments were deposited, that in regions are characterised as bentonitic and sand-rich, with limestone intercalations. In contrast, the upper interval is characterised by an alternating succession of well-developed massive to cyclic oolitic and pisolitic units representing dominated bank margin systems, with partially dolomitized limestones with layers of anhydrite (Horbury, 2002).

Detailed analysis of core data and stratigraphic studies throughout the Campeche Basin by Angeles-Aquino (2001), (Figure 2.14) allowed further subdivision of the Akimpech Formation into four members:

- **Lower Terrigenous Member B:** Thickness varies from 75 m (Cantarell – 2239 well) to 408 m (Zinic-1 well). It consists of mudstones and bentonitic sandy shales, sporadically thinly interbedded with sandstones and bentonitic dolomicrite with anhydrite. This material is more common in the eastern region of the area, and changes laterally into carbonates towards the western region (Figure 2.14, B). This member conformably overlies the Oxfordian Ek-Balam Group, and conformably underlies the calcareous Member C.

- **Lower Calcareous Member C:** Thickness varies from 37 m to 267 m and it is found mainly in the central region of the Campeche shelf and consists of microcrystalline to mesocrystallline dolomites, packstones with partial dolomitization, isolated interbeds of mudstone and olive-grey, sand rich shales. Member C overlies conformably the terrigenous unit B, and underlies conformably the algal member D. Member C is distributed along the central and eastern regions of the Campeche shelf that passes laterally into more terrigenous rocks towards the east (Figure 2.14, C).

- **Terrigenous Member D:** It consists of claystone, mudstone, and shale interbedded with carbonates and abundant algal material, found at well Kokay-1. Reddish mudstones are interbedded with marine siliciclastic rocks. This unit thins and disappears towards the west (Figure2.14, D).

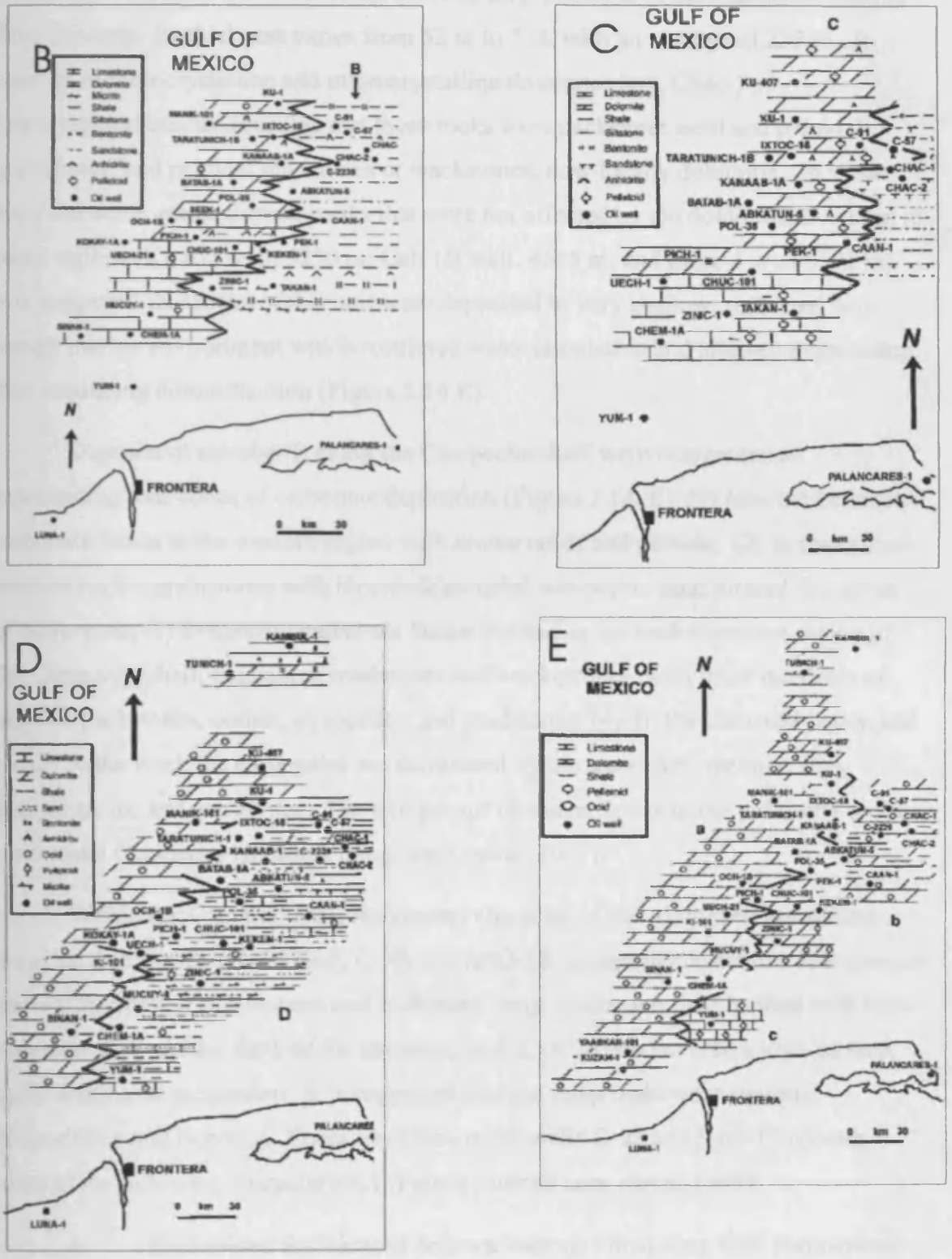

Figure 2.14
Maps representing the areal distribution for the Kimmeridgian lithofacies. Four units were defined: (B) consists of a lower terrigenous member towards the west that grades into carbonates towards the west; (C) carbonate member that appears to be prograding eastwards, note the extent of the terrigenous facies decreased; (D) Terrigenous member with abundant carbonates and algal material. The terrigenous material is suggested to be marine in origin; (E) meso to micorcrystallne dolomites. After Angeles-Aquino, 2001.

Calcareous Member E: Most of the Jurassic oil production of the Campeche shelf is from this unit. Its thickness varies from 52 m to 373, with an average of 225 m. It consists of mesocrystalline and microcrystalline dolomites (e.g. Chac-1). Petrographical studies revealed that these rocks were packstone, ooid and peloidal grainstones, and peloidal mudstones or wackstones, now locally dolomitic. In some areas the ooids grains formed banks that were not affected by the dolomitization seen in other regions (Ki-102 well, 5250 m; Och 1B well, 4585 m; and Zinic-1 well 5592 m). It is suggested that rocks of this unit were deposited in very shallow, restricted high energy marine environment which restricted water circulation and allowed evaporation, thus enhancing dolomitization (Figure 2.14 E).

Deposits of member E along the Campeche shelf were recognized as representing four zones of carbonate deposition (Figure 2.14, E): (1) Micritic bentonitic carbonate facies in the western region with scarce ooids and peloids; (2) In the central-western region grainstones with bioclastic material and oolitic sand formed in a series of oolite bars; (3) Evaporitic carbonate facies situated in the central-eastern region of the Campeche shelf, containing mudstones and wackestones, with some interbeds of peloidal packstones, oolites, evaporties, and mudstones; (4) In the Cantarell region and locally to the west, the carbonates are dominated by terrigenous mudstones, fine-grained sands, and anhydrites. The terrigenous character is due to the proximity to the continental Campeche landmass (Angeles-Aquino, 2001).

Within the Cantarell area, the general character of the Akimpech Formation, based on data from wells C-3068, C-98, and Sihil-19, is seen to consist of a low gamma interval interpreted as a dolomitized carbonate ramp succession, interbedded with high gamma shales. At the flank of the structure, well C-3026 encountered a high gamma, shale-dominated succession. It is suggested that the ramp underwent repeated progradation and flooding. Cores from the crestal wells C-98 and Sihil-19 contain some of the following characteristics (Pemex internal core report, 1999):

- Bioturbated argillaceous dolowackestone / mudstone with periplatform bioclastic carbonate sand and mud deposited in a very low energy, well-oxygenated environment below normal wave base. This facies is associated with gamma peaks interpreted as flooding events.

- Core 4 in well C-98 taken from a high gamma interval contains pebble to cobble-sized intraformational dolowackestone clastss in an argillaceous, bioclastic dolowackestone matrix. This has been redeposited at the base of a slope or in a distally steepened carbonate ramp setting.

- Dolomitized bioturbated bioclastic wackstone deposited in a low energy subtidal setting.

- A shale dominated succession, revealed by well C-3026 which is different to the successions seen in crestal wells suggest a deeper ramp succession at the C-3026 well location

In summary, the Kimmeridgian interval is interpreted to consist of a carbonate ramp succession that underwent progressive and cyclic progradation and flooding. The ramp, overall, deepened towards the west - north-west (Pemex Internal report, 2001). The end of the Kimmeridgian is marked by a gradual upward-deepening flooding event (Ortuno-Maldonado, 1999).

2.2.3.4 Tithonian

In general the Early Tithonian sediments are characterised by deeper water facies than the underlying Kimmeridgian rocks (Cantu-C., 1992; Ortuno-Maldonado, 1999; Angeles-Aquino, 2001). Santiago (1992) suggests that the Tithonian marks a period of maximum inundation, where deposits consist mainly of shaly limestones with inclusions of black shale. During the Middle Tithonian, on a regional scale, a period of sea-level highstand is interpreted by Salvador (1987) and Wilson (1990). Ortuno-Maldonado, (1999) associates this event in the Campeche Basin with deposition of organic rich-mudstones. Late Tithonian sediments are interpreted to consist of shallower origin than the Middle Tithonian (Ortuno-Maldonado, 1999).

Angeles-Aquino (2001) coined the term Edzna Formation for the Tithonian rocks found in the Campeche Basin. These are equivalent to the Pimienta Formation of eastern Mexico (Magoon, 2001). The Pimienta Formation contains more terrigenous rocks that the Edzna Formation that has considerably more carbonate rocks.

The Edzna Formation is further subdivided into three members: F, G, and H from bottom to top (Figure 2.15):

- Member (F) consists of a clayey mudstone, light grey to dark brown in colour, with abundant organic material deposited irregularly over Kimmeridgian rocks, where carbonate sedimentation predominates. Well information suggests that a general trend exists such that the carbonates gradually become more dolomitized toward the east (Figure 2.15, F).

- The (G) Member is more uniformly and widely distributed (Figure 2.15, G), consisting of calcareous sandy shales of grey to black colour, mixed together with dark-coloured clayey limestone. It is suggested that this Member is the main source rock in the Campeche Shelf, and is easily recognised on gamma logs due to its high shale content.

Geochemical and biological marker analyses performed by (Guzman-Vega M. A., 1999), suggest that Tithonian rocks are important source rocks for the oil produced in the Campeche Basin in reservoirs ranging in age from the Kimmeridgian to the Pliocene. The environments associated to the Tithonian source rocks based on geochemical analysis consist of: (1) an anoxic marine-carbonate environment of confined basin geometry, (2) an anoxic marine-carbonate regime associated to a shallow, gentle broad marine-carbonate ramp and (3) a clay-rich suboxic-anoxic environment proximal to a carbonate platform.

- Member H is the most widely distributed of the three members that constitute the Tithonian (Figure 2.15, H). It consists of a clayey and bentonitic lime mudstone, with a chalky appearance that becomes dolomitized towards the east. The top H member lies conformably over the (G) member and transitionally with the Cretaceous units.

Horbury (2000) indicated that within the Cantarell region, the Tithonian gamma ray log response is characterised by high API marly limestones that show aggradation into the Early Cretaceous as expressed by decreasing API of the gamma ray log.

The model that Pemex embraces suggests that a carbonate ramp established during the Kimmeridgian and drowned during the Tithonian. The onset of this

Figure 2.15
Maps representing the lithofacies distribution for members F, G and H for the Tithonian, refer to stratigraphic column Figure 2.11 from Angeles-Aquino (2001). (F) area "b" consists of clayey limestones, towards the east it becomes terrigenous with continental influence due to the proximity to the Campeche shelf; Member (G) lithofaceis tend to be carbonate towards the east and is considered as the principal source rock for hydrocarbons in the Campeche shelf; Member (H) consists of a calcareous-clayey (a) and clayey dolomite (b) in the Campeche shelf.

transgression has been interpreted at the Kimmeridgian/Tithonian pick with the occurrence of shale deposits.

To the north of the Cantarell area, within the locality of Bacab and Lum fields the Tithonian has an average thickness of 130 metres. The upper contact with the Early Cretaceous has been interpreted as discordant based on the following observations:

1. There is an abrupt change in lithology form the Tithonian into the Cretaceous, this abrupt change is observed in the well log response in wells: Lum-1, Chacmol-1, Bacab-201, and Ek-Balam-DL3.

2. The Tithonian is almost absent in well Lum-DL1 and there is a thickness difference among the mentioned wells.

3. The index fauna identified at the apparent top Tithonian in well Lum-1 consisted of *Saccocoma,* whose biozone belongs to the Late Tithonian but not the culmination of it. The end of the Tithonian is conformed and marked by the index fauna *Crassicolaria sp. and Calpionella alpine.*

4. The only well that appears to contain the entire Tithonian sequence is Sam-1, suggested from the gradual lithological change into the Cretaceous and also observed from well logs. Also the index fauna earlier mentioned that marks the culmination of the Tithonian has been encountered in core 2 of well Sam-1.

It has been interpreted that the discordance here described corresponds to an erosional hiatus. However it is important to mention that at the end of the Jurassic a half graben topography existed (Figure 2.9) in which erosion and non-deposition was a probably localised process along crests of fault blocks (García-Hernández, 2000).

2.2.4 Cretaceous

During the Cretaceous it has been suggested that the Yucatan block had reached its current position (Pindell, 1985); crustal cooling and flexural subsidence occurred (Buffler, 1985 and 1991), allowing the seeding of carbonate and evaporite deposition along the Yucatan Platform for the first time (Viniegra-Osorio, 1981).

The Campeche Basin along the shelf margin was a site of deep water (>200 m) carbonate sedimentation (see Section 2.3). The palaeomorphology of the shelf margin during the Cretaceous as suggested by Winker (1988), consisted of a high relief

platform margin continuously aggrading up to the Middle Cretaceous, represented by a maximum flooding surface which corresponds to a shale unit of Aptian age referred to as the Otates Formation. In Mexico, the Middle Cretaceous includes beds of Albian and Cenomanian age (McFarlan, 1991). Viniegra-Osorio (1981) and Winker (1988) suggested that the lowering in sea level, together with the pre-existing high relief carbonate platform margin provided the key elements for carbonate slope sedimentation in the Campeche Basin.

The Upper or Late Cretaceous (Turonian-Maastrichtian) is of great economic interest and it also contains many unanswered questions about its genesis and the subsequent diagenetic processes. It is in this interval where breccia type facies occur, their mode and genesis has been a topic of great controversy. Three models have been proposed (Viniegra-Osorio 1981; Grajales 2000; Horbury 2000). In this chapter only a description of the regional stratigraphic development will be presented. A discussion and analysis of the current proposed models for the Upper Cretaceous will be presented in Chapter 3.

For purposes of detailed lithological and depositional description, the Cretaceous has been subdivided into three: Early Cretaceous, Mid Cretaceous and Late Cretaceous (Figure 2.16). This division follows to a degree the major sequence boundaries recognised by different authors in previous studies (Viniegra-Osorio, 1981; Winker, 1988; Horbury, 2000 and 2002; Pacheco-Gutierrez, 2002). For the study area, the divisions above presented are difficult to identify. This is attributed mainly to the fact that the Cretaceous has been strongly dolomitized through different diagenetic processes, which makes the stratigraphic division problematic. In places, fossils are difficult to identify or are completely absent making the stratigraphic subdivision subjective and heavily based on the well log response. The three fold division adopted is pertinent in that the Late Cretaceous represents a fundamental change in the depositional environment.

2.2.4.1 Early Cretaceous (Neocomian-Aptian 142 – 112 Ma)

During the Early Cretaceous a marine transgression covered most of Mexico. The area that covered the Yucatan Peninsula was covered by very shallow water in which carbonate sediments and evaporites were deposited (Viniegra-Osorio, 1981). To

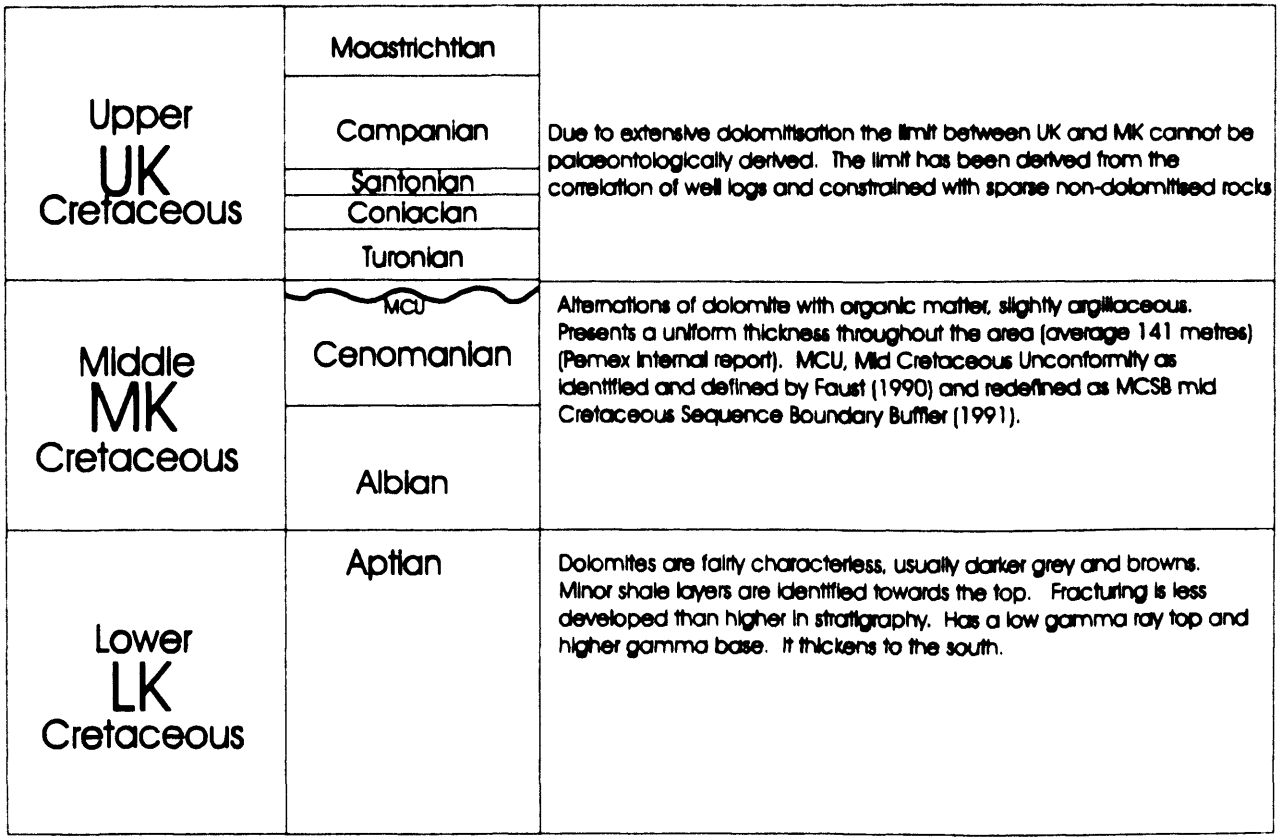

Figure 2.16
Stratigraphic subdivision for the Cretaceous: Lower, Middle and Upper, and the representative lithologic summary encountered within the Campeche Basin, as suggested by Pemex.

the west of the Yucatan Peninsula, towards the study area, the carbonates deposited corresponded to a deeper water environments (Figure 2.17; Viniegra-Osorio, 1981). It has been suggested that the thickness variations occurring within the study area are probably the result of a renewed episode of halokinesis (Horbury, 2002), and / or to the levelling out of an irregular underlying topography (García-Hernandez, 2000).

In the Cantarell area, core 5 in well C-418D exhibits dolowackstone/ carbonate mudstone that displays a general bioturbation mottling with burrows and winnowed bioclasts layers, having a high gamma signature which is suggestive of being deposited in deep-water settings or just beneath base level. The episodes of winnowing are probably related to storms. FMI image logs and core shows that Lower Cretaceous resedimented carbonates are characterised by packages 10-15 m thick of amalgamated, mainly clast-supported graded breccio-conglomerate beds 1-5 m thick with cobble- and granule-sized clasts. These have a generally low gamma signature with some minor internal gamma peaks. The conglomerates are suggested to represent deposits of debris flows sourced from a shallower water platform carbonate (Pemex, internal reports 2003).

2.2.4.2 Middle Cretaceous (Albian-Cenomanian 112 – 93 Ma)

Viniegra-Osorio (1981) reports, without any time constraints, a maximum marine transgression during Albian-Cenomanian times, which resulted in deep water facies surrounding the palaeo-highs of the Yucatan Platform to the east. Within the study area, base of slope carbonate breccias are identified whose lithoclasts are polymictic, which can be interpreted as lowstand shedding, or as a product of highstand shedding when incorporating the contemporaneous and neighbouring spatial distribution of facies assemblages. McFarlan (1991) suggests that the Albian to Cenomanian is composed of a prograding and aggrading sequence where subsidence and eustatic rise in sea level were factors influencing stratigraphic development. Albian time began with the deposition of regressive carbonates being deposited conformably on the underlying upper Aptian shales around most of the northern and southern margins of the Gulf of Mexico basin area. On the Yucatan peninsula Albian carbonates and evaporites overlie conformably Aptian carbonates.

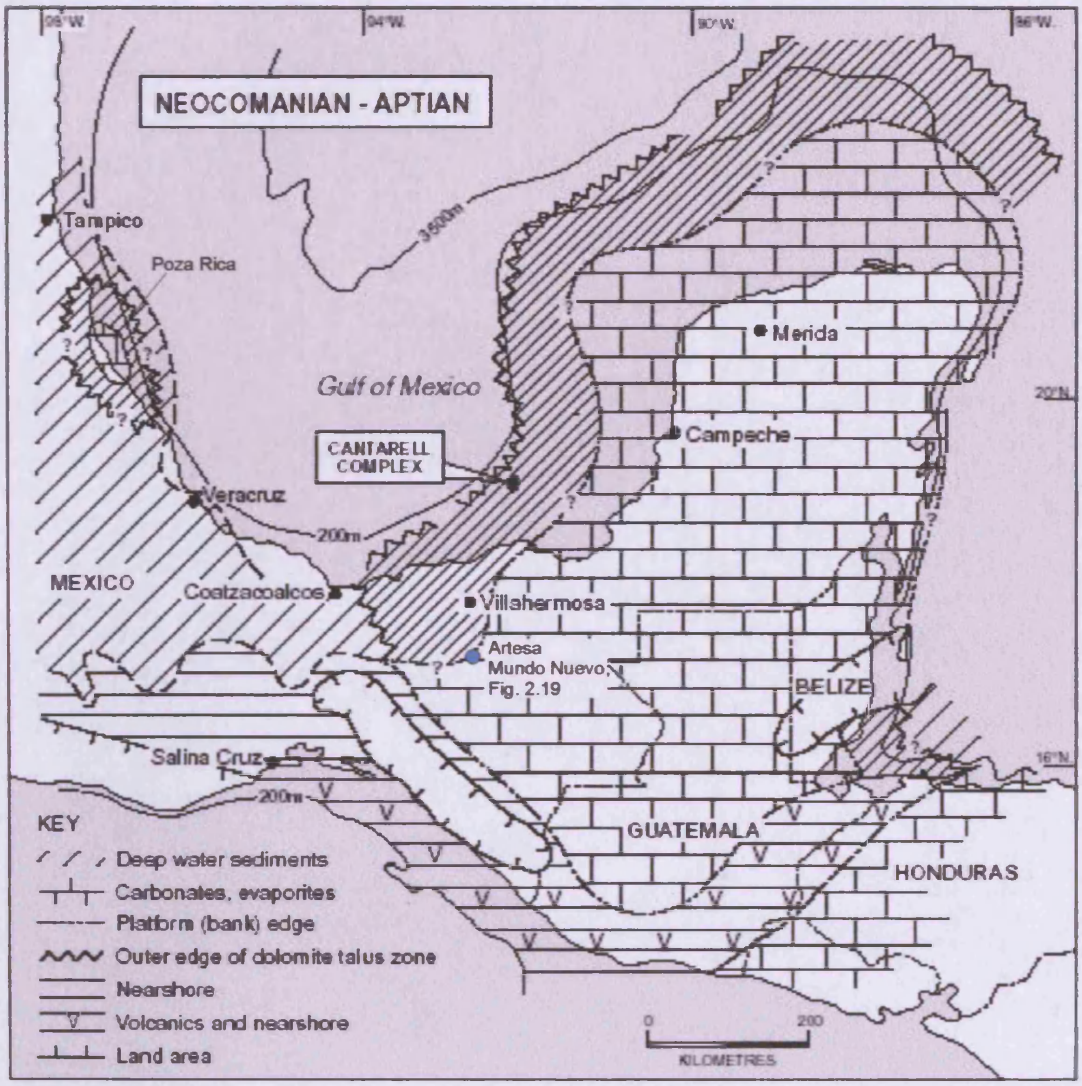

Figure 2.17
Early Cretaceous palaeo-geographic map for southern Mexico. Note the position of the Cantarell area relative to the Yucatan Platform, which suggests it was within an area of deep water. After Viniegra-Osorio, 1981.

Regionally, north of the study area near to Cuba, the Middle Cretaceous has been recognised through seismic lines as a high-amplitude reflection that can be easily mapped throughout the deep basin, and in regions of the Gulf of Mexico margin (Faust, 1990). Buffler (1991) and Marton (1999) describe this seismic reflection as a major unconformity along the southern and eastern margins of the Gulf of Mexico basin and have named it the Middle Cretaceous Unconformity (MCU). Towards the centre of the basin the seismic reflection becomes conformable with the gross stratigraphy. The MCU is inferred to be mid Cenomanian in age (Buffler et al., 1980; Buffler and Sawyer, 1985; Shaub, 1987; Faust 1990; Schlager, 1994), and has been tentatively correlated with a mid-Cenomanian drop in sea level (Vail, 1977; Figure 2.18).

Miranda-C (2000) suggests that during the mid-Cenomanian many Cretaceous platforms of the Campeche Basin were subaerially exposed, based on the development of extensive breccia sheets, as observed in the onshore Mesozoic parts of the Campeche Basin. From this, Horbury (2002) suggests a regional shallowing of the area coupled with lowstand shedding.

During the Late Cenomanian a period of relative sea level rise occurred as expressed in the Artesa-Mundo Nuevo platform located onshore south of Villahermosa, Tabasco (Figure 2.19; Horbury, 2002). This drowning event is identified in Cantarell well logs as an increase in gamma ray at the top of the MK marker (Figure 2.16). Refer to Chapter 3 for a detailed description on the Cantarell well data.

2.2.4.3 Late Cretaceous (Turonian-Maastrichtian 93 – 65 Ma)

Regionally, the Late Cretaceous history is marked as a general time of oceanic highstand in which onset of deep-marine sedimentation within the west and central areas of the Gulf of Mexico Basin occurred (Sohl, 1991). Within the Yucatan Platform, platformal carbonates that at times are interbedded with evaporites dominate this interval. The geologic setting that dominated the southern Campeche Basin consisted of carbonate rocks that developed in various platform margin, ramp and basinal settings. The stability of the Yucatan platform is noteworthy, because platform margin and slope deposits were developed here throughout a large part of the Cretaceous and into the Palaeocene (Galloway et al., 1991; McFarlan and Meneses, 1991; Sohl et al., 1991; Santiago and Baro 1992).

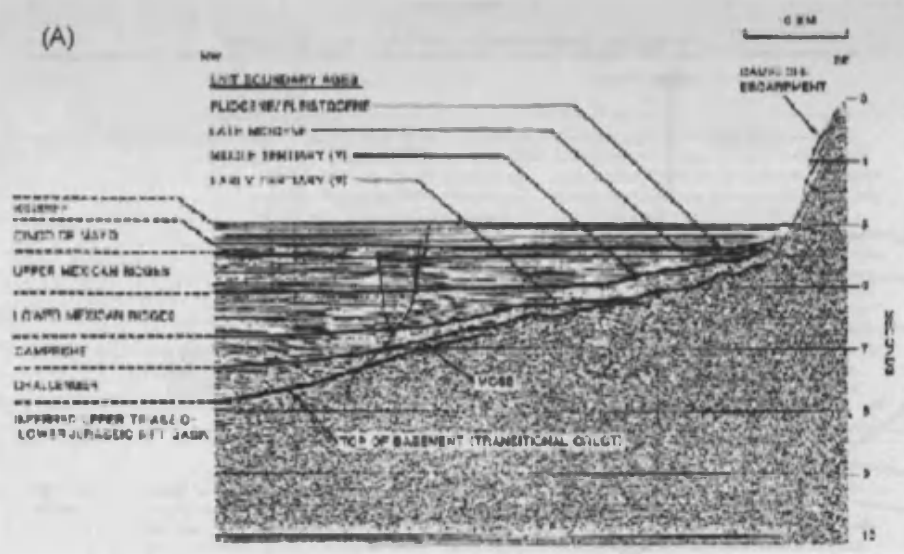

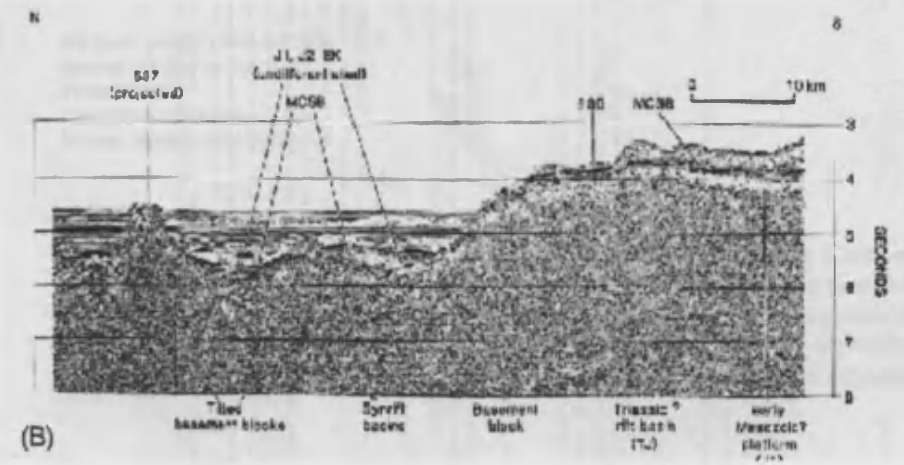

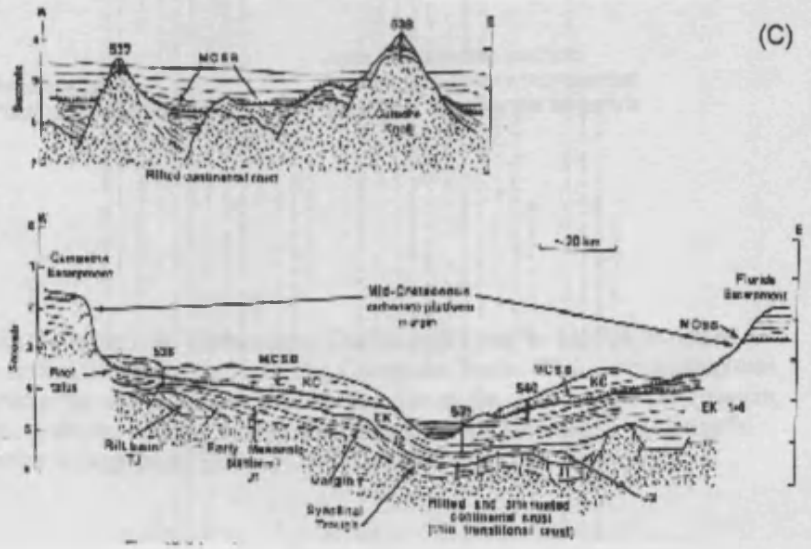

Figure 2.18
Seismic sections illustrating the character of the thick to transitional basement and the Mid Cretaceous Sequence Boundary (MCSB) also referred to as the Mid Cretaceous Unconformity (MCU), after Buffler, 1991.
(A) Portion of UT seismic line CE-2 showing names, ages, and stratigraphic relations of deep Gulf of Mexico seismic sequences along the base of the Campeche Escarpment as defined by Shaub and others (1984). (B) Portion of UT seismic line GT3-75 near the base of the Campeche Escarpment showing regional settin and stratigraphic reflections at DSDP sites 536 and 537. (C) Schematic cross section (two-way traveltime in seconds) across the southeastern Gulf of Mexico showing major geologic features, seismic sequences, and locations of DSDP Leg 77 sites. Modified from Schlager and others (1984b). See Figure 2.7 for location of lines.

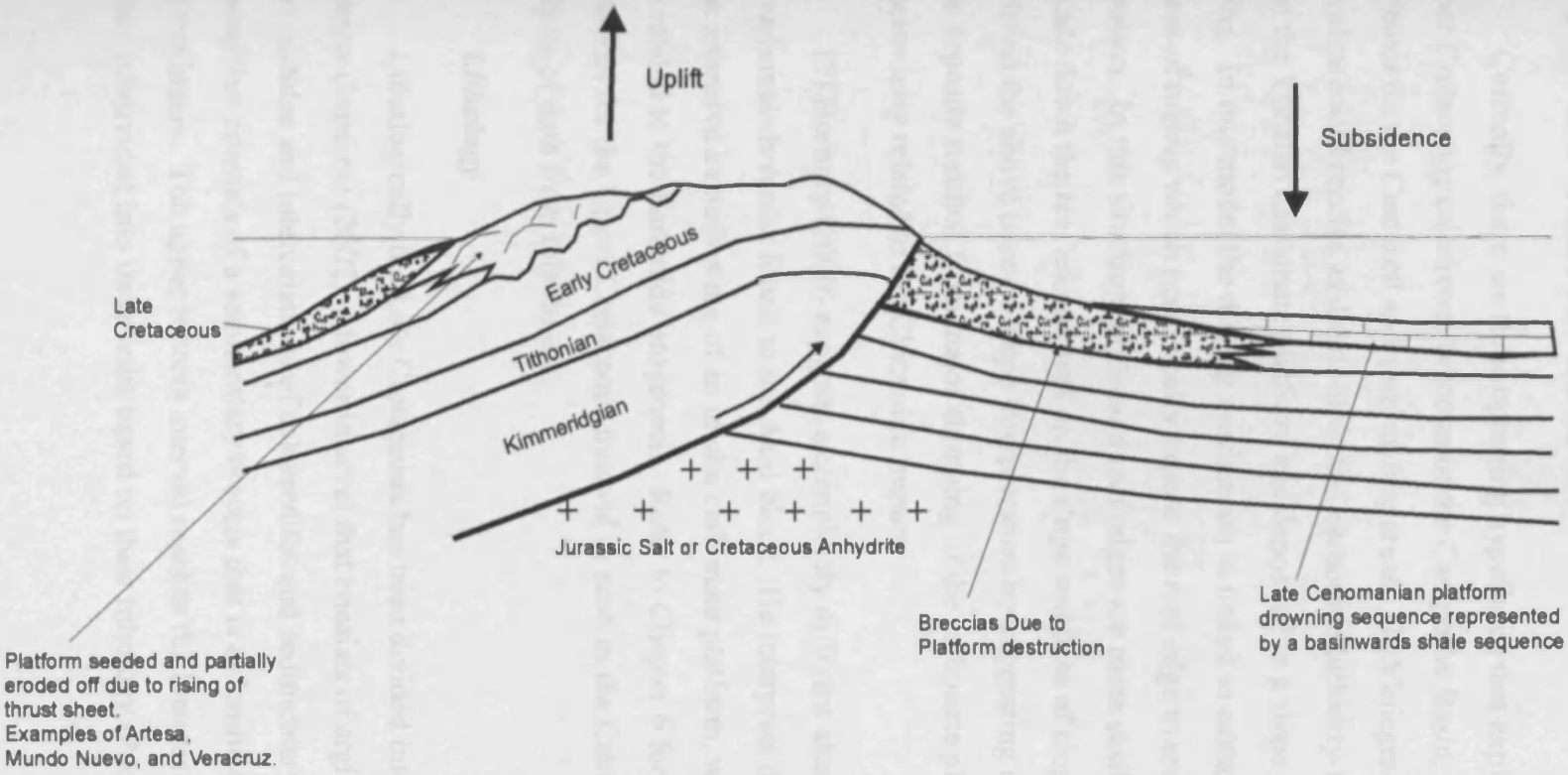

Figure 2.19
Sketch illustrating the Cretaceous platform during Late Cretaceous. This example may be applied to Artesa, Mundo Nuevo platforms which are located at the basin margin of the Campeche Basin. This basin margin was subject to subaerial exposure due to structuring and possible sea level drop during the early to mid Cenomanian, which resulted in the deposition of breccia sheets. During the late Cenomanian rapid subsidence resulting in basinward widespread deposition of shales is suggested (Horbury, 2003). See Figure 2.17 for location.

The geology contained in the Upper Cretaceous stratigraphy is of great economical interest due to the fact that most of the current oil production in the Campeche Basin is derived from it. The deposits found in the Cantarell area and surrounding areas consists mainly of calcareous breccias that have a widespread distribution among the Campeche Basin (Figure 2.20 and 2.21).

Currently, there are three opposing hypothesis that explain the genesis of the Upper Cretaceous calcareous breccias of the Campeche Basin, and with special emphasis on the Cantarell and surrounding areas. (1) Viniegra-Osorio (1981) interprets the calcareous breccias as debris-flow and carbonate turbidity-flow deposits derived from the Yucatan Carbonate platform and deposited in a slope and base of slope setting. In this model the driving mechanism is linked to eustatic sea-level fluctuations of tens of meters which periodically expose the reef edge to erosion and diagenetic alteration. In this situation, highstand reef edges are more easily broken off and cascade down the reef escarpment on the slope and base of slope. (2) Grajales (2000) modified the above base-of-slope interpretation by suggesting that the base of slope talus deposits resulted from major slumping of the carbonate platform margin triggered by seismicity related to the Chicxulub impact.

(3) Horbury (2000) suggests a completely different alternative for the origin of the carbonate breccias found in the Akal block. He interprets the breccias to result from intensive karstification of an in situ carbonate platform, whose subareal exposure was related to the Laramide orogenesis. Refer to Chapter 6 for a detailed discussion on the model for the Upper Cretaceous interval as seen in the Cantarell area based on the analysis of data from this thesis.

Lithology

Lithologically the Late Cretaceous has been divided into two intervals by Pacheco-Gutierrez (2002), a lower interval that consists of argillaceous limestones with chert nodules and intercalations of calcarenites and sedimentary breccias, and an upper interval that consists of a sedimentary breccia that is dolomitised and contains sporadic shale stringers. The upper breccia interval reaches thicknesses up to 200 m, and is further subdivided into three units based on their lithology (Pacheco-Gutierrez, 2002):

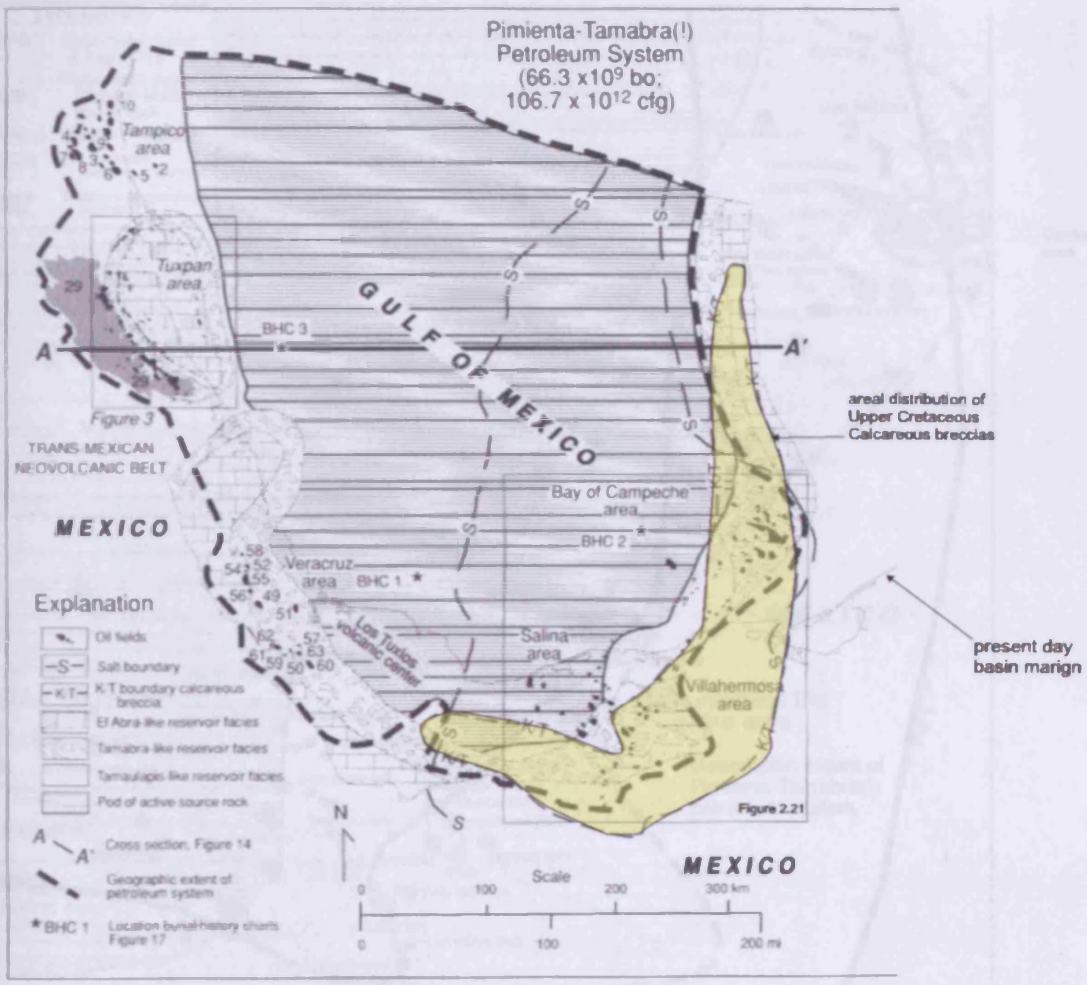

Figure 2.20
Map showing the areal distribution of the Upper Cretaceous calcareous breccias among the Gulf of Mexico (modified after Magoon, 2001).

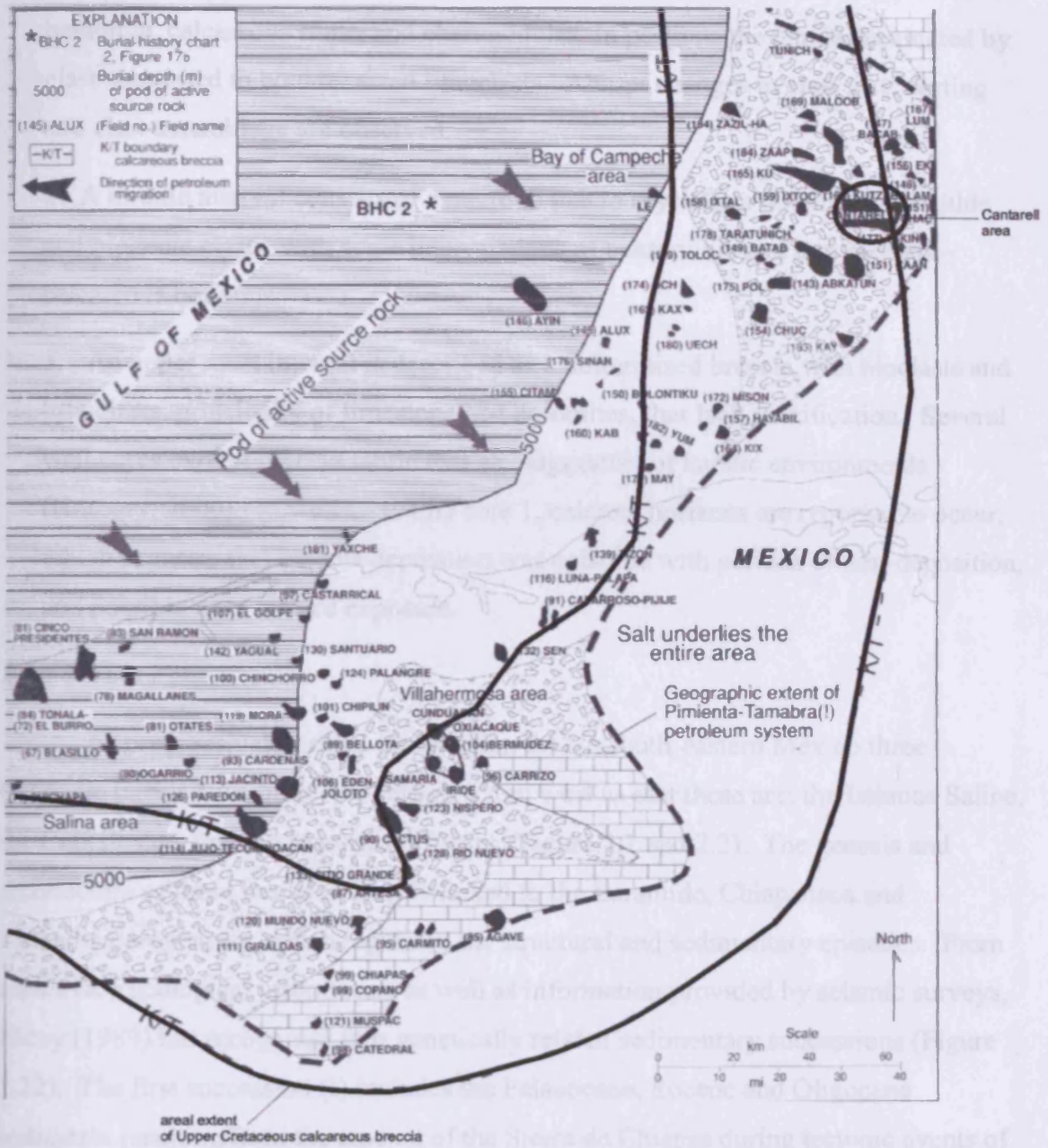

Figure 2.21
Map showing the areal distribution of the Upper Cretaceous calcareous breccia, note the Cantarell area (circle) (after Magoon, 2001).

1. A lowermost interval is represented by a sequence of fined textured dolomites with dolomitised mudstone and wackestone with intercalations of fine layers of bentonite, calcareous shale, and chert nodules. In portions the unit is dominated by clast-supported to boulder sized lithoclasts. Abrupt changes in clast size, sorting and clast assemblage are observed.

2. A middle interval consists of a micro to macro crystalline dolomite with lithic and biogenic clasts, with some intercalations of bentonithic and argillaceous – calcareous horizons.

3. An upper most interval is described as a dolomitised breccia with bioclasts and lithoclasts, principally of limestone and dolomites, that lack stratification. Several well cores exhibit breccia fabric that are suggestive of karstic environments (Horbury, 2000). In well C-3945D core 1, calcrete horizons are reported to occur, which suggests that breccia deposition was episodic with periods of non-deposition, and possible near surface exposure.

2.2.5 Tertiary

As previously described (see Section 2.1) in south-eastern Mexico three Cenozoic basins have been recognised. From west to east these are: the Isthmus Saline, the Comalcalco, and the Macuspana basins (Figure 2.1 and 2.2). The genesis and architecture of these basins is closely linked to the Laramide, Chiapaneca and Cascadian orogenesis, which regulated the structural and sedimentary episodes. From subsurface geological information as well as information provided by seismic surveys, Ricoy (1989) has recognised four genetically related sedimentary successions (Figure 2.22). The first succession (I) includes the Palaeocene, Eocene and Oligocene sediments resulting from the erosion of the Sierra de Chiapas during tectonic events of the early Cenozoic. The Palaeocene to Oligocene section is predominantly composed of shales (the Nanchital Shale and the La Laja Formation). Towards the western front of the Sierra de Chiapas the Eocene-Oligocene sequence contains lenticular conglomerates probably deposited as turbidity currents in submarine fans. In the Campeche Basin and the study area a dolomitized breccia occurs straddling at the Cretaceous/Palaeocene boundary. It has a wide distribution extending southward to the states of Chiapas and Tabasco. The breccia is transitionally covered by argillaceous limestones and marls, which grade up into fine-grained terrigenous sediments- shales

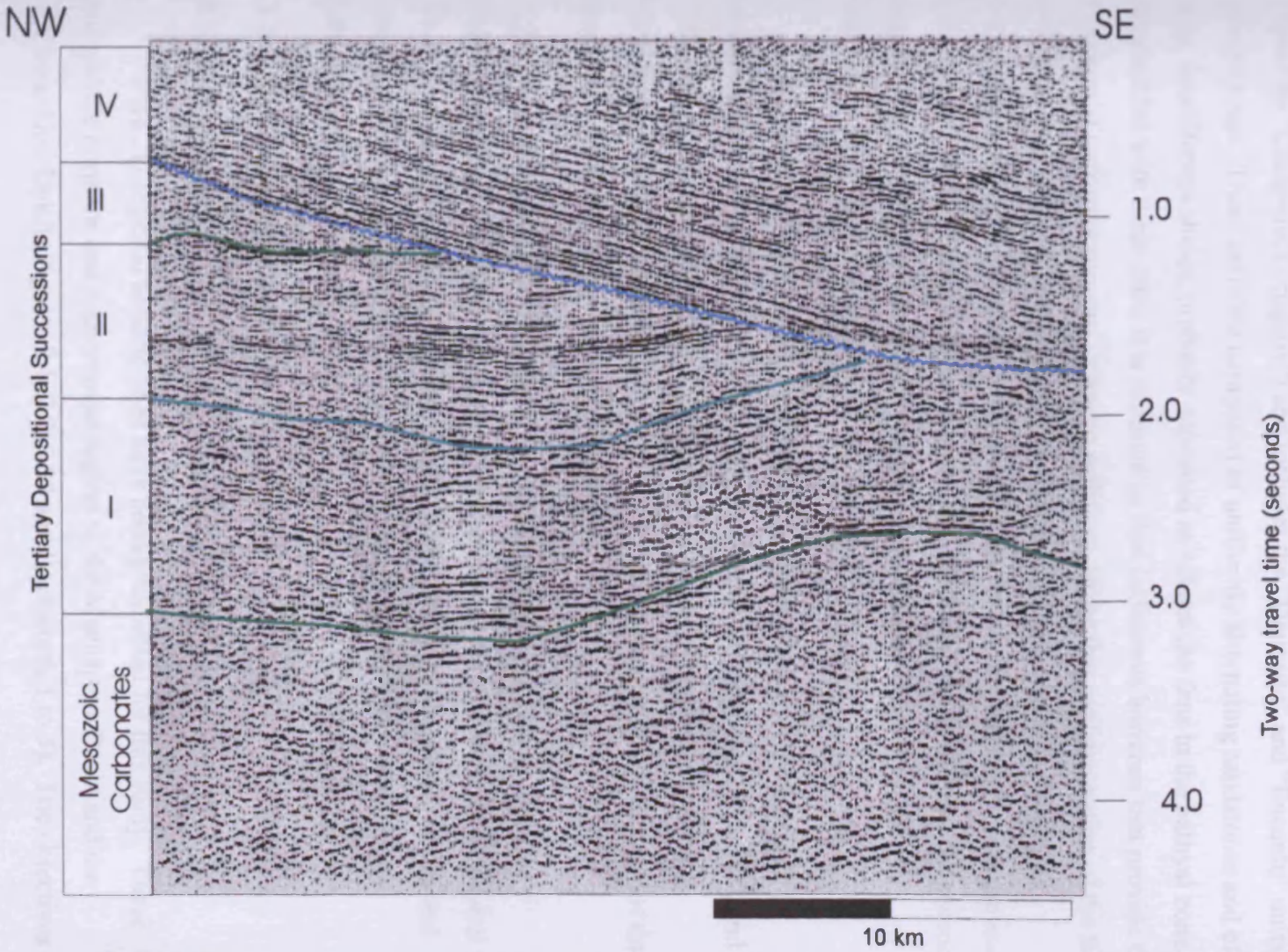

Figure 2.22
Seismic section showing Tertiary sedimentary sequence within the Comalcalco Basin, see figure 2.2 for location. From Ricoy, 1998.

and bentonitic shales. Eocene sediments are composed of bentonitic greenish-grey shales with pyrite grains. Calcarenitic intercalations are present deposited by turbiditic currents flowing from the western margin of the Yucatan Platform. The Oligocene is predominantly composed of shales, partly bentonitic; containing variable sand-size clastics and occasional lenticular bodies of conglomerate (Ricoy, 1989).

The second succession (II) (Figure 2.22) is related to an early Miocene tectonic event (the "Chiapaneca orogeny") and includes the "Deposito" and "Encanto" units of Miocene age. These units are composed of uniformly alternating sandstones and bluish grey, fossiliferous shales, probably deposited as submarine fans in the bathyal zone. Interbedded with these units it is common to find tuffaceous horizons that provide the evidence of contemporaneous volcanic activity. Along the northern region of the Sierra de Chiapas the succession is composed of marly shales, sandstones, bioclastic limestones and sandy limestones with an abundant benthonic fauna (the Macuspana Limestone). In the Macuspana Basin and along the Reforma-Akal Uplift the second sequence is composed predominately of grey fossiliferous shales with some intercalations of fine- to medium grained sandstones.

The third succession (III) (Figure 2.22) is associated with the Cascadian tectonic event and includes the "Concepcion Inferior", "Concepcion Superior", and "Filisola" units deposited during the Pliocene. This sedimentary succession is composed of grey fossiliferous shales with abundant intercalations of micaceous quartz sandstones deposited in a platform environment.

The fourth succession (IV) (Figure 2.22) includes the "Paraje Solo", "Agueguexquite", and "Cedral" units, deposited during the Pleistocene. In general they are composed of prograding and aggradational sequences of alternating shales and sandstones with occasional conglomerates. They prograded from southeast to northwest.

2.3 2D Regional seismic lines

2.3.1 Introduction

Five 2D regional seismic lines have been interpreted for this study. These traverse the northern and westernmost region of the Macuspana Basin and the Reforma-Akal Uplift (Figures 2.1, 2.2, 2.23 and Enclosures 1 to 5). The objectives of

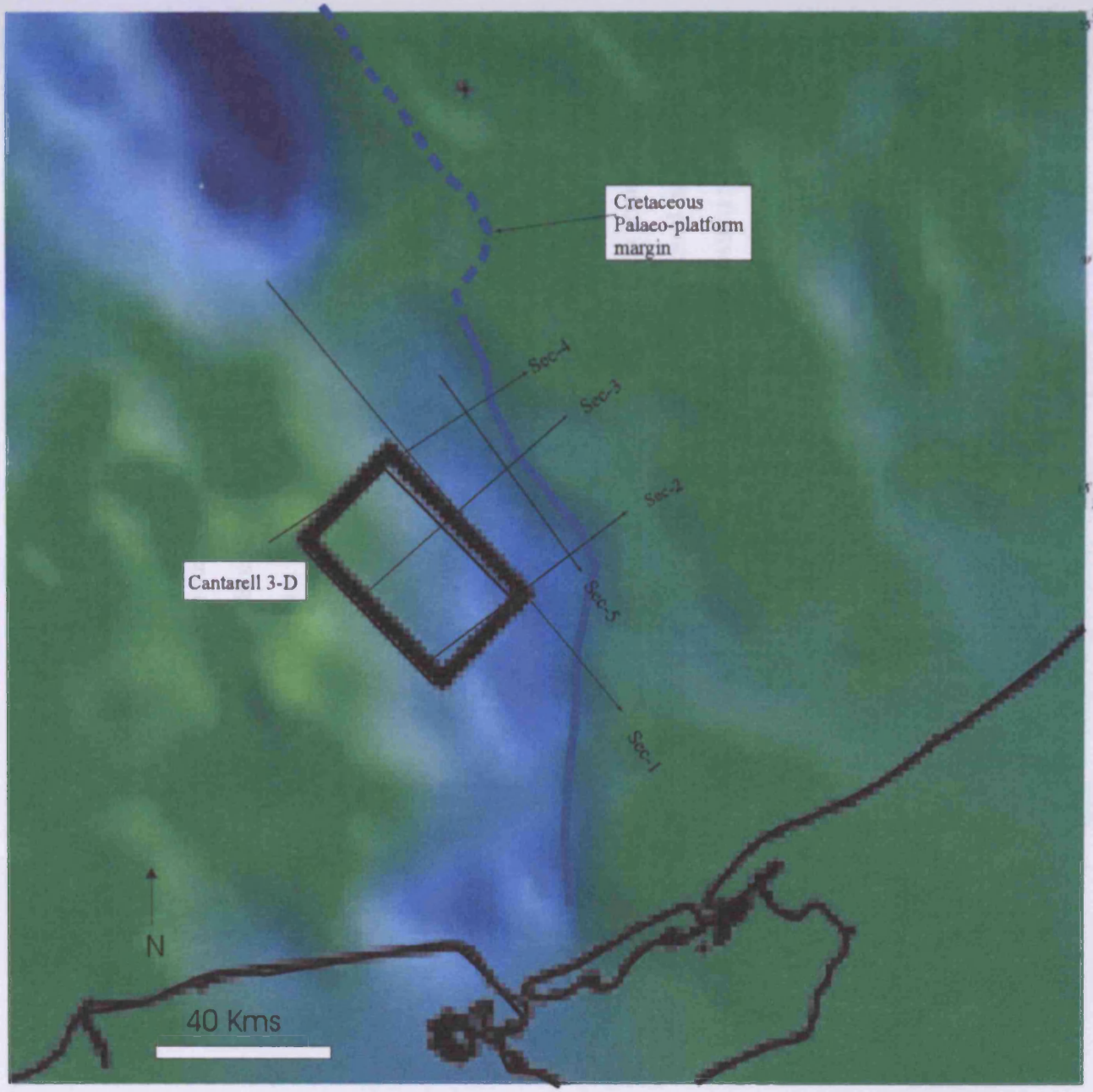

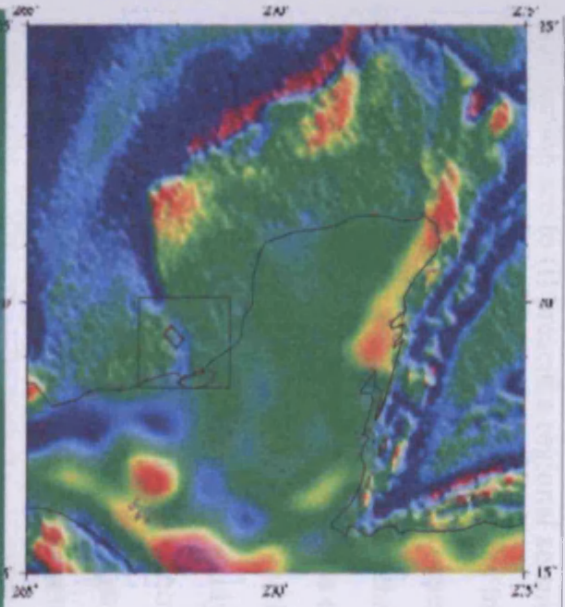

Figure 2.23
Gravity map of the Gulf of Mexico showing the location of the 3D seismic cube and 2D seismic lines (after GEODAS, 2004).

this section are to (i) present a regional seismic - stratigraphic framework based on observations and interpretations of the five transects and (ii) to investigate the significance of the seismic-stratigraphic observations related to the previous lithologic-stratigraphic descriptions presented above that are derived from literature and Pemex manuscripts (see Section 2.2). The analysis of the geometry, configuration, and continuity of seismic reflections in the five 2D regional lines, provides a general regional depositional framework for the study area. The location of these transects has allowed the description of the setting and morphology of the basin margin, and the spatial relationship between the platform margin and the basinal area, where the Cantarell study area is located. The interpretation of regional seismic horizons defines nine seismic units. Their morphology and distribution shed light on different geological processes (sedimentary and tectonic) that are an expression of the stratigraphic development of the basin margin at this location. From the morphology and distribution of the nine seismic units, two main episodes of stratigraphic development are proposed: (i) Jurassic to Palaeogene and (ii) Miocene to Recent (see Section 2.3.4).

2.3.2 Data and methods

The five transects consists of composites of different 3D data sets. Each 3D data set has been processed and migrated using different algorithms. This makes the seismic appearance different from one data set to the other. Some of the differences consist of: apparent amplitude contrasts for a given seismic reflection from one data set to the other; discrepancy in reflectivity; and vertical resolution. These differences complicate the horizon correlations and therefore their degree of certainty. The vertical extent of the data ranges from 0 to 4.6 seconds, which disables the elucidation of deeper structures.

The methodology undertaken for the interpretation of the five transects consisted of delineating and interpreting different seismic horizons that were correlated from transect to transect. The basis for choosing a specific seismic reflection was based mainly on (i) lateral continuity and (ii) where considerable changes in style of the seismic reflection configuration were noted. This approach is similar to the concepts and techniques developed by Brown & Fisher (1977), Mitchum et al. (1977b) and Vail et al (1977b).

Eight main seismic boundaries were identified and interpreted; their given names from base to top are: (i) Base Kimmeridgian; (ii) Top Jurassic; (iii) Base Tertiary; (iv) Mid-Miocene; (v) P-1; (vi) Pliocene; (vii) P-2; (viii) P-3. Together, these seismic boundaries make up nine seismic units that internally have a degree of heterogeneity, represented in terms of their seismic reflection configuration (Table 2.2).

The identification and definition of the (i) Base Kimmeridgian; (ii) Top Jurassic; (iii) Base Tertiary; (iv) Mid-Miocene; and (vi) Pliocene seismic horizons coincided with horizon definitions of Pemex as presented in García-Hernández (2000), and whose time definitions were utilised for the current interpretation. For the Base Tertiary and Top Jurassic seismic horizons, their stratigraphic timing is supported by the interpretation carried out in the Cantarell area where well data is employed to calibrate the seismic horizons.

The age definitions extracted from García-Hernández (2000), are from seismic line 10830 of the Ek-Balam 3D seismic cube (Figure 2.8). These age definitions are calibrated using biostratigraphic data from well Balam-101. The seismic inline 10830 (Figure 2.8) was taken as the benchmark to assist the age calibration for the seismic horizons in seismic Transect 1, (Enclosure 1) and from this line are correlated throughout the other five regional seismic lines. This approach is taken on the basis that the sector of Transect 1 that corresponds to the Ek-Balam 3D cube is subparallel to the seismic section presented in Figure 2.8. The seismic section in Figure 2.8 corresponds to inline 10830 and the Ek-Balam sector of Transect 5 is situated approximately 1.5 km south-west apart of inline 10830.

2.3.3 Transect descriptions

The description for each of the transects is presented below, starting with Transect 1, which has been taken as the reference section due to well calibration.

2.3.3.1 Transect 1

Transect 1 is located to the east of the Cantarell 3D survey area, it is oriented south-east, north-west (Figure 2.2 and Enclosure 1). This transect is composed of part sections from five different 3D seismic cubes, whose seismic quality is considered as medium to good. The Ek-Balam sector has been processed with a gain algorithm for

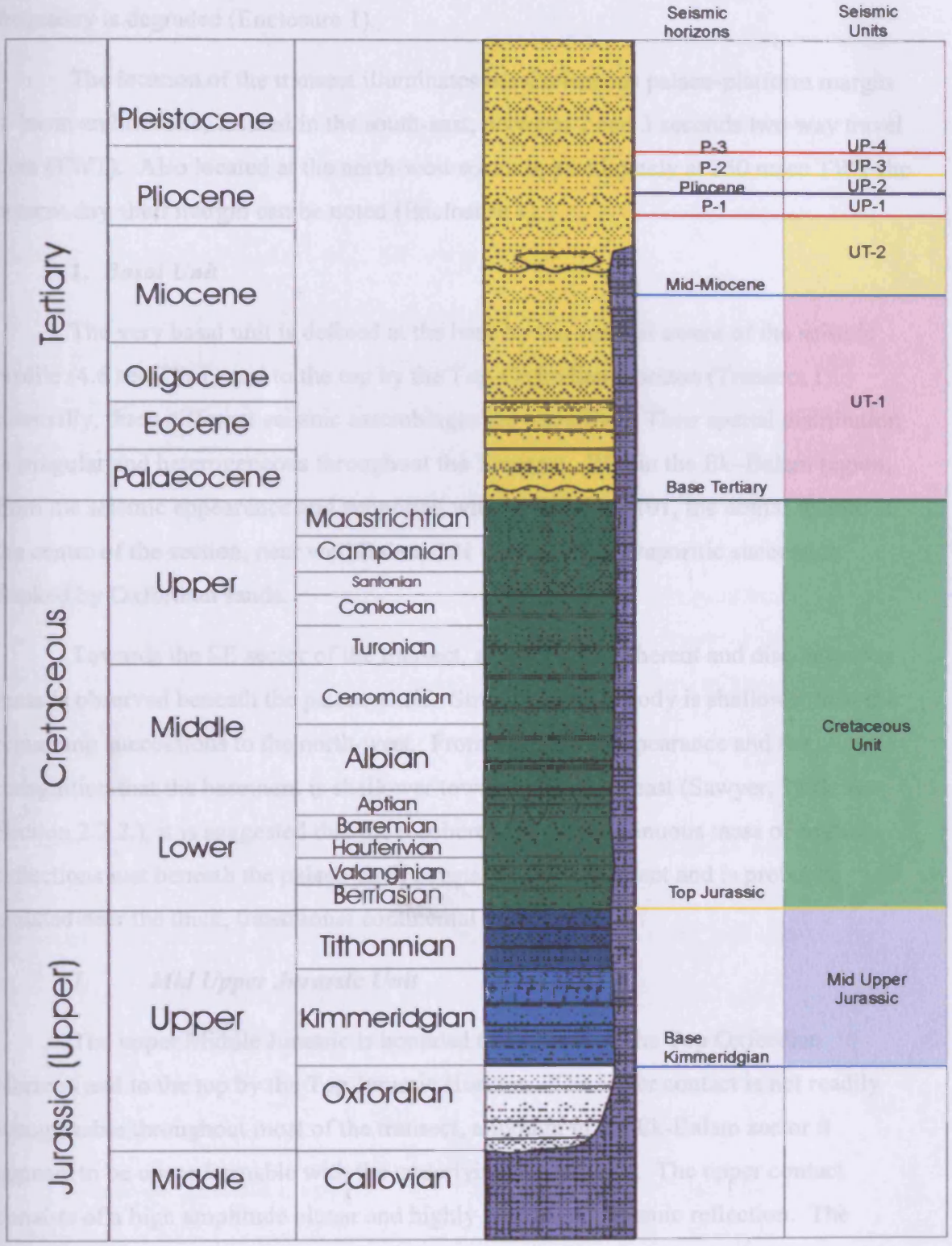

Table 2.2
Stratigraphic table and relation to the seismic horizons and units that are interpreted throughout the five 2D regional lines.

the lower 2 seconds, which gives an enhanced amplitude appearance; although its frequency is degraded (Enclosure 1).

The location of the transect illuminates the Cretaceous palaeo-platform margin to basin architecture, located in the south-east, between 2 and 3 seconds two way travel time (TWT). Also located at the north-west sector approximately at 250 msec TWT the present day shelf margin can be noted (Enclosure 1).

1. *Basal Unit*

The very basal unit is defined at the base by the vertical extent of the seismic profile (4.6 sec TWT) and to the top by the Top-Oxfordian Horizon (Transect 1). Internally, three different seismic assemblages are identified. Their spatial distribution is irregular and heterogeneous throughout the Transect. Within the Ek–Balam region, from the seismic appearance and supported with well Balam-101, the domal feature at the centre of the section, near well Balam-101 consist of an evaporitic succession flanked by Oxfordian sands.

Towards the SE sector of the transect, a massive, incoherent and discontinuous mass is observed beneath the palaeo-shelf. Structurally this body is shallower than the remaining successions to the north-west. From its seismic appearance and the recognition that the basement is shallower towards the south-east (Sawyer, 1991; see Section 2.2.2.), it is suggested that the incoherent and discontinuous mass of seismic reflections just beneath the palaeo-shelf consists of the basement and is probably situated near the thick, transitional continental crust boundary.

1. Mid Upper Jurassic Unit

The upper Middle Jurassic is bounded to the base by the Top Oxfordian Horizon and to the top by the Top Jurassic Horizon. The lower contact is not readily recognisable throughout most of the transect, although in the Ek-Balam sector it appears to be unconformable with the underlying successions. The upper contact consists of a high amplitude planar and highly continuous seismic reflection. The internal character of the unit changes throughout. The basal part is marked by discontinuous reflections of alternating high and low amplitude. Towards the upper region these become continuous, of high amplitude and with higher frequency seismic facies.

2. Cretaceous Unit

The Cretaceous Unit is bounded to the base by the Top Jurassic Horizon and to the top by the Base Tertiary Horizon. The basal horizon (Top Jurassic) appears conformable with the underlying Jurassic successions over most of the transect. Towards the Cretaceous palaeo-platform margin this unit thins noticeably, possibly due to non-deposition of the Tithonian marine shales, such that the Kimmeridgian carbonates lie in direct contact with the Lower Cretaceous.

The overall geometry of the Cretaceous consists of a shallow NW dipping unit that thickens towards the palaeo-slope and platform margin (south-east). Internally the Cretaceous exhibits concordant, continuous high amplitude parallel and planar seismic reflections, mostly homogeneous throughout. A second localised seismic assemblage is recognised which is transparent (discontinuous and low amplitude reflective events).

The top boundary defined by the Base Tertiary horizon consists of a high amplitude, highly continuous reflection. Locally it appears to be unconformable with the overlying Tertiary strata, especially towards the north-western sector where the Base Tertiary Horizon is marked by an undulating reflection being onlapped by the overlying reflections (Enclosure 1).

3. Unit UT-1

This interval is marked to the base by the Base Tertiary Horizon and the top by the Mid-Miocene Horizon. Its overall morphology is almost planar to lensoidal that drapes over the platform, paralleling the underlying Mesozoic carbonate successions.

Its thickness varies throughout, its lensoidal morphology marked by repeated thinning and thickening. In the Ek-Balam section, Unit UT-1 is completely absent. Internally the seismic character consists of parallel continuous and planar high amplitude reflections.

The upper boundary is defined by the Mid-Miocene Horizon, erosional truncation is observed at this boundary. Based on the erosional truncation configuration it is suggested that the irregular thickness of unit UT-1 resulted from the erosional event marked by the Mid-Miocene Horizon.

4. Unit UT-2

The base of this unit is defined by the Mid-Miocene Horizon and its top by the P-1 horizon. The morphology of the Mid-Miocene horizon is flat, appearing to be draping and onlapping the underlying sequences. It pinches out against the palaeo-platform. The onlapping character is more evident near the palaeo-platform base and margin.

The basal boundary marked by the Mid-Miocene Horizon is characterised by an irregular undulating surface which becomes most noticeable at the Ek-Balam sector, and where it is marked by three concave upward depressions that resemble palaeo-canyons or channels. Their dimensions are c. 2 - 3 km wide and about 200 metres deep (Enclosure 1).

The thickness of the unit varies throughout. At the Cretaceous palaeo-platform margin it is reduced to its minimal expression of about 10 msec twt (14 m), from which it thickens to its maximum at the platform base and along the slope. From this position and into the basin its thickness is regularly thinning and thickening although a general thinning trend is observed.

Internally the seismic character changes laterally and vertically. For descriptive reasons the platform to basin profile has been subdivided into three sub-areas: (i) Palaeo slope-shelf margin consisting of the palaeo-shelf and slope, (ii) inner basin plain (iii) outer basin plain, (Enclosure 1).

(i) Along the palaeo-platform and slope, contorted reflections infill the underlying Mid – Miocene Horizon irregular palaeo-bathymetry. The seismic reflection configurations are difficult to elucidate, no apparent downlaping or onlapping is observed. In general the lower part is characterised by semi-continuous parallel reflections of variable amplitude that become divergent and contorted towards the top and platform base. Just at the platform base, a concave upward feature is noticeable which is filled in with a seismic assemblage that exhibits semi-continuous transparent reflections.

(ii) The inner basin plain interval comprises features that are interpreted as "channels" or "palaeo-canyons" based on their external geometry, internal fill, and similarity to incised features described in Brown & Fisher (1977) and Galloway (1991).

Vertically, the lower part that infills the Mid – Miocene "channels" or "palaeo canyons", are typified by high amplitude reflections that onlap against both lateral walls of the channels or palaeo canyons, and are limited to their vertical extent. The upper part appears to drape underlying units and exhibits a combination of transparent and parallel continuous, high amplitude reflections.

(iii) The outer basin plain is similar to the proximal basin plain, where a basal part is dominated by concordant, high amplitude, continuous reflections overlain by transparent reflections. The overall thickness decreases by twofold in a downdip direction.

6. Unit UP-1

The upper and lower boundaries are the Pliocene and P-1 horizons respectively. The geometry of this unit consists of a wedge shape that thins towards the palaeo-platform and thickens in a basinwards direction, with a considerable thinning at the Ek –Balam sector.

Internally, parallel, continuous, medium amplitude reflections are apparent. Along the slope, discontinuous low amplitude and higher frequency reflections occur. The transition with the overlying deposits is gradual, and downlapping terminations onto the Pliocene horizon are observed.

7. Unit UP-2

This unit is defined to the top by the Progradation-2 horizon and to the base by the Pliocene horizon. The overall morphology consists of a wedge that tapers against the palaeo-platform, and thins out basinwards just at the Ek –Balam area. Internally, it consists of a characterless, transparent seismic assemblage. In some parts, the seismic reflections can be seen to exhibit a downlapping relationship (Enclosures 2 to 4).

8. Unit UP-3

This unit also has a wedge-like sigmoidal shape, and it has a composite basal surface defined by the P-2 and the Pliocene horizons. The upper limit is marked by the P-3 surface. Internally it consists of a sequence of stacked topsets and clinoformal reflections that dip north-west.

9. Unit UP-4

This unit is defined at the base by the Propagation -3 and the Pliocene horizons, its top is defined by the seafloor. Its morphology and internal character is similar to unit UP-3, although there is a considerable volume increase for this unit. Internally progradation is very noticeable from the SE extent of the seismic line until the present day shelf break.

2.3.3.4 Transect 2

Transect 2 is oriented south-west to north-east, and is made of two 3D seismic cubes (Figures 2.2, 2.23 and Enclosure 2). The south-western sector of this line crosses the northernmost region of the Cantarell 3D area, although the seismic section belongs to the Nezalih 3D data set (Enclosure 2). The orientation and length of this section sheds light on the basin to palaeo-platform margin architecture (Enclosure 2). The profile consists of a flat topped palaeo-platform located at the north-east sector of the section. Towards the south-west, the slope-to-platform-base transition displays a gentle and continuous dip of 5-9 degrees, about 10 km measuring in length.

All of the eight seismic surfaces previously defined were identified and interpreted in this transect; the nine units were also encountered, however unit UT-1 indicates a considerable thickness development and preservation compared to the other sections.

The following is a detailed description of each seismic surface and its defined seismic units from the base upwards.

1. Basal Unit

This unit is present at the base of the entire section. Stratigraphically it comprises the basement, the Callovian evaporitic successions if present, and the Oxfordian successions. Of these successions, the occurrence of the evaporitic successions is not conclusive from the seismic character alone. On the basis of the seismic reflection configuration, three seismic assemblages are recognised within this unit: (i) highly discontinuous subhorizotal reflections functioning as the base for the palaeo-shelf margin at the north-eastern most sector; (ii) a transitional area in which the

continuity of the reflection increases towards the south-west, locally appearing with a south-west dip, and (iii) continuous, parallel, medium amplitude south-west dipping reflections. Towards the palaeo-platform, the overlying Kimmeridgian successions consist of continuous reflections, which appear to onlap the basal discontinuous reflections. Along the slope this boundary is not so obvious. It appears unconformable and the seismic appearance consists of basal steeply dipping semi-continuous reflections, overlain by the Kimmeridgian continuous reflections (Enclosure 2).

2. Mid-Upper Jurassic Unit

This seismic package is characterised as a tabular well defined unit with a continuous dip towards the north-east. Structurally it is disrupted by reverse and normal faults. The thickness is relatively homogenous, but slightly thickens and then thins in a basinwards direction. Internally it consists of continuous, medium to high amplitudes reflections.

The upper limit is marked by the Top Jurassic Horizon, best described as a highly continuous and high amplitude reflection that appears to be concordant with the overlying package in the basinal setting, and discordant near the palaeo-platform margin.

3. Cretaceous Unit

The base for the Cretaceous is the Top Jurassic Horizon, and the top the Base Tertiary Horizon (see Enclosure 2). The top boundary appears concordant; there is no clear evidence that there was erosional truncation at the Base Tertiary boundary. However, at the upper slope there are significant onlapping reflections onto the Base Tertiary horizon.

Internally, the unit consists of a well defined, thick tabular unit with a continuous dip towards the north-east. It flattens out at the palaeo-platform margin. Towards the south-west it is disrupted by two parallel reverse faults that dip north-east, which display minor displacement and are antithetic to the extensional faults related to rifting of the Gulf of Mexico, here evidenced by the basal normal faults interpreted at the basement.

There is an apparent thickness increase towards the shelf. Internally it consists mainly of transparent reflections that pass into the overlying Tertiary successions as continuous high amplitude reflections.

4. Unit UT-1

Unit UT-1 is bounded to the base by the Base Tertiary Horizon and to the top by the Mid-Miocene Horizon. The base contact is marked by a high amplitude, high continuity reflection that is easily traced across the section. Its top is readily identified and traced along the palaeo-slope, which becomes difficult to trace basinwards and into the Cantarell area. The overall geometry of this unit consists of a wedge which thins towards the palaeo-platform margin.

Internally its seismic character varies, at the basinal regions it consists of a thicker unit of concordant parallel reflections of high amplitude. Thinning up-slope, two seismic assemblages are observed: a lower one consisting of continuous, high amplitude, onlapping reflections, and an upper one of relatively higher frequency, medium to low amplitude semi-continuous reflections. The upper one totally pinches out at the lower slope by the upper Mid-Miocene boundary.

The upper slope is characterised by a thin unit with high amplitude, continuous onlapping reflections, in regions with a hummocky appearance. At the palaeo-platform margin a minor depression feature is apparent. Internally, mixed assemblages occur from continuous to discontinuous, with an overall low amplitude and higher frequency. Overlying the depression feature, parallel, continuous, higher frequency reflections occur that appear to have a minor downward sagging deformational pattern.

The upper boundary for this unit is manifested by the Mid Miocene Horizon. The overall morphology of the Mid Miocene profile resembles a concave upward shape with a degree of asymmetry. Structural highs are located on both sides of the section, to the north-east besides the shelf, and to the south-west, the periphery of the prominent Cantarell structure, (see Chapter 4 for the description of the structure).

The overlying reflections downlap on to the Mid Miocene horizon. The downlapping direction appears to be emanating from the structural highs, mainly from the shelf, although downlapping reflections coming from the Cantarell periphery are also noticeable.

5. Unit UT-2

The occurrence of this unit is restricted to the upper slope region. It has a wedge shape. Its lower boundary is defined by the Mid Miocene horizon, and its upper by the P-1 horizon having a distinctively high amplitude and continuous character. The P-1 horizon merges with the Mid Miocene horizon.

Internally, it consist of a predominantly downlapping, concordant, oblique parallel reflections. The lower part appears to be disturbed, as suggested from the hummocky reflections.

6. Unit UP-1

The basal contact is the Mid–Miocene horizon at the basin to lower slope region, and by the P-1 horizon at the upper slope and shelf region. The upper limit is marked by the Pliocene horizon which appears to be slightly discordant with the overlying deposits. It has a wedge-shaped appearance, thinning over the shelf and Cantarell periphery areas. Internally it consists predominantly of downlapping sigmoidal reflections.

7. Unit UP-2

The basal contact is conformed throughout by the Pliocene horizon and the upper limit by the P-2 horizon. It has a wedge morphology that thins against the shelf and maintains a uniform increased thickness in a basinal direction. Internally, it consists of downlapping, high frequency, continuous parallel, medium amplitude reflections.

8. Unit UP-3

It is defined to the base by P-2 and top by P-3 horizons, both contacts appear transitional. Evidence suggesting erosional truncation is not apparent. The upper contact appears almost horizontal throughout. The lower interval of this unit fills in the underlying platform to basin profile. At the upper portion of this unit the shelf to basin transition is not present.

This unit has a wedge shape which thins towards the shelf, and thickens in a basinal direction where it exhibits a homogeneous thickness. Internally it consists of parallel, concordant, high frequency, medium amplitude reflections. Vertically, a

change in morphology is observed from slightly divergent in a basinwards direction, to parallel concordant reflections at the top portion, which further suggests an infilling pattern of the underlying shelf-slope-basin transition and, therefore, shelf progradation.

9. Unit UP-4

The uppermost unit is defined to the base by horizon P-4 and top the seafloor. It consists of a tabular horizontal package with minor thickness variations. Internally it is characterised by very homogeneous and highly continuous, parallel, high frequency reflections, of medium to high amplitude.

2.3.3.3 Transect 3

Transect 3 (see Enclosure 3) is oriented south-west – north-east crossing the Cantarell, the Ek-Balam and the Chanix 3D surveys. The location and orientation of this transect sheds light on the palaeo-platform to basin architecture and the spatial relationship of the Cantarell area with the Cretaceous palaeo-platform margin (Transect 3). To the south-west is situated the prominent Cantarell structural high. This structure resulted from a complex Oligocene-Miocene structural deformation which gave rise to a complex array of a major thrust and subsidiary normal and reverse faults (see Chapter 4). This section is orientated almost perpendicular to the northerly thrust vergence. The thrust plane is marked as a heavy dashed line (see Enclosure 3). The Cretaceous palaeo-platform margin is observed to the north-east of the section. The basinal plain extends towards the south-west.

1. Basal Unit

The basal unit is located throughout the entire section as confirmed by well penetrations within the Cantarell area reaching the Oxfordian sands. The Callovian evaporites have been encountered out of their stratigraphic context by wells intruded along fault planes. The seismic appearance of the basal unit within the Ek-Balam and Chanix areas is similar to that described in Transects 2 and 1. Within the Cantarell area, a massive body with a concave downward morphology of discontinuous, semi-concordant, high amplitude reflections lies underneath the main thrust block which measures over 6 km across.

2. *Mid Upper-Jurassic Unit*

The Upper Mid Jurassic Unit is present throughout the entire section and is repeated twice at the Thrust Block, as a result of thrusting (see Chapter 4). Its overall geometry is tabular. In regions it has been structurally altered by faulting and folding (See Chapter 4).

Internally, it is made up of high amplitude, continuous reflections, which in parts are discontinuous. Its lower boundary appears to be unconformable with the underlying reflections. The upper boundary also appears unconformable, whereas the overlying reflections appear to be draping this unit.

3. Cretaceous Unit

This unit is present throughout the entire section, it is structurally altered and defines thickness changes across faults. Internally, it consists of concordant highly continuous, high amplitude reflections. No preferential onlapping or downlapping direction for the stratal architecture is observed. It is suggested that the reflection configurations constitute an aggradational system.

4. Unit UT-1

This unit is present in the entire section, and vertically repeated throughout the Thrust Block section. Its overall morphology is tabular, with a decrease in thickness towards the paleo-platform and an increase basinwards. Its base is defined by the Base Tertiary, which is continuous and smooth. The top boundary is defined by the Mid-Miocene Horizon, which exhibits an irregular morphology towards the base of the palaeo-platform, and where erosional truncation can be readily observed (see Enclosure 3 and Figures 2.24 and 2.25). In a basinwards direction, within the Thrust Block, the interpretation of the Mid-Miocene Horizon is problematic. Well stratigraphic data suggests that the Mid-Miocene sediments are only present in the hangingwall, therefore the interpretation delineates the horizon over the structure. Within the Thrust Block, the top boundary of Unit UT-1 can also be seen to be defined by the thrust plane. However, the stratigraphy encountered beneath the thrust plane varies in age, from Oligocene to Mid-Eocene, as suggested from well stratigraphic data (See Chapter 4, Figure 4.32).

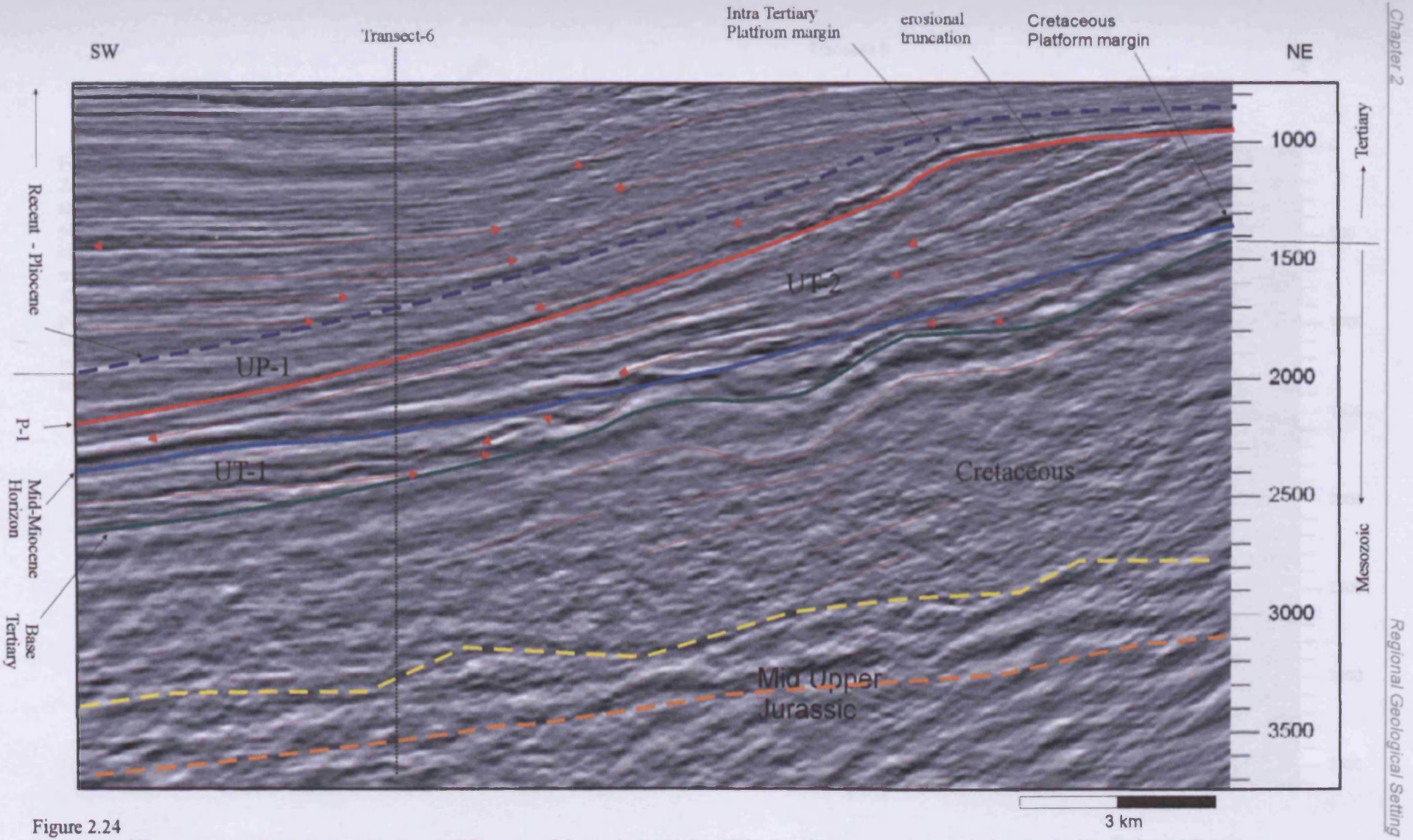

Figure 2.24
Zoom box of Transect 4 (see Enclosure 4) showing the NE sector of the section, which exhibits the platform margin architecture for the Mesozoic and Tertiary times and the slope morphology of the Base Tertiary, and overlying units. Note the considerable thickness development of the Cretaceous successions towards the NE. The undulating morphology at the base of the Cretaceous platform within the UT-1 unit and upper interval of the Cretaceous. Reflections that have concave upward morphology infill this undulating morphology as well as downlapping reflections. For definition of letters see text.

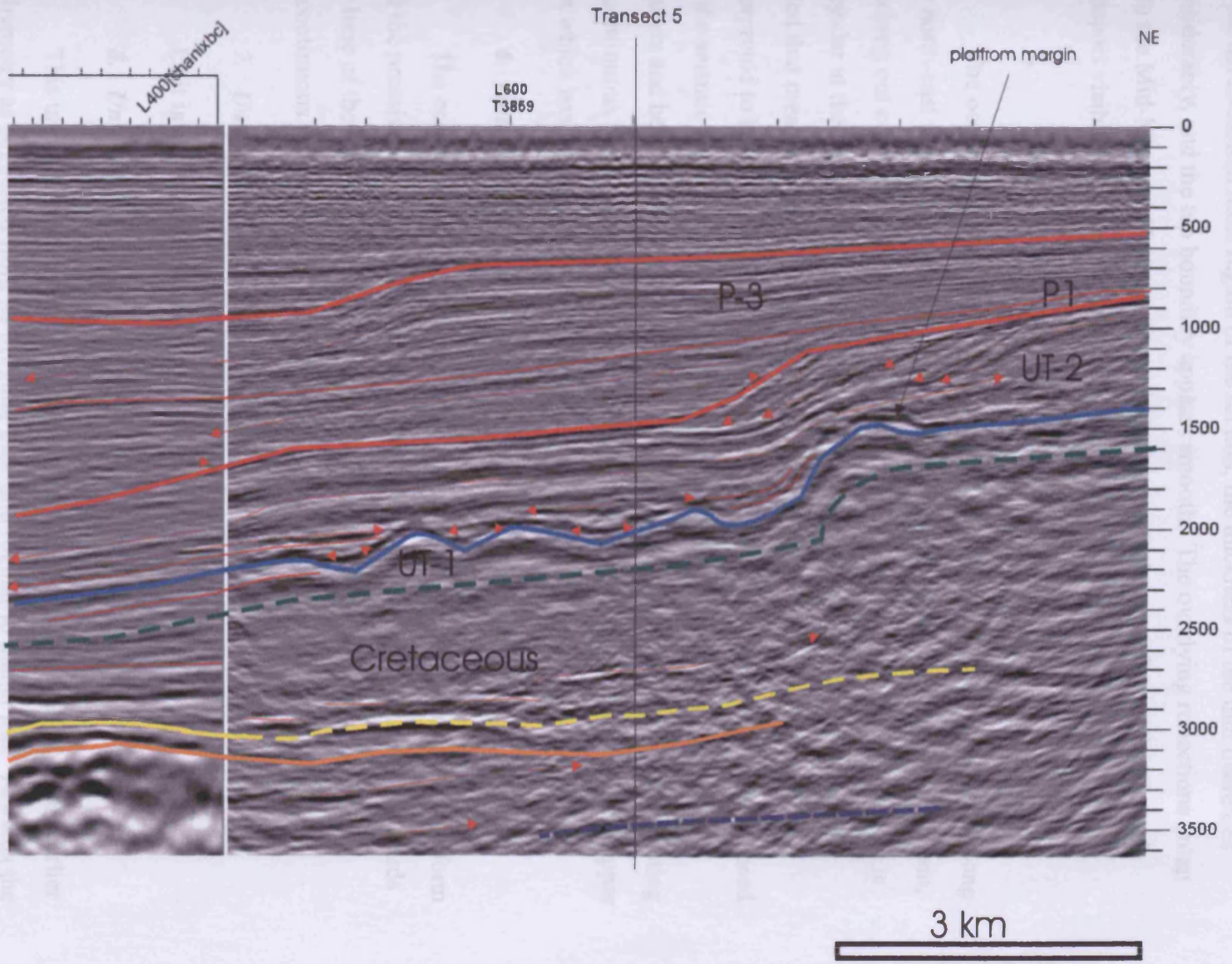

Figure 2.25
Zoom of Transect 3 showing the palaeo-platform margin and slope base . Note the undulating morphology along the slope at the base of the platform margin. For significance of the labelling letters refer to text and Enclosure 3.

At the north-eastern most region of the section, the thickness of the unit decreases considerably, and the top boundary appears smooth. The overlying reflections onlap onto the Mid-Miocene Horizon, appearing as drape with no preferred direction of transport visible from stratal geometry alone.

5. Unit UT-2

The occurrence of this unit is restricted to the slope and palaeo-platform, along the north-east region of the section. It has a wedge shape that thins towards the basin, pinching out completely at the base of the prominent Cantarell structure. The base is irregular at the palaeo-platform top and base, where concave-upwards features are noted that measure approximately 0.5 km in width. Normal faults have been interpreted to bound these features, although this interpretation is not conclusive based on the seismic appearance. The top of the unit is uniform, consisting of topsets, foresets and bottomsets. Internally, it can be divided in two parts, the lower consisting of continuous higher amplitude reflections appearing to be downlapping, and the upper part which has a transparent assemblage (see Enclosure 3).

6. Unit UP-1

The occurrence of this unit is restricted to the area between the palaeo-platform and the prominent Cantarell structure. Its thickness is minimal (250 msecs). Towards the base of the Cantarell structure the seismic character is seen to consist of discontinuous and incoherent reflections.

7. Unit UP-2

Unit is absent due to non-deposition.

8. Unit UP-3

This unit is present over the entire section. It appears to be filling in the earlier bathymetry as suggested from its irregular base and regular to planar top. Towards the north-east, the unit is structurally disrupted by normal faults. The internal progradational reflection architecture is best observed in Transect 1. The reflections architecture in this transect appears downlapping, and infilling the depression areas situated between the Cantarell structure and the paleo shelf.

9. Unit UP-4

This unit is defined to the base by the P-3 Horizon and the present-day seafloor. Its internal architecture is seen in this section to consist of parallel, continuous high amplitude reflections. Minor normal faults appear to have displaced the reflections.

2.3.3.2 Transect 4

This transect is oriented north-east to south-west, and passes through the southern sector of the extent of the Cantarell seismic survey (Figures 2.2, 2.23 and Enclosure 4). And comprising parts of the the Nezalih seismic survey (Figure 2.23). The location and layout of this transect sheds light on the morphology of the palaeo-platform to basin transition for Cretaceous times. Towards the north-east, the uppermost sector of the palaeo-slope passes laterally to the Cretaceous platform margin. However, the edge of the palaeo-platform margin is not readily observed in this section. If preserved it would lie further north-east of this section. Towards the south-west, the palaeo-slope, which is defined as the transition of the platform margin and into a basinal or deeper open water setting, is observed (Enclosure 4). At higher stratigraphic levels, within the Tertiary successions, a shelf margin is observed, which appears in the north-eastern sector of this section overlying the Cretaceous platform margin. Towards the south-west, along the base of slope, reverse faults are observed that displace the Mesozoic carbonates. This faulting is related to the Oligocene-Miocene structural deformation which resulted in a complex array of a major thrust and subsidiary normal and reverses faults, found throughout the study area (See Chapter 4).

Only five units were defined of the eight seismic surfaces previously identified and defined in Transect 1 (Fig 2.23, B). The post-Pliocene units were treated as a single unit due to their internally similar seismic characteristics (Enclosure 4). Unit UP-2 is also absent in this section which is the same for Transect 3. The Tertiary successions are interpreted to be derived from the erosion of the Sierra de Chiapas (see Section 2.2.5; Ricoy, 1989).

1. Basal Unit

This unit is present at the base of the entire section, and stratigraphically is similar to the basal units present in all 2D sections; however the existence of Callovian evaporitic sequences is not conclusive, based on the seismic character. The overall

thickness of this unit is not observed due to the vertical extent of the seismic data, which prohibits deeper imaging of the unit. The internal reflection configuration consists of highly discontinuous, south-western dipping reflections at the north-eastern sector of the section, that become chaotic towards the south-west beneath the reverse faults. The upper boundary is defined by the Base Kimmeridgian surface, however, this limit is not identified from a seismic perspective. Instead, it was defined by cross-correlations with Transects 1 and 5.

2. Mid Upper Jurassic Unit

This seismic succession is characterised as tabular well defined unit with a generally homogeneous thickness which thins slightly in a basinwards direction. Structurally, it is disrupted by reverse faults that dip to the south-west. Internally, the seismic character, towards the north-east sector of the section, consists of discontinuous reflections of medium amplitude. Towards the top of the unit the reflections become more continuous. These represent the Tithonian sediments. The continuity of this reflection package diminishes in a basinwards direction. The upper boundary against the Cretaceous carbonates is not readily apparent. Its current position was correlated from Transects 1 and 5. Towards the south-western sector of the section, the internal character appears different to that seen in the north-eastern sector because of differences processing parameters. The seismic character consists of discontinuous reflections at the base of the unit that become more continuous and layered towards the top of the Tithonian successions. Towards the south-western sector, beneath the reverse faults, the seismic reflections are discontinuous and chaotically arranged. The general morphology and internal seismic character of this unit is similar to the Basal Units described in other transects.

3. Cretaceous Unit

This unit is defined to its base by the Top Jurassic Horizon and to the top by the Base Tertiary horizon. The shape of this unit is tabular with a considerable thickness development towards the north-eastern sector near the platform margin. Structuring is observed in the form of reverse faults in the south-western sector of the section. The top boundary consists of high amplitude, highly continuous reflections. Towards the north-eastern sector onlapping reflections are observed onto the Base Tertiary horizon. Towards the south-western sector, the boundary becomes concordant with the

overlying stratigraphy. At the base of the platform margin and along slope an undulating morphology is observed (Figure 2.24). Similar morphological features are observed along the base of slope in Transects 2 and 3. No faults are recognised below or above this horizon. Reflections onlap and infill this undulating morphology.

4. Unit UT-1

Unit UT-1 is bounded to the base by the Base Tertiary horizon and to the top by the Mid-Miocene Horizon. Its base, the Base Tertiary horizon, is easily identified throughout the section (see Sections 2.3.3.1 to 2.3.3.3). The top, defined by the Mid-Miocene Horizon, is also identifiable at the slope section, which becomes difficult to trace in a basinwards direction.

The overall geometry consists of a wedge which thins considerably towards the slope and onlaps the underlying Cretaceous successions. The morphology of this unit is similar to all of the four dip sections previously described (Transects 2 and 3).

Internally, its seismic character varies; at the basinal location (south-west), it consists of medium amplitude, continuous seismic reflections that appear folded and faulted. The seismic quality in this sector is from poor to medium. Up-slope continuous, high amplitude, onlapping reflections are noted. The upper slope region is characterised by a thin interval of high amplitude, continuous onlapping reflections that locally have a hummocky appearance that fill in the underlying irregular morphology.

5. Unit UT-2

This unit is bounded to the top by P-1 horizon and to the base by the Mid-Miocene Horizon. The occurrence of this unit is restricted to the slope, along the north-east region of the section, similar to the distribution of this unit in Transect 2 and 3. Its overall geometry is similar to Transects 2 and 3, which consists of a wedge shape that thins basinwards, pinching out completely at the base of the slope. Internally, it consists of reflections of continuous, high frequency and medium amplitude slope foresets and bottomsets that appear to be downlapping (Figure 2.24).

6. Unit UP-1

This unit is bounded to its base by the P-1 horizon and to its top by the Pliocene horizon (Enclosure 4). The lower and upper boundaries of this unit are unconformable;

erosional truncation is observed at the basal contact at the intra-Tertiary platform margin (Figure 2.24). Overlying onlapping reflections are observed towards the south-western sector of the section, the onlapping architecture and thickness suggests a rapid infilling pattern, and a high sediment supply. Up along slope at the platform margin downlapping reflections are observed (Figure 2.24). The geometry of this unit is clinoformal, internally it consists of topsets, forests and bottomsets, which are not so evident.

The internal seismic character consists of parallel medium frequency and medium amplitude reflections at the south-western sector. Locally, the seismic quality is poor, resulting in a discontinuous seismic appearance. Towards the north-eastern sector, the internal seismic reflection architecture is mainly transparent (discontinuous and low amplitude reflective events). At the base of the platform margin a relatively higher amplitude reflection, with a corrugated texture is observed, on which onlapping reflections occur (Figure 2.24).

7. Units UP-2

Absent due to non-deposition, refer to Enclosure 1.

8. Unit UP-3 and UP-4

Units UP-3 and UP-4 were not differentiated in this section, the internal seismic reflection configuration is very similar throughout this sedimentary package. Therefore, the base of this package is defined by the Pliocene horizon and its top by the present day seafloor. Its morphology consists of a concave upward base and a planar top. Its thickness is irregular, which results from infilling the previous, irregular bathymetry. It thickens toward the centre of the section, thinning towards the platform margin and against the structural high that is situated towards the south-western sector of the section.

Internally it consists of parallel reflections of medium frequency, and medium amplitude, and of high continuity. The reflections architecture suggests a parallel infill whose main sedimentary source was from the south, south-east.

2.3.3.5 Transect 5

This transect is oriented north-west to south-east, almost parallel to Transect 1 (Figures 2.2, 2.23 and Enclosure 5). The data presented consists of a single seismic cube (Chanix bc), located the north-east of the Cantarell study area. The orientation and length of this section permits the elucidation of the seismic expression of the Cretaceous palaeo-platform margin from a strike perspective, since the section is almost parallel to it (Figure 2.2, and 2.23).

This transect profile captures all of the nine seismic units identified in Transect 1. However, some units are not differentiated in this transect. The Basal Unit and the Upper Mid-Jurassic Unit are merged into a single unit because the internal character does not allow for the accurate differentiation. Units UP-3 and UP-4 are also described as a single unit, although the seismic horizon P-3 is defined and shown in this transect.

The Mesozoic successions display an overall uniform thickness throughout the transect (Enclosure 5). The top boundary for Unit UT-1 displays an irregular undulating surface marked by concave upward depressions that resemble palaeo-canyons, or channels, similar to those observed in transect 1. These concave upward features that are filled in by seismic reflections found within unit UT-2.

Towards the middle of the transect a mound-like features are observed (Figure 2.26), whose growth is suggested to have commenced by Mid Miocene times, based on (i) the homogeneous and concordant thickness found within Unit UT-1 and the Mesozoic successions and (ii) the thinning and onlapping style of Unit UT-2 towards the mound-like feature.

Overlying the UT-1 and UT-2 Units are Units UP-1 and UP-2 and UP-3, which appear downlapping on to the underlying successions and prograding in a north-western direction.

1. Basal Unit and Upper-Mid Jurassic Unit

The Basal Unit and the Upper-Mid Jurassic Unit exhibit a well developed tabular morphology that thickens towards the south-east. The Top Jurassic Horizon that is posted in Transect 5 has been correlated from the other Transects (2, 3, and 4) and its base is limited by the extent of the seismic data 4600 msec twt.

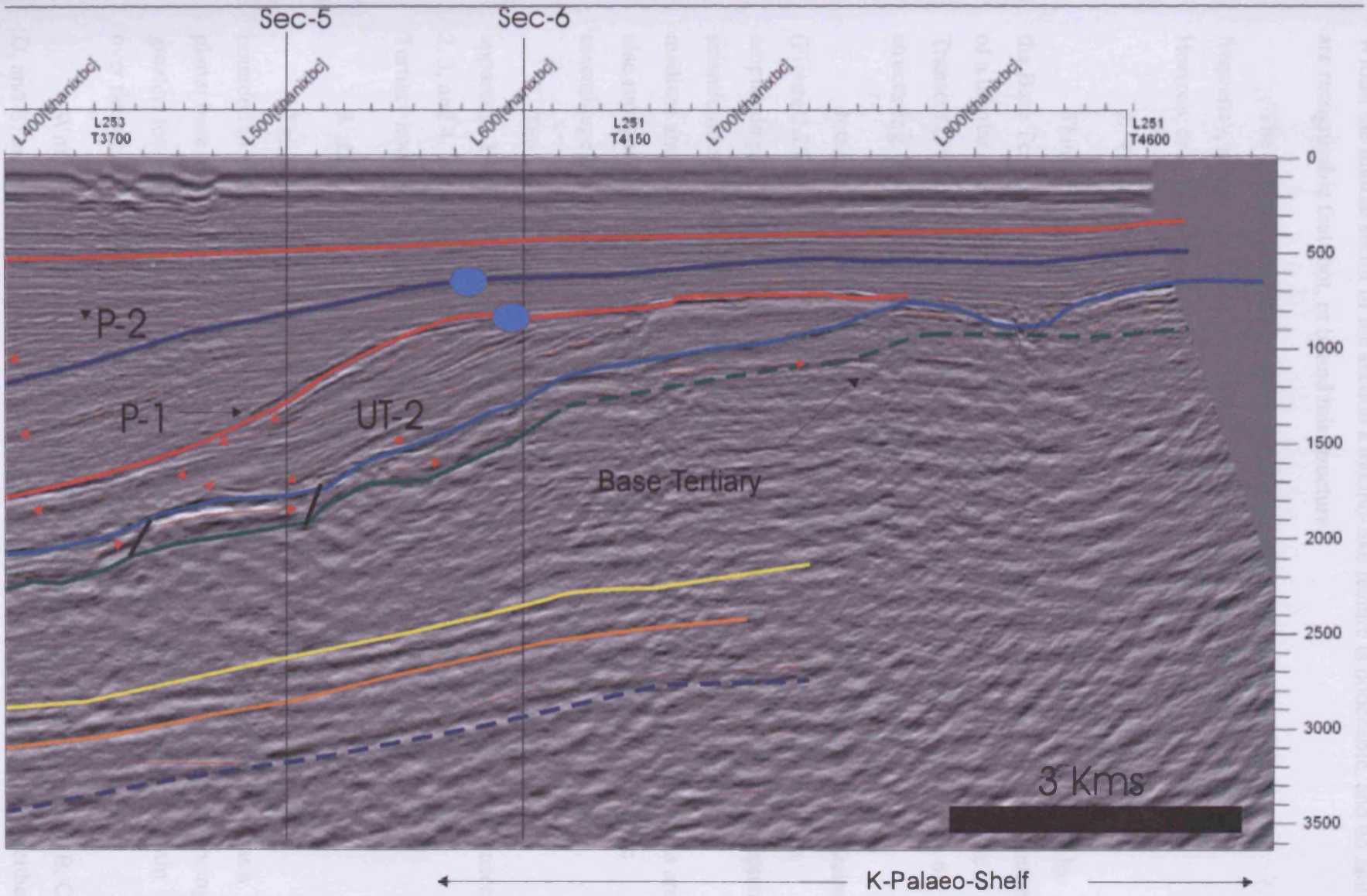

Figure 2.26
Zoom of transect 2 displaying the Cretaceous paleo-platform margin and its overlying defined units, for significance of labelling letters refer to text and Enclosure 2.

Within the middle sector of the section a mound-like feature is noticeable, and no faults are recognisable that root, or bound this structure.

The internal seismic character consists generally of discontinuous, high frequency, medium amplitude reflections. Towards the top, near the Tithonian Horizon, continuous and high amplitude reflections are seen.

2. Cretaceous Unit

This unit is bounded to its base by the Top Jurassic Horizon, and at its top by the Base Tertiary Horizon. The overall geometry of the Cretaceous succession consists of a tabular, well defined unit that exhibits a mound-like feature at the centre of the Transect (Figure 2.26 and Transect 5). This feature does not exhibit any evidence of structuring, neither to the sides or towards the base.

Internally the Cretaceous successions exhibits two main types of seismic facies (Figure 2.27 and 2.28); toward the base it consists of concordant, continuous, high amplitude parallel and planar reflections, mostly homogeneous throughout. The upper seismic interval that exhibits transparent seismic reflections, that in areas are of medium amplitude appearing in localised patches. These two seismic assemblages are also recognised in Transects 1; although in Transect 4 only the transparent seismic assemblage is noted.

The upper boundary defined by the Base Tertiary Horizon is not readily apparent. The definition of it has been mainly derived from the correlation of Transects 2, 3, and 4. It is very difficult to asses the relationship between the Cretaceous – Tertiary boundary as unconformable or conformable.

3. Unit UT-1

This interval is marked with the onset of the Tertiary sedimentation and is bounded to its top by the Mid-Miocene Horizon. Its overall geometry varies, it has a planar base and an irregular, undulating top; its thickness also varies throughout, being greatest towards the south-east, thinning towards the northwest and thickening again over the mound feature (Figures 2.27 and 2.28).

Within the top undulating surface, five main concave upward features (A, B, C, D, and E) are recognised (Figures 2.27 and Enclosure 5) which are interpreted as either

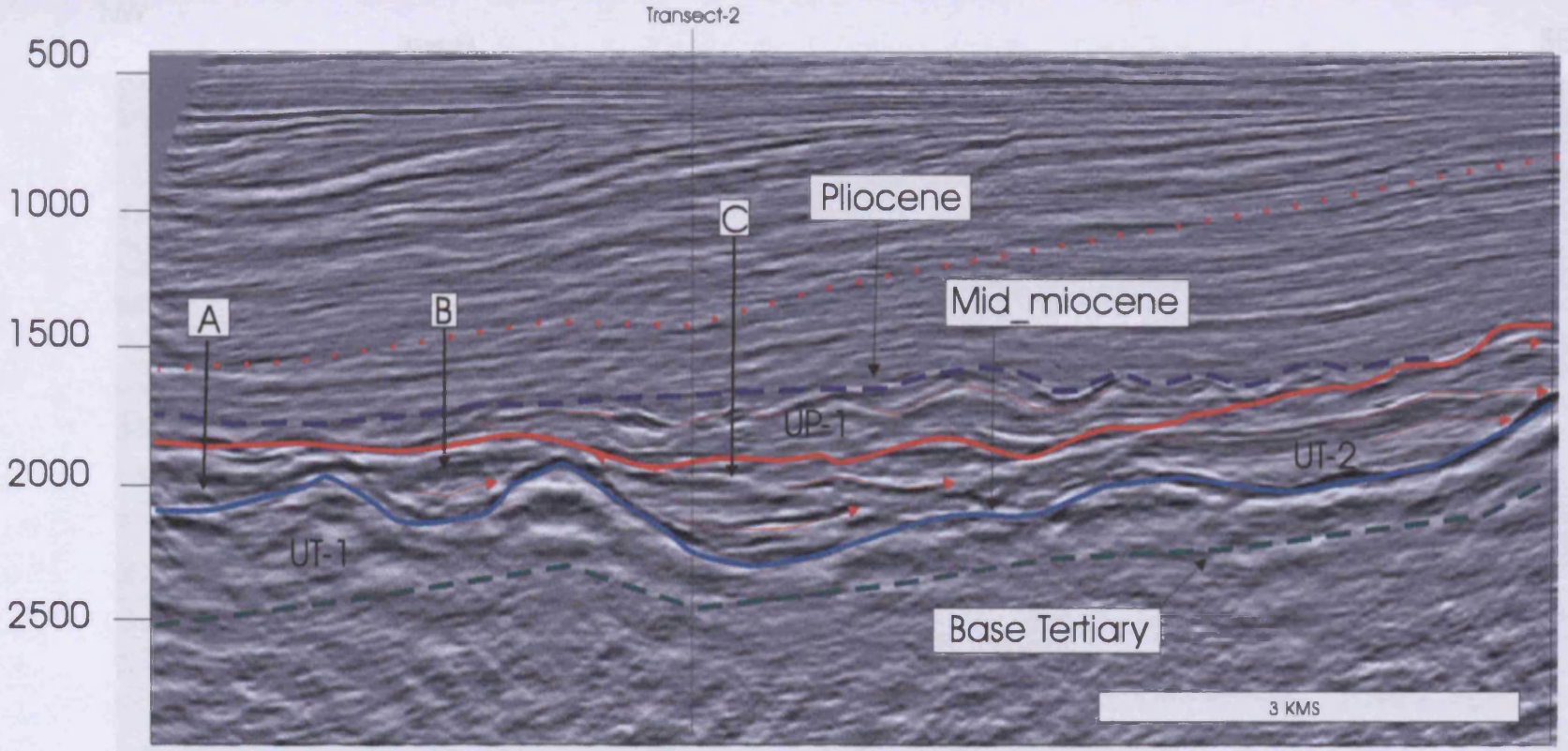

Figure 2.27
Zoom of Transect 5; Cretaceous and Tertiary successions are displayed. Note the concave upward features labeled A, B and C, and the seismic character that is filling in these features. These similar features are found within the same UT-1 and UT-2 successions in Transect 1, and appear aligned in a NE-SW trend. These characteristics point towards a channel system or palaeo-canyon system.

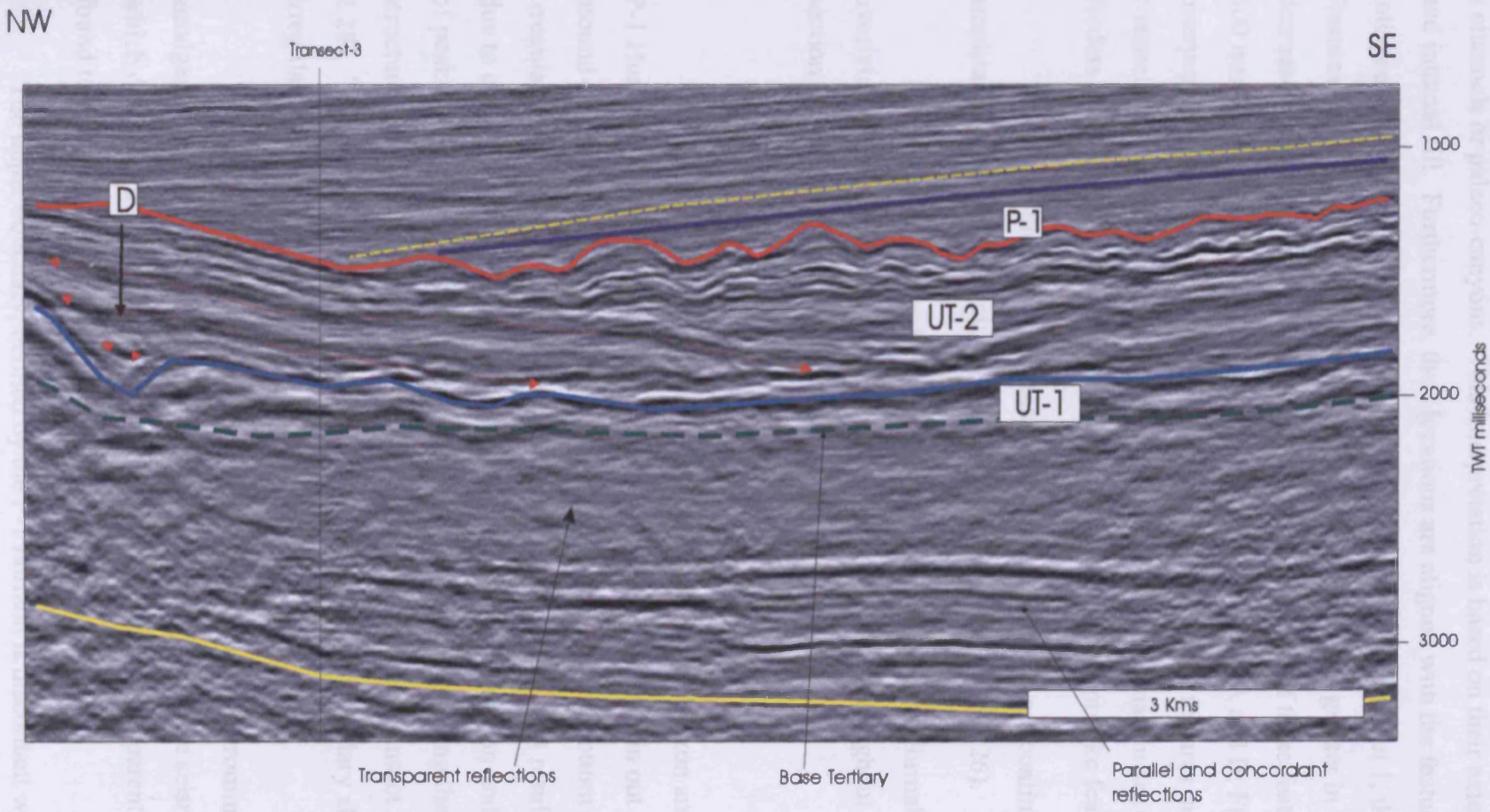

Figure 2.28
Zoom from Transect 5, displaying the Cretaceous and overlying seismic units. Note the irregular character of Horizon P-1 seen towards the south-east that may be the result of erosion and becomes planar towards the north-west, adjacent to the mound-like structure. This difference in morphology suggests that within the mound-like feature the seismic facies are more resistant to erosion, which in turn suggest that the mound-like feature may represent a reef structure.

a channels or palaeo-canyons. This interpretation is based on their external geometry, and internal fill. Furthermore, their locations are aligned with the features also interpreted as channels or palaeo-canyons in transect 1. In transect 1, three of these features were recognised. The amplitude of these features is greater in transect 1 which decreases considerable in this transect. The vertical extent of these features varies from 300 msec twt (C and D) to shallow 200 msec twt incisions (A and B; Figure 2.27). One interpretation that may answer these differences is that these features may consist of channels that incise the shelf margin. Proximal to the shelf margin are the tributary feeders that with distance merge into larger channels to canyon-like features.

Within the mound-like feature the seismic reflections are continuous, of high amplitude and low frequency, and no faults are evident (Figure 2.26).

The upper boundary, the Mid-Miocene Horizon, is unconformable with the overlying UT-2 successions, erosional truncation is evident throughout the entire section (Figure 2.28, and Enclosure 5).

4. Unit UT-2

The base of this unit is defined by the Mid-Miocene Horizon and its top by the P-1 Horizon. Its overall geometry consists of two wedges that thin out against the mound-like feature (Transect 5 and Figure 2.29). Both top and bottom boundaries are irregular; the base fills in the underlying irregular bathymetry that resulted from erosion due to channelling. To the south-east of the mound like feature, an undulating surface of peaks and troughs is noted, which become more prominent along the relative structural lows, and flatten out above an elevation datum (see Transect 5 and Figure 2.28). To the north-west of the mound-like feature, the top boundary also exhibits an irregular surface.

Internally, two general seismic assemblages occur: (i) a prominent, undulating, amalgamated, continuous, high frequency, and medium amplitude seismic reflections, which dominate the upper sector of the unit; and (ii) a basal transparent package that is found to onlap the mound-like feature.

The upper boundary, defined by the P-1 horizon is discordant with the overlying successions, which appear to onlap the P-1 Horizon.

5. Unit UP-1

The base of this unit is defined by the P-1 Horizon, and its top by the Pliocene Horizon. The occurrence of this unit is restricted to the north-west and south-east sectors of the transect and absent over the mound-like feature. The south-eastern region consists of a thin layer that pinches out towards the north-west. The north-western sector consists of a lensoidal body which also thins out completely towards the south-east, against the mound feature (Figure 2.29). The internal character of the south-eastern body consists of parallel, continuous, high frequency reflections; whereas the internal character for the north-western lensoidal body exhibits contorted to hummocky medium amplitude reflections (Figure 2.27).

6. Unit UP-2

This unit is defined at its base by the Pliocene Horizon, and the upper limit by the P-2 Horizon. Its occurrence is limited to the SE region of the section where it displays a very thin veneer draping over the underlying unit UP-1. The internal character is made of continuous, low amplitude, shallow clinoforms (Enclosure 5). Both top and bottom contacts appear conformable.

7. Units UP-3 and UP-4

Both of these units are described together, due to their external and internal seismic geometry similarities. Unit UP-3 is seen to have an unconformable base on which, from south-east to the north-west, horizons P-2, P-1, and Pliocene downlap onto the base of Unit UP-3 (Transect 5). Its top is defined throughout the entire section by the P-3 Horizon. The lower and upper boundaries of UP-4 Unit are defined by the P-3 and current sea floor respectively. This succession has a wedge-like geometry with an irregular base and a flat top. Internally, the stratal configuration consists of clinoforms that infill the previous bathymetric relief defined by the basal contact of Unit UP-3.

The clinoform architecture is best evidenced towards the north-western sector of the Transect. These clinoform geometries differ in shape to the ones observed in Transect 1. In Transect 1 the clinoform geometries consists of topsets, foresets and bottomsets; whereas in Transect 5 the clinoform geometry is limited to mainly foresets with erosional topsets, and the bottomsets are not as well developed as the ones observed in Transect 1.

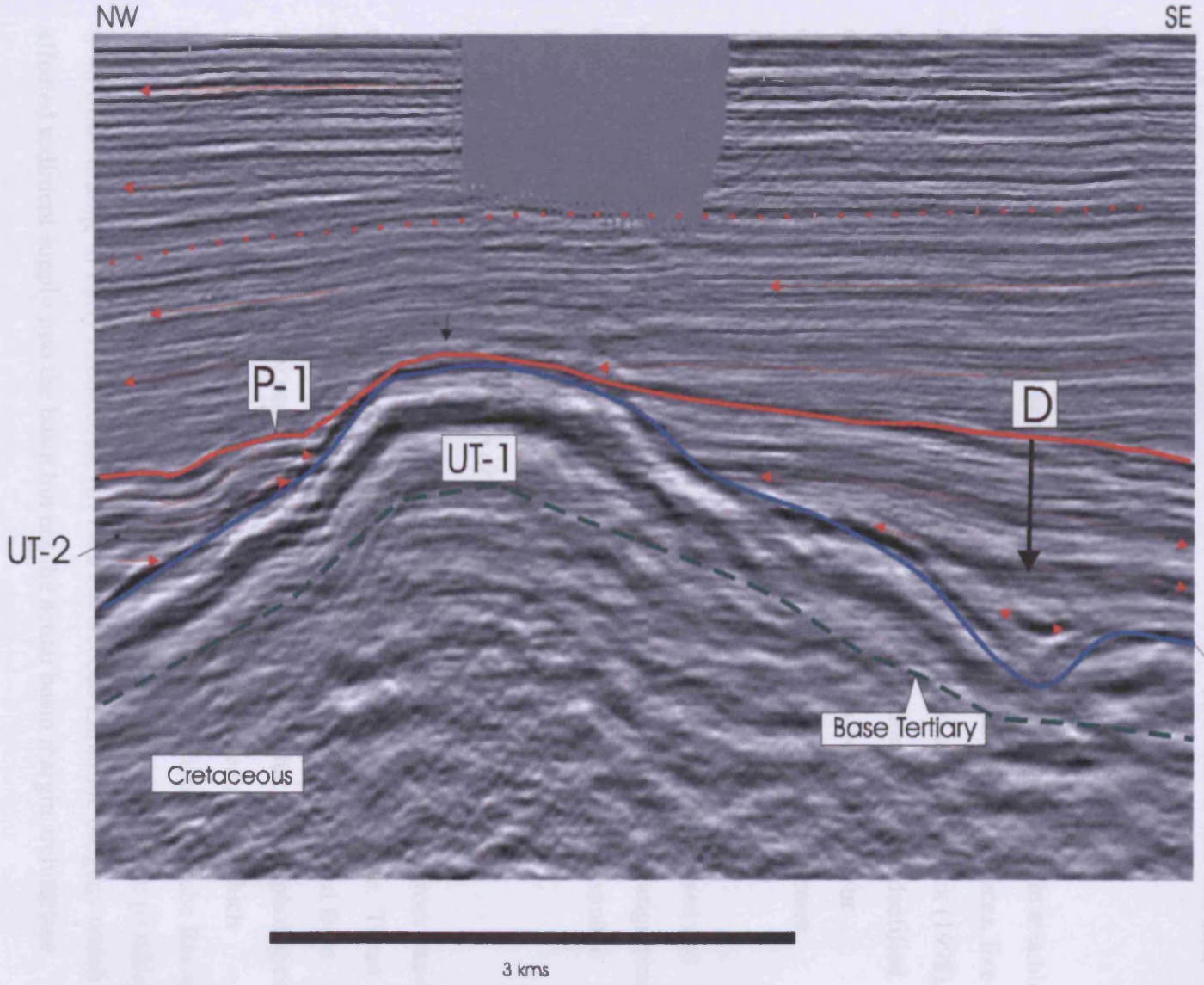

Figure 2.29
Zoom of mound-like feature shown in Transect 5. Note the continuous seismic character hosted in Unit UT-1, whereas in the Cretaceous Unit a transparent to semi-continuous seismic character predominates. Towards the south-western base of the mound structure note the incised channel-like feature (D), filled in with apparent concave upwards reflections. Within Unit UT-2 seismic reflections onlap onto the mound-like structure.

The angle between the foresets and topsets in Transect 1 is much shallower than the angle observed in Transect 5, suggestive of a higher slope gradient during the deposition of the foresets.

It is important to mention that this apparent difference in clinofrom geometry observed in from Transect 1 and 5 may be due to the relative orientation of these with respect to the real depositional dip of the clinoforms and the sediment source. These possible differences in clinoform geometry may only be resolved with the further analysis of three-dimensional seismic data. However, it is unfortunate that this data was not available for this project.

2.3.4 Summary and discussion

The analysis of five 2-D seismic lines provided the delineation of eight seismic boundaries (Figure 2.23 and Enclosures 1 to 5). From the eight seismic surfaces, five are coincident with the seismic-stratigraphic picks defined and used by Pemex (1998), enabling the dating of the five horizons. The remaining two horizons were identified on the basis of their prominent regional continuity where the underlying and/or overlying reflections terminate against them. The six horizons defined by Pemex adhere to this basis.

From the analysis of the five sections the following points are addressed and discussed: (1) basin margin architecture, and structural trends influencing stratigraphic development (2) stratigraphic development, and (3) development of unconformable horizons and their driving mechanisms.

2.3.4.1 Evolution of the basin margin architecture

The location of the five transects permitted the interpretation of the gross basin margin architecture and its structural-stratigraphic development through time. These findings, integrated with the basin evolution of the Gulf of Mexico as distilled from various authors and previously presented in section 2.2, suggest that the morphological evolution of the basin margin architecture can be divided into three stages which influenced the stratigraphic development patterns encountered in the Campeche Basin. The three suggested stages correspond to major tectonic events (Figure 2.30): (i) rifting from Mid-Jurassic to Early Cretaceous; (ii) Late Cretaceous Laramide orogeny which affected sediment supply into the basin but not the actual basin margin architecture.

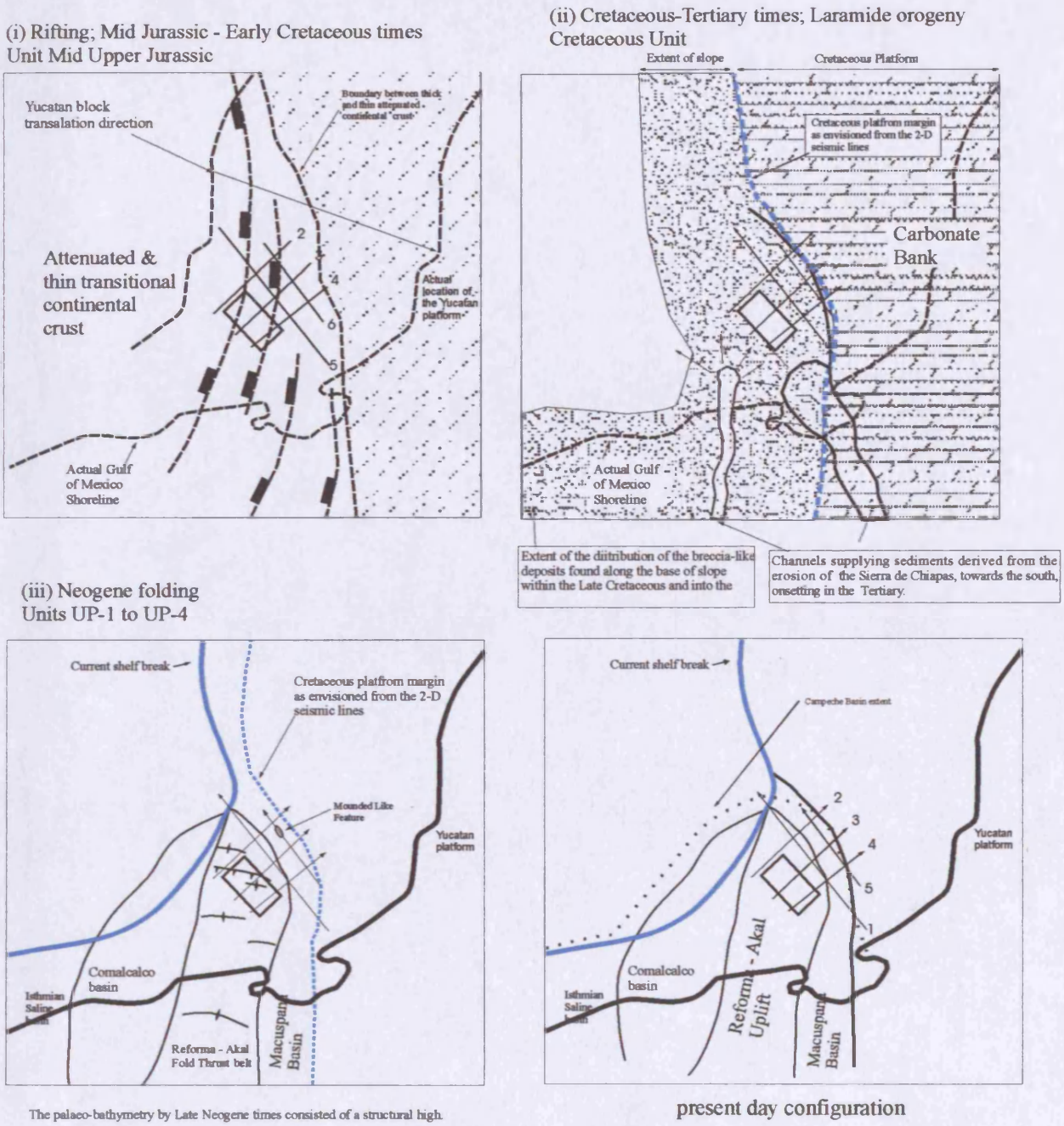

Figure 2.30
Sketches representing the three different development stages of the basin margin and the resulting structural trends that influenced the stratigraphic development. See Figure 2.2 for the regional context. (i) Opening of the Gulf of Mexico occurred during the Mid-Upper Jurassic to early Cretaceous, the Yucatan block drifted southward from the actual Texas shoreline; extensional faults occur throughout the study area that displace Jurassic sequences and in portions root into the acoustic basement. Sketch is representative for the deposition of the Mid Upper Jurassic Unit. (ii) In the Early Cretaceous times the Yucatan block had reached is current position, and the gross Gulf of Mexico configuration was established; a carbonate bank was seeded upon the Yucatan block, whose carbonate production peaked during the Cretaceous time, aggrading and shedding vast amounts of carbonate down slope and into the basin. Note that the extent of the carbonate bank was controlled by the distribution of thick continental crust, compare (i and ii). Sketch representative for deposition of the Cretaceous Unit (iii) During the Neogene along the western margin of Mexico the Chortis block collides with the Sierra de Chiapas generating complex strike slip tectonics, as a result of this event folding and thrusting occurred along the Reforma-Akal Uplift region . Sketch representative of deposition of Units UP-1 to UP-4.

Instead, the Laramide orogeny resulted in the formation of folds along the western Mexican margin (Sierra Madre Occidental), resulting in the exhumation of sedimentary successions and formation of igneous bodies whose erosive by-products fed the Campeche Basin; (iii) Neogene folding resulted from the collision of the Chortis Block against the Sierra de Chiapas and the suturing of the Caribbean sea, referred to as the Chiapaneca orogeny (Galloway, 1991; Pindell 2000; Figure 2.6D).

From the regional transects, two major basin margins are recognised: the Cretaceous carbonate platform and the present day clastic shelf break (Enclosure 1). The nature of the margin profile of the early Gulf of Mexico (Early to Late Jurassic) is not interpretable from these transects. Instead a conceptual model for the basin margin architecture for this period is proposed, based mainly on previous works (See Chapters 3 and 4).

Palaeomagnetic studies and well data provide evidence that the Yucatan Peninsula is underlain by thick continental crust which changes basinwards into thinner continental crust. The boundary between thick continental crust and thin transitional continental crust appears to be coincident with the envisioned Cretaceous platform margin, as suggested from the 2D seismic lines and the distribution of the crust (Buffler, 1985) and (Figures 2.7 and 2.2). Although this assumption is not conclusive because the vertical extent of the seismic data (0 to 4.6 msec) does not permit the recognition of the basement geology. If the above suggestion is the case, then the distribution of the thick continental crust controlled the seeding and areal development of the Yucatan carbonate bank, and in consequence the basin margin arrangement.

The Cretaceous margin, as envisioned from the five interpreted transects, resembles an embayment that opened north to northwest and parallels the shoreline of the Yucatan Peninsula (Figure 2.30). The transition from the platform into the open sea consisted of a shallow continuous dipping (5°-10° degrees), broad slope. The platform was flat topped and locally a rugged margin texture is observed, with overlying downlapping reflections (Enclosures 2 and 3 and Figure 2.30). The stratal configuration observed within the Mesozoic succession, is consistent with the hypothesis that the Mesozoic sediments of the Cantarell area were deposited in a deepish setting (see Sections 2.2.3. and 2.2.4. of this Chapter). This environmental setting is further supported with the facies and the biostratigraphic record observed in

core data (see Appendices 1 and 2). However, the precise depth range cannot be inferred from the seismic evidence, and the biostratigraphic reports provided by Pemex do not suggest any depth range.

2.3.4.2 Seismic stratigraphic development

From the reflection configurations three types of major stratigraphic packages are suggested as modes of basin fill (Figure 2.31). (i) The interval from the Mid Jurassic to Mid Miocene (Mid Upper Jurassic, Cretaceous and UT-1 seismic units) was dominantly aggradational, possibly with cycles of retrogradation and progradation (Figure 2.31, stages 1-4). However these are not readily observed, due to the limited vertical resolution of the seismic data. Internally the stratigraphy consists of carbonates found within the Mesozoic succession; which passes into clastic sedimentation during the Palaeogene. This stratigraphic package is bounded at the top by the Mid-Miocene Horizon, which locally has eroded the underlying successions. This erosion is interpreted as palaeo-canyons or large channels. The orientation of these erosional features is north-east to south-west, and they are interpreted to be incised by currents flowing from the north-east platform margin, on the basis that the concave upward features observed in Transect 5 are aligned with those observed in Transect 1 and become enlarged in Transect 1 (Figure 2.31)

From the basin margin architecture observed in the seismic transects, and the internal seismic fill assemblage geometries, a ramp or distally over-steepened ramp depositional system is suggested for the Early to Upper Cretaceous (Campanian). The Early Cretaceous basin margin consisted of a gentle slope (3-10 degrees) that broadly extended into the deeper inner basin. The upper slope to platform margin is not well constrained in the interpreted transects (Enclosures 2 to 4). It is assumed that the slope to platform boundary lies landwards from the actual transects.

During the Late Cretaceous and into the Early Palaeocene it is proposed that the over-steepened ramp system experienced structuration and development of a platform margin, which possibly collapsed and backstepped, as suggested by the seismic appearance of the Upper Cretaceous margin (Figures 2.24 to 2.26 and figure 2.31 (2A)). Further supporting evidence consists of widespread occurrence of 80 to 200 metres thick Late Cretaceous – Early Palaeocene polymictic breccia, which blankets a large area deposited over calcareous rocks of hemipelagic origin. Internally, this Late

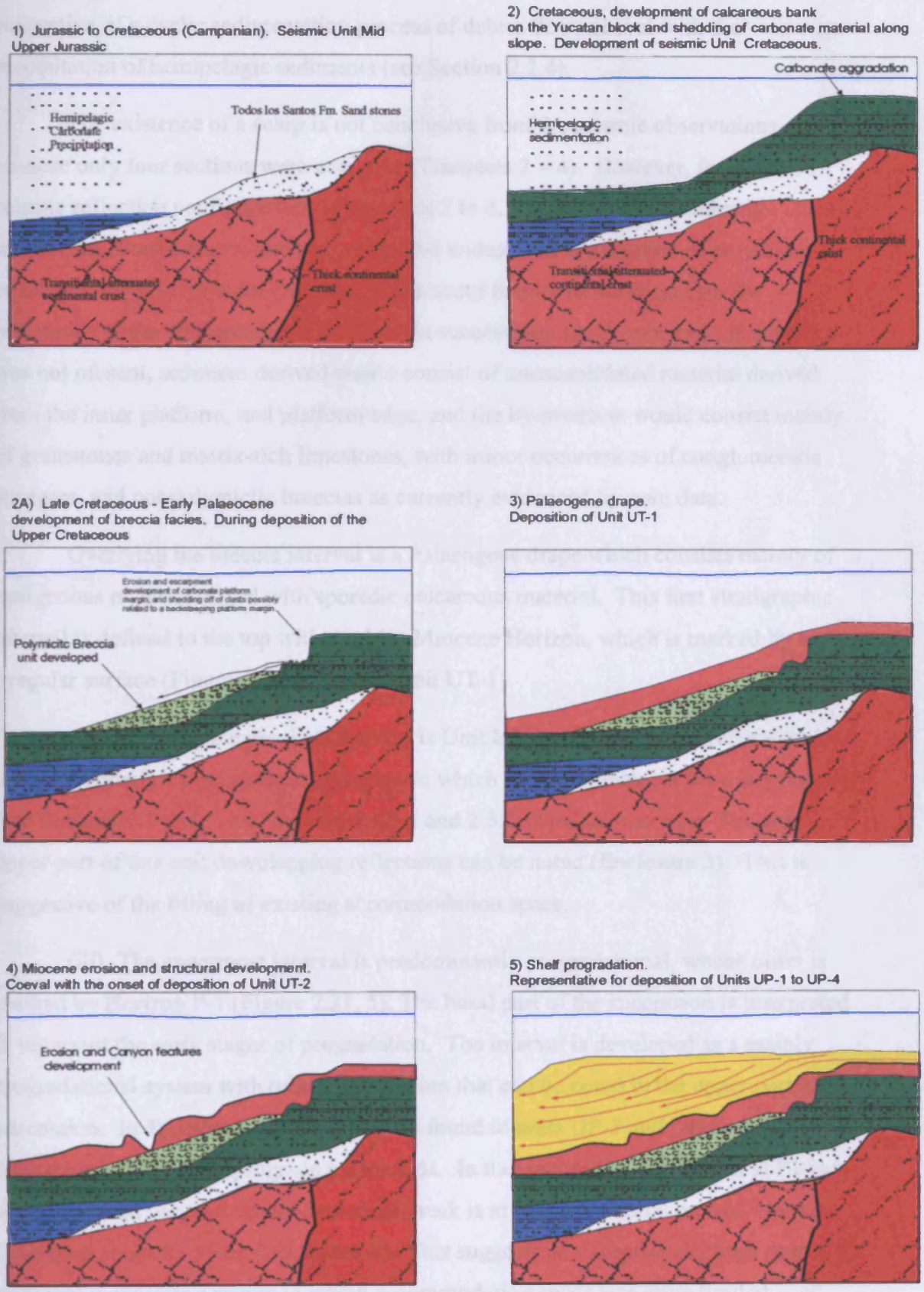

Figure 2.31
Schematic profiles illustrating the stratigraphic development through time for the basin margin configuration of the Campeche Basin. The stratigraphic development is presented from the Late Jurassic to Recent in six stages. This conceptual evolutionary model is derived from the analysis of five seismic transects (Enclosures 1 to 5), and the integration of previous geological literature.

Cretaceous breccia contains intercalations of hemipelagic sediments which are suggestive of a cyclic sedimentation process of debris flows coeval with the precipitation of hemipelagic sediments (see Section 2.2.4).

The existence of a scarp is not conclusive from the seismic observations, because only four sections were available (Transects 2 – 4). However, from the seismic reflection configurations in transects 2 to 4, a scarp can be confidently interpreted. Furthermore, the occurrence and widespread distribution of polymictic breccia deposits favours the occurrence of a scarp feature as the source for the polymictic clasts encountered in this breccia succession. On the contrary, if the scarp was not present, sediment derived would consist of unconsolidated material derived from the inner platform, and platform edge, and the by-products would consist mainly of grainstones and matrix-rich limestones, with minor occurrences of conglomeratic stringers, and not polymictic breccias as currently evidenced by core data.

Overlying the breccia interval is a Palaeogene drape which consists mainly of terrigenous material mixed with sporadic calcareous material. This first stratigraphic interval is defined to the top with the Mid-Miocene Horizon, which is marked by an irregular surface (Figure 2.31, 3, seismic unit UT-1).

(ii) Overlying the previous interval is Unit UT-2, which exhibits reflections that infill the underlying irregular bathymetry on which erosional features were developed (see Enclosure 1 and 5, and Section 2.3.3.1 and 2.3.3.5) palaeo-canyons. Towards the upper part of this unit downlapping reflections can be noted (Enclosure 3). This is suggestive of the filling of existing accommodation space.

(iii) The uppermost interval is predominantly progradational, whose onset is marked by Horizon P-1 (Figure 2.31, 5). The basal part of the succession is interpreted to represent the early stages of progradation. The interval is developed as a mainly progradational system with minor aggradation that can be noted in the upper part of the succession. In Transect 1 the offlap breaks found in units UP-3 and UP-4 appear almost horizontally and prograde basinwards. In this section the shelf break at P1 is at about 1 second twt, and the modern shelf break is at about 250 milliseconds, having prograded about 87.5 km, (Enclosure 1). This suggests an exceptionally high rate of sediment input over a region in which accommodation space was quite limited, favouring a progradational depositional system for units UP-3 and UP-4. The seismic

reflection configuration observed within this interval are downlapping, consisting of clinoforms with topsets that are characteristic of prograding basin margins (Galloway, 1989). Well data shows that this massive progradational system is largely terrestrial in origin, and this system is therefore interpreted as a large delta.

The timing of the onset to a phase of full development of the progradational sequence is coincident with the development of the Sierra de Chiapas, 250 km south of the Cantarell area. Meneses-Rocha (2001) suggests that the Sierra de Chiapas develops as result of a triple junction collision of the Caribbean, American and Cocos plates. The structuring began at the end of the Cretaceous and lasted until the Late Miocene to Pliocene, with episodes of structural quiescence and structural rejuvenation (Meneses-Rocha, 2001). It is noteworthy that fluvial discharge of the Sierra de Chiapas is still found south of the Cantarell area. This further strengthens the interpretation of a post Mid Miocene delta along part of the continental margin. The development of this major clastic flux is highly significant for petroleum generation, migration and entrapment.

2.3.4.3 Development of Unconformity

The top of the aggradational system is marked by the Mid-Miocene Horizon. This horizon exhibits characteristics that can be interpreted as a result of pervasive erosion. Erosional truncation and downlapping are readily apparent and prominent. The palaeo-platform has a flat profile at this level, and the palaeo platform margin appears to have been strongly affected by erosion, with evidence of slope failure and incision (Enclosure 5, and Figure 2.27). At the base of slope, reflections exhibit concave-up erosional features that can represent shelf erosion as a result of along-shore currents. Along the slope, at the base of slope, three "palaeo-canyons" or "channel" features are also evident (see Enclosures 1 and 5).

From the seismic reflection terminations it is suggested that the Mid-Miocene Horizon represents a period of relative sea level fall which probably exposed the shelf and most importantly, structural highs (the Cantarell structure). Projection of the likely position of greatest lowstand from the exposed platform into the basin, shows that the crest of Cantarell could have been exposed at this time (Figure 2.32 and Enclosure 3). Additionally well core evidence exhibits dissolution vugs and fracture patterns that have been previously interpreted as karstic fabrics (Horbury, 2001; see Chapter 3,

Section 3.4.3.3). Furthermore, the seismic analysis of the Cantarell seismic cube shows the local occurrence of the Mid-Miocene Horizon in direct contact with Cretaceous successions at the crestal zones of the structure. Furthermore, faults found within the crest of the structure are recognised to propagate up stratigraphy reaching the unconformity surface. This fault and fracture network provides direct pathways for fluid migration into the Cretaceous successions (see Chapter 6).

2.4 Conclusions

The geological regional setting proposed in this Chapter is a result of a detailed analysis of five 2D regional seismic lines and previous works. The most important observations derived in this Chapter include:

1. The Cantarell area is located in an area that is underlain by thin transitional continental crust. The stratigraphy consist of a carbonate dominated interval for the Upper Mezosoic and terrigeneous dominated for the Cenozoic.
2. The depositional setting is interpreted to have evolved from a shallow ramp setting during the Jurassic to a scarp dominated platform margin setting at the end of the Cretaceous. During the Cenozoic the basin underwent further significant subsidence, the carbonate factory switched off and major supply of terrigenous sediments entered the basin.
3. Two types of major stratigraphic packages are seen from the seismic lines which consist of a dominant aggradation interval (Mid Jurassic to Mid Miocene) and an overlying progradational system.
4. The present day structural configuration as seen from Transect 4 allows suggesting that the crest of the Cantarell structure was possibly subject to subaerial exposure. As seen from a projection of the likely position of greatest lowstand from the exposed platform margin into the basin.

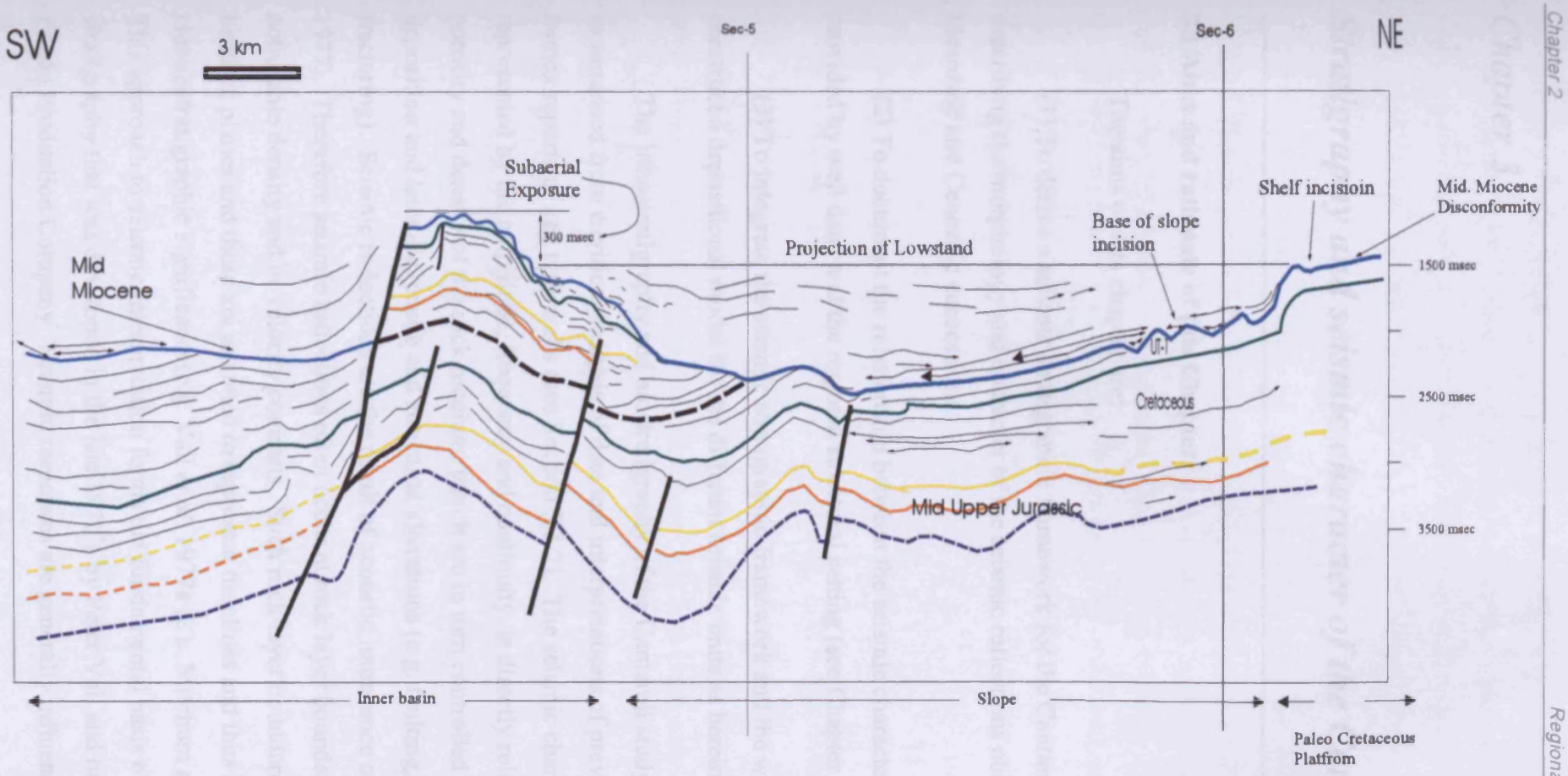

Figure 2.32
Seismic line drawing for Transect 3 depicting the projection of possible greatest lowstand related to structural development. Note the crestal area of Cantarell was possibly subject to subaerial exposure where an average of 300 msec twt is calculated for the relief of exposure.

Chapter 3

Stratigraphy and seismic character of the Cantarell area

3.1 Aims and rationale of this Chapter

The aims of this chapter are:

(1) To derive a seismic stratigraphic framework for the Cantarell Field, by describing the morphology and character of the seismic reflections observed within the Mesozoic and Cenozoic successions.

(2) To document the relationship between the seismic character, lithology provided by well data, and the regional structural setting (see Chapter 4).

(3) To integrate the seismic stratigraphic framework and the well data to construct a depositional model for the different seismic units as herein defined.

The lithostratigraphy and biostratigraphy of the Cantarell study area is summarised from a critical analysis of data and interpretations of previous internal Pemex reports of key type wells (see Section 3.3.2). The seismic character, which is represented by the amplitude, frequency and continuity, is directly related to the porosity and density of the rock medium, which are in turn controlled by the initial deposition and later diagenetic and structural alterations (e.g. faulting, folding, fracturing). Seismic reflections are the result of acoustic impedance contrasts (Sheriff, 1977). Therefore seismic reflections often occur at rock layer boundaries that have noticeable density and/or velocity contrasts. Such rock layer boundaries include bedding planes and these are assumed to represent timelines and thus have chronostratigraphic significance(e.g. Vail *et al.* 1977a & b, Mitchum and Vail 1977). This approach to seismic interpretation forms the fundamental basis of seismic stratigraphy that was developed in the late 1970's by Peter Vail and his co-workers at Exxon Production Company. Seismic responses are generally influenced by the

porosity, pore compressibility, fluid saturation, fluid type and mineralogy of the host rock (Gregory, 1977). Carbonate rocks tend to have complicated pore systems, such as vugs, moulds, channels, and fractures. Different types of pores have different compressibility, which in turn affect seismic wave velocities in a different manner (Wang, 1997).

The layout of this chapter takes the form of four main sections. Section 3.3 presents the data and the methodology for the definition of the stratigraphic framework of this study. Section 3.4 presents a lithologic and biostratigraphic description for the defined seismic units based on well data. Section 3.5 presents the seismic character of the defined seismic units. Section 3.6 integrates the previous observations into a model that best represents the depositional environments interpreted for each seismic unit. This model provides insights into the different sedimentary and structural processes interpreted.

3.2 Data

A vast amount of well data (over 260 wells), were available for this study. Each well represents a significant amount of lithological, petrophysical and age data. However the quality of the well data differs markedly and thus three different well sets were defined to analyse and underpin the different interpretative tasks; these being chronostratigraphic, lithologic and structural constraints (Figure 3.1). The first well set was defined to chronostratigraphically constrain the interpreted seismic horizons and tie the reflection seismic data to the Pemex stratigraphic markers. A second well set characterises the lithologies found within the different seismic units, and a third set was established to aid in the structural interpretation of the major thrust plane and the delineation of the footwall and hangingwall structural blocks (see Chapter 4).

The criteria defined for the well sets used in the lithostratigraphic calibration of the interpreted seismic units consists solely of those Pemex wells which have both well and core reports (Figure 3.1). Particular priority was given to wells with lithologic calibration of the petrophysical logs. For the structural interpretation, the defined well sets consist of wells that have both check-shot data and penetrated the footwall block (Figure 3.1). Biostratigraphic reports were primarily extracted from unpublished Pemex and IMP reports, as well as isolated published reports (Salazar-Medina, 2001).

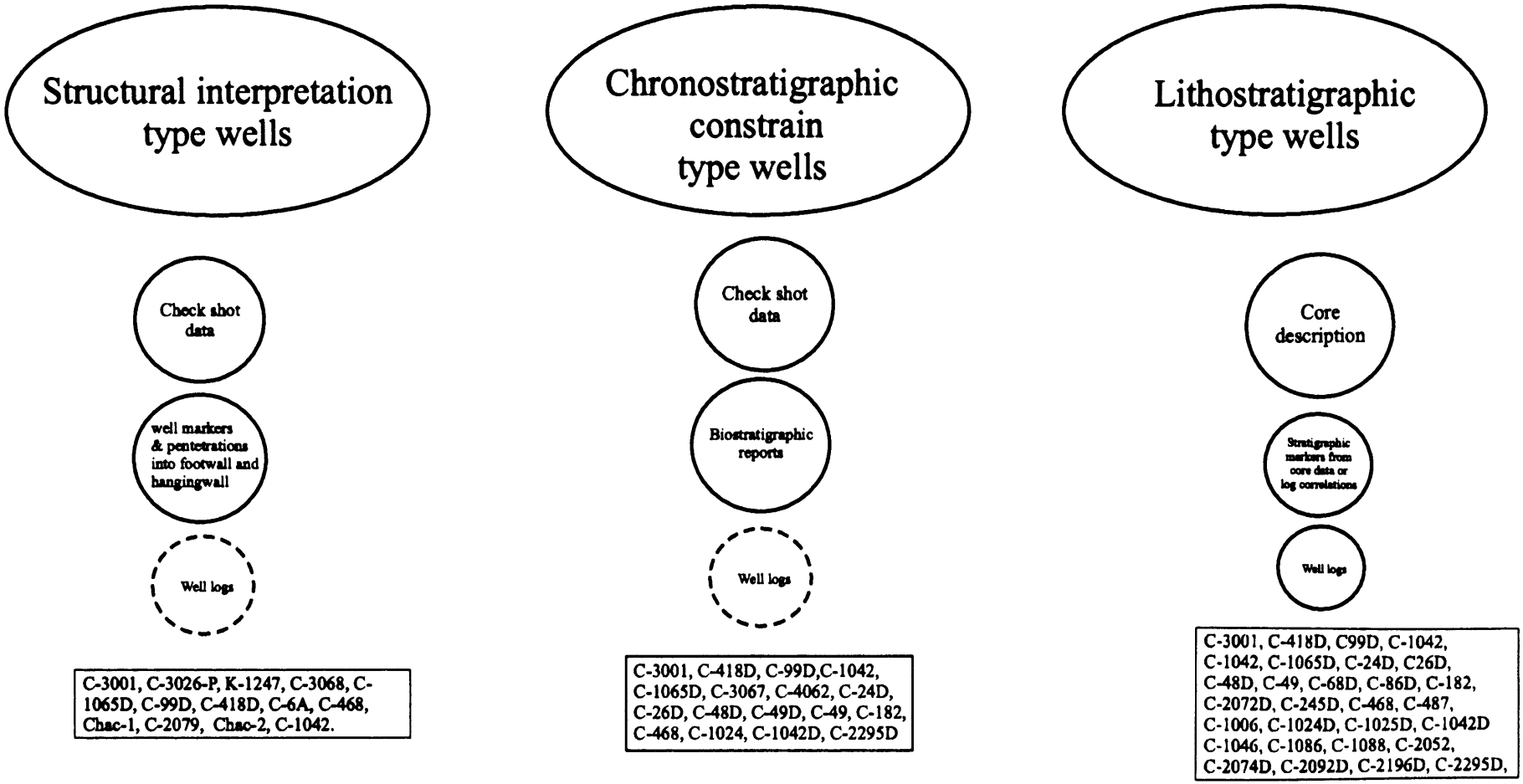

Figure 3.1
Diagram showing the different sets of wells defined as type wells and their associated well information. The different sets of type wells were defined according to the interpretative needs, these are shown in larger ellipses. The associated well data are shown in circles. The size of the circle denotes the degree of importance.

These reports were used to constrain the age of the different seismic horizons. Unfortunately no palaeo-bathymetric data has been released by Pemex, and no published reports exist for the Cantarell study area, and thus does not allow the integration of palaeo-water depth data for the different seismic units studied.

An ocean-bottom-cable (OBC) 3-D seismic survey (Figure 3.2) acquired over the Ixtoc, Akal, Sihil, Nohoch, Chac and Kutz oil fields (covering 750 km2) was used to identify and map the lower and upper boundaries of the seismic units. Other seismic reflection terminations such as erosional truncation, and onlap were subsequently mapped and interpreted in accordance with standard seismic-stratigraphic methodology advocated by Mitchum et al (1977) and Brown and Fisher (1977).

3.3 Stratigraphic nomenclature

3.3.1 Introduction

An informal stratigraphic scheme is presented, based on the interpretation of key seismic reflections (Figure 3.3). These were chronostratigraphically and lithostratigraphically calibrated with the stratigraphic nomenclature defined by Pemex using key wells. Five gross seismic units (J-1, K-1, T1, T2 and T3) were defined (Figure 3.3). Various seismic horizons have been interpreted internally within these units to add detail in specific areas of interest.

The well stratigraphic scheme developed by Pemex geologists and consultants was based on palaeontological analysis and correlation of well logs. Biostratigraphic analyses were performed on cores, later calibrated against various well log responses (gamma, sonic, resistivity). The well log signatures were then correlated to other wells to define the current stratigraphic framework that Pemex employs. This stratigraphic framework is mainly based on an extrapolation of one-dimensional data (well data), lateral continuity provided by seismic data has been mainly omitted. This omission means that there is a clear requirement to test the accuracy of the lithostratigraphic scheme against the seismic data.

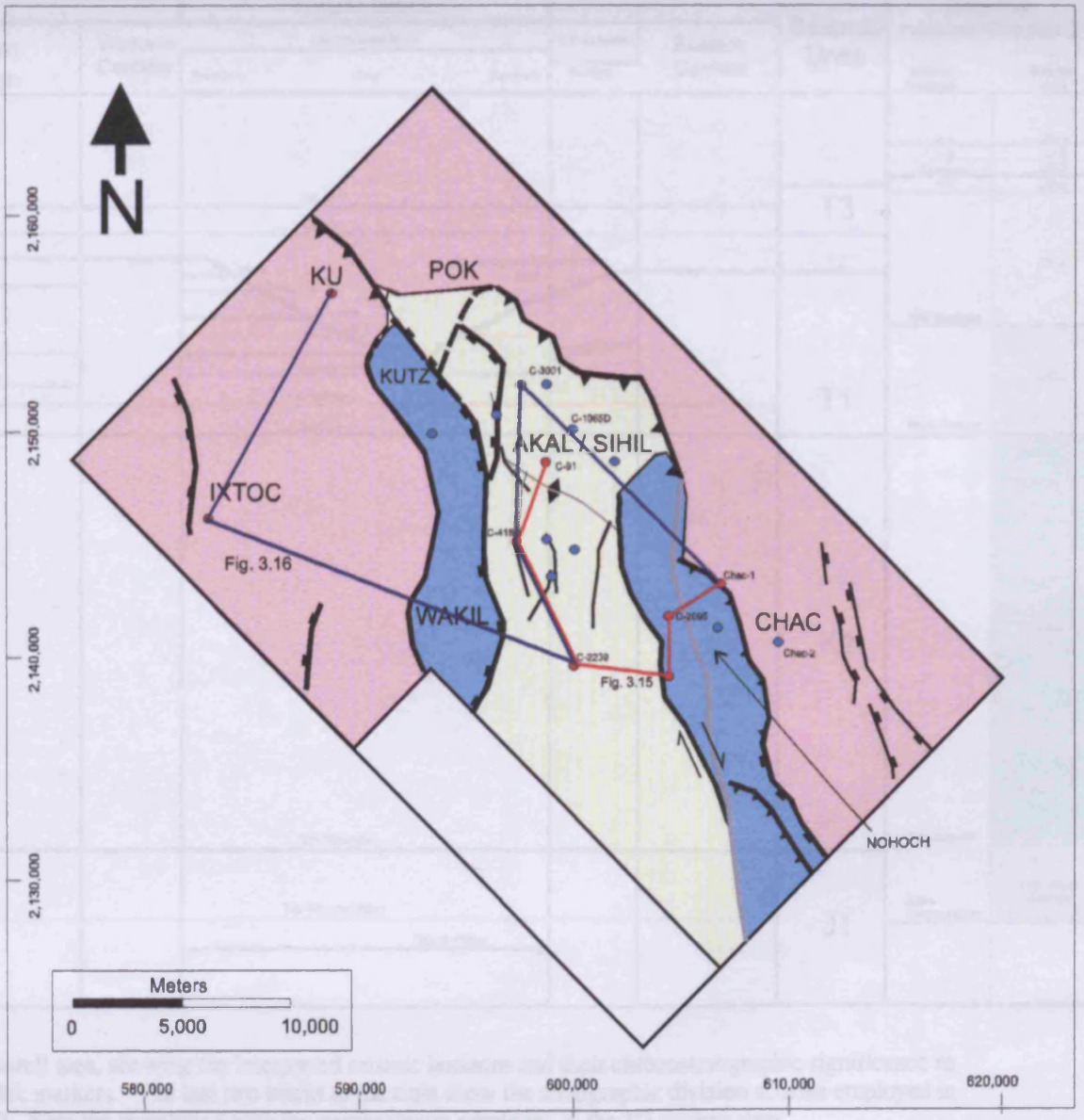

Figure 3.2
Layout of the seismic survey, and the defined structural elements. Wells are posted (blue dots) that have check-shot data used to age calibrate the different defined seismic horizons. Note the three structural elements defined: (1) at the centre, coloured in yellow, the main Thrust Block which contains the Sihil reservoir in the footwall and the Akal reservoir in the hangingwall; (2) adjacent to the Thrust Block, two narrow Fault Corridors shaded in blue (Eastern Fault Corridor and Western Fault Corridor) these contain the Kutz and Nohoch reservoirs, respectively; (3) two outermost least deformed areas Western and Eastern Platforms, these contain Ixtoc and Chac resevoirs, respectively.

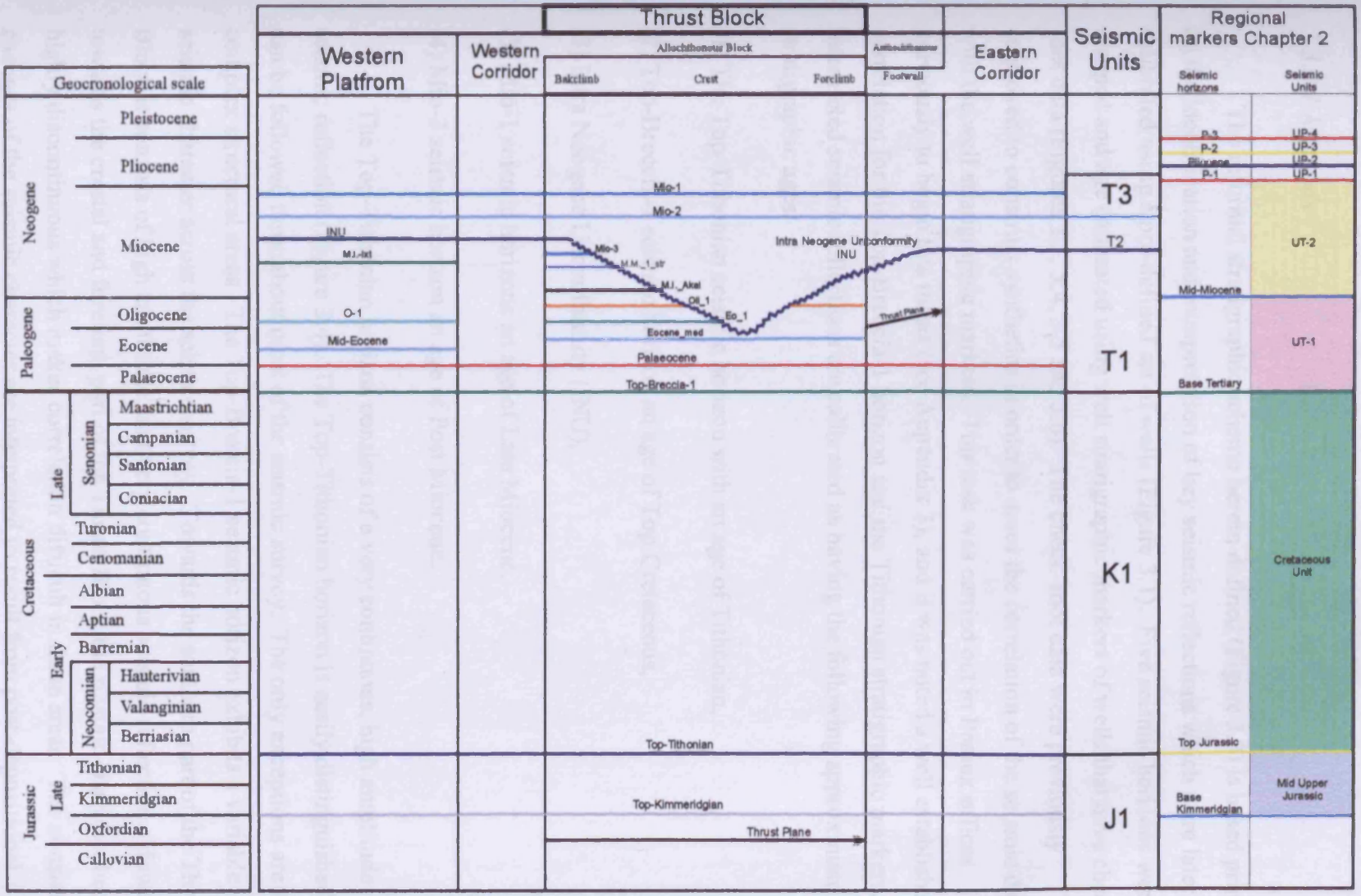

Figure 3.3
Stratigraphic chart for the Cantarell area, showing the interpreted seismic horizons and their chronostratigraphic significance as calibrated from well stratigraphic markers. The last two tracks to the right show the stratigraphic division scheme employed in the regional data, see Chapter 2. Note the correlation with the nomenclature employed in the 3D seismic data.

3.3.2 Methods and definitions

3.3.2.1 Methods

The informal stratigraphic scheme herein defined (Figure 3.3) is based primarily on the identification and interpretation of key seismic reflections which were later age calibrated using a pre-defined set of wells (Figure 3.1). Five seismic horizons were mapped and age calibrated using well stratigraphic markers of wells that have check-shot data (Figures 3.3, 3.4, 3.5 and 3.6). The check-shot data were previously employed to construct synthetics in order to asses the correlation of the seismic data with the well stratigraphic markers. This task was carried out in Pemex offices previously to begin this thesis (see Appendix 3), and it was noted a well established correlation for the Top-Breccia-1 horizon and the Tithonian stratigraphic markers. The interpreted seismic reflections are calibrated as having the following approximate stratigraphic ages:

(1) The Top-Tithonian seismic horizon with an age of Tithonian,

(2) Top-Breccia-1 seismic horizon an age of Top Cretaceous,

(3) Intra Neogene Unconformity (INU),

(3) Mio-1 seismic horizons an age of Late Miocene,

(4) Mio-2 seismic horizon an age of Post Miocene.

The Top-Tithonian horizon consists of a very continuous, high amplitude seismic reflection (Figure 3.4). The Top-Tithonian horizon is easily distinguished and can be followed throughout most of the seismic survey. The only exceptions are in complex structural areas. The Top-Breccia-1 seismic horizon exhibits a variable seismic character across the seismic survey. Towards the southern part of the Thrust Block it consists of high amplitude, and very continuous seismic reflection. However towards the crestal and forelimb part of the Thrust Block the seismic character becomes highly discontinuous which makes correlation difficult in these areas. The considerable changes of the seismic character are interpreted to result from post-depositional processes (tectonism and diagenesis, see Chapter 6). The Intra Neogene Unconformity (INU) horizon is defined based on seismic character (e.g. erosional truncation and

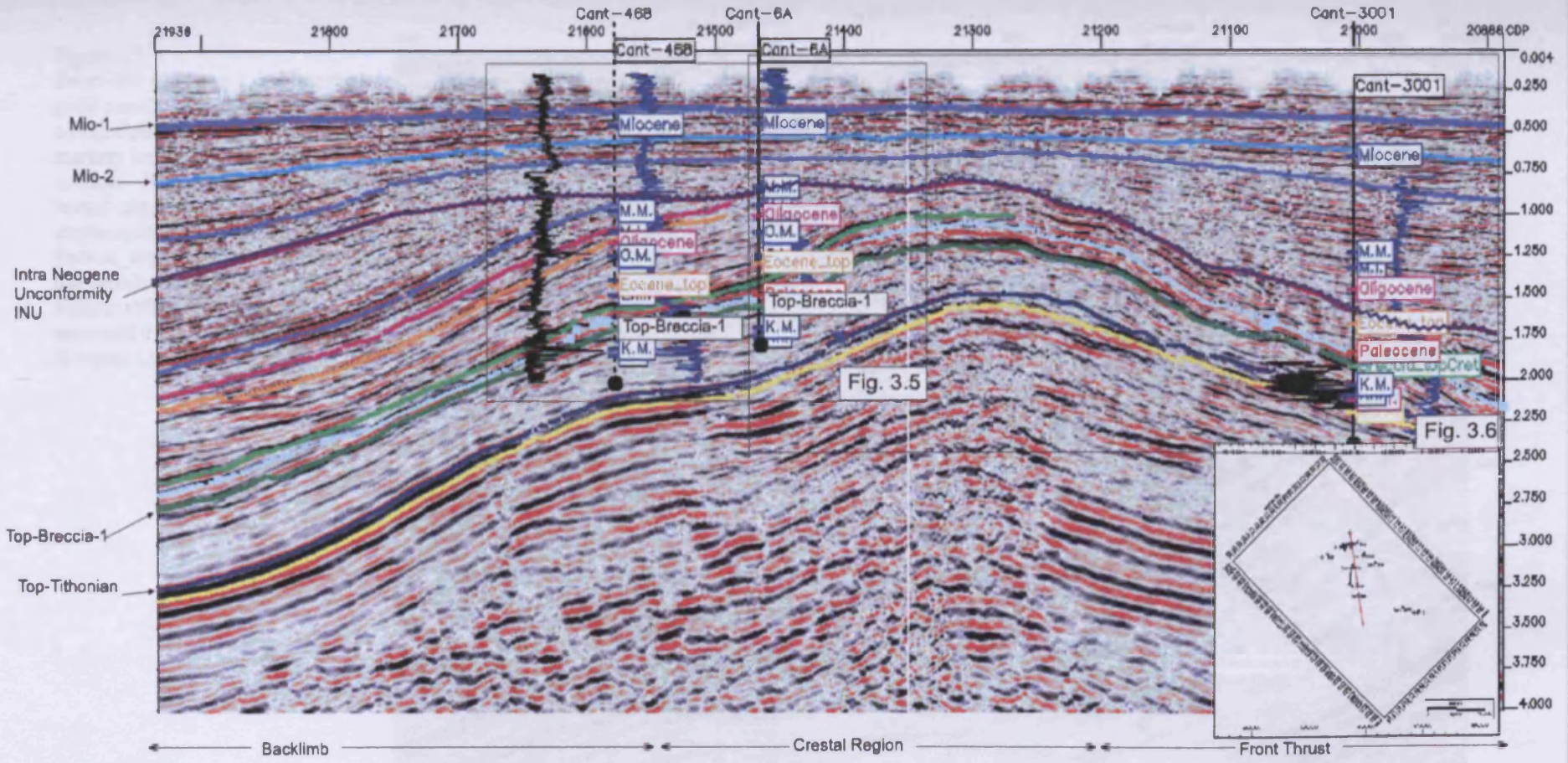

Figure 3.4
Seismic section oriented SE-NW with wells posted containing well stratigraphic markers as defined by Pemex. These wells have check-shot data that provided a good depth to time correlation. The seismic horizons have been defined seismically and time constrained using the well stratigraphic markers. Note the horizons defined within the Mesozoic (Top-Tithonian, Top-Breccia-1 and Palaeocene) show good correlation with the established stratigraphic markers at the three different well locations. Within the Cenozoic the well to seismic correlation is not well established.

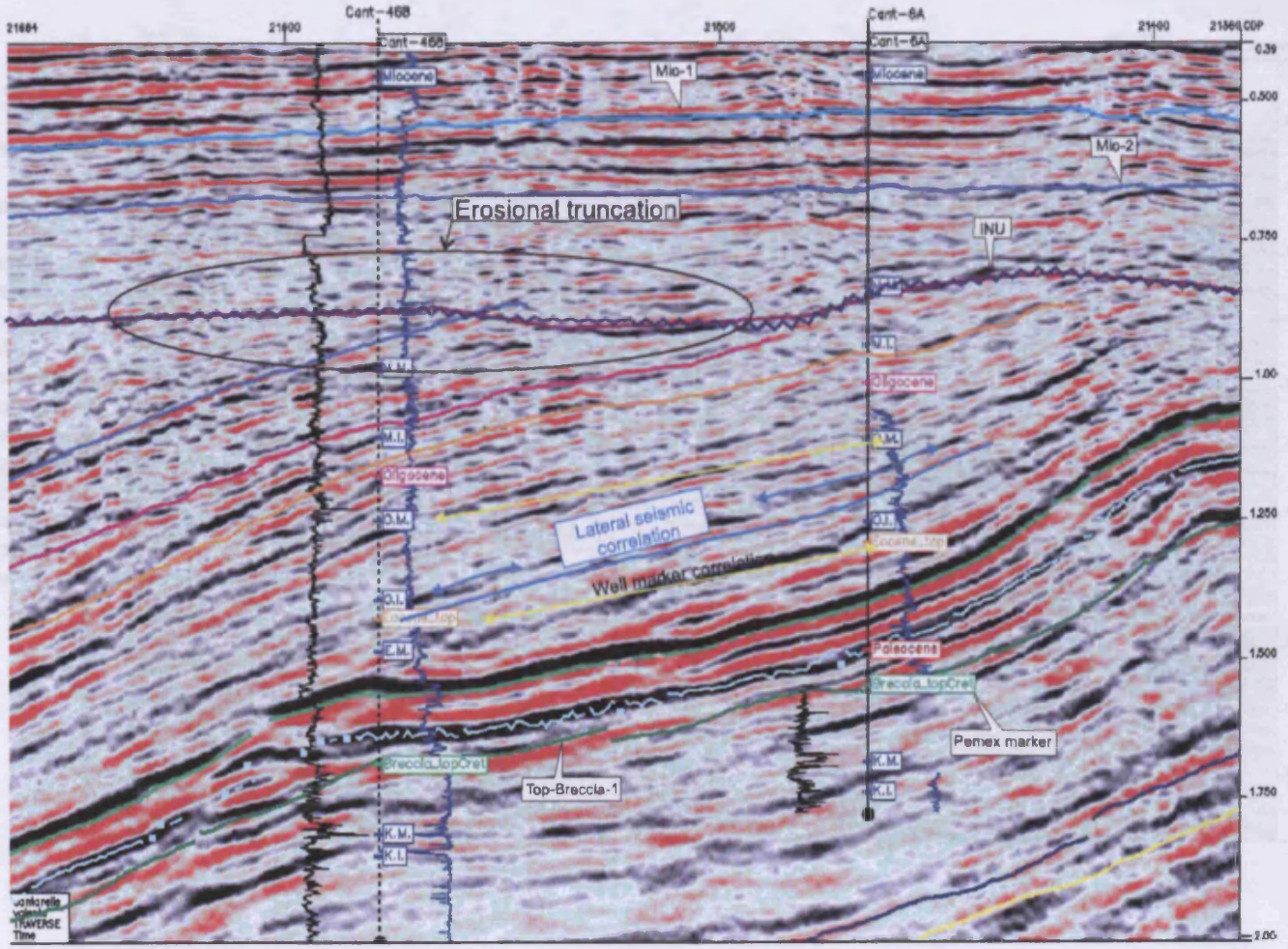

Figure 3.5
Zoom box of Figure 3.4. Note the good correlation between the seismic correlations and the well stratigraphic markers for the Top-Breccia-1 horizon. However by studying the lateral correlation of the well stratigraphic markers O.M., O.I. and Eocene_top, it is noted that these do not correlate consistently with the seismic reflections. Note the erosional truncation beneath the Intra Neogene Unconformity INU.

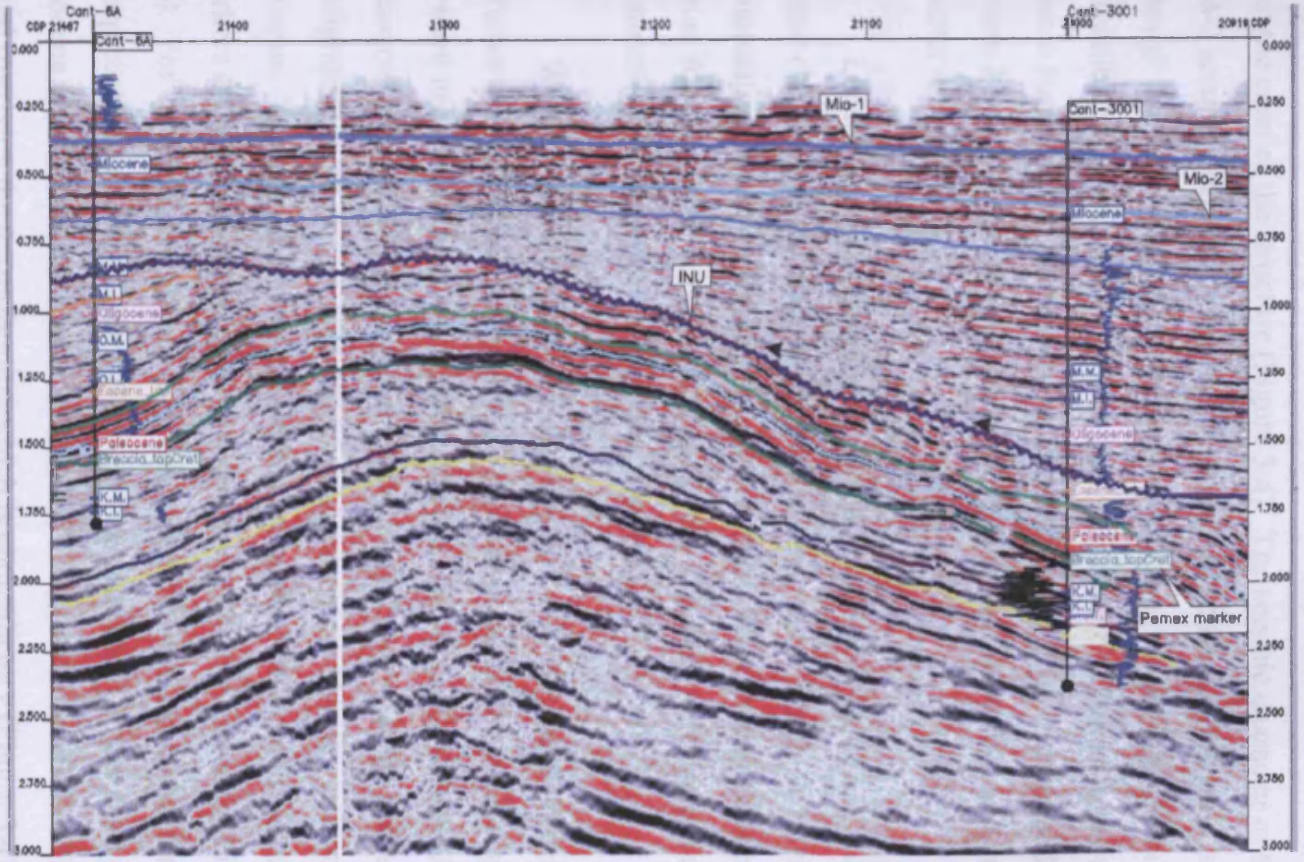

Figure 3.6
Zoom box from Figure 3.3, showing the well stratigraphic markers and the correlation with the seismic reflection horizons. Note that there is a good correlation between the seismic horizons Top-Breccia-1, Palaeocene, and mid Eocene, with both stratigraphic markers in wells C-6A and C-3001. The interpreted unconformity Intra Neogene Unconformity (INU) is located just beneath the M.M. marker as observed in well C-6A, however in well C-3001, the INU horizon intercepts the wellbore just above the Eocene_top marker. This is an example of the degree of uncertainty with the well stratigraphic markers that occur within the Cenozoic succession. Note onlapping configuration that occurs overlying the INU horizon.

onlap). The INU is interpreted as an unconformity that becomes conformable away from the crest of the structure (Figure 3.4). The seismic character of the Mio-1 and Mio-2 seismic horizons consists of medium amplitude continuous seismic reflections, although the seismic quality at shallow stratigraphic levels inhibits the accurate correlation of these surfaces (Figures 3.4, 3.5 and 3.6). From the above interpreted seismic horizons, the Intra Neogene Unconformity (INU) is described in detail in Section 3.5.5, whereas the other seismic horizons are described and interpreted in Chapter 4.

Local horizons were interpreted and correlated within the Cenozoic interval to further characterise and date the defined seismic units. Due to the structural complexities, it was impossible to jump-correlate these seismic reflections from the Thrust Block to the Platforms and through the Fault Corridors which are structural elements that were herein defined (see Chapter 4).

Wells containing check-shot data (Figure 3.2) were used to age constrain the different interpreted seismic horizons, which also revealed a general good correlation between the well derived stratigraphy and the seismic horizons hosted on the Upper Mesozoic interval. For the Cenozoic interval, uncertainty in the defined well stratigraphic markers was revealed when these were tied to the interpreted seismic horizons. There is not a well-established correlation between the interpreted seismic markers and the well picks, especially within the Miocene interval (Figures 3.4, 3.5 and 3.6). For example, stratigraphic markers of wells C-6A and C-468 that penetrate the interpreted unconformity (Intra-Neogene Unconformity), intersects a post middle Miocene interval, but in contrast well C-3001 suggests that middle Miocene strata are found overlying the unconformity, which is contradictory (Figure 3.4). Also minor well to seismic discrepancies have been documented within the Palaeogene (Figure 3.5).

3.3.2.2 Definition of structural framework

The areal extents of the interpreted seismic horizons are restricted and controlled by the structural complexities of the study area (Figure 3.2). Based on the seismic reflection configurations and fault arrangement, the study area has been divided into five structural blocks (Figure 3.2). The outermost and least deformed of these

structural blocks are referred to as the Western and Eastern Platforms. The central Thrust Block is defined as the most structurally complex area and is delineated on both sides by the Western and Eastern Fault Corridors. The Thrust Block is further subdivided into the hangingwall block and the footwall block. The hangingwall is subdivided into three regions: backlimb, crestal region, and the forelimb areas (Figure 3.2). In terms of reservoir names as used by Pemex, the hangingwall contains the Akal reservoir, the footwall the Sihil, and within the Fault Corridors, to the west is the Kutz and to the east the Nohoch reservoirs, respectively. The Western Platform contains the Ixtoc, and the Eastern Platform the Chac, reservoirs. For detailed description and discussion of the structural features of the Cantarell see Chapter 4.

3.4 Lithostratigraphic and biostratigraphic description

3.4.1 Introduction

This section presents the lithostratigraphic and biostratigraphic descriptions for the different successions as defined by Pemex, based on core and well cuttings of selected wells located in the different structural blocks. The information has been extracted from Pemex in-house well reports (Appendix 5). Composite logs were constructed for key wells (C-418D, C-91, C-2239, Chac-1, Chac-2, C-2095, C-3001, and C-1065D; Figures 3.7 to 3.14; for location see Figure 3.2). All of these wells except Chac-1 and Chac-2 are located within the Thrust Block of the study area. These composite well logs contain the following information: well logs (gamma ray GR, calliper Cali, sonic DT, density RHOB and resistivity, LLD and LLS); well stratigraphic markers as defined by Pemex and a summarised lithological description and biostratigraphic fossil indexes. The above-mentioned wells are used in the following descriptions that correspond to those judged to consist of the best quality and most representative data.

3.4.2 Jurassic

Sedimentary successions ranging in age from Oxfordian to Tithonian were encountered in various wells throughout the entire seismic survey (e.g. C-418D, C-91, C-2239, Chac-1, Chac-2, C-2095, and C-2011). The lithostratigraphy and biostratigraphy herein described were obtained from Pemex in-house well reports.

well C-418D

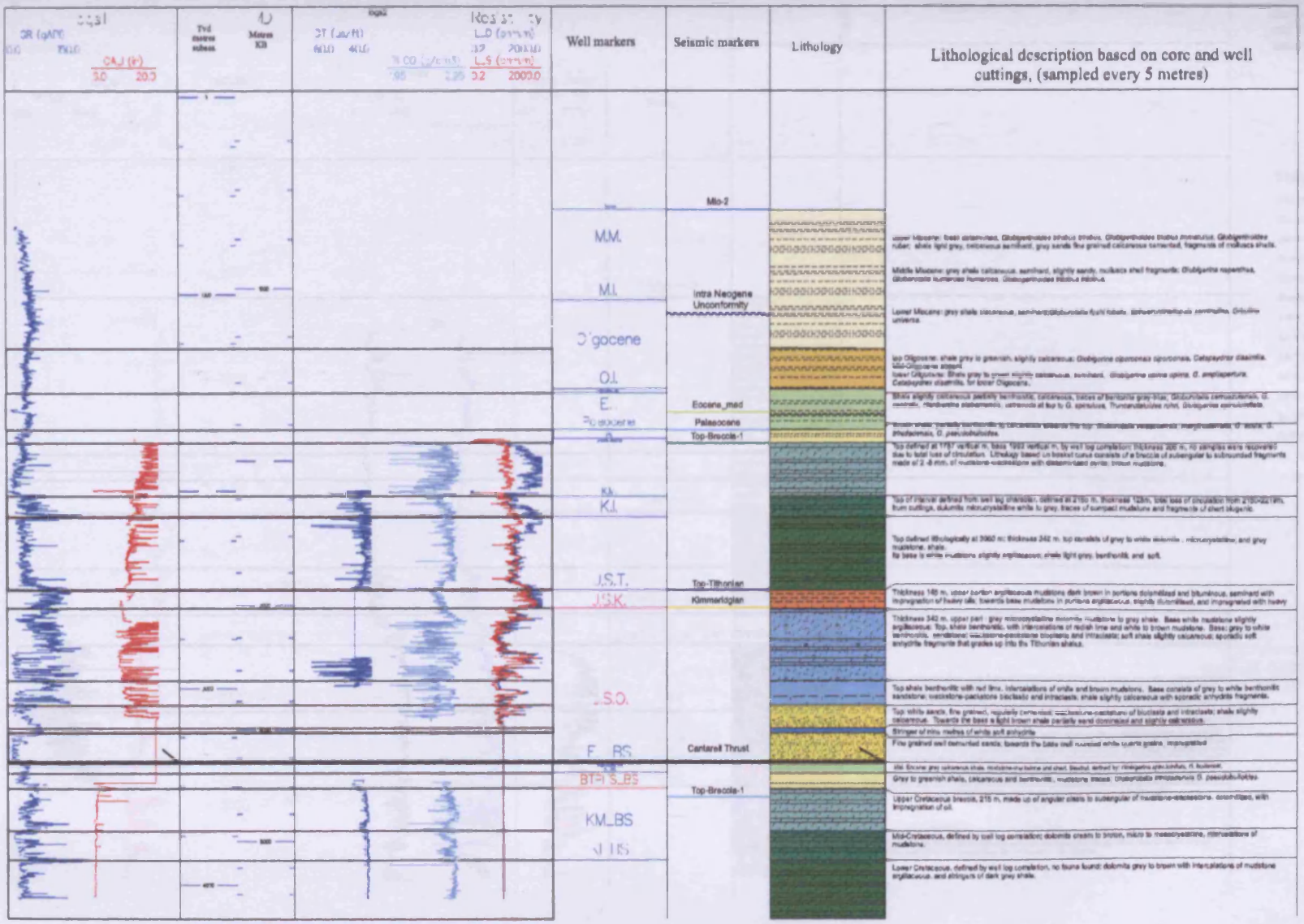

Figure 3.7
Composite log for well C-418D, displaying well logs, well stratigraphic markers provided by Pemex, seismic markers, lithologic and biostratigraphic descriptions based on well cuttings and core data. The seismic markers are calibrated using the defined stratigraphic nomenclature defined by Pemex. This well penetrates into the footwall block. For well location see Figure 3.2.

Figure 3.13
Composite log for well C-3001, displaying well logs, lithologic and biostratigraphic descriptions based on core data.

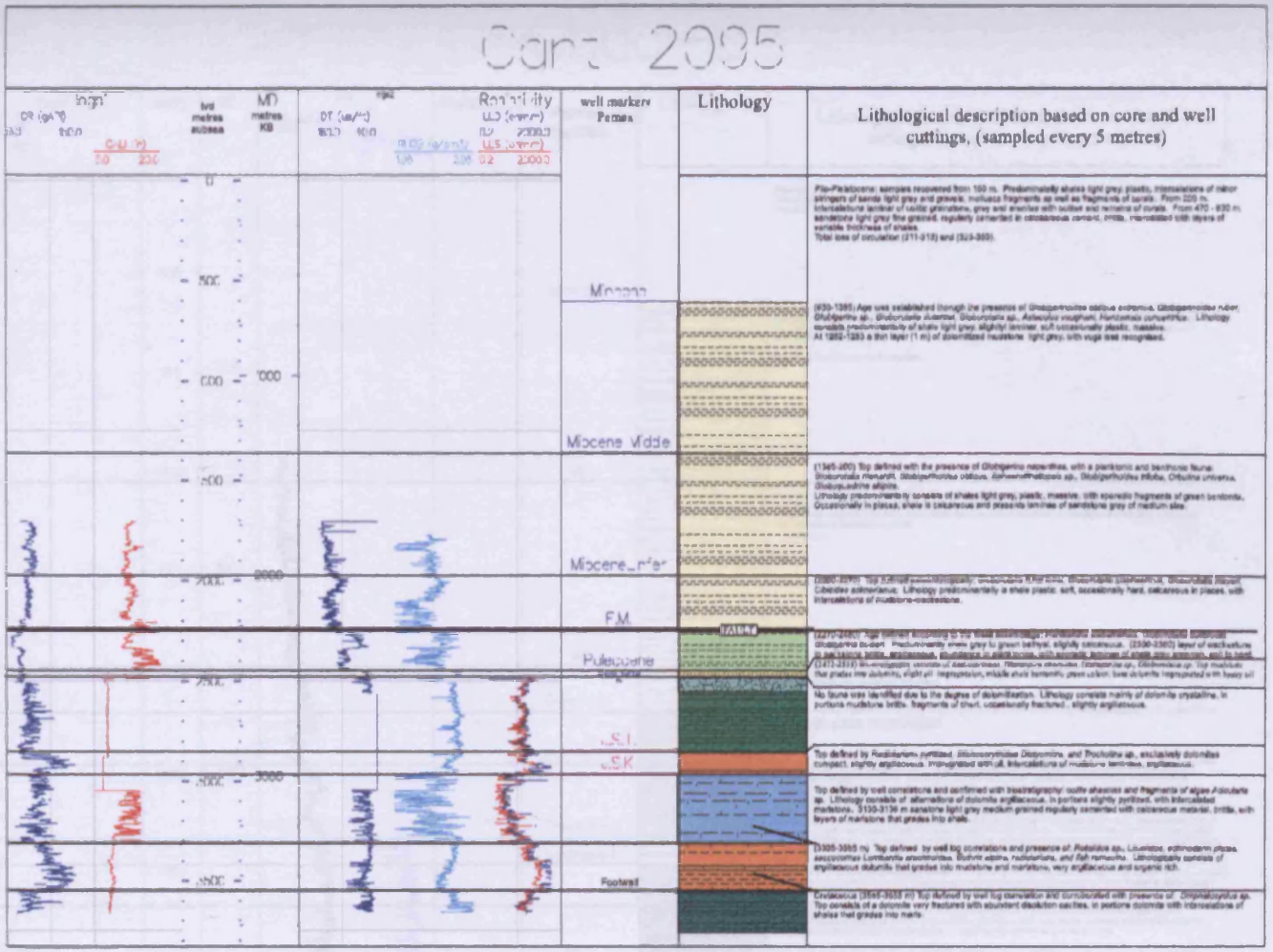

Figure 3.12
Composite log for well C-2095, displaying well logs, lithologic and biostratigraphic descriptions, and the stratigraphic nomenclature as distilled from Pemex inhouse well reports (Informe Final del pozo Cantarell No. 2095, Diciembre 1977 - Octubre 1978).

Stratigraphic key

M.M.=Middle Miocene
M. I. Lower Miocene
Oligocene
O.I.= Lower Oligocene
E.I.= Lower Eocene
Brecha_topCret= Top Cretaceous
K.M = Middle Cretaceous
K.I. = Lower Cretaceous
J.S.T. = Top Tithonian
J.S.K. = Top Kimmeridgian
J.S.O. = Top Oxfordian
E.I.-BS= Lower Eocene Footwall block
BTPKS_BS= Top Cretaceous footwall block
KM_BS= Middle Cretaceous footwall block
KI_BS= Lower Cretaceous footwall block

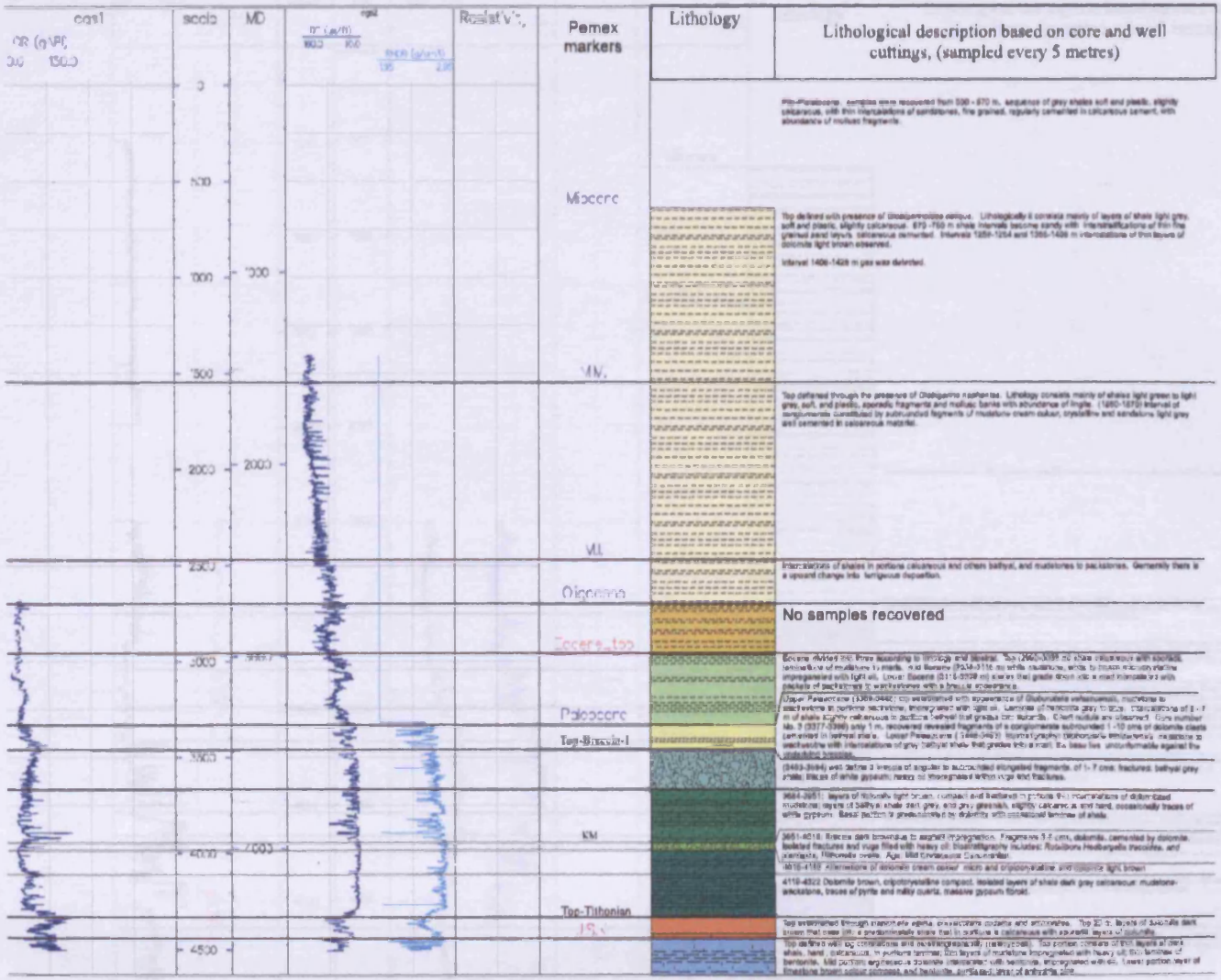

Figure 3.11
Composite log for well Chac-2, displaying well logs, lithologic and biostratigraphic descriptions, and the stratigraphic nomenclature as distilled from Pemex inhouse well reports (Informe Final del pozo Chac-2, Junio 1977 - Marzo 2 1978).

Stratigraphic key

M.M.=Middle Miocene

M. I. Lower Miocene

Oligocene

O.I.= Lower Oligocene

E.I.= Lower Eocene

Brecda_topCret= Top Cretaceous

K.M.= Middle Cretaceous

K.I. = Lower Cretaceous

J.S.T. = Top Tithonian

J.S.K. = Top Kimmeridgian

J.S.O. = Top Oxfordian

E.I.-BB= Lower Eocene Footwall block

BTPKS_BB= Top Cretaceous footwall block

KM_BB= Middle Cretaceous footwall block

KI_BB= Lower Cretaceous footwall block

Chac-1

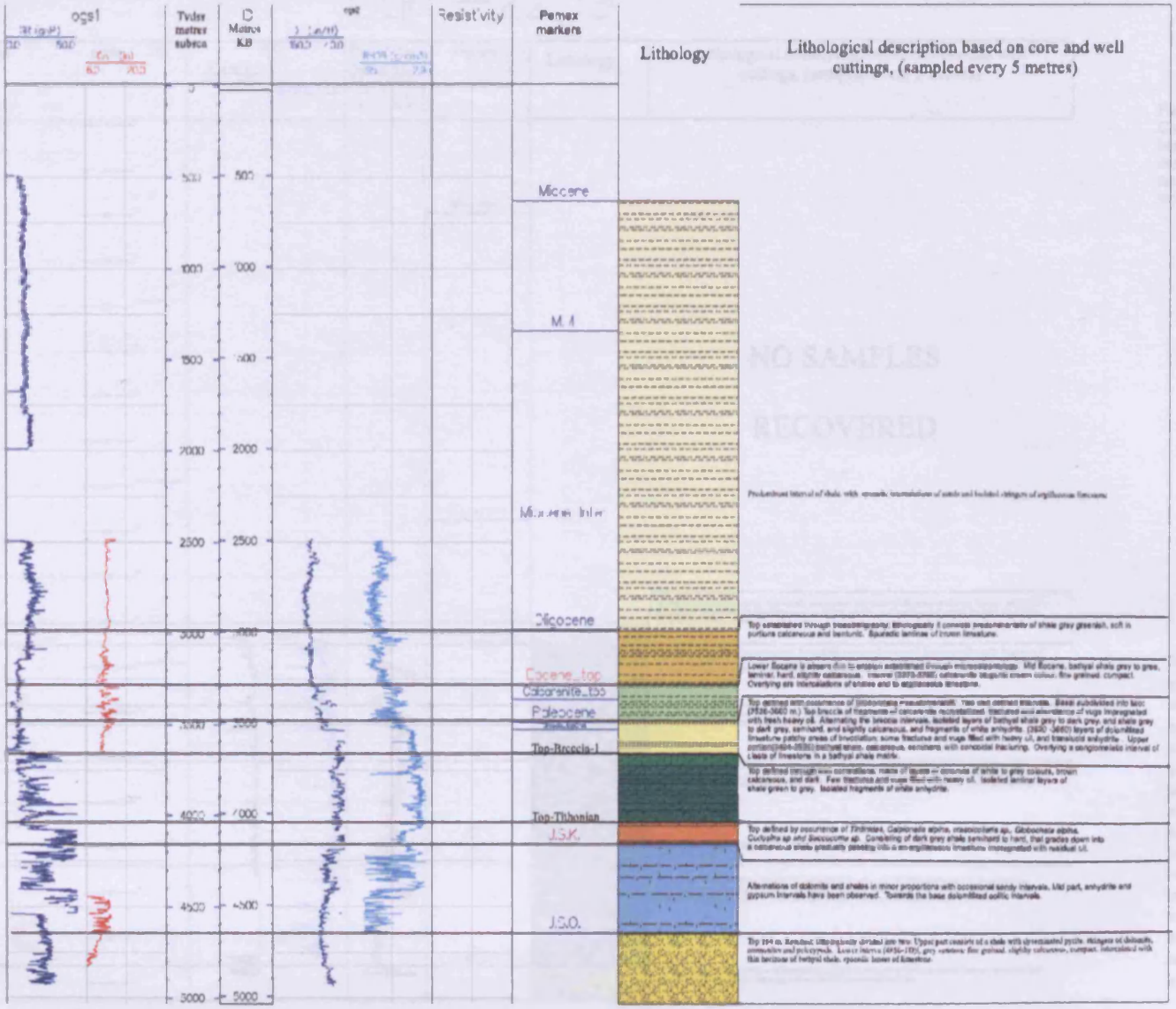

Figure 3.10
Composite log for well Chac-1 displaying well logs, lithologic and biostratigraphic nomenclature as obtained and defined from Pemex in house well reports (Informe Geologico final del Pozo Chac 2, 7045, junio 74 - marzo 76).

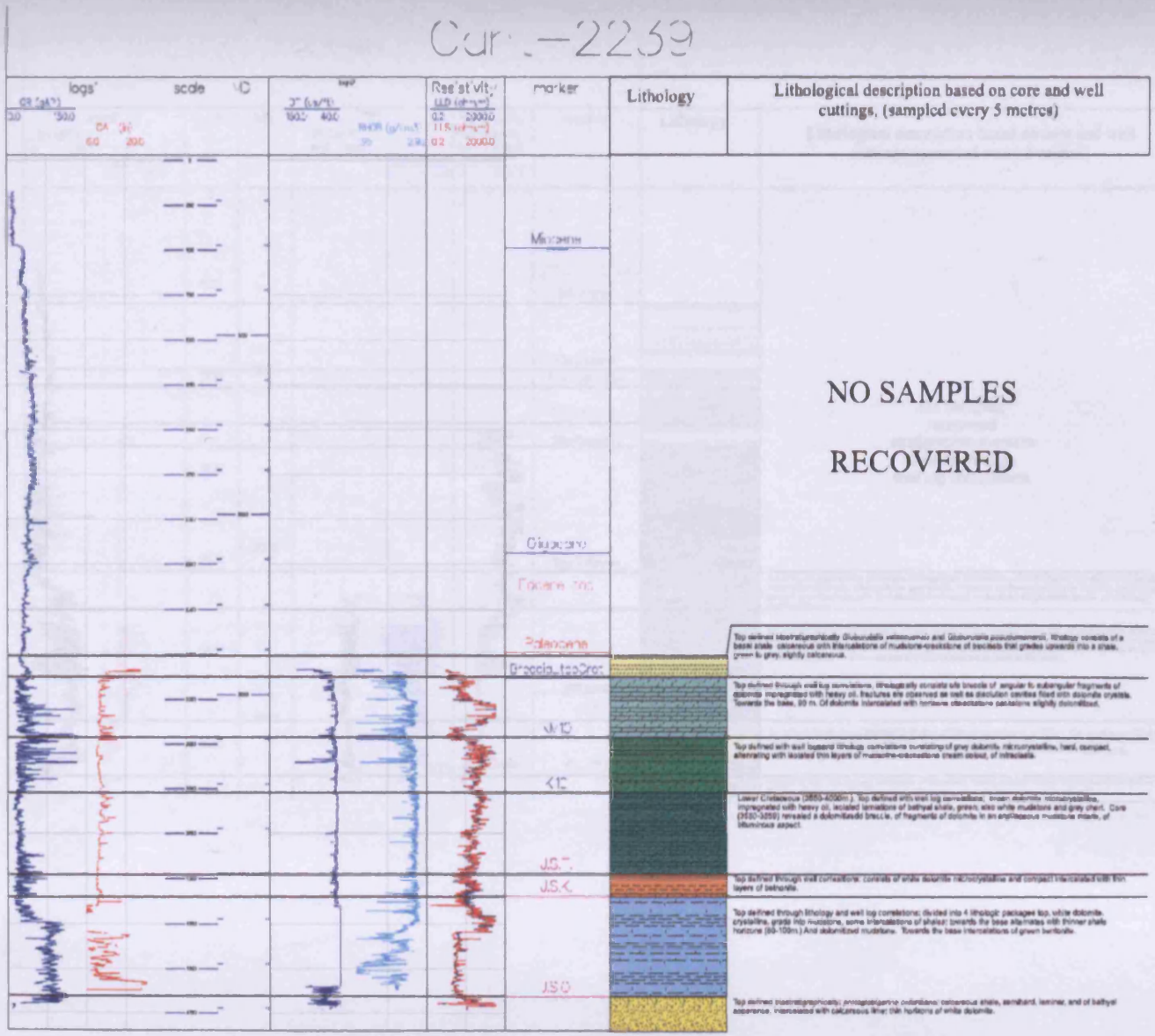

Figure 3.9
Composite log for well C-2239, displaying well logs, lithologic and biostratigraphic descriptions, and the stratigraphic nomenclature as distilled from Pemex in house well reports (Informe Final del pozo C-2239).

Stratigraphic key

M.M.=Middle Miocene

M. I. Lower Miocene

Oligocene

O.I.= Lower Oligocene

E.I.= Lower Eocene

Breccia_topCret = Top Cretaceous = Top-Breccia-1 horizon

K.M.= Middle Cretaceous

K.I. = Lower Cretaceous

J.S.T. = Top Tithonian = Top-Tithonian seismic horizon

J.S.K. = Top Kimmeridgian

J.S.O. = Top Oxfordian

E.I.-BS= Lower Eocene Footwall block

BTPK@_BS= Top Cretaceous footwall block

KM_BS= Middle Cretaceous footwall block

KI_BS= Lower Cretaceous footwall block

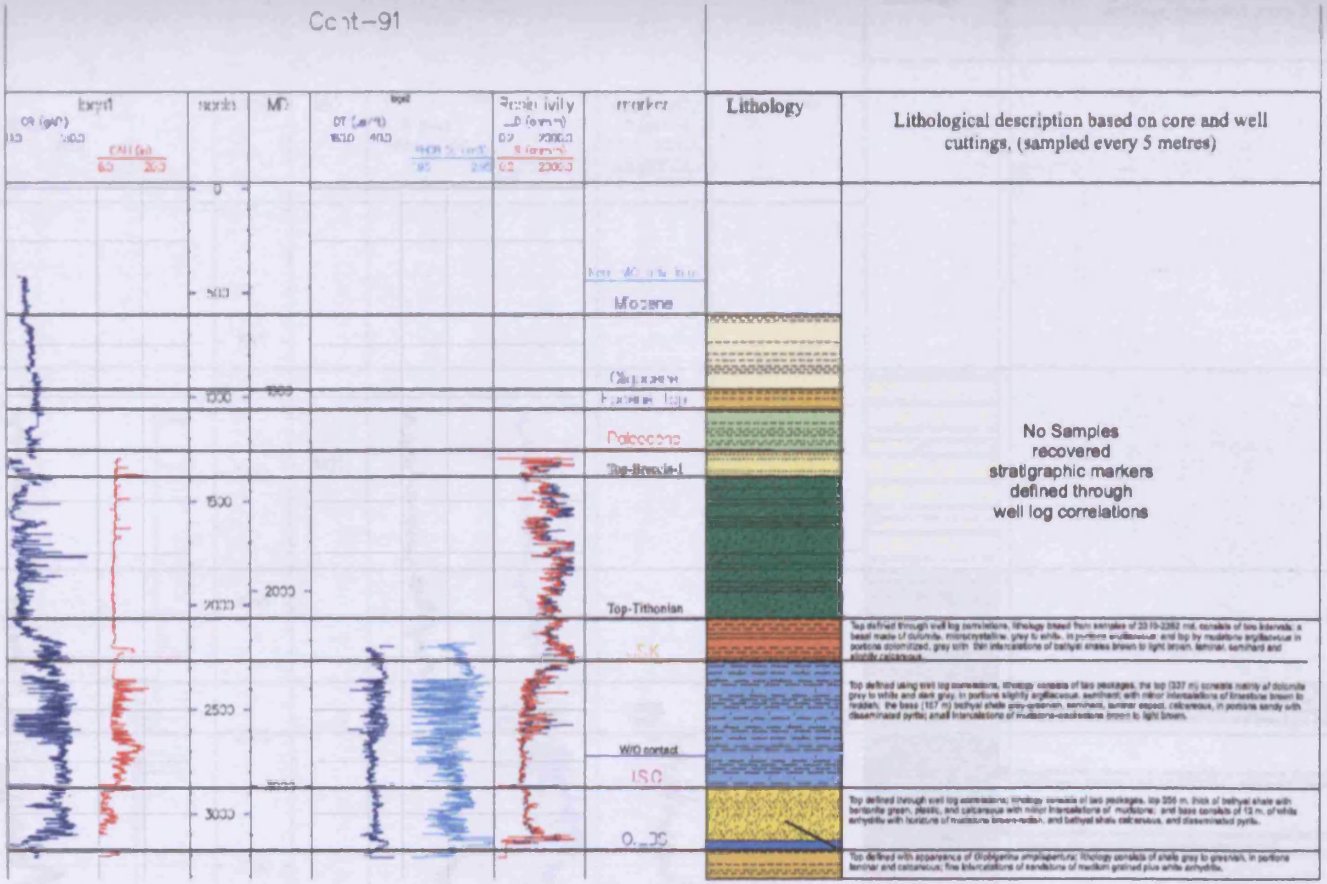

Figure 3.8
Composite log for well C-91 displaying well logs, lithologic and biostratigraphic descriptions, and the stratigraphic nomenclature as distilled from Pemex inhouse well reports (Informe Final del pozo Cantarell No. 91, 4-6-557). Well cuttings were recovered from the Tithonian to total depth. The economical objective of this well was to encounter oil production within the Oxfordian interval, which resulted water invaded. Instead Oligocene rocks were found beneath the Oxfordian successions. Oil and gas production was obtained from the Kimmeridgian interval (2650-2695 m).

Stratigraphic key

M.M.=Middle Miocene
M. I. Lower Miocene
Oligocene
O.I.= Lower Oligocene
E.I.= Lower Eocene
Brecia_topCret= Top Cretaceous
K.M.= Middle Cretaceous
K.I. = Lower Cretaceous
J.S.T. = Top Tithonian
J.S.K. = Top Kimmeridgian
J.S.O. = Top Orfordian
E.I.-BS= Lower Eocene Footwall block
STPKB_BS= Top Cretaceous footwall block
KM_BS= Middle Cretaceous footwall block
KI_BS= Lower Cretaceous footwall block

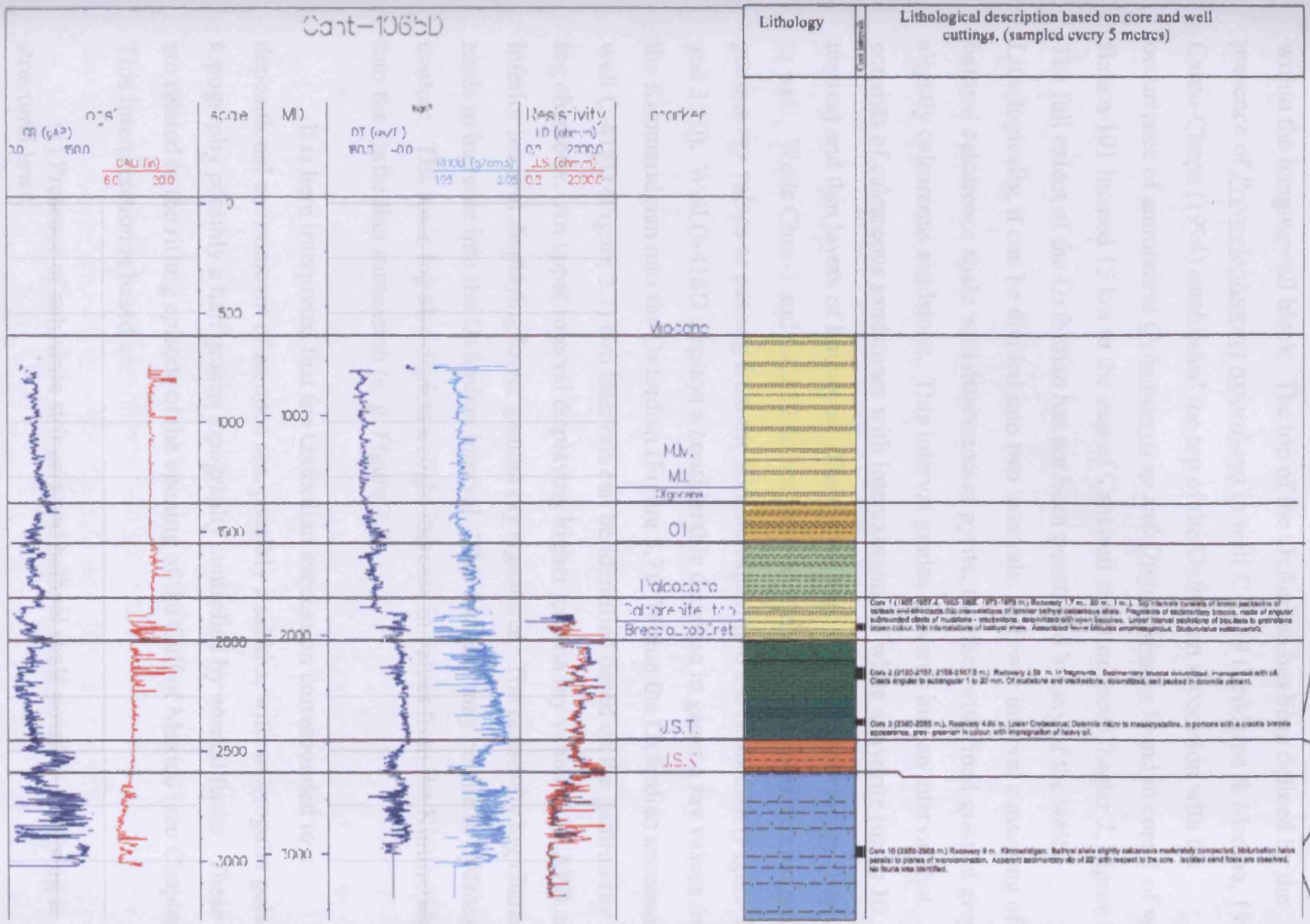

Figure 3.14
Composite log for well C-1065D, displaying well logs, lithologic and biostratigraphic descriptions are derived from core reports from Pemex inhouse well reports (Cantarell 1065D core 1, 2, 3 and 10).

Stratigraphic key

M.M.=Middle Miocene
M. I. Lower Miocene
Oligocene
O.I.= Lower Oligocene
E.I.= Lower Eocene
Breccia_topCret= Top Cretaceous
K.M.= Middle Cretaceous
K.I. = Lower Cretaceous
J.S.T. = Top Tithonian
J.S.K. = Top Kimmeridgian
J.S.O. = Top Oxfordian
E.I.-BS= Lower Eocene Footwall block
BTPKB_BS= Top Cretaceous footwall block
KM_BS= Middle Cretaceous footwall block
KI_BS= Lower Cretaceous footwall block

3.4.2.1 Oxfordian

The Oxfordian rocks were penetrated by wells C-418D, C-91, C-2239, and Chac-1 wells (Figures 3.7, 3.8, 3.9 and 3.10). Of these wells all but Chac-1 are located within the hangingwall block. The top of the Oxfordian has been defined by the presence of *Protoglobigerina oxfordiana* in well C-2239 (Landeros & Medina, 1993). Cantú-Chapa (1994) established the top of the Oxfordian succession with the occurrence of ammonites *Ochetoceras sp* and *Discosphinctes* found in core 3 of well Balam-101 located 15 km to the east of Cantarell structure (see Chapter 2, Figure 2.3). The full extent of the Oxfordian has not been penetrated by any of the wells. Lithologically, it can be divided into two intervals: A lower interval consisting of bathyal calcareous shale with disseminated pyrite, together with fined grained grey slightly calcareous sandstone. This interval grades upwards into an interval that consists of calcareous sandstones with intercalations of white anhydrite (up to 10 metres) and thin layers of limestone. The overall well log character changes from well to well. Wells Chac-1 and C-2239 do not show any internal considerable changes in gamma ray values or passing from the Kimmeridgian into the Oxfordian (Figure 3.9 and 3.10). Well C-418D displays a considerable decrease in gamma ray values from the Kimmeridgian into the Oxfordian (Figure 3.7). Within the Oxfordian succession in well C-418D (Figure 3.7) two intervals can be identified based on the gamma ray well log character. An upper interval displaying higher gamma ray values (100 API) and a inferior interval displaying lower gamma ray signatures. The resistivity log character tends to increase into the Oxfordian interval. This increase may be due to hydrocarbon content. The sonic log also depicts a slight increase in values from the Kimmeridgian into the Oxfordian succession (e. g. Figure 3.8).

It is here interpreted that the Oxfordian succession corresponded to a depositional environment of an open sea, possibly a sabkha, with an irregular palaeo-topography possibly a half graben topography controlled by normal faults. These faults are related to the rifting episode of the opening of the Gulf of Mexico (see Chapter 2). This interpretation is based on:

(1) Presence of anhydrite stringers and bathyal shale possibly occurring at structural lows.

(2) Stringers of limestone

(3) Occurrence of calcareous sandstones.

3.4.2.2 Kimmeridgian

This succession was penetrated by wells C-418D, C-91, C-2239, Chac-1, Chac-2, Cant-2095, and C-2011 wells (Figures 3.7 to 3.12 and 3.15, 3.16). The top marker for the Kimmeridgian was defined with the occurrence of *codiaceas* algae (*Cayeuxia sp, Rhaxella sorbyana* and *sponge spines;* Landeros & Medina, 1993). Cantú-Chapa (1994) identified ammonites *Nebrodites and Taramelliceras sp.* Ortuno-Maldonado (2002) defined the top of the Kimmeridgian at the first dolomitized layer beneath the Tithonian succession where a significant decrease in API values and an increase in resistivity values are generally observed. The total thickness as evidenced by well penetrations varies from 350 metres to 560 metres (Ortuno-Maldonado, 2002). Lithologically is heterogeneous with alternations of dolomite, shale and sand-rich intervals. Occasional disseminated pyrite is present as well as layers of emerald green bentonite. The basal boundary is marked by lithology changes from an overall cleaner sandstone body (Oxfordian) to a more silt-rich lithology (Kimmeridgian), and the presence of carbonate stringers (thin and covering small areas) in the form of dolomite and limestone, plus the occurrence of intercalated layers of bentonite.

Towards the north of the Thrust Block structure within the forelimb, as evidenced by well C-91 (Figure 3.8), the Kimmeridgian succession is seen to be 504 m thick and is divided into two intervals based on lithology. A basal interval of 167 m that consists of grey to green, semi-hard, calcareous bathyal shale. Locally, sand-prone with intercalations of mudstone-wackestone of an oolitic texture with disseminated pyrite. An upper interval (337 m thick) consisting of grey to white microcrystalline dolomite, that is slightly argillaceous with occasional thin intercalations of limestone and green bentonite.

Towards the west within the crestal area of the Thrust Block, the Kimmeridgian was penetrated by well C-418D, (Figure 3.7, 508 m thick) and divided into three intervals. The basal interval comprises mainly a terrigenous interval of bathyal shale that is grey to grey greenish in colour. Occasional reddish limestone is seen with intercalations of white to cream bathyal mudstone. The middle interval consists of sand-rich shale succession that is slightly calcareous, and has occasional fragments of anhydrite and is semi-hard. The uppermost interval has a thickness of 342 m and

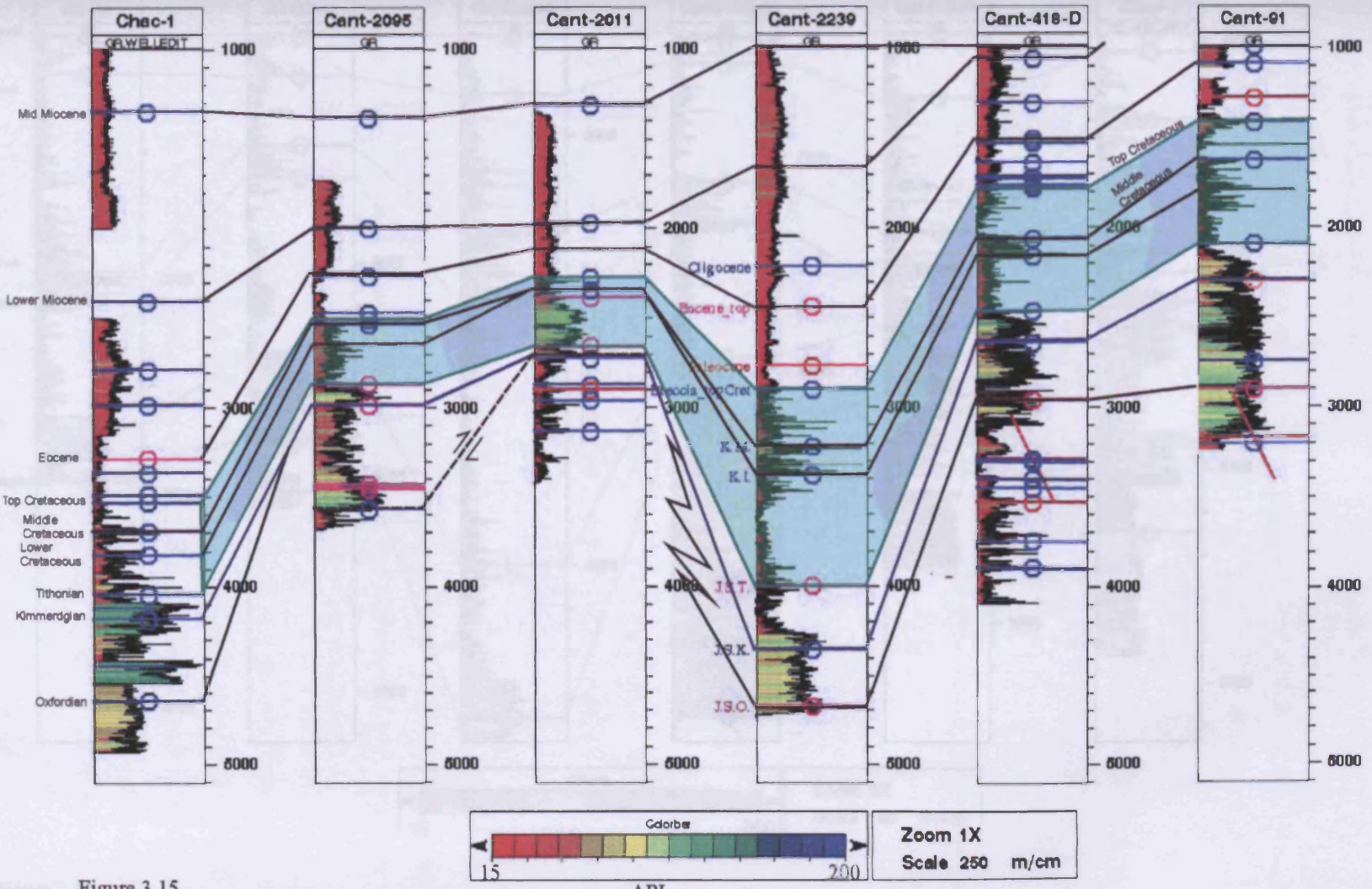

Figure 3.15
Well log (gamma ray) correlation panel of some wells that penetrated Jurassic successions. For well locations refer to Figure 3.2. Not to scale horizontally.

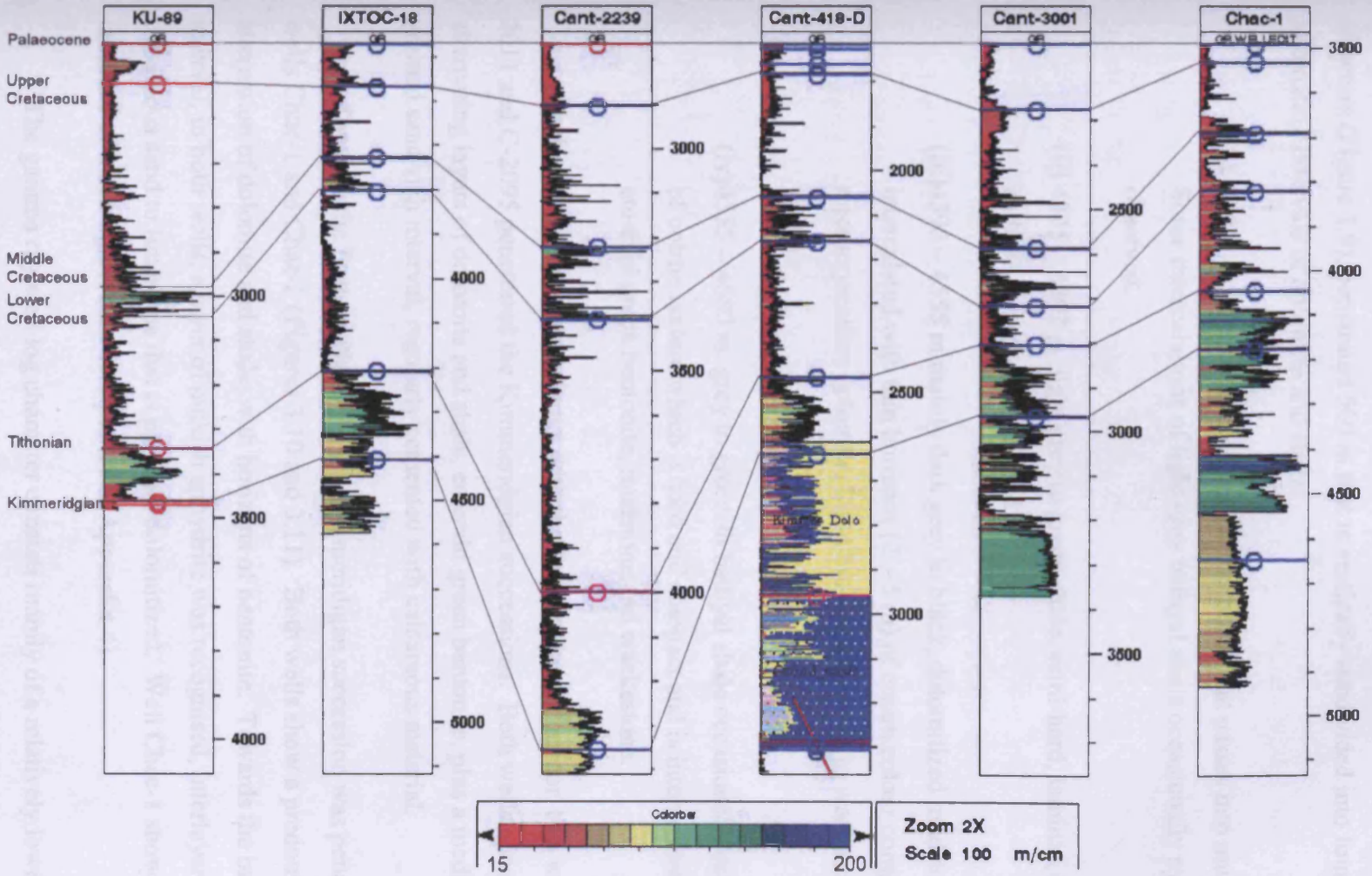

Figure 3.16
Well log (gamma ray) correlation for the Mesozoic successions, flattened at the top Palaeocene stratigraphic marker; vertical scale is posted as TVD; for well locations refer to Figure 3.2. Note the thickness variations for the Lower Cretaceous succession. Not to scale horizontally.

consists of white bathyal mudstone that grades upwards into grey dolomite with mudstone and occasional shale.

Well C-2239 located in the southern region of the backlimb of the Thrust Block structure (Figure 3.9), penetrated 560 m that is vertically subdivided into four alternating intervals of dolomite and shale:

(i) 4120 – 4325 m white crystalline dolomite that passes into mudstone. Some intercalations of light grey bathyal shale occasionally pyritized are observed.

(ii) 4325 – 4392 m light grey to green shale, semi-hard, laminar, slightly bathyal, in portions pyritized.

(iii)4392 – 4555 m mainly dark grey to black, dolomitized mudstone, intercalated with thin horizons (2 – 5 m) of cream colour compact microcrystalline dolomite. Light brown mudstones to wackestone also occur.

(iv)4555 – 4680 m grey to greenish bathyal shale occasionally calcareous of oolitic texture which is hard and compact and is intercalated with emerald green bentonite, mudstone and wackestone.

In the southeast near the limits with the Eastern Fault Corridor, two wells C-2011 and C-2095 penetrated the Kimmeridgian successions. Both wells encountered alternating layers of dolomite and shale, emerald green bentonite, plus a medium grained sand-rich interval, regularly cemented with calcareous material.

Towards the Eastern Platform, the Kimmeridigan succession was penetrated by wells Chac-1 and Chac-2 (Figures 3.10 and 3.11). Both wells show a predominant alternation of dolomite and shale, with horizons of bentonite. Towards the base of the interval, in both wells, a layer of pinkish anhydrite was recognised, interlayered with calcareous sand to limestone that is partially dolomitized. Well Chac-1 showed the presence of black lignite (see core photos in Appendix 4).

The gamma ray well log character consists mainly of a relatively lower API values than the upper interval. Most wells show an increase of API values with depth.

The resistivity log, exhibits considerably lower values than the overlying Tithonian interval, with the upper interval showing higher resistivity (e.g. Figure 3.8). The resistivity values are directly linked to the fluid content of the formation, whether water, oil or gas saturated. Lower resistivity tend to be related to water charged formations, although this interpretation is not conclusive. Intervals that have been good hydrocarbon producers within the Kimmeridgian successions exhibit higher resistivity values (Figure 3.8).

In summary, the Kimmeridgian succession consists of a lower part of shale and limestone that have been interpreted to be deposited in a shallow, low-energy water environment (Ortuno-Malodnado, 2000). Towards the top the Kimmeridgian consists of an interval of light brown microcrystalline dolomite made up off grainstone to packstone with localised patches of pellets and oolite bank deposits, intercalated with thin layers of reddish marls and stringers of anhydrite. These facies are here interpreted to correspond to a low angle carbonate ramp environment possibly situated in a mid to inner ramp setting. The ramp most likely had a terraced half-graben palaeo-topography (Figures 3.17 and 3.18). Where the structural highs provided by the half-graben topography were the loci for pellet and oolite bank deposition and development (see Section 3.6, Figure 3.17 and 3.18). This interpretation coincides with previous authors (Garcia-Hernandez, 2000 and Ortuno-Maldonado, 2000).

3.4.2.3 Tithonian

The Tithonian succession as evidenced from wells C-418D, C-91, C-2239, Chac-1, Chac-2, Cant-2095, and C-2011 consists mainly of an upper interval of siltstone that grades to shale (Figures 3.7 to 3.12). Towards the basal section argillaceous dolomite occurs. The Tithonian stratigraphic age has been defined through the occurrence of, *Saccocoma arachnoidea, Eotrihis alpina, Suarites sp; Lombardia angulosa, Lombardia filamentosa, Campionella alpina, Crassicollaria massutiniana, Durangites sp; Salinites sp;* and *protoncycloceras sp.* (Landeros & Medina, 1993). Cantú-Chapa, (1982), confirmed the Jurassic – Cretaceous boundary with the occurrence of ammonites (*Durangites sp. Salinites sp., Protancyloceras sp.* and *Suarites sp.*).

Figure 3.17
Sketch representing the geological setting during the Kimmeridgian, that is interpreted to consist of a ramp with a half-graben topography.

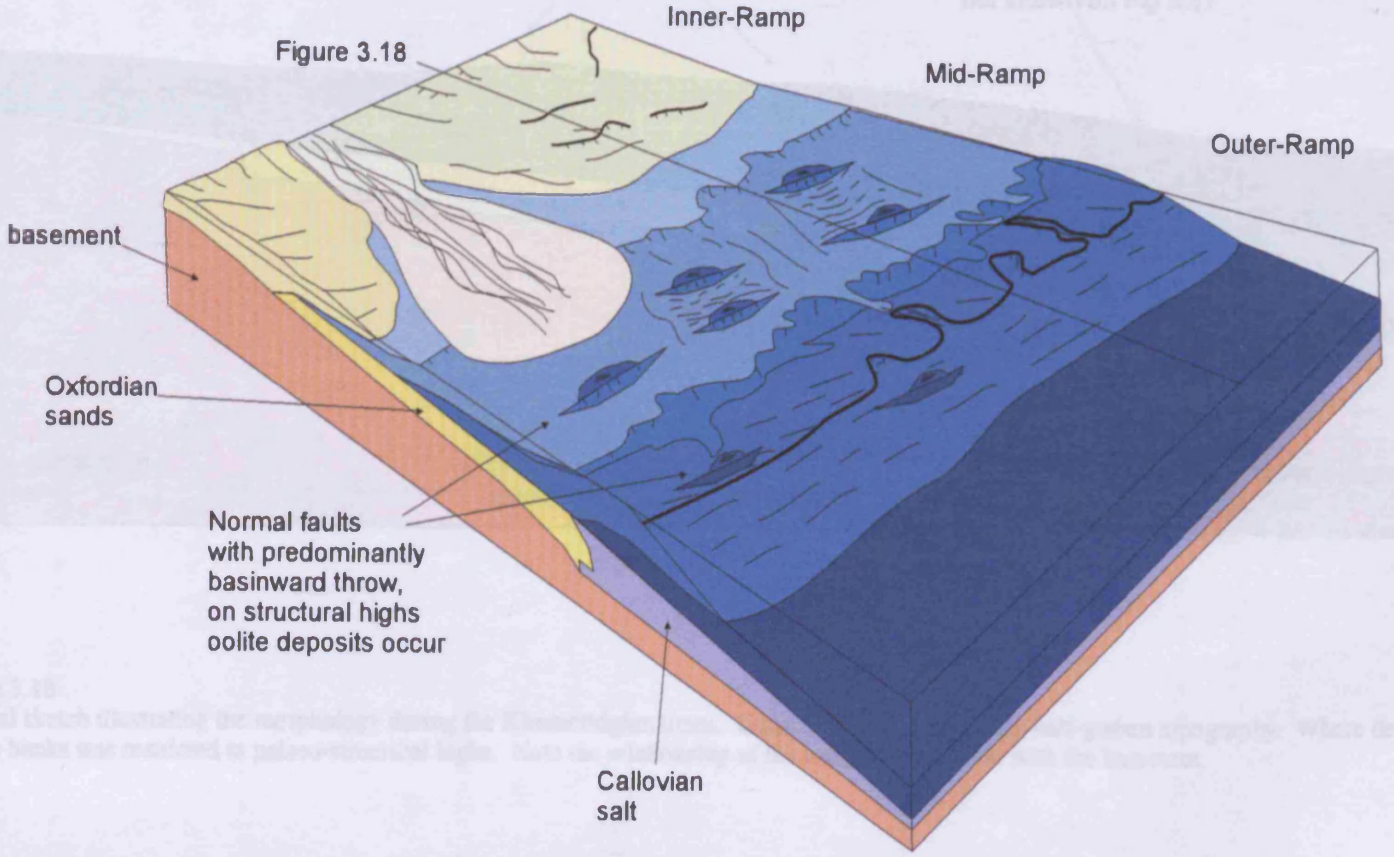

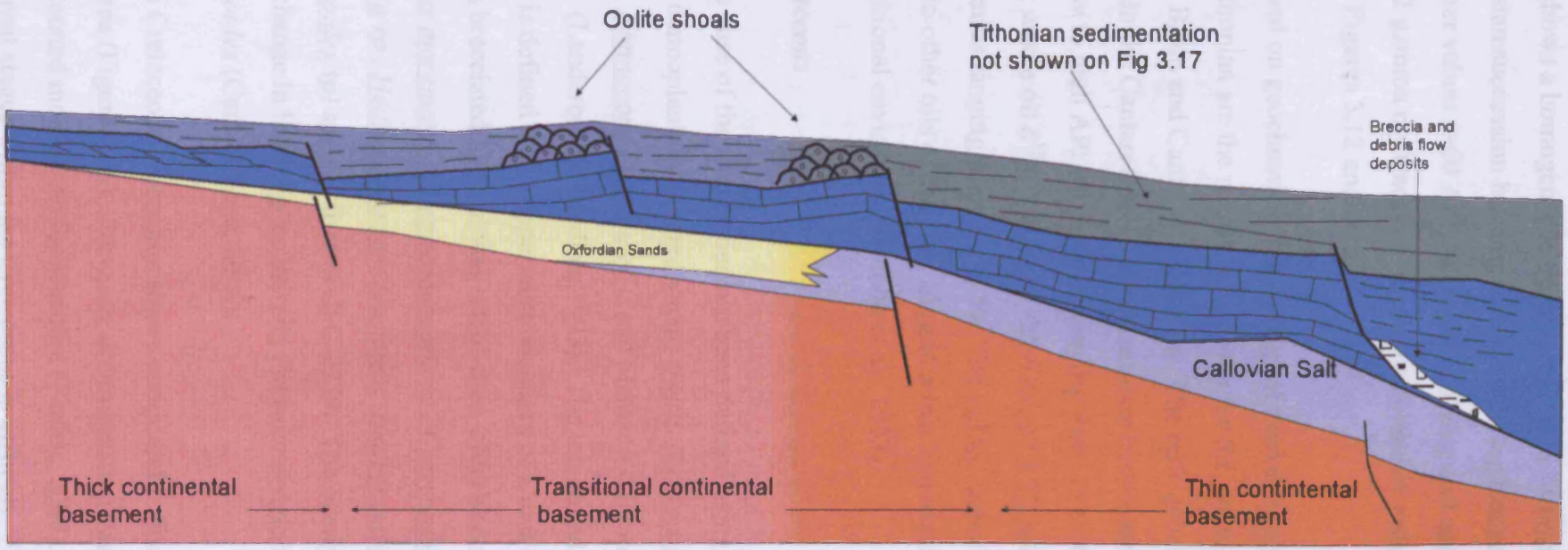

Figure 3.18
Vertical sketch illustrating the morphology during the Kimmeridgian times. Consisting of a ramp with a half-graben topography. Where deposition of oolitic banks was restricted to palaeo-structural highs. Note the relationship of the ramp configuration with the basement.

Well data reveals thickness variations from 63 m (Chac-1) to 260 m (C-2239), although generally shows a homogeneous thickness (100 to 140 m) throughout (Figure 3.15). The Tithonian succession has a distinctive well log character. The gamma ray log shows higher values (>60 API) than the overlying and underlying successions (e.g. Figure 3.12 gamma ray track). The resistivity shows generally higher values > 1500 ohms (e.g. Figures 3.12 and 3.13).

Based on geochemical and biological marker analyses, Guzman (1999) suggests that the Tithonian are the main source rocks for the produced hydrocarbons of the Campeche Basin and Cantarell reservoirs. The bulk geochemical character for the oils found within the Cantarell area include saturate hydrocarbon contents ranging from 21 to 63%, low to high API oil gravities ranging from 15 to 47 %; sulphur content from 0.1 to 6 %; whole oil δ^{13}C values of –25.6 to –27.8 ‰ with most values around –27 ‰ and V/Ni ratios ranging from 1 to 5 %. The lighter carbon isotope values of these oils compared to other oils of the area, suggest a less hypersaline condition in the source rock depositional environment (Mello et al., 1993).

3.4.3 Cretaceous

The base of the Cretaceous has been defined using the following microfossils calcareous nannoplankton (*Nannoconnus truitii, Nannoconus bucheri and Nannoconus Kamtcheri, Nannoconus bermudezi);* and planktonic forams *Globigerinelloides algerianus* (Landeros and Medina, 1993). The top boundary of the Cretaceous succession is defined at the uppermost boundary of a unit of dolomitised breccia. The age for this brecciated interval was established with the occurrence of *Globotruncana* (*Heterohelix moremanii, Marginotruncana sp., Clavibedbergella moremanii, Loeblichella sp., Hedbergella portdownensis, Hedbergellia delrioensis y Globigerinoides sp)* species from well C-2239. The overlying succession (Palaeocene) exhibits a change in lithology containing *Parvularugoglobigerina trinidadensis* and *Pa. pseudobulloides* (Cantú-Chapa, 2001).

The Cretaceous succession shows considerable thickness variations across the Cantarell area (Figure 3.15). Pervasive dolomitization has been reported to occur, which obliterated most of the fossil record (Pemex, 2000). Therefore consistent dating of the different stages within the Cretaceous is difficult. Furthermore, the recognition

of primary depositional sedimentary structures is also difficult. However, a threefold subdivision has been proposed (Pemex, 2000) Lower, Middle and Upper, based on general lithological trends and well log responses. Some wells (e.g. C-2095, C-3001, C-418D) contained limited biostratigraphic data that supported the different assigned ages. Herein, the Lower Cretaceous is considered from the Neocomian to Aptian, the Middle Cretaceous to the Albian - Cenomanian and the Upper Cretaceous to the Turonian – Maastrichtian (see Chapter 2 section 2.2.4.1). The Upper Cretaceous interval is of significant interest because it is pervasively brecciated and the genesis and subsequent geological modification of these breccia have contributed to the formation of a reservoir interval that has exceptionally good reservoir properties (e.g. porosity > 15 Phi (Φ) and permeability ranging from 3 -5 darcy).

3.4.3.1 Lower Cretaceous

Of the entire Cretaceous successions, the Lower Cretaceous exhibits the most significant thickness variations, from 100 m in well C-3001 to 600 m in well C-2239 (Figure 3.16). Lithologically, it almost always consists of a basal silt-rich dolomite that generally cleans upwards. Within it, intercalations of re-sedimented calcareous conglomerates to breccia packages and wackestone can be seen (see core photos Appendix 4). Well C-3001, core 5 consists of dolomitised wackestone to mudstone that displays a general bioturbation mottling appearance with burrows and winnowed bioclastic layer; these have a high API signature (Pemex well-completion logs).

Pemex internal reports (2003) report that the image logs and cores exhibit resedimented conglomerate intervals that are characterised by 10 to 15 m thick of amalgamated, mainly clast-supported graded breccio-conglomerate beds and 1-5 m thick beds of cobble- to granule-sized clasts. These have a generally low gamma signature with some minor internal gamma peaks. The conglomerates are suggested to represent deposits of debris flows sourced from a shallower water platform carbonates, (after Pemex, internal reports, 2003; see Appendix 5).

The well log character consists of relative lower API values towards the base with increased spikes in the middle and an overall increase in API values at the upper boundary against the overlying Middle Cretaceous. The resistivity consists of medium

to high values. Towards the top a thin clay-rich layer exhibits high API values and medium resistivity values (100 – 200 ohms).

The interpretation in this thesis is that the conglomerate - breccia intervals were deposited in a base of slope or in a distally over-steepened ramp setting (see Section 3.6). Where the emplacement of the breccia packages probably occurred as turbidity flows. This suggestion is based on:

(1) The identification of sedimentary structures found within the breccia (elongated clast and imbrication).

(2) The gross clast fabric that is found in association with the presence of bathyal shale and mudstone.

(3) The basin margin architecture as observed from seismic profiles (see Chapter 2, Section 2.3.4.1).

3.4.3.2 Middle Cretaceous

The Middle Cretaceous was defined with the occurrence of *Globigerinelloides bentonensis, Praeglobotruncana delrioensis, Whiteinella aprica, Hedbergella delrioensis, Globigerinelloides sp., Pessagniella cf. Ovifera* and silicified radiolarians of Cenomanian age (Landeros & Medina, 1993). The top marker for the Middle Cretaceous was defined by Ortuno-Maldonado (2001) occurring 25 to 30 m beneath the overlying Upper Cretaceous breccias. The Middle Cretaceous lithology is predominated by dolomite that occasionally is interbedded with bathyal shale and mudstone. Cores from well C-3001 encountered a layered dolomite that is intercalated with reworked bituminous material. Dissolution vugs are present as well as intensive fracturing that inter-connects the vugular porosity. A sedimentary breccia was also observed that is composed of meso-crystalline dolomite of sub-angular to sub-rounded clasts with an abundance of vugs (see core photos Appendix 4). This interval shows a significant increase in API values. This increase in API values is very distinctive of the Middle Cretaceous (Figure 3.15 and 3.16), which allows the readily identification of this succession. At the well scale, the thickness of the Middle Cretaceous interval shows minor lateral variations (Figure 3.16).

3.4.3.3 Upper Cretaceous

The top marker of the Upper Cretaceous succession has been established to occur just beneath a shale unit that is interpreted to be Palaeocene in age (Ortuno-Maldonado, 2001). This shale unit is almost always observed in most wells as a 25 to 45 m thick interval exhibiting high API values and very low resistivity values (Figure 3.16). The base marker for the Upper Cretaceous was established using gamma ray logs (Ortuno-Maldonado 2001, PEMEX Exploración y Producción 1996), at a significant increase in the API values (Figure 3.16).

The age of this unit was defined with the presence *Heterohelix moremanii, Marginotruncana sp., Clavibedbergella moremanii, Loeblichella sp., Hedbergella portdownensis, Hedbergellia delrioensis* and *Globigerinoides sp.* that suggest a Maastrichtian – Campanian age (Landeros & Medina, 1993).

The top of the Upper Cretaceous is characterised by low API values of corrected gamma ray and higher resistivity values (1000 ohms; e.g. Figure 3.16). Generally, during well perforation, total loss of drilling mud occurred when penetrating the top of the Upper Cretaceous succession (Ortuno-Maldonado 2001). The core recovery within this interval is generally poor (Figure 3.19), especially within the uppermost interval of the Upper Cretaceous and in wells located in the forelimb region of the Thrust Block (see Chapter 4, for structural definition). The thickness of the Upper Cretaceous is variable across the study area (Figure 3.16). Within the Thrust Block the thickness is relatively homogeneous with an average thickness of 280 m that thins considerably in the Eastern and Western Platforms as suggested from wells Chac-1 and Ixtoc-18 (Figure 3.16).

The Upper Cretaceous lithology is characterised at the base by a dolomite interval. Some intervals are intensively fractured and show minor intercalations of bathyal shale and siltstones (see core photos Appendix 4). Stringers of green bentonite are as well documented within this basal interval. Towards the top of this succession a characteristic sedimentary breccia occurs, whose thickness reaches from 200 m and up to 300 in places as indicated by Grajales-Nishimura (2000).

The areal distribution of this calcareous breccia is considered to be widespread across the entire study area and throughout the Campeche Basin based on the

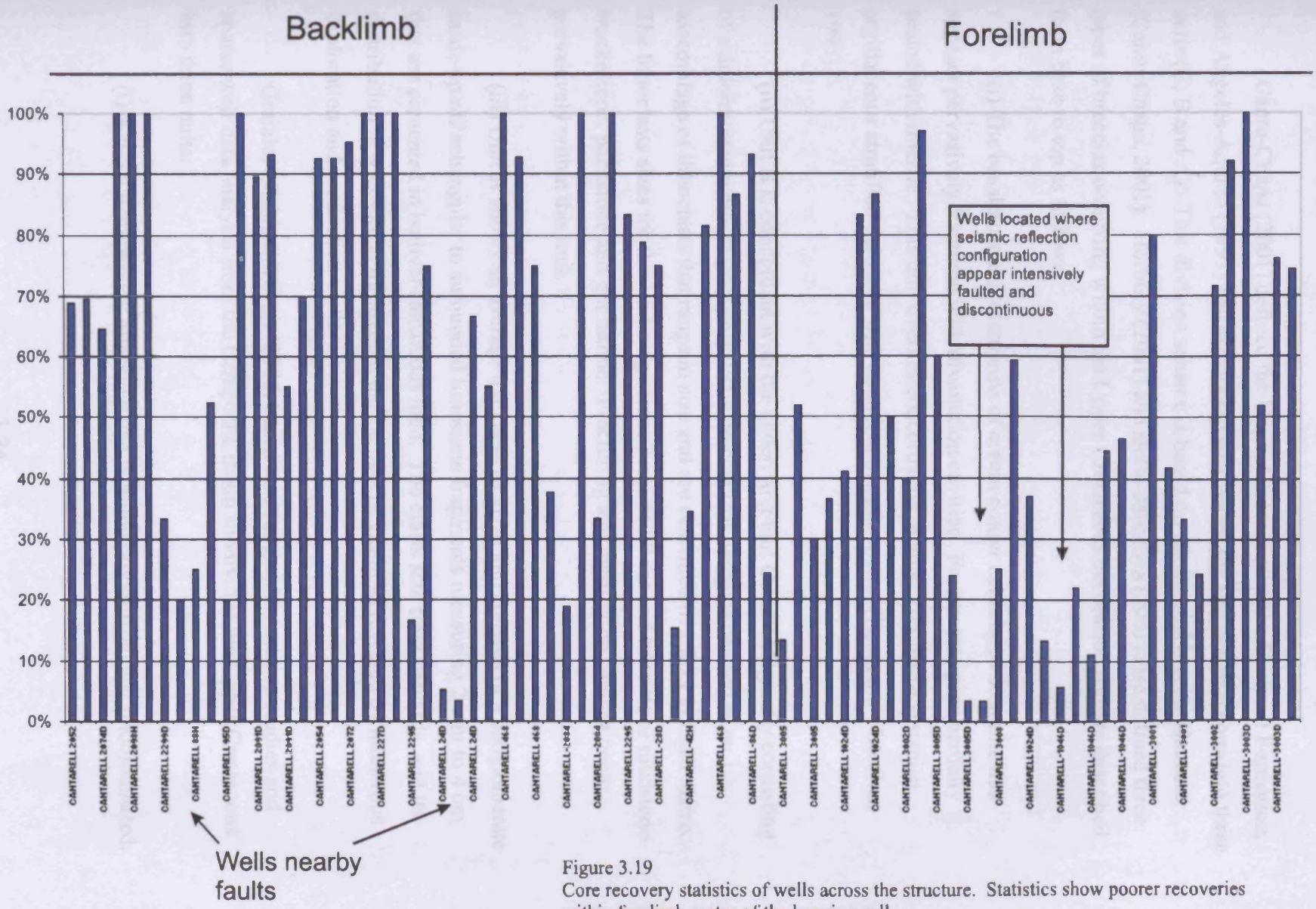

Figure 3.19
Core recovery statistics of wells across the structure. Statistics show poorer recoveries within forelimb sector of the hangingwall.

occurrence in numerous exploration and production wells (see Chapter 2, Figures 2.20 and 2.21; Magoon et. al. 2001). However, the poor core recovery limits the accurate characterisation of the vertical and aereal variations of these sedimentary breccias.

Cantu-Chapa (2001) defined the Upper Cretaceous as the Cantarell Formation, and Angeles-Aquino (1991) had previously subdivided the Upper Cretaceous into three units (C, B and A). This division scheme is based on the internal breccia character (Cantu-Chapa, 2001). Horbury (2001) and Bello-Montoya (2001) also defined three types of breccias occurring within the Upper Cretaceous succession and are described from base to top as follows:

(i) The basalmost unit C consists of cream colour calcareous dolomite that appears pervasively fractured with dissolution cavities. Fractures appear partially sealed with micrite. This unit overlies concordantly against Turonian-Coniacian argillaceous stratified dolomite with abundant organic matter (Landeros y Medina, 1993).

(ii) Unit B is concordant with the underlying unit C. Lithologically consisting of a dolomitized white to grey polymictic breccia that herein is defined as an assemblage of lithoclasts that range in size and are cemented in a finer grained matrix. The lithoclasts sizes for this unit range from 2 mm to 30 cm and consists of mudstone-wackestone, packstone and grainstone. Fracturing and dissolution cavities occur pervasively within this unit.

(iii) Unit A shows an average thickness of 20 m and consists of a conglomerate made up off subangular to surounded limestone fragments measuring 2 mm to 4 cm that are cemented in bathyal calcareous mud. The clasts size fines upwards, and its distribution is widespread throughout the Campeche Basin as revealed by numerous exploration and production wells.

Grajales-Nishimura et al. (2000) based on stratigraphic outcrop studies and sparse well data analysis from the Campeche Basin subdivided the Upper Cretaceous into three units:

(i) A basal hemipelagic limestone that is found dolomitized and undolomitized.

(ii) An approximate 300 m thick dolomitized limestone breccia that exhibits secondary vuggy porosity due to dissolution. Its average porosity varies from 8 % to 12% and permeability is 3000 – 5000 mD.

(ii) An upper average 30 m thick unit consisting of clast- or matrix- supported polymictic breccia or conglomerate composed mainly of shallow-water limestone and dolomite fragments. Shocked quartz and plagioclase were found in the upper breccias at the Bacab-1 well (well located 13 km north of the Cantarell structure).

The presence of a sedimentary polymictic and monomictic breccia fabrics is undisputed as evidenced by cores (see core photos Appendix 4). These cores show different sizes and types of clasts. This variation changes rapidly vertically and from well to well. Vugular porosity can be seen, and some vugs appear interconnected by fractures. Some of the fractures exhibit oil impregnation.

As previously described in Chapter 2 (Section 2.2.4.3) various hypothesis have been suggested for the origin of the Upper Cretaceous calcareous breccias. In this thesis, both the origin and the nature of the internal stratigraphic architecture of the breccias are still herein questioned. It remains to be seen whether one single geological event (Grajales-Nishimura et. al., 2000) caused the deposition of the breccia layer, or a series of cyclic sedimentary breccias were deposited in a talus apron setting (Viniegra-Osorio, 1981). Both of these interpretations are compatible, as suggested solely by the core data. However these hypotheses and others will be reviewed and discussed in great detail in Chapter 6.

3.4.4 Cenozoic

The base of the Cenozoic is defined with good quality biostratigraphic data whose fossil index are: *Globorotalia pseudobulloides, Globorotalia trinidadensis, Globorotalia angulata y Globorotalia compressa* (Landeros & Medina 1993). There is a marked change in the sedimentation pattern from the Cretaceous to the Cenozoic: from a carbonate dominated setting to a more siliciclastic dominated one. The overall thickness of the Cenozoic varies from 1000 m to 3000 m (Figures 3.15 and 3.16). This variability is primarily due to the late-stage structural deformation during the Neogene that took place on large-scale, thus modifying both the amount and location of available accommodation space.

3.4.4.1 Palaeocene

The Palaeocene succession averages 120 m in thickness, and appears to be present across almost the entire seismic survey area as suggested from well reports. The certain occurrence of Palaeocene sediments within specific areas of the crest of the Thrust Block structure is however more problematic due to the presence of an unconformity that appears to locally erode these sediments (See section 3.4.3). Although most of the wells situated along the crestal region report the occurrence of Palaeocene strata.

Lithologically this succession has been divided into two:

(i) Lower Palaeocene which has been named formally as the Abkatun Formation by Cantú-Chapa (2002). This unit consists of an average 30 m of brown to reddish calcareous shale that is found to be widespread across the Campeche Basin.

(ii) Upper Palaeocene interval that consists of alternating layers of bathyal shale (often calcareous) and conglomerate layers (Figure 3.20). The clasts of the conglomerates are dominated by bioclasts and lithoclasts that are Upper Cretaceous (Maastrichtian – Cenomanian) in age embedded in a Palaeocene matrix that contain *Globorotalia velascoencis, Globorotalia aequa,* index fossils (Landeros and Medina, 1993). Bioclastic packstones were also found coexisting with minor intercalations of bathyal shale. The intervals of conglomeratic breccia are not reported in all of the wells (Figures 3.14).

The log character of the Palaeocene consists of two well defined intervals, an upper that shows lower API values and a lower that displays higher API values. The boundary between these two intervals is sharp in some wells (e.g. C-Ku-89 in Figure 3.16) and transitional in others (e.g. C-2239 in Figure 3.16). The sonic log displays two well-defined intervals. The upper interval shows lower velocity with respect to the underlying higher velocity interval.

The interpretation in this thesis is that the depositional environment for the Palaeocene consisted of a deeper marine setting than the Upper Cretaceous. It is very probable that the carbonate factory switched off, possibly due to major terrigenous

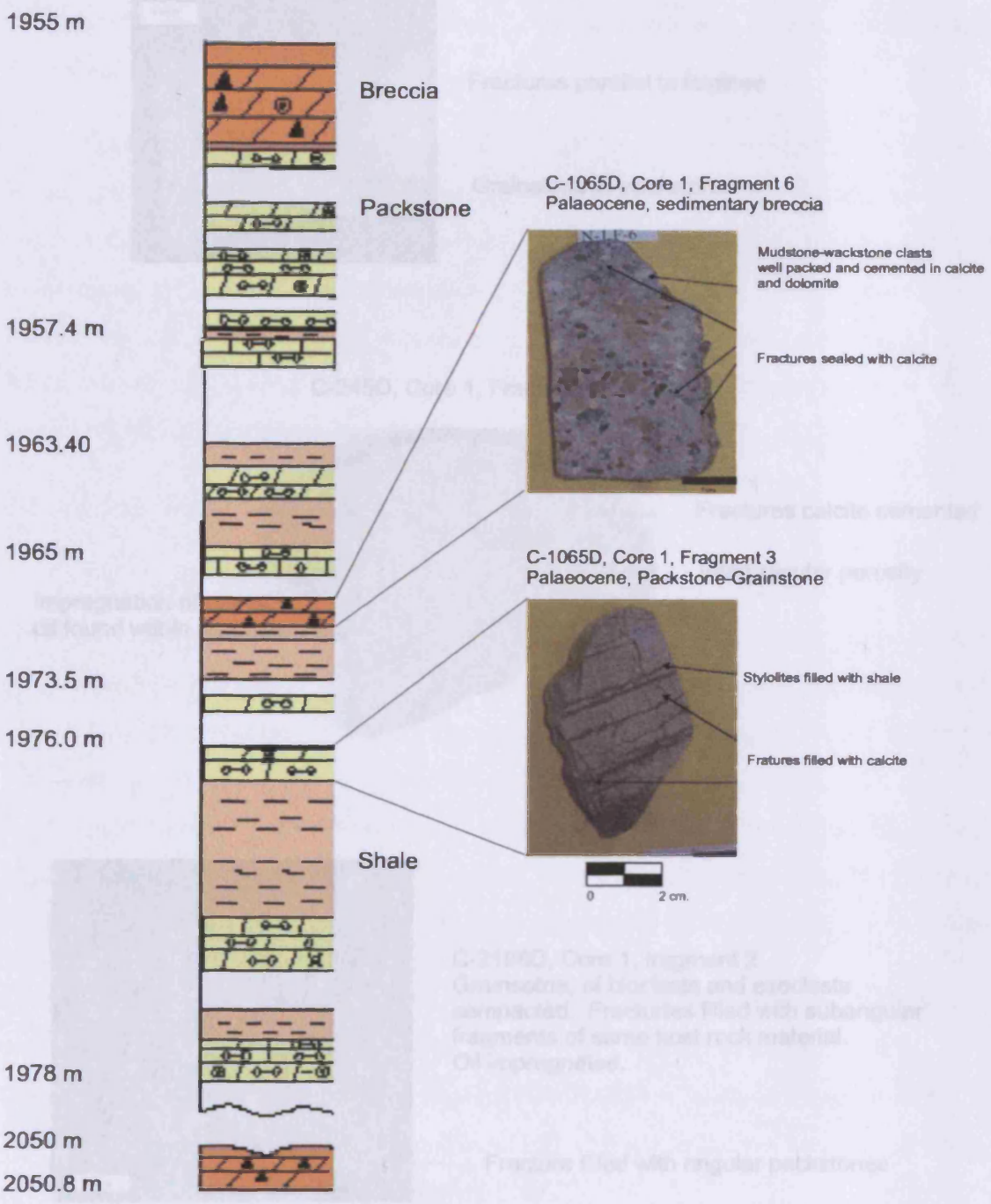

Figure 3.20
Lithological track derived from core 1 well C-1065D, within the Palaeocene stratigraphic interval. Note the intercalations of sedimentary breccias with packstones and bathyal shales. Depth scale is in vertical metres subsea.

C-182, core 1, fragment 27
med Eocene

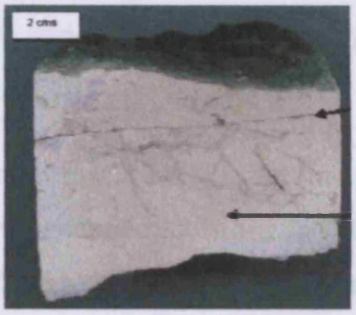

C-245D, Core 1, Fragment 32

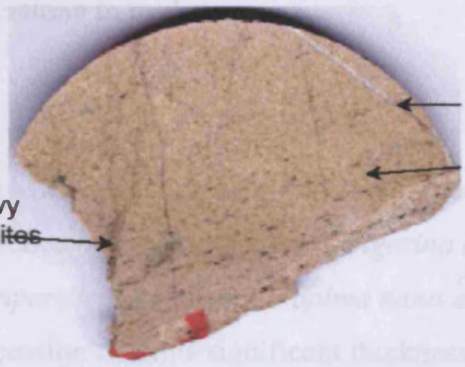

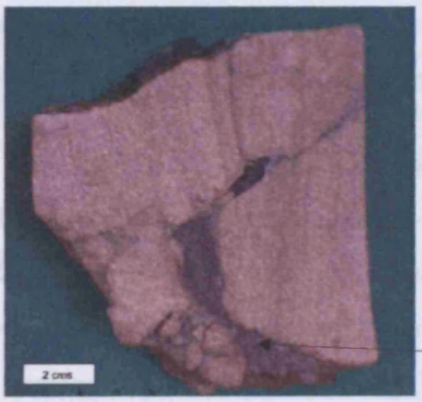

C-2196D, Core 1, fragment 2
Grainsotne, of bioclasts and exoclasts compacted. Fracturtes filled with subangular fragments of same host rock material.
Oil impregnated.

Fracture filled with angular packstones

Figure 3.21
Core photographs displaying the lithological character for the Mid-Eocene.

3.4.4.3 Oligocene

The Oligocene succession has been chronostratigraphically defined with the occurrence of *Globigerina ampliapertura* associated with *Globorotalia opima* and *Globigerina tripartite, Globorotalia opima nana* associated with *Ciperoensis* (Landeros & Medina, 1993).

The average thickness for this interval is 200 m. Along the crest of the Thrust Block, the Oligocene succession is not present due to erosion. Seismic observations have revealed erosional features within the Oligocene interval that are herein suggested to be related to the structural deformation history (see Section 3.4.3). However, wells located towards the backlimb of the structure show that the entire Oligocene (220 m thick) interval is preserved. Lithologically consists of a bathyal calcareous shale with intercalations of wackestone to packstone.

3.4.4.4 Miocene

The age of the Miocene succession was determined by Landeros and Medina (1993) with the occurrence of fossil indices: *Globigerina ampliapertura, Globorotalia opima, Globigerina tripartite, Globorotalia opima nana associated with Ciperoensis.* This sedimentary succession exhibits significant thickness variations (Figure 3.22), which are herein associated with the structural deformation (see Chapter 4, Section 3.5.4). A relatively thinner Miocene unit occurs over the crest of the Thrust Block that increases in thickness away from the structure. The thickness varies from 2011 m at C-2074 to 1085 m in well C-1 where the Middle Miocene interval is reported to be absent.

Lithologically it consists of bathyal calcareous shale that interlayer with grey sand-rich, carbonate cemented intervals. Occasional 1 to 2 m thick cream colour mudstone layers occur intercalated with dark plastic shale. Towards the top of the Miocene succession wackestone to mudstone intervals are found with occasional sand-rich horizons that show oil staining (Figure 3.23).

The Miocene succession has been interpreted to be deposited in a neritic environment (PEMEX, Exploración y Producción, 1999). Based on 2D seismic lines, the Upper Miocene succession correspond to a highly progradational package

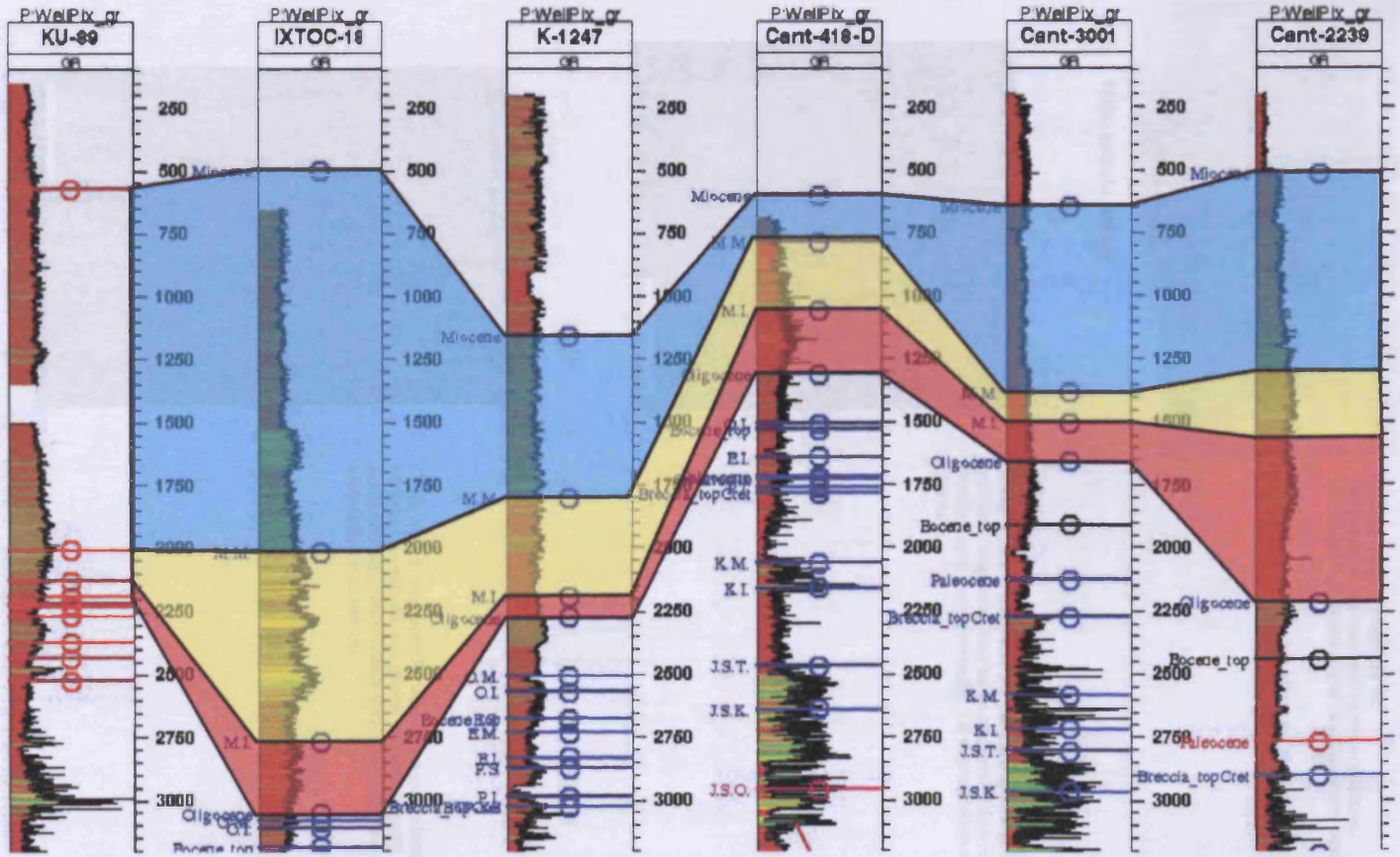

Figure 3.22
Well log correlation (gamma ray) displaying the Miocene succession subdivided into three units, Lower Middle and Upper. Subdivision scheme designed by Pemex (2000). For well location refer to Figure 3.2. Note the thickness variations observed in the Upper Miocene unit. In part is due to the poor correlations of picks of the Miocene marker. However there is a significant thinning over the crest of the structure. Not to scale horizontally.

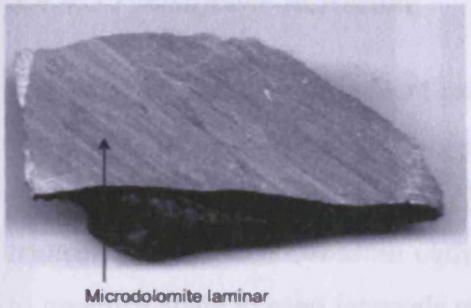

C-49D, core 1, fragment 16
wackestone, bathyal and sandy in portions,
to mudtone-wackestone of lithoclasts and bioclasts

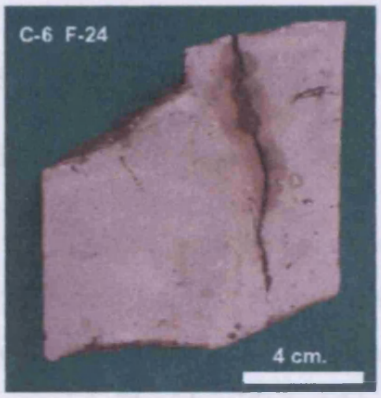

C-49, Core 1, fragment 24, packstone sandy, intraclasts and pelloids, bioclastic, detrital quartz grains well consolidated; fracture and matrix porosity. Oil impregnation limited to the fracture.

C-49, core 1, fragment 7; wackstone-packstone, sandy of intraclasts, pelloids and grains of detrital quartz, poorly consolidated, brown colour due oil impregnation. Intensive bioturation is observed.

Figure 3.23
Core photographs for the Upper Miocene interval.

(see Chapter 2; Enclosure 5). From this, it is interpreted that the Upper Miocene possibly corresponded to a distal deltaic system.

3.4.4.5 Pleistocene to Recent

The Pleistocene to recent successions have been aged calibrated with the occurrence of fossil indices: *Globigerinoides triloba triloba, Globigerinoides triloba inmatura, Globigerinoides ruber, Globorrotalia crassiformis, Globorotalia truncatulinoides and Orbulina Universa*. Lithologically it consists of interlayered grey to greenish shale to sand intervals with abundance of mollusc remains (Ortuno-Maldonado, 2002).

3.5 Seismic stratigraphic framework

3.5.1 Aims and methods

This section aims to document the seismic reflection configuration in a three-dimensional framework for the five defined seismic units (Figure 3.3). These consist of two units defined within the Mesozoic successions and three seismic units within the Cenozoic. The identified and interpreted Intra Neogene Unconformity (INU) will be described in great detail in Section 3.5.5. In this section, it will be discussed the relevance of the INU in terms of the reservoir system.

Eight seismic profiles that are taken as the most representative were interpreted and are used to illustrate the seismic reflection configurations (Figures 3.25 to 3.33). Each of the presented seismic sections consists of a non-interpreted full colour seismic section followed by a geoseismic interpreted section. Use of a colour filter has enabled the seismic reflection configurations to be enhanced by the removal of all negative amplitudes. The internal stratal configurations are described using established seismic stratigraphic methods (e.g. Vail *et al.* 1977, Mitchum et al. 1977; Brown and Fisher 1977).

3.5.2 Rationale for defining the seismic units

The rationale employed for the definition of the seismic units represents the various stages of structural deformation as: pre- syn- and post- structural development intervals (Figure 3.34). Where the pre- deformation seismic units correspond to the

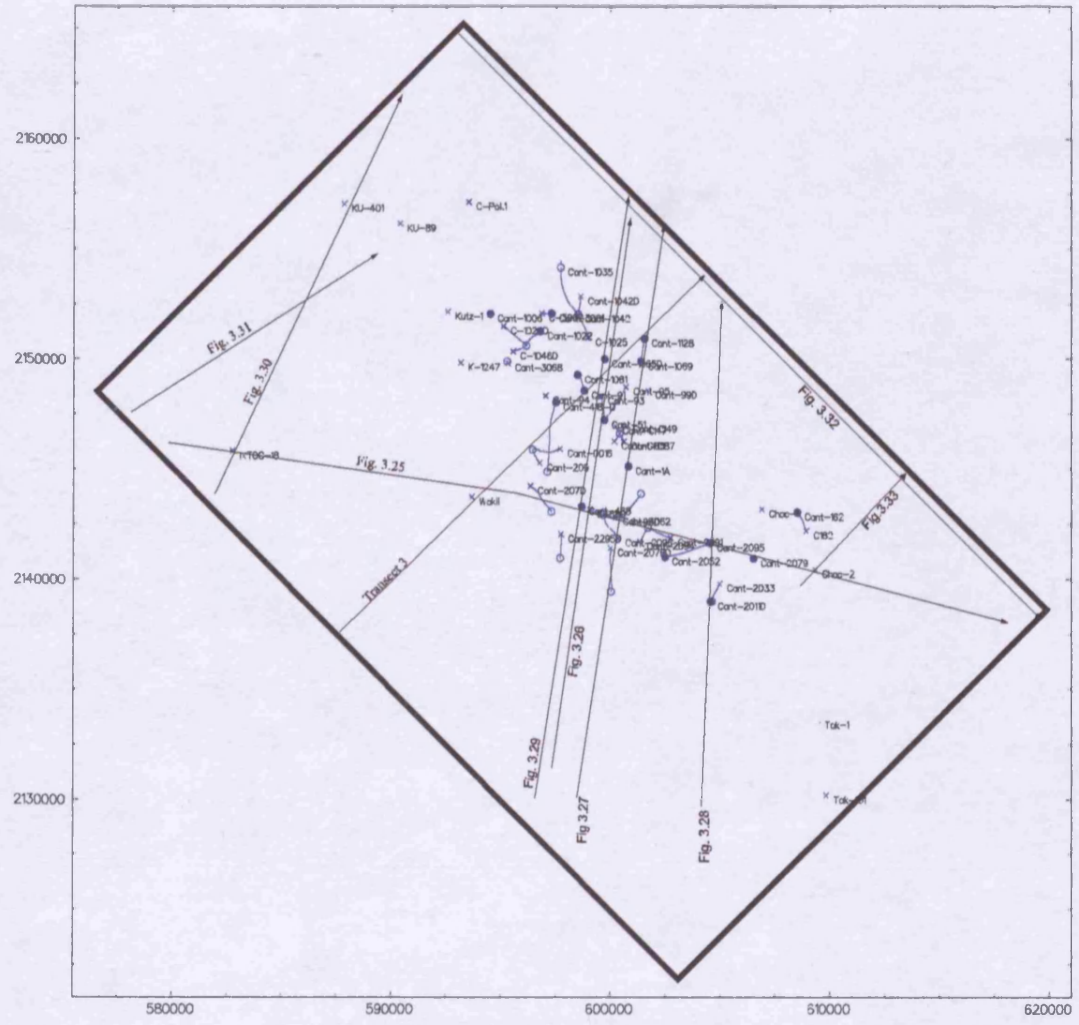

Figure 3.24
Layout of Geoseismic sections and well locations within the Cantarell 3D survey.

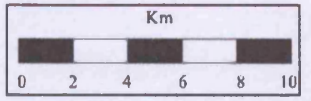

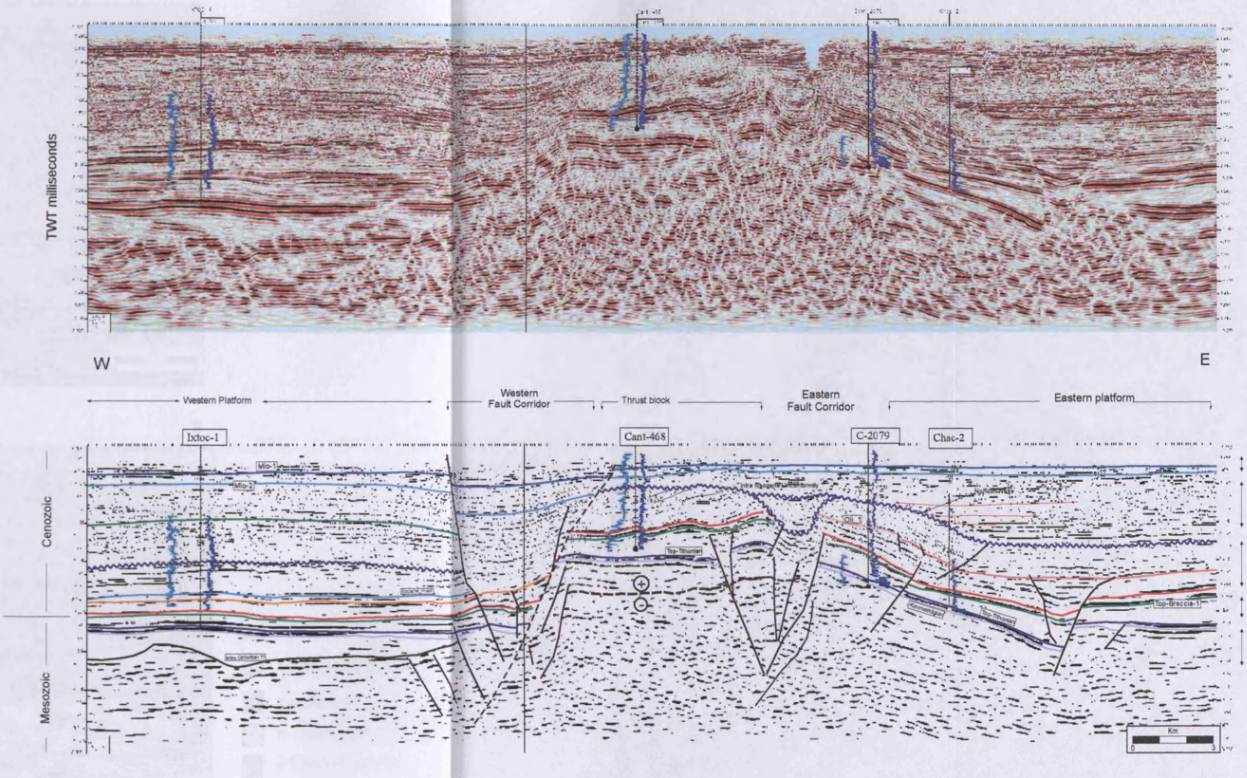

Figure 3.25
Seismic section and geoseisimic interpretation oriented W-E and illustrating the defined structural blocks and interpreted seismic horizons. The Western Platform consists of a relatively undeformed block with general parallel bedding. The Oxfordian base has been inferred based on seismic character, the remaining seismic horizons have been calibrated using well Ixtoc-1. Within both Western and Eastern Fault Corridors the interpreted seismic horizons is uncertain. Note within the Western Fault Corridor a major normal west dipping fault, dashed line, with subsidiary branching faults, and an eastern dipping antithetic fault system; faults are interpreted that have a complex deformational history. Within the Thrust Block, the thrust plane is interpreted "A" dashed line, where the encircled plus sign refers to the into page hangingwall relative motion. For a relationship of the marker scheme herein presented with the regional stratigraphic scheme refer to Figure 3.3.

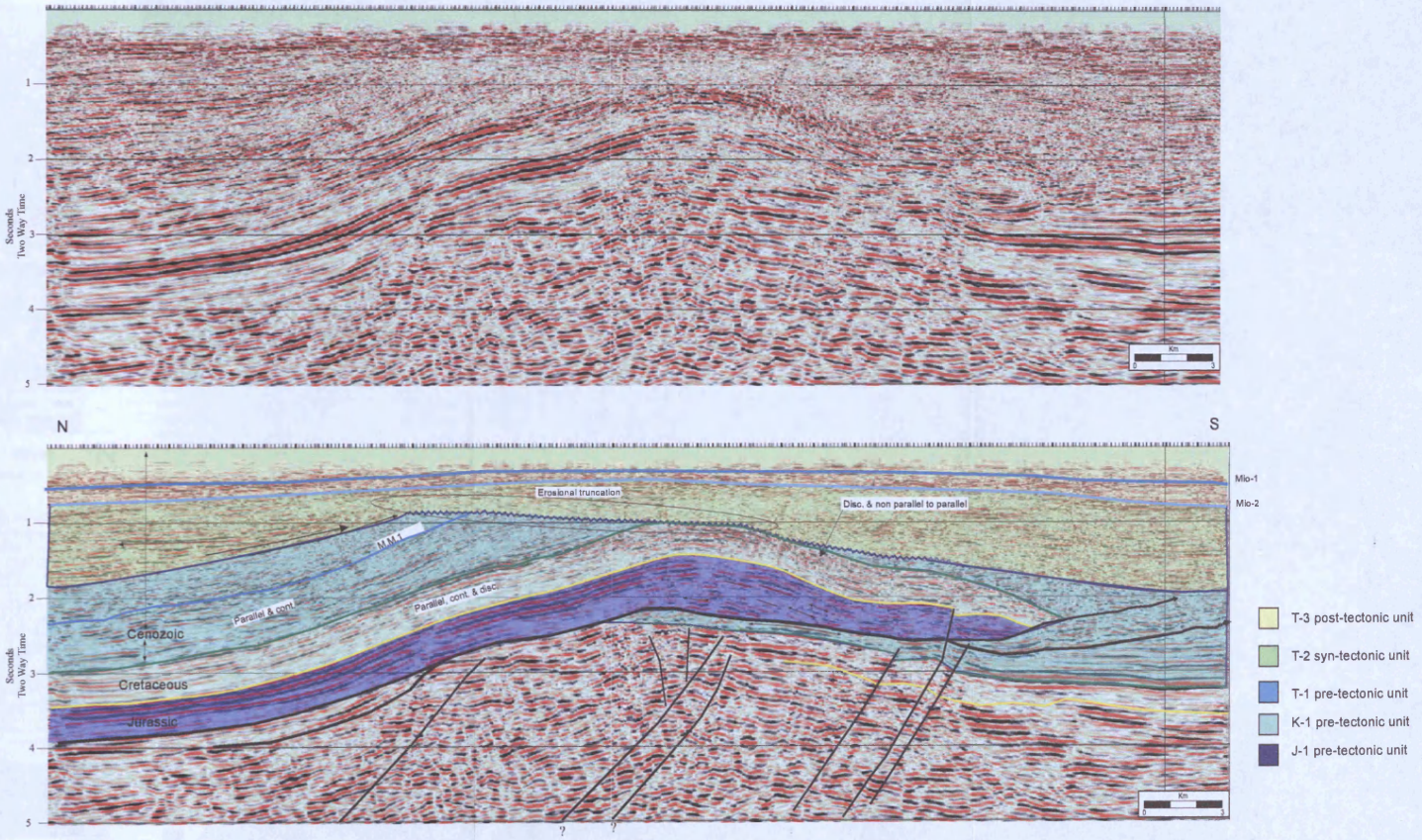

Figure3.26
Seismic and interpreted geoseismic section, oriented S-N; for precise location refer to Figure 3.24. Note the overall continuous character for both the Jurassic and Cretaceous intervals. The Cretaceous, towards the crestal and forelimb regions, is characterised by discontinuous, semi-parallel seismic reflections. The backlimb region consists of concordant reflections from the Jurassic to the INU seismic horizon. The INU along the crestal portion denotes erosional truncation features, away from it becomes concordant with overlying and underlying strata. Along the crest of the structure the unconformity appears to be in direct contact with Mesozoic rocks.

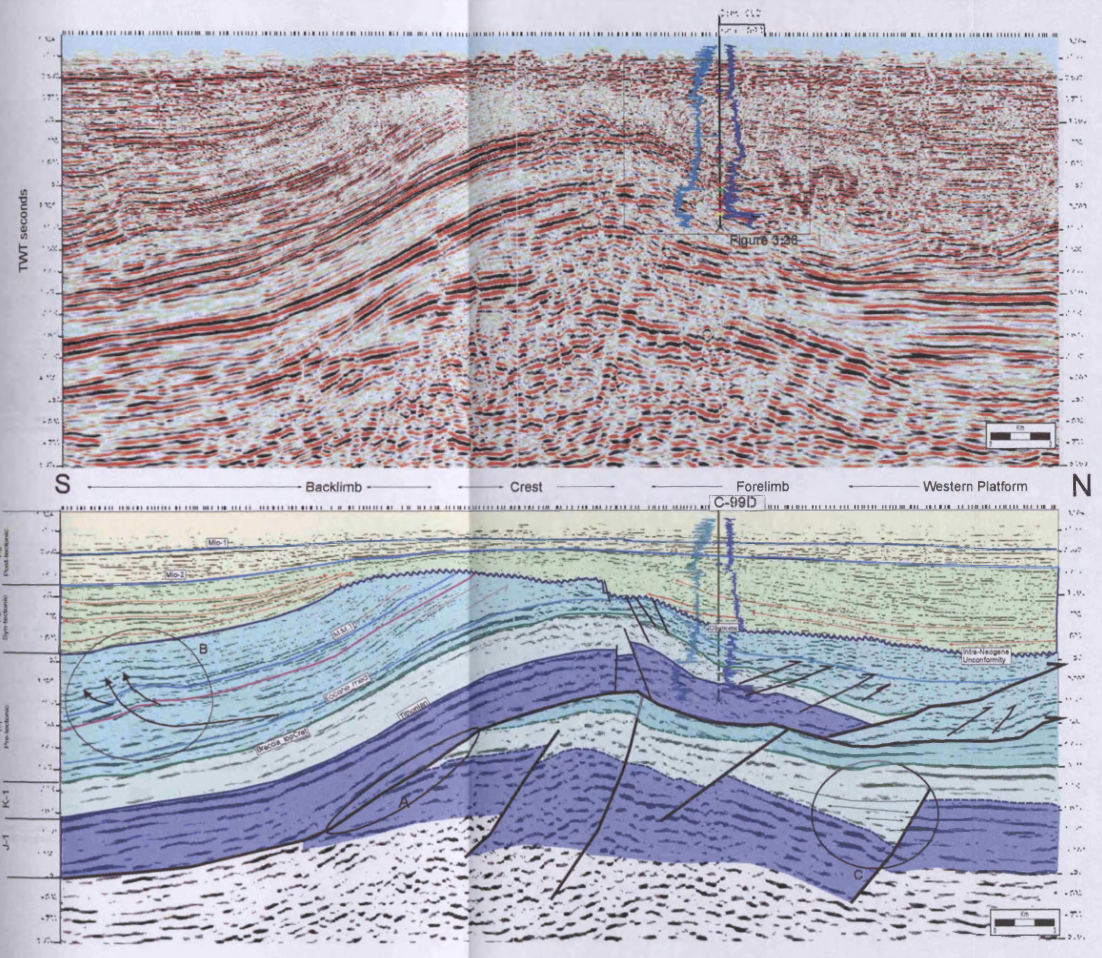

Figure 3.27
Seismic line uninterpreted and geoseismic inertptreted sections oriented almost S-, through the thrusted structural block refer to figure 3.24. Well C-99D is posted with gamma ray log at right and soinc log at left of wellbore. Both hanging(HW) and footwall (FW) are visible; the HW reveals folding, minor faults are illuminated at the crest of the structure; the internal character of the Cretaceous successions is continuous and concordant at the backlimb which becomes considerably discontinuous towards the crest and forelimb, shaded in green; its overall thicknesses increases southerly within the HW; the FW reveals variable thickness which appear fault controlled, circle (C), decreasing southerly. Note the deep rooted faults within the FW block; along the ramp reflection truncations are well imaged encircled (A). Towards the front thrust syndeformation package region discontinuous medium amplitude, slightly contorted reflection occur, minor backthrust have been interpreted that accommodate the shortening due to thrusting; Note the erosional truncation occurring in the backlimb region beneath the INU (Intra Neogene Unconformity) horizon, and the onlapping configuration at the forelimb region. Cirlce "A" highlights a minor fold bend occurring at the base of the backlimb within Palaeogene strata, the master thrust fault detachment limit is found at the "med Eocene" contact, where core data of other wells have revealed a carbonate-shale boundary; seismically a change in acoustic character is appreciated between the folded and underlying packages.

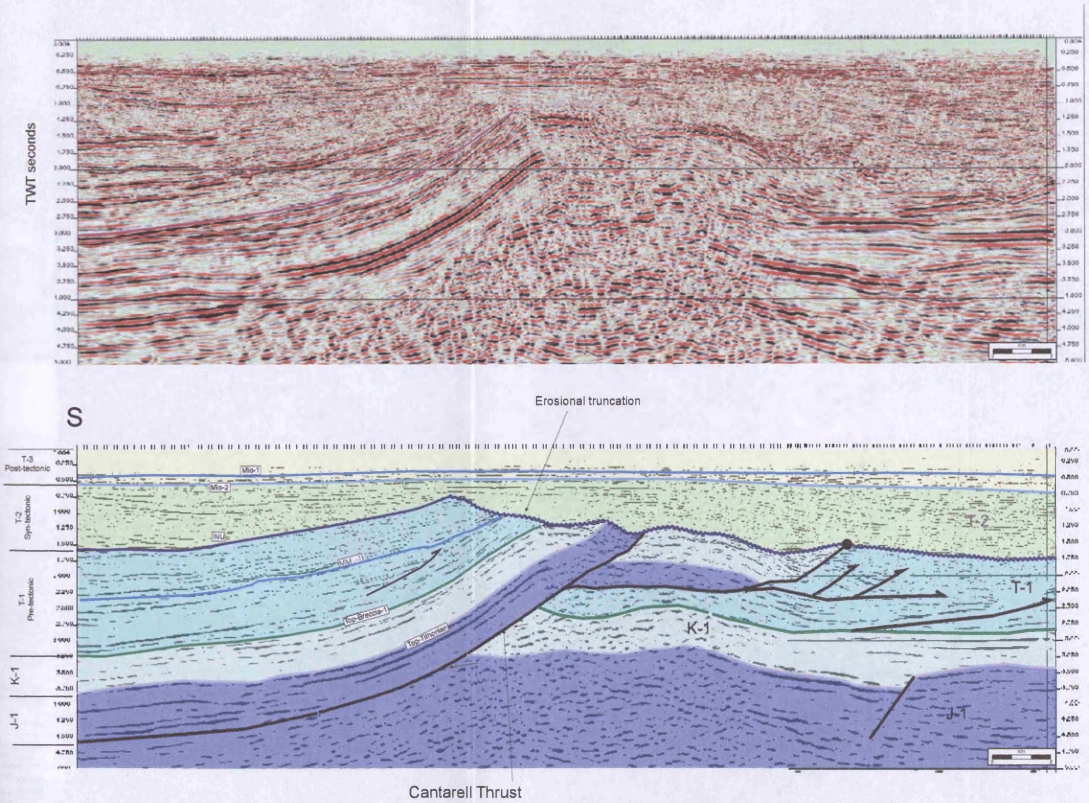

Figure 3.28
Seismic section and interpreted geoseismic section; for location refer to Figure 3.24. Note the four seismic units and their structural deformation style; the extent and morphology of the unconformtiy, the erosional truncation; extensional normal faults at the base of the Cretaceous, seismic unit K1. The structural style reflect morphological similarities to duplex structures, or double thrust systems.

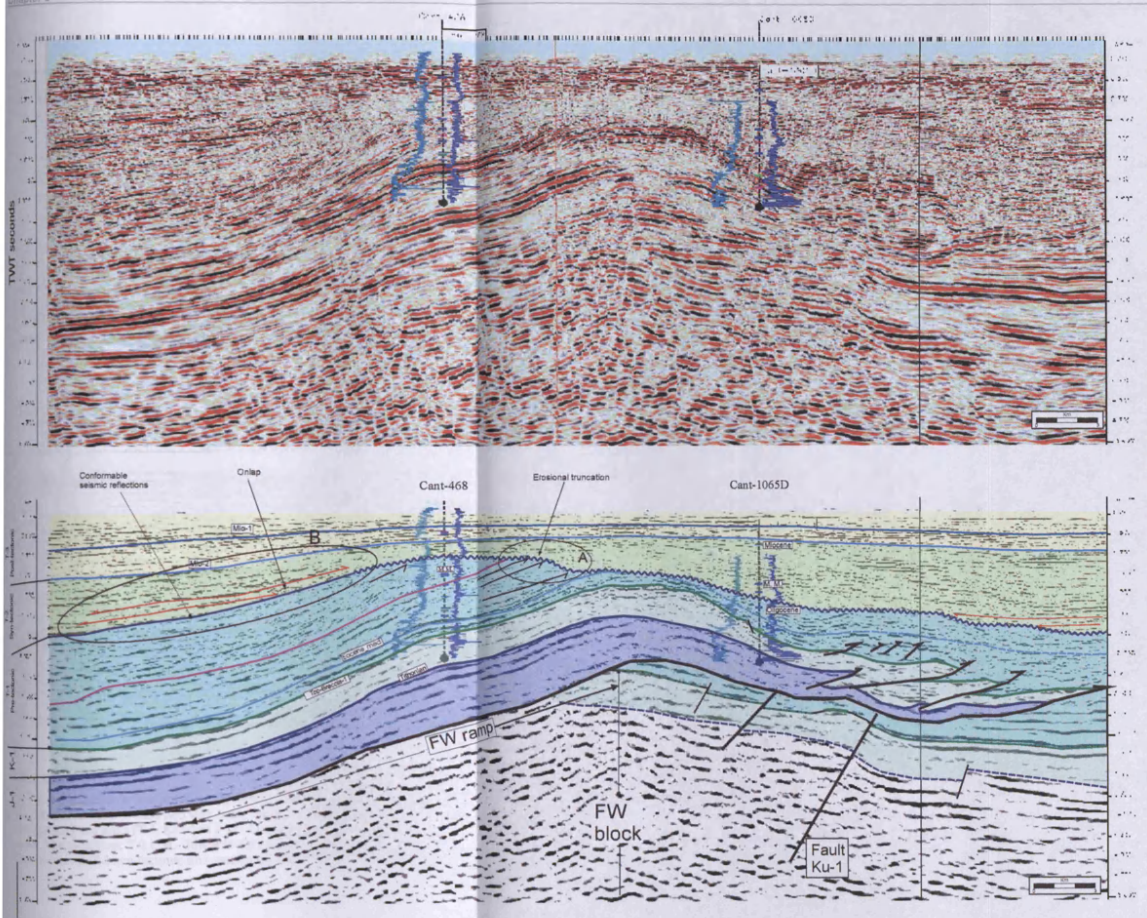

Figure 3.29
Seismic line and geoseismic interpreted sections oriented S-N through the Thrust Block. Refer to Figure 3.24 for location. Illustrating seismic units (J-1, K-1, T-1, T-2, and T-3). Wells C-468 and C-1065D are posted with gamma ray and sonic log, right and left respectively. Both hanging(HW) and footwall (FW) are noticeable. The internal seismic character of the Cenozoic HW exhibits continuous and concordant reflections within the backlimb region which become considerably discontinuous towards the crest and forelimb of the Thrust Block. Within the HW, the overall thickness for J-1 and K-1 units increases towards the south.
The FW shows an overall wedge like morphology, with a relative continuous dip along the "FW ramp". Internally, faults with a south dip are interpreted. Towards the Eastern Platform region these faults reveal a growth package which occur at the Jurassic-Cretaceous boundary. Similar faults have been observed elsewhere e.g. Figures 4.53 and 4.54.
The thrust plane exhibits an apparent concave downward morphology which is due to a velocity pull-up effect. The thrust plane appears to be tipping out within Palaeogene successions seen at the northernmost region of the section. Note the concave downward morphology of the Intra Neogene Unconformity interpreted horizon. Erosional truncation, circle "A", is observed at the southern region of the crest. Towards the forelimb, onlapping reflections occur overlying the INU horizon.
Circle B highlights the seismic reflections of unit T-2 showing onlap and having very shallow dips that converge onto the structure

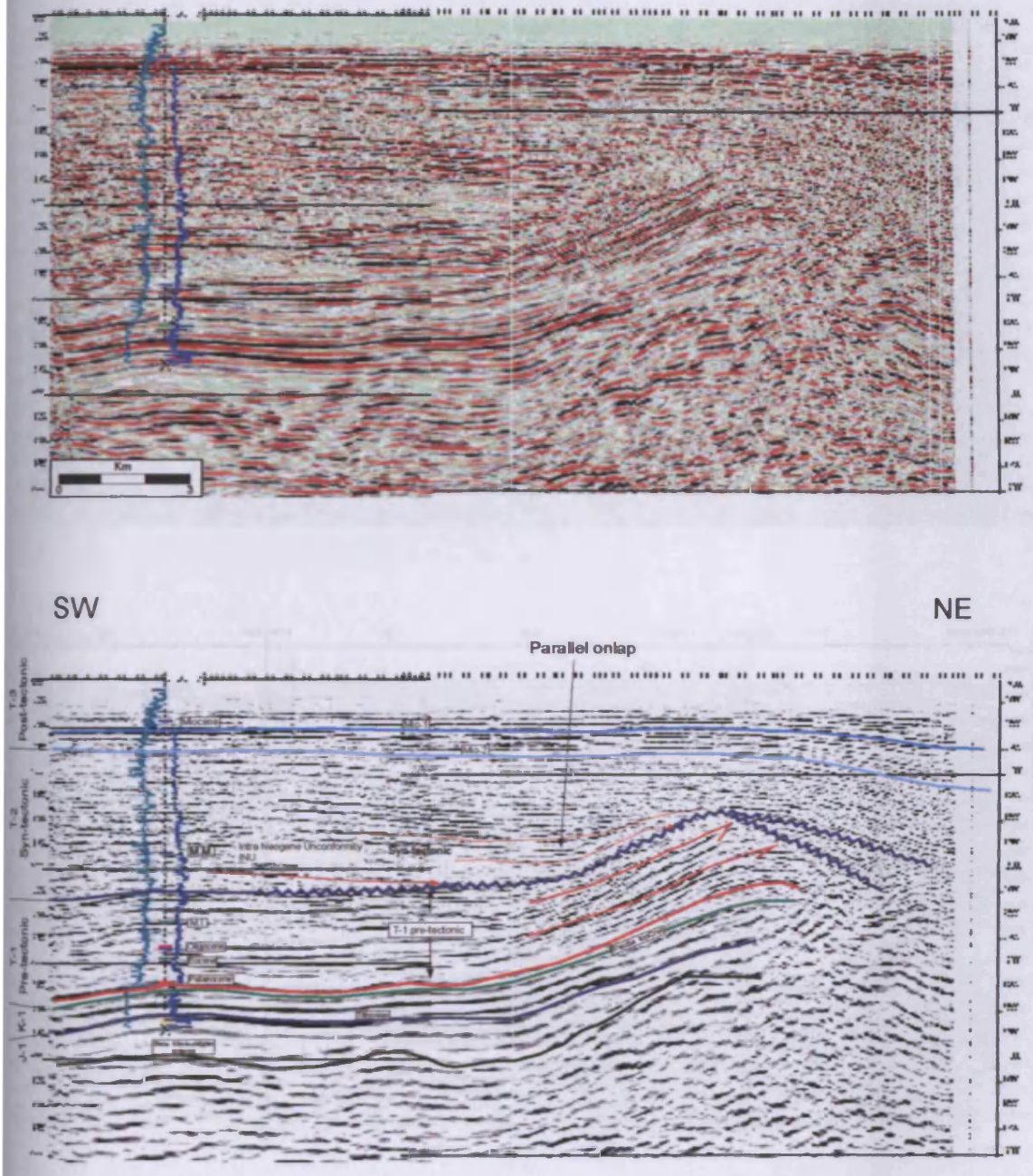

Figure 3.30
Seismic and geoseismic section along the Western Platform, refer to figure 3.24 for location. Vertical scale in milliseconds two way time. Note the parallel concordant seismic character of the pre-tectonic units (T-1, K-1 and J-1). Convergent onlap is observed onto the fold within the syn-tectonic T-2 unit. Towards the crest, erosional truncation is observed. Growth interval, T-2 syn-tectonic unit associated with folding is shaded in blue.

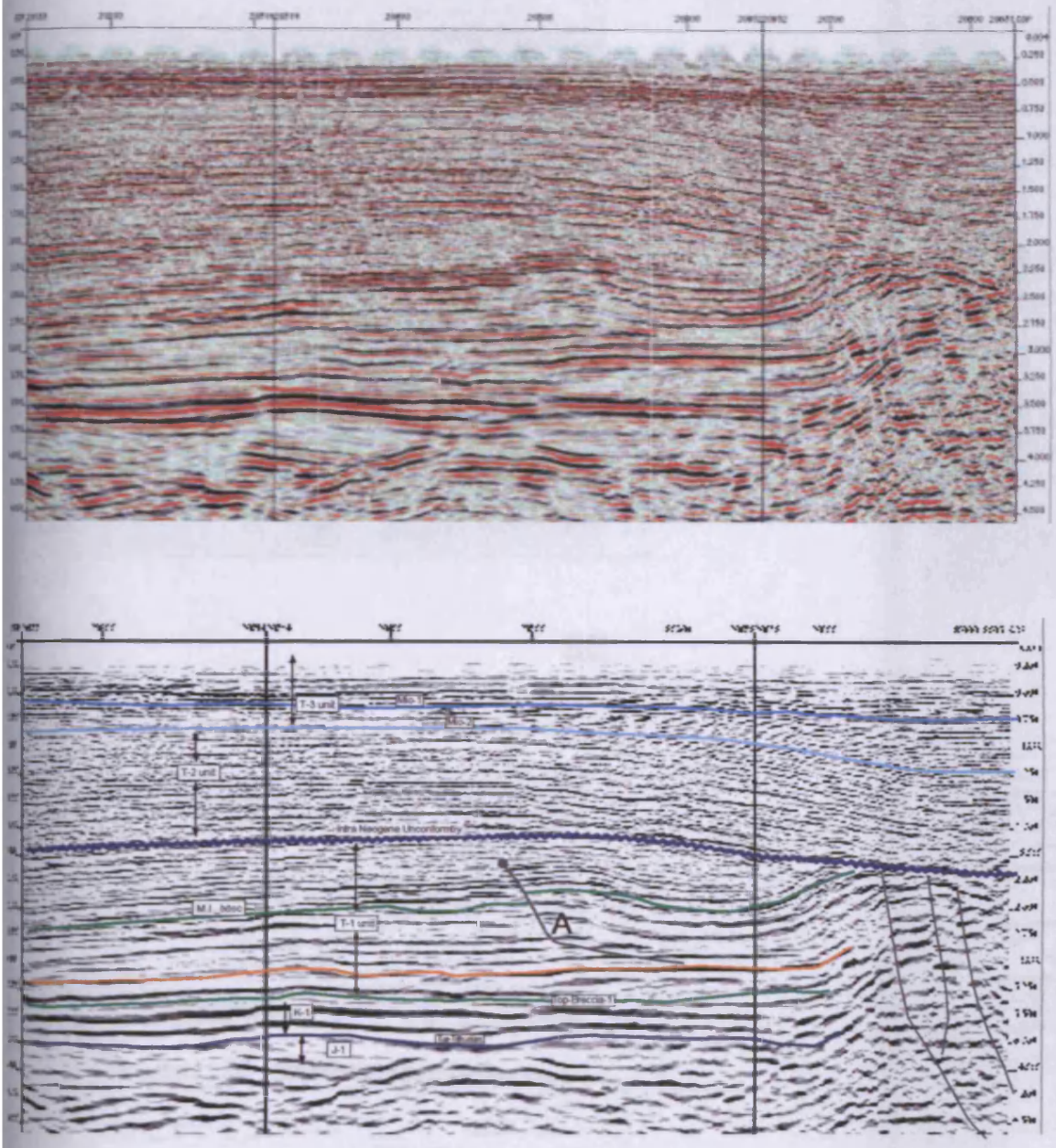

Figure 3.31
Seismic line and geoseismic interpretation along the Eastern Platform; for location refer to Figure 3.24. Note the thrust structure labelled "A" , the M.I._Ixtoc horizon appears displaced by about 100 msec twt. The thrust is contained and tips out within Unit T-1.

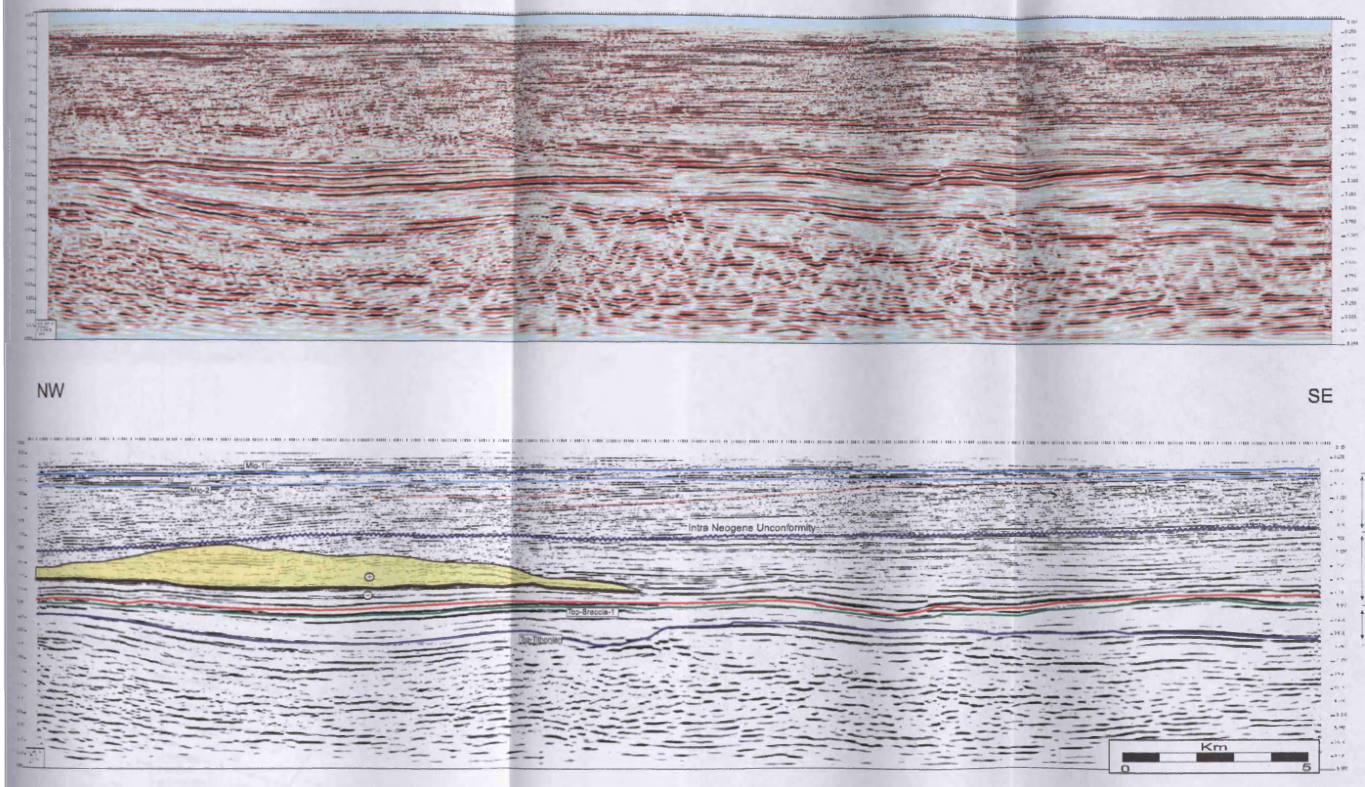

Figure 3.32
Seismic and interpreted geoseismic inline 3808, along the Eastern Platform. Note the overall flat and concordant appearance of the seismic reflections. The Cretaceous interval has a basal non-reflective character that exhibits higher amplitude towards the top. Note the irregular base defined by the Top-Tithonian seismic horizon. Towards the NW portion of the section, coloured in yellow consists of a thrusted Tertiary sequence with minor translation refer to Figures 3-6 and 3-9. The thrust gliding plane is encased within Tertiary shales, and linked to the major thrust plane found in the major thrusted block. The unconformity here presented corresponds to the area of correlative conformity, hence no erosional truncation nor onlapping is evident.

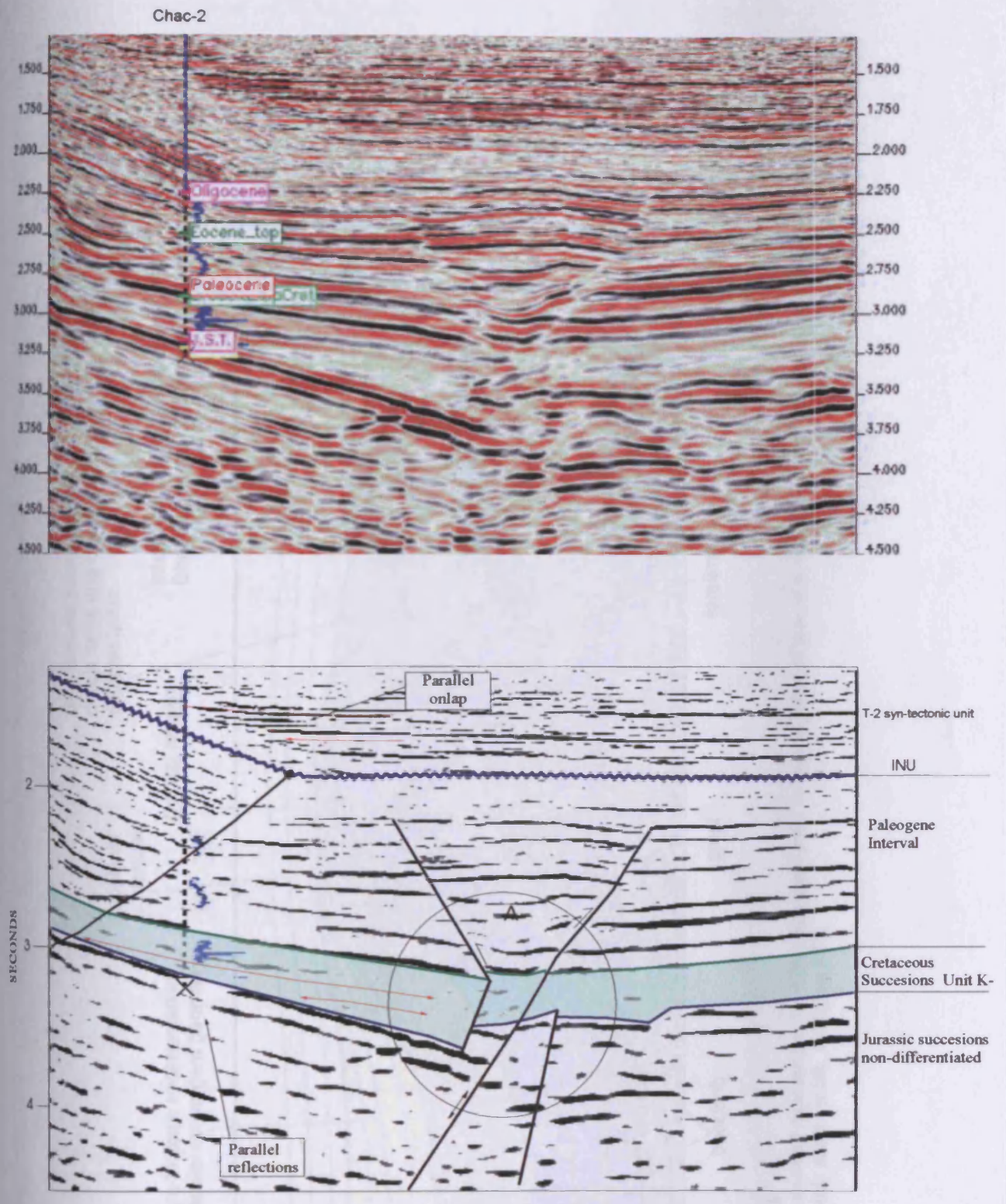

Figure 3.33
Seismic section and interpreted geoseismic section. For location see Figure 3.24. Note the irregular thickness for the Cretaceous interval. Thickness increase is observed in the downthrown side of the normal fault circle A. It is interpreted that this normal fault resulted from early phases of structural extension that appears reactivated at later stages through compressive stresses related to the formation of the thrust and fold structure. Note the INU unconformity at 1.5 secs. related to the structural deformation of Cantarell. Convergent onlap is observed at the base of seismic unit T-2.

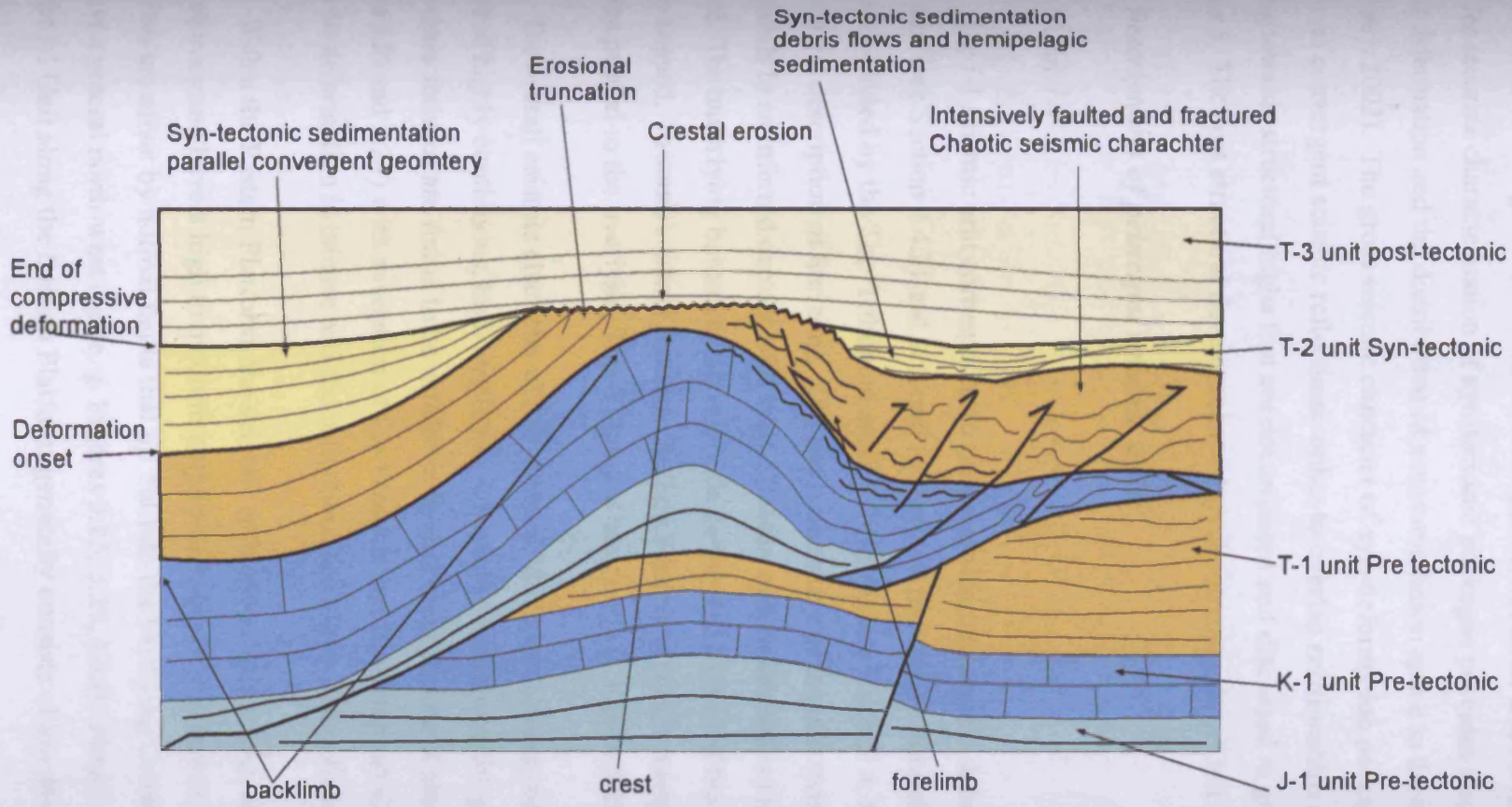

Figure 3.34
Schematic drawing representing the different seismic units defined in terms of pre-, syn- and post-tectonic sedimentation. Line is oriented approximately north - south, see figure 3.27.

consists of convergent seismic reflections, onlap to overlap relationships and thickness thinning towards structural highs that are documented and discussed in greater detail in Chapter 5. The post structural development interval corresponds to Unit T-3.

3.5.3 Descriptions of principal seismic units

3.5.3.1 Unit J-1

The J-1 seismic unit corresponds to the entire Upper Jurassic sedimentary succession (see Section 3.4.2) and is found throughout the entire Cantarell study area. The top is defined by the Top-Tithonian seismic horizon (see Chapter 4, Section 4.2.2.4 for structural description of horizon). The basal boundary of the unit (which corresponds to an inferred contact with the Callovian evaporates below) has not been mapped. The underlying basement has not been penetrated by any of the wells nor has it been mapped. In some seismic sections the Top Kimmeridgian is interpreted which is almost parallel to the overlying Top-Tithonian horizon (e.g. Figure 3.25).

The overall seismic character of the interpreted Upper Jurassic succession consists of highly continuous, high amplitude reflections with a parallel geometry. These characteristics are found to be similar in the different structural blocks (e. g. Figures 3.25 and 3.27) with exception of the Western and Eastern Fault Corridors, where the deformation is intense and the reflections are highly discontinuous.

Within the Eastern Platform, the seismic reflections are parallel, continuous, of low frequency and have a high to medium amplitude response. In places, the reflections are offset by normal faults that tip out into the overlying Cretaceous interval and have a general north-west dip (e. g. Figures 3.25, 3.27, 3.33). Note that in Figure 3.26, the J-1 Unit along the Eastern Platform generally consists of low frequency,

tinuous reflections, although localised areas of high to low amplitude reflection figurations are observed.

Towards the Western Platform near the Ixtoc-1 well, the reflection figurations are distinguished by high amplitude, parallel and highly continuous mic reflections (Figures 3.25, 3.30 and 3.31). These reflections are underlain by an rval of about 500 ms of low to medium amplitude, semi-continuous reflections. is medium amplitude interval appears to be infilling an irregular surface where the mic character changes to higher amplitude discontinuous seismic reflections. This ndary has been interpreted as the possible Basal Oxfordian (Figures 3.25 and 3.30).

Within the Thrust Block in the footwall the occurrence of the Jurassic cession is inferred from seismic reflection correlations, and supported with wells penetrated into the lowermost Cretaceous succession, since no wells have ifically penetrated into the Jurassic.

The hangingwall block is divided into three areas: backlimb, crestal and limb areas (Figure 3.27). The backlimb area, consist of well stacked, parallel, tinuous, high amplitude and low frequency reflections that steeply dip (20°) towards south. Along the hangingwall ramp the basal part of the J-1 unit is defined by the st plane. This thrust plane has been mainly interpreted from the seismic character ncation) and is constrained with the other interpreted seismic horizons (Figures 6, 3.27, and 3.29) and direct well calibrations (see Chapter 4, Section 4.4.1).

Along the footwall ramp region, sub-parallel and sub-horizontal reflections are rlain and truncated by seismic reflections that have been interpreted as part of the gingwall block (Figure 3.29). The Jurassic interval has a distinguishable seismic racter that consists of high amplitude and very continuous reflections (e.g. Figures 7 and 3.29). Within the crestal region, the lower part of the J-1 unit, is characterised more discontinuous chaotic reflections.

In the footwall block within the crestal area, the Jurassic succession exhibits parallel and sub-horizontal seismic reflections of high amplitudes and low quency. The seismic reflections exhibit various degrees of continuity (e. g. Figures 7 to 3.29).

The areal distribution of the J-1 thickness was not calculated because no basal horizon is interpreted. The thickness reported in the well completion logs (Pemex) are calculated from well penetrations into the Upper Jurassic (see Section 3.4.2).

3.5.3.2 Unit K-1

The K-1 seismic unit represents the Cretaceous succession. Defined to the base by the Top-Tithonian seismic horizon and to the top by the Top-Breccia-1 seismic horizon. Both horizons are interpreted throughout the entire 3D seismic volume. The Cretaceous interval has been penetrated by the majority of the wells present in the study area, and thus provides a vast amount of data. This large dataset offers many control points, (core coverage, lithostratigraphic and biostratigraphic controls, well log information, and check-shots) to enable the calibration of the seismic data, however the amount is overwhelming and is thus very difficult and time consuming to quality control. This has resulted in confusion in constraining the seismic interpretation to the stratigraphic markers provided by Pemex. Some well markers as defined by Pemex are calibrated consistently on a specific reflection, whereas others fall randomly within a time window of about 250-350 ms.

The Cretaceous thickness varies significantly throughout the study area (Figure 3.35). Within the Western Platform isochrones appear homogeneous from 300 to 400 ms. Within the hangingwall Thrust Block, isochron values decrease significantly from 500-400 ms to 250 - 350 ms twt (e. g. Figures 3.26 and 3.29). The southern area of the Thrust Block shows relatively minor isochron variations and a general decrease in thickness towards the west (Figure 3.35). The Eastern Platform also shows thickness variations (Figure 3.35). The south-western region reveals general isochron values ranging from 200 to 400 ms twt. Thickening usually is seen across normal faults within the hangingwall block and against the fault plane in an eastern direction (Figures 3.25, 3.27 and 3.33). The irregular thickness of unit K-1 is herein interpreted to be related to the infillment of an irregular Top Tithonian palaeo-bathymetry. The basal contact of unit K-1 defined by the Top-Tithonian seismic horizon is irregular. These irregularities are provided by normal faults that throw in basinwards direction, towards the west. The vertical extent of these normal faults is limited to the basal interval of the Early Cretaceous succession (Figure 3.33, circle).

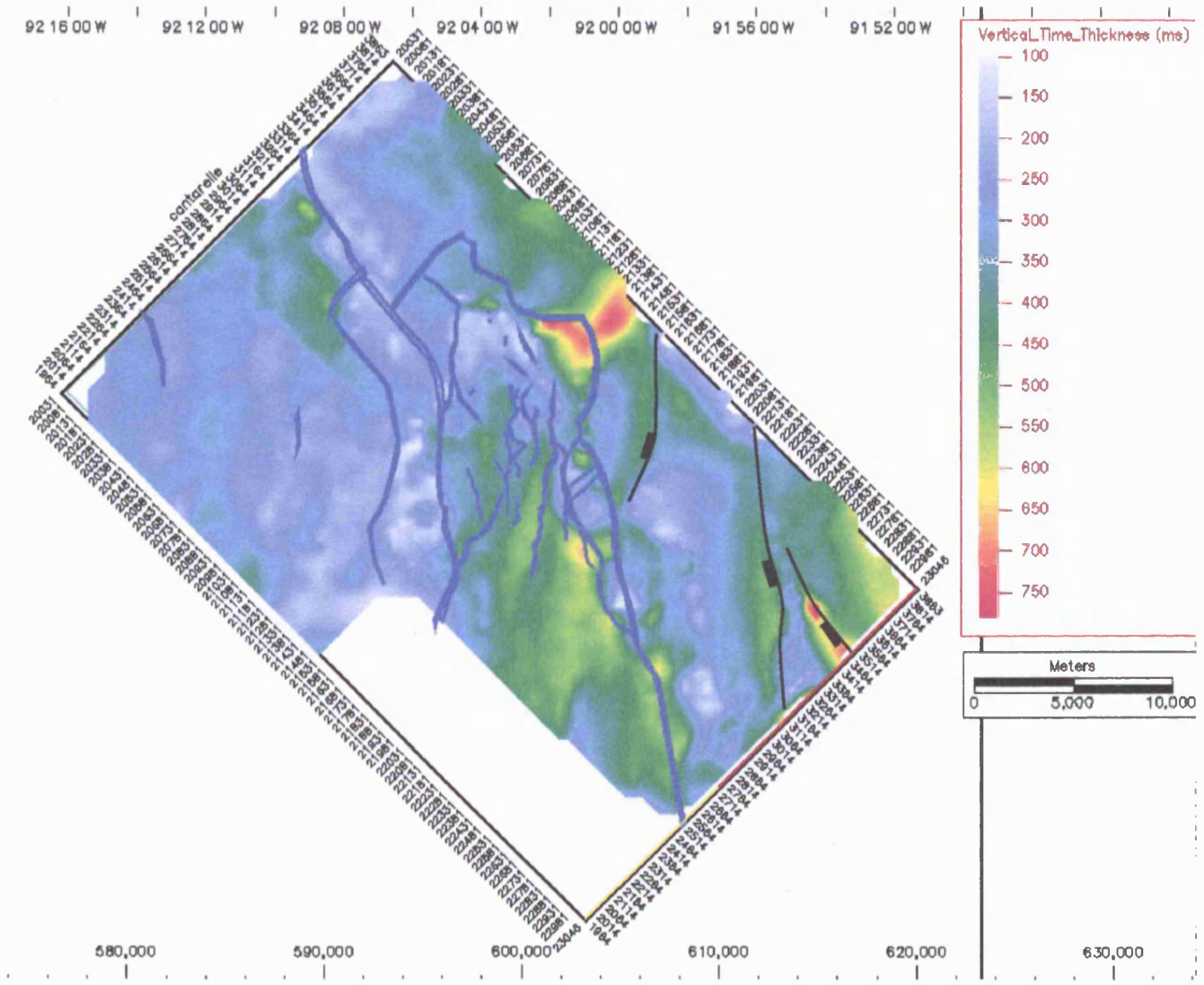

Figure 3.35
Isochrone map for seismic unit K-1, the hangingwall isochrone of the Thrust Block is displayed. Reds indicate thicker areas and blues thinner areas. Top Cretaceous fault arrays, blue coloured, and Upper Jurassic, black lines, are posted for structural reference. Areas within the Western and Eastern Fault Corridors are considered of high uncertainty. Note within the Thrust Block thickness thinning towards the north. Within the Eastern Platform thickness thickening occurs within the hangingwall blocks of Late Jurassic to Early Cretaceous normal faults.

The seismic character for unit K-1 generally consists of a basal non-reflective interval that becomes higher in amplitude and more continuous towards the top. However, there are areas where the frequency and amplitude are distinctively high throughout the entire Cretaceous interval. These areas generally correspond to the Western and Eastern Platforms (Figures 3.25 and 3.30 to 3.33).

In the Western Platform of the study area, the Cretaceous interval consists of high amplitude, low frequency, continuous reflections which are generally flat-lying and near horizontal (Figures 3.25, 3.30 and 3.31). The Eastern Platform shows a combination of very low amplitude reflections and high amplitude, parallel continuous, low frequency seismic reflections occur (Figure 3.32). Within the Thrust Block, the hangingwall block exhibits a similar seismic character to the reflections observed within the Eastern Platform (e.g. low amplitude at the base and high amplitude, high continuous reflections towards the top). At the crest and forelimb areas of the structure, the seismic character changes considerably, distinctive higher frequencies are seen and the reflections are less continuous. Towards the base of the forelimb the seismic reflections appear very discontinuous. This discontinuous character is interpreted to result mainly from structuring (e. g. Figures 3.26 and 3.29; see Chapter 4, Section 4.4.2.3).

Along the crestal and forelimb regions of the structure, the uppermost limit of the K-1 Unit exhibits a highly discontinuous character which prohibits the accurate interpretation on a line to line basis (Figures 3.26 to 3.29). In localized areas of the crest the Top-Breccia-1 horizon appears to coincide with the Intra Neogene Unconformity boundary (Figure 3.26). It is difficult to assess the vertical depth of erosion of the INU solely based on seismic character. Significant change in acoustic impedance is observed along the crestal and forelimb region where the INU is in close proximity with the Top-Breccia-1 horizon. In places along the crest and forelimb, seismic reflections of the uppermost K-1 Unit are discontinuous, of high frequency, and low amplitude (e. g. Figures 3.26 to 3.29). In contrast, the Cenozoic well stratigraphic markers provided by Pemex does not refer to an unconformity. Instead a layered stratigraphy is suggested for most of the stratigraphic successions with localised thinning.

The K-1 Unit in the footwall block consists of high amplitude, low frequency seismic reflections that appear discontinuous as a result of structuration. The fault and fracture orientations are not readily apparent, (see Chapter 4, Section 4.4.3).

In summary, the Mesozoic seismic reflections are overall parallel, continuous and concordant. The amplitude noted for the Upper Jurassic (J-1 Unit) is distinctively high. For the Cretaceous (K-1 Unit) low amplitude reflections are apparent, discontinuous to chaotic seismic reflections were noted specially along the crestal and forelimb regions. The nature of the discontinuous seismic character is interpreted to be related to the structural evolution of the area (see Chapters 4 and 6).

3.5.4 Cenozoic successions

3.5.4.1 Introduction

The Cenozoic interval is characterised by a change in sedimentation from a carbonate-dominated succession during the Cretaceous to a more siliciclastic one (see Chapter 2 and Sections 3.4.3 and 3.4.4). During the Neogene major structural deformation occurred resulting in a complex thrust system (see Chapters 4 and 5).

The Cenozoic successions are herein divided into three seismic units: T-1, T-2 and T-3. The seismic horizons Mio-1, Mio-2 and the Intra Neogene Unconformity defined the seismic units (Figure 3.3). These units were defined based according to their internal seismic reflection configurations (concordant, vs. convergent and divergent) and their geometrical relationships to the underlying thrust and fold structure (concordant and/or convergent with the fold and thrust structure). Unit T-1 represents the pre-growth strata; Unit T-2 represents the sedimentation coeval with structural growth; and Unit T-3 represent the sedimentation once structural compression terminated (Figures 3.33 and 3.29).

An attempt was made to age calibrate the seismic horizons using well markers provided by Pemex. However, it was noted that the well-to-seismic correlation was quite poor, especially within the youngest and shallowest intervals (top Miocene), where the well markers do not tie consistently the seismic horizons Mio-1 and Mio-2 (Figure 3.4). The intra-Miocene horizons are clearly discordant to those units deformed in the underlying thrust structure. From the regional seismic lines (see

Chapter 2, and Enclosure 5) the seismic horizons Mio-1 and Mio-2 are seen to coincide with the progradational seismic packages defined regionally. Based on the discordant geometry and the relationship to the INU, the chronostratigraphic age for these horizons is viewed as post dating the structural compression that resulted in thrusting and folding (see Chapter 4).

The INU unconformity was identified and interpreted based on mainly erosional truncation seismic reflection terminations (e.g. Figures 3.26 to 3.29). Some wells that penetrated the unconformity display strong and sharp deflections on well logs (Figure 3.29). This suggests a significant change in lithology across the unconformity surface. The hiatal range represented by the INU surface was constrained using the well markers that penetrated the surface. However, as mentioned above, the uncertainty of the well picks within the Upper Cenozoic succession is large and thus the well marker ages are merely approximate. The INU will be described and discussed in greater detail in Section 3.5.5.

3.5.4.2 Unit T-1

Seismic Unit T-1 corresponds to the pre-tectonic Cenozoic interval. The base is defined by the Top-Breccia-1 seismic horizon. The top of Unit T-1 is defined by the Intra Neogene Unconformity INU (Figure 3.3). The seismic quality of the Cenozoic interval is medium to poor, especially over the crest of the structure. This is partially due to the seismic processing of the seismic data which was processed to enhance the deeper structures. Despite the modest quality of the seismic data within shallower intervals, various relevant sedimentary and structural features have been observed.

Within the footwall of the Thrust Block, well penetrations have encountered Cenozoic sediments of Oligocene to Palaeocene age, (Figures 3.7 and 3.8). From their seismic character these cannot easily differentiate from the Mesozoic carbonates (e. g. Figures 3.26 to 3.29). The thickness of unit T-1 varies throughout the study area (Figure 3.36). The thinner isochron areas are coincident with the structural highs.

Within the hangingwall, towards the backlimb region, the seismic data is characterised by concordant, parallel, continuous, moderate amplitude seismic reflections. Towards the crestal region, the reflection configurations of unit T-1 exhibit considerable localised erosional truncation (e. g. Figures 3.5 and 3.27).

Figure 3.36
Isochron map for seismic unit T-1 in msec twt .
Note that the thinner thickness are coincident with the structural highs.

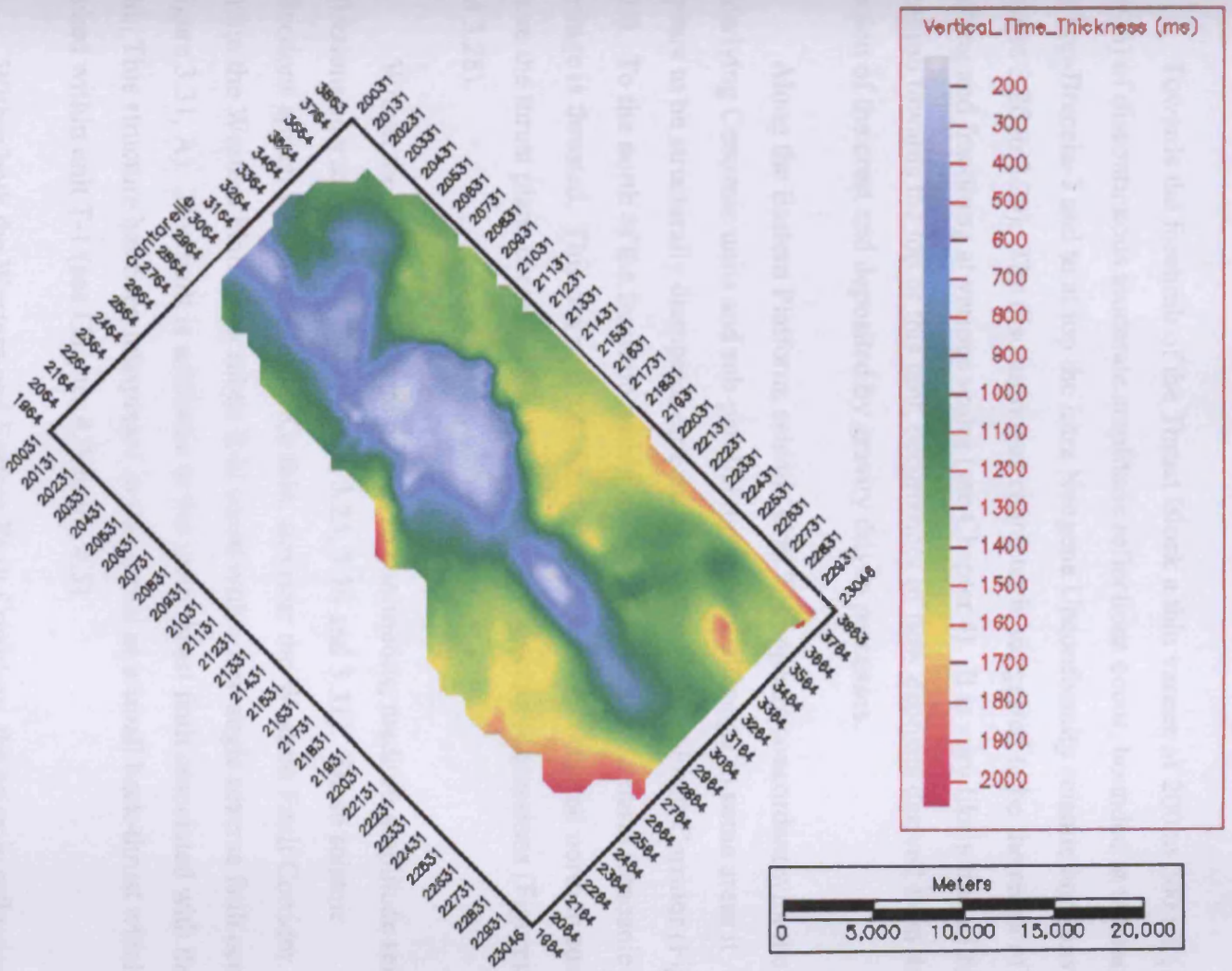

From the seismic interpretation, it appears that most Unit T-1 has been removed by over the crestal region.

Towards the forelimb of the Thrust Block a thin veneer of 200 to 300 ms (140 – 200 m) of discontinuous moderate amplitude reflections occur, bounded at the base by the Top-Breccia-1 and to at top the Intra Neogene Unconformity seismic horizons (e.g. Figures 3.26 to 3.29). The discontinuous character is suggested to be the result of faulting and fracturing at various scales (see Chapter 4). It is very likely that within the forelimb towards the top of this unit, occurrences of flow deposits derived from the erosion of the crest and deposited by gravity driven processes.

Along the Eastern Platform, seismic Unit T-1 appears concordant with the underlying Cenozoic units and sub-parallel throughout although in some areas it appears to be structurally disrupted, especially near the Eastern Fault Corridor (Figure 3.25). To the north of the forelimb within the Eastern Platform, a basal Cenozoic package is thrusted. This can be noted from vertical sections oriented north to south, where the thrust plane occurs within the Eocene – Oligocene successions (Figures 3.26 and 3.28).

Within the Western Platform parallel to continuous, medium amplitude seismic reflections characterise Unit T-1 (Figures 3.25, 3.30 and 3.31). These seismic reflections appear folded within the Ku fold, and near the Western Fault Corridor. Within the Western Platform a subtle fold cored with a low angle reverse fault occurs (Figure 3.31, A). This fault is antithetic to the main thrust fault associated with the Ku fold. This structure has been interpreted in this thesis as a small back-thrust which is packed within unit T-1 (see Chapter 4, Section 4.5).

Within both the Western and Eastern Fault Corridors, the seismic reflections are pervasively disrupted by structuring which prohibits any accurate interpretation.

3.5.4.3 Unit T-2

Seismic Unit T-2 represents the syn-tectonic sedimentary unit of the structural evolution. This unit will be documented in greater detail in Chapter 5 using a seismic streamer data set that allows a better imaging of the seismic configurations at shallow stratigraphic levels. The base of seismic Unit T-2 is defined by the Intra Neogene

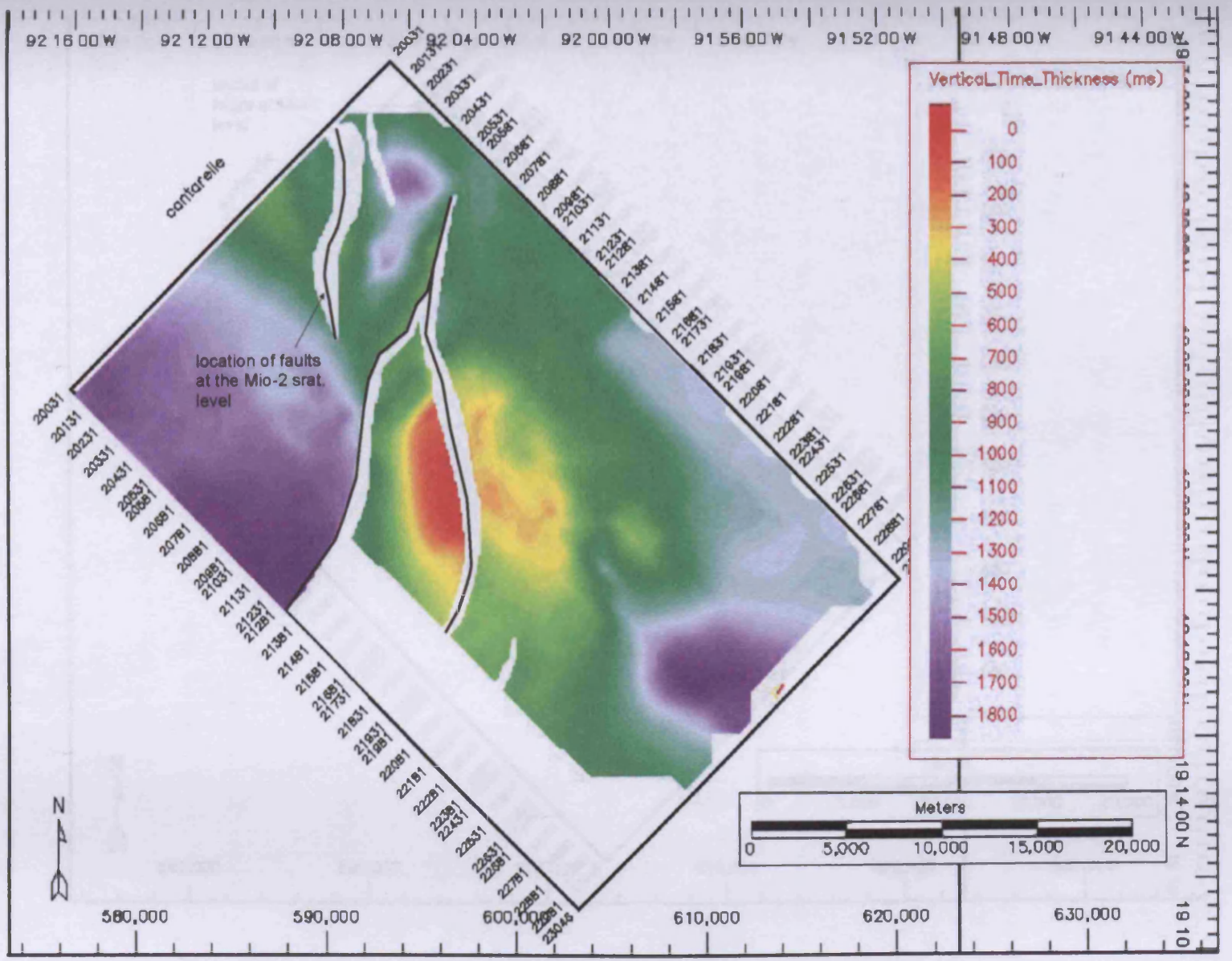

Figure 3.36.a Isochrone map for seismic unit T-2 in msec TWT. Note the thinnest thickness is coincident with the structural highs (Thrust Block). Black lines represent the location of the

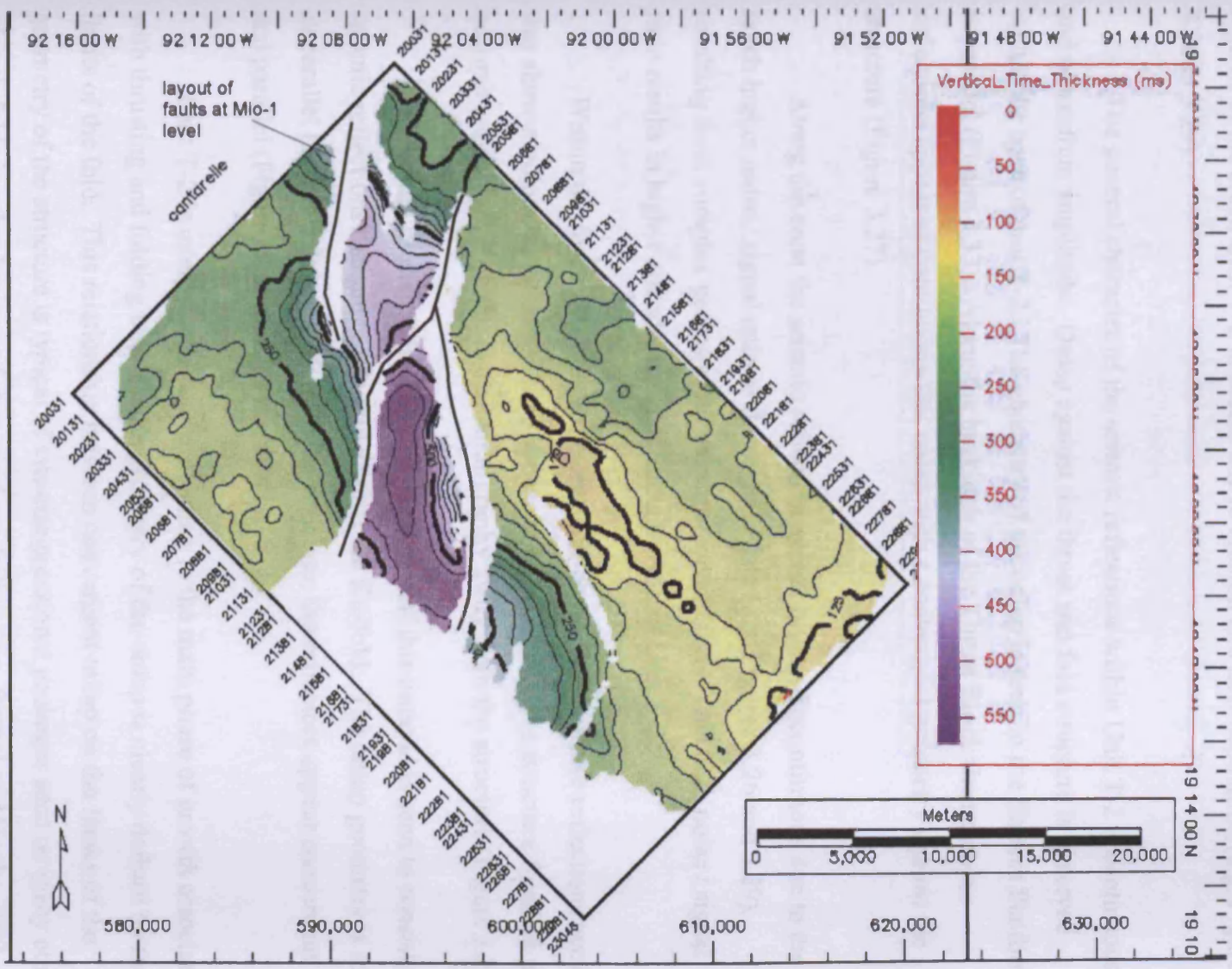

Figure 3.36.b Isochrone map for seismic unit T3 in msec TWT. Note the thinnest thickness is coincident with the structural highs (Thrust Block). Black lines represent the location of the

Unconformity (INU) and the top by the Mio-2 seismic horizon (Figure 3.3). Within regions of the crest, Unit T-2 is absent due to erosion and non-deposition (e.g. Figures 3.26 to 3.29).

The general character of the seismic reflections within Unit T-2 is continuous, and of medium amplitude. Onlap against the thrust and fold structure is observed within the base of unit T-2. The geometry of the onlap is seen in the Eastern Platform is parallel (Figure 3.33). Along the backlimb of the Thrust Block the seismic reflections appear as continuous that onlap with a convergent geometry against the structure (Figure 3.27).

Along the crest the seismic reflection appear highly discontinuous due to the much higher noise / signal ratio of the seismic data (e.g. Figures 3.26 and 3.29), resulting from complex geology and transmission artefacts. This high noise / signal ratio results in higher uncertainty in defining the top of Unit T-2.

Within the forelimb of the structure semi-continuous seismic reflections occur that show medium amplitude. These appear to onlap against the structure forelimb and become concordant with the overall stratigraphy away from the structure (Figure 3.27).

Within the Western Platform, the basal part of this interval is seen to consist of seismic reflections that onlap and thin against the Ku-fold. The onlap geometry is seen as parallel (Figure 3.30). Away from the structure, the reflectors appear concordant and parallel (Figures 3.30 and 3.31).

Unit T-2 is interpreted as corresponding to the main phase of growth associated with thrusting and folding because the geometry of the onlap is clearly defined by the limits of the fold. This relationship between convergent onlap on the flanks of the geometry of the structure is typical of syn-compressional packages seen on many other growth folds in other basins and numerical modelling (e.g. Bernal and Hardy, 2002; Flemings and Jordan, 1990; Chalaron et al., 1996; Garcia-Castellano et al., 1997; Zoetemeijer et al., 1992, 1993; Poblet and Hardy, 1995). The internal seismic configuration of the syn-tectonic Unit T-2 is studied in greater detail in Chapter 5.

3.5.4.4 Unit T-3

Seismic unit T-3 represents the post-tectonic sedimentary package. The base is defined by the Mio-2 seismic horizon and the top by the modern day seabed. The seismic reflection configurations observed within this unit are mainly parallel and concordant with minor thickening and thinning variations (Figure 3.25). Thickness variations are seen in this interval and occur throughout the study area (800 ms twt – 2200 ms twt).

Within the Western Platform concordant, semi-continuous seismic reflections that show local areas of relative thickening occur. The thickening is possibly associated with areas that experienced greater accommodation space, and that were located beneath wave-base action.

Within the Thrust Block, towards the Backlimb and the forelimb areas, onlaping seismic reflections onto the structure are noted. The thickness of this interval decreases towards the crest (from 1500 to 800 ms). Along the crest, the seismic reflections appear highly discontinuous due to apparent low resolution of the seismic data (e.g. Figures 3.26, and 3.27).

The Eastern Platform exhibits continuous, concordant, parallel, medium amplitude seismic reflections that dip towards the NW (basinwards). As previously documented in Chapter 2, Section 2.3.4, this package corresponds to a highly progradational unit.

3.5.5 Intra Neogene Unconformity

3.5.5.1 Introduction

As previously mentioned, an unconformity, the Intra Neogene Unconformity (INU), was recognised within the Tertiary interval based on the termination configurations of seismic reflections (Figures 3.26 to 3.29). The identification and interpretation of this surface posed great difficulties because: (1) the unconformity itself did not reveal a clear seismic reflection and (2) in areas away from the structural highs the unconformity passes laterally into areas where it is seen to become conformable with the gross stratigraphy. It was most clearly picked and correlated

within the crest and backlimb of the thrust and fold structure using arbitrary seismic sections as well as inlines and crosslines (e.g. Figures 3.26 and 3.27). Within the backlimb and southern parts of the crest of the structure erosional truncation is widely noted which serves as the basis for the interpretation and correlation of the INU (Figure 3.27).

The INU seismic interpretation was gridded using an IESX algorithm (Figure 3.37). The gridded surface represents the areas of erosional truncation, onlap and correlative conformity. Reflections that exhibit erosional truncation patterns occur towards the southern region of the crest of the Thrust Block, whilst away from the structure a correlative conformity is seen (Figures 3.25 and 3.36). Enclosure 3 reveals that the INU extends eastwards. Onlap is observed onto the Yucatan platform margin (section 2.3.3.3. and Figures 2.24 to 2.26).

This section (3.5.5) is subdivided further into three subsections (3.5.5.2 to 3.5.5.4). Section 3.5.5.2 describes the erosive extent and the stratigraphic age of the INU. Section 3.5.5.3 details the areal morphology of the INU and the seismic character of the INU and the overlying and underlying seismic character. Section 3.5.5.4 presents an interpretation of geological features that can be associated to the INU and in consequence influence the reservoir system.

3.5.5.2 Erosive extent and stratigraphic age

The well stratigraphic markers do not provide any documentation as to the magnitude of the erosional truncation over the structure. Instead most of the stratigraphic column is reported to be complete in the operator completion reports. However, seismic sections along the crestal region of the Thrust Block reveal considerable erosional truncation. Based solely on (i) the reflection configurations associated to the INU and (ii) the extent of erosion upon the crest of the Thrust Block it can be interpreted an almost complete removal of Eocene to possibly upper Cretaceous beds over localised areas of the crestal region of the Thrust Block (e.g. Figure 3.26).

The stratigraphic age of the INU was constrained using different wells. Well C-99D (Figure 3.38) indicates the presence of Oligocene strata immediately beneath the unconformity, and Miocene strata immediately overlying the unconformity, however no precise age data (in Ma) are available (Figures 3.27 and 3.38). Pemex stratigraphic

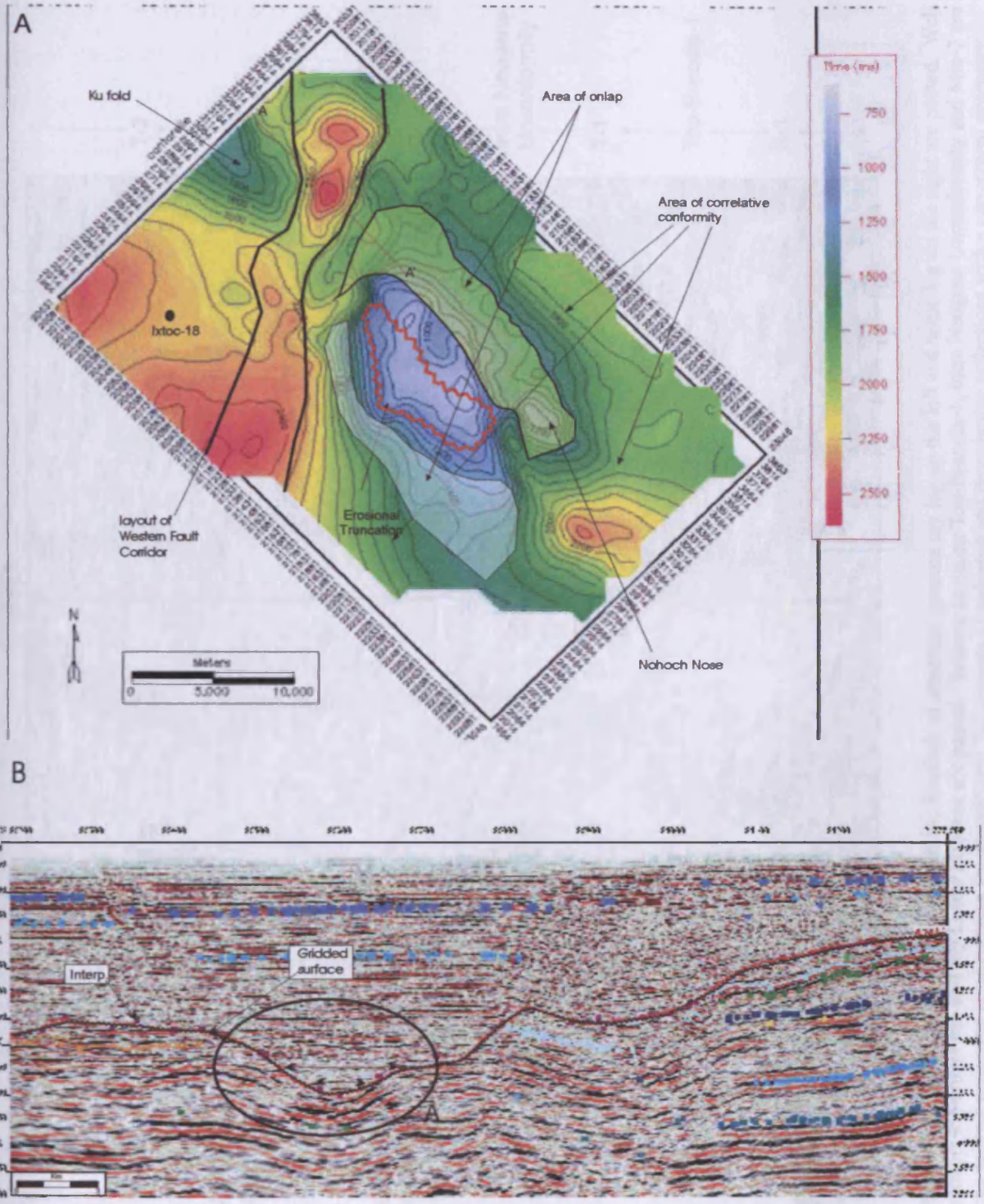

Figure 3.37
(A) Gridded map of the Intra Neogene Unconformtiy seismic horizon in two way time and (B) seismic line A-A' showing the interpretation and the gridded surface. Note in (A) the structural highs are coincident where the seismic character reveal erosional truncation (e.g. Figures 3.26, 3.27, 3.28). Towards the forelimb region onlap is noted, shaded in yellow. The shaded area correspond to the region where correlation between the reflections above and below the unconformity appear conformable. Towards the western part of the section an elongated depression occur with a concave upward morphology where infillmment of horizontal reflections are observed, circle A.

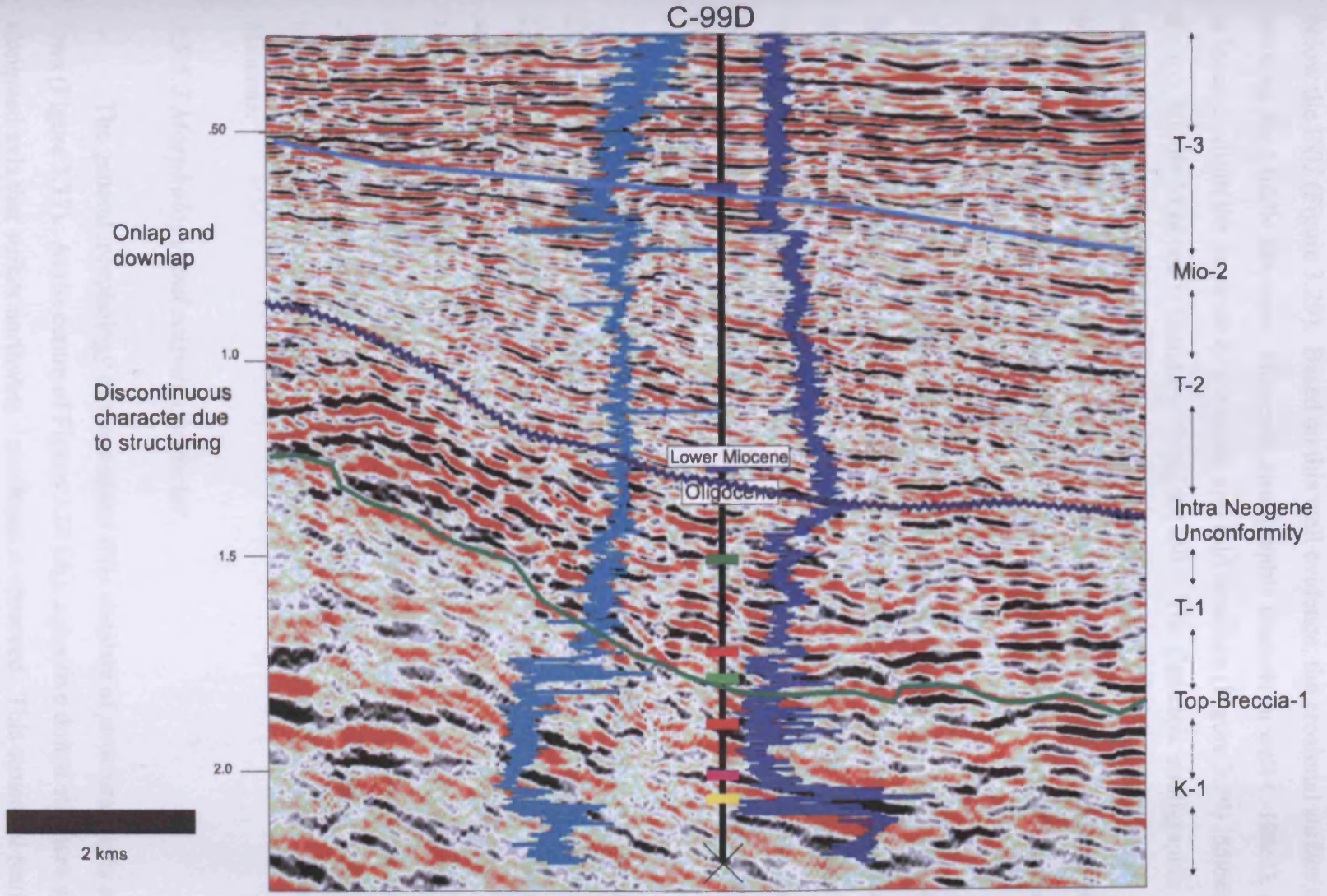

Figure 3.38
Zoom box of figure 3.27. Well C-99D penetrating into the forelimb of structure; gamma ray log on the left and sonic log on the right are posted. Well stratigraphic markers top Oligocene and top Lower Miocene are posted. Seismic horizons Top-Breccia-1, Intra Neogene Unconformity and Mio-2 are posted. Note the seismic reflection configuration for seismic unit T-2 consists of onlaping and downlaping reflections with a convergent geometry. Within seismic unit T-1, the seismic configurations consists of discontinuous seismic reflections that resulted from pervassive structural deformation.

markers for well C-468 (Figure 3.4) indicates that Middle Miocene sediments are found below the INU (Figure 3.29). Based on this well evidence, the erosional surface should postdate the Middle Miocene. However, stratigraphic markers in well C-1065D, which is located within the forelimb of the thrust and fold structure (Figure 3.29) indicate that the top Middle Miocene is found overlying the INU. The Cenozoic stratigraphic markers of wells C-468 and C-1065D are in conflict. This is an example of the uncertainty that some wells pose in their stratigraphic markers. If Mid Miocene strata are indeed present within the pre-INU horizon, then no Mid-Miocene strata should be found overlying it.

Towards the Eastern Platform with a stratigraphic control provided by well Ixtoc-18, the INU horizon is seen to occur beneath the Middle Miocene stratigraphic marker (Figure 3.30). Well Ixtoc-18 is considered to be a key well in the context of analysis of this unconformity due to the consistency between seismic horizons and the well stratigraphic markers plus the well location, that correspond to areas of minor structural deformation.

In summary, the precise age for the INU horizon is difficult to constrain using all of Pemex stratigraphic markers due to conflicting well to seismic correlations. However, it is suggested that the duration of erosion represented by the INU horizon and syn-sedimentary deposition roughly corresponds to an age of lower middle Miocene to lower late Miocene. In Figure 3.30, it is observed that while erosion occurred the crest of the Ku fold, background syn-tectonic sedimentation took place away from the structure. Unit T-2 presents this syn-tectonic sedimentation. The age interval for this syn-tectonic interval corresponds to early middle Miocene to lower late Miocene.

3.5.5.3 Morphology and seismic character

The general morphology of the mapped INU consists of structural highs and lows (Figure 3.37). At the centre of Figure 3.37 (A), a positive domal structure with an elongated axis that strikes northwest – southeast is observed. This structural feature corresponds to the crestal region of the Thrust Block. Within this crestal region in plan form a sub-rectangular feature is seen that measures 2 km across and is bounded by north-south trending faults (Figure 3.39 label C). In vertical sections (Figure 3.40), the

1A

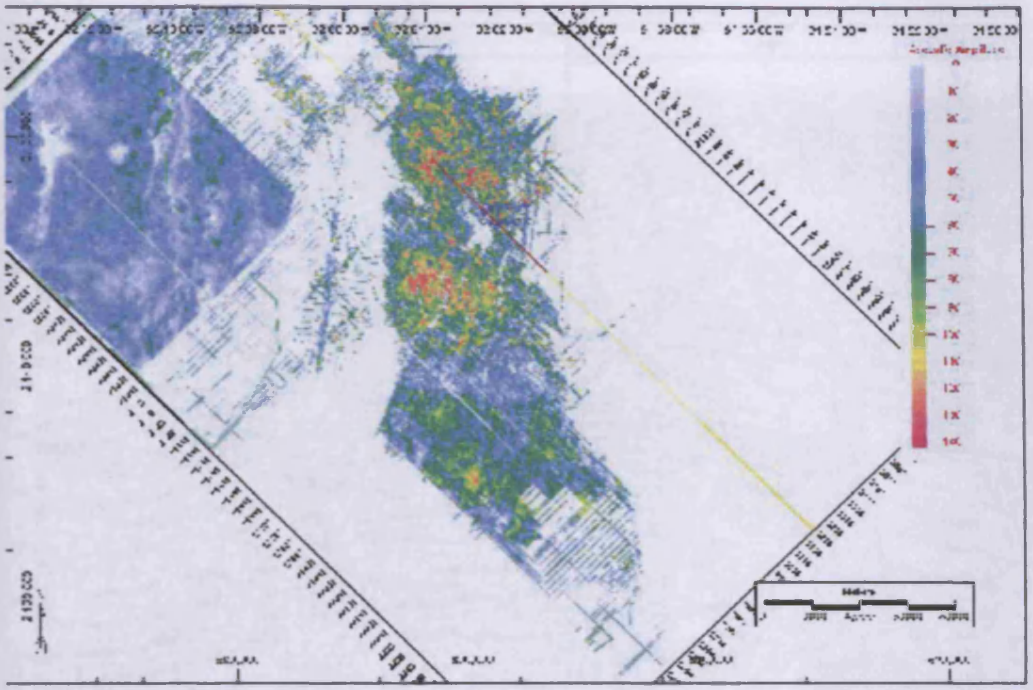

2B

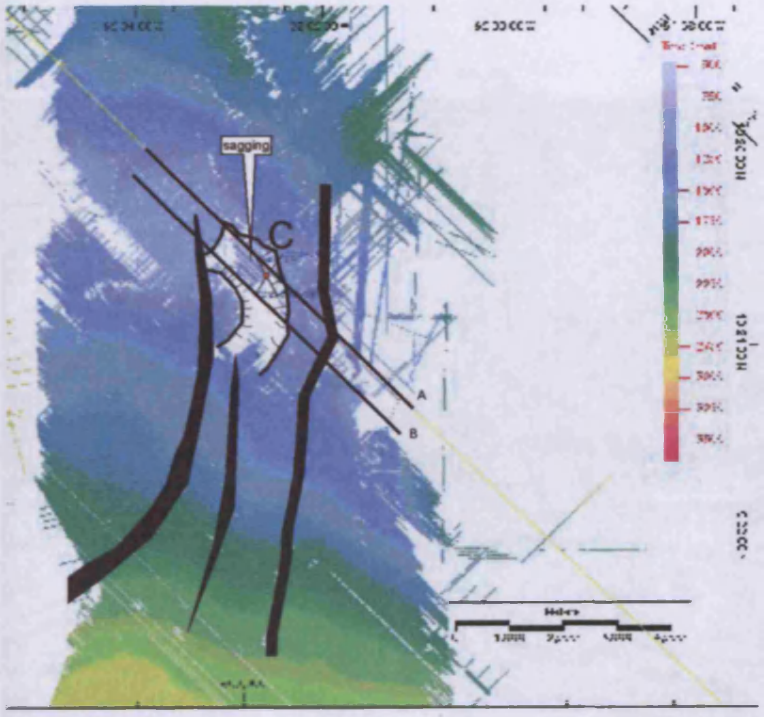

Figure 3.39
Map 1A displays the amplitude for the Top-Breccia-1 seismic horizon along the TB and WP; (2B) displays the Thrust Block in msec twt and the depression-like feature C found at the crestal area of the Thrust Block; nitrogen injection wells are posted (red circle). Seismic lines A & B are displayed in Figure 3.40.

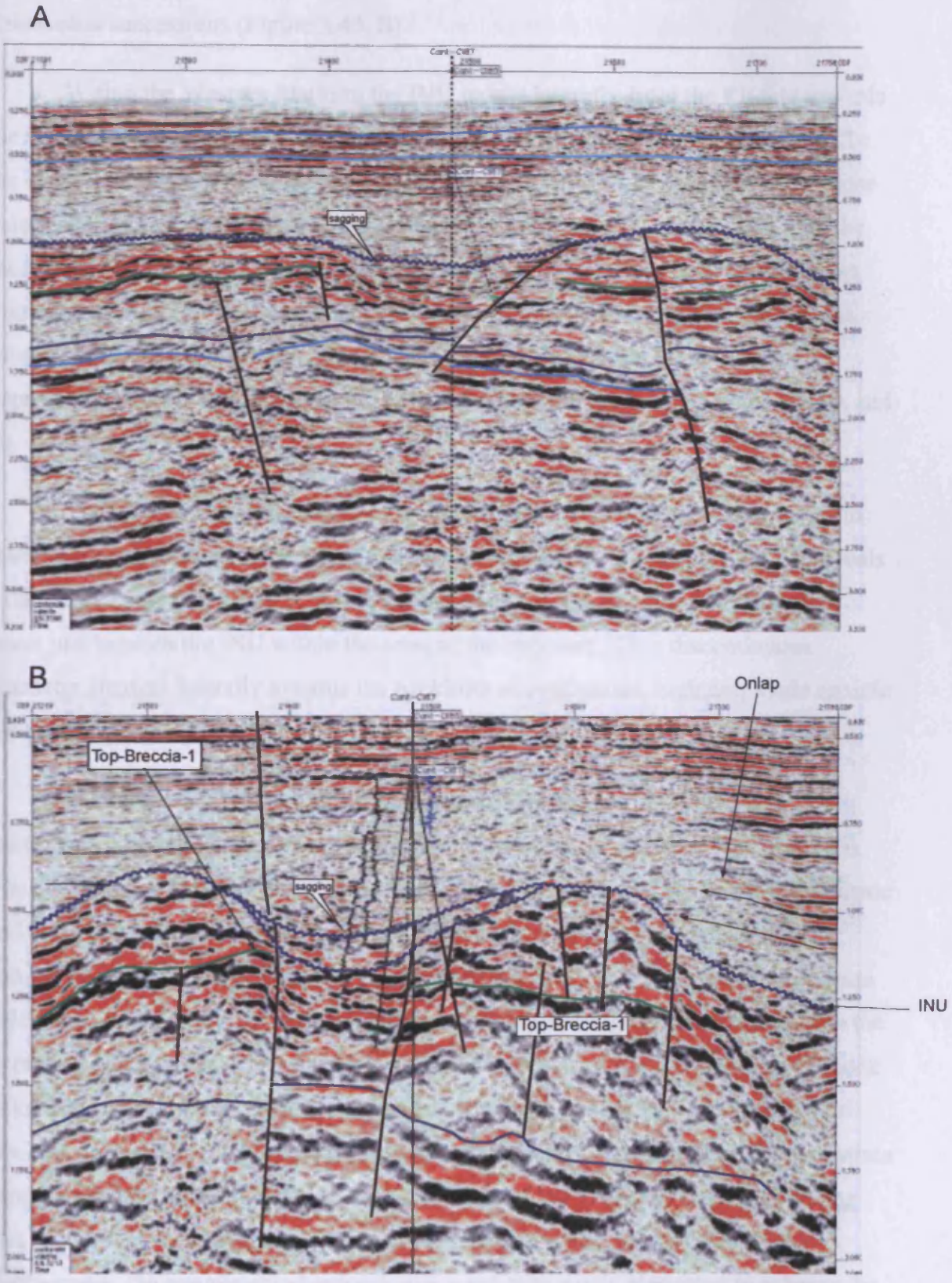

Figure 3.40
Seismic sections along the crestal area of the Thrust Block; for orientation refer to Figure 3.39. Nitrogen injection wells posted for reference. Note the depression like feature and the change in seismic character within it. Faults bound it to both sides, in section B faults are observed to displace Mesozoic and overlying Tertiary successions, providing vertical permeability conduits for fluid flow.

INU surface across this depression appears to be in direct contact with or near to the Cretaceous successions (Figure 3.40, B).

Within the Western Platform the INU passes laterally from the Ku fold towards the south (at well Ixtoc-18) with a smoother and planar topography (Figure 3.37). To the east of the Eastern Platform, an elongated depression (> 5 km across) occur whose axis strikes almost north-south. This elongated depression feature coincides with the locations of the Western Fault Corridor. Compare the location of both features from Figures 3.37 and 3.2. The entire length of this feature is limited by the extent of the seismic data. To the southeast quadrant adjacent to the Nohoch Nose, a minor depression is observed that appears to extend towards the southeast (Figure 3.37, A and B).

The seismic character observed underlying the INU consists of continuous to discontinuous, sub-horizontal seismic reflections (Figure 3.40). Figure 3.40, B reveals a classic example of the highly discontinuous nature of the seismic reflections that occur just beneath the INU within the crest of the structure. This discontinuous character changes laterally towards the backlimb as continuous, high amplitude seismic reflections (Figure 3.27).

Overlying the INU, the seismic reflections appear sub-horizontal and continuous, although high noise / signal ratio is observed (e.g. Figure 3.27 and 3.40). The poor seismic imaging along the crest is speculated to be a result of various intrinsic and extrinsic geological and acquisition / processing aspects. The geological complexity in this area gives rise to large lateral velocity contrasts. The crestal region below the unconformity is marked by higher velocity and higher density rocks than the overlying successions. Intrinsically, the reservoir hosted within the hangingwall block (Akal reservoir) has a large gas cap, that it is known to be leaking. The geophysical attribute contrasts (density and transient velocity), the geological setting, (dipping strata beneath sub-horizontal strata), and the occurrence of gas produces a complex setting that restricts the accurate imaging the seismic data at higher seismic resolutions. Furthermore, the seismic data has been processed with a gain algorithm to enhance the deeper sections, which in turn decreases the seismic quality throughout the shallower sections.

Within the forelimb region, the seismic reflections overlying the INU show evidence of onlap. These appear discontinuous, which is interpreted to be due to the seismic processing (Figure 3.27). The underlying seismic reflections also appear discontinuous. This discontinuous appearance is interpreted to be due to the seismic processing and also to faulting and fracturing at a subseismic scale.

Within the Western Platform (Figure 3.30), the seismic reflections that overlie the INU show onlapping geometries that are continuous of medium amplitude. The underlying package consists of continuous, parallel and concordant seismic reflections.

Within the Eastern Platform, next to the Nohoch structure, seismic reflections that exhibit a parallel onlap configuration are observed (Figure 3.21 and 3.22).

3.5.5.4 Features associated with the Intra Neogene Unconformity

Over the crest of the Thrust Block, and beneath the INU, a near rectangular depression feature is present that is bounded to the east and west by faults that appear almost vertical (Figures 3.39 and 3.40). The depression like feature opens towards the south (Figure 3.39). In vertical sections the depression-like feature exhibits a considerable change in seismic character consisting of highly disrupted seismic reflections of higher frequency, high amplitude (Figure 3.40 A, flagged as "sagging"). Overlying the INU sub-parallel and sub-horizontal reflections occur that appear to be infilling the depression like feature. There is an overall acoustic impedance change between the overlying and underlying successions. Beneath the depression, the basal Cretaceous and Jurassic successions are present. These successions are severely faulted with the fault planes having a diffuse seismic appearance. No sagging and depression- like features are apparent beneath the depression-like feature.

Based on (1) The different seismic characters noted within the crestal region, (2) the morphologies noted (depression like-features; Figure 3.40), (3) the proximity of the depression-like feature to the INU, (4) the vertical connectivity of the depression-like feature with the INU provided by faults (5) the lithologic fabrics observed in cores, and (6) the regional context and the vertical structural relief in reference to the Yucatan platform margin (see Chapter 2, Section 2.3.4.3 and Figure 2.32), it is proposed that the crestal area was subject to subaerial exposure which in turn permits the proposal that the depression-like feature possibly consists of a cave collapse structure. The vertical

connectivity of the reservoir units with the surface is then suggested to have been provided by faults, and where brines infiltrated into the Upper Cretaceous reservoir enhancing the reservoir properties (porosity and permeability) by dissolution of matrix and widening of fracture networks (Figure 3.40).

3.6 Discussion: stratigraphic development

This section integrates the relevant regional stratigraphy (Chapter 2) with the local stratigraphy (Chapter 3). Interpretation of 2D regional seismic lines (Chapter 2), locates the Cantarell study area within the continental shelf. It is proposed that during the upper Jurassic to Cretaceous times, Cantarell was located in basinal margin environment. This proposal is based on the distribution of lithological facies and seismic reflection configurations (Enclosures 1-5). Based on the vertical and aereal lithological facies arrangement, and the land to basin profiles, it is suggested here that during the Late Jurassic to Cretaceous, the study area evolved from a ramp to a base-of-slope by the end of the Cretaceous.

During the Kimmeridgian and into the Tithonian a low angle ramp with terraced half-graben palaeo-topography is envisaged (Figure 3.17 and 3.18). The half-graben topography was controlled by normal faults, few of which are preserved within the Cantarell area. Carbonate deposition predominated with minor anhydrite precipitation, organic matter influx, and deposition of shale. Probable oolitic banks as suggested from well C-91 accumulated along restricted palaeo-structural highs provided by the terraced half-graben topography. The above lithological assemblages coupled with concordant, parallel and highly continuous seismic reflections configuration points towards a carbonate ramp environment as previously described by Burchette (1992). Solely based on the analysis of the 3D seismic data it is very difficult to precisely define the area of the carbonate ramp (inner versus outer) in which Cantarell is located. However, by integrating the interpreted 2D regional lines (Enclosures 2-4), with the lithologic assemblages (basal silt-rich that grades into dolomite and limestones with anhydrite nodules, and oolithic graistones to packsotnes) suggests that the Cantarell area was most likely situated in a mid- to inner-ramp setting with a variable slope gradient governed by the half graben topography. Evaporite precipitation may have occurred in shallower and restricted areas. This current interpretation is analogous to the Cotton Valley lime reservoirs located within a carbonate ramp as described by

Montgomery (1996). The lithologic (facies distributions), tectonic setting and age are comparable to the geological setting found within the Cantarell area.

The Tithonian marks a period of relative sea-level rise, judging from the lithological assemblages (argillacesous dolomite, siltstones that grade into shale with high organic content).

During the Cretaceous, major carbonate deposition occurred located in a base of slope setting, as suggested by the regional 2D lines (Chapter 2) and the lithology provided by well data. The seismic reflection within the Cretaceous interval appear mainly concordant. Breccia intervals found intermittently within the lower, mid and upper Cretaceous are suggested here to have been derived from a scarp dominated platform margin. It is suggested that the increase in brecciated congolomeratic material encountered within the upper most Cretaceous interval resulted from the possible structural development and fault activation along the Yucatan platform margin. The intercalations of bathyal shale with conglomeratic breccias, strongly favours a cyclic sedimentary pattern with episodes of coarse breccia interbedded with finer grained sediments. Similar processes have been documented in the Garagano-Murge region of southern Italy (Borgomano, 2000).

The monomictic and crackle breccia fabrics observed from the core data (see Section 3.4.3.3) are herein interpreted to post-date the Cretaceous times and are instead associated to the structural development that occurred during the middle Miocene (see Chapter 4).

During the Tertiary there was a significant change in the mode of sedimentation from a carbonate-dominated to a clastic-dominated (see Chapter 2). This change in sedimentation is coincident with the formation of the Sierra de Chiapas, located ≅ 250 km south of the study area. It is speculated that the change in sedimentation is the result of the degradation of the uplifting Sierra de Chiapas. This clastic input is considered as important factor contributing to the lowering to shutting off of the and / or translation of the carbonate factory. Furthermore, this clastic sedimentary supply was penecontemporaneous to synchronous with the structural deformation that resulted in the thrust and folding of the Cantarell area.

3.7 Concluding remarks

A seismic stratigraphic framework was established for the Cantarell study area based on seismic reflection configurations and coupled with well and regional data that allowed to give geological insights in the depositional systems. Seismic horizons were defined and interpreted at a number of stratigraphic levels, which allowed for the subdivision of five seismic units. In terms of the timing of the structural deformation, seismic units J-1, K-1 and T-1 correspond to the pre-tectonic units. Seismic unit T-2 correspond to the syn-tectonic sediments (growth strata) whose geometry reflects a deformation style of a submarine thrust-fold structure with some background sedimentation and erosion along the crest. From the previous documentation and interpretation of seismic data coupled with well data the most important concluding remarks are as follow:

1. During the Kimmeridgian, the Cantarell area was situated in a mid to outer ramp setting, with a half-graben topography in which carbonate precipitation was predominant.

2. During the Tithonian relative sea level rise occurred.

3. During the Cretaceous, the Cantarell area was situated in a base of slope setting and the identified breccia intervals were probably derived from a scarp dominated basin margin. This breccia intervals became more prominent at higher stratigraphic intervals.

4. Two types of breccia predominate: monomyctic crackle breccia and polymictic breccia. Crackle breccia facies are interpreted to result from structuring.

5. The mode of sedimentation changes significantly during the Tertiary from a carbonate dominated to a clastic dominated.

6. During the Tertiary the stratigraphy is divided into three units: T-1, T-2 and T3. These are associated to the modes of sedimentation that are mainly structurally controlled: pre-tectonic, syn-tectonic and post-tectonic. During deposition of T-2 a major phase of structural deformation occurs.

7. Whilst structural development occurred, development of the INU occurred and possible subaerial exposure which modified the internal petrophysical arrangement of the reservoir hosted within the hangingwall block.

Chapter 4

Structural geology of Cantarell

4.1 Introduction

The Cantarell Field is a geologically complex structure that resulted from a number of different phases of deformation. These deformational phases have modified the external and internal architecture of the reservoir and surrounding rock system. At the macro or seismic scale the structure has been deformed into a thrust complex with highly complicated fault patterns. At a meso and micro scale, the intricate fracture network organization, has exerted a major control on porosity and permeability distribution contributing greatly to a world-class reservoir with high porosity and permeability on the order of over 15 % Phi and permeability of 1 to 3 Darcies, (Limon-Hernandez, 1999).

This chapter will show evidence of three episodes of structural deformation. These are derived from the structural interpretation of number seismic horizons at various stratigraphic levels and the analysis of key seismic sections. Based on the detailed analysis of interpreted structural maps, cross sections and the distribution of faults at different structural levels, the following structural elements are defined: (1) Western Platform, (2) Western Fault Corridor, (3) Thrust Block, (4) Eastern Fault Corridor, (5) Eastern Platform, and (6) the Ku Fold (Figure 4.1).

Understanding how regional and local tectonics have shaped the Cantarell Field is of great importance. It will allow some of the many questions that surround the Cantarell system to be answered. Some of the questions can be grouped into themes such as, structural development, timing of hydrocarbon generation and migration, secondary recovery, formation evaluation, and oil field development.

Most of the previous seismic structural studies of the Cantarell Field have been conducted by the operator, Pemex, and focused primarily on the definition of the

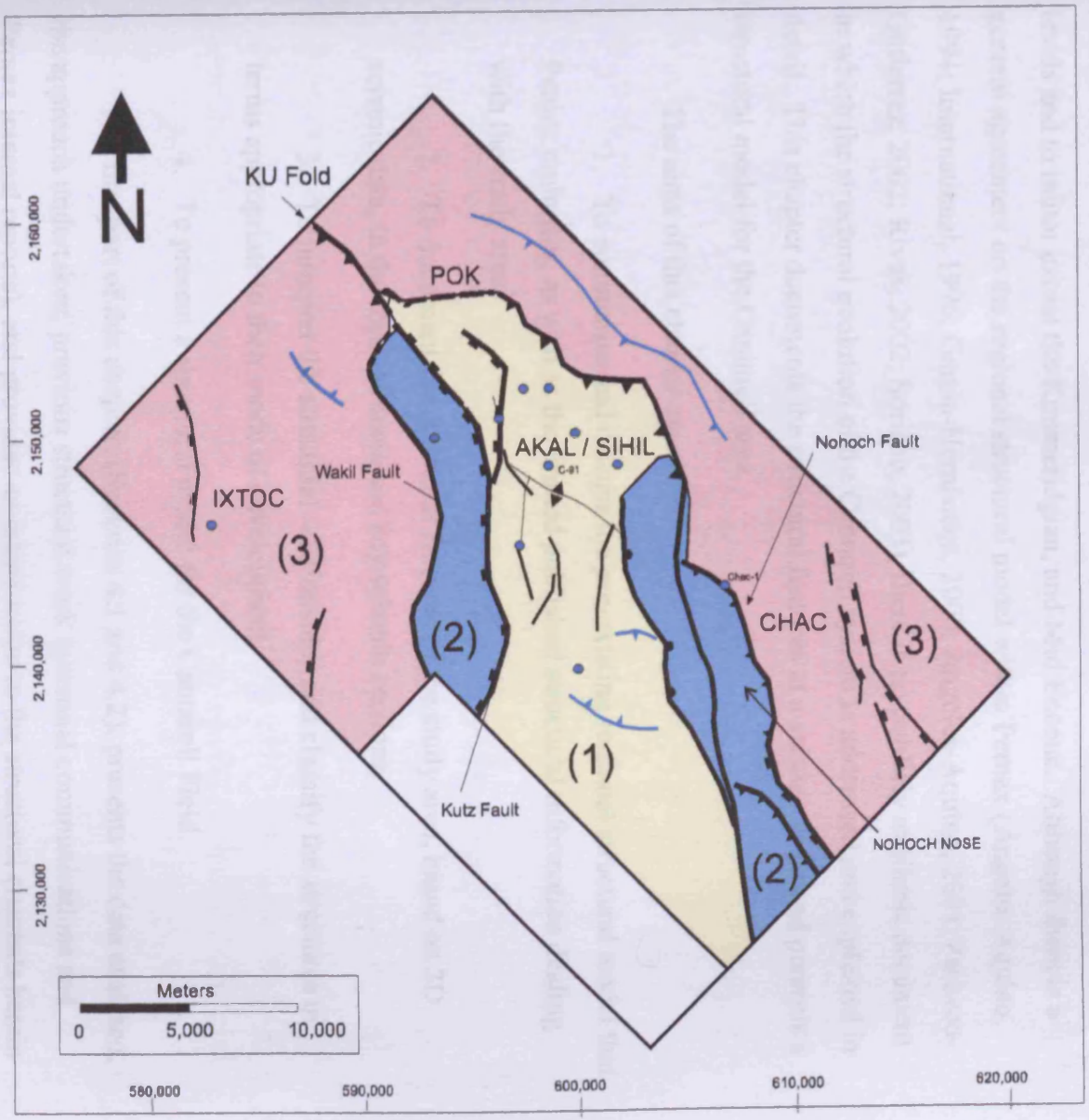

Figure 4.1
Structural elements that resulted from the compressive event. Note the three areas that share similar structural styles: (1) at the centre, coloured in yellow, the main Thrust Block is located which hosts the Sihil reservoir in the footwall and the Akal reservoir in the hangingwall; (2) adjacent to the Thrust Block, two narrow Fault Corridors shaded in blue the Eastern Fault Corridor and the Western Fault Corridor. These host the Kutz and Nohoch reservoirs, respectively; (3) two outermost least deformed areas Western and Eastern Platforms, these host the Ixtoc and Chac reservoirs, respectively. Fault array names are posted. Fault lineaments coloured in blue are hosted within the T-1 seismic unit (Base Tertiary). Blue circles correspond to wells that contain check shot data.

Reverse faults occurring in the T-1 seismic unit (early Mesozoic)

Reverse faults occuring within the J-1, K-1 and T-1 seismic units (late Mesozoic, early Cenozoic)

Mesozoic reservoir architecture: mainly the Top Cretaceous and Tithonian stratigraphic levels and to minor extent the Kimmeridgian, and Mid Eocene. Although there is a general agreement on the regional structural model within Pemex (Angeles-Aquino, 1994; International, 1996; García-Hernández, 2000; Angeles-Aquino, 2001; Pacheco-Gutierrez, 2002; Rivas, 2002; Soriano, 2003), there is no publicly available document in which the structural evolution of the Cantarell system is addressed and explained in detail. This chapter documents the structural features at a seismic scale and presents a structural model for the Cantarell area.

The aims of this chapter are:

1. To summarise and discuss the pre-existing regional structural model that Pemex embraces, as well as the limited published structural information dealing with the study area.

2. To document the structural features of the study area, based on 3D seismic data, in the form of maps and key seismic sections.

3. To interpret the structural relationships and classify the structures in terms appropriate to their mode of development.

4. To present a structural model for the Cantarell Field.

The first part of this chapter, (Sections 4.1 and 4.2), presents the data analysed, the approach undertaken, previous structural work (personal communications and Pemex internal reports), and provides an introduction to the structural elements herein defined. The second part of the chapter (Sections 4.3 to 4.6) provides a detailed account of the three-dimensional structural geometries, internal seismic character, and the fault patterns observed in each of the defined structural blocks. The chapter concludes by synthesising the structural framework and the spatial significance of each structural block in relation to the entire holistic structural model here presented.

4.1.2 Data and methodology

Data from a three-dimensional (3-D) Ocean Bottom Cable seismic survey acquired in 1998 over the Cantarell area (Figure 4.1) were interpreted in detail. Stratigraphic markers from wells that penetrate the footwall were used to constrain the

interpretation of the thrust plane and calibrate the interpreted seismic horizons (see Chapter 3, Section 3.2 and Figure 3.1). Pemex in house reports were collated and used to summarize the current structural model that Pemex embraces.

The methodology undertaken for the description of structural styles observed in the seismic data consisted primarily of detailed mapping of seismic horizons at different stratigraphic levels. These seismic maps were analysed with the objective of extracting the general structural morphology and the location of major fault arrays. Fault delineation and interpretation was also carried out and this involved measuring the strike and dip of the main faults and their vertical extent in relation to the stratigraphic framework.

4.1.3 Previous work on the Regional Structural Context of the Cantarell study area

The structural model developed by Pemex is based on the detailed analysis of cores, image logs, and seismic data. The structural interpretation for the Cantarell and surrounding areas has mainly been derived from structural features observed at different stratigraphic levels within the Mesozoic (e.g. Top Cretaceous, Kimmeridgian and Top Tithonian). Little discussion of the structural evolution during the Cenozoic is included in the available unpublished and published documents (Angeles-Aquino et al. 1994, 2001; Garcia-Hernandez et al., 2000; Pacheco-Gutierrez, 2002; Rivas, 2002; unedited AGI Mexicana, 2002). This lack of detailed discussion is a serious deficiency in the current understanding of the Cantarell Field.

The Cantarell area is located in the Campeche Basin, at the north-easternmost end of the Reforma-Akal Uplift. Within the Campeche Basin three provinces have been defined: the Comalcalco Depocentre, Reforma-Akal Uplift, and the Macuspana Depocentre (Figure 4.2 and see Chapter 2, Figure 2.2). The name of Reforma-Akal Uplift has been given to a region that is structurally higher than the surrounding areas and is bounded by the Comalcalco and Macuspana depocentres (Meneses-Rocha, 1991). The Macuspana and Comalcalco Depocentres correspond to areas of shale remobilisation (Ambrose *et al.*, 2003), that formed during the Paleogene, contemporaneous with the development of fold and thrusts structures within the Reforma-Akal Uplift region (Murillo, 2004, pers. comm.). Within the Reforma-Akal

Figure 4.2
Structural map of the Top Cretaceous stratigraphic level in the Campeche Basin. The structural provinces : Reforma-Akal Uplift is located at the centre and is limited to both sides by the Comalcalco and Macuspana Basins (coloured in blue). The rectangle defines the extent of the Ocean Bottom Cable (OBC) 3D seismic data of the Cantarell area; modified from García-Hernández, J. et. al. (2002).

Uplift region, reverse faults, folds and thrusts occur in the pre mid Miocene stratigraphic section (Figures 4.2 and 4.3).

The structural model for the Cantarell Field developed by Pemex is primarily based on regional studies (García-Hernández, *et al,* 2000; Meneses-Rocha, 2001; and Murillo pers. comm. 2004). García-Hernández, *et al* (2000) and Pacheco-Gutierrez (2002) suggested two major structural events as responsible for the structures encountered in the area:

(1) An extensional structural episode during the end of the Jurassic and beginning of Cretaceous. The structures related to this event are defined as half grabens, whose normal faults strike north to south and north-west to south-east and dip toward the west and southeast (basinwards). These normal faults strike sub-parallel to the Yucatan Jurassic margin (north-south to northwest – southeast).

(2) A transpressive - transtensile event is interpreted (García-Hernández *et al.,* 2000) to occur by the end of the Oligocene or beginning of the early Miocene and culminating in the late Miocene to Pliocene. A combination of folds, thrusts, thrust imbricates, reverse faulting and strike-slip deformation resulted from this transpressive event. This structural event affected entire sedimentary successions and underlying basement. The driving mechanisms for this structural deformation have been interpreted by Meneses-Rocha (2001) to be the result of the movement of tectonic plates along the Motagua-Polochic strike-slip fault system. These tectonic plate movements resulted in a compressive stress vector oriented north to northeast within the Reforma-Akal Uplift (Meneses-Rocha, 2001). It is speculated that Upper Mesozoic and Lower Tertiary successions detached and translated over Callovian evaporitic successions in a northerly direction against the Jurassic basin margin adjacent to the Yucatan Platform (García-Hernández *et al.,* 2000; Meneses-Rocha, 2001; Murillo, 2004). This northerly translation resulted in the development of a series of folds, reverse faults, thrusting and dextral strike – slip faults along the Reform-Akal Uplift (García-Hernández *et al.,* 2000; Meneses-Rocha, 2001; Murillo, pers. comm. 2004). Murillo (pers. comm. 2004) suggests a tectonic evolutionary model for the current basin configuration that resulted from a northerly to northwest translation of upper Mesozoic and lower Paleogene sedimentary successions. This northerly translation

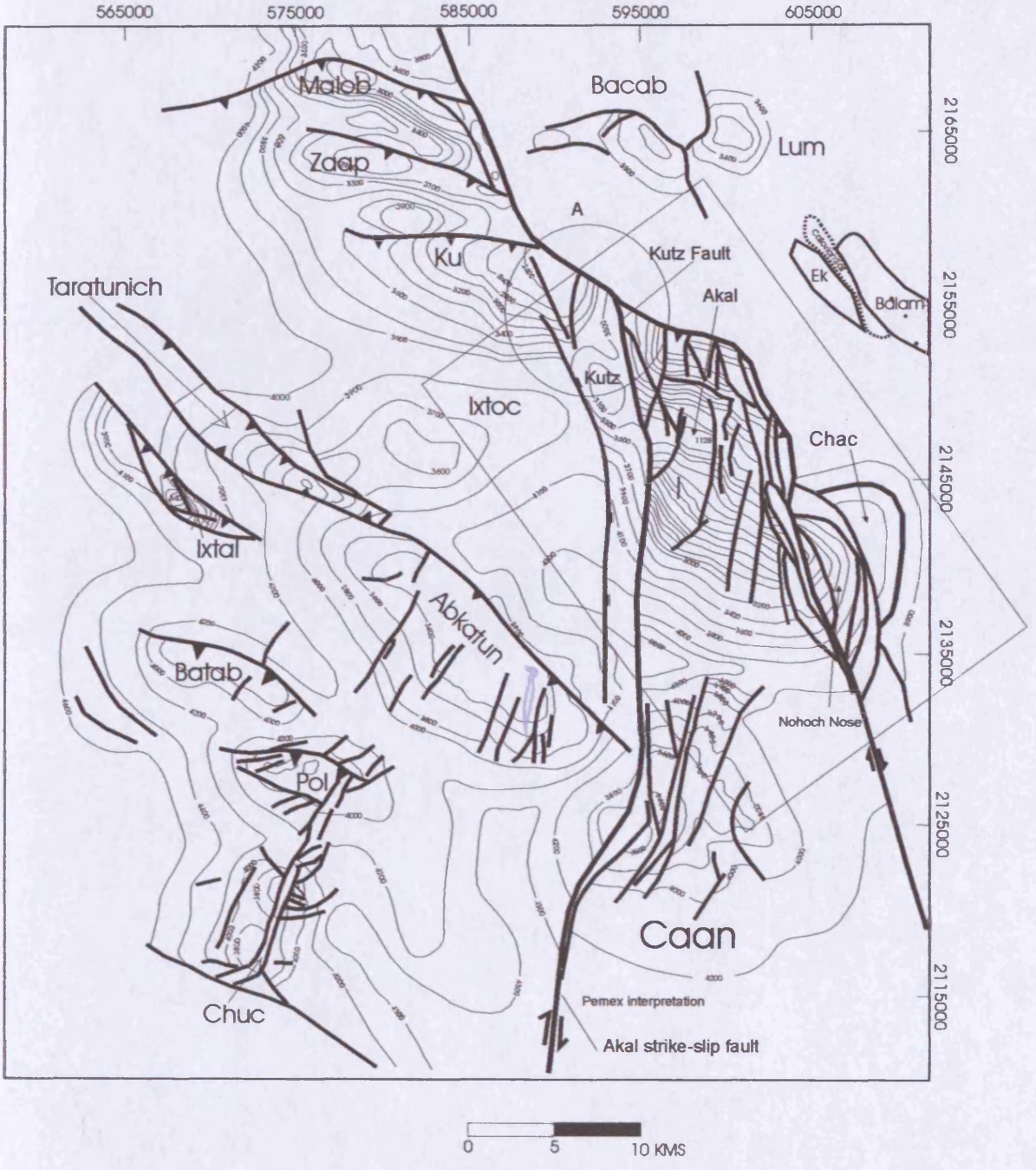

Figure 4.3
Structural map of the Top Cretaceous stratigraphic level, for the Campeche Basin. Modified from Netherland (1999). Note the structural setting is dominated by fold structures that have a general northwest to southeast strike. Note the fault layout of the "Akal strike-slip fault" exhibits a curve plan form geometry circle A. Note the extent of the 3D OBC survey.

became limited towards the north by the Yucatan Block. The Yucatan Block is underlain by thick continental crust which has been structurally stable since the Cretaceous (see Chapter 2, Section 2.2.2) and is considered to have acted as an obstacle to the northerly translation of the Upper Mesozoic and Lower Paleogene sedimentary succession steering it towards the northwest, instead of allowing it to ramp up the Yucatan Block (Murillo, pers. comm. 2004). This steering resulted in transtension and development of the Macuspana and Comalcalo depocentres, and strike-slip fault systems, specifically the fault that separates the Akal block from the Ixtoc block (Murillo, 2004, pers. comm.; Figures 4.1, 4.2 and 4.3). This model suggests that the western fold closure of the Akal fold corresponds to the Ku structure. This is supported by well log, facies, and thickness correlations from the Ku structure to the Akal structure (Murillo, pers. comm. 2004).

The Pemex model emphasises that the Callovian evaporitic successions have played an important role in the deformation of this area, although none of the wells within the Cantarell study area have penetrated in situ salt. However, salt has been penetrated by some wells located in the boundaries between the Thrust Block and the Eastern Fault Corridor. South of the Cantarell structure salt has been found in the core of the Caan structure (Figures 4.2 and 4.3). Angeles-Aquino (2001) interpreted the Callovian evaporitic succession as the main detachment level and gliding plane for the contractional structures encountered in the study area.

4.2 Structural Elements

The aims of this section are: (1) to familiarise the reader with the structural nomenclature herein defined; and (2) to illustrate and document the spatial distribution of the key structural elements within the context of the study area (Figure 4.1). The main structural geometries encountered in the study area are first highlighted using a number of representative seismic profiles previously presented in Chapter 3 and their spatial relationship are then described with reference to a number of key structural time contour maps derived from 3D interpretation.

The structural elements defined within the three-dimensional seismic survey area are illustrated in Figure 4.1. From west to east these are: the Western Platform (WP), Western Fault Corridor (WFC), Thrust Block (TB), Eastern Fault Corridor

(EFC), and Eastern Platform (EP). The Western Platform is a relatively undeformed region that is limited to the east by the Western Fault Corridor. Towards the north the extent of the WP has been defined at the Ku Fold, where the limit of the Eastern Platform has also been defined. The Eastern Platform is also a relatively undeformed region. Structural features within the EP, interpreted as normal faults can be seen towards the southern quadrant of the 3D seismic survey (Figure 4.1). The western limit of the EP is defined by the Eastern Fault Corridor and the Thrust Block.

The Eastern Fault Corridor consists of an elongated, thoroughgoing and narrow zone that internally exhibit disrupted to chaotic seismic reflections. This structural element trends north-west. To the north and east the EFC is limited by the Eastern Platform and to the west by the Thrust Block. The Western Fault Corridor also consist of an elongated thoroughgoing and narrow zone of intense deformation. The dimensions of it are considerably larger that the EFC. The WFC widens in an upwards direction. The WFC also trends north-east and is limited to the east by the Thrust Block and towards the west by the Western Platform. Towards the north the WFC is vertically limited at its base by the Eastern Platform. The upper stratigraphic section (Cenozoic) of the WFC exhibit fault traces that can be correlated further to the north (see Figure 3.25).

The Thrust Block is defined by the spatial extent of a major thrust zone cutting through Mesozoic and Cenozoic successions (see Section 4.4.1). The TB consists of a narrow 12 to 8 km wide in which two structural blocks have been identified: the hangingwall and the footwall (Figure 4.1). The hangingwall appears folded with a fold axis trending north-west to south-east. As previously described the TB is bounded to the west and east by the WFC and EFC respectively and to the north by the EP. Towards the south the backlimb of the hangingwall continues to dip in a southwards direction before it is elevated adjacent to the Caan structure (see Figure 4.3).

4.2.1 Structural elements in cross-section

The cross-sectional structural style of the study area is described with reference to a series of representative seismic profiles (Figures 3.25, 3.26, 3.28, 3.30 and 3.32, see Figure 3.24 for profile orientation).

4.2.1.1 Thrust Block (Figures 3.26 and 3.28)

Figures 3.26 and 3.28 are oriented north – south, cross-cutting the Thrust Block. The structural style of the TB changes along strike and dip (Figures 3.26, and 3.28). In a broad sense, the structure becomes more complex towards the east; from the interpretation of a single thrust-related fold (Figure 3.26) to a thrust-related fold with a double thrust structure occurring in the hangingwall (Figure 3.28). Generally, the internal seismic character of the footwall exhibits disrupted seismic reflections that are accentuated at the central and lower structural levels. A single thrust plane has been interpreted that splits into different splay faults towards the forelimb and frontal tip region. The overall seismic appearance varies within the hangingwall block. The backlimb exhibits the most continuous seismic reflections. These become noticeably disrupted towards the crest and forelimb of the structure, especially along the forelimb.

4.2.1.2 Western Platform (Figure 3.30)

Figure 3.30 is oriented southwest – northeast, along the Western Platform. The structural feature that dominates in this region is an anticlinal fold, herein named the Ku Fold. A reverse fault has been interpreted within the core of the fold based on the relative offset of the stratigraphy, although the seismic character precludes the accurate definition of this interpreted fault plane. The seismic units that appear folded are: J-1, K-1 and T-1 (see Chapter 3, Section 3.5.2 for definition of seismic units). The overlying seismic units T-2 and T-3 do not show any structural deformation. Although folding is pervasive, no major faults are recognised nor interpreted within the Western Platform apart from the reverse fault that forms the core to the Ku Fold.

4.2.1.3 Eastern Platform (Figure 3.32)

The Eastern Platform consists of a broad area that appears mainly undeformed. This is well illustrated in Figure 3.32 that is oriented northwest – southeast. From Figure 3.32 it is noted that planar seismic reflections predominate. No major structural features (faults and folds) are recognised. Towards the north-western sector of the seismic profile coloured in yellow represent an interval of seismic reflections that exhibit slightly higher frequency than the underlying interval. Based on the correlation of seismic horizons, the interval coloured in yellow consists of Tertiary strata that have

been displaced along the splay faults of the thrust forelimb. These are better illustrated in Figure 3.26. The relative sense of motion of these strata is oriented towards the north. Note above the INU and beneath the Mio-2 seismic horizons, seismic reflections that are downlapping (Figure 3.32 red lines). This interval represents the progradational units that are interpreted in the regional Transects (see Enclosures 1 and 5, and Chapter 2, Section 2.2.3).

4.2.1.4 Western Fault Corridor and Eastern Fault Corridor (Figure 3.25)

The Western Fault Corridor (WFC) and Eastern Fault Corridor (EFC) in vertical cross section oriented west to east are seen to bound the Thrust Block. The WFC is defined by two steeply dipping faults that appear deep-rooted and extend vertically to higher stratigraphic levels (present day sea floor). Internally the Mesozoic interval exhibits highly disrupted seismic reflections, whilst the Cenozoic interval continuous seismic reflections that have a slightly down faulted and downwards sagging appearance. The EFC corridor observed in vertical profiles oriented west to east, perpendicular to the EFC exhibit a narrow zone that is defined by steeply dipping faults. This zone becomes relatively wider at higher stratigraphic and structural levels, similarly to the WFC. The overall geometry of the EFC resembles the WFC geometry, however, the dimensions are considerably smaller that the WFC. Some of the similarities that the EFC and the WFC share consist of: (i) internally, the Mesozoic interval also exhibits disrupted seismic reflections, whilst (ii) the Cenozoic interval exhibits continuous seismic reflections that appear to be sagging downwards (Figure 3.25).

4.2.2 Structural outline based on 3D horizon mapping

The aim of this section is to document the structural features observed in plan view of four interpreted seismic horizons (Mio-1, Mio-2, Top-Breccia-1 and Top-Tithonian) with reference to seismic sections. These four seismic horizons were previously defined in Chapter 3 (refer to Section 3.3 and Figure 3.3). The four horizons were selected for mapping in order to capture the full range of structural geometries observed within the best-imaged parts of the seismic cube. The shallow horizons (Mio-1 and Mio-2) exhibit structural styles that contrast markedly with the

deeper horizons (Top-Breccia-1 and Top-Tithonian) where the major change in structural style occurs across the level of the INU.

4.2.2.1 Structure of the Mio-1 seismic horizon (Late Miocene)

The structure for the Mio-1 seismic horizon consists of three main structural blocks: the West Flank, East Flank, and the Kutz-Wakil Graben (Figure 4.4) that are defined based on their seismic character and the occurrence of major faults. The different seismic characteristics and array of faults are well imaged in time slices (Figure 4.5). All faults encountered at the Mio-1 level are interpreted as normal faults. Their vertical displacement varies along the fault strike and from fault to fault (Figure 4.6). Throw values along the faults that bound the graben range from 12 m to 215 m.

The East Flank consists of an irregular broad wide anticlinal fold that opens to the east – southeast. The Kutz-Wakil Graben is structurally subdivided into two segments, the northern and southern segments, which separate the East Flank from the West Flank. The Kutz-Wakil Graben is bounded by fault segments that exhibit the characteristics of accommodation zones as seen in other graben systems (Morley, 1990). Fault throws decrease towards the fault tips in a complementary manner at two relay ramps in a fashion similar seen for other relay structures (Peacock & Sanderson, 1991; Trudgill & Cartwright, 1994). The structural features observed at this level suggest that it was formed under an extensional regime.

4.2.2.2 Structure of the Mio-2 seismic horizon (middle Miocene)

The structural framework evident at this stratigraphic level is very similar to that described for the Mio-1 structure. Both horizons reveal similar structural features and their fault array is comparable. Two relatively undeformed flanks (East Flank and West Flank) are divided by a segmented central graben (Kutz-Wakil Graben) that trends north - south (Figure 4.7).

The faults at this stratigraphic level appear as a number of sub-parallel closely spaced faults that form a fault zone. The seismic reflections within these fault zones appear highly discontinuous and the imaging is such that individual fault planes cannot be resolved (Figure 4.8). The nature of this seismic discontinuity is not well understood, it could be related to gas seepage, severe shearing, or poor seismic

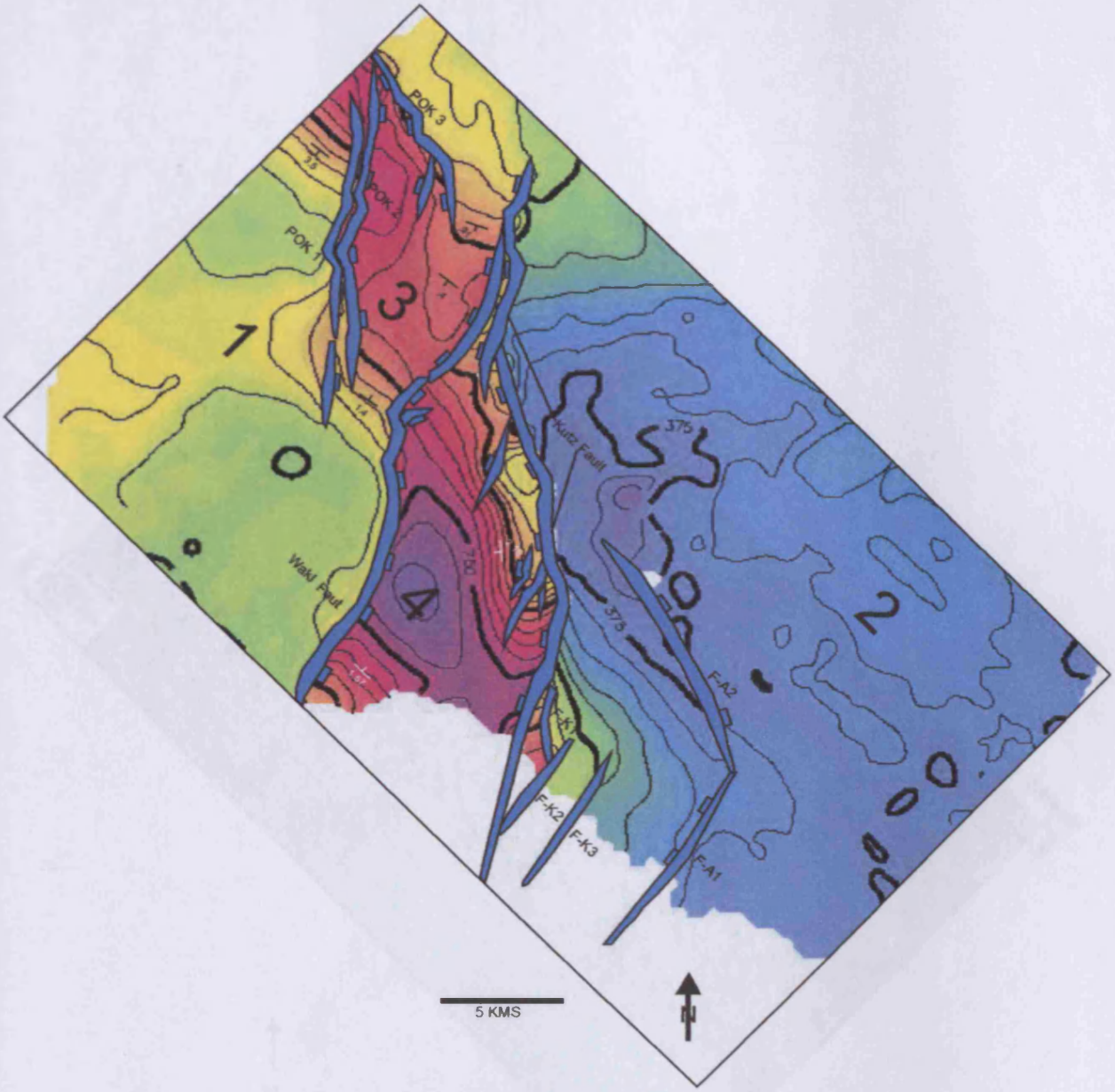

Figure 4.4
Structural map in msec twt of the Mio-1 seismic horizon (Late Miocene). The colour scale consists of reds being deeper and blues shallower. The different defined structural blocks consists of: (1) West Flank, (2) East Flank, (3) Northern Segment and (4) Southern Segment. Northern and Southern segments make up what has been herein defined as the Kutz-Wakil Graben. The fault names are labelled.

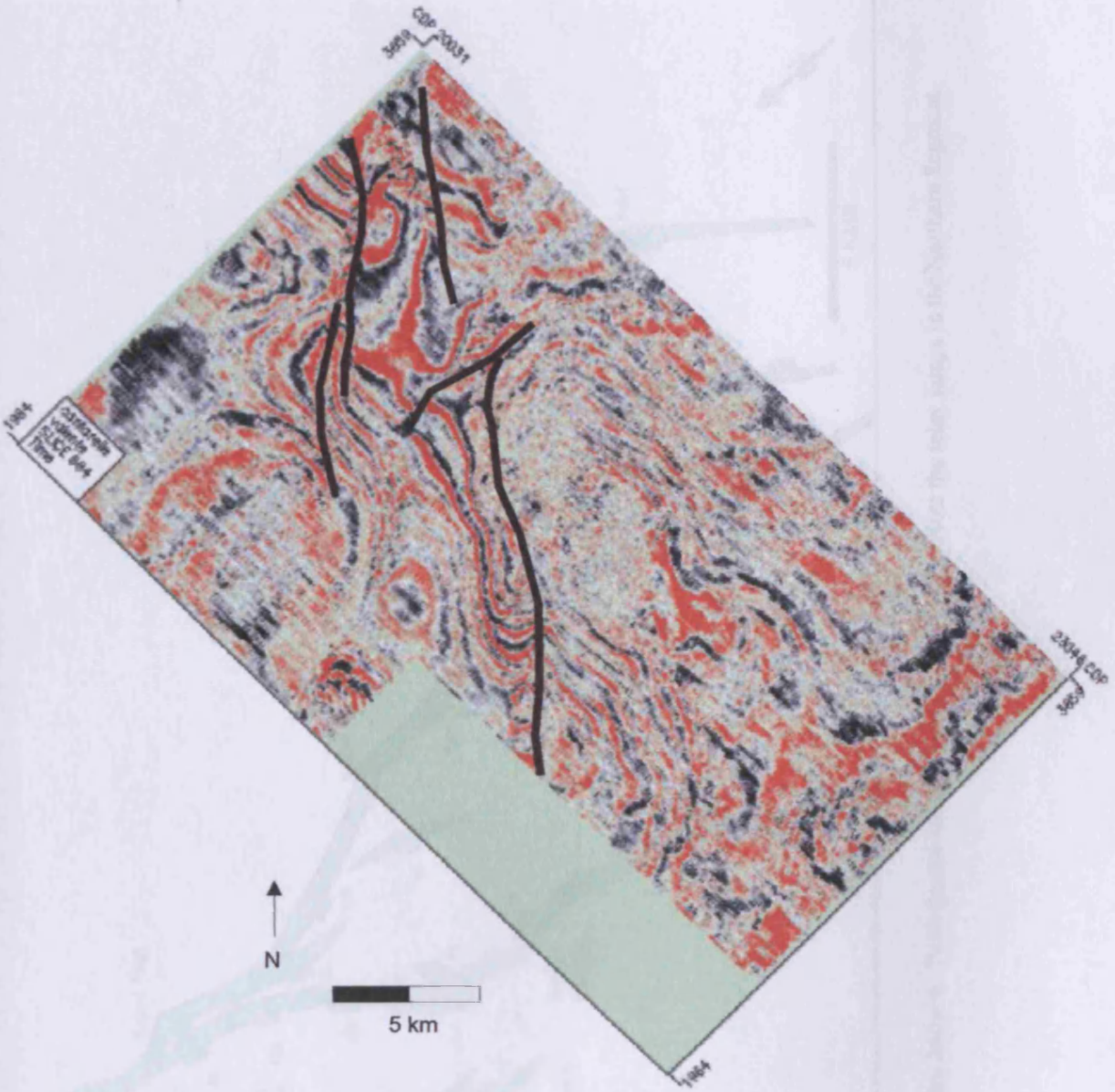

Figure 4.5
Time slice at 684 ms. Note the lineations that strike almost N-S, these are interpreted as the faults that bound the Kutz-Wakil Graben.

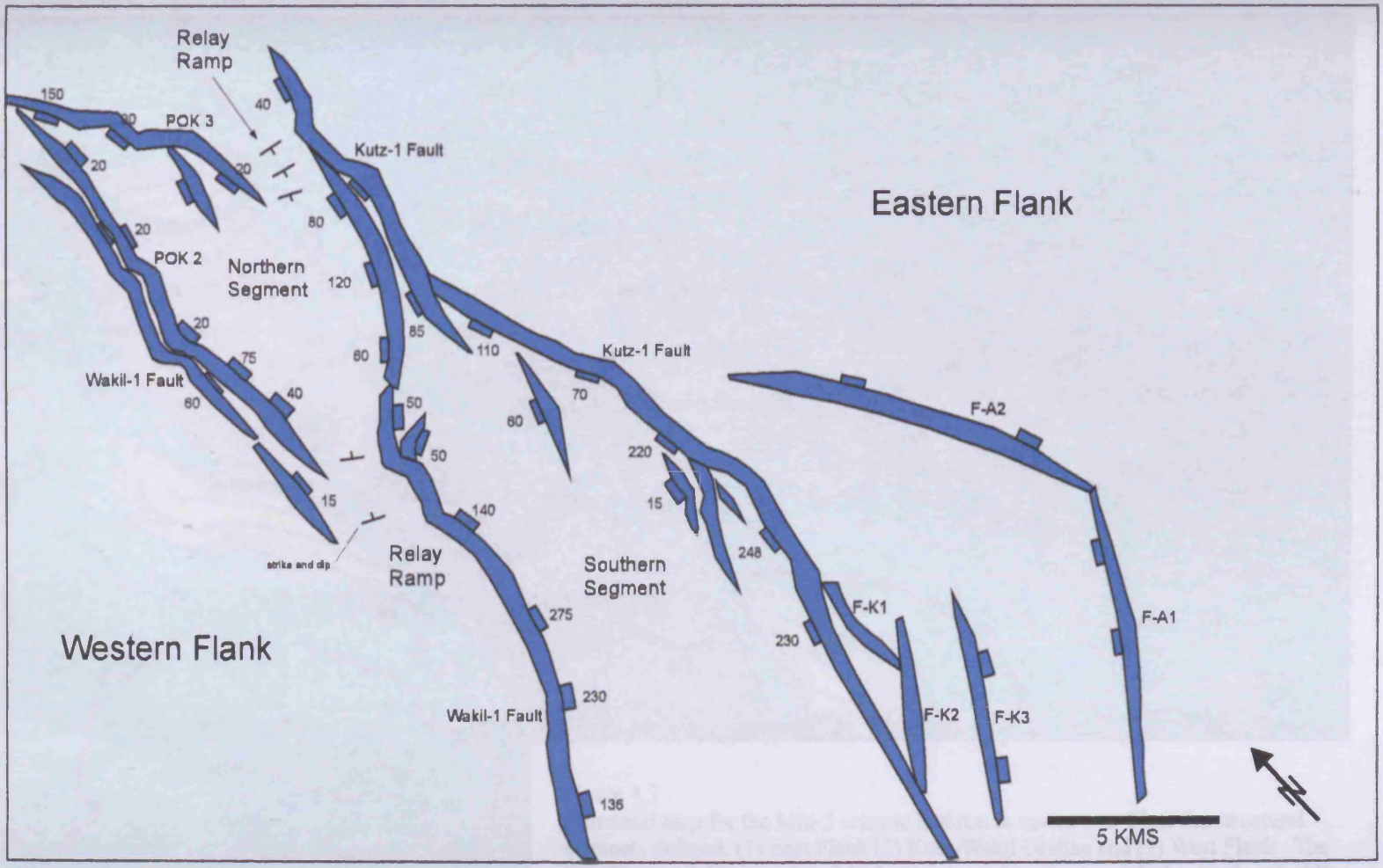

Figure 4.6
Fault layout for the Mio-1 seismic horizon. Fault throws are displayed in msec TWT. Note the relay ramps in the Northern Segment.

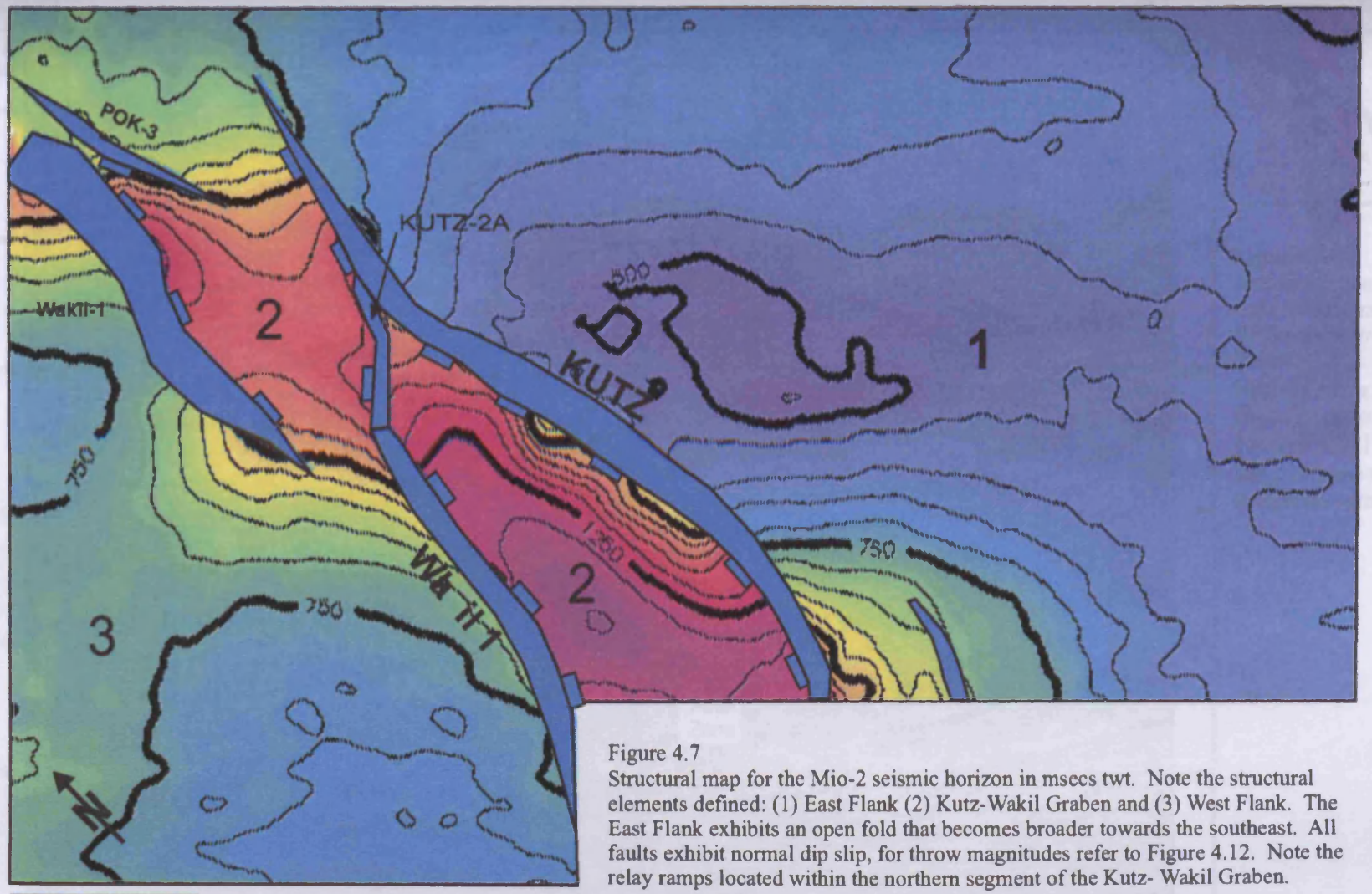

Figure 4.7
Structural map for the Mio-2 seismic horizon in msecs twt. Note the structural elements defined: (1) East Flank (2) Kutz-Wakil Graben and (3) West Flank. The East Flank exhibits an open fold that becomes broader towards the southeast. All faults exhibit normal dip slip, for throw magnitudes refer to Figure 4.12. Note the relay ramps located within the northern segment of the Kutz- Wakil Graben.

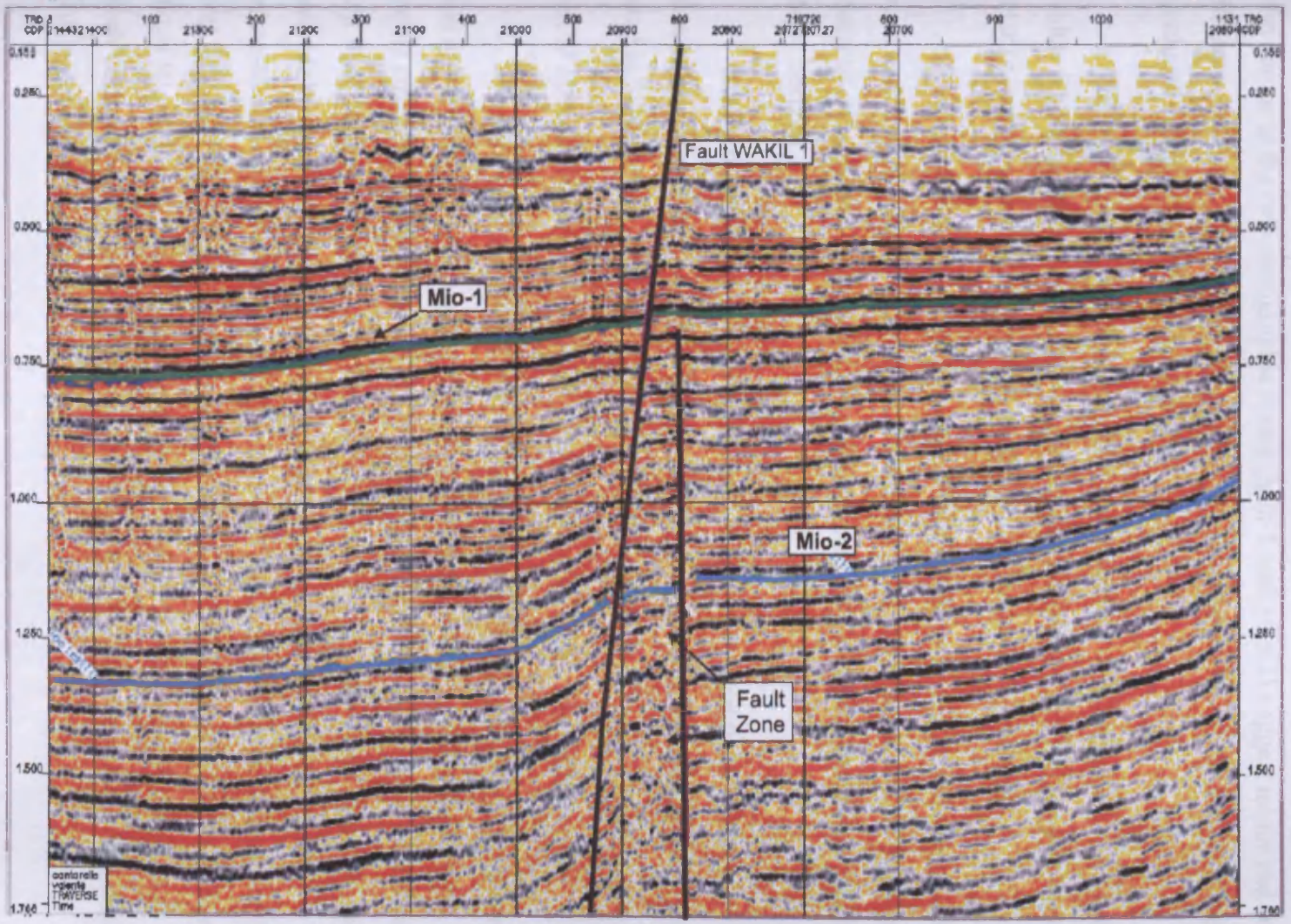

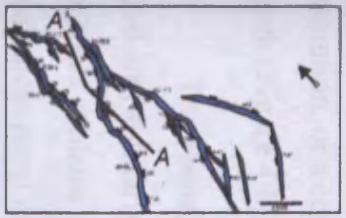

Figure 4.8
Seismic section through Kutz-Wakil Graben, showing the Southern to Northern Segments.

Note the minor fault displacement at seismic horizons Mio-1 and Mio-2. The fault zone width appears to increase with depth.

resolution, or a combination of all these. The width of the fault zone increases with depth (Figure 4.8).

The central Kutz-Wakil Graben is divided into two segments (northern and southern) similarly to the structure at the Mio-1 stratigraphic level. The northern segment contains a relay ramp structure. This structure differs slightly from the equivalent ramp mapped at the Mio-1 horizon. Measurements of the dimensions of the relay ramps at the two stratigraphic levels (Mio-1 and Mio-2) suggest minor and subtle differences (Figure 4.9). At the Mio-2 horizon, the overall size of the southern segment is reduced compared to the Mio-1 horizon.

The northern and southern segments are separated by the Wakil-1 and Kutz-1 Faults. These faults tip out against each other at a position where a change in fault polarity occurs, as was also observed on the Mio-1 horizon (Figure 4.9).

The structural character of the East Flank is similar to that of the West Flank at the Mio-1 horizon. However, the anticline at this level is smoother and no faults are observed. The West Flank has an almost identical morphology to that defined at the Mio-1 horizon.

Both structural maps Mio-1 and Mio-2 exhibit structural features that are interpreted to occur in an extensional tectonic regime. This will be discussed in greater detail in Section 4.6.

4.2.2.3 Structure of the Top-Breccia-1 seismic horizon (Base Cenozoic)

From the interpretation and analysis of the Top-Breccia-1 seismic horizon and fault arrays that displace this horizon, three main domains that among them share similar structural characteristics have been defined (Figure 4.1). Seismic time slices help illustrate the geometry of these structural domains (Figure 4.10). From the outer parts of the seismic survey towards the centre these consist of: (1) two slightly deformed outermost Platform areas (Western and Eastern Platforms); (2) two narrow corridors that exhibit highly fragmented to chaotic seismic reflections; and (3) the main Thrust Block region that is located at the centre of the seismic survey. The Thrust Block consists of a folded hangingwall and a footwall block, in which the Akal and Sihil reservoirs are located, respectively.

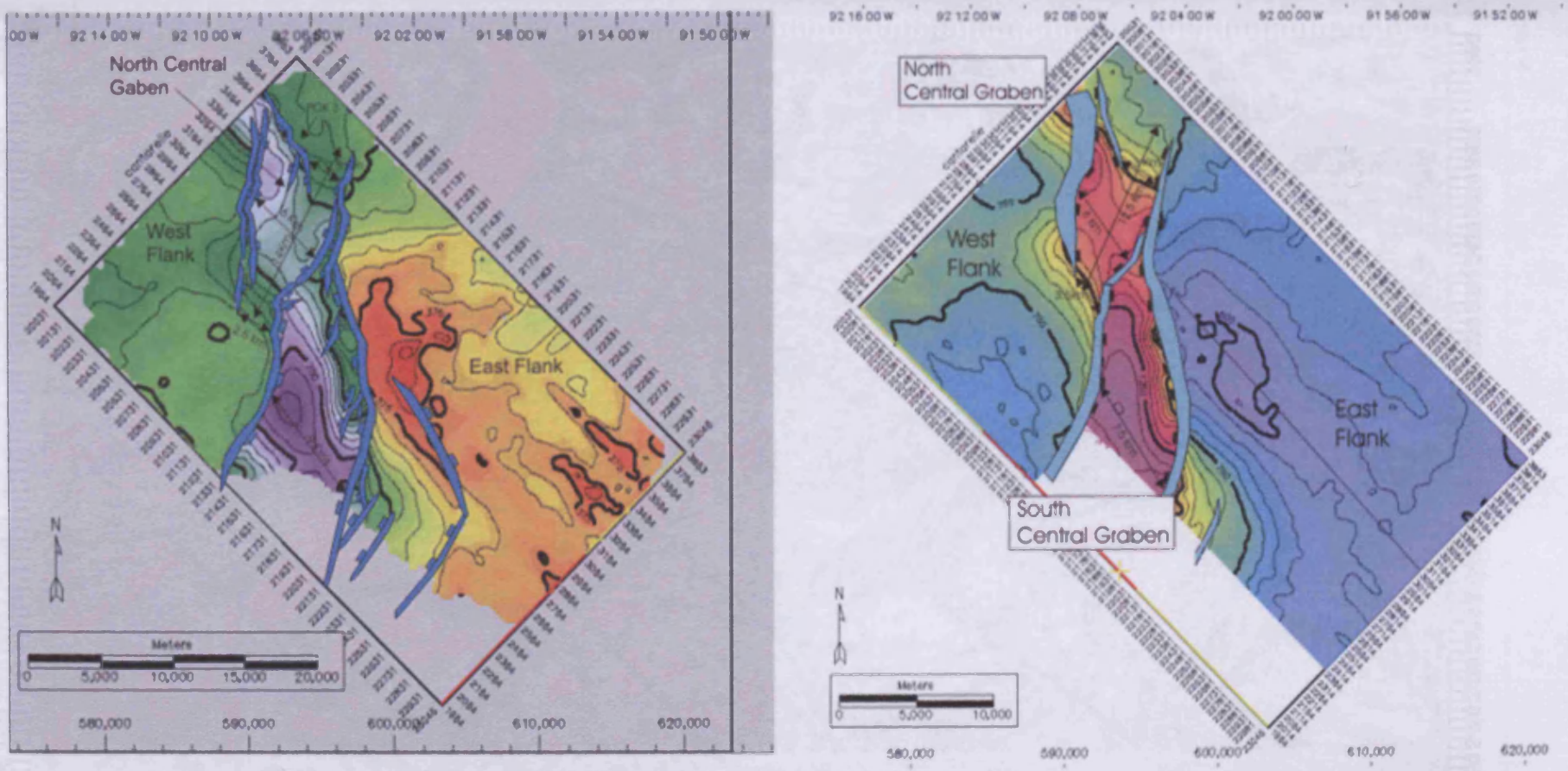

Figure 4.9
(a) Map of the Mio-1 structure msec TWT showing the dimensions of the relay ramp structure, yellow colours are shallow and purples deeper. (b) Map of the Mio-2 structure. Note both structural styles are very similar. Subtle dimensional changes occur within the graben. The East Flank of the Mio-1 horizon is less smooth and contain normal faults that were not visible in Mio-2 horizon. Blue colours are shallow and purple to red deeper.

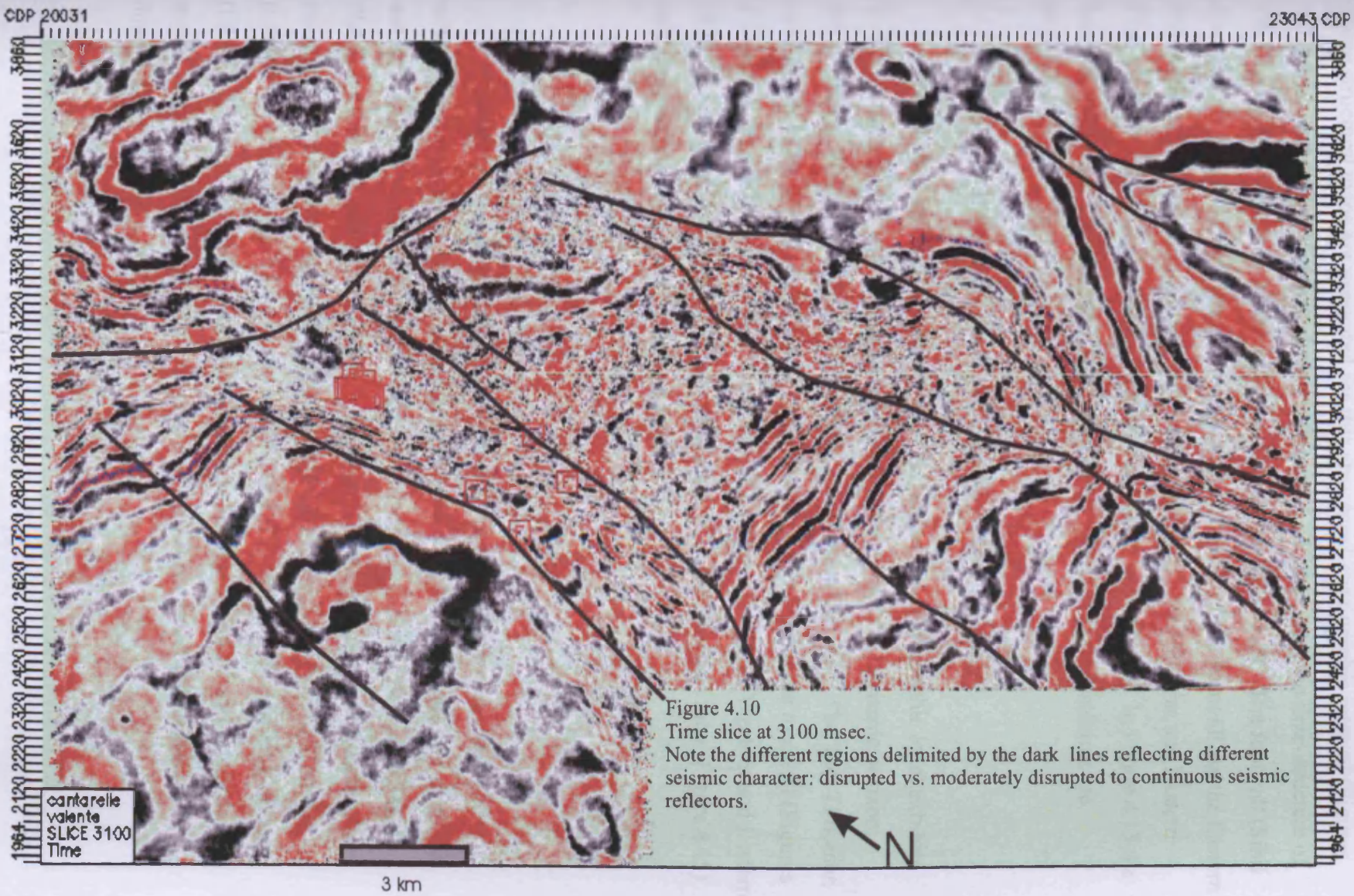

Figure 4.10
Time slice at 3100 msec.
Note the different regions delimited by the dark lines reflecting different seismic character: disrupted vs. moderately disrupted to continuous seismic reflectors.

Three structural maps are presented for this structural-stratigraphic interval (Figures 4.11, 4.12, and 4.13). The map shown in Figure 4.11 illustrates the time-structure of the Top-Breccia-1 seismic horizon displaying the footwall block. The footwall (Sihil reservoir) is located at the centre of the map. Either side of the footwall are the Eastern and Western Fault Corridors that in turn are delimited by the Western and Eastern Platforms. In Figure 4.12 only the hangingwall block is displayed. In Figure 4.13 the hangingwall block, the Western and Eastern Fault Corridors and Platforms are displayed.

4.2.2.4 Structure of the Top-Tithonian seismic horizon (Tithonian)

The mapped seismic horizon for the Top-Tithonian stratigraphic level exhibits similar structural elements to those defined at the Top-Breccia-1 seismic horizon: Thrust Block, Western and Eastern Platforms and Fault Corridors. The Top-Tithonian structural horizon is presented in two maps: the hangingwall and the footwall (Figures 4.14 and 4.15). In Figure 4.14 the Western and Eastern Platforms, Western and Eastern Fault Corridors and the footwall block are shown. The hangingwall map (Figure 4.15) only images the area located beneath the thrust plane.

In summary, the structural styles observed from seismic profiles and maps exhibit vertical variations in structural geometries and styles. At shallower structural and stratigraphic levels three structural blocks are defined: the Western and Eastern Platforms and the Kutz-Wakil Graben. At deeper levels five structural elements are interpreted: (1) the Western Fault Corridor (WFC), (2) the Eastern Fault Corridor (EFC), (3) Thrust Block (TB), (4) Western Platform (WP) and (5) Eastern Platform (EP) (Figure 4.1). The following sections document the structural characteristics, spatial layout, and the structural significance of the above structural elements in a three-dimensional framework.

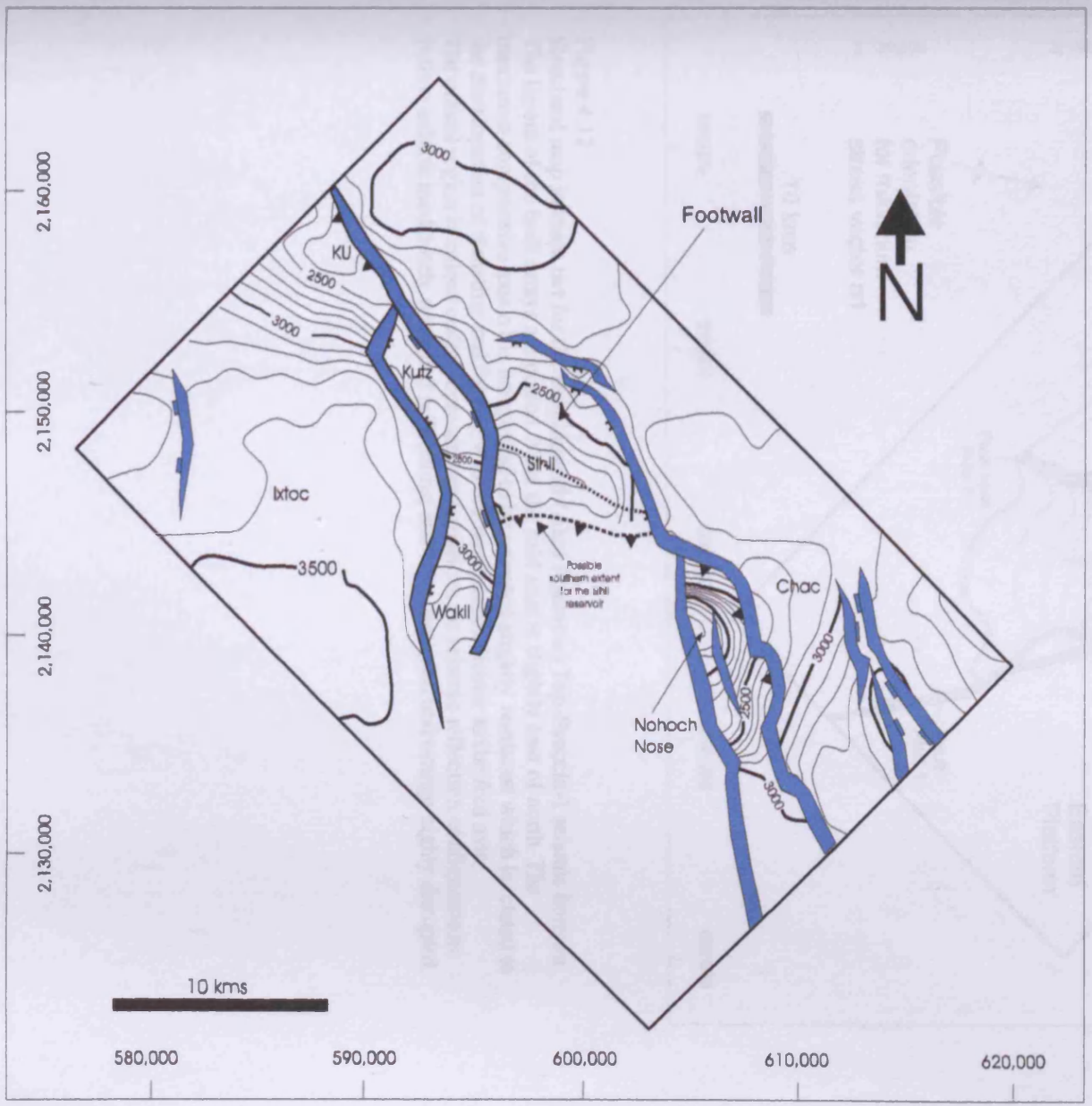

Figure 4.11
Structural map in time twt for the Top-Breccia-1 seismic horizon displaying the footwall structural block. At the centre the Sihil reservoir, adjacent regions Western and Eastern Fault Corridors, and outermost Western and Eastern Platforms. The southern limit of Sihil is defined by the thrust plane cutoff (dashed line).
Note that in the Thrust Block the contours exhibit a fold morphology, although this appearance is a result of pull-up effects, as demonstrated from Figure 4.29 and 4.32.

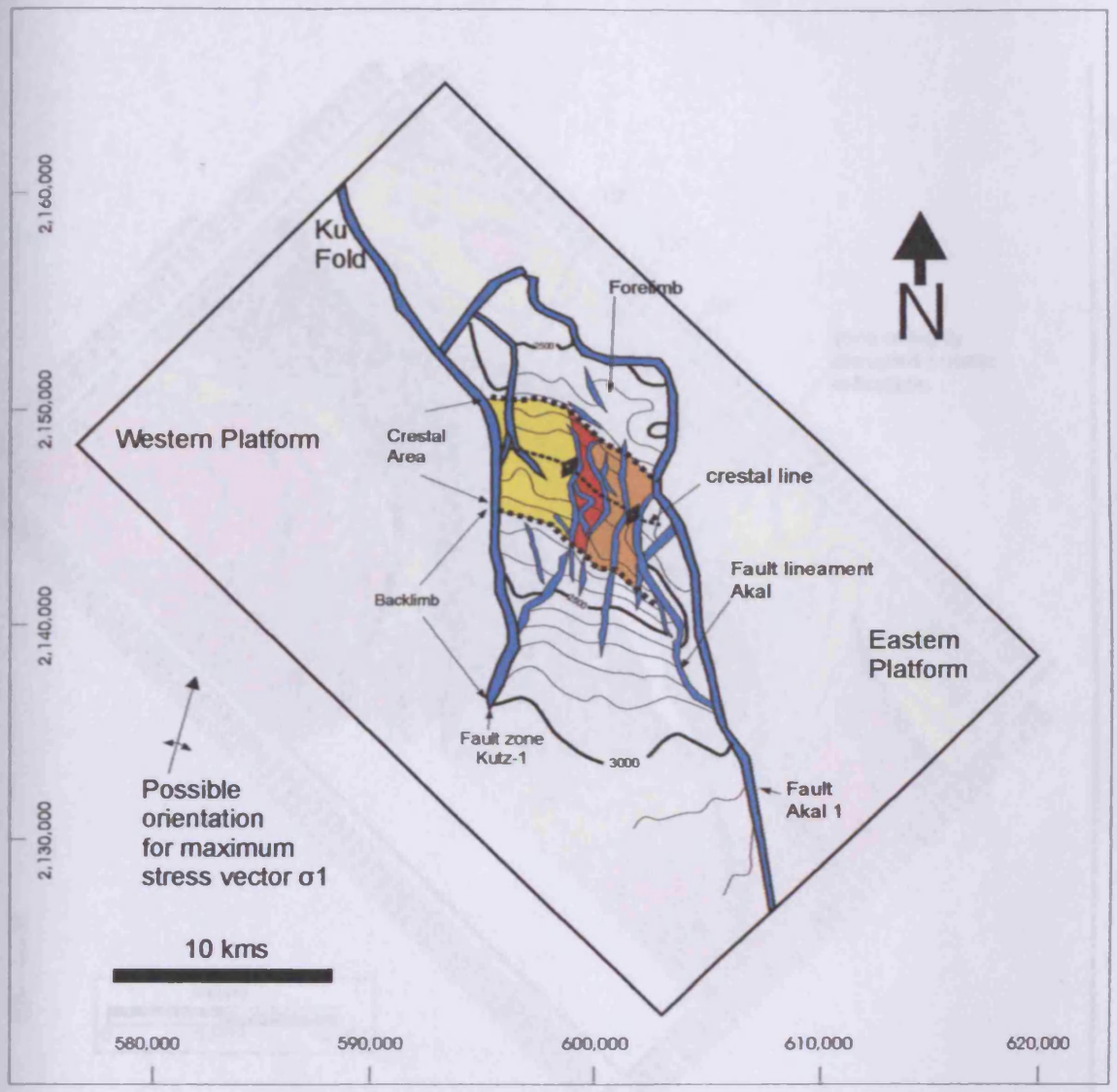

Figure 4.12
Structural map in msec twt for the hangingwall (Akal reservoir) Top-Breccia-1 seismic horizon. The layout of the fault arrays are posted. Note the fold axis is slightly east of north. The maximum compressive axis σ1 is interpreted to be oriented slightly northeast which is related to the development of thrusting and folding was oriented perpendicular to the fold axis.
The crestal region is colour coded representing variations on seismic reflection configurations: yellow exhibit moderately disrupted reflections; red very disrupted and orange highly disrupted.

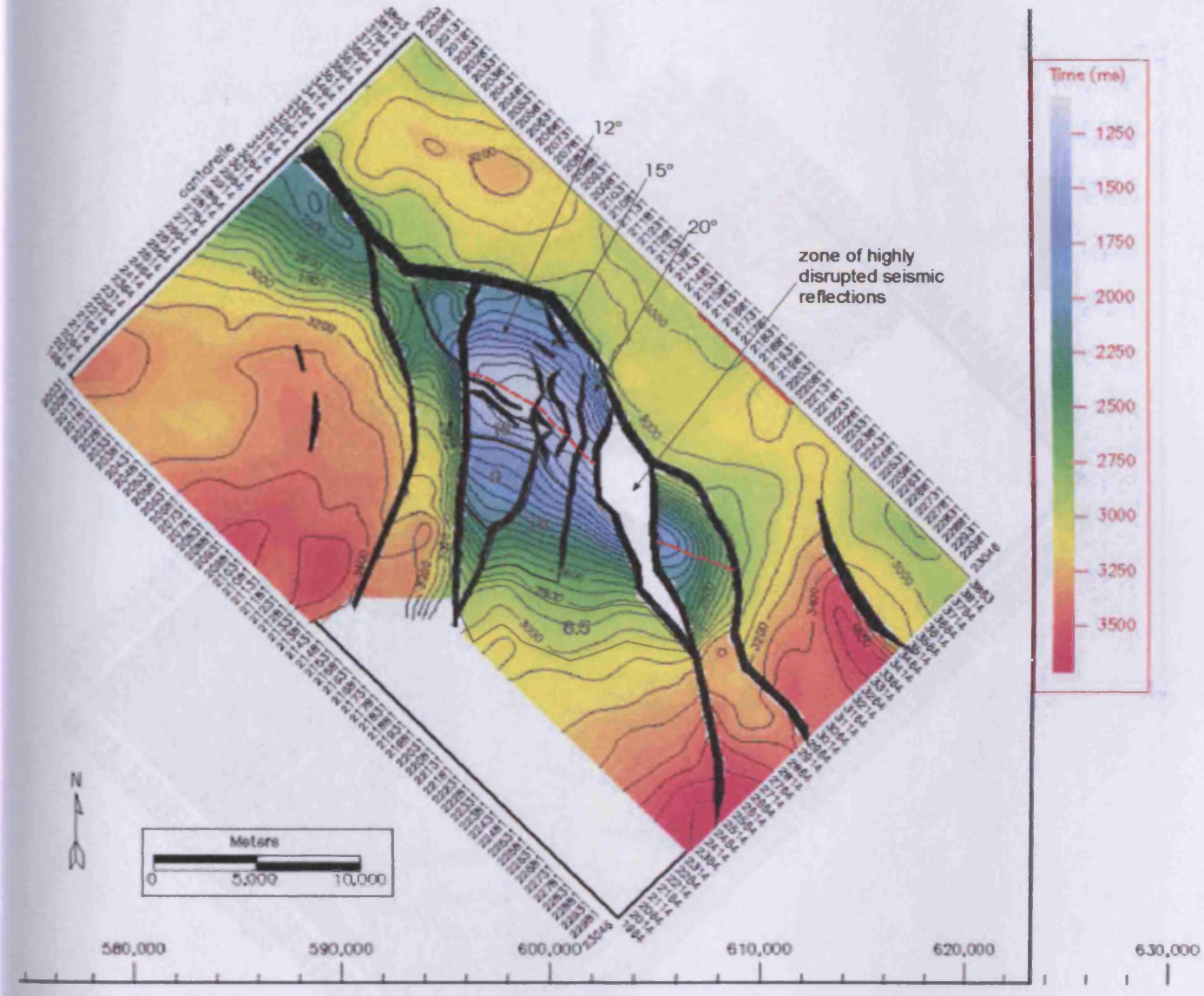

Figure 4.13
Areal view of the Top-Breccia-1 seismic horizon, the shown map was gridded using a convergent blanking IESX algorithm. Within the Thrust Block, regions exhibit the average calculated dip. Note towards the eastern sector the beheaded fold morphology of the anticlinal fold with respect to the Nohoch Nose.

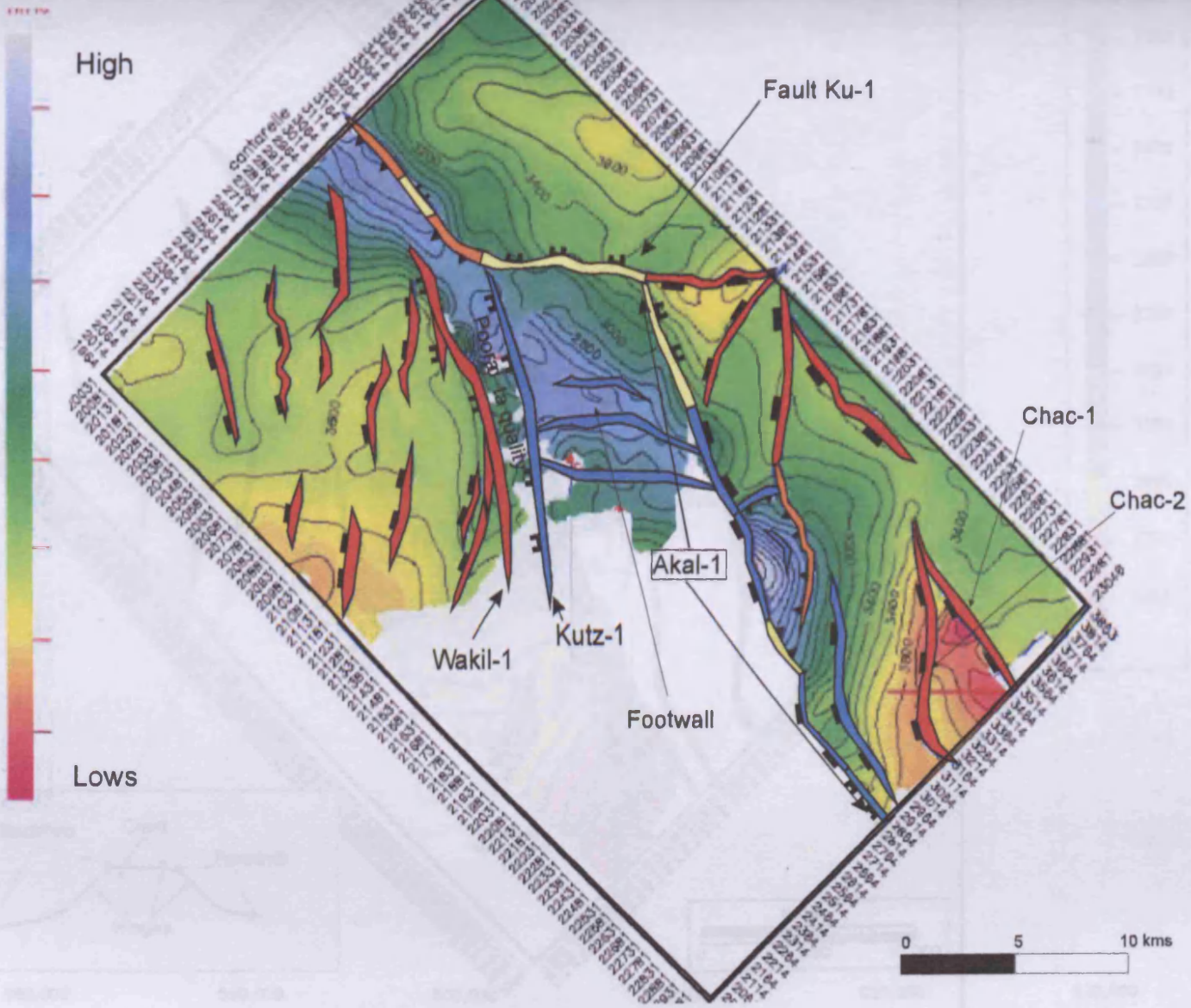

Figure 4.14
Structural map for the footwall Top-Tithonian seismic horizon. Fault polygons are colour coded, which displace different stratigraphic intervals: reflect red traces are found to only displace Jurassic to Early Cretaceous strata, some are deep-rooted. The remaining fault traces displace various stratigraphic intervals. The different given colours are associated with the various fault styles observed: blue steeply dipping normal faulting; orange low angle reverse; light yellow steep reverse dip slip.

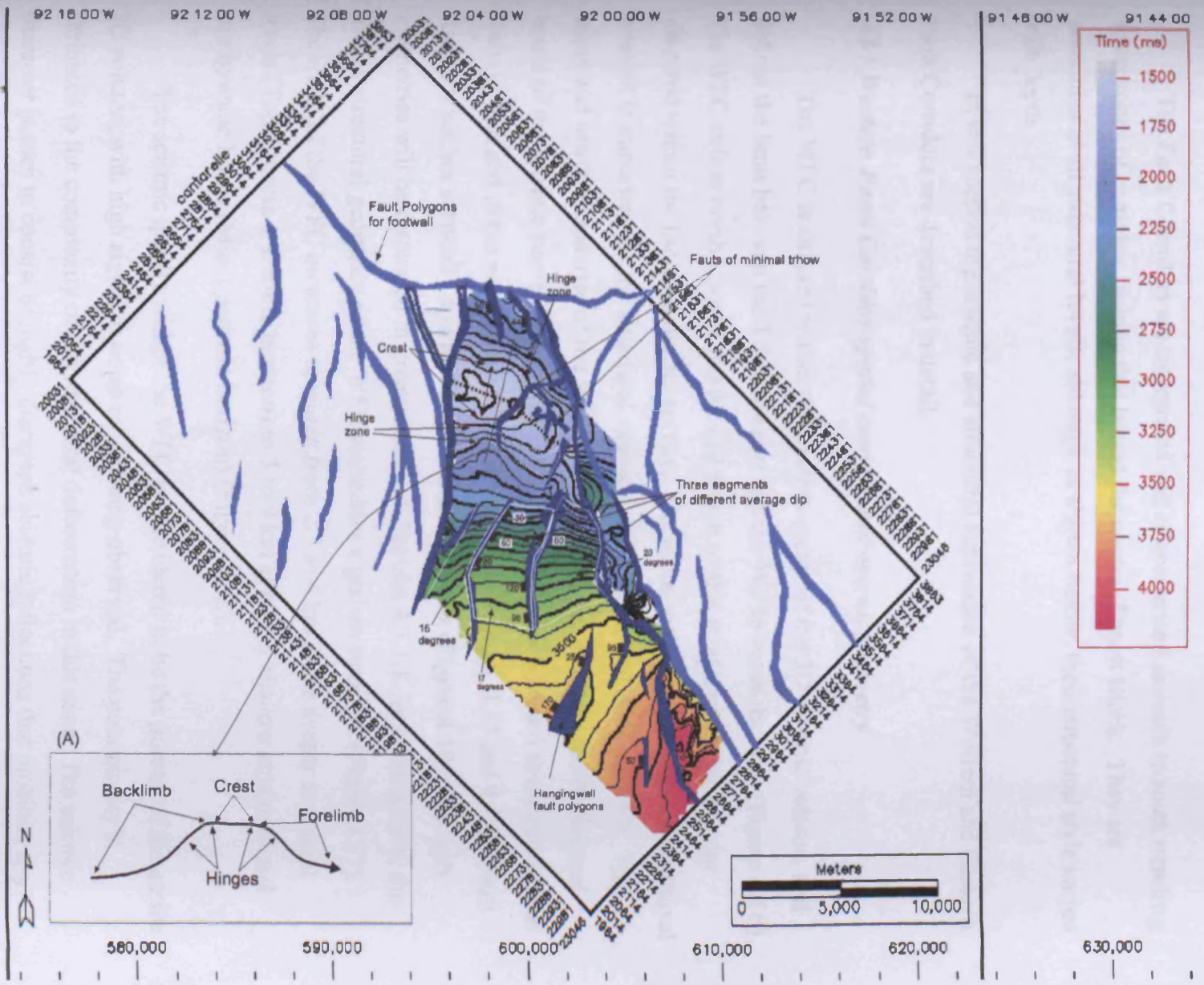

Figure 4.15
Structural map in msec twt for the Top-Tithonian seismic horizon within the hangingwall, which hosts the Akal reservoir. Throw magnitudes and direction of throw are posted. Fault lineaments coloured in light blue are present in the block. Average calculated dips are shown for the backlimb area.

4.3 Fault Corridors

The Fault Corridors are interpreted and characterised as north to south trending linear zones of complex faulting that bound the central Thrust Block. They are prominent at all structural levels, although as shown below, their structural style varies with depth.

In this section the seismic and structural expression of the Western and Eastern Fault Corridors are described in detail.

4.3.1 Western Fault Corridor spatial context and overall geometry

The WFC is situated within the western sector of the 3D seismic volume, and defines the limit between the TB to the east and the WP towards the west (Figure 4.16). The WFC strikes north – south and the full extent of this structural element is not observed within the limits of the 3D survey. The more regional extent of this structural element is important for the structural analysis and is described in Section 4.6. The upper and lower boundaries of the WFC are defined by the seafloor and the vertical extent of the seismic survey (6 seconds TWT). The WFC is bounded to the east by the Kutz-1 Fault and to the west by the Wakil-1 Fault (Figure 4.16, 4.17 and 4.18). Fault Kutz-1 branches vertically upwards into various segments (Figure 4.18). The fault geometries will be discussed in greater detail in Section 4.3.1.1. In cross section, the overall structural geometry of the WFC resembles a graben structure (Figure 4.17). The width of the WFC increases upwards from 2.5 to 4 km at the deeper structural levels (Top-Breccia-1 seismic horizon) to 5 to 9 km at higher shallow structural and stratigraphic levels (Mio-1 seismic horizon) (Figure 4.18).

The seismic quality within the WFC is considered to be the poorest of the entire 3D volume, with high signal to noise ratios being observed. The poor quality is attributed to the complexity of the structural deformation in this zone. The seismic character is seen to consist of highly disrupted seismic reflections that prohibits any accurate and detailed interpretation of seismic horizons within this complexly deformed zone (Figure 4.17 and 4.18).

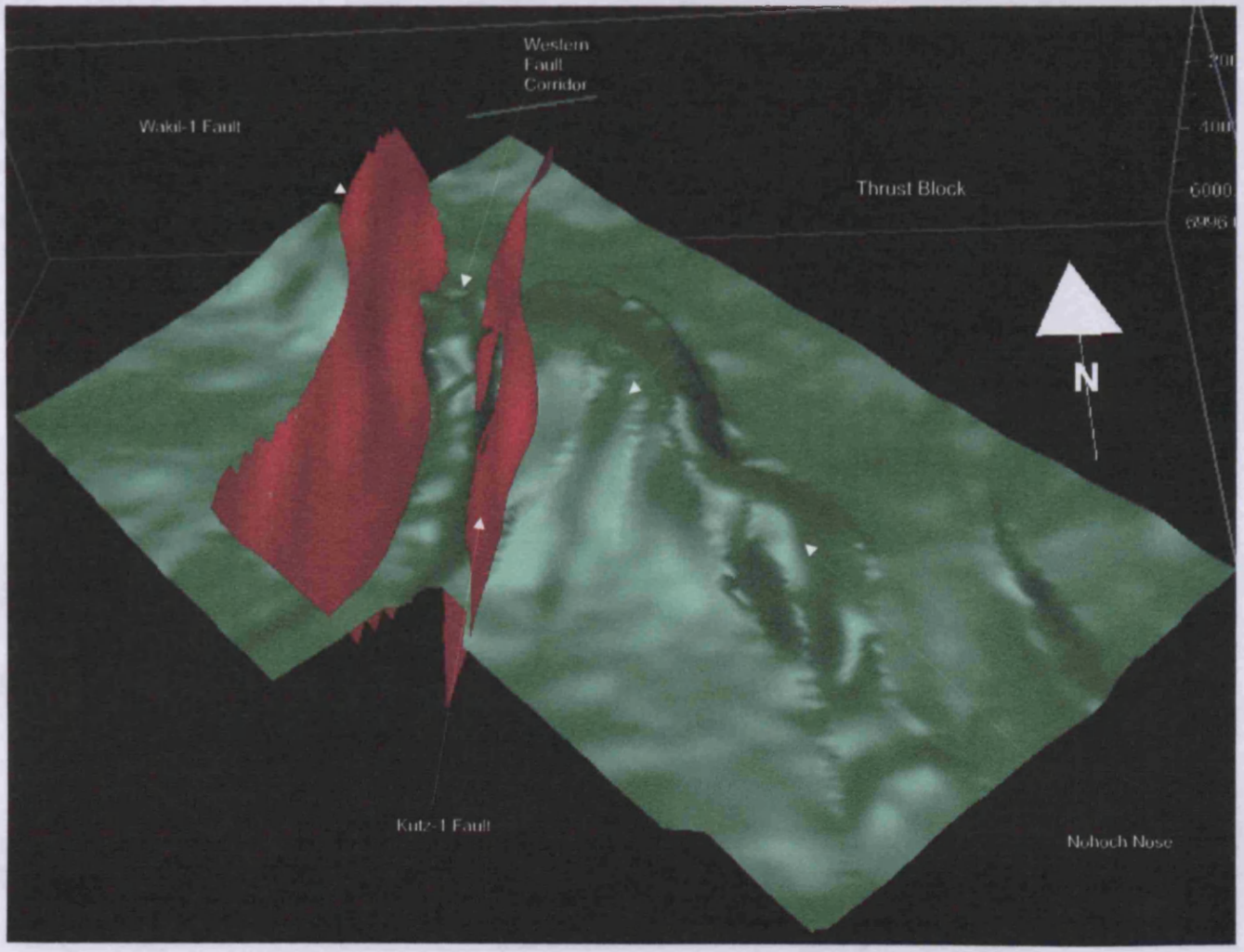

Figure 4.16
Geoviz image displaying the Top-Breccia-1 seismic horizon and the faults that bound the Western Fault Corridor zone.

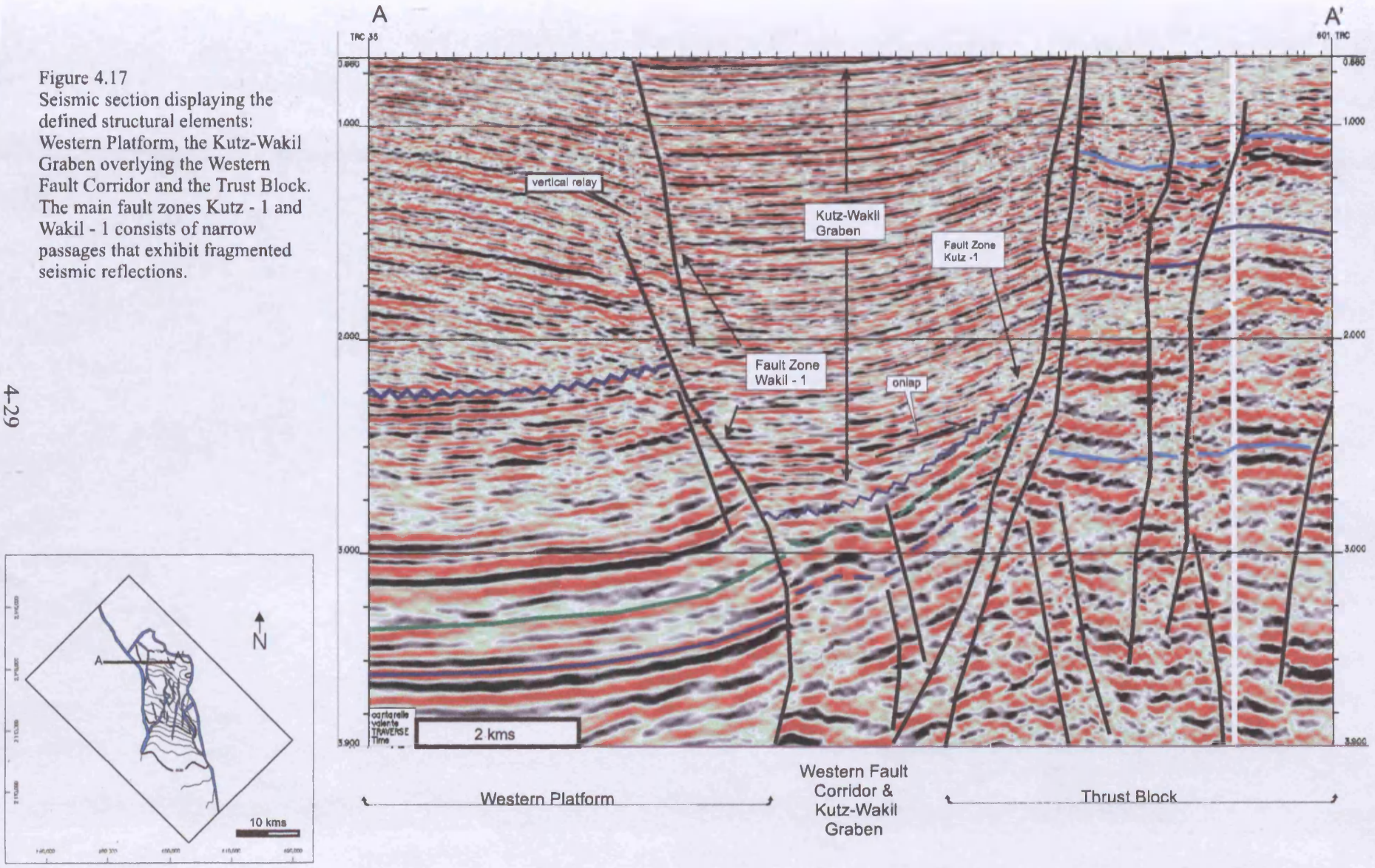

Figure 4.17
Seismic section displaying the defined structural elements: Western Platform, the Kutz-Wakil Graben overlying the Western Fault Corridor and the Trust Block. The main fault zones Kutz - 1 and Wakil - 1 consists of narrow passages that exhibit fragmented seismic reflections.

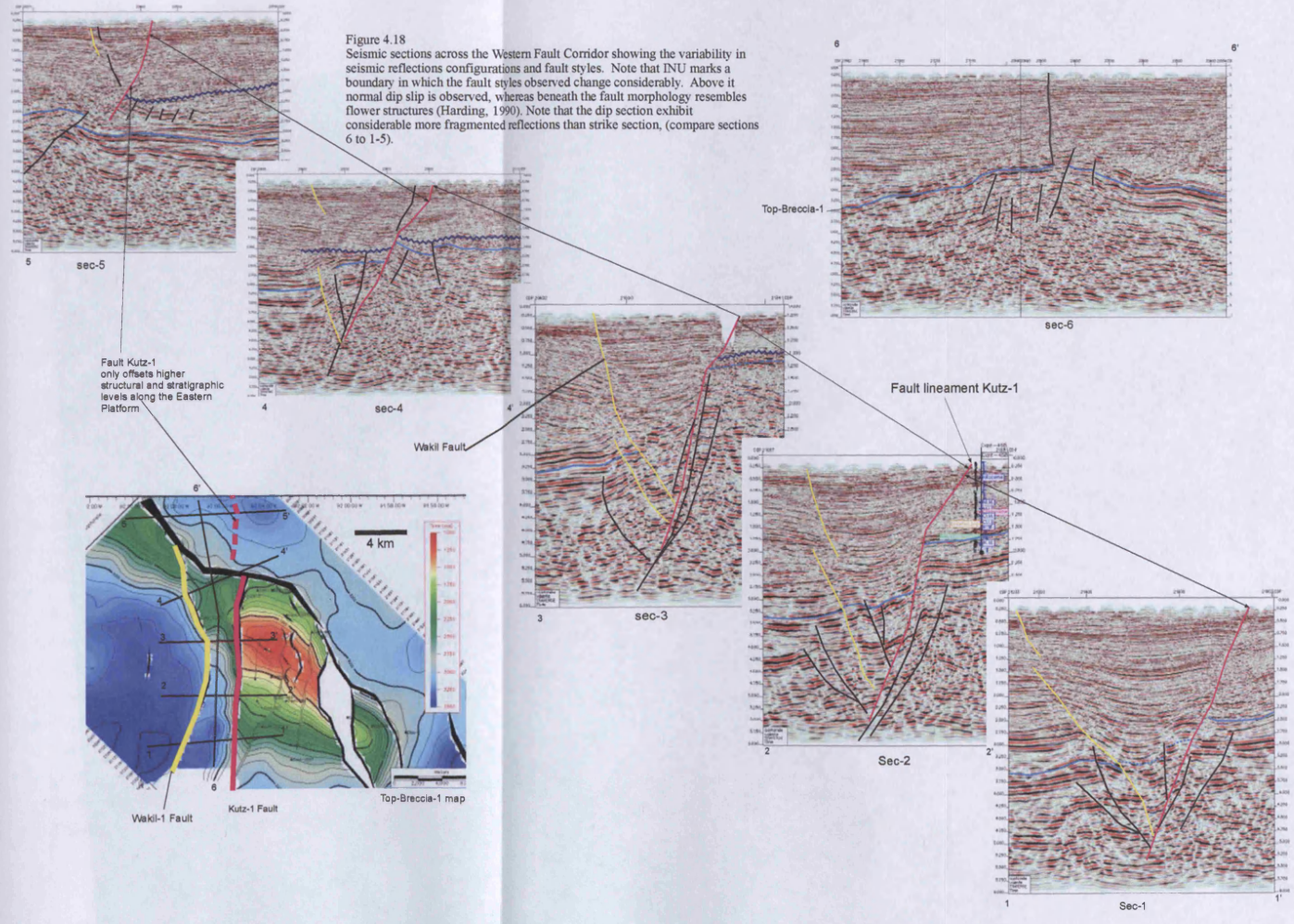

Figure 4.18
Seismic sections across the Western Fault Corridor showing the variability in seismic reflections configurations and fault styles. Note that INU marks a boundary in which the fault styles observed change considerably. Above it normal dip slip is observed, whereas beneath the fault morphology resembles flower structures (Harding, 1990). Note that the dip section exhibit considerable more fragmented reflections than strike section, (compare sections 6 to 1-5).

4.3.1.1 Three-Dimensional Geometry of Bounding Faults

The geometry of the Kutz-1 and Wakil-1 Faults vary vertically and along strike with various complexities in fault geometry being observed along their lengths (e.g. relay ramps, vertical ramps, branching and splaying faults; Figures 4.17 and 4.18).

The Kutz-1 Fault that separates the WFC from the TB consists of a narrow fault zone in which a master fault and various fault segments are interpreted vertically and laterally (Figure 4.17). The strike of the Kutz-1 Fault is approximately north – south and it is found to be deep-rooted (5.6 sec twt) in areas adjacent to the Thrust Block (Figure 4.18). North of the Thrust Block, along the WFC, the Kutz-1 Fault only offsets Cenozoic rocks (Figures 4.16 and 4.18, sec 5). At deeper structural levels, the Kutz-1 Fault generally exhibits a steep dip (> 65 °) that becomes shallower (45 °) at higher structural levels. The steeper segments of the Kutz-1 Fault occur adjacent to the Thrust Block (Figure 4.18).

Fault throws have been calculated along the Kutz-1 Fault at the Top-Breccia-1 (Figure 4.19), the Mio-2 and Mio-1 seismic horizons (Figure 4.6). The largest fault throws were observed at the Top-Breccia-1 seismic horizon (from 850 m to 300 m). At higher structural and stratigraphic levels (Mio-1 seismic horizon, Figure 4.6), the fault throws decrease (430 m to 0 m), and at shallower structural and stratigraphic levels, the fault throw decrease further (215 m to 0 m). The apparent sense of motion on the Kutz-1 Fault is normal as observed from seismic profiles (Figure 4.18). Further analysis of the fault kinematics will be discussed in Section 4.6.

The western boundary of the WFC is defined by the Wakil-1 Fault that consists of various fault segments (horizontally and vertically) and strike north – south (Figure 4.18). Like the Kutz-1 Fault, the Wakil-1 Fault is found to penetrate into deep structural and stratigraphic levels. A considerable number of fault segments have been interpreted at deeper structural levels adjacent to the Thrust Block. Towards the north these fault segments decrease and die out at deeper structural levels. At shallower structural and stratigraphic levels, the number of fault segments decreases and the width of the fault zone decreases vertically upwards (Figure 4.17). In some cross sections (Figure 4.18, secs. 2-2'and 4-4'), vertical relays occur within the shallower

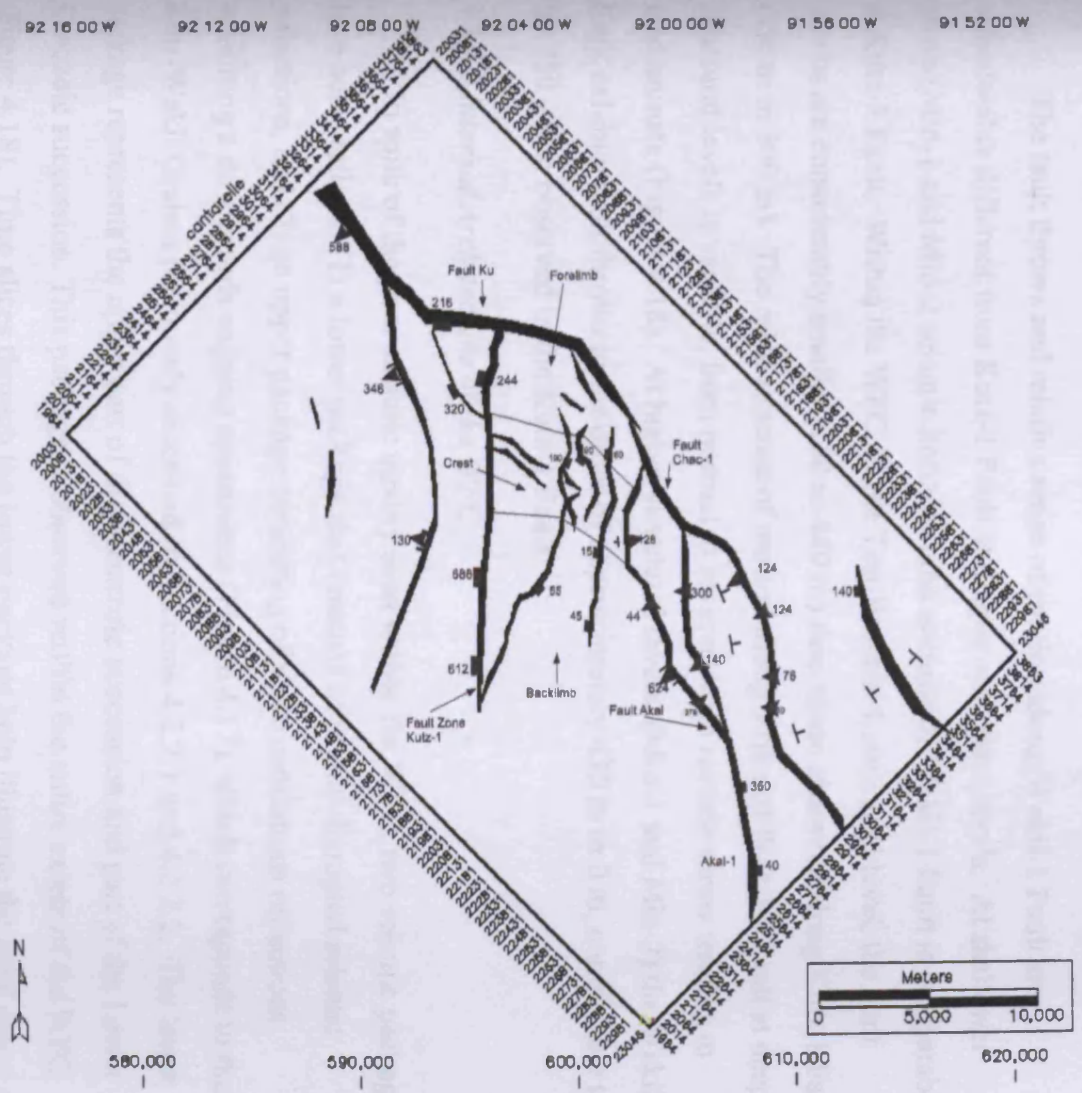

Figure 4.19
Fault layout for the Top -Breccia-1 seismic horizon, (Base Tertiary stratigraphic level). Fault arrays, relative throws, throw direction, and throw magnitudes are displayed. Throw magnitudes calculated in msec twt. Note the alternating throw values along fault Akal. Fault Akal bounds the Eastern Fault Corridor which in cross section exhibits variable styles, that have been interpreted as a flower structure (refer to Figure 4.18).

Cenozoic successions. Laterally, these relays eventually coalesce into a single fault segment.

The fault throws and relative sense of motion along Wakil-1 Fault are considerable different from Kutz-1 Fault at deeper structural levels. At shallower levels (Mio-1 and Mio-2 seismic horizons) the attitude of Wakil-1 Fault is comparable to Kutz-1 Fault. Within the WFC, at the Top-Breccia-1 structural level, the fault throws are considerably smaller (160 to 440 m) than those observed along Kutz-1 Fault (850 m to 300 m). The relative sense of motion along strike of Wakil-1 Fault at deeper structural levels is variable, from normal to reverse, with reverse throw tending to predominate (Figure 4.18). At higher structural levels, (Mio-1 and Mio-2) the Wakil-1 Fault exhibits fault throws in the order of approximately 430 m to 0 m, comparable to the 250 – 0 m observed in the Kutz-1 Fault.

4.3.1.2 Internal Architecture of the WFC

In spite of the poor seismic quality seen within the WFC, two seismic packages have been defined: (1) a lower package that consists of highly disrupted seismic reflections, and (2) an upper package consisting of more continuous reflections exhibiting a downwards-sagging appearance (Figure 4.17), which corresponds to the Kutz-Wakil Graben previously described in Sections 4.2.2.1 and 4.2.2.2. The lower package represents the upper part of the Mesozoic succession and part of the Lower Cenozoic succession. This package is observed within the entire extent of the WFC (Figure 4.18). Time slices through the lower package help illustrate the areal extent of the WFC. The upper package extends beyond the Ku Fault to the north (Figure 4.18).

Considering the fragmented seismic appearance, the overall structural style of the WFC, and the structural context of the WFC with respect to the Thrust Block, it is suggested that the highly disrupted appearance of this lower package reflects a severely sheared zone (Figure 4.18). Similar loss of coherency I reported from highly sheared sedimentary sequences elsewhere in highly deformed sedimentary basins (Harding, 1990).

The upper region was referred to as the Kutz-Wakil Graben in earlier sections of this Chapter (4.2.2.1 and 4.2.2.2). It trends north - south and extends across the full length of the seismic survey (Figures 4.4 and 4.18).

4.3.2 Eastern Fault Corridor

The Eastern Fault Corridor is defined as a narrow (up to 5 km in width) and elongated zone of intense deformation that exhibits disrupted seismic reflections. It is located to the east of the Thrust Block and to the west of the Western Platform (Figures 4.1 and 4.4) and is defined by the bounding Akal and Nohoch Faults (Figure 4.20). Towards the north the Akal and Nohoch Faults converge and the northern extent of the EFC is coincident with the extent of the TB (Figure 4.1). Towards the south the entire extent of the EFC is not appreciated due to the extent of the seismic data.

4.3.2.1 Three-Dimensional Geometry of Bounding Faults

The Akal and Nohoch Faults that define the boundaries of the EFC strike approximately north - south and are sub-parallel to each other. The apparent sense of throw on these faults varies vertically and along strike (Figure 4.20 and 4.21).

The Akal Fault defines the western boundary of the EFC and occurs adjacent to the TB (Figure 4.21). This fault consists of a master fault with an adjacent narrow zone of vertical to steeply dipping fault slices (Figure4.20 and 4.21). The fault displacement along the Akal Fault occurs mainly below the INU, but in some regions seismic reflections near the present seafloor appear slightly displaced (Figures4.20 and 4.21). Variations in fault dip and throw were observed laterally and vertically. Vertically the EFC can be divided into two intervals separated by the INU. The fault attitude above the INU exhibits normal dip-slip throws whereas within the interval beneath the INU, the fault style changes rapidly vertically and along strike (Figures 4.21 and 4.22). These rapid changes are well illustrated at the Top-Tithonian level where various fault segments were recognised along the strike of the Akal Fault (reverse and normal, Figure 4.14). These exhibit variations in fault throw and dip. The northernmost segment (Figure 4.14) appears with a reverse sense of movement. In contrast, towards the south the relative sense of motion appears to have a normal sense of throw and the dip of the fault appears to be towards the east (Figure 4.14). The southern most segment of the fault located adjacent to the Nohoch Nose, consists of a series of parallel, almost vertical and north – south striking normal faults with an apparent throw towards the west (Figures 4.14 and 4.22).

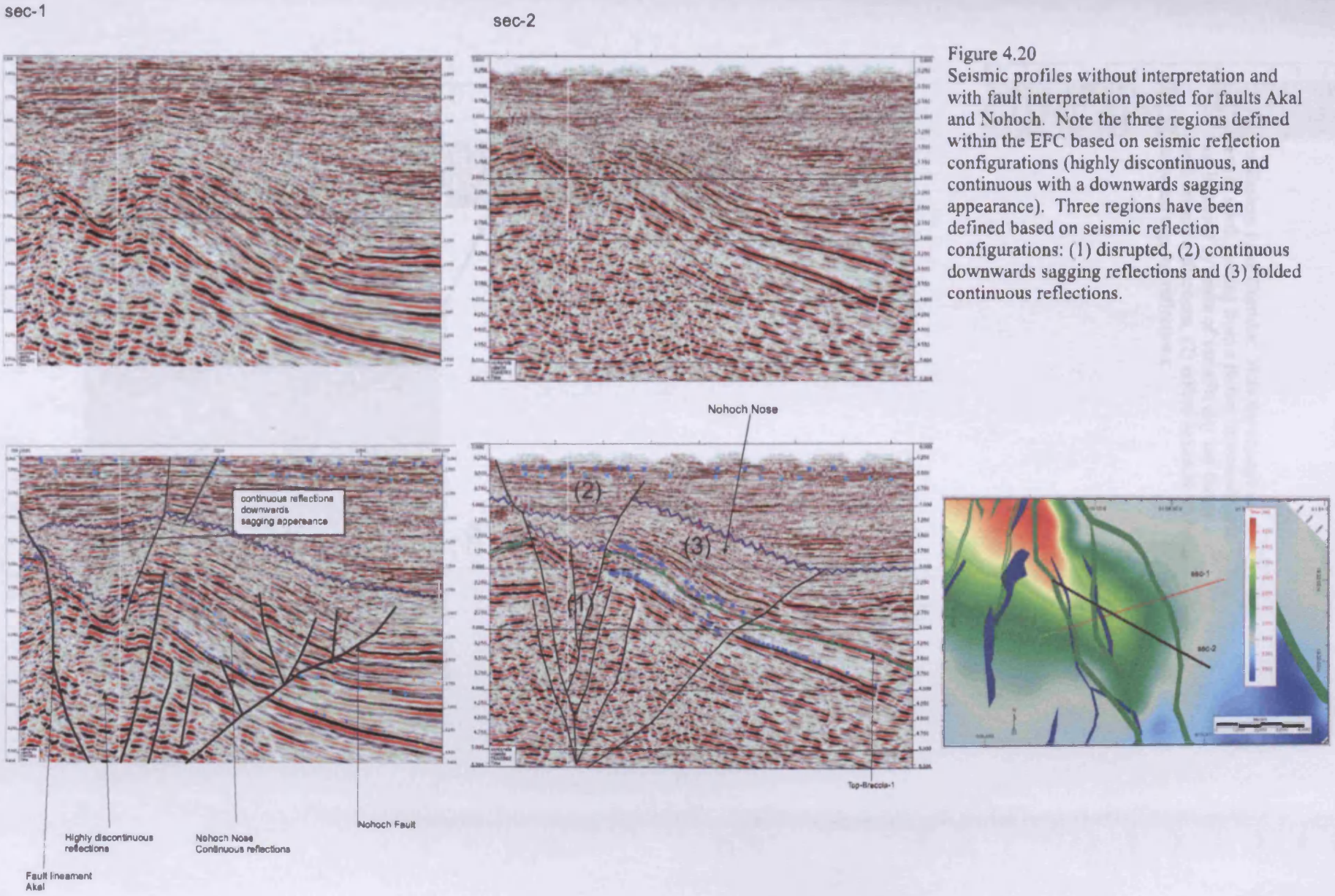

Figure 4.20
Seismic profiles without interpretation and with fault interpretation posted for faults Akal and Nohoch. Note the three regions defined within the EFC based on seismic reflection configurations (highly discontinuous, and continuous with a downwards sagging appearance). Three regions have been defined based on seismic reflection configurations: (1) disrupted, (2) continuous downwards sagging reflections and (3) folded continuous reflections.

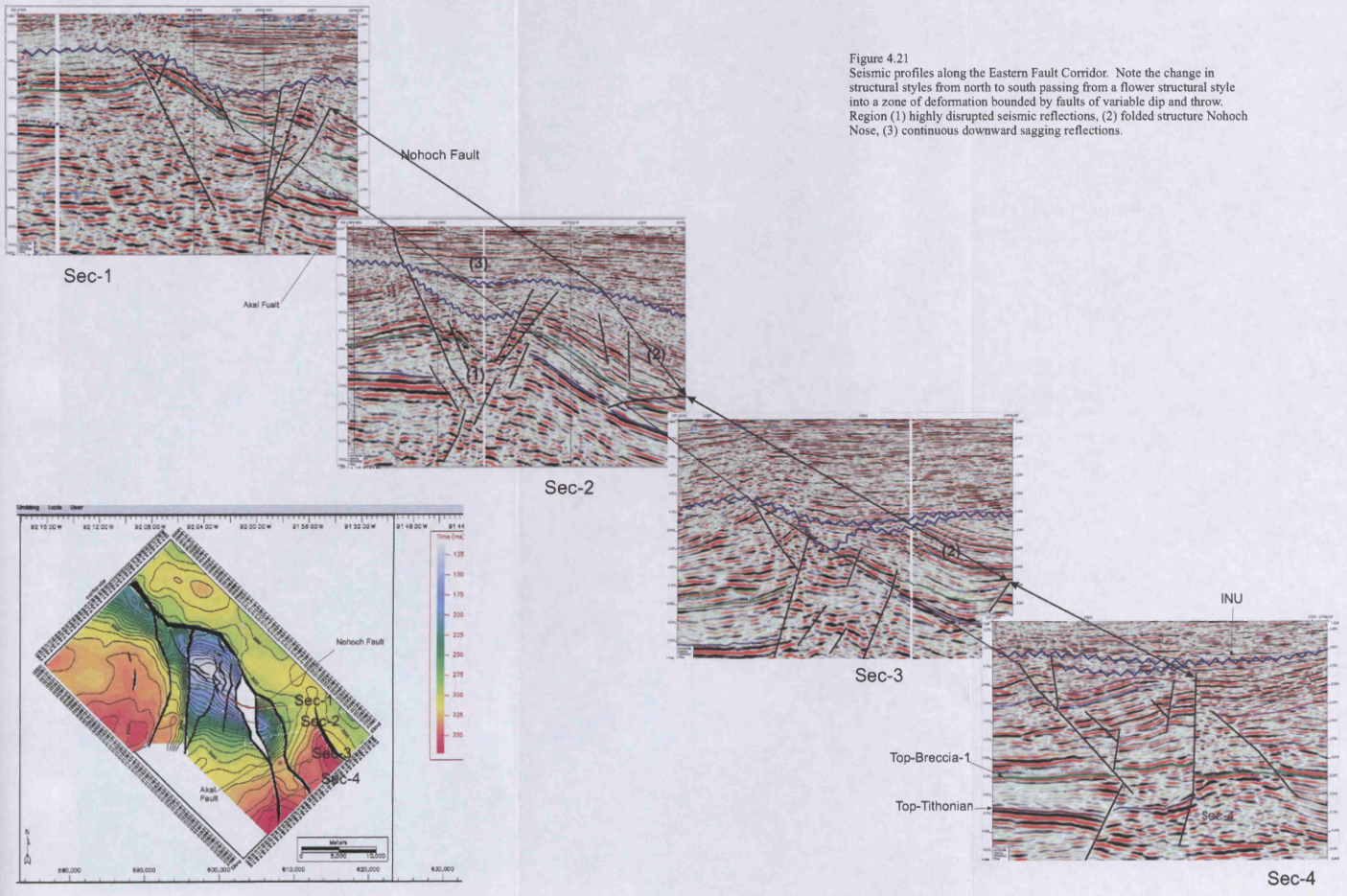

Figure 4.21
Seismic profiles along the Eastern Fault Corridor. Note the change in structural styles from north to south passing from a flower structural style into a zone of deformation bounded by faults of variable dip and throw. Region (1) highly disrupted seismic reflections, (2) folded structure Nohoch Nose, (3) continuous downward sagging reflections.

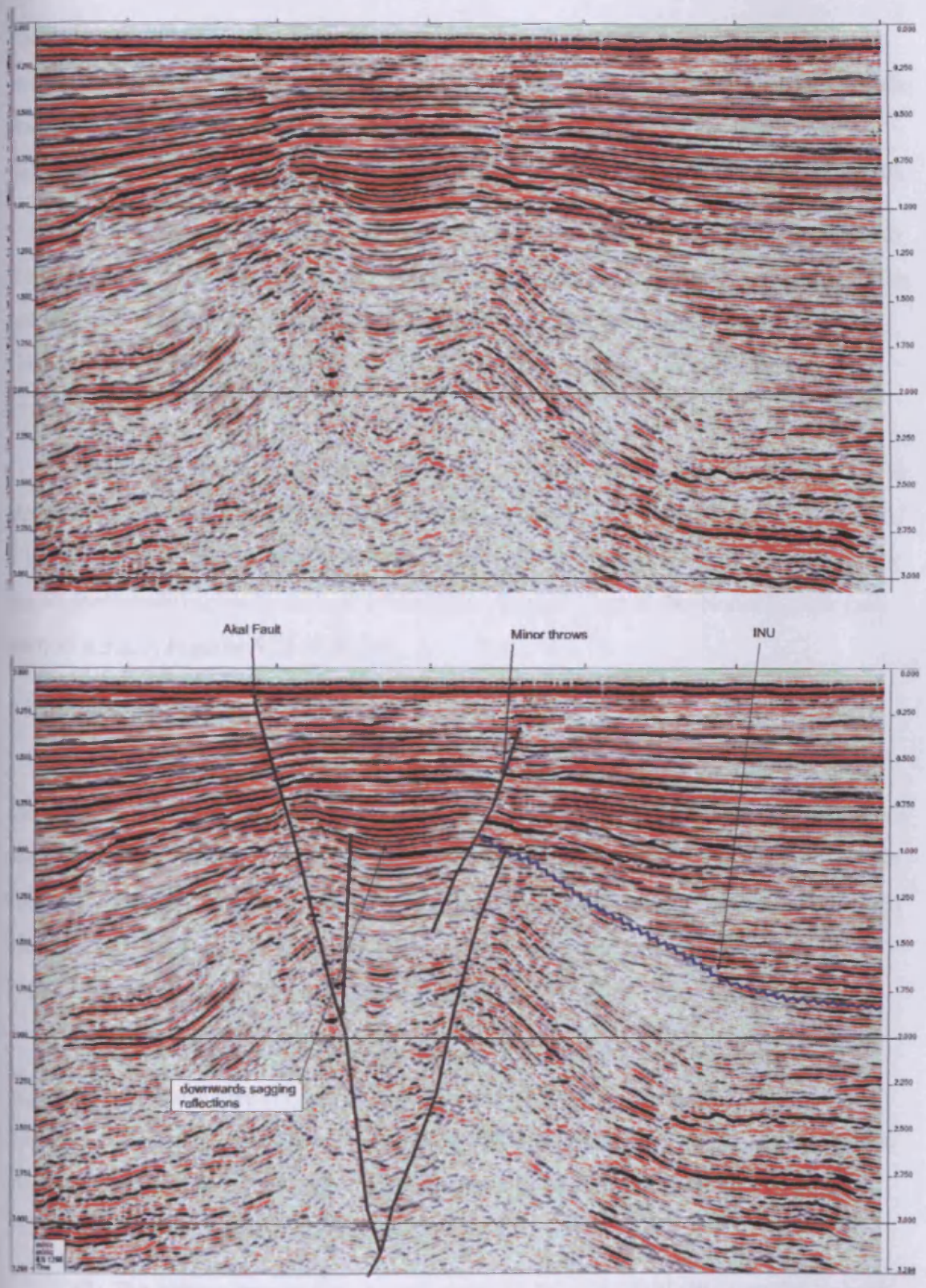

Figure 4.22
Seismic profiles non interpreted and interpreted oriented west - east from the first 3D streamer seismic data, across the EFC (Eastern Fault Corridor). Note the regions above the EFC exhibits continuous reflections that have a downwards sagging morphology and are bounded by faults with minor normal slip throws.

The most diagnostic aspect of the preceding description of the Akal Fault is the rapid lateral and vertical changes in the sense and direction of throw. These are characteristic features observed in strike-slip faults that may occur at various scales from wrench faulting to detached tear faults associated with fold and thrust systems (Harding, 1990).

The Nohoch Fault defines the eastern boundary of the EFC. Towards the north it converges into the Akal Fault, and towards the south it is truncated by the edge of the seismic survey. Based on Pemex regional interpretation shown in Figure 4.2, the Nohoch Fault appears to continue further to the south tipping out in the Macuspana depocentre.

Vertically, the Nohoch Fault offsets basal seismic reflections that correspond to Upper Mesozoic and Lower Cenozoic successions before dying out just above the INU (Figure 4.20 and 4.21). Along strike the fault style changes drastically from normal at the southernmost region to a thrust plane (flat – ramp – flat) at the Nohoch Nose (see Section 4.3.2.3; Figures 4.21 and4.23).

4.3.2.2 Internal Architecture of the EFC

Within the EFC, three regions have been defined based on seismic reflection configurations. The three regions consists of: (1) an elongated western region of highly disrupted reflections and (2) an eastern region that consists of a folded structure herein defined as the Nohoch Nose, and (3) a region of continuous seismic reflections located directly above region 1, adjacent to the Nohoch Nose (Figures 4.20 and4.21). Following, these regions are documented in greater detail:

(1) In cross section the western region (Figure 4.20 and 4.21) resembles a negative flower structure comparable to those described by Harding (1990), and Sylvester (1988), (see Section 4.6). Harding (1990) associates these type of structures to (i) detached tear faults in fold-thrust belts and (ii) faults that form as a result of folding and lead to a shift of the fold axis.

(2) The eastern region consists of a smooth but tight fold structure the Nohoch Nose with a northwest - southeast fold axis that is subparallel to the hinge line defined in the TB (Figure 4.12; see Section 4.2.2.3). However, the fold axis is located towards the south with respect to the fold axis of the TB (Figure 4.12). The fold axis of the

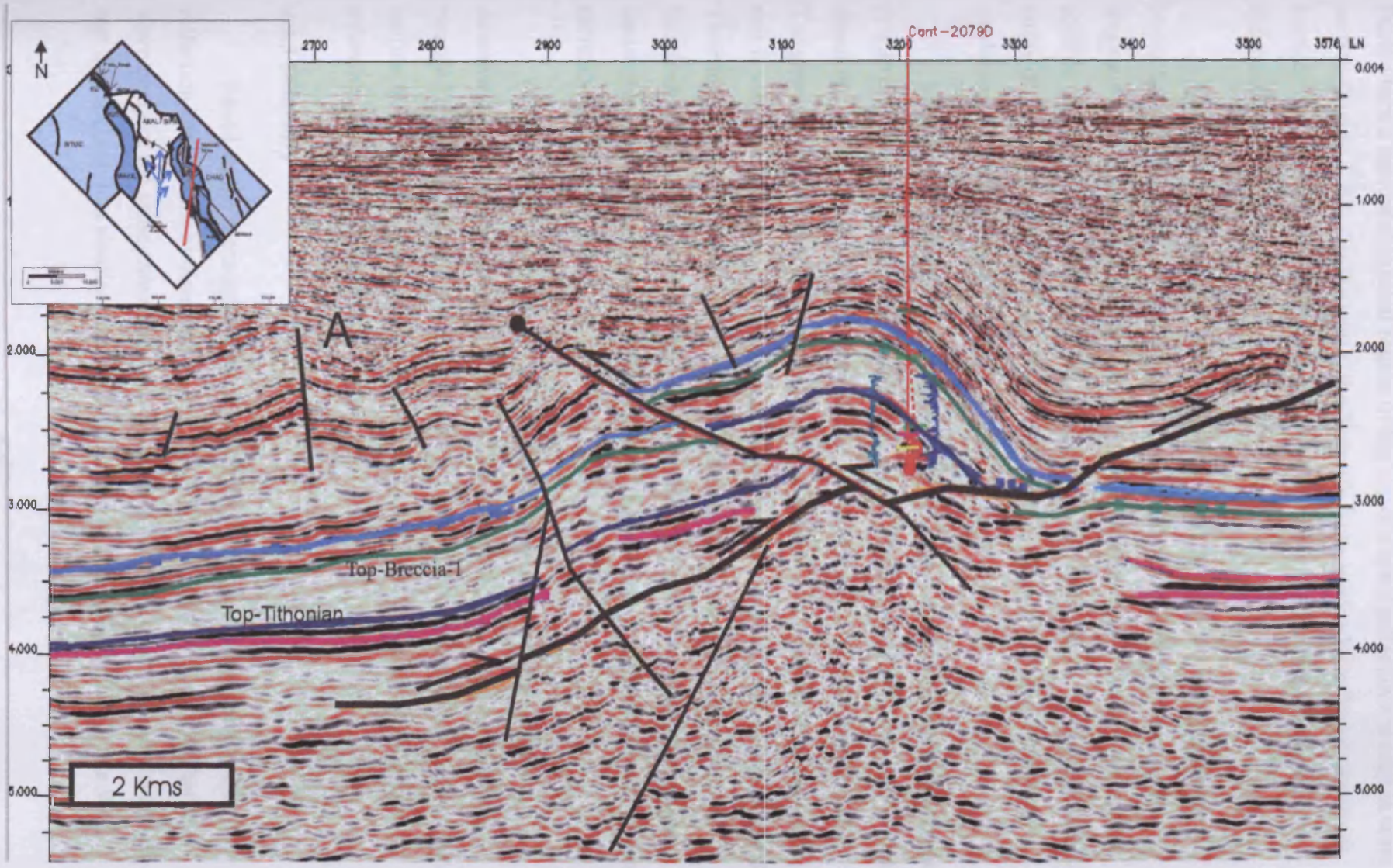

Figure 4.23
Section illustrating main thrust fault , in black, related to the major thrust emplacement of the Akal block being at later stages of deformation displaced by a back thrust, in red. Note the fold labelled A located to the south of the backthrust. Horizons, Top-Breccia-1; and Top-Tithonian.

Nohoch Nose is delimited to the east by the Nohoch Fault, to the west by the Akal Fault where a narrow elongated region of highly disrupted reflections is seen in cross section (Figure 4.20). To the south, the Nohoch Nose passes laterally into a narrow corridor that exhibits moderately disrupted reflections. Towards the north it is delimited by the Nohoch Fault.

The seismic reflection character varies vertically and laterally, within the Nohoch Nose (Figure 4.20). At the base, beneath the Top-Tithonian horizons, fragmented to chaotic reflections occur, whilst above the Top-Tithonian horizon the seismic reflections are relatively continuous, but slightly offset by normal and reverse faults (Figure 4.20). South of the Nohoch Nose the seismic reflections become moderately disrupted (Figure 4.21).

In cross-sections oriented north – south (Figure 4.23), the Nohoch Nose is seen to sole on a low angle, long and continuous thrust plane that exhibits a northerly thrust direction. A backthrust verging towards the south is also interpreted (Figure 4.23). The geometry of the northerly verging thrust plane exhibits a flat-ramp-flat geometry that is very similar to that of the thrust plane observed within the TB (see Section 4.4). Their lower and upper flats are located within similar stratigraphic and structural locations. The thrust plane interpreted within the Nohoch Nose could be the same thrust plane as that interpreted within the TB. However, it is not possible to confidently correlate it across the EFC.

(3) The region found above the INU and the western region exhibits a downward sagging morphology (Figure 4.22). The downward sagging feature is bounded by faults that are vertically connected with the underlying fault system (see section 4.3.2.1). This feature is interpreted to have formed as a result of (i) mild extension, and/or (ii) differential compaction.

4.3.3 Summary

Based on the preceding description of the structural arrangement and seismic reflection configurations observed within the EFC and WFC, it is evident that they share many of the same characteristics. However, the dimensions vary considerably in that the EFC exhibits smaller dimensions (5 km vs 9 km) (Figure 3.25). The WFC

extends north of the TB whilst the northernmost extent of the EFC is coincident with the extent of the TB. In summary, the WFC and EFC share the following characteristics:

(1) They are narrow, elongated, straight, and through going zones of deformation that are bound by two parallel fault zones.

(2) The delimiting fault zones exhibit steep to moderate dips that generally are steeper at depth.

(3) Along the fault zones, changes in relative sense of throw, separation and fault dip with depth are recognised.

The three-dimensional geometry of these structures strongly suggests that the WFC and EFC most likely represent lateral ramps or *tear faults*. In the next section more evidence is presented reinforcing such an interpretation.

4.4 Thrust Block

In this section the seismic and structural characteristics of the Thrust Block are described. The Thrust Block is divided into three structural elements: thrust plane, the hangingwall, and the footwall (Figures 4.11, 4.12 and 4.24) all these are described separately in the following sections. A structural model in which the geometrical relationships of the three structural elements are integrated, will be presented in Section 4.6.

4.4.1 The Cantarell Thrust

The occurrence of a major thrust fault in the Cantarell area was first revealed with direct evidence provided by well C-418D (Pemex well completion log, 1996; Figure 3.7). This well penetrated a repeated section of Upper Mesozoic to Lower Cenozoic strata (Figure 4.25 and 4.26). Later wells (C-99D, C-3001, C-1128, C-1035, C-91, C-1022, C-3068) also penetrated repeated sections of Upper Mesozoic to Lower Cenozoic stratigraphy, which further indicated the existence of a major thrust structure (e.g. refer to Figures 3.7, 3.8, 3.12, 3.27). This main thrust fault is herein defined formally as the Cantarell Thrust.

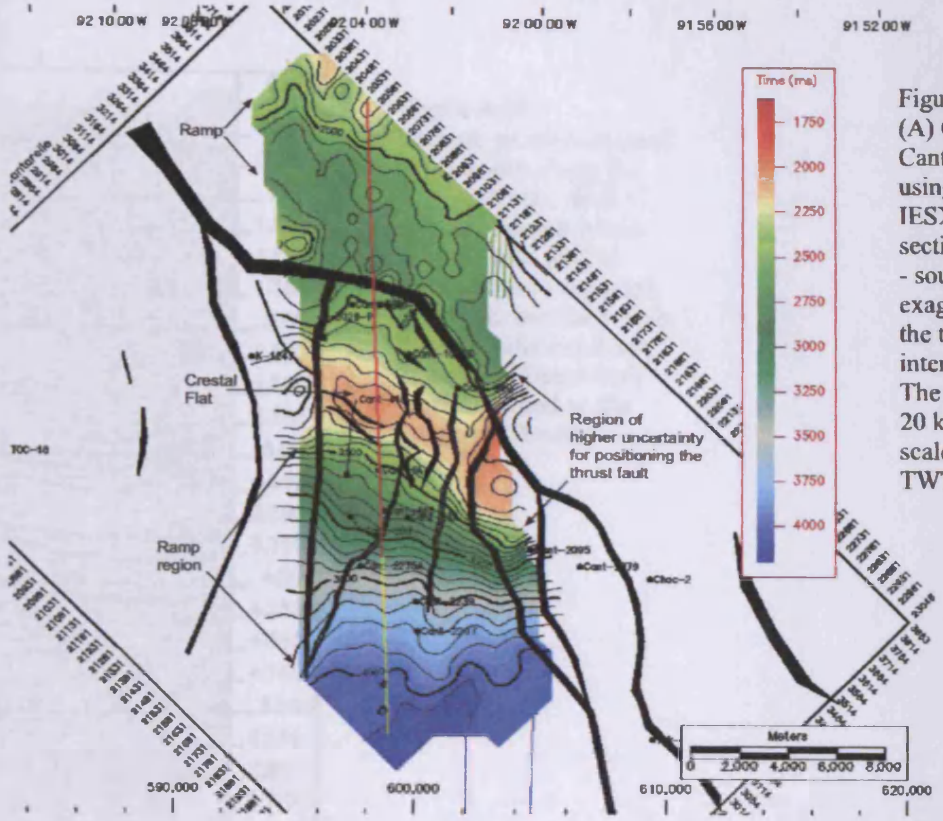

Figure 4.24
(A) Gridded map of the Cantarell Thrust plane using a convergent IESX algorithm; (B) section is oriented north - south and vertically exaggerated 3 x with the thrust plane interpretation posted. The section measures 20 km, the vertical scale is given in msec TWT.

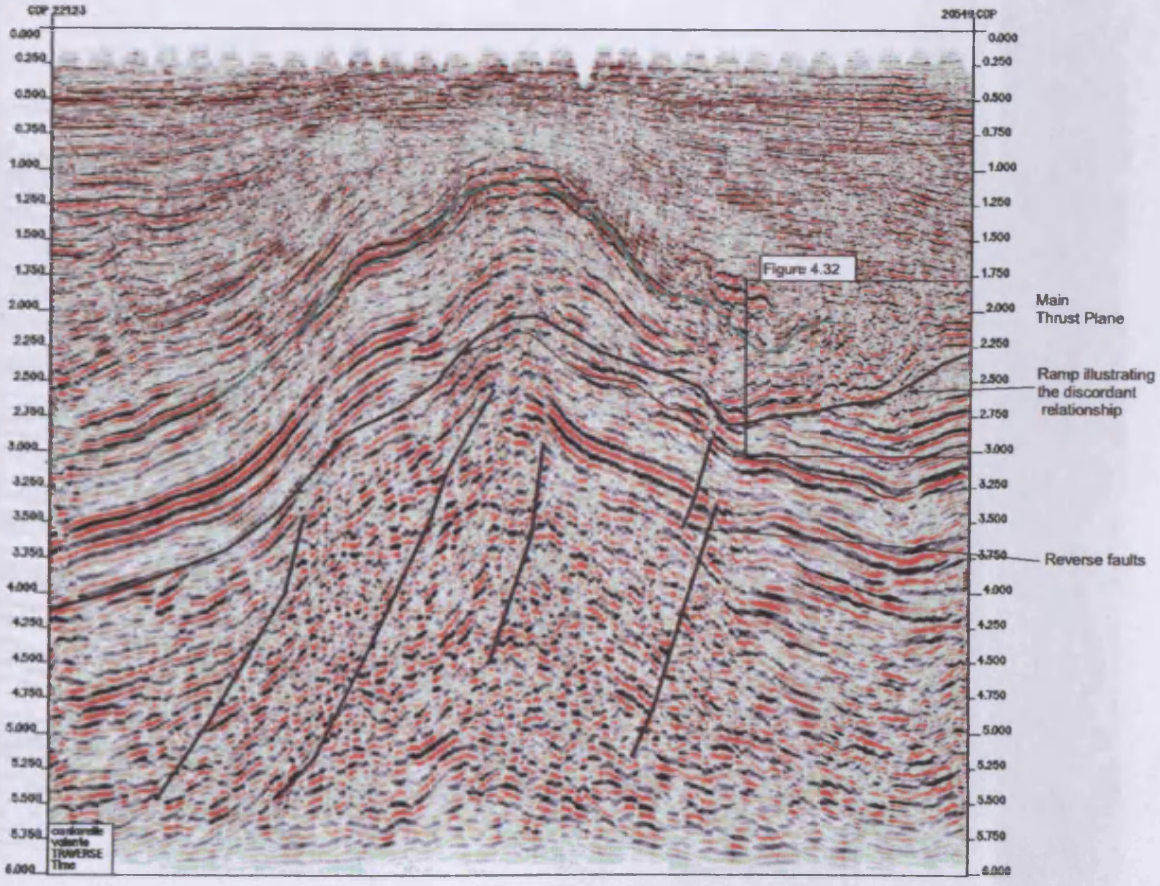

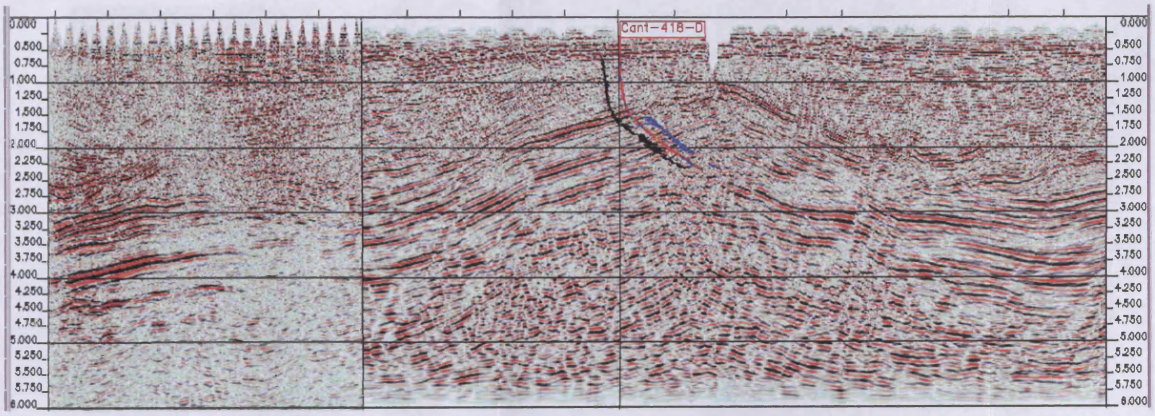

Figure 4.25
Seismic profile oriented north-south along the Thrust Block. Well C-418D is posted which was the first well to penetrate into repeated Mesozoic section which indicated the existence of a major thrust fault herein defined as the Cantarell Thrust.

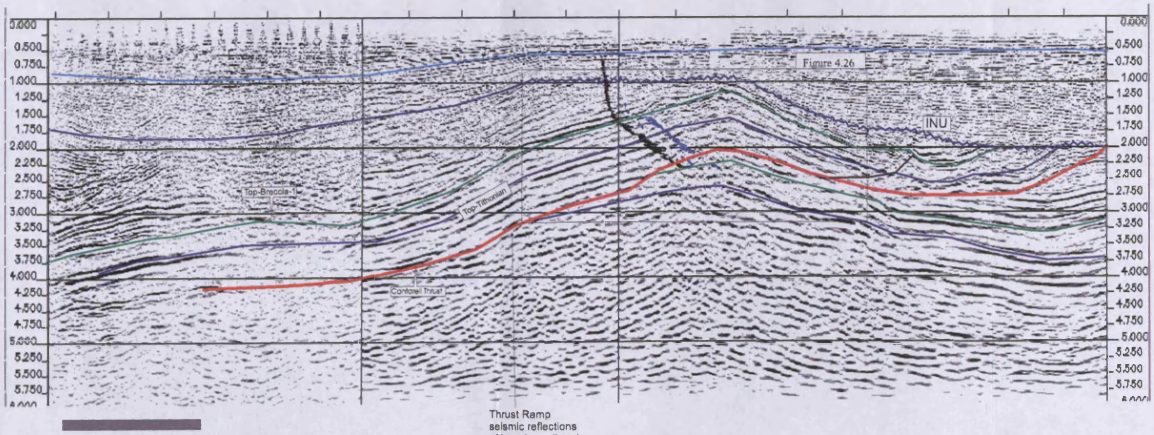

5 km

Thrust Ramp
seismic reflections
of hangingwall and
footwall show a discordant
relationship

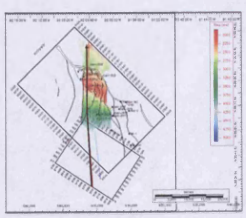

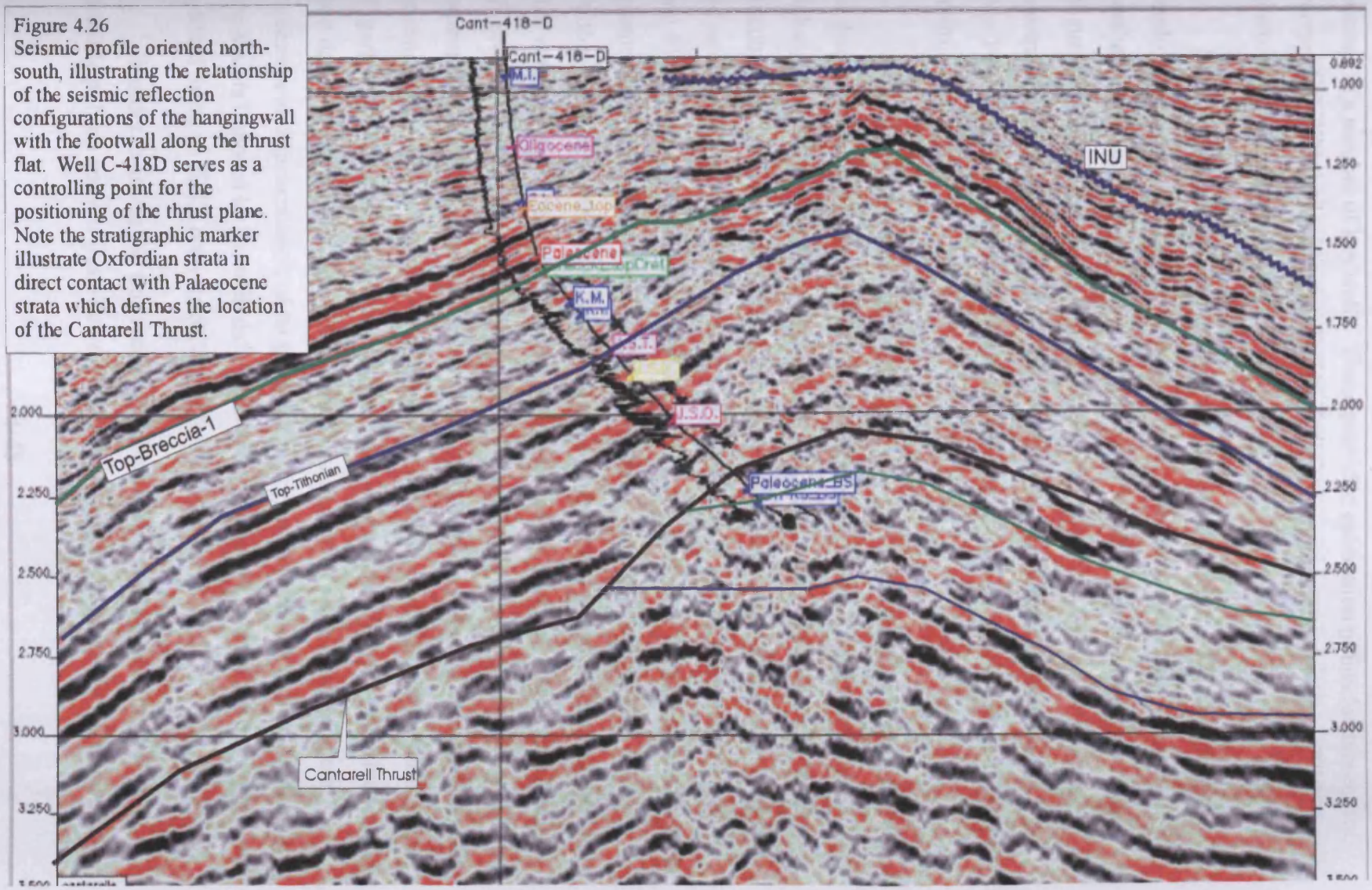

Figure 4.26
Seismic profile oriented north-south, illustrating the relationship of the seismic reflection configurations of the hangingwall with the footwall along the thrust flat. Well C-418D serves as a controlling point for the positioning of the thrust plane. Note the stratigraphic marker illustrate Oxfordian strata in direct contact with Palaeocene strata which defines the location of the Cantarell Thrust.

4.4.1.1 Constraining the geometry of the Cantarell Thrust

The Cantarell Thrust was defined initially based on the identification of repeated sections in a number of key wells. These provided calibration points for subsequent interpretation of the thrust using seismic reflection geometry as the primary interpretational constraints.

Seismic sections oriented northeast – southwest along the Thrust Block were employed to interpret the thrust fault geometry. Seismic profiles that intersect the well boreholes mentioned above provide good control on the location of the thrust plane (Figure 4.25 and 4.26). Away from the well boreholes, the Cantarell Thrust was constrained using the extent of the seismic stratigraphic horizons (Top-Breccia-1 and Top-Tithonian) interpreted within the footwall and hangingwall, as well as the overall seismic character.

Away from the well control points, the position of the thrust was identified based on discordant relationships between the hangingwall and the footwall structural reflections. These discordant relationships here used to define a surface of stratal discontinuity within an envelope of interpretational uncertainty approximately of 100 ms as in vertical extent. The geometry of this surface was clearly incompatible with any possible stratigraphic interpretation (e. g. unconformable). This approach led to the interpretation of a major south-west dipping thrust ramp structure (Figure 4.27). Further to the north-east of this ramp, the thrust appears to flatten off into a major thrust flat, where stratal reflections in the hangingwall and footwall are almost concordant (Figure 4.28). Accurate positioning of the thrust along the thrust flat region is extremely difficult to constrain from the seismic geometry alone. This limitation of the seismic data results in an interval of uncertainty for the positioning of the thrust plane (Figure 4.28). Therefore the interpretation in this area is relied more extensively on the well data when available. The interpretation of the thrust plane presented here represents an approximation of its gross geometry, with localised vertical positioning constraints imposed by the well data. The seismic interpretation of the thrust plane was gridded using an IESX convergent algorithm (Figure 4.24).

In order to assess the true morphology of the thrust fault, and eliminate any possible pull-up and / or push-down effects, a seismic profile considered as the most

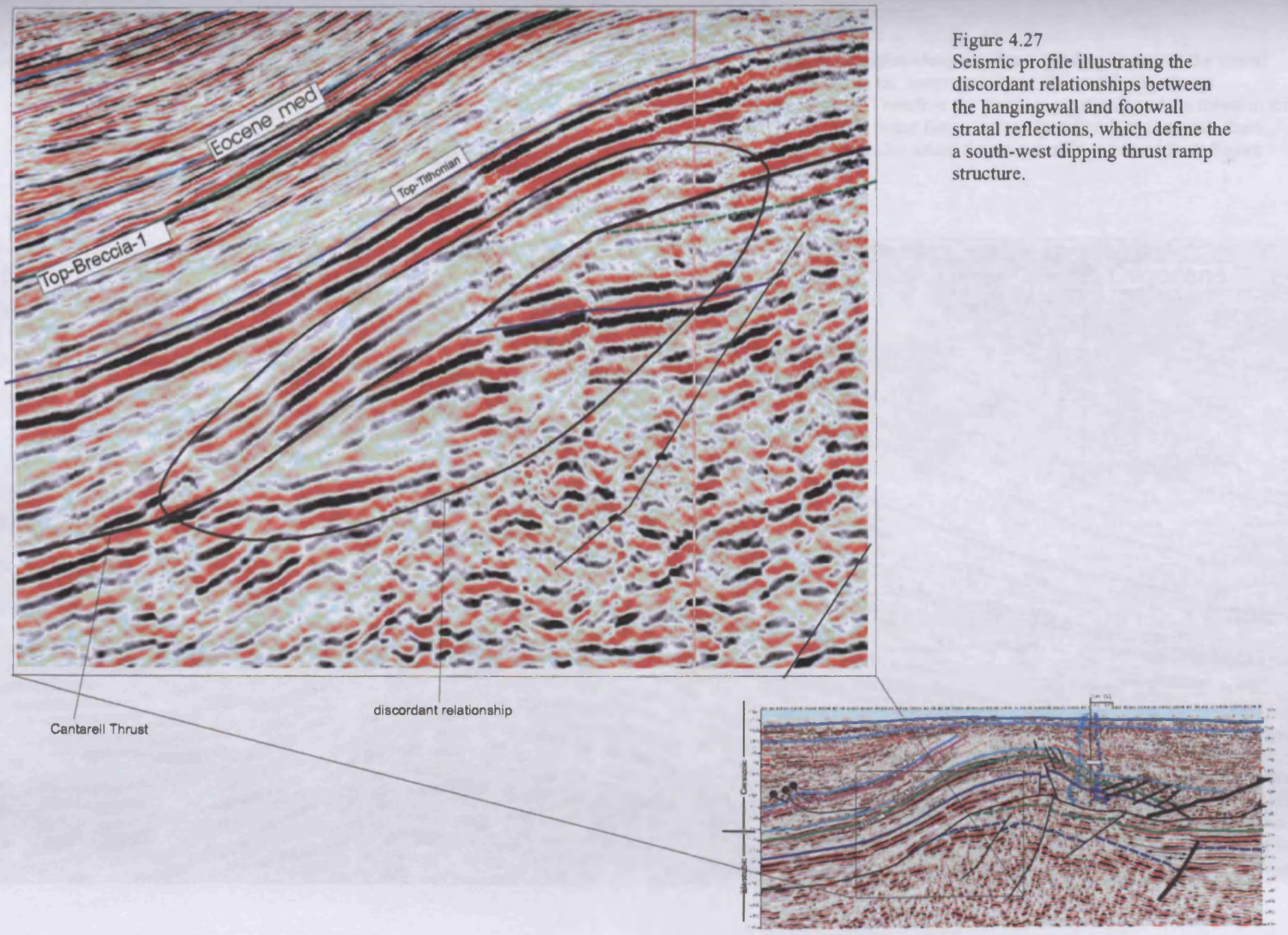

Figure 4.27
Seismic profile illustrating the discordant relationships between the hangingwall and footwall stratal reflections, which define the a south-west dipping thrust ramp structure.

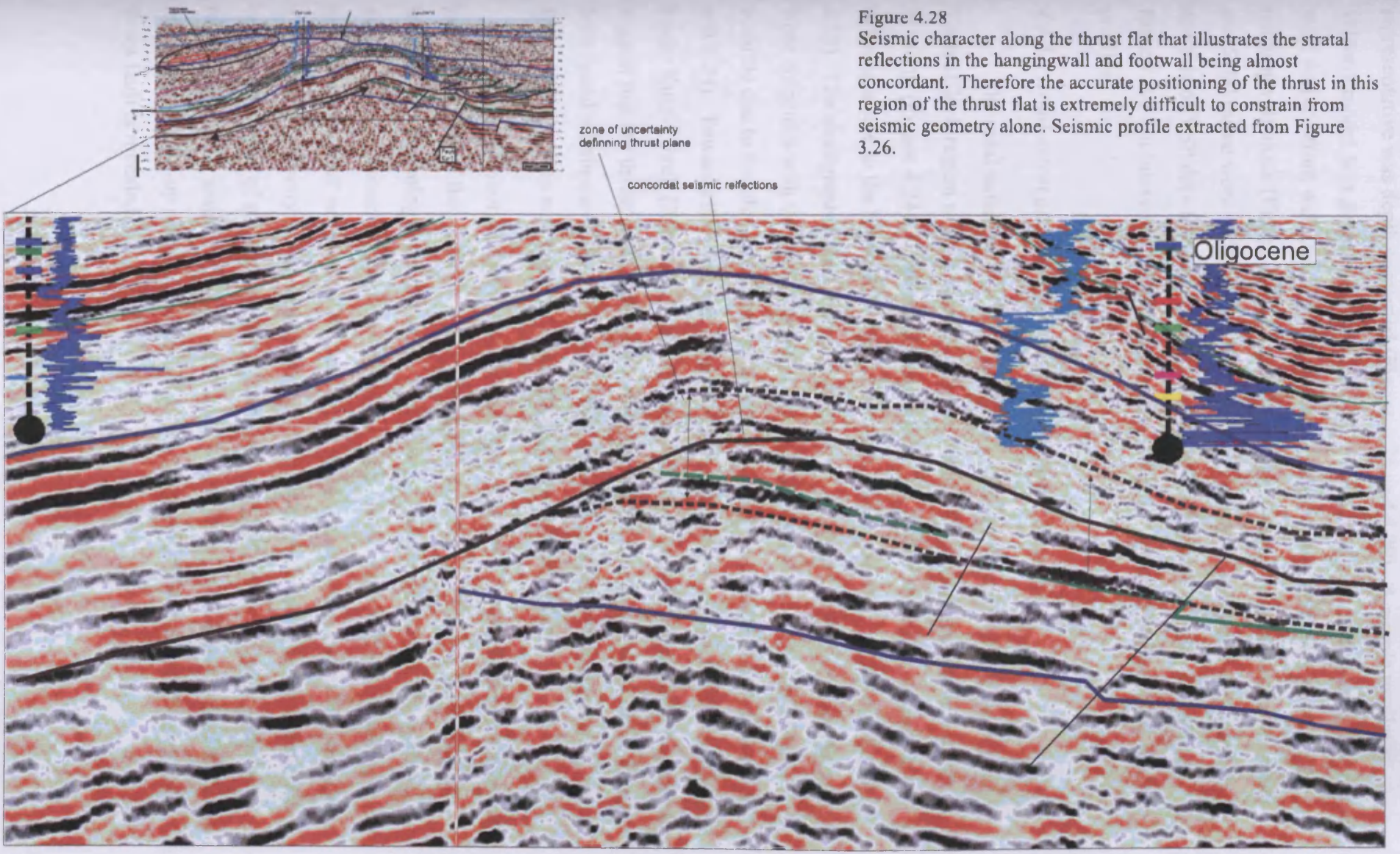

Figure 4.28
Seismic character along the thrust flat that illustrates the stratal reflections in the hangingwall and footwall being almost concordant. Therefore the accurate positioning of the thrust in this region of the thrust flat is extremely difficult to constrain from seismic geometry alone. Seismic profile extracted from Figure 3.26.

representative was depth converted (Figure 3.23 and 4.29). A simple two-layer velocity model was generated (Figure 4.30). The interval velocities used in this model were derived from well check-shots of wells C-418D and C-99D that penetrate the hangingwall block (Figure 4.31). Uniform average seismic velocities of 2500 m/sec and 5100 m/sec were assigned for the upper and lower units respectively based on analysis of VSP data from crestal wells. Twenty two control points were defined spaced at 3 km intervals to depth convert the thrust plane and Top-Breccia-1 seismic profiles.

4.4.1.2 Areal extent and morphology of the Cantarell Thrust

The areal extent of the thrust fault has been interpreted to cover the entire Thrust Block region as well as an area to the north of it located within the Eastern Platform (Figure 4.24). Towards the east of the TB, within the EFC, a thrust fault defining a sole to the Nohoch Nose was interpreted (see Section 4.3.2.3 and Figure 4.23). The stratigraphic and structural position of the thrust fault within the Nohoch Nose coincides with the main Cantarell Thrust, although direct correlation is not possible due to the elongated zone of discontinuous seismic reflections (Figure 4.16 and 4.24). Towards the west, the Cantarell Thrust is abruptly truncated and terminated by the Kutz-1 Fault (Figure 3.25 and 4.16) and there is no well penetration evidence to suggest that the thrust fault is present within the WFC. The dimensions of the thrust fault found within the Nohoch Nose together with the Cantarell Thrust cover an area of 15 km from west to east and more than 30 km from north to south.

The gross morphology of the thrust fault as observed from the depth converted profile consists of flat - ramp – flat geometry (Figure 4.23). Conversely, a 'folded' thrust fault morphology is observed in time seismic profiles (Figure 3.27) and the gridded TWT seismic interpretation (Figure 4.22). However on close inspection, it is noted that the 'fold' occurs just beneath the major hangingwall anticline that consists of a unit of high velocity rocks, which decreases in gross thickness away from the crest region. This type of structural setting (localised high velocity over lower velocity rocks) is typically associated with significant velocity pull-up effects (Koyi, 1992). By removing the pull-up effect in the depth-converted section the true morphology of the thrust fault is revealed.

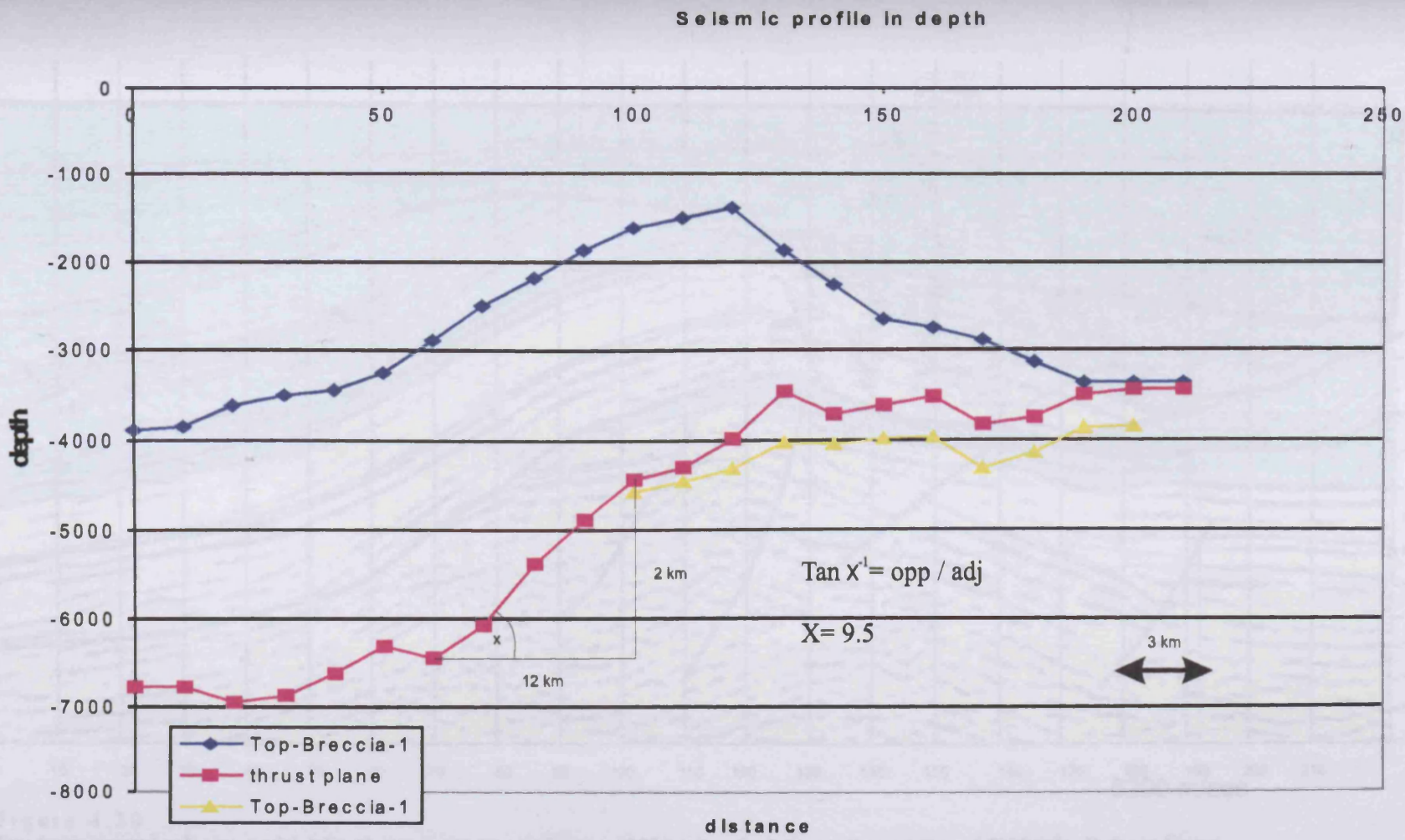

Figure 4.29
Depth converted seismic section shown in Figure 4.30.
Note that in this depth converted section the footwall does not exhibits a folded strucutre as is the case for the same time section.

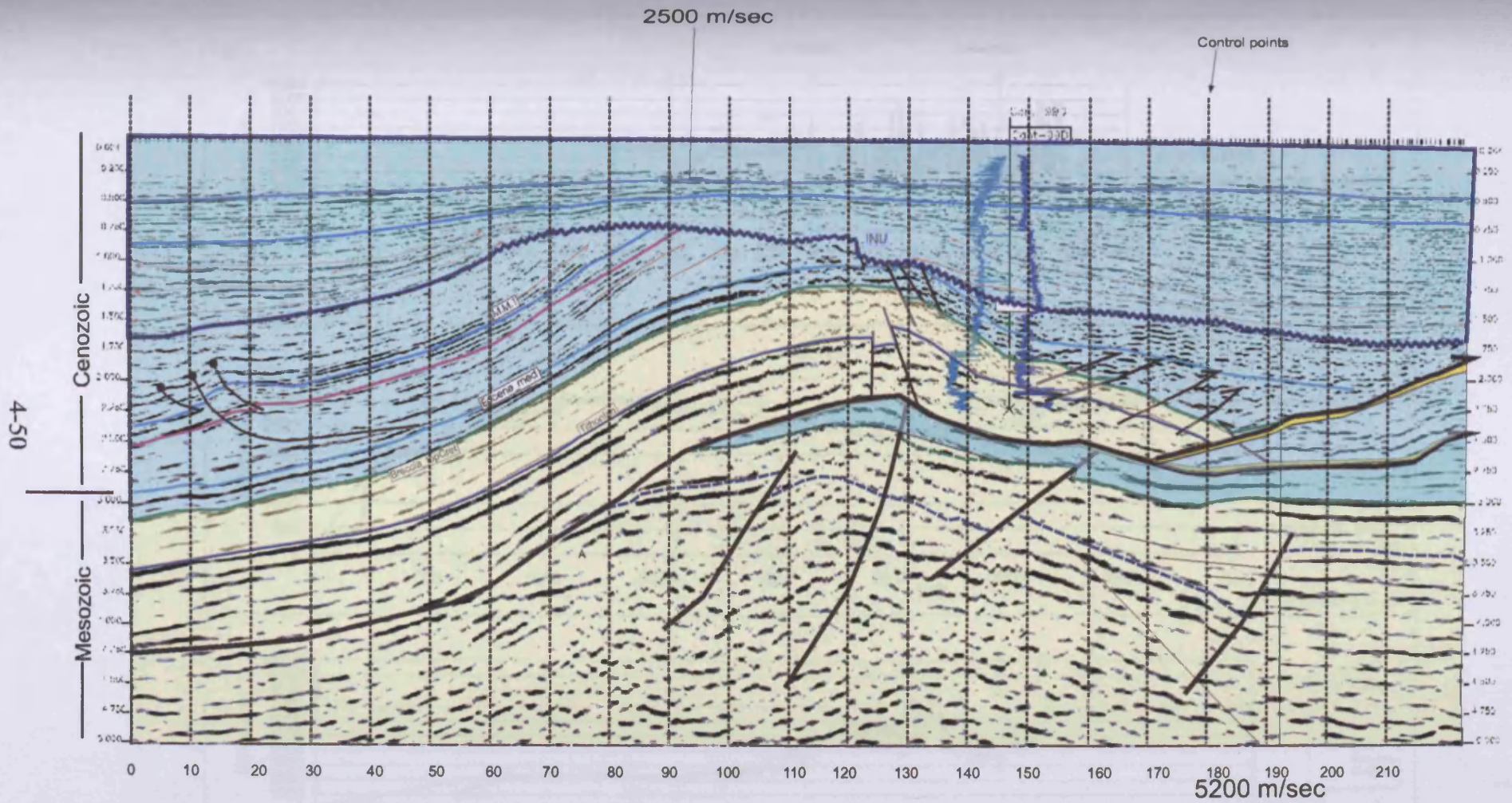

Figure 4.30
Two layer interval velocity model defined, an upper unit consisting of 2500 m/s and a lower unit consisting of 5200 m/s. Refer to Figure 4.31 for well velocity data from which the above velocities were derived.
Twenty one control points evenly spaced at 1 km were used to calculate the depth profile.

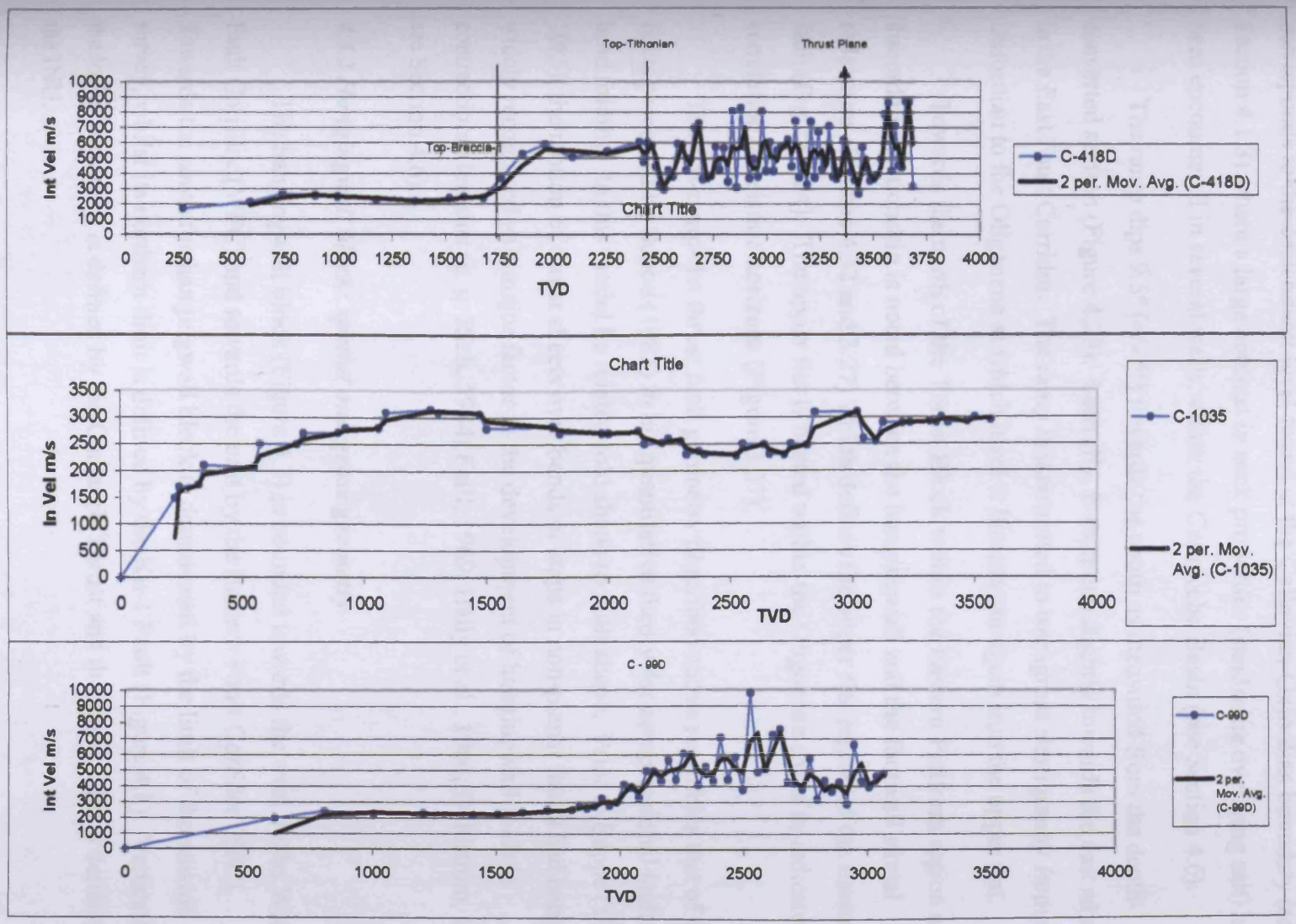

Figure 4.3l Velocity profiles of wells C-418D, C-99D and C-1035D

The lower flat is interpreted where the overall geometry of the seismic reflections become planar towards the south. Stratigraphically, it is speculated that the lower flat corresponds to the detachment level found at the Callovian-Oxfordian boundary (see Section 4.1.3) where a large contrast in rock properties (sandstone overlying salt) has been encountered in several wells within the Campeche Basin (see Section 4.6).

The ramp dips 9.5° (+/- 5°) towards the south as measured from the depth-converted section (Figure 4.29). Laterally, it steepens slightly towards the east adjacent to the East Fault Corridor. The ramp is interpreted to transgress stratigraphy from the Oxfordian to the Oligocene at which level it flattens out again into the upper flat.

Towards the north of the Thrust Block within the Eastern Platform region a discordant relationship is noted between the hangingwall and the footwall stratal reflections (Figures 4.32 and 3.27) which defines the upper flat region of the thrust fault (Figure 4.24). The upper flat is hosted within the Oligocene strata as indicated by correlation of seismic horizons (Figure 3.27).

The flat-ramp-flat thrust fault geometry described above resembles that of thrust faults presented by Suppe (1983) in his quantitative theory for compressional fault-bend folding. In this model he related fold shape to fault shape. Prior to Suppe (1983, 1985), the motion of thrust sheets over bends or steps in non-planar faults had been widely recognised as a major factor in the development of hangingwall folds in contractional terrains (e. g. Rich, 1934; Faill, 1969; Bally et al., 1966; Dahlstrom, 1970; see Section 4.6).

4.4.2 Hangingwall block: spatial and gross geometry

The hangingwall block (Figure 4.1) is bounded towards the west by the Western Fault Corridor (WFC) and towards the east by the Eastern Fault Corridor (EFC). Towards the south the hangingwall block is demarcated by the limit of the seismic survey, whilst its northern limit is defined by the Ku-1 Fault (Figure 4.1). Vertically, the lower boundary is defined by the Cantarell Thrust and the upper limit is defined by the INU.

The overall geometry of the hangingwall block as seen at the Top-Breccia-1 and Top-Tithonian levels consists of a gentle open anticlinal fold with an approximate

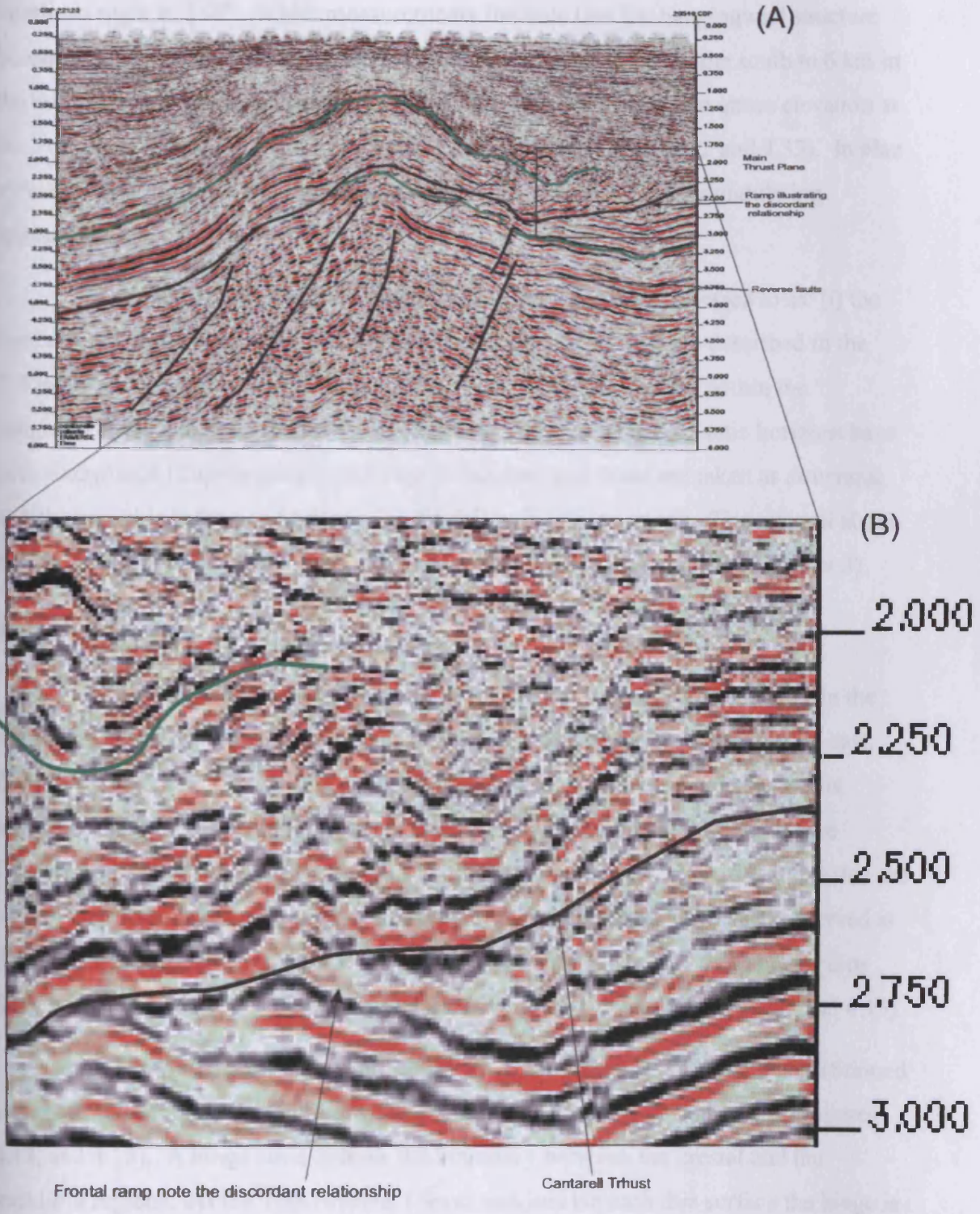

Figure 4.32
Seismic profile showing the frontal ramp region. Note the discordant relationships between the hangingwall and footwall stratal reflections. Note that the thrust plane is hosted within Cenozoic successions, see the green horizon in (A) corresponds to the Top-Breccia-1 horizon (Base Tertiary). For location of seismic profile refer to Figure 4.24.

interlimb angle of 150°. Width measurements indicate that the hangingwall structure becomes narrower towards the north, varying from about 11 km in the south to 6 km in the north (Figures 4.11, 4.12 and 4.13). The crest line or line of maximum elevation at the Top-Breccia-1 level, strikes northwest to southeast (Figures 4.12 and 4.33). In plan view the crest line does not appear as a straight line but has a gently undulating appearance.

The hangingwall block has been divided into three areas referred to as: (i) the forelimb, (ii) the crestal region, and (iii) the backlimb and these are described in the following sections (Figure 4.12 and 4.33). The stratigraphy hosted within the hangingwall ranges from Oxfordian to Miocene. Internally two seismic horizons have been interpreted (Top-Breccia-1 and Top-Tithonian) and these are taken as structural and stratigraphic reference horizons for the following descriptions. The interval above the Top-Breccia-1 has been previously defined as Unit T-1 interval (see Chapter 3).

4.4.2.1 Hangingwall Backlimb

The backlimb dips towards the south and generally becomes shallower in the southern direction. At the Top-Breccia-1 the dip becomes steeper from west to east, from an average of 9° to 20° (Figure 4.13). The seismic reflection configurations observed along the backlimb within the defined seismic units J1, K1 and T1 (see Chapter 3, Section 3.5), consist of highly continuous and concordant reflections that are slightly offset by faults. However, variations in dip magnitudes have been observed at the Top-Tithonian level, particularly in at the westernmost region where higher dips than those observed at the Top-Breccia-1 level were calculated (Figures 4.13 and 4.15).

At both the Top-Breccia-1 and Top-Tithonian levels, the backlimb is partitioned into three sub-rectangular fault bounded segments that exhibit different dips (Figures 4.13, and 4.15). A hinge zone defines the boundary between the crestal and the backlimb regions. At the Top-Breccia-1 level and just beneath this surface the hinge is more pronounced than overlying and underlying stratigraphic units, and exhibits relatively higher dips (Figure 4.34).

Hosted within Unit T1, in the southern part of the central segment, an asymmetric fold with a thrust structure has been interpreted and named the JAC

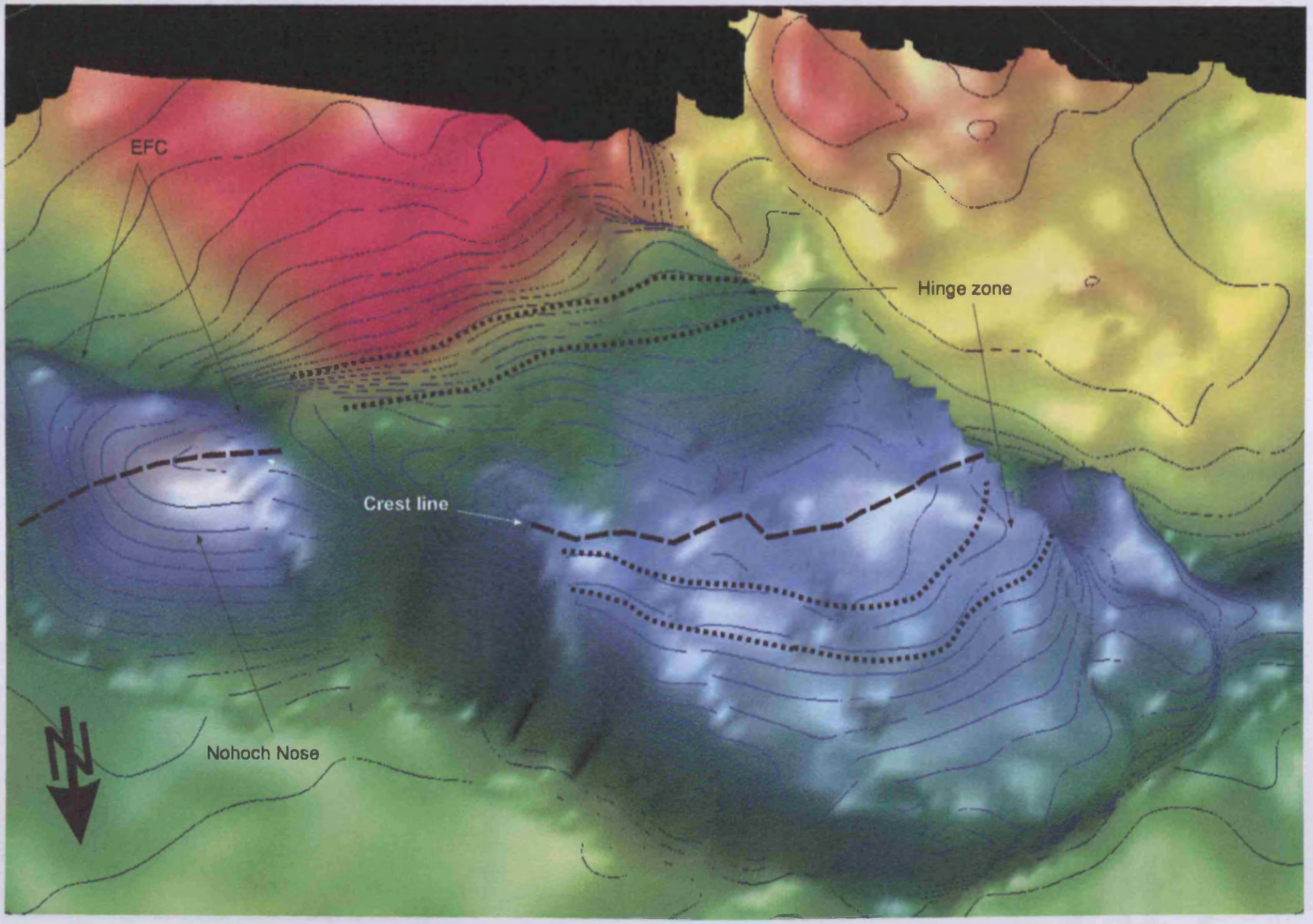

Figure 4.33 Isometric Geoviz image of the structural map Top-Breccia-1, zoomed on the crestal area to the thrust block. The crestal line, and hinge zones are labelled. Note the crestal line being displaced from the thrust block to the Nohoch Nose, separated by the Eastern Fault Corridor (EFC).

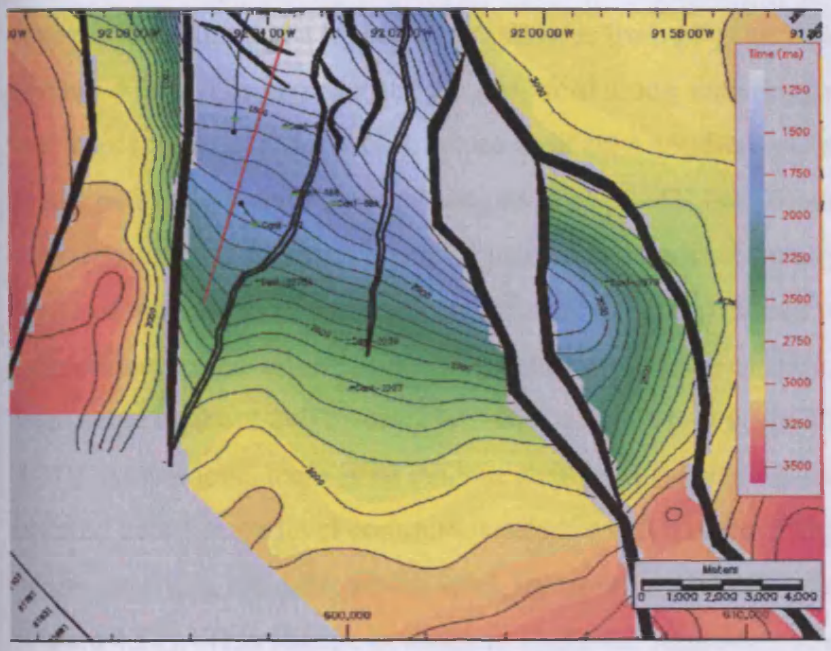

Figure 4.34
(A) Structural map for the Top-Breccia-1 showing the backlimb of the thrust structure. (B) seismic section along the westernmost segment of the backlimb. Note the hinge zone and the erosional truncation defined by the INU (Intra Neogene Unconformity).

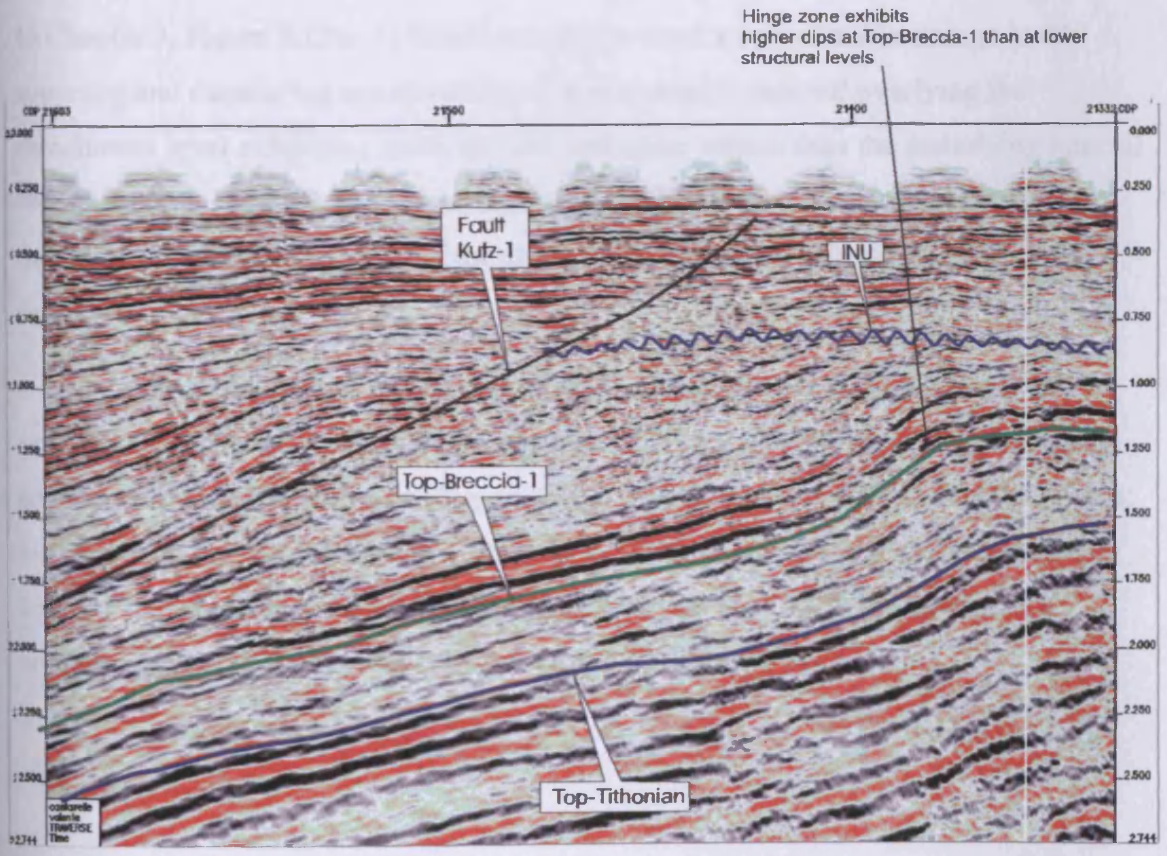

structure. This structure is bounded at its basal contact by an interpreted minor thrust plane (Figure 3.27, 4.35 and 4.36). Towards the west and east, the JAC fold dies out near the WFC and EFC. The JAC fold has a shorter and steeper limb (8°) that dips towards the south and a longer and shallower limb (4°) that dips towards the north (Figure 4.36). The geometry of the JAC fold along with the geometry of the master and minor thrusts of the JAC structure indicate a southern propagation direction. This is antithetic to the main thrust propagation of the TB (see Section 4.4.4). The lithology in which the JAC structure is hosted primarily consists of bathyal shale with minor layers of wackstone to packstone as inferred from correlation to the nearby well C-2095 (see to Chapter 3 section 3.4.4). The detachment level of the JAC structure is interpreted at about 200 msecs TWT above the Top-Breccia-1 seismic horizon (Figure 4.37). At this level there is an evident change in seismic character. Beneath the inferred detachment level continuous seismic reflections of high amplitude are present, whilst overlying the detachment level, transparent seismic reflections are observed (Figure 4.37). This change in acoustic character suggests a marked change in rock properties (lithology and density). Based on well correlations C-2095, C-2207 and C-2095, this detachment level corresponds to the mid Eocene stratigraphic marker (refer to Chapter 3, Figure 3.12). At this stratigraphic level a considerable change in the sonic log and density log are observed, with the seismic interval overlying the detachment level exhibiting lower density and sonic values than the underlying interval (see Chapter 3; Figure 3.12). The detachment level can also be interpreted as a rheologic boundary, above which the strata deform in a more ductile manner than below it.

In the north-eastern region and towards the upper part of the backlimb an asymmetric northwest-southeast striking tight and very localised fold was identified and named the CECY structure (Figure 4.38). The crestal line measures about 1.5 km, the shorter and shallower limb (12°) dips towards the north and the longer and steeper limb (18°) dips towards the south. The asymmetry of the CECY fold indicates a northern propagation direction similar to the TB (Figure 4.38).

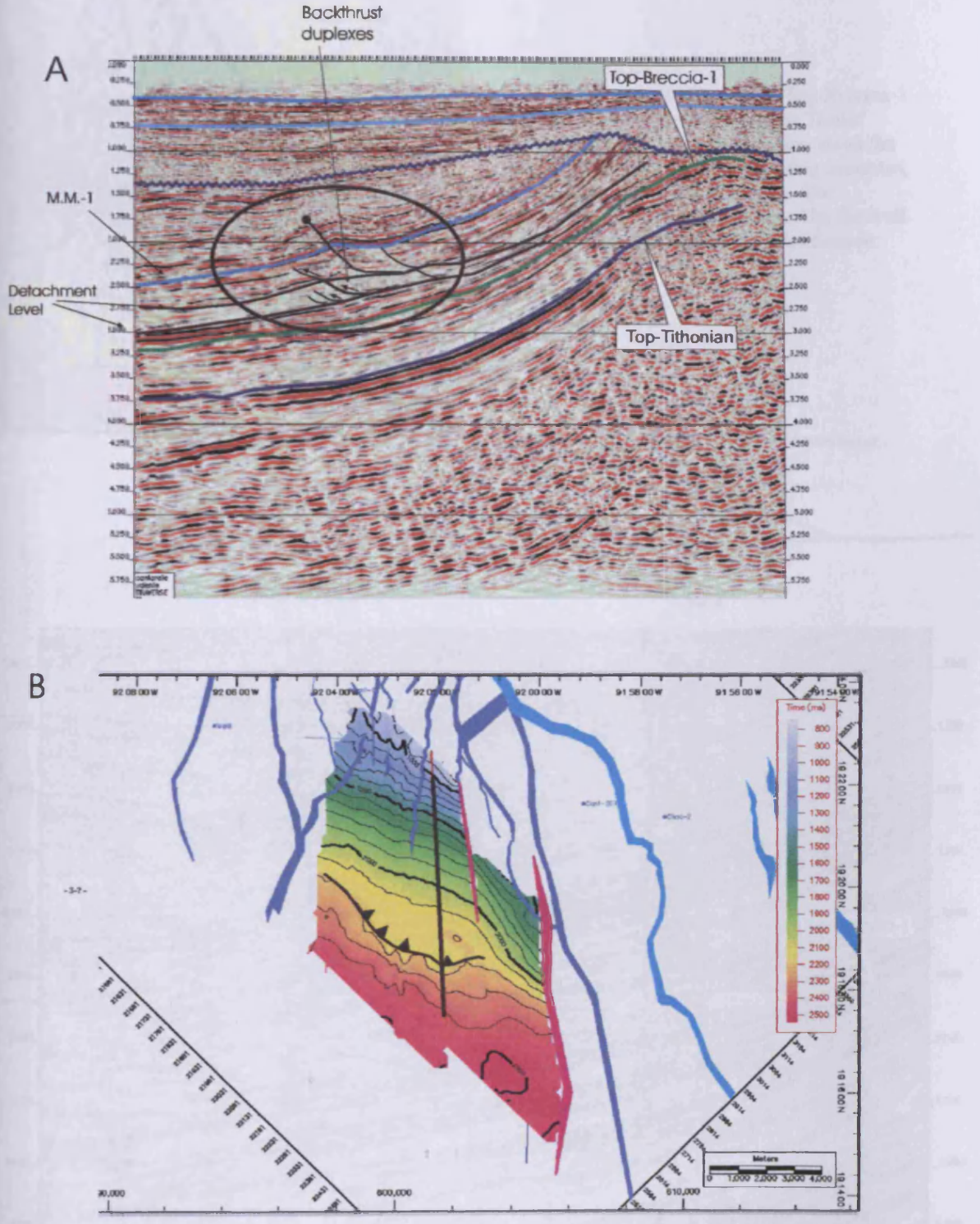

Figure 4.35
(A) Seismic section oriented north-south displaying the backlimb character and associated structure. Note the JAC folded structure near the base of the backlimb (encircled). (B) structural map of M.M.-1 seismic horizon, an intra T-1 horizon.

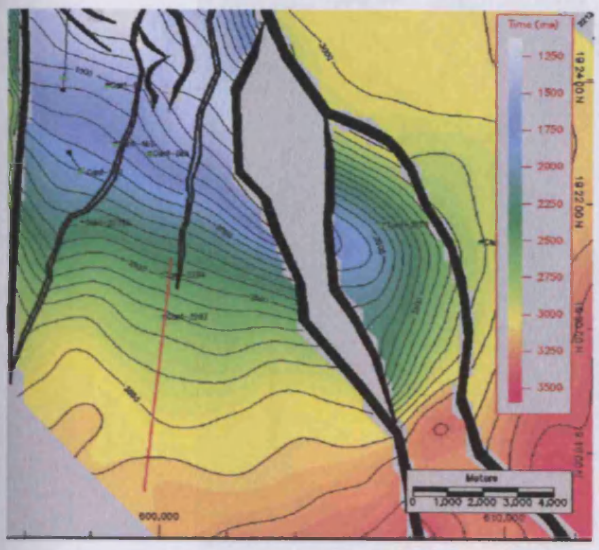

Figure 4.36
(A) Structural map for the Top-Breccia-1 showing the backlimb of the Thrust structure. (B) seismic section along the base of the. Note the thrusting occurring at the base of the backlimb. The detachment level is indicated by the well stratigraphic markers as intra Eocene.

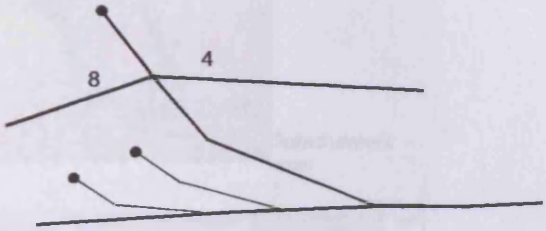

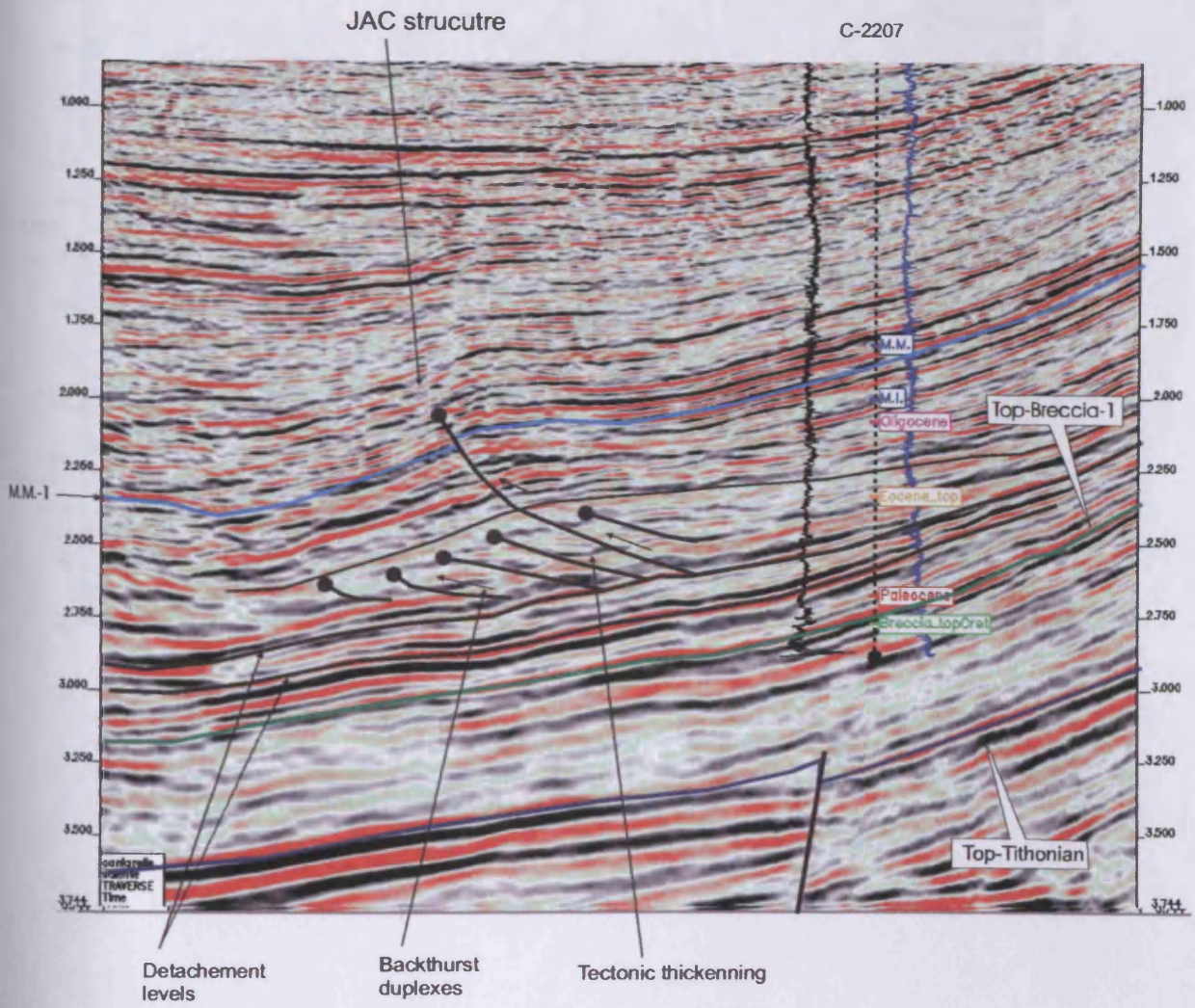

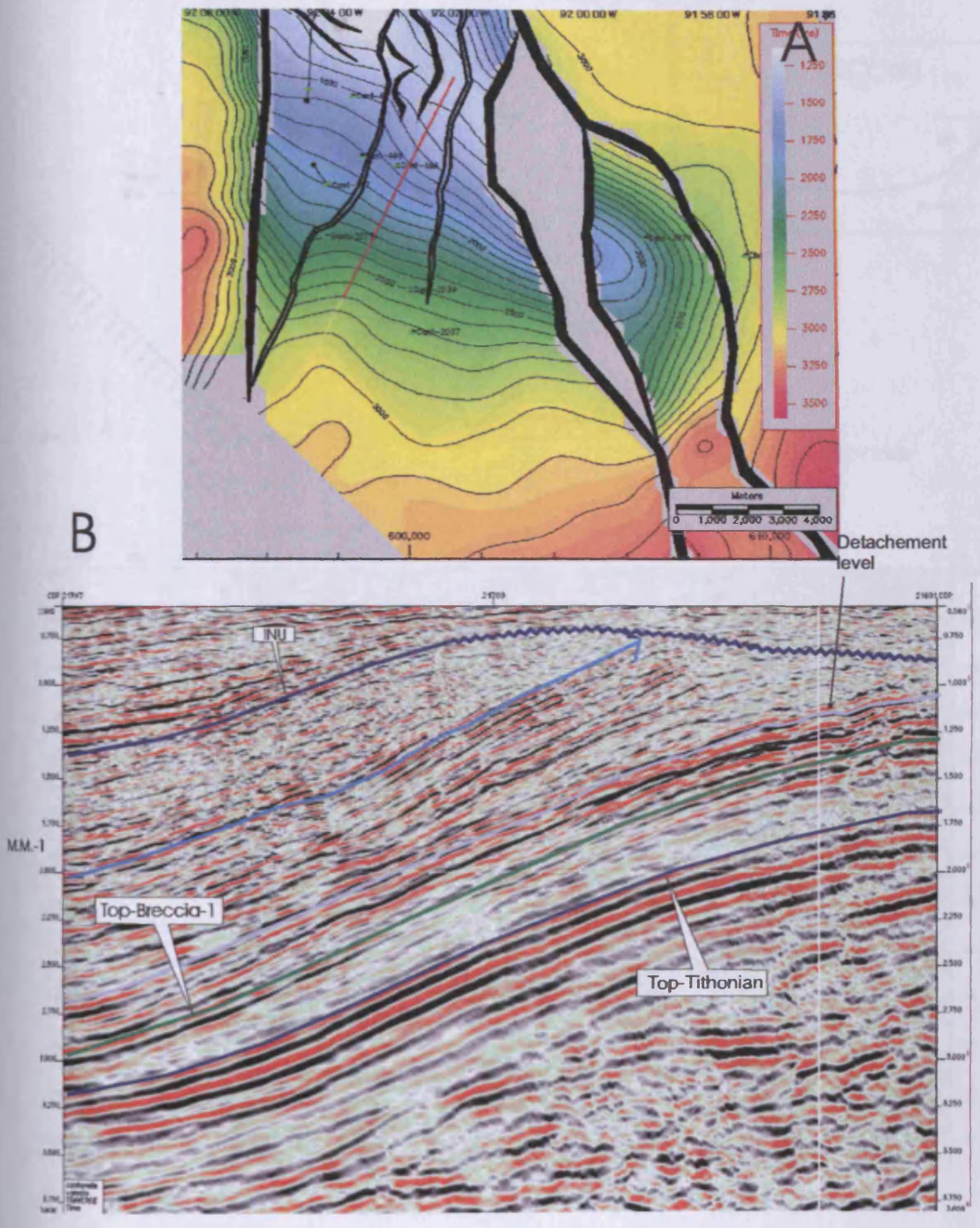

Figure 4.37
(A) Structural map for the Top-Breccia-1 showing the backlimb of the Thrust structure. (B) seismic section along the central segment showing the profile of the backlimb. Refer to (A) for location of seismic line. Seismic horizons Top-Breccia-1 in green, M.M.-1 in blue, and the detachment level in black are posted.

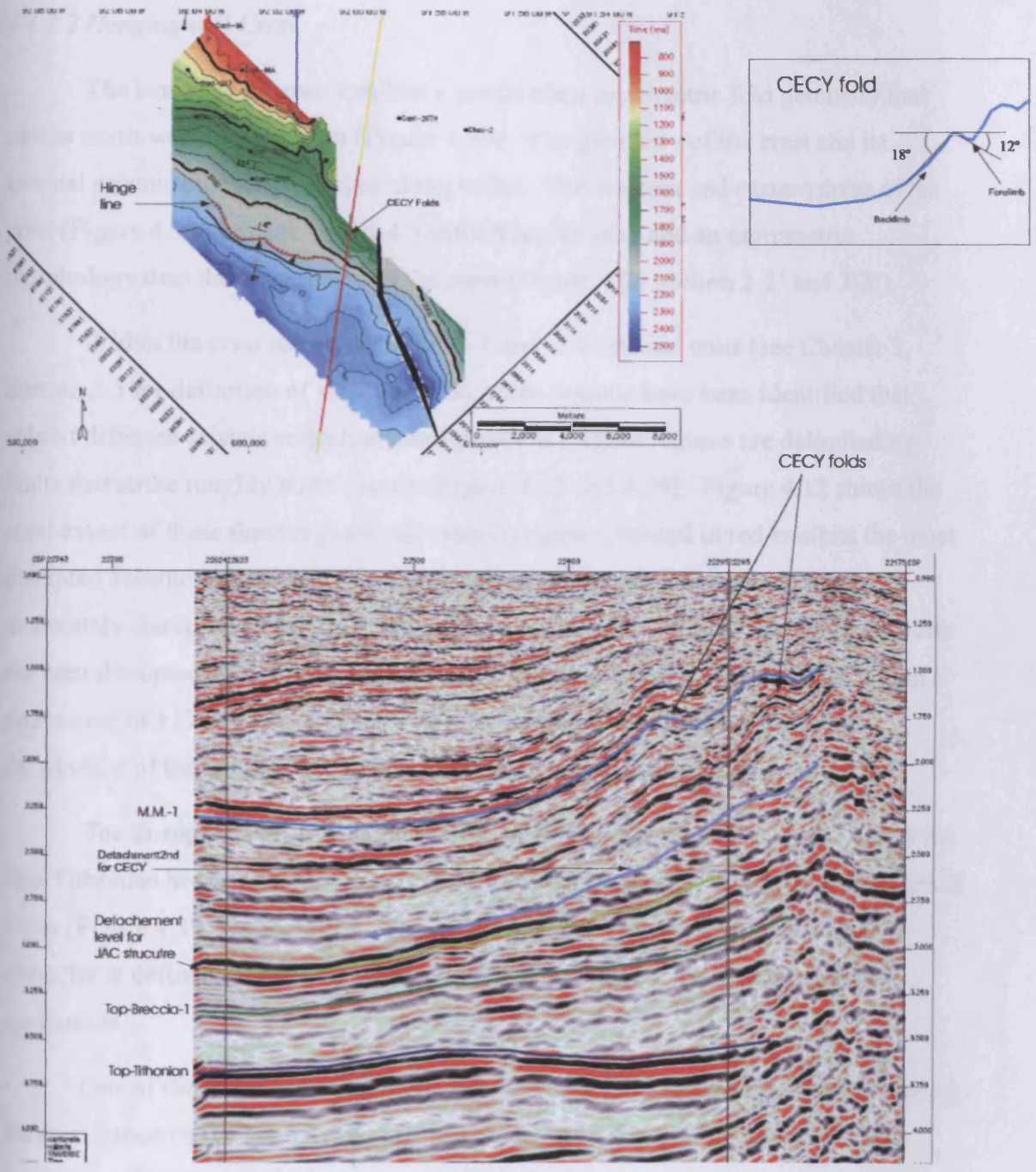

Figure 4.38
(A) Structural map for the M.M.1 seismic horizon in msec twt. (B) seismic profile showing tight parasitic folds near the crest of the backlimb, named the CECY fold.

4.4.2.2 Hangingwall Crest

The hangingwall crest exhibits a gentle open asymmetric fold geometry that strikes north-west to south-east (Figure 4.39). The geometry of the crest and its internal seismic character changes along strike. The western and eastern areas of the crest (Figure 4.39 lines 1-1' and 4-4') exhibit higher dips and an asymmetric morphology than the central area of the crest (Figure 4.39 section 2-2' and 3-3').

Within the crest restricted to the K-1 and T-1 seismic units (see Chapter 3, Section 3.5 for definition of seismic units), three regions have been identified that exhibit different seismic reflection configurations. These regions are delimited by faults that strike roughly north –south (Figure 4.12 and 4.39). Figure 4.12 shows the areal extent of these three regions: the central region coloured in red exhibits the most disrupted seismic reflections; the eastern region, coloured in orange, exhibits moderately disrupted reflections; and the western region, coloured in orange, exhibits the least disrupted reflections although still fragmented. Seismic time slices within a time frame of 1170 to 1280 msec TWT (Figure 4.40) help illustrate the areal distribution of the variable intensity of disrupted seismic reflections.

The disrupted seismic character decreases considerably with depth. Below the Top-Tithonian horizon, continuous reflections are displaced by continuous sub-vertical faults (Figure 4.39, section 5-5'). The upper boundary for the disrupted seismic character is defined by the INU, above this level the seismic reflections appear continuous.

One of the most important observations made from the seismic character along the crest concerns the lateral and vertical variations in stratal reflection continuity across the major fold in the hangingwall. This is important in relation to establishing a possible link between fold geometry and fracture intensity. The disrupted seismic character observed in the crestal region of the hangingwall is interpreted as a qualitative representation of the degree of faulting, fracturing and vugular porosity. This interpretation is supported by statistical data of core recovery percentages across the hangingwall structure (see Chapter 6 discussion of the reservoir geology), where an increase in poor core recovery is associated with the zone of increased seismic fragmentation seen in the crestal region of the hangingwall.

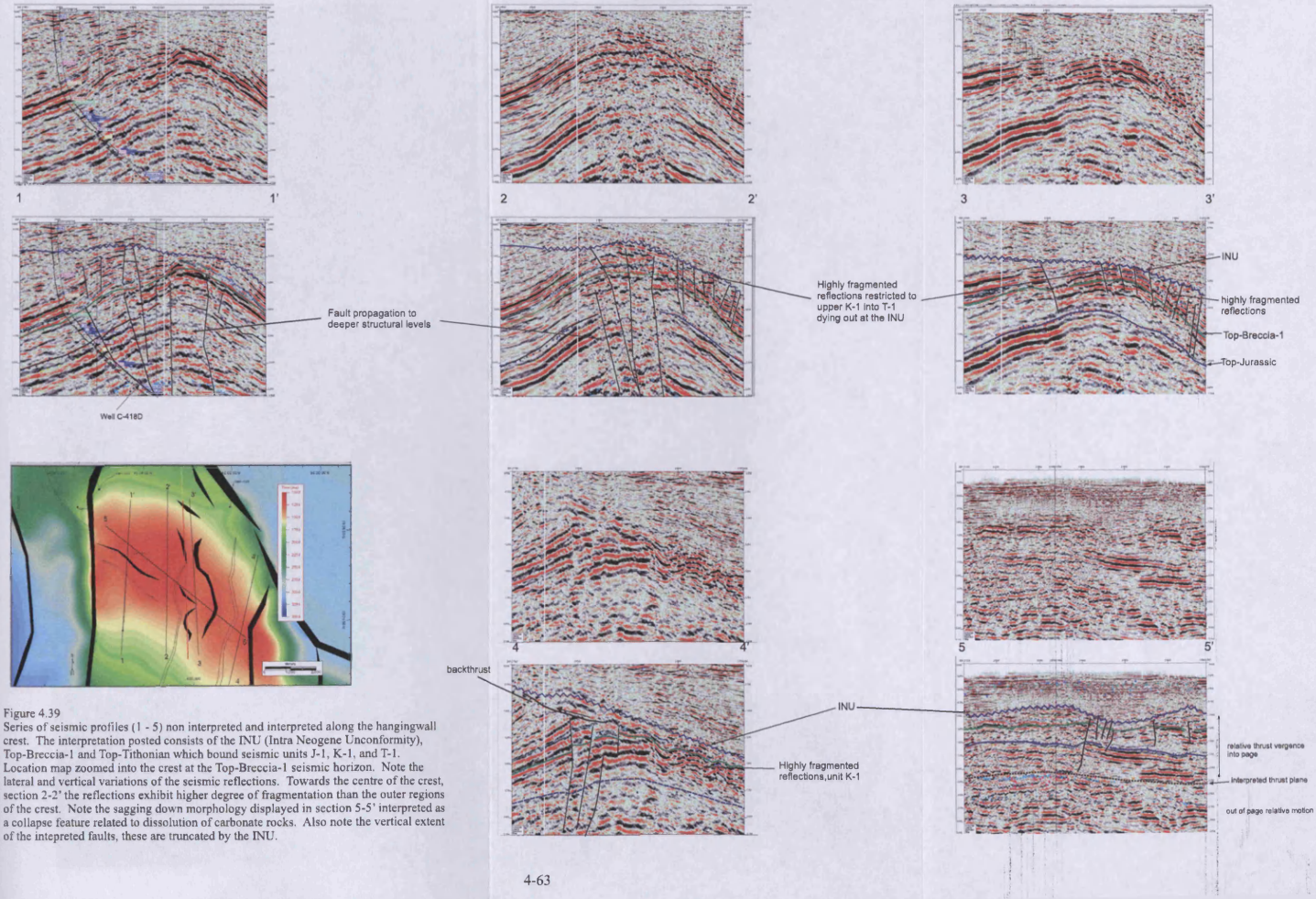

Figure 4.39
Series of seismic profiles (1 - 5) non interpreted and interpreted along the hangingwall crest. The interpretation posted consists of the INU (Intra Neogene Unconformity), Top-Breccia-1 and Top-Tithonian which bound seismic units J-1, K-1, and T-1. Location map zoomed into the crest at the Top-Breccia-1 seismic horizon. Note the lateral and vertical variations of the seismic reflections. Towards the centre of the crest, section 2-2' the reflections exhibit higher degree of fragmentation than the outer regions of the crest. Note the sagging down morphology displayed in section 5-5' interpreted as a collapse feature related to dissolution of carbonate rocks. Also note the vertical extent of the intepreted faults, these are truncated by the INU.

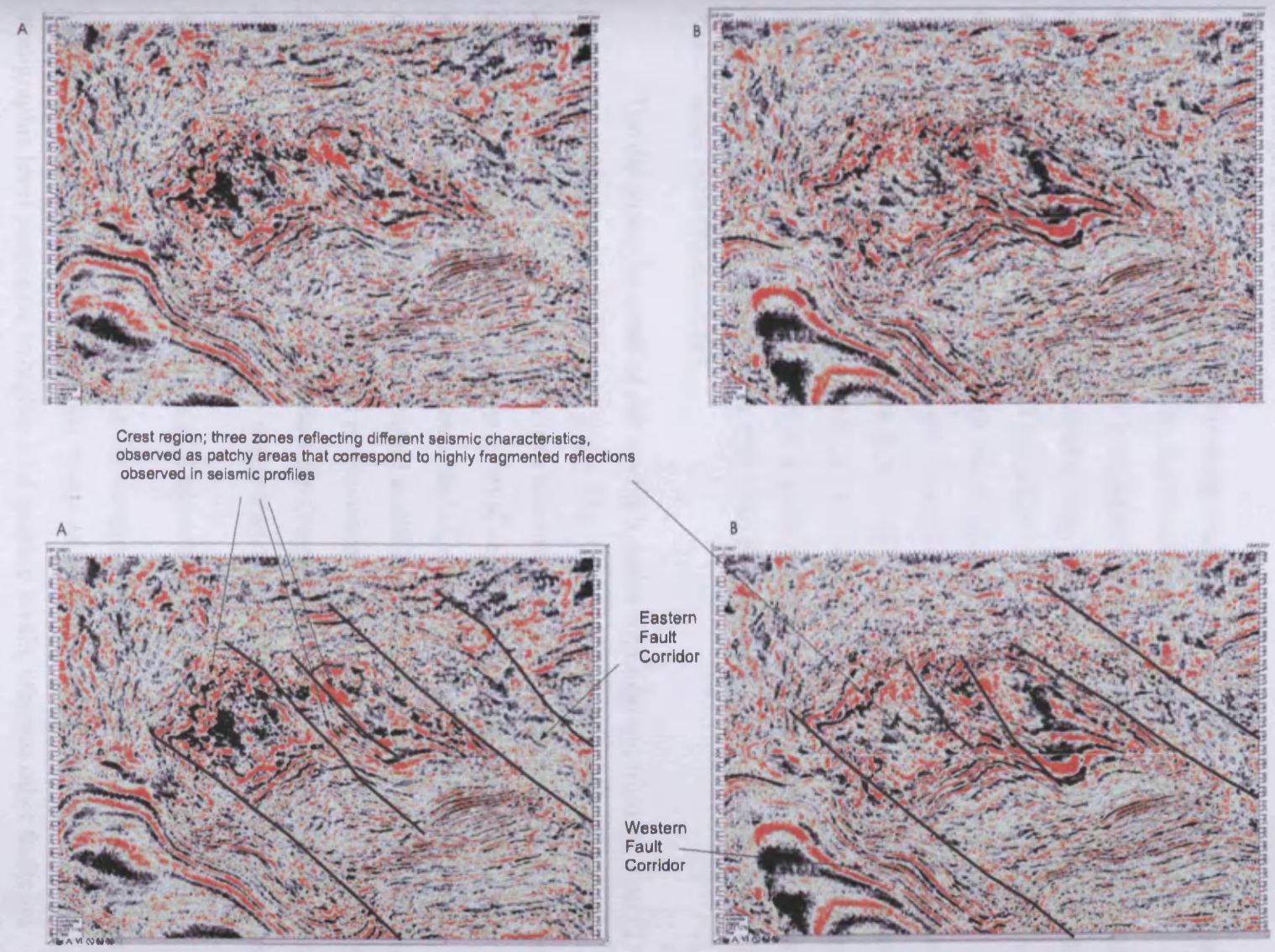

Figure 4.40
Time slices at (A) 1176, and (B) 1276 msecs twt illustrating the crest region of the hangingwall. Note the three regions defined that exhibit different seismic reflections configurations defined as discontinuous vs. continuous.

4.4.2.3 Hangingwall Forelimb

The overall morphology and internal seismic character of the forelimb changes rapidly laterally and vertically and the seismic character is considered to differ markedly from the other areas of the hangingwall (Figures 4.41 to 4.45). The accurate correlation of seismic horizons and faults along the forelimb is extremely difficult due to the highly discontinuous nature of the seismic reflection configurations, suggestive of a chaotic fault and fracture network occurring at seismic and sub-seismic scales. This interpretation is supported by poor core recovery statistics at the forelimb, and a high degree of fracturing observed in the few core samples in this region (see Chapter 6 Discussion of reservoir geology and Figures 3.14 and 3.16). Towards the westernmost region of the forelimb a block with a triangular appearance in plan view is seen. This block appears to have subsided with respect to the remaining forelimb along one of the Kutz-1 splay fault (Figure 4.41).

The dip along the trend of the forelimb varies significantly, from the west (27°) to the east (19°) (Figures 4.42, 4.43 and 4.44). Lateral variations in the overburden average interval velocity were taken into account when the dip along the forelimb was calculated. The variations in average interval velocities along the forelimb (2300 m/sec at the western sector, 2450 at the central sector, and 2300 at the eastern sector) were deduced from well velocity data sampled at different well locations along the forelimb. A localised backthrust is interpreted in the eastern region of the uppermost sector of the forelimb where this exhibits its greatest dip (Figure 4.45, circle A). This interpretation is based purely on seismic character where truncations of seismic reflections are seen.

4.4.2.4 Three Dimensional geometry of faults within the hangingwall

Faults were interpreted within the hangingwall block at different stratigraphic intervals (Figures 4.15, 4.19 and 4.46). Some of the faults that occur at the Jurassic stratigraphic level propagate to higher stratigraphic levels, whereas other faults are restricted to either the Jurassic or Cretaceous interval (Figures 4.15, 4.19 and 4.47).

At deeper stratigraphic and structural levels (Top-Tithonian), the faults identified and interpreted strike northwest – southeast. Fault throws vary from 170 to 30 twt msecs (about 340 to 60 m using an interval vel of 4000 m/sec). Most of the

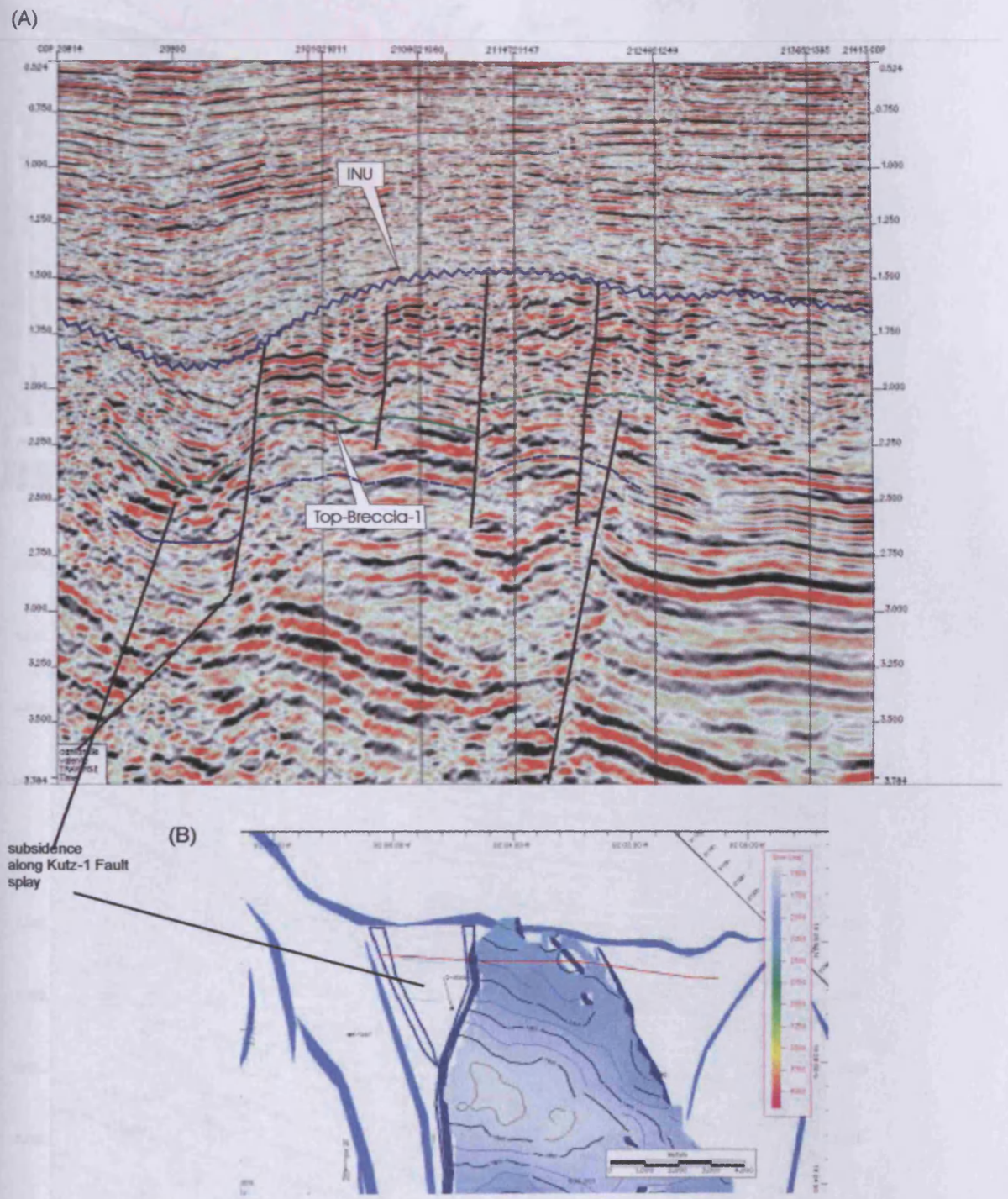

Figure 4.41
(A) Seismic profile along strike of the forelimb. The INU (Intra Neogene Unconformity) surface, and Top-Breccia seismic horizons are posted. Note the faults occurring are restricted vertically by the INU. (B) Map displaying location of seismic line and structural grid of the Top-Tithonian at the hangingwall.

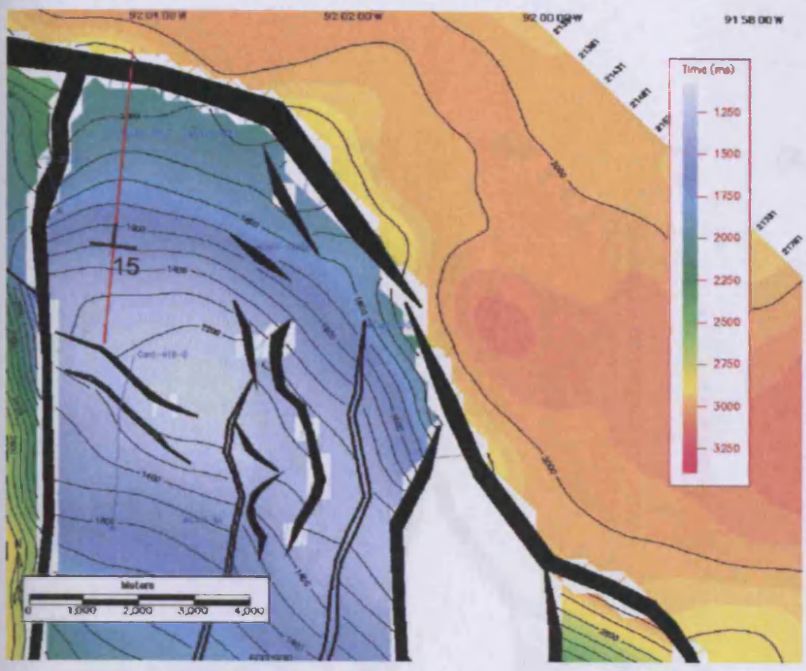

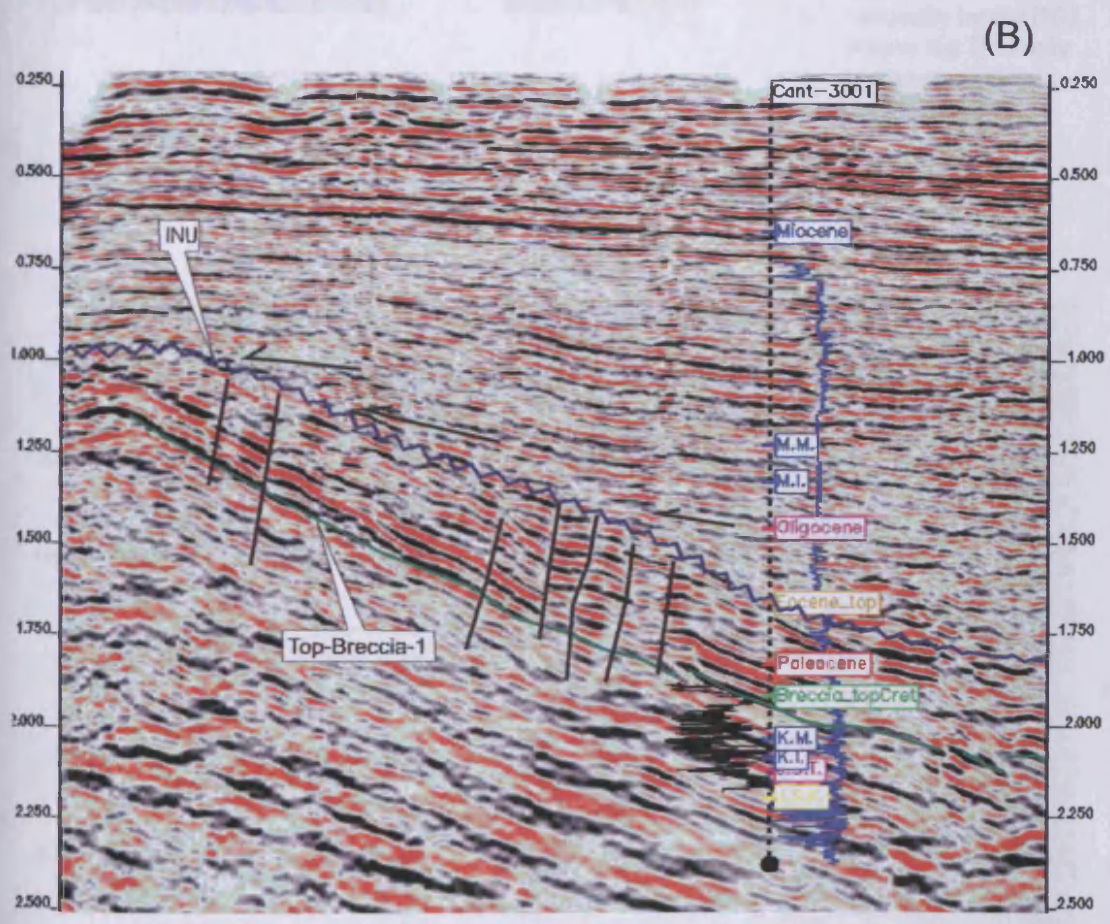

Figure 4.42
(A) Structural map for the Top-Breccia-1 level showing the forelimb region of the thrust block, and location of seismic profile. (B) seismic profile showing the forelimb sector of the Thrust Block. An average dip of 15 degrees was calculated using an average interval velocity to the Top-Breccia-1 seismic horizon of 2372 m/sec. Note the moderately fragmented character of the seismic reflections beneath the INU (Intra Neogene Unconformity). Note the onlapping seismic reflections onto the INU.

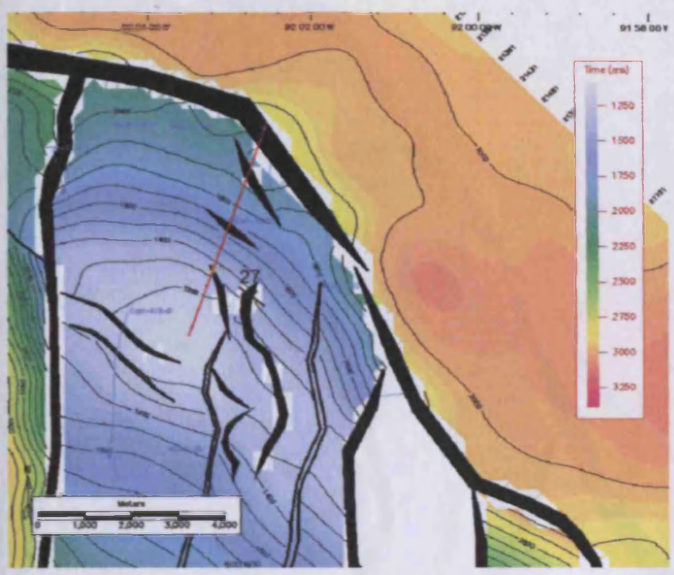

(A)

Figure 4.43
(A) structural map for the Top-Breccia-1 seismic horizon displaying the forelimb region of the thrust block. (B) seismic profile along the forelimb exhibits an average dip of 27 degrees, calculated using an average interval velocity to the Top-Breccia-1 seismic horizon of 2413 m/sec. Note the fragmented character. The faults and fragmented character are limited vertically by the INU. Above the INU only continuous seismic reflections are

(B)

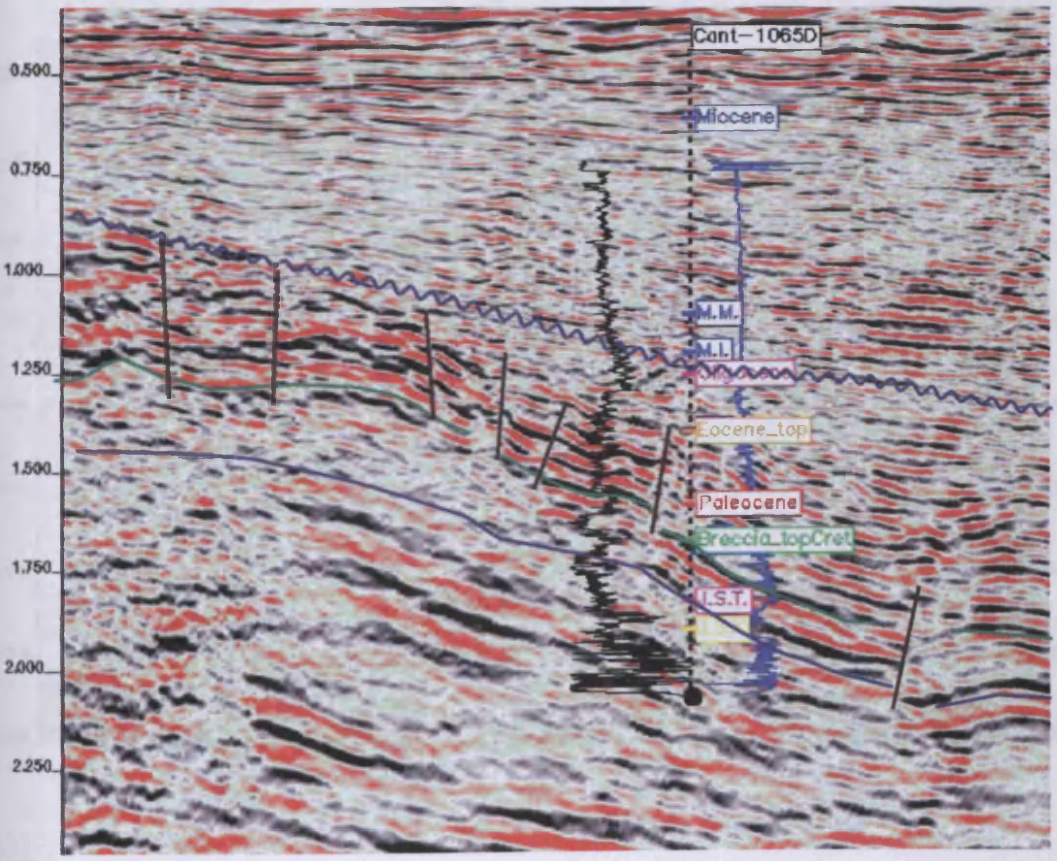

Figure 4.44
(A) structural map for the Top-Breccia-1 seismic horizon displaying the forelimb region of the thrust block. (B) seismic profile along the forelimb exhibits an average dip of 19 degrees, calculated using an average interval velocity to the Top-Breccia-1 seismic horizon of 2300 m/sec. Note the fragmented character. The faults and fragmented character are limited vertically by the INU. Above the INU only continuous seismic reflections are observed.

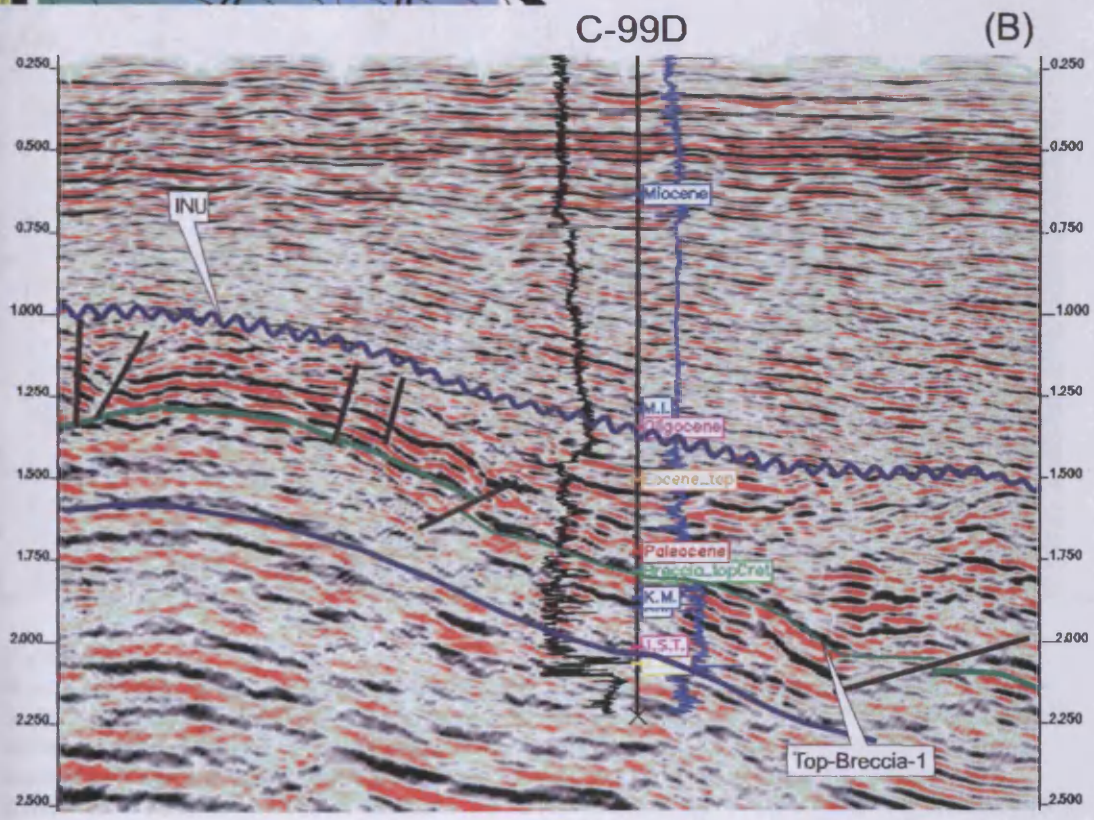

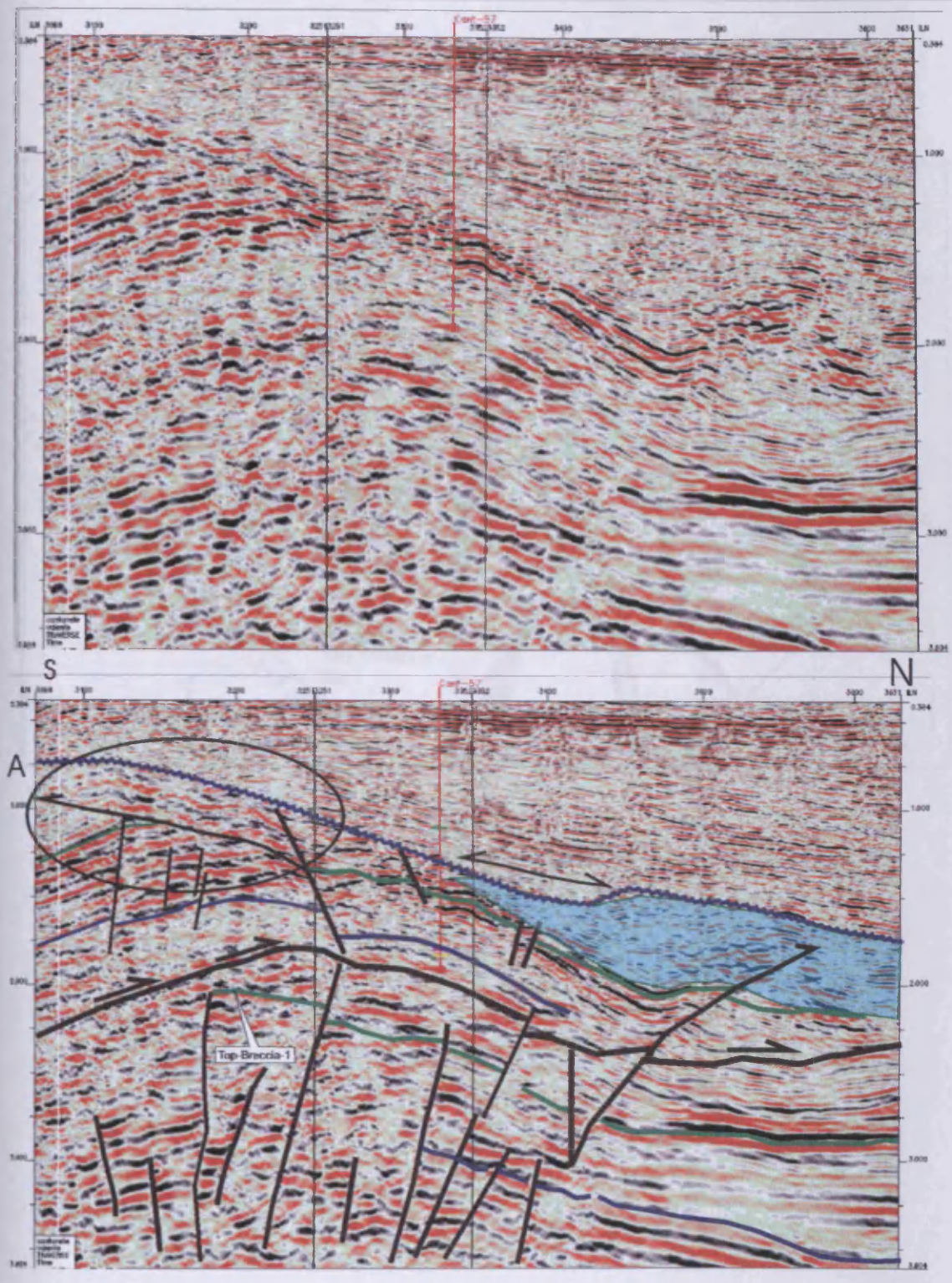

Figure 4.45
Seismic sections non interpreted and interpreted, oriented north to south showoing the forelimb sector of the Thrust Block. Seismic horizons are calibrated with well C-57. Note the difference in seismic character (amplitude, continuity and frequency) observed along the forelimb of the structure. Along the crest a backthrust has been interpreted based on seismic character and truncation of seismic reflections circle A. The occurrence of this backthrust is very localised. Note the fragmented seismic character is vertically limited by the INU (Intra Neogene Unconformity).

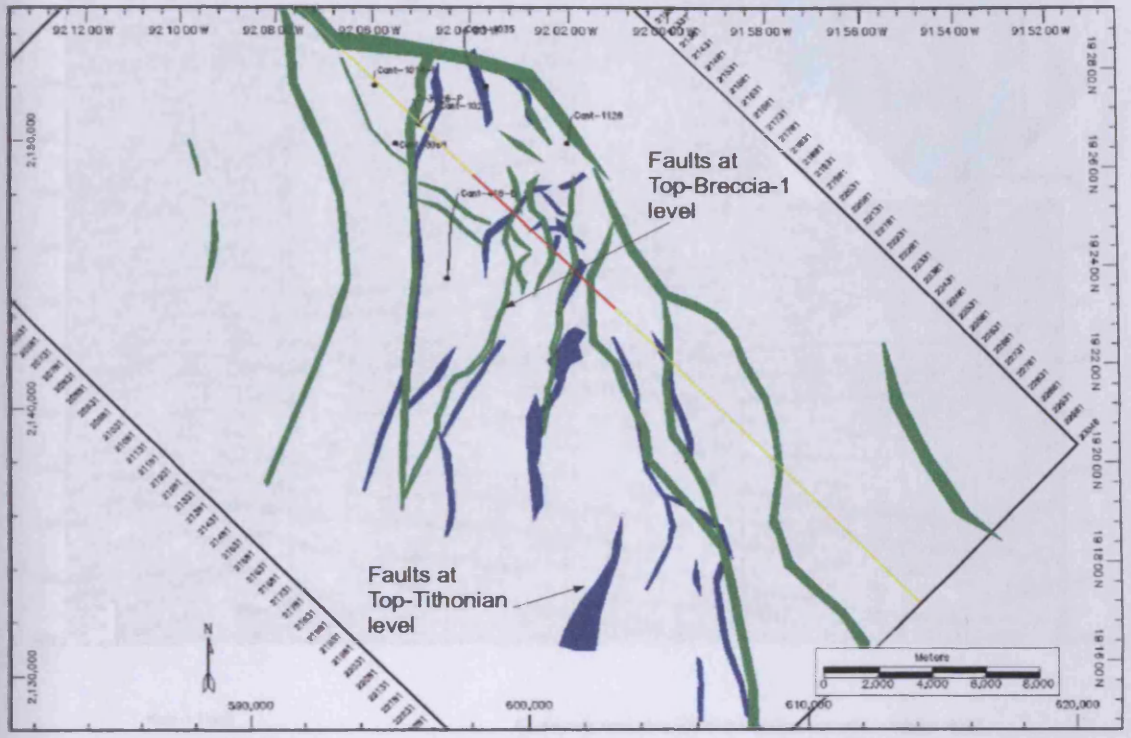

Figure 4.46
Fault layout occurring at the Top-Breccia-1 (green coloured) and Top-Tithonian-1 (blue coloured) stratigraphic levels at the hangingwall block.

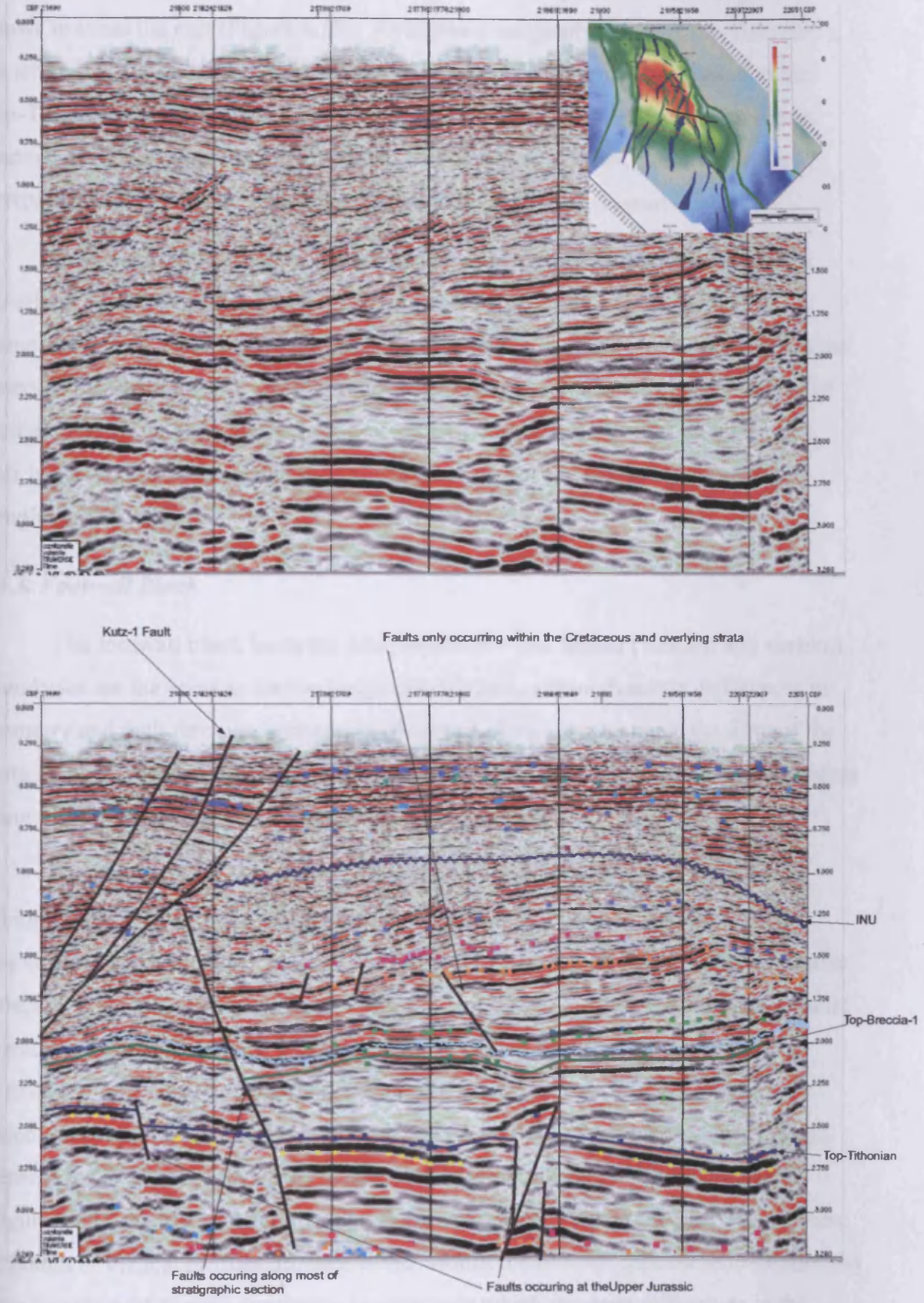

Figure 4.47
Seismic profiles oriented west to east exhibiting fault occurrences at different stratigraphic and structural levels. Faults that only occur at the Jurassic succession, faults along most of the stratigraphic interval, and faults restricted to the Cretaceous strata.

faults exhibit northwest to westerly throw directions except for one fault lineament that throws towards the east (Figure 4.15). At higher stratigraphic levels (Top-Breccia-1), the strike (northwest – southeast) and location of the fault network is similar to the Top-Tithonian level. Vertically, faults occur within Upper Jurassic and Cretaceous successions. The upper limit of the faults and disrupted seismic character that is interpreted to be related to fracturing, is defined by the INU (Figure 4.39).

In summary, the seismic expression of the hangingwall shows considerable variations from the backlimb to the forelimb with a general increase in stratal disruption concentrated within the crestal and forelimb regions. It is proposed that the observed disrupted seismic expression is a qualitative representation of the degree of faulting, fracturing and vugular porosity occurring at seismic to sub-seismic scales. This interpretation is supported by statistical core recovery percentages and core samples (see Chapter 6).

4.4.3. Footwall Block

The footwall block hosts the Sihil reservoir. The lateral (western and eastern) boundaries are the same as for the hangingwall block, although subtle differences in geometry and fault throw magnitudes were noted. Towards the north the limit of the footwall block is defined by the Ku-1 Fault. The southern limit is defined by the thrust plane and the intersection with the footwall (Figure 4.11).

The footwall as seen from vertical seismic profiles oriented north to south exhibit continuous to highly discontinuous seismic reflections (e.g. Figure 3.26). Towards the southern most region of the footwall, concordant, high amplitude seismic reflections that are continuous up to 4 km are seen. Most of the discontinuous seismic character is concentrated just beneath the hangingwall fold (Figure 3.26 centre of seismic profile). Further towards the north the seismic reflections are seen as concordant and of high amplitude that are relatively continuous up to 5 km in length. Vertical seismic profiles oriented west - east, exhibit a different seismic character (Figure 4.48), mostly, semi-concordant discontinuous seismic configurations are seen. Although in vertical profiles oriented north –south the seismic appears semi-continuous their lateral (west to east) continuity is very poor which imposes difficulties in the

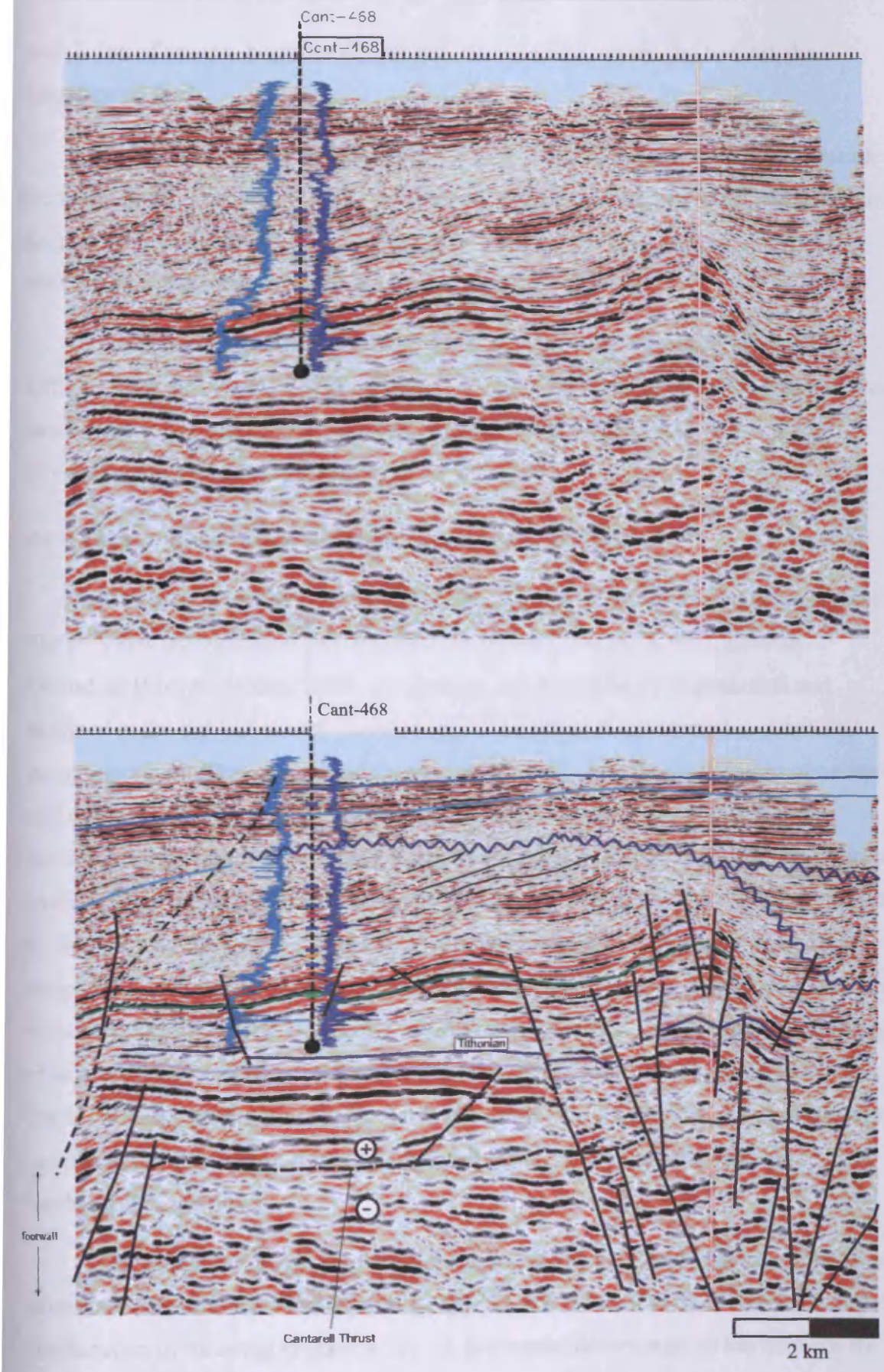

Figure 4.48
Zoom from Figure 3.25, showing the Thrust Block, for location refer to figure 3.24. Note the eastern region of thrust block exhibits increased fragmentation of seismic reflections. The seismic reflection configuration within the footwall is seen as discontinuous, semi-concordant.

correlation of seismic horizons throughout the footwall, especially beneath the hangingwall fold.

In cross section the morphology of the footwall is seen as folded just beneath the hangingwall fold (e.g. Figures 4.25 and 3.23), however as previously described in Section 4.1.1.1 this fold feature is a result of a pull-up effect. Instead, in depth converted profiles (Figure 4.29) the footwall appears as planar.

Accurate correlation of seismic horizons within the footwall is extremely difficult from the seismic geometry alone. The interpretation within the footwall area needs to be relied more extensively on well data. As further wells penetrate the footwall a better constrained map may be produced.

4.4.4 Thrust displacement, direction and detachment level

This section presents the interpretation for the thrust displacement and direction. The previous interpretation that the detachment level occurs at the Callovian – Oxfordian (Menses-Rocha, 2000, see Section, 4.1.3) boundary is evaluated and analysed in the light of earlier observations. The thrust displacement is quantified using seismic profiles oriented northeast – southwest. The thrust direction of transport was defined based on: (i) the fold axis trend (NW – SE) which implied that the maximum stress vector σ_1 was oriented perpendicular to the fold axis; (ii) the strike and south-western dip of the thrust fault ramp; (iii) the asymmetry of the hangingwall fold structure where the longer limb faces towards the south-west similarly to the thrust ramp and the shorter limb towards the north; and (iv) the distribution of fold structures within the Reforma-Akal Uplift region (Figure 4.2 and 4.3) that exhibit a similar degree of asymmetry as the Cantarell thrust where the longer limb faces towards the south (backlimb) and the shorter faces towards the north (forelimb). The above observations provide evidence to suggest that the direction of thrust transport is oriented north to northeast (Figure 4.49).

The amount of thrust displacement along the thrust plane was quantified from a seismic profile oriented north - south, perpendicular to the fold axis and near parallel to the direction of thrusting (Figure 4.50). A horizontal distance of 10 km between the hangingwall cutoff and the footwall cutoff was calculated (Figure 4.50). This linear

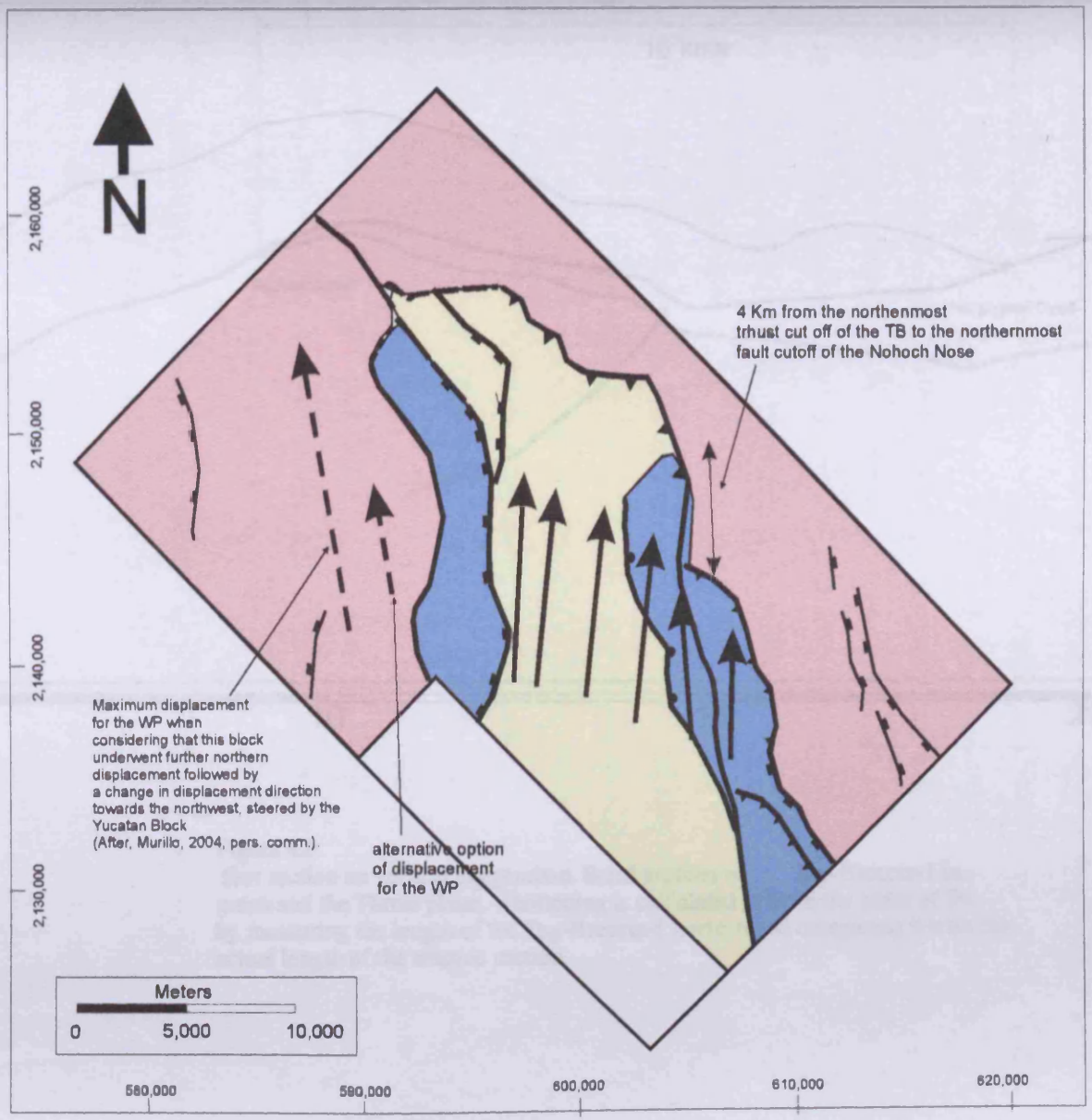

Figure 4. 49
Structural elements map showing vectors of relative thrust displacement. The size of the arrow represents the magnitude of displacement. Within the Thrust Block 12 km of displacement were calculated.

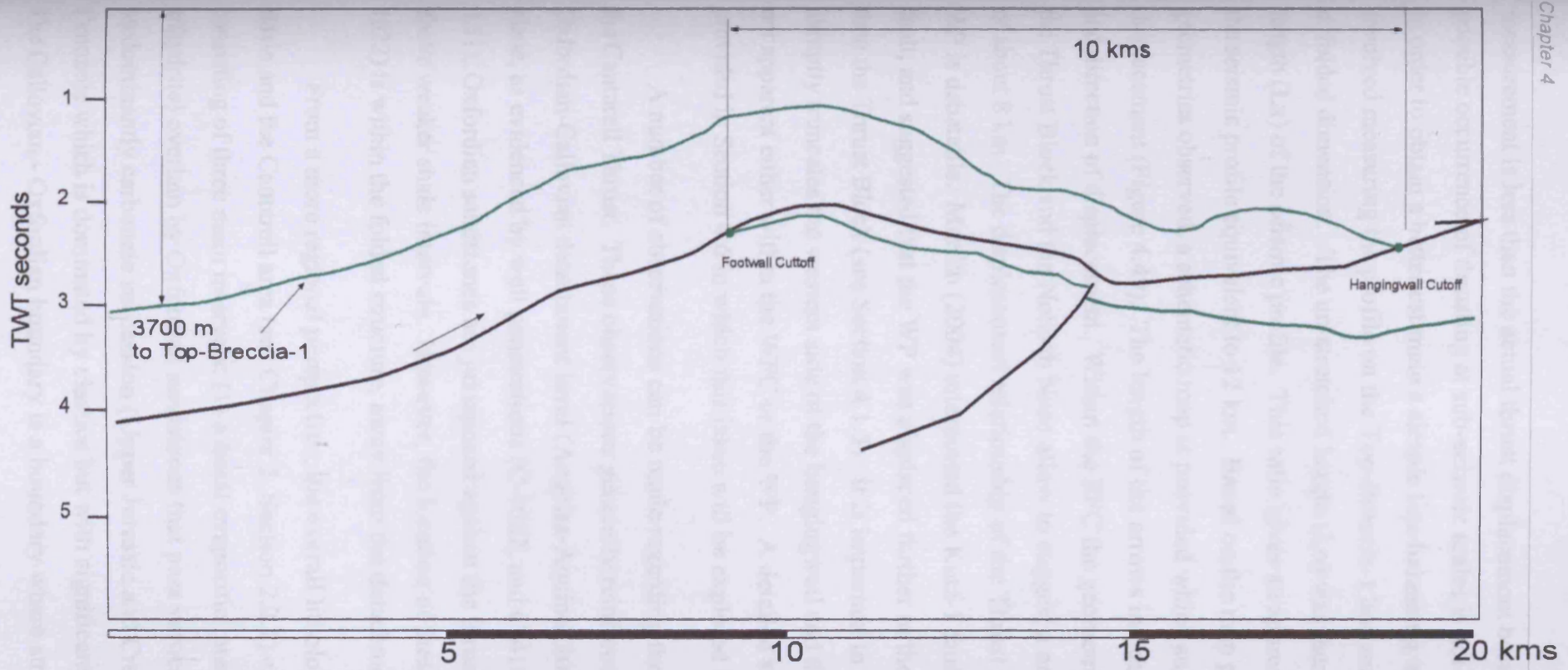

Figure 4.6
Cross section no vertical exaggeration. Dotted profiles of Top-Breccia-1 in green and the Thrust plane. Shortening is calculated to be in the order of 3% by measuring the length of the Top-Breccia-1 horizon and comparing it with the actual length of the seismic section.

measurement is less than the actual thrust displacement because folding and / or the possible occurrence of thrusting at sub-seismic scales is not taken into consideration. In order to obtain a better estimate a simple line balancing technique was applied. This involved measuring the profile on the Top-Breccia-1 horizon and then measuring the unfolded dimension. The un-stretched length (Lo) was then compared to the actual length (Lx) of the seismic profile. This ratio gives an approximated displacement along the seismic profile equivalent to 12 km. Based on the map perspective and the geometries observed, a schematic map is provided which suggests vectors of thrust displacement (Figure 4.49). The length of the arrows indicates the relative magnitude and direction of displacement. Within the EFC the geometrical relationship between the Thrust Block and the Nohoch Nose allow to suggest a minor displacement gradient of about 8 km. The displacement relationship of the Thrust Block with respect to the WP is debatable. Murillo (2004) interpreted the Kutz-1 fault as a dextral strike – slip fault, and suggested that the WP was displaced further in the north-western direction than the Thrust Block (see Section 4.1.3). It is important to note that the Kutz-1 Fault abruptly truncates the western side of the hangingwall and that the hangingwall fold is not apparent either within the WFC or the WP. A detailed structural discussion is provided in Section 4.6 in which this issue will be explored in greater detail.

A number of observations can be made regarding the main detachment level for the Cantarell Thrust. These observations generally reinforce the interpretation of an Oxfordian-Callovian detachment level (Angeles-Aquino, 2000). Along the thrust plane, as evidenced by well penetrations (C-1022, and C-418D see Figures 3.7 and 4.51), Oxfordian sandstones are juxtaposed against the thrust fault and are situated above weaker shale intervals. However, the location of these wells (C-418D and C-1022) is within the folded structure, away from the detachment level.

From a more regional perspective, the overall lithology within the Campeche Basin and the Cantarell area (see Chapter 2, Section 2.2.2) can be summarised as consisting of three main intervals: (1) a basal evaporitic interval (Callovian salt and anhydrite) overlain by Oxfordian sandstones that pass vertically upwards to (2) a predominantly carbonate succession (Upper Jurassic and Cretaceous) and (3) the Cenozoic which is dominated by clastics but with significant proportion of carbonates. The Callovian - Oxfordian boundary is a boundary where stronger rocks are underlain

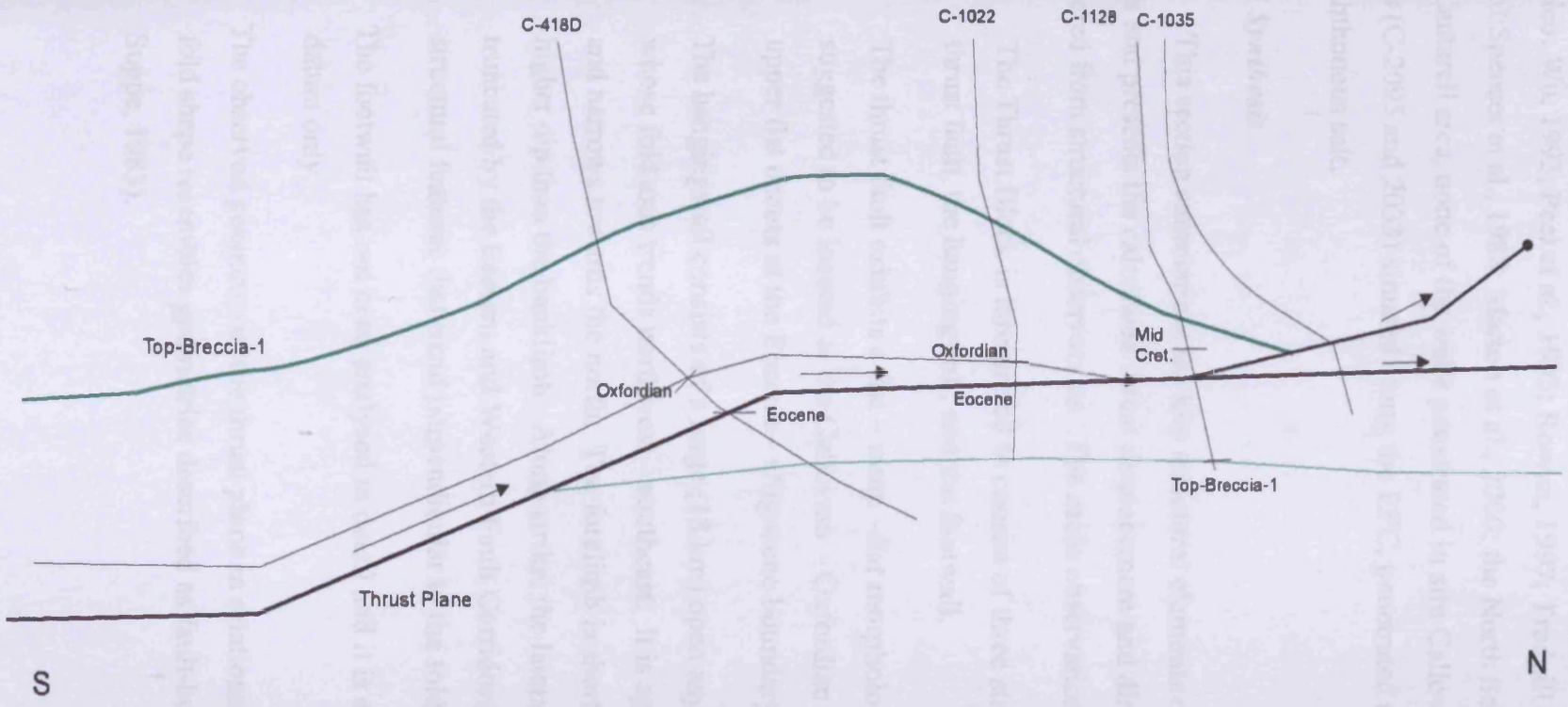

Figure 4.51
Schematic cross section oriented north - south, wells posted that have penetrated the thrust plane and the stratigraphic intervals found above and beneath the thrust plane. The wells are projected onto section in their relative position with respect to the folded structure (backlimb and forelimb).

by weaker rocks. This boundary may be considered as a detachment level, which is similar to other detachment levels, recognised in other basins of the world (e.g. Gulf of Mexico: Wu, 1993; Peel et al., 1995; Rowan, 1997; Trudgill et al., 1999; Angola and Brazil:Spencer et al., 1988; Marton et al., 2000; the North Sea: Stewart, 1995). Within the Cantarell area, none of the wells penetrated in situ Callovian salt, instead, some wells (C-2095 and 2033) situated along the EFC, penetrated minor amounts of allochthonous salt.

4.4.5 Synthesis

This section summarizes the key structural elements observed within the Thrust Block and presents the calculated thrust displacement and direction of thrusting extracted from structural observations. The main observations are:

(1) The Thrust Block is interpreted to consist of three structural elements, the thrust fault, the hangingwall, and the footwall.

(2) The thrust fault exhibits a flat – ramp –flat morphology. The lower flat is suggested to be located at the Callovian – Oxfordian stratigraphic level. The upper flat occurs at the Eocene – Oligocene boundary.

(3) The hangingwall consists of a large (18 km) open asymmetric fold structure whose fold axis trends northwest – southeast. It is approximately 9 km wide and narrows towards the north. The forelimb is shorter and exhibits a slightly higher dip than the backlimb. Along strike, the lateral fold terminations are truncated by the Eastern and Western Fault Corridors. These Corridors are structural features that trend perpendicular to the fold axis (NW – SE).

(4) The footwall has not been analysed in detail and it is considered as a structural datum only.

(5) The observed geometry of the thrust plane in relationship to the hangingwall fold shape resembles geometries described as fault-bend folds (Rich, 1934; Suppe, 1983).

4.5. Western and Eastern Platforms

The Western and Eastern Platforms consist mainly of relatively undeformed seismic reflections. However, structural features that are indicative of a structural event predating thrusting have been identified and interpreted within these platform areas. These structural features are documented in the following paragraphs. Normal faults occur within the Western and Eastern Platforms.

As previously described (see Sections 4.2.2.4 and 4.2.2.5), normal faults in the Western and Eastern Platform exhibit the following characteristics (Figures 4.14, 4.52, 4.53 and 4.54): (i) they subtly offset the Top-Breccia-1 horizon, (ii) most of the displacement occurs at deeper intervals below the Top-Tithonian, and (iii) they are located and most easily interpreted within the least deformed areas of the platforms. These characteristics suggest that these faults formed in an extensional event which lasted from the Late Jurassic through to the Cretaceous, and appear not to have been structurally reactivated during the subsequent development of the Thrust Block.

In the Western Platform, near the boundary with the Ku Fold, a contractional structural feature is observed within the seismic unit T-1 (Eocene – Miocene stratigraphy; Figure 4.55). On close inspection of Figure 4.55, it is observed that the contractional feature resembles a fold structure that is bounded by a reverse fault. The detachment level for this fault is interpreted to occur at the Oligocene-Miocene boundary as indicated by well Ixtoc-18. The ramp of the thrust fault dips towards the northeast, which in turn suggests a southwest direction of thrusting due to the strike and dip of this fold, its relation to the Ku-fold and its vergence (Figure 4.55). It is interpreted that this structure was developed contemporaneously with the emplacement of the Thrust Block. The structural morphology and the stratigraphy associated with this fold may serve as a potential hydrocarbon prospect.

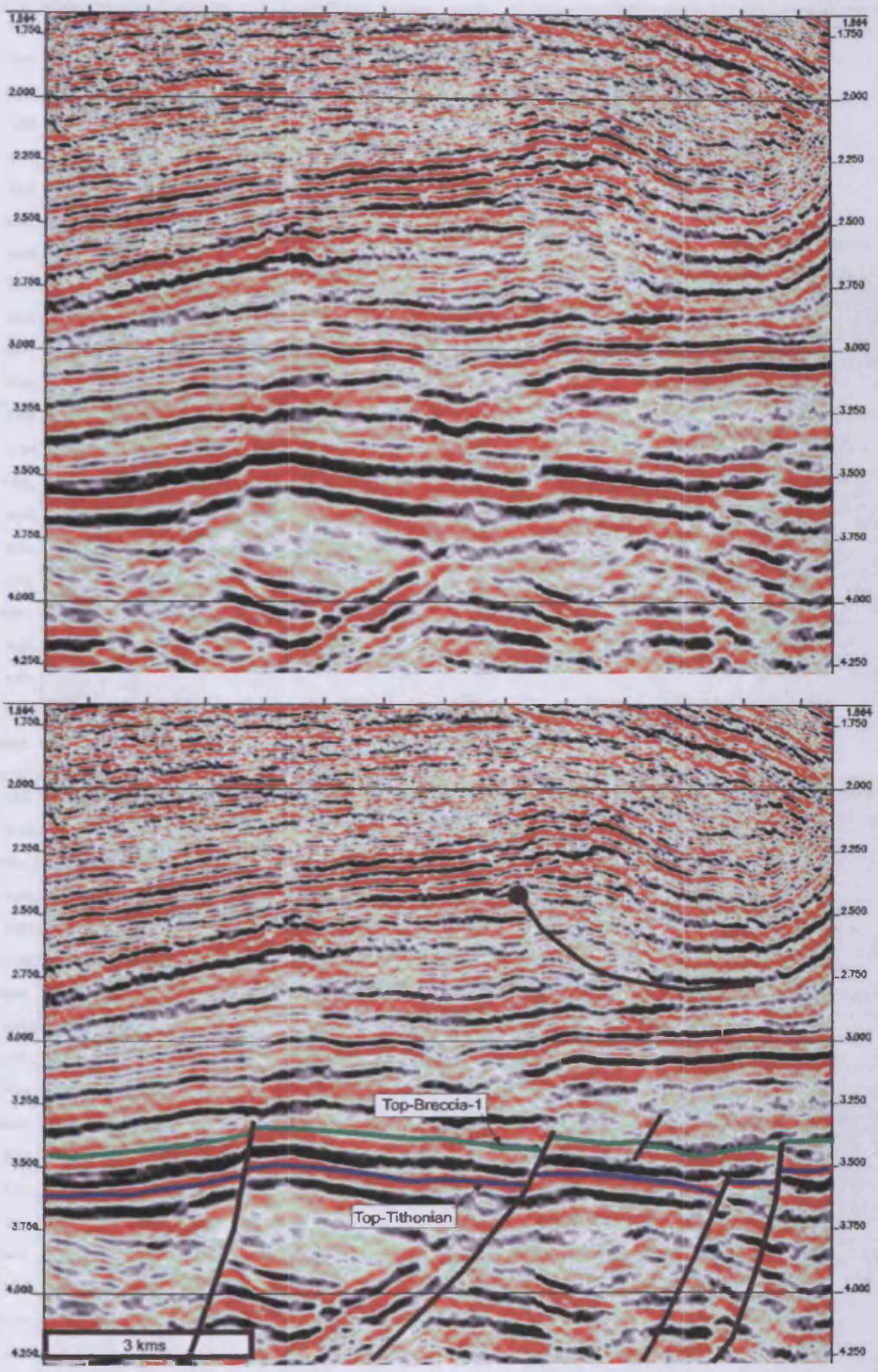

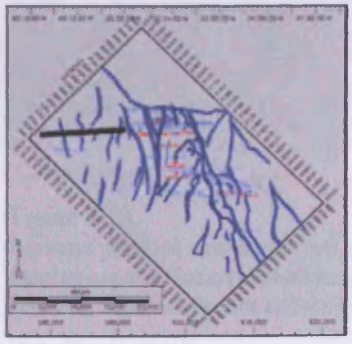

Figure 4.52
Seismic section along the Western Platform. Top-Breccia-1 and the Top-Tithonian horizons displayed. Note the normal faults that offsets the basal interval, and subtly the Top-Breccia-1 horizon.

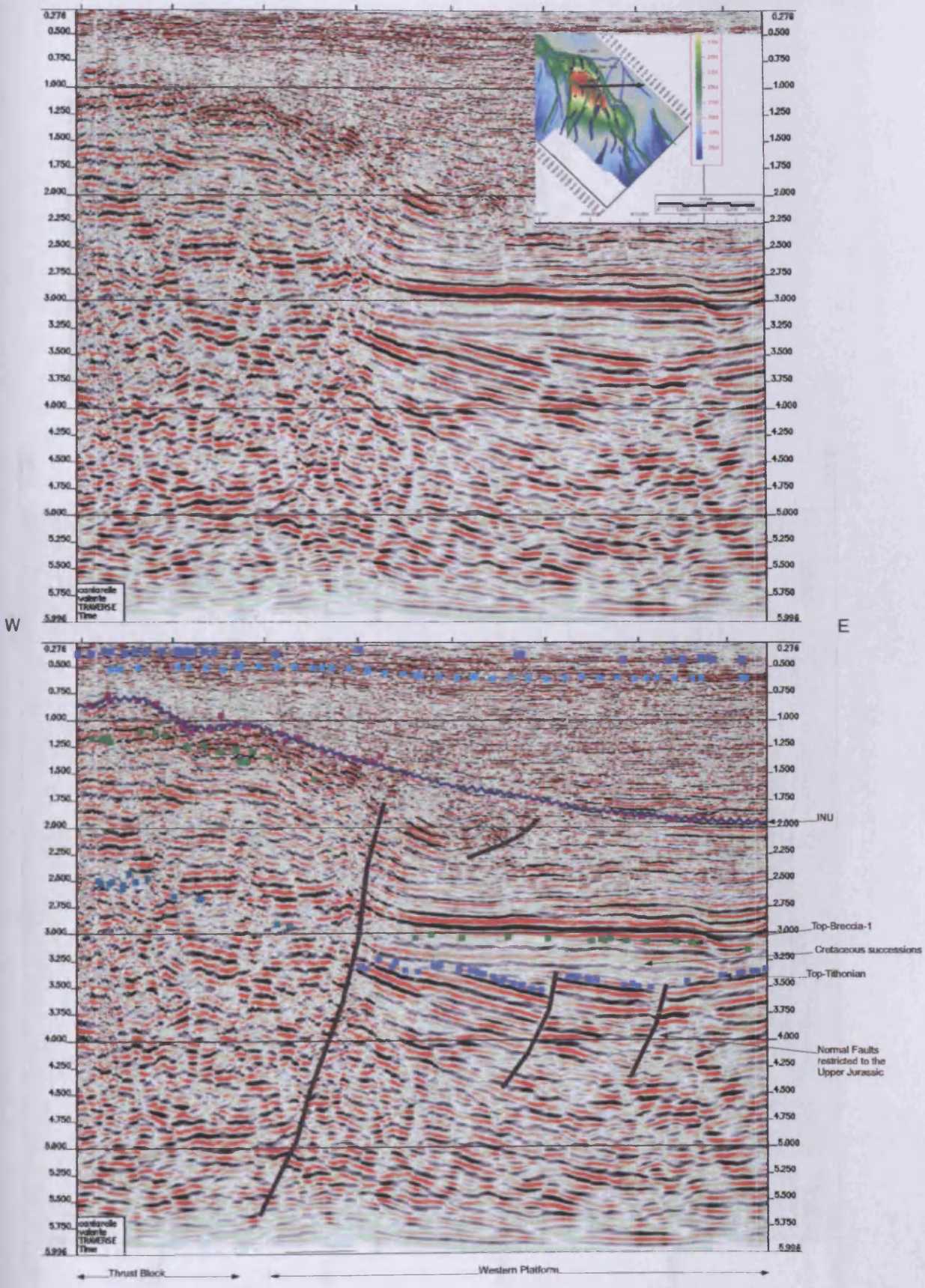

Figure 4.53
Seismic profiles uninterpreted and interpretation, oriented northwest southeast displaying the Eastern Platform. Note the faults that occur within the upper Jurassic interval do not offset higher stratigraphic levels.

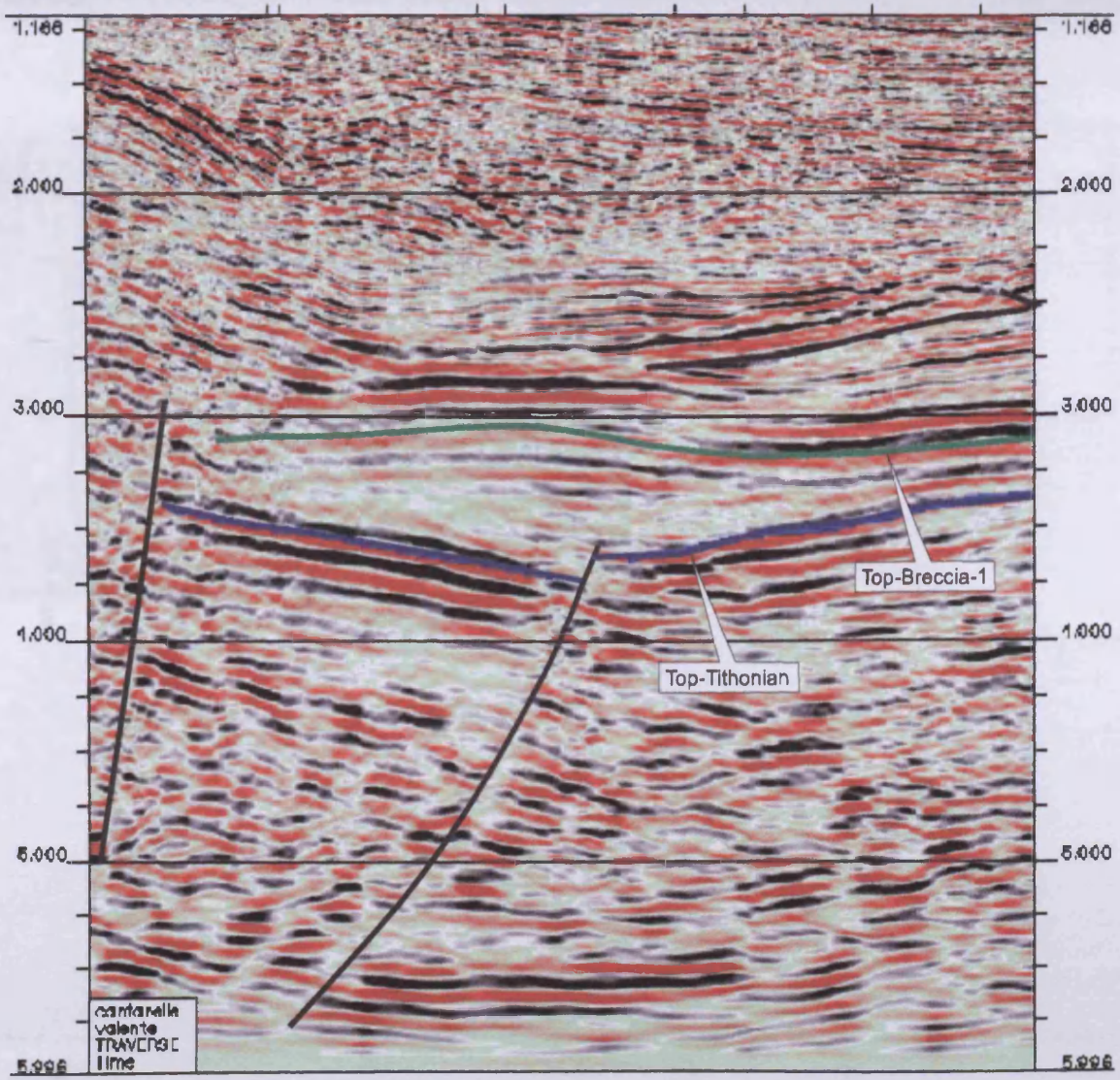

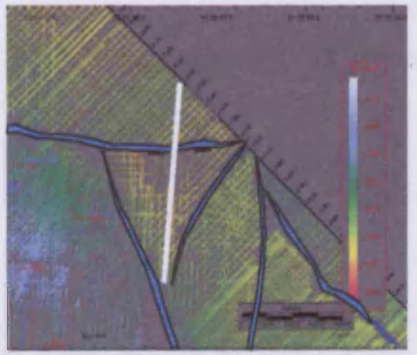

Figure 4.54
Seismic section running north south imaging the easternmost portion of fault Ku-1. Note that the fault is deep rooted, possibly into basement rocks. Note that the overlying Cretaceous strata are not displaced by the deep rooted faults.

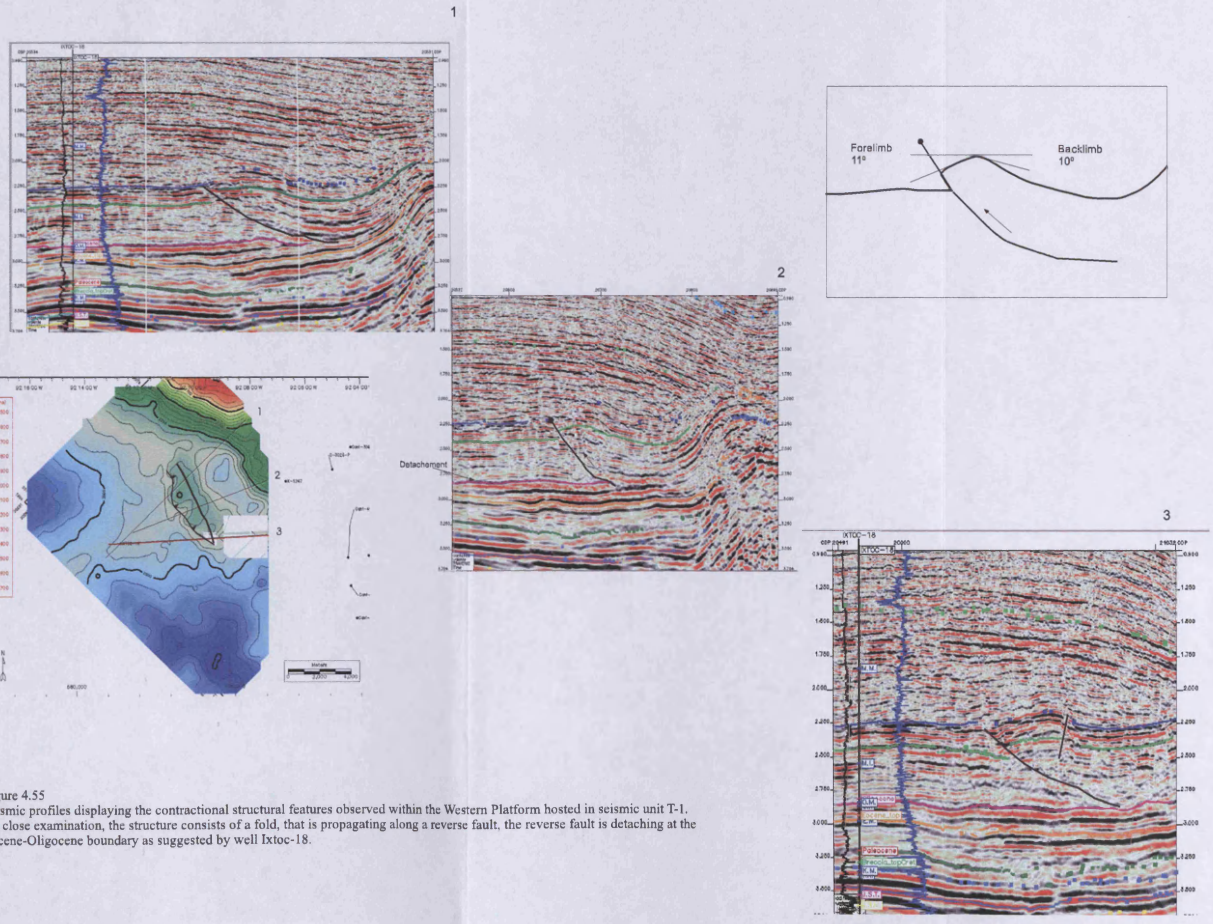

Figure 4.55
Seismic profiles displaying the contractional structural features observed within the Western Platform hosted in seismic unit T-1. On close examination, the structure consists of a fold, that is propagating along a reverse fault, the reverse fault is detaching at the Eocene-Oligocene boundary as suggested by well Ixtoc-18.

4.6 Discussion: Structural Analysis

4.6.1 Introduction

The structural features described above demonstrate that the Cantarell area was shaped by several episodes of structural deformation. These exhibit contrasting structural styles suggestive of different modes of deformation. From the preceding descriptions and interpretations the following questions can be addressed:

(1) How many episodes of structural deformation occurred? Is there any evidence for structural reactivation?

(2) What is the structural relationship and role of each of the structural elements during the deformational history of the Cantarell structure?

(3) Is the deformational style of the Thrust Block thin- or thick- skinned? The above subject includes the issue of the putative detachment level of the Thrust Block.

In the following sections evidence is provided and discussed that will address the above questions. The layout of this section takes the form of two sections. The first section (4.6.2) discusses the evidence that supports the different episodes for the evolution of the structural deformation. The second section (4.6.3) presents a four-fold model of the structural evolution of the Cantarell area in which the role of each structural element is presented and discussed. In this later section the third question is addressed and discussed.

4.6.2 Evidence for three structural events

Faults and structural morphological styles demonstrate the sequential evolution of the study area in the form of three structural events: early extension, compression, and late extension.

4.6.2.1 Early Extension

The early extension has been highly overprinted by compressional tectonics. However, on close inspection of the Upper Jurassic and Lower Cretaceous interval, as previously described (see Sections 4.2.2.4 and 4.2.2.5) normal faults were observed. These are most evident within the EP and WP exhibiting a westerly throw in a

basinwards direction as previously observed in Figures 4.52, 4.53 and 4.54. The fault dips, throw directions and different thickness across faults are evidence that supports the hypothesis that during the Late Jurassic to Early Cretaceous was a period of tectonic extension. Previous authors (García-Hernández, *et al.*, 2000; see Chapter 2), have suggested an extensional event during the Late Jurassic and Early Cretaceous, and describe a 'half graben topography' as a result of this event.

In the north-eastern and south-eastern sectors of the Gulf of Mexico an earlier Mesozoic (Late Triassic-Early Jurassic) extensional episode has been interpreted associated with a rifted, passively subsiding continental margin resulting in a half-graben setting (MacRae, 1996; Marton and Buffler, 1999). Within the Gulf of Mexico Basin the distribution of the overlying Upper Jurassic sediments reflects the overall morphology of the basin that was established during the Jurassic. Deposition of the Lower Cretaceous strata in the central part of the basin was enhanced by local subsidence due to sediment loading. In contrast, the Late Cretaceous and Cenozoic sediments reflect uniform deposition in a tectonic setting characterised by subsidence through lithospheric cooling.

Based on the observations of MacRae (1996) and Marton and Buffler (1999) the extensional event associated to rifting of the Gulf of Mexico occurred during the Late Triassic-Early Jurassic. Within the Cantarell 3D survey the Late Triassic to Early Jurassic succession is not imaged, most likely due to the lateral and vertical limits of the 3D seismic data. This limitation of data coverage does not permit comparison of the Cantarell structures to previous observations (MacRae, 1996; Marton and Buffler, 1999; García-Hernández, *et al.*, 2000). However, a normal faulted terrain is seen within the Upper Jurassic to Lower Cretaceous succession and their structural character is similar to those described by MacRae (1996), which he interprets to be the very latest stages of the extensional event coupled with local subsidence.

From the above discussion the extensional terrain that is observed across the Cantarell 3D survey is interpreted to represent the very latest stages of an extensional event associated to the opening of the Gulf of Mexico.

4.6.2.2 Compression

As previously described (see Section 4.4) the structural framework consists of: (1) a Thrust Block that consists of a folded hangingwall, a footwall and a thrust fault, with an approximate thrust displacement of 12 km and a north to northeast direction, (2) adjacent to the TB two elongated and narrow structural domains (EFC and WFC) that exhibit highly disrupted seismic reflections (see Section 4.3), and (4) a smooth but tight fold the Nohoch Nose (Figure 4.56). At sub-seismic scales, faulting and fracturing has been recognised from core and wire-line data (Pacheco-Gutierrez, 2000). These structural styles were evidently formed under a compressive tectonic regime. This regime resulted from a compressive regime in which the maximum principal compression stress was horizontal and disclosed between north and south and north-east (see Section 4.4.4).

Previous studies (Angeles-Aquino, 2001 and Garcia-Hernandez, et al. 2000) have interpreted within the Sierra de Chiapas (see Chapter 2) alternating phases of tectonic quiescence with phases of mild tectonism to compressional and transpressional regimes. Angeles-Aquino (2001) proposed three periods of regional compression during the Campanian, End of Early Eocene and Late Eocene. He also suggested alternating transpressive and transtensile regimes during the Miocene. The middle Miocene transpressive event that is known to have occurred in the Sierra de Chiapas has been interpreted to be linked to a south-west to north-east oriented maximum compressive stress within the area of the Reforma-Akal Uplift. This compressive event is associated with the development of folds, and reverse faults (Angeles-Aquino, 2001). The timing for the development of the compressive structural framework encountered within the Cantarell area will be documented and reviewed in Chapter 5.

In the context of a compressional phase of deformation, the structural relationship among the WFC, EFC and the TB exhibits a coherent geometry and structural relationship based on their location, the strike of both the WFC and EFC with respect to the thrusting direction of the TB (Figures 4.1 and 4.56), the internal seismic character and morphology of the WFC and EFC (see Section 4.3), and the similarities of the WFC and EFC to strike slip fault systems previously observed and documented (e.g. Sylvester, 1988; Harding, 1990; see section 4.3.3). From the above, the WFC and

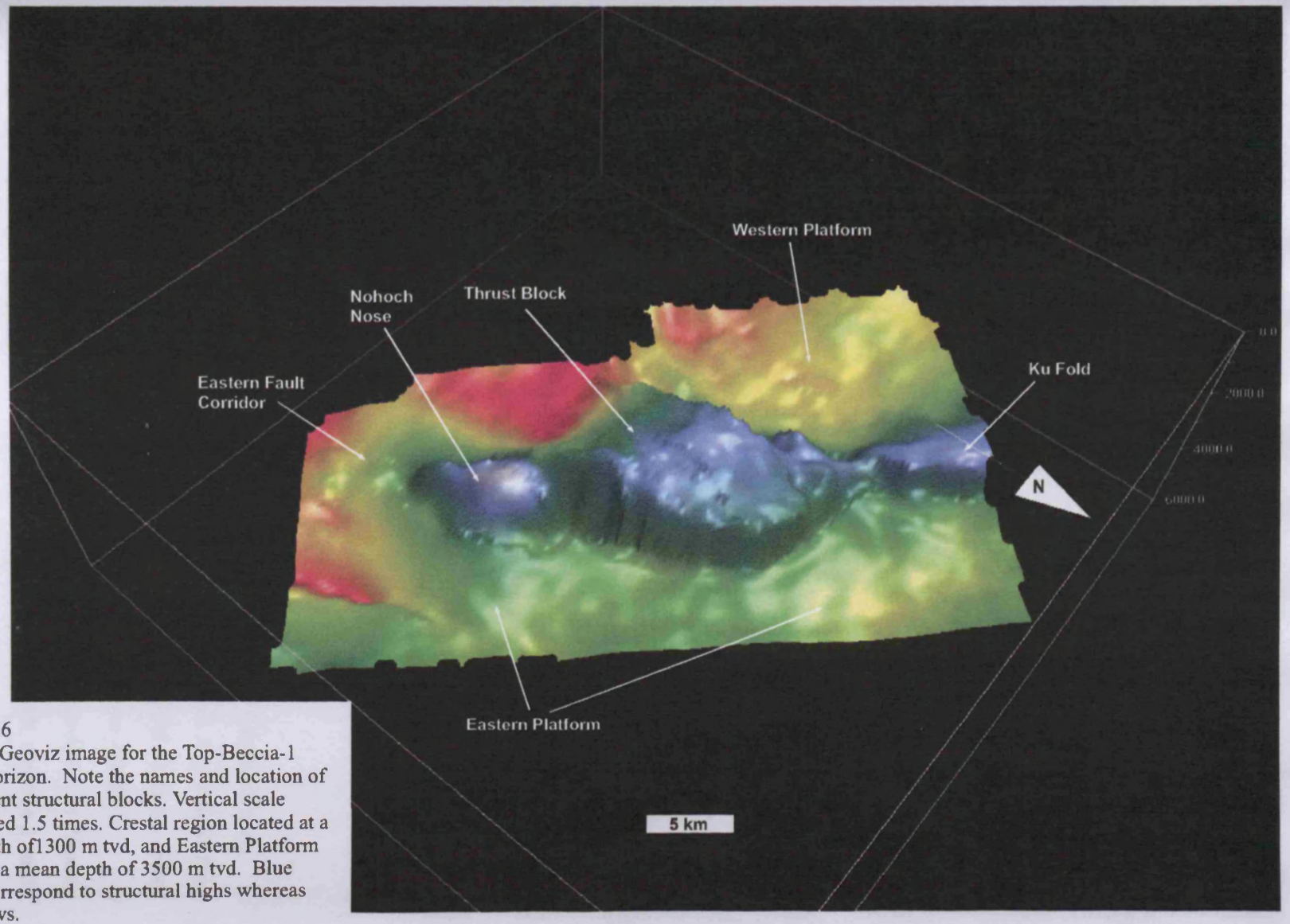

Figure 4.56
Isometric Geoviz image for the Top-Beccia-1 seismic horizon. Note the names and location of the different structural blocks. Vertical scale exaggerated 1.5 times. Crestal region located at a mean depth of1300 m tvd, and Eastern Platform located at a mean depth of 3500 m tvd. Blue colours correspond to structural highs whereas reds to lows.

EFC have been interpreted as lateral ramps or *tear faults* (Sylvester, 1988; Harding, 1990) of the TB.

The structural geometries documented earlier in the Chapter (see Sections, 4.3 and 4.4) can be interpreted in a structural model in which the Cantarell structure is considered to be thrusted and folded in two stages. These stages will be presented in detail and discussed in Sections (4.6.3.3 and 4.6.3.4). The first stage involved major folding with minor thrusting and the second stage includes major thrust displacement with minor folding. This is suggested based on the occurrence of the smooth but tight fold, the Nohoch Nose, which appears displaced by the EFC and the abrupt termination of the hangingwall fold.

4.6.2.3 Late Extension

The late extensional event has been established based on: (1) the occurrence of normal faults at shallow stratigraphic levels located within the WFC and EFC (Figures 4.7 and 4.8), (2) relay ramp structures associated to the normal faults and (3) a graben like structure, the Kutz-Wakil Graben, situated over the WFC trend (see Section 4.2.2.1 and 4.2.2.2, Figure 4.18).

Two structural scenarios are explored as significant for the development of normal faults that bound the Kuz-Wakil Graben: (1) transtension (Murillo, 2004; pers. comm.) and (2) pure east-west extension. These structural scenarios will be presented and discussed in Section 4.6.3.5.

4.6.3 Structural evolution

This section presents a structural evolutionary model of the Cantarell area, based on the previous observations and interpretations of them. This model describes the evolution and the structural relationships of each defined structural element. From the three structural events previously discussed, a five-stage structural model is suggested for the evolution of the Cantarell structure: (1) Early Extension, (2) Passive basin infill, (3) Compressive event, episode 1, (4) Compressive event, episode 2, and (5) Late Extensional event.

4.6.3.1 Early Extension (Jurassic to Early Cretaceous)

Based on earlier observations a tectonic scenario for the Jurassic to Early Cretaceous is presented (Figure 4.57). This map has been constructed based on: (1) the fault geometry at the Top-Tithonian seismic horizon, (2) the deep structured fault styles observed within the Western and Eastern Platforms, (3) thickness variations across main faults, and (4) the vertical extent of the faults.

The structural framework that resulted from the early extensional event (Jurassic to Early Cretaceous) has been interpreted to consist of three main blocks divided by normal faults with a possible half-graben arrangement (Figure 4.57). Importantly, the locations of these three blocks are coincident with the location of the WP, the TB and the EP. In addition, as previously described, the normal faults strike north-south to northwest-southeast with a basinwards throw. The arrangement of the faults is such that towards the north of the TB a relay ramp that passes laterally to a normal fault with little throw is inferred. The possible occurrence of this structural arrangement has been established based mainly on the correlation of the Top-Breccia-1 horizon from the WP into the footwall block (Figure 4.11). This structural arrangement is associated with the site on which the thrust ramps up stratigraphy during the subsequent compressive event. Similar structural styles have been suggested previously for other structures (Rowan, et al., 2000), in which the thrust ramps up over underlying normal faults.

Within the TB, the Upper Cenozoic succession thickens towards the south and against the Akal Fault (see Chapter 3 and Figure 3.20.1). From the thickness distributions it is speculated that the TB region had a primary southern to southeast depositional dip, which strengthens the above suggested structural arrangement.

4.6.3.2 Passive basin infill (Cretaceous to Miocene)

Prior to the onset of the compressive event, burial of the previous structural framework occurred (Figure 4.58). Based purely on seismic observations it is interpreted that normal faulting coalesced at this stage. Possibly minor normal faults were present bounding the TB, resulted as differential compaction over a relict irregular bathymetry. Furthermore, previous studies (Sawyer, 1980) suggested that the transition of thick continental crust to stretched continental crust occurred within the vicinity of

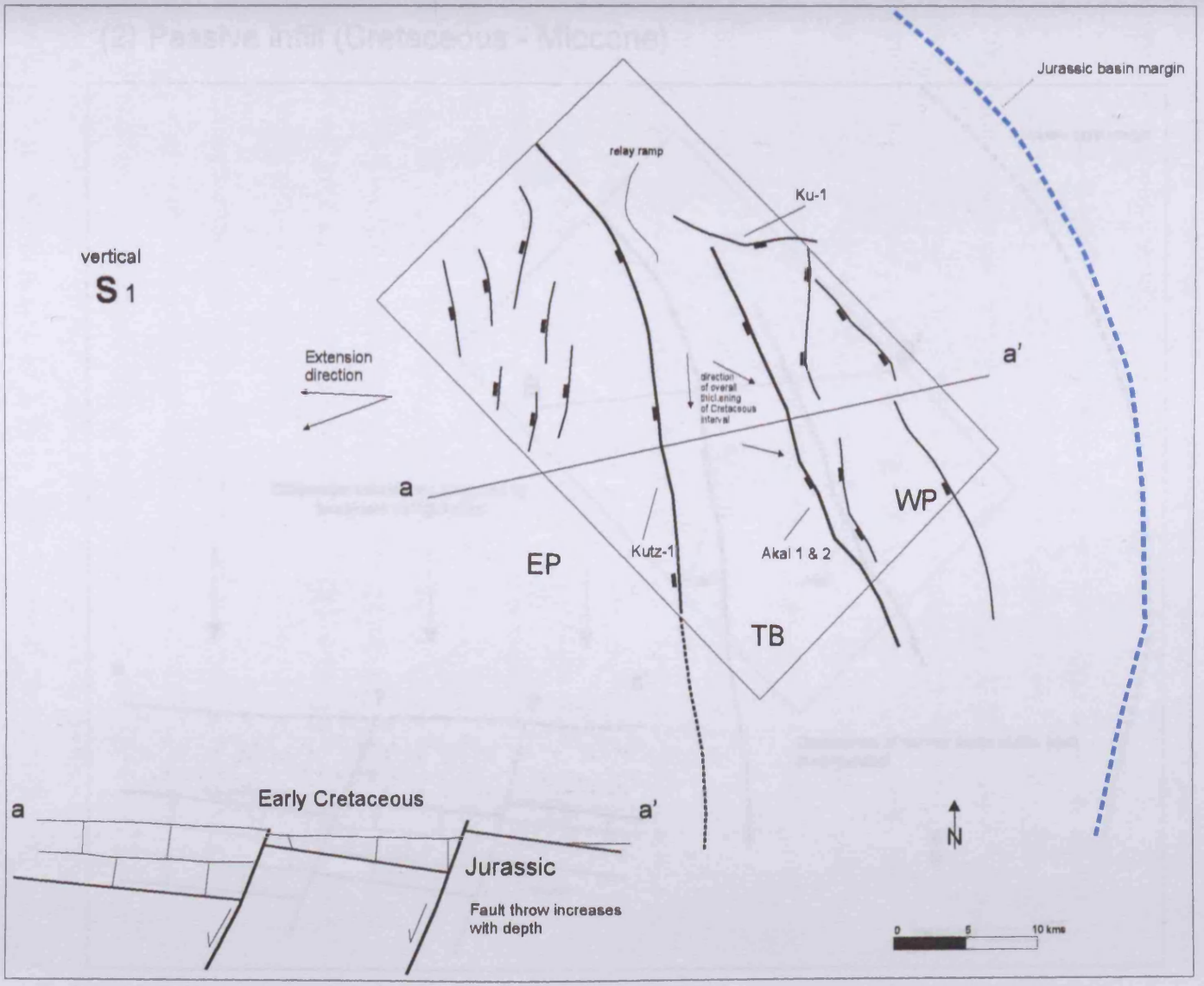

Figure 4.57
Geologic sketch of structural evolution stage 1: early extension, occurred during the Jurassic to Early Cretaceous.
Note the terrain is dominated by normal faults with a west to south west throw. Three structural blocks were defined partitioned by normal faults, these are coincident with the EP, TB and WP. The TB block had a depositional dip which deepened towards the south southeast. This interpretation is based on thickness distribution within the TB and across the normal faults.

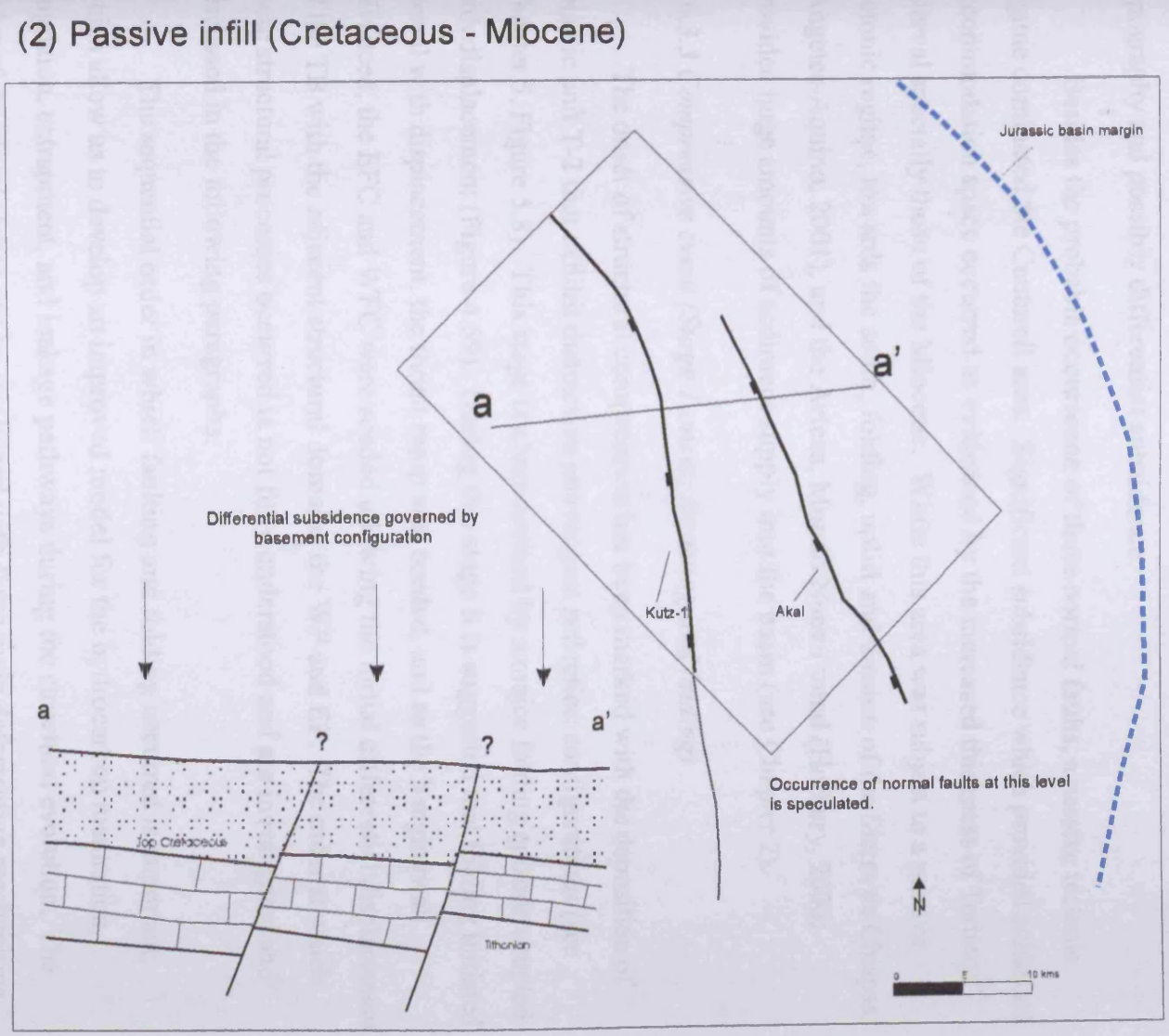

Figure 4.58
Geologic sketch for structural evolution stage 2: Passive infill, during Cretaceous to Miocene times. Three structural blocks are interpreted which are coincident with the WP, TB, and WP. This interpretation is not definite due to the overprinting of the structural compression at later stages. However, the normal faults are suggested to occur as extensions of earlier structures resultant of differential compaction, and possibly differential subsidence governed by basement configuration.

the Cantarell area (see Chapter 2), which may have provided an enhanced irregular topography and possibly differential subsidence.

Besides the probable occurrence of these normal faults, a passive tectonic regime dominated the Cantarell area. Significant subsidence which provided enhanced accommodation space occurred as evidenced by the increased thickness of Tertiary interval specially those of the Miocene. While this area was subject to a passive tectonic regime, towards the south, folding, uplift and erosion of the Sierra de Chiapas (Angeles-Aquino, 2001), and the Artesa, Mundo Nuevo trend (Horbury, 2000) provided huge amounts of sediment supply into the basin (see Chapter 2).

4.6.3.3 Compressive event (Stage 1 onset: thrusting and folding)

The onset of structural compression has been marked with the deposition of seismic unit T-2 that exhibit distinctive convergent reflection configurations (see Chapter 5, Figure 5.8). This stage is characterised by a major folding episode coupled with displacement (Figure 4.59). During this stage it is suggested that folding initiated coeval with displacement, the thrust ramp was seeded, and as the hangingwall advanced, the EFC and WFC were seeded allowing the initial differential displacement of the TB with the adjacent structural domains the WP and EP. The order at which these structural processes occurred is not fully understood and are investigated and discussed in the following paragraphs.

The sequential order in which faulting and folding occurred is important, which allow us to develop an improved model for the hydrocarbon maturation, migration, entrapment, and leakage pathways during the structural evolution. The order of structural stages can be explained with three main deformation mechanisms previously modelled and described (Suppe, 1983; Suppe & Medwedeff, 1990; and Mitra 2002). These include: (1) Fault bend folding (Suppe, 1983), where the displacement of the hangingwall and development of the fold develops over bends of a pre-existing faulted terrain, (2) Fault- propagation folding (Suppe and Medwwdeff, 1990) occurs when strata deforms by folding coeval with propagation and growth of the fault tip, and (3) faulted detachment folds (Mitra, 2002) in which folding first develop over a planar decollement, followed by ramping up the thrust plane (Figure 4.60).

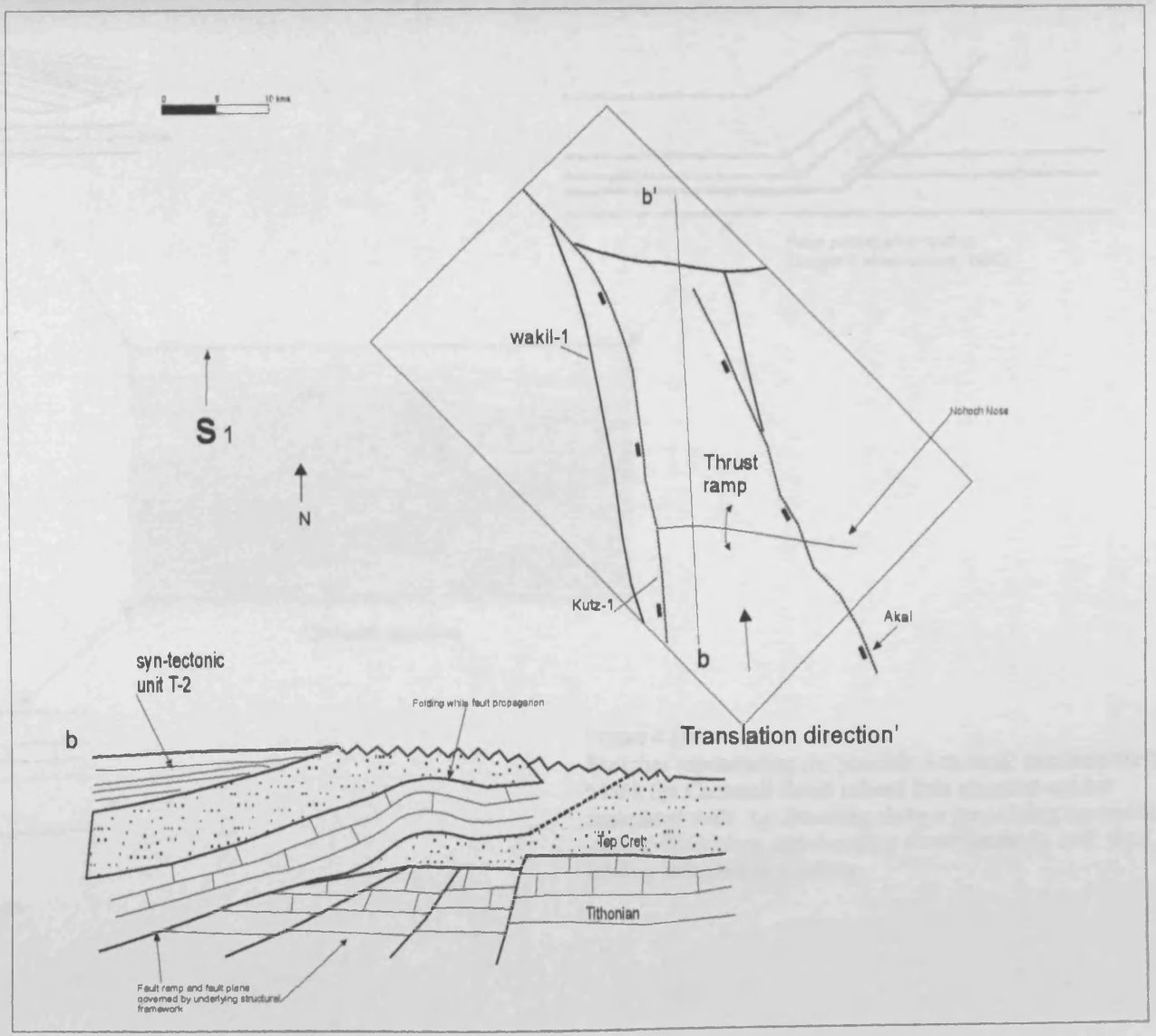

Figure 4.59
Geological sketch of the structural evolution, stage 3: compression, episode 1. Fault ramp is seeded, within the southern part of the TB, lateral ramps are seeded at the preexisting normal faults, and displacement is coeval with folding

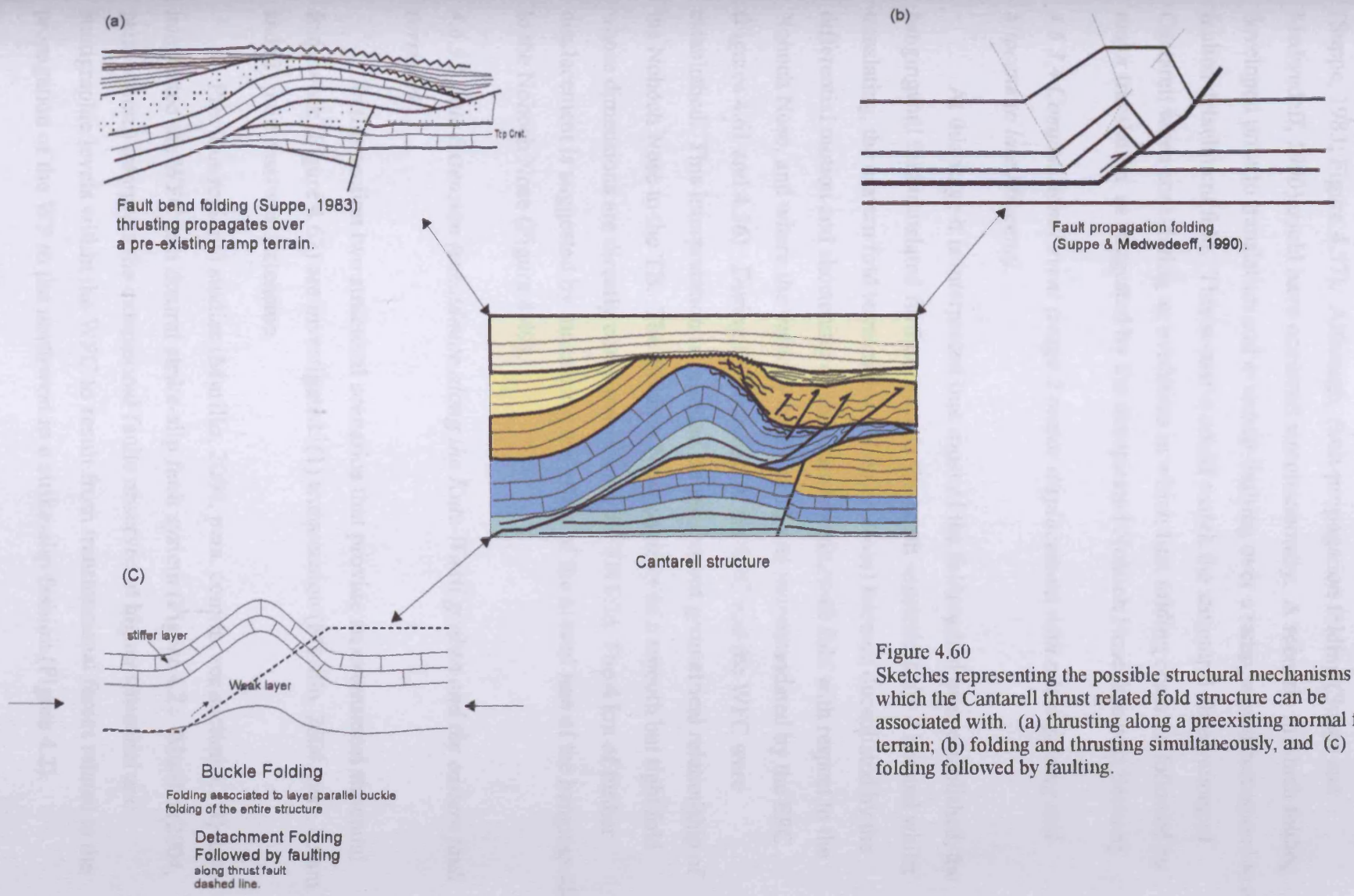

Figure 4.60
Sketches representing the possible structural mechanisms to which the Cantarell thrust related fold structure can be associated with. (a) thrusting along a preexisting normal faulted terrain; (b) folding and thrusting simultaneously, and (c) folding followed by faulting.

A structural scenario in which the underlying structural setting, plays a major control on the location of the thrust ramp, would be analogous with the fault-bend-fold model (Suppe, 1983; Figure 4.57). Although, fault-propagation folding (Suppe and Medwedeff, 1990) could have occurred simultaneously. A scenario in which folding developed prior to translation and eventual faulting over a ramp, would correspond to a faulted detachment fold. This scenario could match the structural observations of Cantarell when considering an evolution in which first folding occurred followed by major translation as suggested by the decapitated Nohoch Nose (see next Section).

4.6.3.4 Compressional event (stage 2 major displacement with minor folding mid Miocene to late Miocene).

At this stage it is interpreted that most of the folding had been established, the hangingwall fold translated further towards the north approximately 4 km and whilst translating, the eastern fold termination (Nohoch Nose) became decapitated by the differential motion and shortening of the main hangingwall fold with respect to the Nohoch Nose, and where the velocity differential was accommodated by the EFC (Figures 4.61 and 4.56). During this translation the EFC and the WFC were established. This interpretation is founded on the current geometrical relationship of the Nohoch Nose to the TB. The Nohoch Nose consists of a smooth but tight fold whose dimensions are directly comparable with the TB fold. The 4 km of further displacement is suggested by measuring the offset of the crestal line of the hangingwall to the Nohoch Nose (Figure 4.49).

4.6.3.5 Late Extension (subsidence along the Kutz-Wakil graben and the eastern fault corridor)

In this section two structural scenarios that provide an extensional structural framework (Figure 4.62) are investigated: (1) transtension (Murillo, 2004, pers. comm.) and (2) pure east-west extension.

Previous regional studies (Murillo, 2004, pers. comm., see section 4.1.3) have interpreted the WFC as a dextral strike-slip fault system (Figure 4.2). Murillo (2004, pers. comm.) interprets the extensional faults observed at higher structural and stratigraphic levels within the WFC to result from transtensional forces related to the propagation of the WP to the northwest in a strike-slip fashion (Figure 4.2).

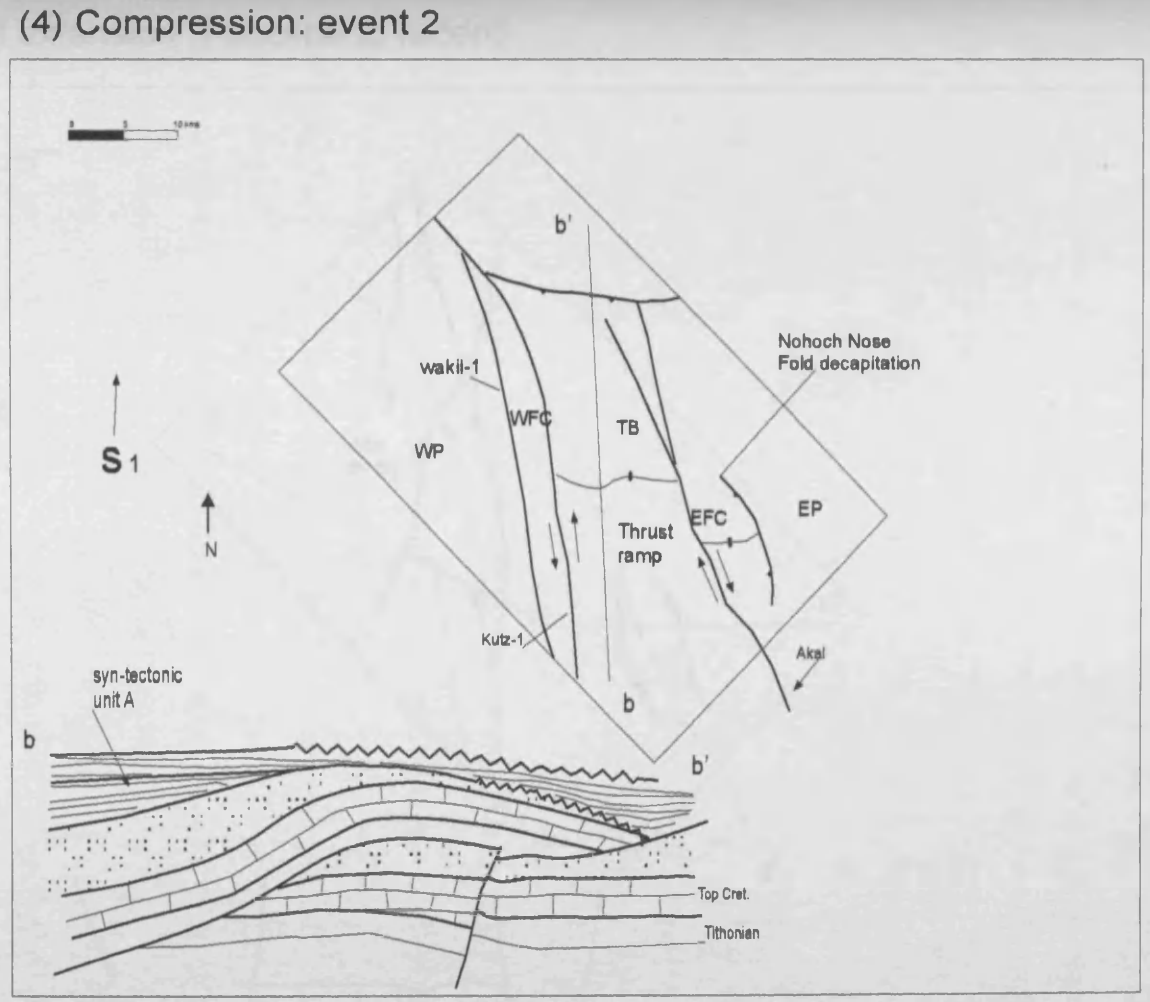

Figure 4.61
Geological sketch of the structural evolution, stage 4: Compressive event 2. Major displacement of hangingwall fold, decapitation of the Nohoch Nose and full development of the lateral ramps of tear faults the WFC and EFC.

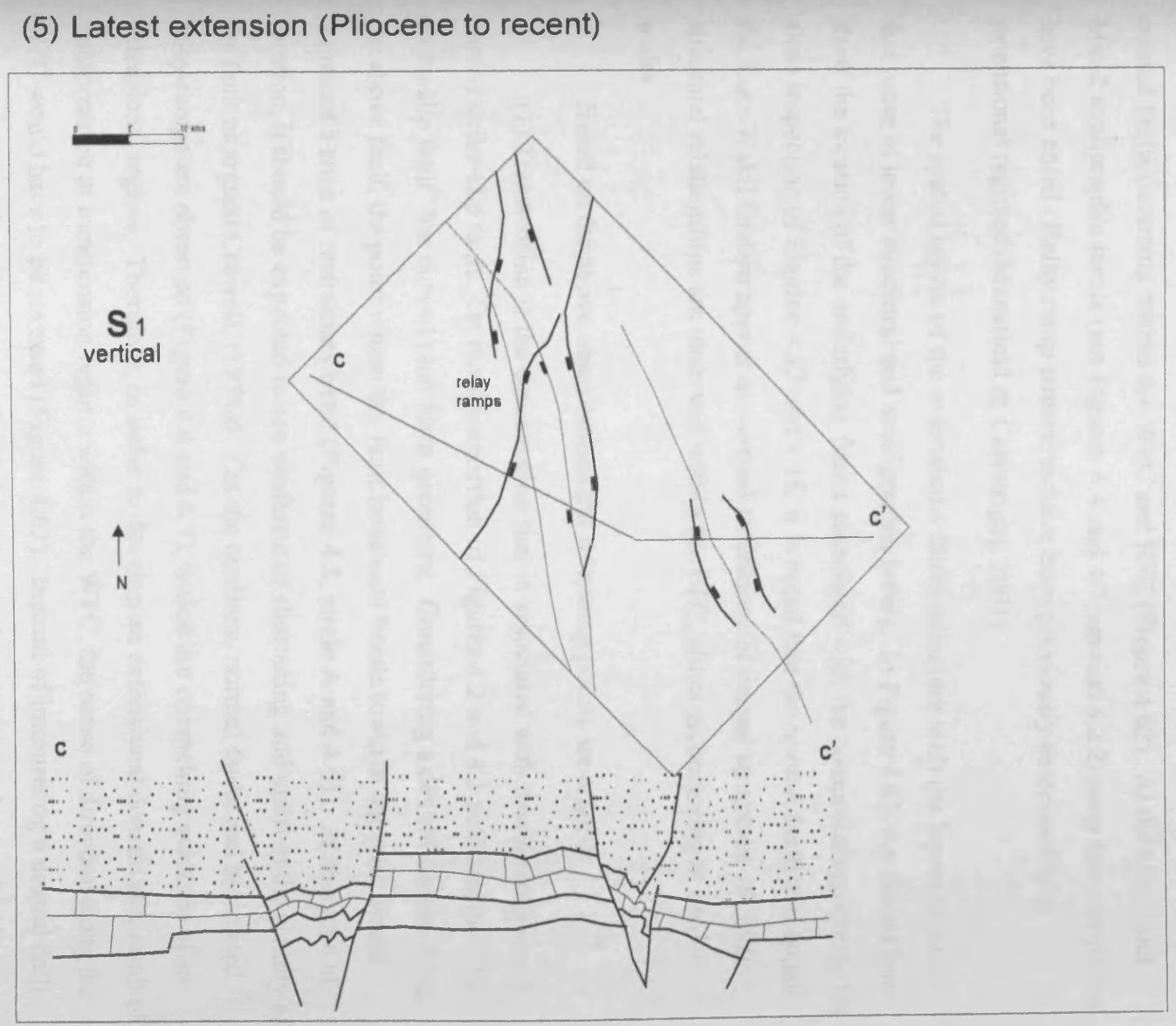

Figure 4.62
Geologic sketch for the structural evolution stage 5: Late mild extension. Development of normal faults and associated relay ramp structures. Occurring directly above the WFC and EFC.

Here a mild late extensional event is interpreted that resulted in the propagation of normal faults occurring within the WFC and EFC (Figure 4.62). At the Mio-1 and Mio-2 stratigraphic levels (see Figures 4.4 and 4.7; section 4.2.2) relay ramp structures have been noted. Relay ramp structures have been previously associated with extensional regimes (Mansfield & Cartwright, 2001).

The spatial layout of the extensional faults coincides with the layout of faults that occur at lower structural and stratigraphic levels. In Figure 4.62, the dashed lines show the location of the underlying faults associated with the compressional event. On close inspection of Figures 4.17 and 4.18, it is noted that the normal faults that bound the Kutz-Wakil Graben appear as vertical extensions of deeper structures. Similar structural relationships are observed within the EFC, although occurring at smaller scales.

Based on the above observations the following points are argued:

(1) Transtension is the deformation that is associated with movement along a curved strike-slip fault. On close inspection of Figures 4.2 and 4.3 note that the "Akal strike-slip fault" has curved plan form geometry. Considering a dextral motion along the above fault, the point where the fault lineament bends towards the west would represent a zone of restraining bend (Figures 4.3, circle A and 4.63). At this type of location, it should be expected to see evidence of shortening and uplift in the vicinity of the fault as argued Crowell, (1974a). On the contrary, normal faults and associated relay-ramps are observed (Figure 4.4 and 4.7), which are compelling evidence of an extensional regime. Therefore, in order to develop an extensional domain as a result of transpression or transtension regime within the WFC, the sense of direction along the WFC would have to be reversed (Figure 4.63). Instead of interpreting a dextral fault system, a sinistral one is suggested. In this structural scenario, a releasing bend is formed at the same location resulting in an overall extension of the terrain, where the Kutz-Wakil Graben is developed (see Section 4.2.2.1).

(2) A pure extensional structural scenario is also considered a possibility. Based on the structural configuration of the Kutz-Wakil Graben at the Mio-1 and Mio-2 seismic horizons, an east – west extension would be the reasonable interpretation

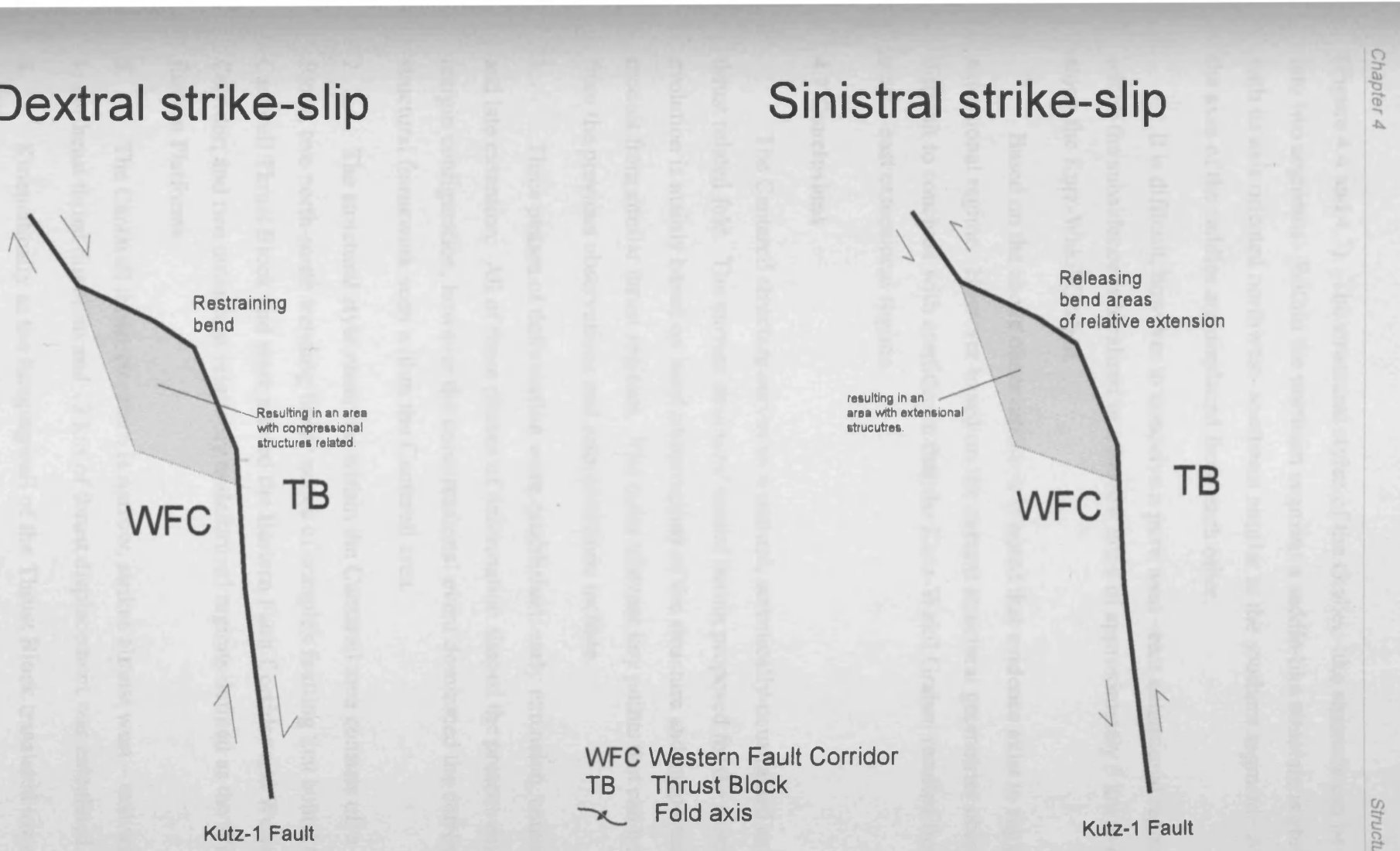

Figure 4.63
Two structural scenarios: synistral and dextral strike slip fault systems and associated structures, after, Christie-Blick and Buddle, 1985.

(Figure 4.4 and 4.7). The structural styles of the Graben-like structure can be separated into two segments. Within the northern segment a saddle-like structure is observed with its axis oriented northwest- southeast similar to the southern segment. Although the axes of the saddles are displaced from each other.

It is difficult, however to conceive a pure west –east extensional regime in which the subsidence is localised in a narrow zone of approximately 5 km as observed along the Kutz-Wakil Graben.

Based on the above observations it is noted that evidence exist to suggest an extensional regime. However based on the current structural geometries observed it is difficult to conclude with confidence that the Kutz-Wakil Graben resulted from a pure west – east extensional regime.

4.7 Conclusions

The Cantarell structure serves as a natural, seismically-constrained example of a thrust related fold. The current structural model herein proposed for the tectonic evolution is mainly based on local observations of the structure and supported by models from similar thrust regimes. The most relevant key points that can be addressed from the previous observations and interpretations include:

1. Three phases of deformation were established: early extension, compression and late extension. All of these phases of deformation shaped the present-day basin margin configuration, however the compressional event dominated the current structural framework seen within the Cantarell area.

2. The structural style observed within the Cantarell area consists of: a Thrust Block, two north-south trending linear zones of complex faulting that bound the Cantarell Thrust Block and were named the Eastern Fault Corridor and Western Fault Corridor; and two outermost relatively undeformed regions defined as the Western and Eastern Platforms.

3. The Cantarell thrust structure is narrow, strikes almost west – east with a north to northeast thrust direction and 12 km of thrust displacement was calculated.

4. Kinematically as the hangingwall of the Thrust Block translated towards the north the Western and Eastern Fault Corridors were seeded as a result of the differential

motion and shortening of the main hangingwall fold with respect to the Nohoch Nose and where the velocity differential was accommodated by the WFC and EFC.

Chapter 5

Kinematics of the main compressional phase of deformation

5.1 Introduction

This Chapter will present a kinematical model for the compressive phase of deformation that developed the Thrust Block situated in the Cantarell area. As previously discussed in Chapter 4, three main tectonic events are recognised as having affected the study area (early extension, compression and late extension). The compressional event controlled to a large extent the structural framework as observed today. As previously described, these consist of a thrust related fold structure bounded by tear faults and these structures dominate the area. The geometry observed in cross sections oriented north-south through the Thrust Block exhibit characteristics analogous to fault-bend fold structures (Suppe, 1983). However, as discussed earlier in Chapter 4 other structural mechanisms (faulted detachment folding and fault propagation folding) can be attributed to the kinematics of the structure. The main objective of this chapter is to document and discuss the structural kinematics involved during the development of the thrust structure through the analysis of the stratal configuration within the syn-tectonic interval complemented with an analysis of the structural relief of the structure.

Constraints on the kinematics of fault related folds can be derived by the following methods: (1) analysis of growth stratal patterns (Poblet and Hardy, 1995; Poblet et al., 1998; Schneider et al., 1996; Butler and Lickorish, 1997) (2) estimating uplift, shortening and/or limb dip values through time from the studies of growth terraces (Rockwell et al., 1988; Molnar et al., 1994; Nicol et al., 1994), (3) sequential restoration of syn-sedimentary strata (DeCelles et al., 1991; Bloch et al., 1997; Suppe et al., 1993; Vergés et al., 1996; Ford et al., 1997; Suppe et al., 1997), (4) paleomagnetism of syn-tectonic unconformities (Holl and Anastasio, 1993). In most of these studies it is assumed that deformation rate for different time intervals was continuous through time. Studies on fold kinematics (Shaw and Suppe, 1994), syn-tectonic unconformities

(e. g. Barnes, 1996), throw along fault scarps (Kelson et al., 1996), terraces and alluvial fan ridges (Muller, 1997) have all suggested that the growth of some natural fault-related folds can be attributed to geologically instantaneous events induced by earthquake related slip on active faults. The formation and amplification of natural fault related folds during well dated earthquakes has been well documented (Yielding et al., 1981; Stein and King, 1984; Klinger and Rockwell, 1989; Lin and Stein, 1989; Phillip et al., 1992; Berberian and Qorashi, 1994). Their observations raised the question of whether deformation occurs as a continuous or a discontinuous process. Suppe (1997) suggested that the periods of deformation and non-deformational events might be geologically instantaneous or steady during a given period of time. Considering rates of structural deformation and folding as either continuous or discontinuous would result in different syn-tectonic sedimentation patterns. Hence the analysis of the syn-tectonic geometries and patterns provide considerable insights into rates and modes of structural deformation.

Sedimentation coeval with the structural growth of the Cantarell area provides an excellent opportunity to study the relationships between sedimentation and thrust and fold development through time. Geometries of growth strata reflect the distribution of accommodation space, where the accommodation space is a function of (1) tectonic uplift, (2) local/regional base level change, (3) style of deformation, and (4) various sedimentological processes such as erosion and / or deposition (Bernal and Hardy, 2000). In consequence the analysis of syn-tectonic strata provides insights into the rates of structural deformation and uplift that can provide critical evidence on whether the deformation is continuous or discontinuous, as previously discussed.

5.2 Data and Methods

Chapter 4 documented the structural characteristics of the Cantarell structure based on an OBC (Ocean Bottom Cable) 3D seismic survey. During August of 2004, the IMP (Instituto Mexicano del Petroleo) made available another 3D seismic survey for interpretation in this thesis. This later seismic survey consists of a streamer data set which was the first survey acquired by Pemex over part of the Cantarell structure (Figure 5.1). The seismic quality throughout the Upper Tertiary is considerably better than for the OBC survey (Figure 5.2). Unfortunately the areal extent of the streamer data set does not cover the entire structural framework that was defined using the OBC data (Figure 5.2). A further limitation is the location of the production

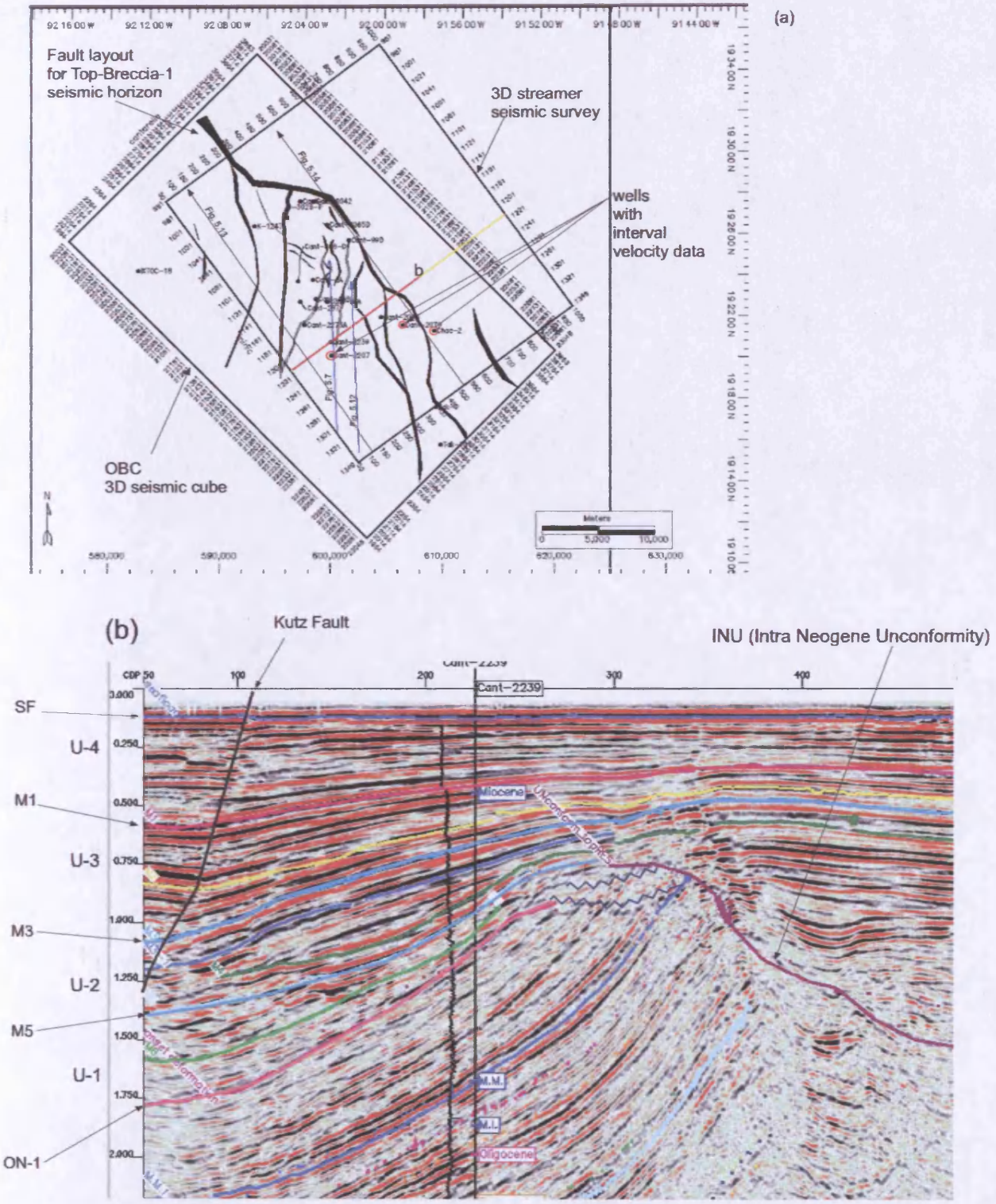

Figure 5.1
Location map (a) and seismic profile showing the seismic horizons interpreted within the syn-tectonic interval (b).

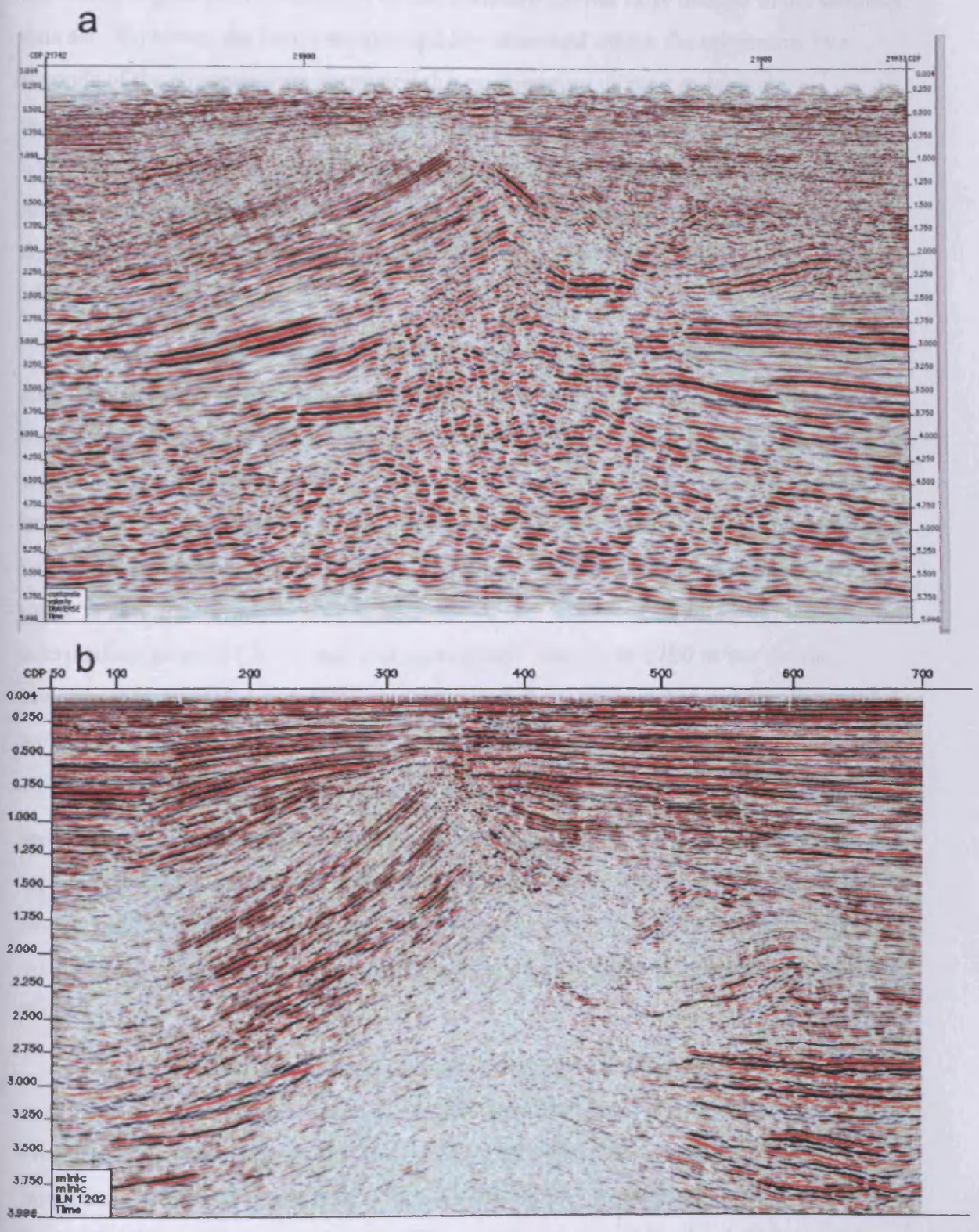

Figure 5.2
Seismic tracks identically oriented of different seismic surveys. (a) Ocean Bottom Cable (OBC) survey and (b) streamer survey that was provided on August of 2004. Note that in the OBC data the deeper structure is better imaged than in the streamer data set.

platforms which prohibited imaging the full extent of the streamer survey. In particular the crestal region and the forelimb of the structure are not fully imaged in the streamer data set. However, the better seismic quality observed within the uppermost two seconds of the streamer data permitted the examination of the syn-tectonic sedimentation associated with the fault-related fold structure of Cantarell, especially within the backlimb and the southernmost region of the crestal region. None of the boreholes and completion logs that penetrate the syn-tectonic package provides a detailed lithologic or stratigraphic description that allowed the lithological calibration of the syn-tectonic interval.

Check-shot data from wells C-2207 and C-2079 that penetrated the syn-tectonic strata at various locations (Figure 5.1) are employed to constrain the interval velocity within the syn-tectonic strata. The syn-tectonic strata are found to occur approximately within a depth interval of 0 sec to 1.6 sec TWT (Figures 5.1). Based on the plotted interval velocities versus depth (Figures 5.3 and 5.4), the following average interval velocities were employed for depth conversion: an average interval velocity of 1800 m/sec is used for the uppermost interval (0 - .5 sec TWT); 2000 m/sec for the intermediate interval (.5 – 1 sec) and an average velocity of 2200 m/sec for the lowermost interval (> 1 sec TWT; see Section 5.5.1, Tables 5.1 to 5.3 and Figures 5.3 and 5.4).

In this Chapter, the syn-tectonic processes of sedimentation and structural uplift are investigated using: (1) the morphology of seismic reflections found within the syn-tectonic package (Poblet and Hardy, 1995; Poblet et al., 1998; Schnider et al., 1996; Bernal and Hardy, 2002) and complemented by (2) the analysis of relative uplift based on the structural relief observed at different geological times (Masaferro et al., 1999 & 2002).

The seismic reflection configuration of the syn-tectonic strata have been documented and analysed in order to obtain insights on how the structure proceeded kinematically. Four seismic horizons (ON-1, M5, M-3, M-1 and SF) have been interpreted within the syn-tectonic package throughout the seismic data. These defined four Units (U1 to U4; Figure 5.1, b). The criteria employed for the definition of the seismic horizons is based primarily on the seismic continuity and the gross geometry and internal seismic configuration of the syn-tectonic units. The stratigraphic situation of these horizons with the regional context is illustrated in Table 5.2b.

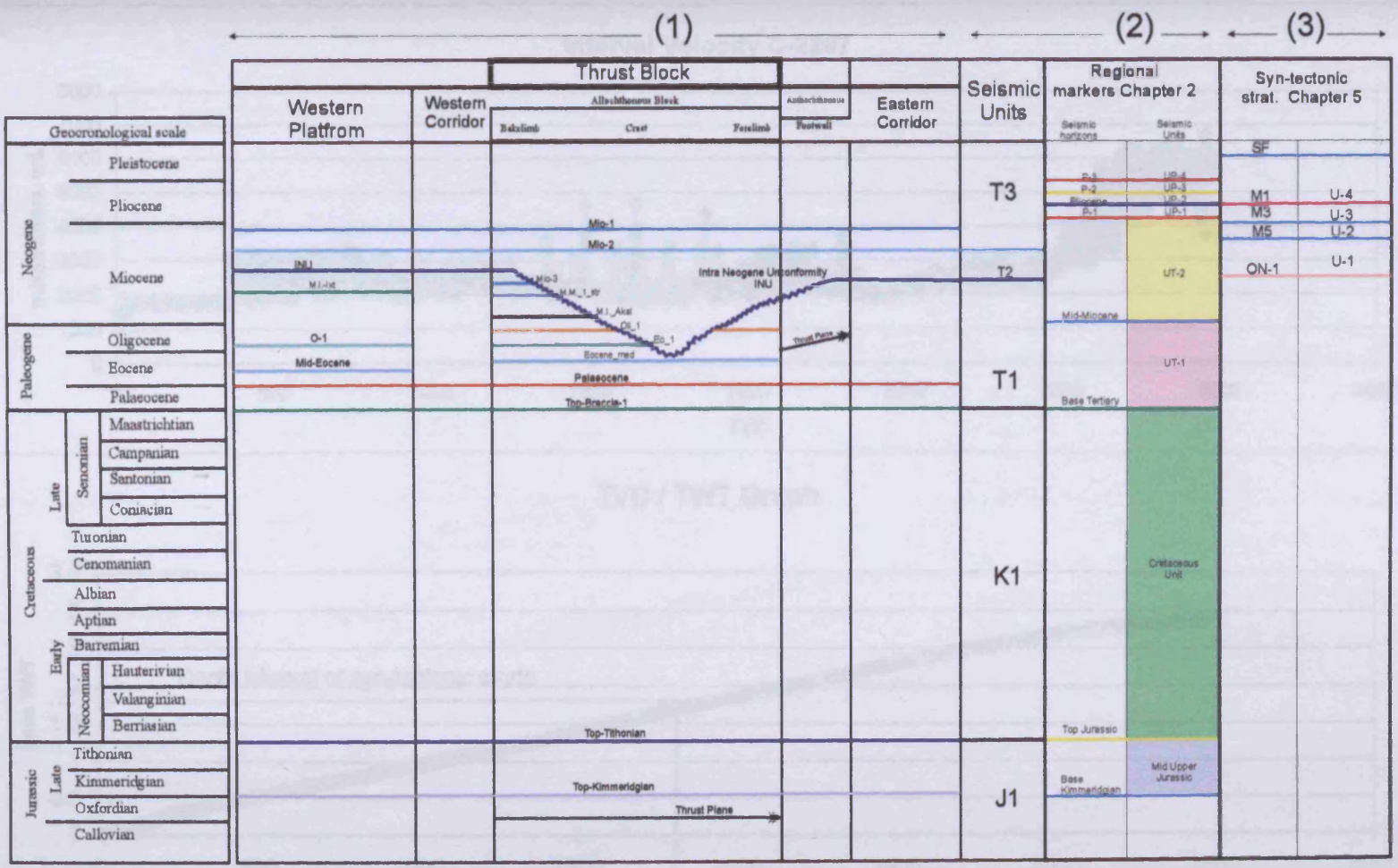

Table 5.1a
Stratigraphic chart for the Cantarell area, showing the interpreted seismic horizons and their chronostratigraphic significance for the horizons interpteted at various scales: (1) 3D seismic survey, (2) the regional scale and (3) for the syn-tectonic interval.

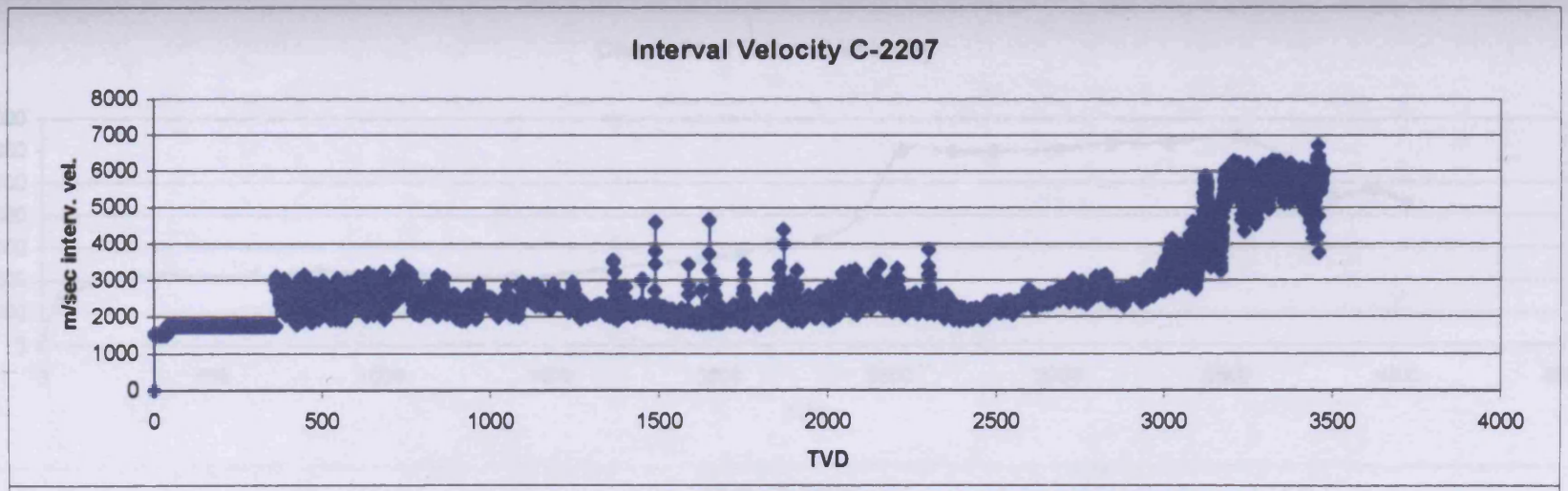

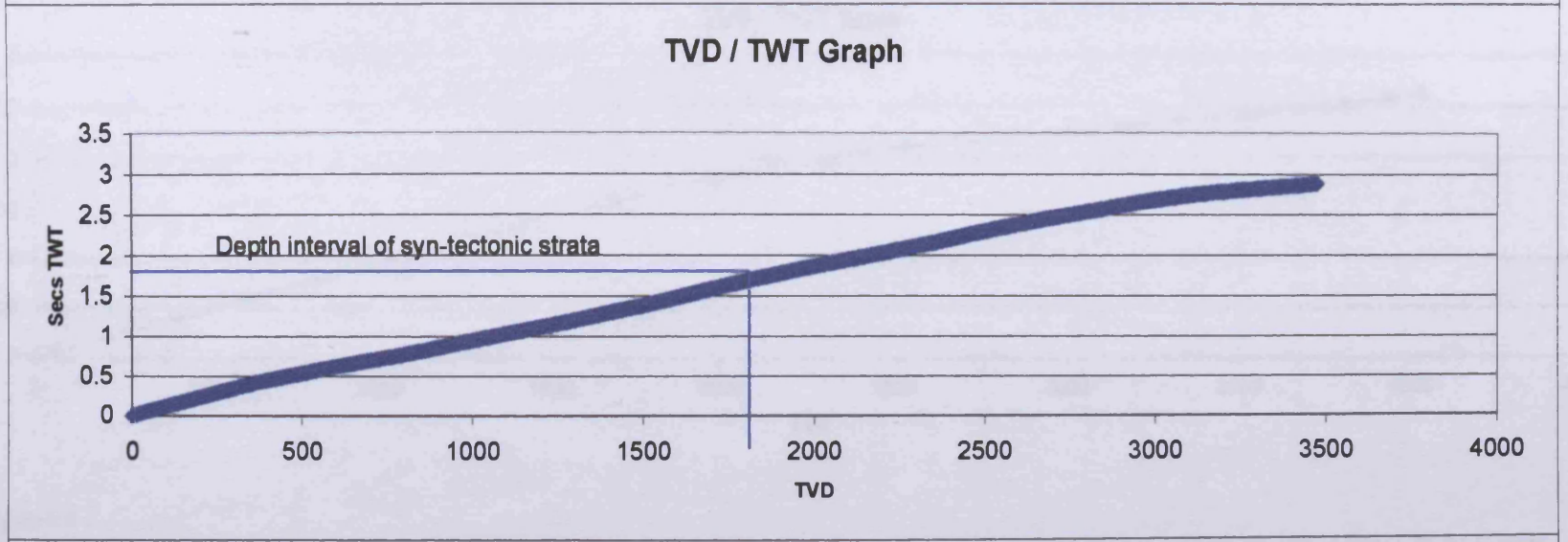

Figure 5.3
Interval velocity and TWT / TVD table of well C-2207, for location see Figure 5.1. Note the depth interval at which the syn-tectonic strata occurs. The average interval velocity calculated for this interval is from 2500 m/sec to 2000 m/sec.

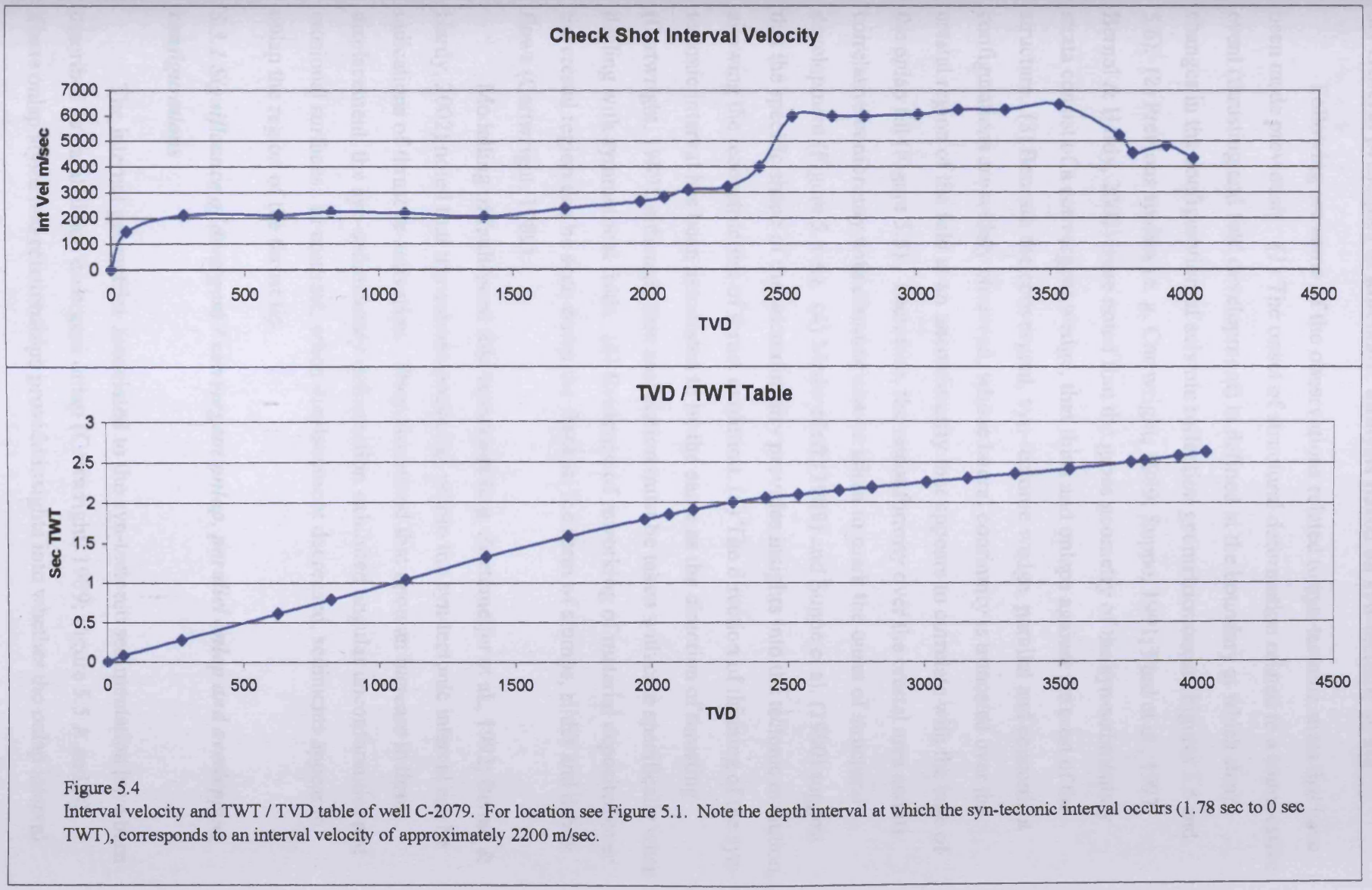

Figure 5.4
Interval velocity and TWT / TVD table of well C-2079. For location see Figure 5.1. Note the depth interval at which the syn-tectonic interval occurs (1.78 sec to 0 sec TWT), corresponds to an interval velocity of approximately 2200 m/sec.

5.3 General principles of kinematic analysis based on syn-tectonic strata

Following are some of the observations related to syn-tectonic strata that have been made previously: (1) The onset of structural deformation related to a compressive event (thrusting and fold development) is defined at the boundary at which sharp changes in the configuration of seismic reflection geometries occur (Figures 5.5 and 5.6). (2) Previous studies (e. g. Cartwright, 1989; Suppe, 1991; Ford et al., 1997; Bernal & Hardy, 2002) have noted that the gross geometry of the syn-sedimentary strata consist of a convergent wedge, that thins and onlaps against the crest of the structure. (3) Beneath the convergent, syn-tectonic wedge, parallel and concordant configurations are widely observed, whose lateral continuity is truncated over the crestal region of the fold at an unconformity that appears to correlate with the base of the onlap fill (Figure 5.5). Therefore, the unconformity over the crestal area and its correlative conformity with distance can be taken to mark the onset of structural development (Figure 5.5 A). (4) Medwedeff (1989) and Suppe et al. (1990) suggest that the specific shape of the unconformity provides insights into the tectonic evolution, allowing the reconstruction of thrust evolution. (5) The direction of thinning of the syn-tectonic interval has been associated to be the same as the direction of thrusting (Cartwright, 1989), although, this association must be taken with care specifically when dealing with symmetrical folds. (6) Evidence of reworking of material deposited over the crestal region can be seen down the flank in the form of slumps, slides and debris flows (Cartwright, 1989).

Modelling of fault-bend fold structures (e.g. Zoetemeijer et al., 1992; Bernal & Hardy, 2002) noted that truncations occurring within the syn-tectonic interval can be indications of thrust re-activation. They also noted that upon an increase in thrust displacement, the syn-sedimentary deformation exhibited angular unconformities and erosional surfaces. In contrast, when displacement decreased, sediments appear to onlap the region of the thrust tip.

5.3.1 Significance of divergent / convergent onlap, parallel onlap and overlapping configurations

The internal geometries associated to the syn-tectonic sedimentation have been described as parallel and divergent onlap (Cartwright, 1989; Figure 5.5 A and B). These onlap styles and relationships provide insights into whether the onlap interval

(A) General seismic reflection configuration of a growth fold pre-, syn, and post-tectonic units.

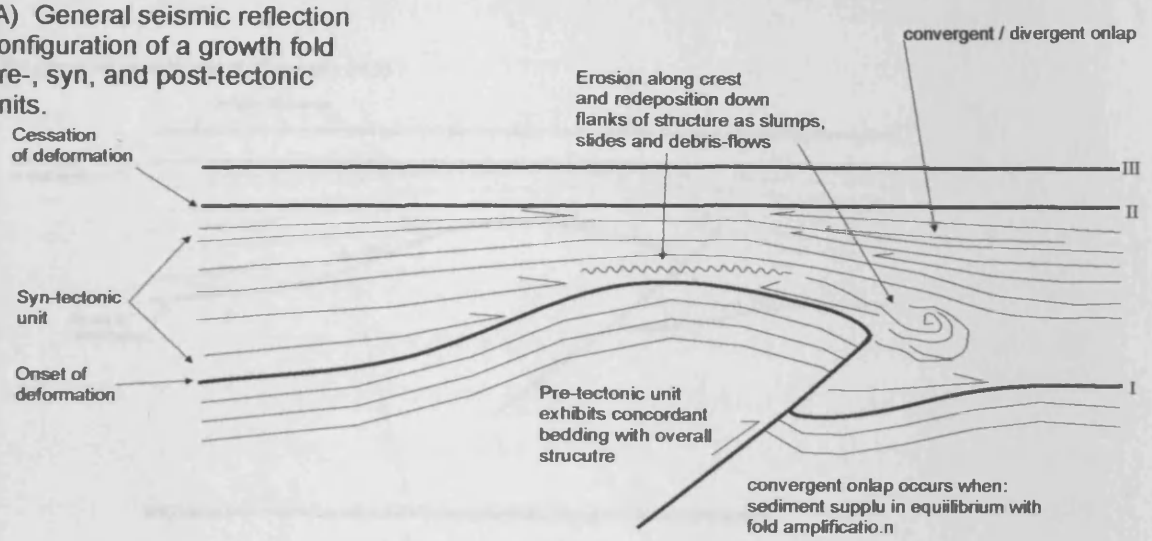

(B) Cessation of compression under pelagic drape sedimentation

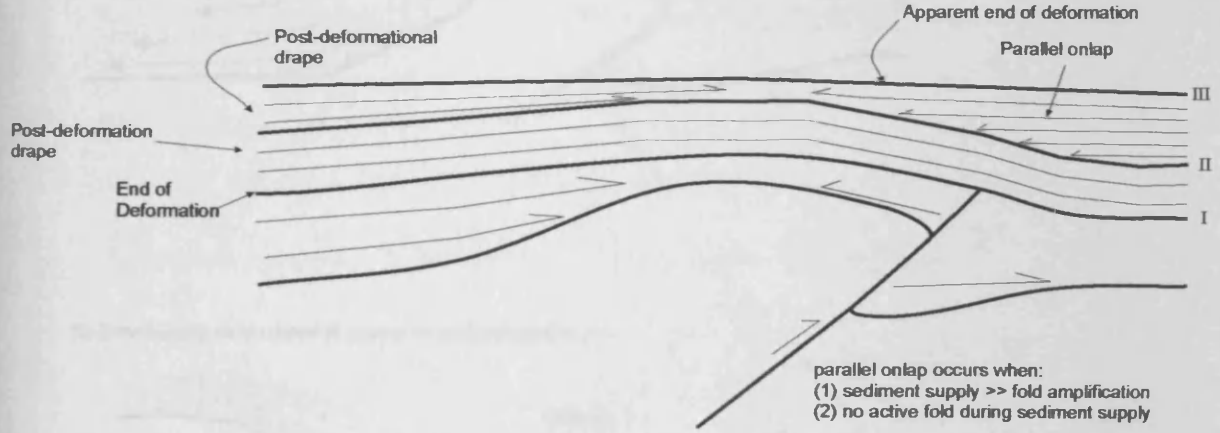

(C) End of compression under non -pelagic deposition

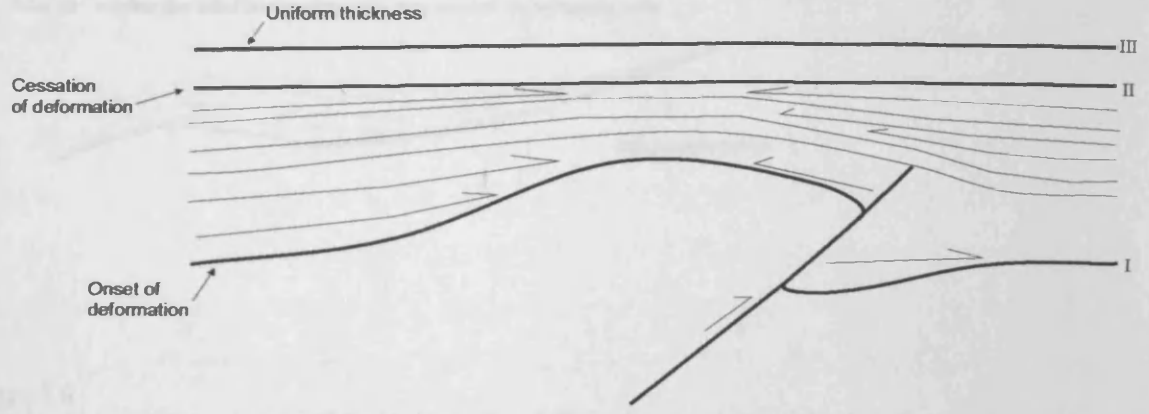

Figure 5.5
Sketched illustrating the different syn-tectonic reflections configurations related to structural growth, or fold amplification. (A) Showing the different seismic reflections configurations patterns from the pre-tectonoic the syn-tectonic and post-tectonic units. (B) Example illustrating the cessation of fold amplification under a pelagic drape sedimentation. (C) End of compression under non-pelagic drape.

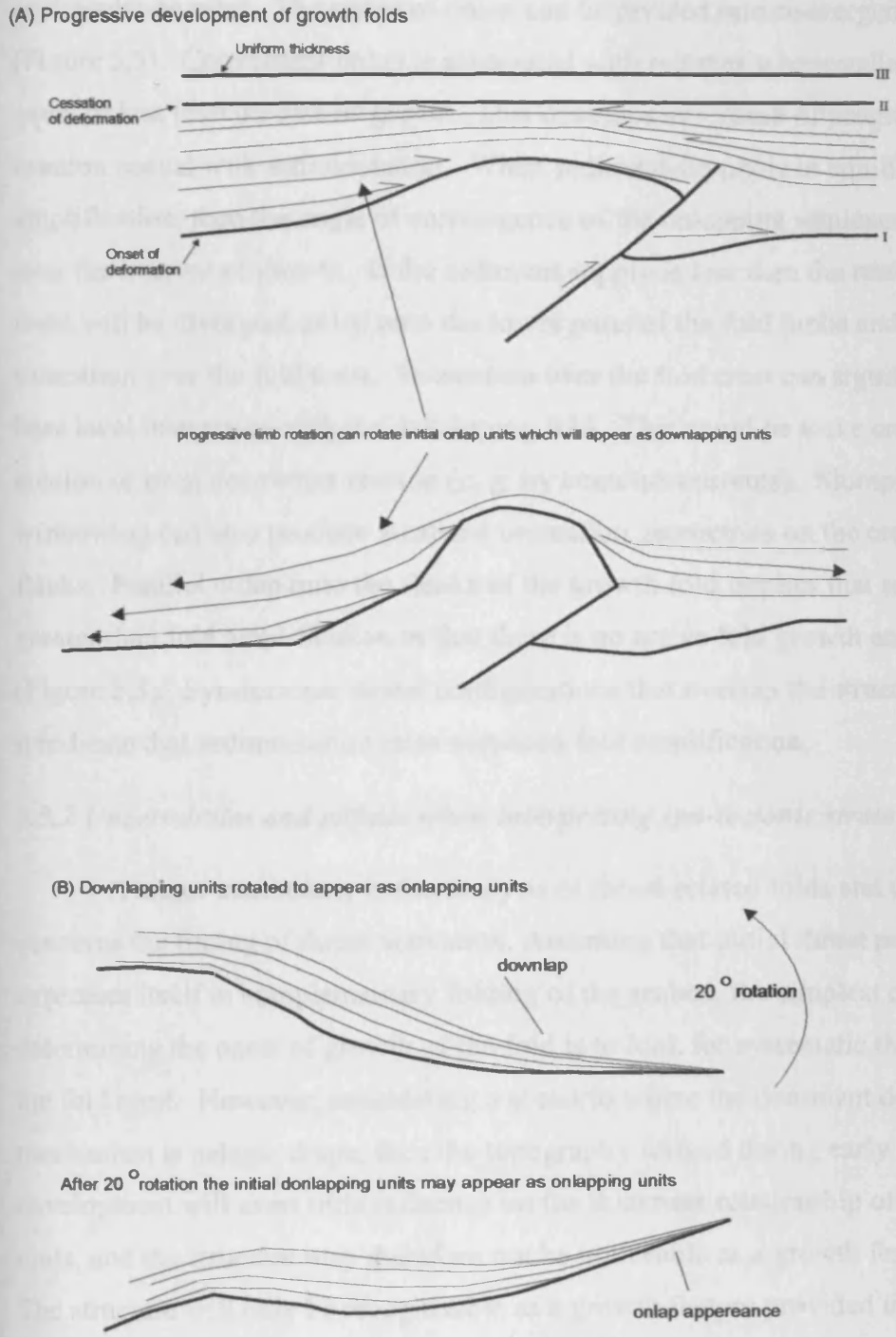

Figure 5.6
Diagram illustrating common pitfalls in the interpretation of syn-tectonic sediments in tectonic settings with progressive limb rotation (B). Where initial onlapping units may become rotated to a position where in their final configuration they may resemble downlapping units, and conversely downlap units can be rotated into onlapping units.

was deposited during or after the deformation occurred and also help constrain the sedimentation rates. The styles of onlap can be divided into convergent and parallel (Figure 5.5). Convergent onlap is associated with regimes where sediment supply is equal or less than the rate of growth. This develops as a result of progressive limb rotation coeval with sedimentation. When sediment supply is in equilibrium with fold amplification, then the angle of convergence of the onlapping sequence will be constant over the interval of growth. If the sediment supply is less than the rate of growth, then there will be divergent onlap onto the lower parts of the fold limbs and there may be truncation over the fold crest. Truncation over the fold crest can signify some form of base level interaction with the developing fold. This could be wave erosion, subaerial erosion or even deepwater erosion (e. g. by contours currents). Slumping and winnowing can also produce localised truncation geometries on the crest or upper flanks. Parallel onlap onto the flanks of the growth fold implies that sediment supply is greater than fold amplification or that there is no active fold growth and limb rotation (Figure 5.5). Syn-tectonic stratal configurations that overlap the structure and thin over it indicate that sedimentation rates outpaced fold amplification.

5.3.2 Uncertainties and pitfalls when interpreting syn-tectonic strata

A major uncertainty in the analysis of thrust-related folds and their evolution concerns the timing of thrust activation. Assuming that initial thrust propagation expresses itself in complementary folding of the seabed, the simplest criteria for determining the onset of growth of the fold is to look for systematic thinning towards the fold crest. However, considering a scenario where the dominant depositional mechanism is pelagic drape, then the topography formed during early stages of fold development will exert little influence on the thickness relationship of the draping units, and the structure may therefore not be noticeable as a growth feature (Figure 5.5). The structure will only be recognisable as a growth feature provided the relief was great enough to induce failure of the drape units deposited on the limbs or if there was enhanced current reworking due to topographic effect (Figure 5.5). A second pitfall in the interpretation of syn-tectonic sediments relates to the progressive development of growth folds. The depositional surface is constantly changing shape and involves limb rotation. As a result of this limb rotation, onlapping units can be rotated to a position where in their final configuration they may resemble downlapping units and conversely downlap units can be rotated into onlapping units (Figures 5.6, B).

The culmination of the compressional activity is often characterised by stratigraphic uniformity across the site of the underlying structure. In the absence of any supporting data this is a reasonable approach, although pitfalls should be considered. Consider first a scenario in which structuring has terminated and the resultant depositional surface has a residual topographic relief inherited from the latest stage of compressional deformation (Figure 5.5, B, marker I). The next depositional stage is dominated by pelagic drape over the inactive structure. This drape would therefore result in a parallel bedded unit (Figure 5.5, B, marker II). Following the drape a period of turbidite deposition in which the remnant topography is onlapped. Looking at the final configuration (Figure 5.5, B) one could interpret that the marker for the end of the deformation is at marker III of Figure 5.5, B. However, as we know from the sequence of events, the real marker that defines the end of deformation is I, which is the base of the pelagic drape.

From the above it is noted that when interpreting syn-tectonic strata besides analysing the internal geometries and stratal configurations, external factors such as sedimentation rates, water depth, compaction rates and a general tectonic history must be taken into consideration, otherwise significant errors may occur in the interpretation.

5.4 Syn-tectonic strata associated with the Cantarell Thrust Block

5.4.1 Introduction

As previously mentioned (see Section 5.3), the syn-tectonic strata are characterised by general thinning against the structure. In Figure 5.7 it is observed that the unit beneath the ON-1 seismic horizon exhibits thinning against the structure, and divergent onlap can be slightly observed. However, above the seismic horizon ON-1 the internal seismic configurations and the thinning against the structure define an interval that can be interpreted as the syn-tectonic strata. The syn-tectonic package is divided into four Units (U1 to U4), defined by five seismic horizons (ON-1, M5, M-3, M-1 and SF). Further seismic horizons were interpreted within these units with the intention of highlighting interesting onlap geometries. As previously described (see Section 5.4.2), the seismic horizons were defined and correlated based principally on seismic continuity that allowed the areal correlation of each horizon among the 3D seismic survey. Isopach maps were calculated for each of the defined units

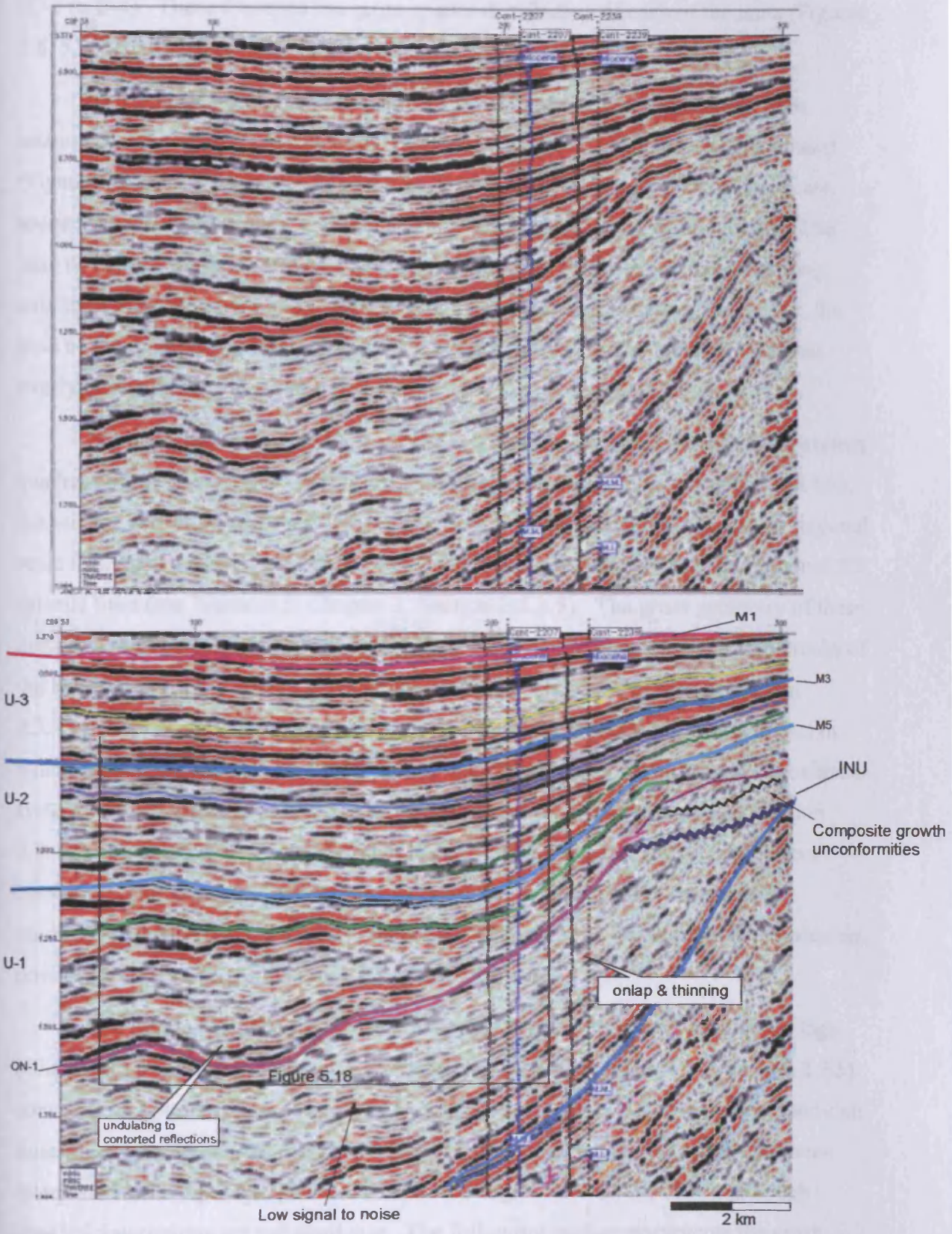

Figure 5.7
(A) Seismic line striking north-south along the backlimb of the Cantarell structure passing over the location of wells C-2207 and C-2239. See figure 5.1 for location. (B) Geological interpretation of seismic line showing the syn-tectonic sediments located at the backlimb of the structure. Zoom box shown in Figure 5.18.

(U-1 to U-4). These illustrate the gross spatial distribution of each of the units (Figures 5.8, 5.9, 5.10 and 5.11).

The general geometry of the entire syn-tectonic interval as observed from seismic profiles oriented north-south (Figures 5.7 and 5.12) and northwest-southeast (Figures 5.13 and 5.14), consists of a wedge that exhibits general thickness increase towards the south-southwest and thickness decrease towards the crestal region. The base of the syn-tectonic interval is seen as irregular, which is due to the underlying structural relief (Figure 5.14). From Figure 5.14 towards the southeastern sector, the base of the syn-tectonic interval is visible to the southeast of the Nohoch Nose just overlying the INU, where parallel seismic reflections onlap the Nohoch Nose.

From seismic sections oriented northwest southeast, located towards the eastern quadrant of the seismic survey (Figure 5.14), hosted principally in Units U-2 and U-3, the seismic reflection configurations exhibit a sigmoidal geometry. On a more regional scale this interval coincides with the UP-2 to UP-4 Units interpreted in the regional 2D seismic lines (see Transect 5; Chapter 2, Section 2.3.3.5). The gross geometry of these units in a regional scale is predominately sigmoidal. In Transect 1, the offlap breaks of the clinoforms appear almost horizontally and prograde basinwards (see Section 2.3.3.1). This suggests an exceptionally high rate of sediment input over a region in which accommodation space was quite limited, favouring a progradational depositional system with a predominant direction towards the north, and northwest (see Section 2.3.4.2). Thus it can be interpreted that the syn-tectonic strata are part of a system consisting of progradation and minor aggradation, where sediment supply was unidirectional (north to northwest) and deposited in a shallow water depth environment, possibly not exceeding 200 m (see Chapter 2, Section 2.3.4).

The lithology of the syn-tectonic strata as derived from well completion logs (Chac-1; Figure 3.10) and regional studies (Ricoy, 1989; see Chapter 2, Section 2.2.5) consist from bottom to top of marly shales, sandstones, bioclastic limestones, sand-rich limestone, with occasional conglomerates. The environment of deposition has been interpreted as hemipelagic (Pemex completion logs well C-2074, 1996), although detailed descriptions are not available. The following section documents the gross geometry of each of the units (U-1 to U-4) as well as their internal stratal configuration

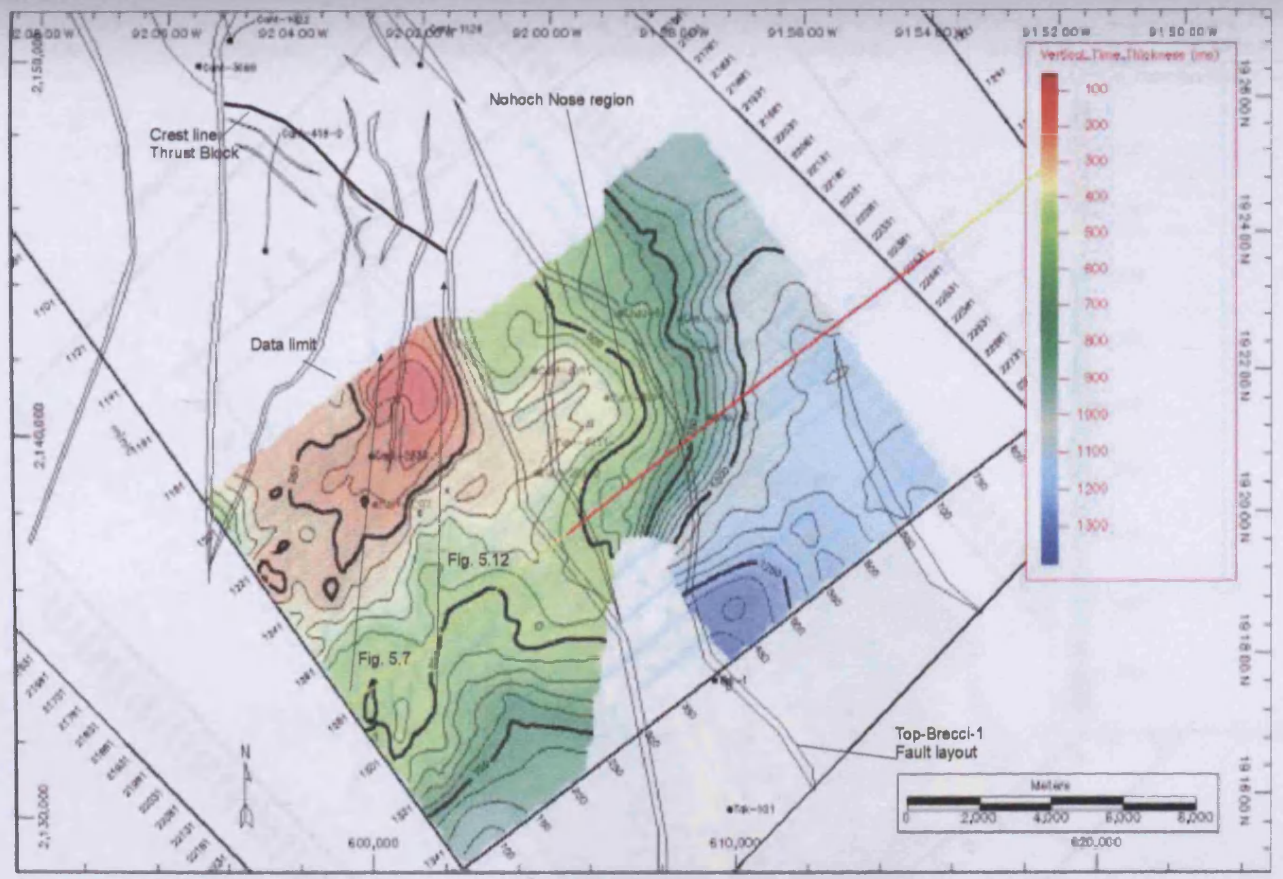

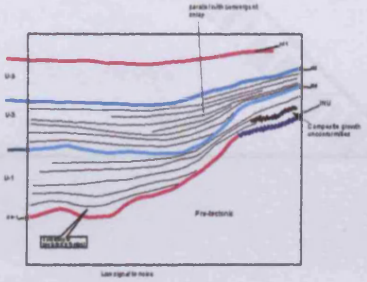

Sketch from Figure 5.7

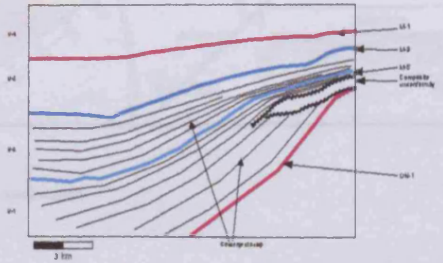

Sketch from Figure 5.12

Figure 5.8
Isopach map of Unit U-1 in meters. Fault layout of the Top-Breccia-1 level shown as thin black polygons.
Thickness ranged from 80 to 1500 msec TWT. Note that an overall thickness reduction occurs against the backlimb and towards the crestal region of the Thrust Block and against the Nohoch Nose.

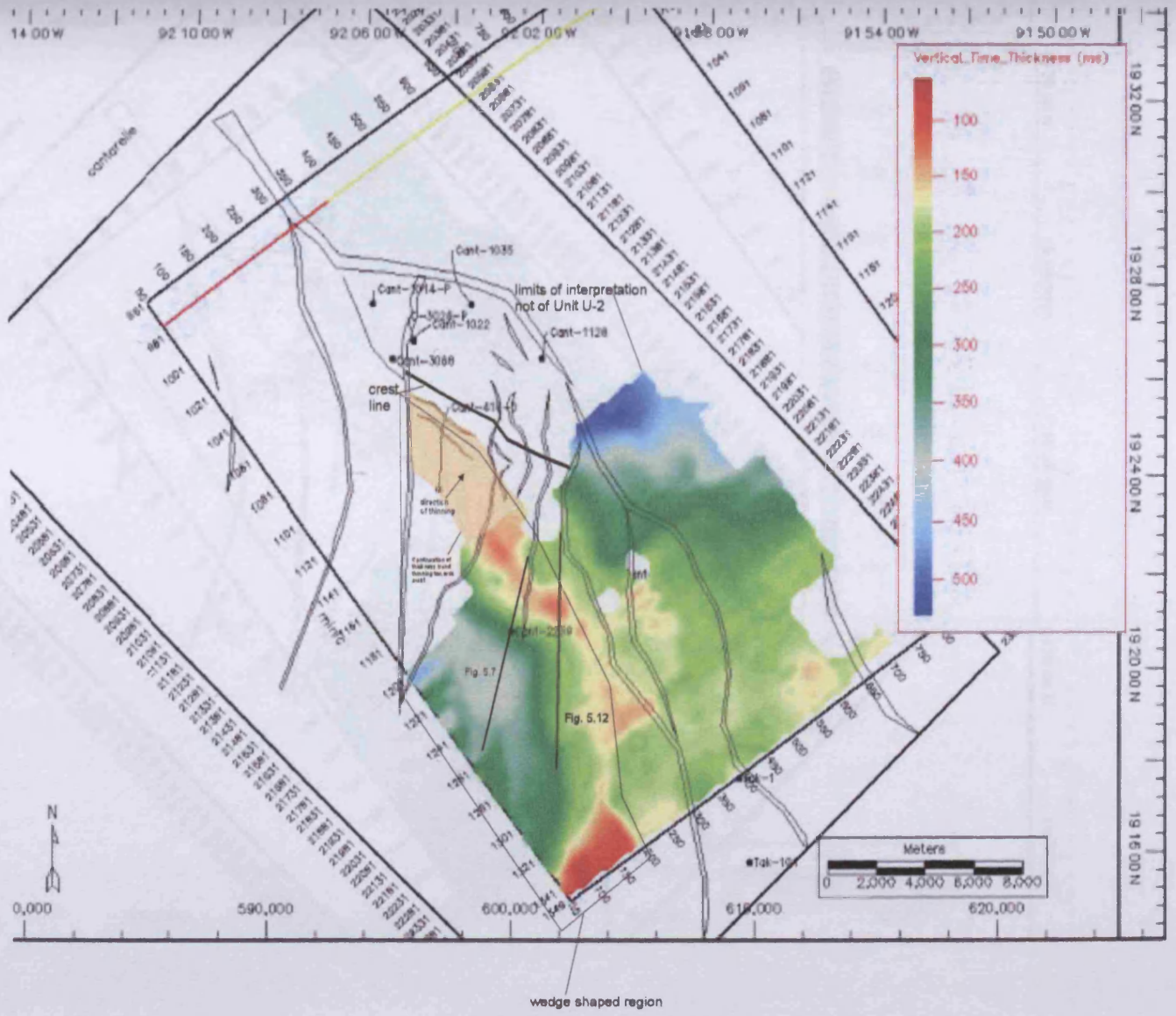

Figure 5.9
Vertical thickness map of Unit U-2 in meters. Fault layout of Horizon Top-Breccia-1 shown in thin black lines. Note that the isopach map is terminated towards the north due to data quality. However the actual occurrence of Unit U-2 prolongates towards the north.

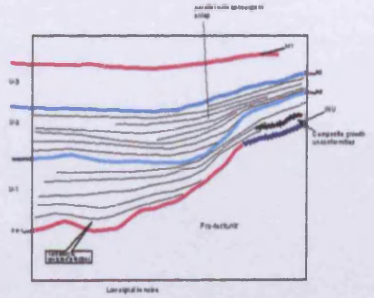

Sketch from Figure 5.7

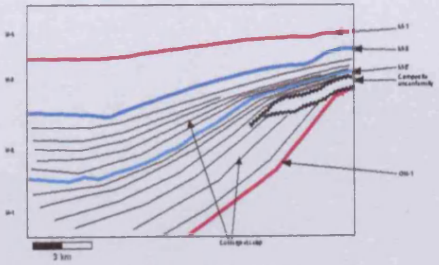

Sketch from Figure 5.12

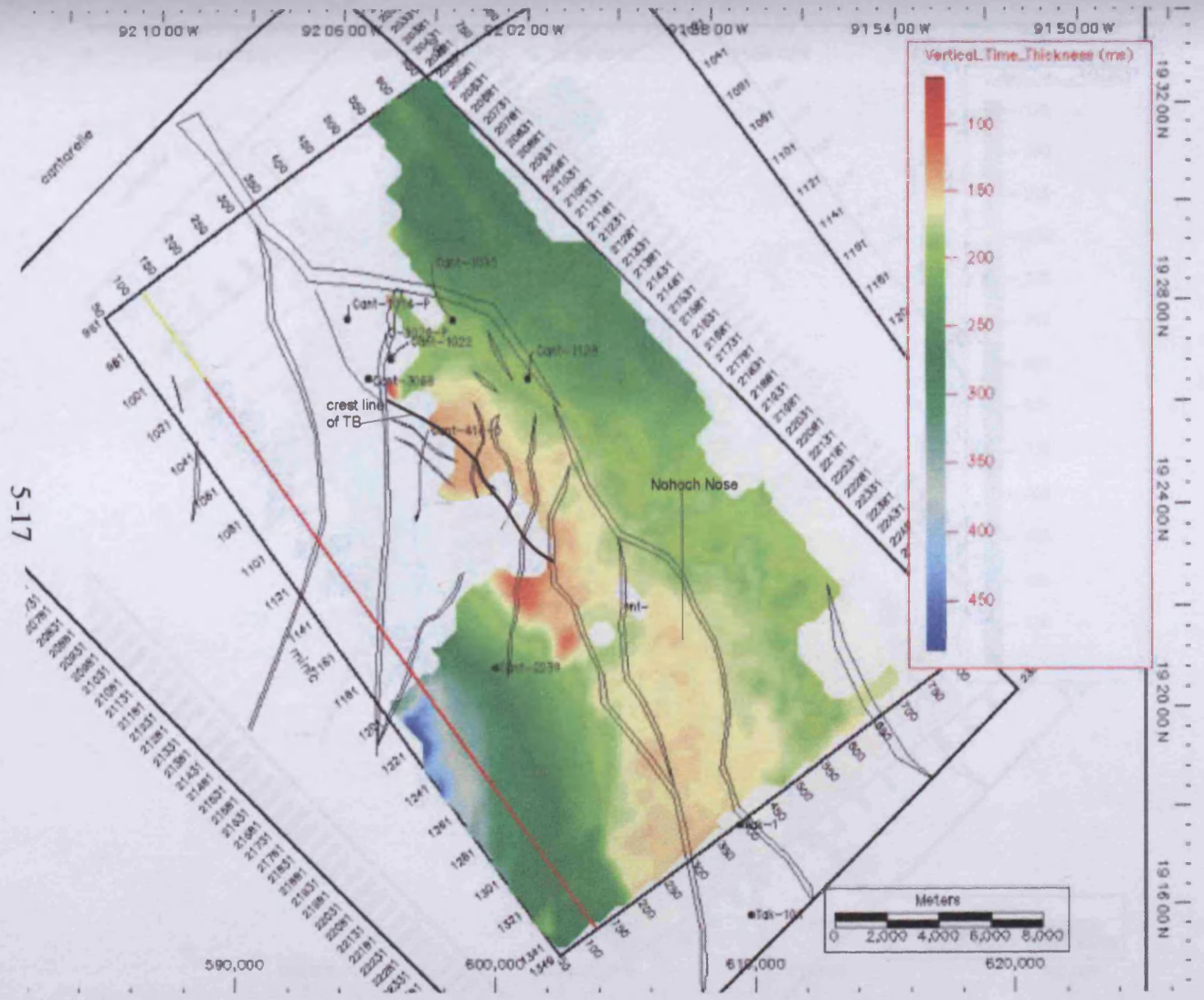

Figure 5.10
Vertical thickness map of Unit U-3 in meters. Fault layout of Horizon Top-Breccia-1 is shown as thin black lines.

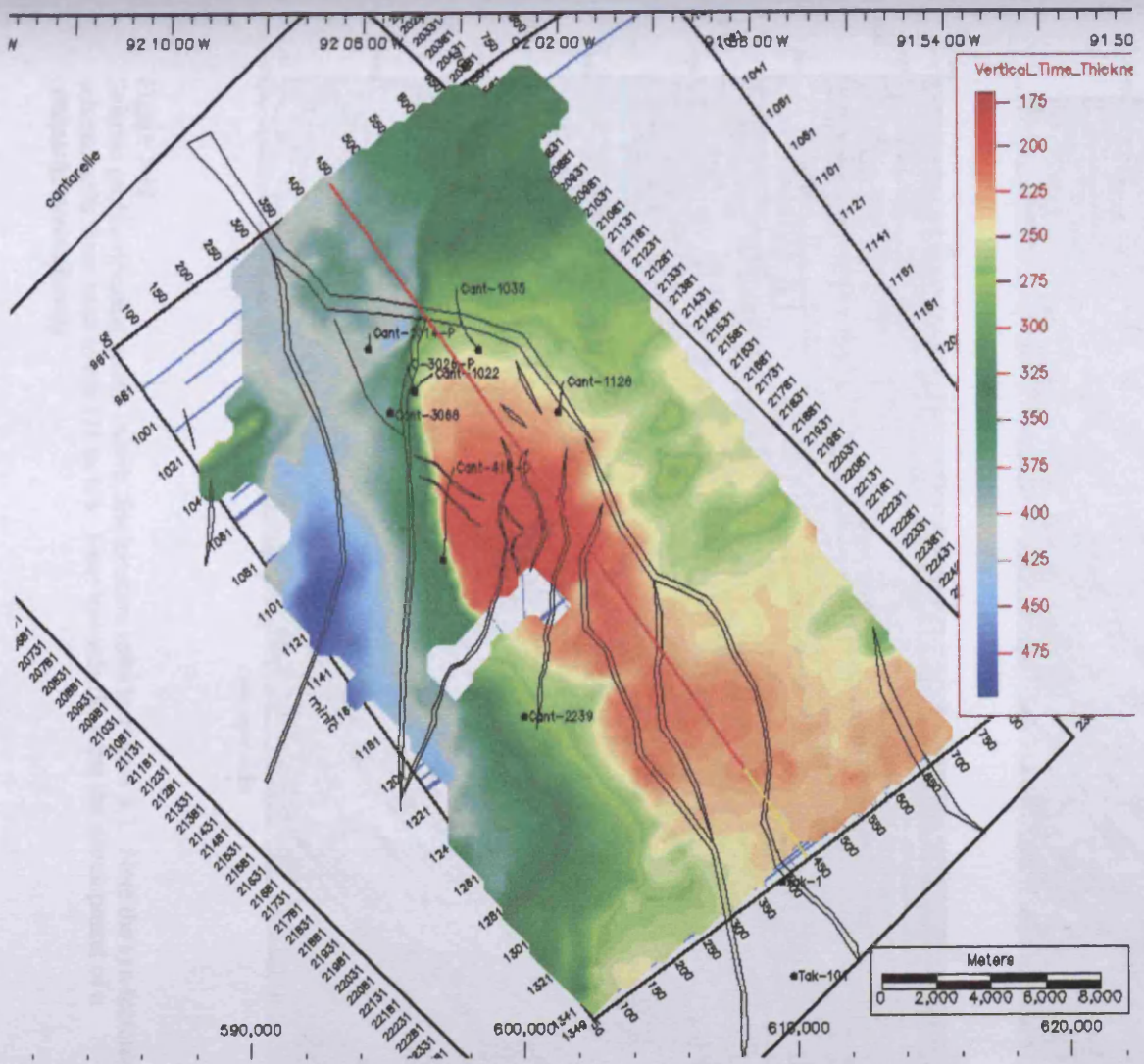

Figure 5.11
Vertical thickness map in msec TWT of Unit U-4. Fault layout of Horizon Top-Breccia-1 is shown in thin black lines.

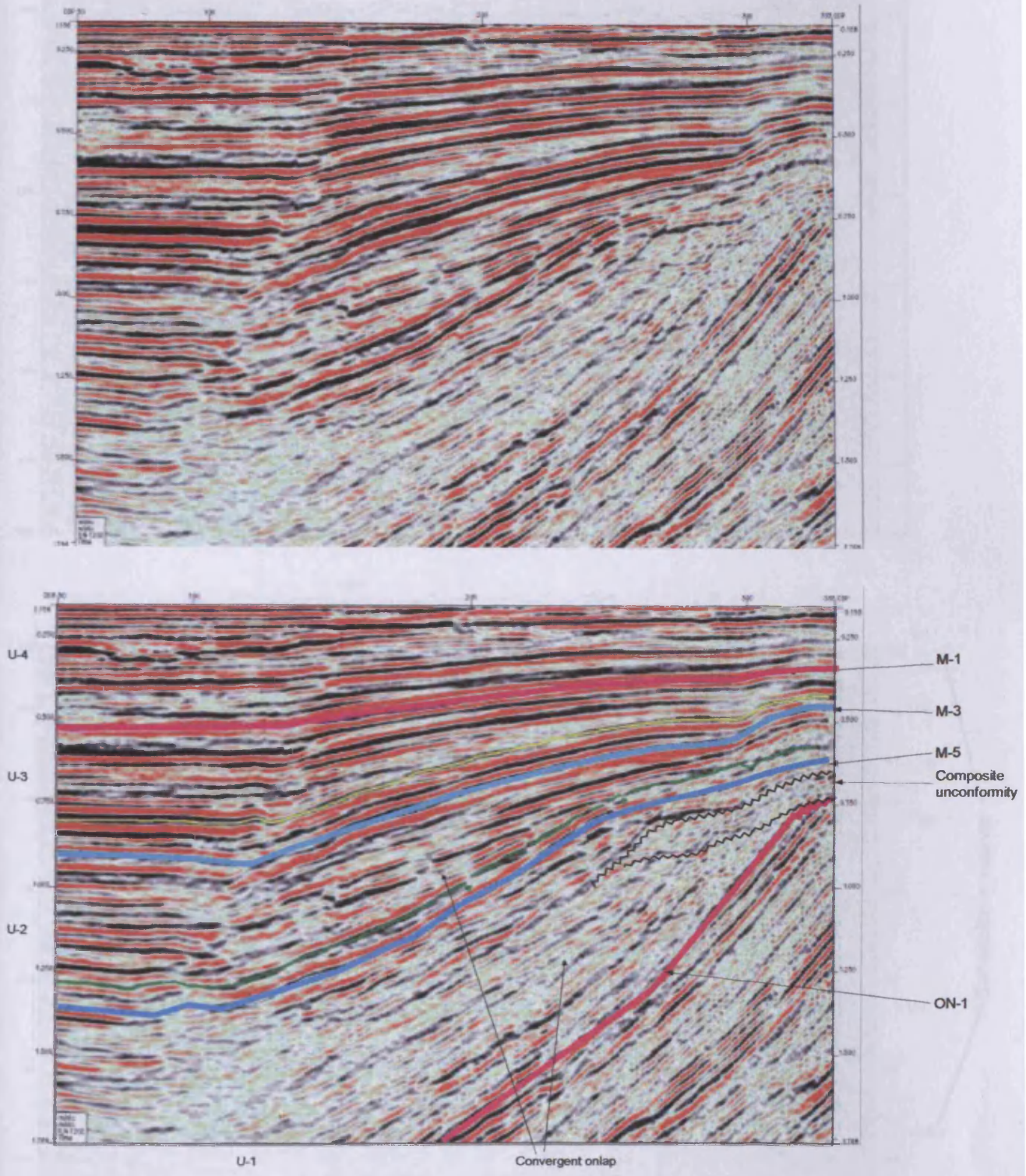

Figure 5.12
Seismic profile oriented south - north, for location refer to Figure 5.1. Note the syn-tectonic seismic units from base to top U1 to U4. Note towards the crest the development of a composite unconformity.

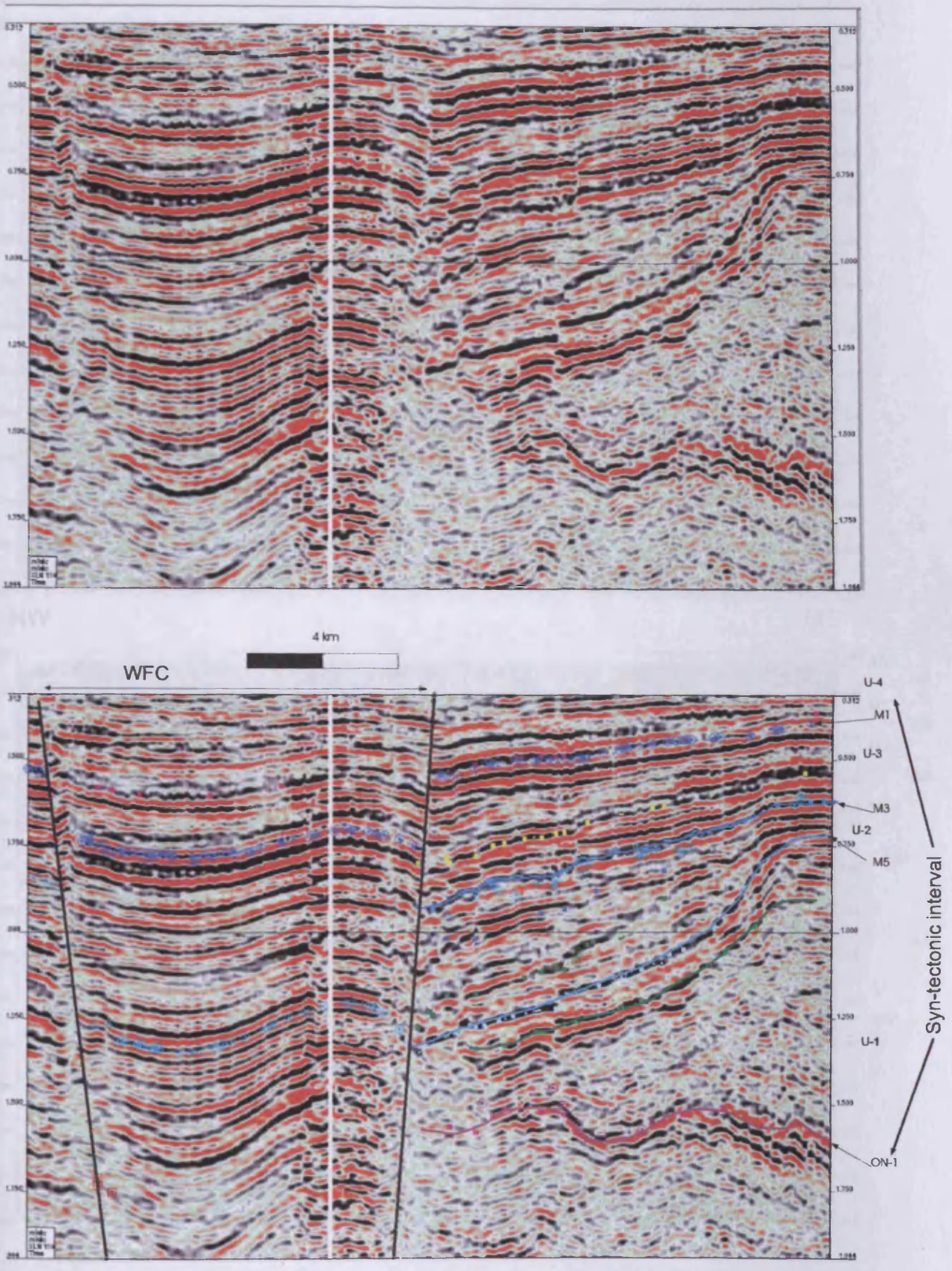

Figure 5.13
Uninterpreted (a) and interpreted (b) versions of seismic profile (location refer to Figure 5.1). Note the internal character of the syn-tectonic interval consists of sigmodidal configurations, progradational configurations, coincident with those observed in Transect 5.

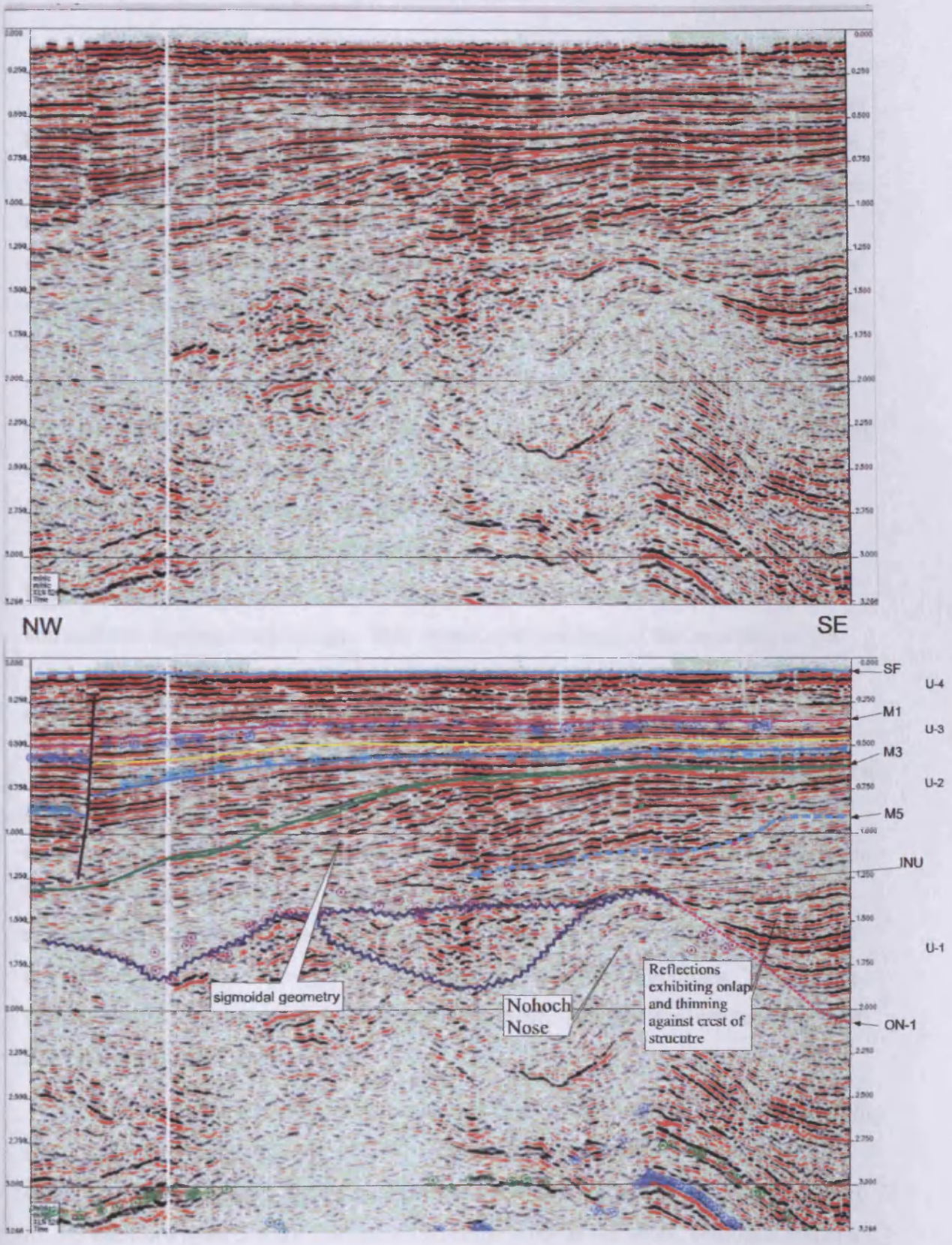

Figure 5.14
Seismic sections oriented northwest southeast, for location see Figure 5.1. The interpretation of the seismic Horizons ON-1 is inferred based on the onlapping reflections and the correlation with the INU. Note that Horizon M5 is absent due to the non correlation over the crest of the structure, see Figure 5.1. Note the syn-tectonic wedge against the Nohoch Nose onlapping over the ON-1 seismic horizon.

5.4.2 Morphological style of the syn-tectonic Units

5.4.2.1 Unit U-1

Unit U-1 is the lowermost unit of the syn-tectonic interval. It is bounded to the base by the Horizon ON-1 and to the top by Horizon M5. The areal extent of Horizon ON-1 interpreted within the southern region of the seismic survey (Figure 5.15), is seen to consist of three main areas. In the central part of Figure 5.15 an elongated region trending northwest is seen. This area corresponds to a high and flat topographic relief according to the contour lines of the interpolated map. This topographically high area coincides with the crestal areal extent of the INU (Figure 5.15). The central part is flanked to the northeast and the southwest by two more areally extensive regions that dip significantly. The region in the northeast exhibits a concave morphology according to its contour lines, and these are seen to become uniform in distance. The uniform region of the ON-1 Horizon occurs at the base of the Nohoch Nose, from where it steepens over it and passes laterally towards the crestal region into the Intra Neogene Unconformity (INU ; Figure 5.15). The region in the west consists of a more planar and uniform dipping morphology. This occurs over the base of the backlimb of the Thrust Block which steepens along the backlimb. Near the crest of the structure the ON-1 Horizon passes laterally into the INU (Figures 5.7, 5.12 and 5.15).

The top of Unit U-1, (Horizon M5), in plan-form is seen to consist of three main areas. In the central part of Figure 5.16a much more extensive elongated region trending northwest is noted. This area corresponds to a topographic high and is seen to broaden in a southeast direction (Figure 5.16). The central part is also flanked to the northeast and southwest by two regions that are less extensive than the ones observed in Figure 5.15. The southwestern region exhibits a convex morphology. The dipping surface exhibit approximately (7 °) towards the west. The northeastern region consists of a uniform shallow dipping area.

The thickness of Unit U-1 as calculated from subtracting the Horizons M5 from ON-1 range from 80 to 1500 msec TWT (Figure 5.8). With an average interval velocity of 2200 m/sec results in an approximate vertical thickness range of 88 to 1650 m. As seen in Figure 5.8 the thickness increases towards the south, southeast and to a minor extent towards the southwest sector. Significant thickness reduction occurs

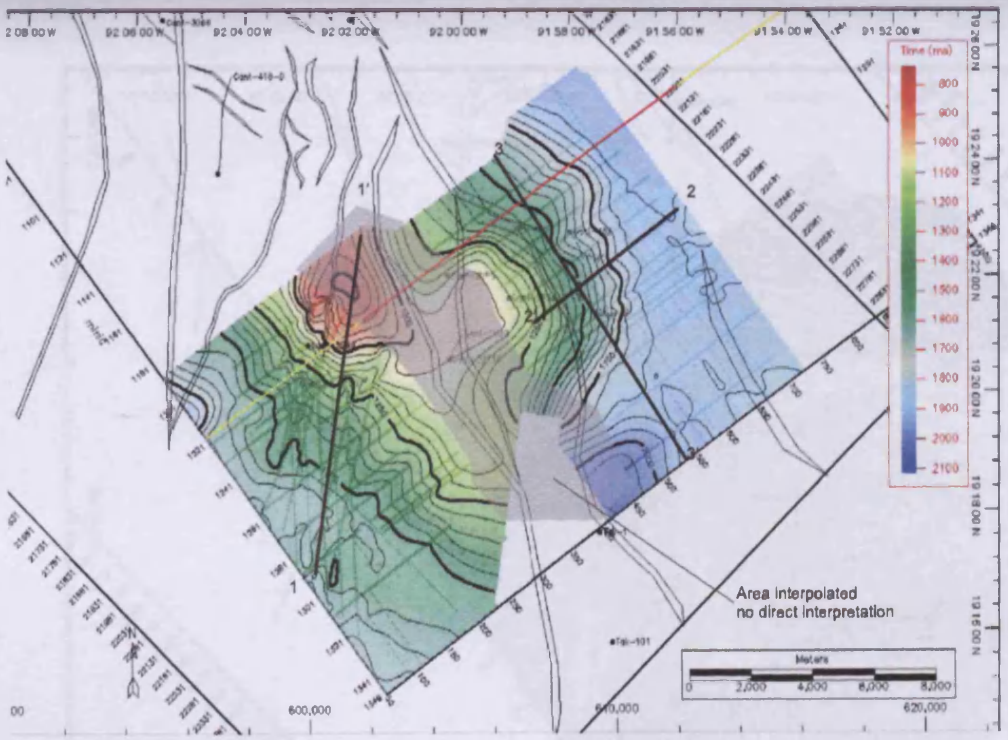

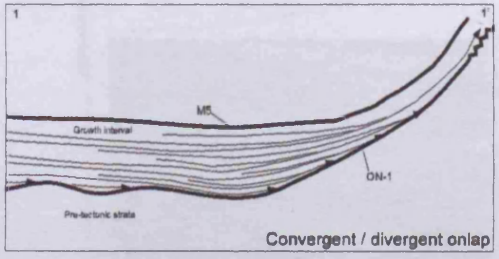

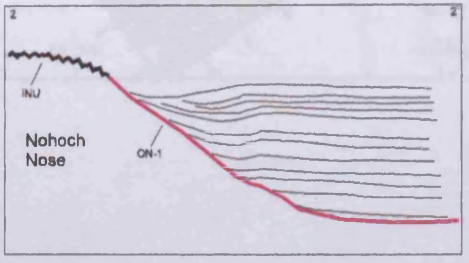

Figure 5. 15
Structural map for seismic horizon ON-1. Gridded from seismic interpretation of various inlines, cross lines and arbitrary lines. Geologic profiles 1-1' and 2-2' display the structural layout of the ON-1 horizon. Seismic profile 3-3' uninterpreted and interpreted displays the different seismic configurations observed from a profile oriented northwest - southeast.

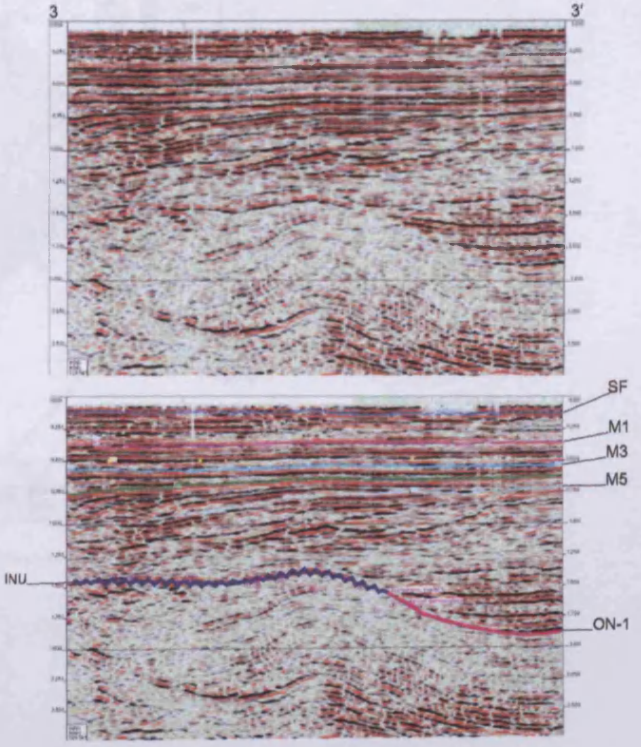

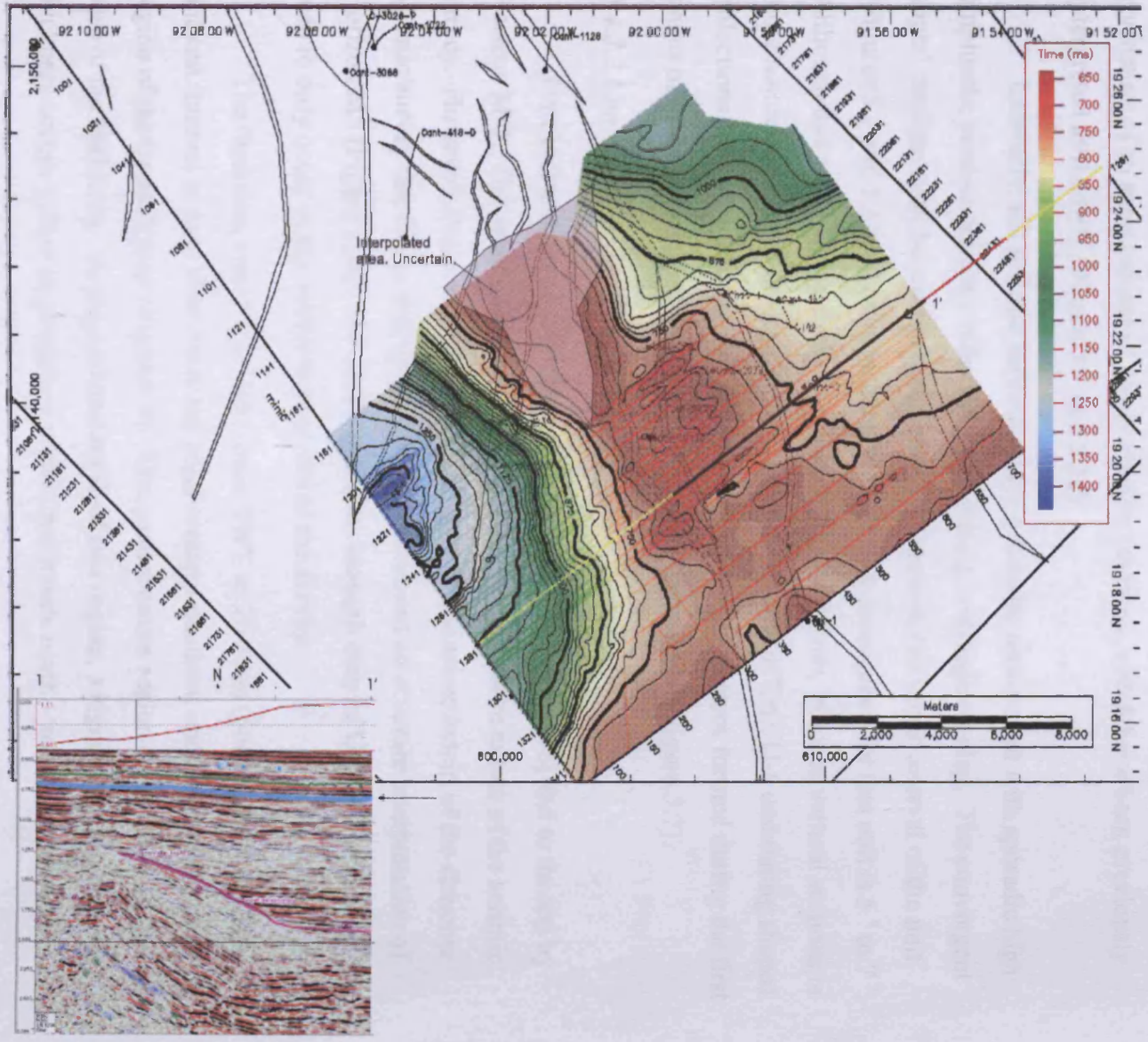

Figure 5.16
Structural map of seismic horizon M5. Note the structure consists of an anticlinal morphology with a narrow crest that trends northwest southeast. The anticlinal structures appears to open towards the southeast.

against the crestal regions of the Thrust Block and along the backlimb (Figure 5.8). The regions that exhibit enhanced thickness reductions along the backlimb correspond to regions in which the structural relief of the Thrust Block are higher.

In vertical sections, Unit U-1 exhibits a wedge like morphology that thins considerably against the crest of the structure. Within the Thrust Block, at the transition between the crestal region and the backlimb of the structure, the basal boundary of the unit passes laterally into the INU. Here a series of amalgamating surfaces where considerable truncation of seismic reflections is noted (Figures 5.7 and 5.12). These surfaces are collectively interpreted as a composite unconformity consisting of an arrangement of minor erosion surfaces, which have been previously interpreted as the INU (Figure 5.7 and 5.12).

Internally, the seismic reflections are generally transparent with sporadic high amplitude, semi-continuous reflections, exhibiting convergent onlap. The convergent stratal configuration becomes more noticeable towards the upper interval of the unit (Figures 5.7 and 5.12). The approximate angle of convergence for this unit is 5 ° to 7 °. Although this angle varies along the strike of the backlimb, in some vertical sections is more noticeable than in others (Figure 5.8). At the base of Unit U-1 undulating shaped reflections are noted that may be indicative of erosional features formed during the first stages of fold development as topographic relief was created (Figure 5.7).

5.4.2.2 Unit U-2

Unit U-2 is defined to its base by Horizon M5 (Figure 5.16) and to the top by Horizon M-3. The areal extent of Unit U-2 occurs in the entire extent of the seismic survey. However, this is not interpreted throughout the entire extent of the streamer seismic survey due to the data quality which prohibited an accurate interpretation of Horizon M5 (Figure 5.16). For this reason, the isopach map of Unit U-2 (Figure 5.9) is seen to only occur in the southern segment of the survey.

The thickness varies from 600 msec TWT to 20 msec (660 m to 22 m). The thickest interval is seen to occur in the southwestern quadrant and the northern most region of the isopach map (Figure5.9). The southwestern region coincides with the base of the backlimb. To the east and north of this region, a significant decrease of thickness occurs within an elongated region that trends north – south to northwest-

southeast (Figure 5.9). The eastern region of the isopach map shows uniform thickness (200 msec TWT).

The gross morphology of Unit U-2 varies throughout the study area. Vertical profiles oriented north – south along the backlimb of the Thrust Block exhibit a wedge that thins against the backlimb (Figures 5.7 and 5.12). In profiles oriented southwest to northeast it is seen as a wedge that thins and overlaps the underlying structure (Figure 5.1). Profiles oriented southeast – northwest (Figure 5.14), exhibit a sigmoidal wedge morphology.

The internal seismic reflection configuration of Unit U-2 seen in the backlimb of the Thrust Block, consists of irregular to regular and continuous reflections (Figures 5.7 and 5.12). A combination of parallel and convergent onlap is seen to occur within the backlimb of the Thrust Block. An approximate angle of 2 ° of convergence was noted in Figure 5.7.

5.4.2.3 Unit U-3

Unit U-3 is defined to the base by Horizon M-3 and towards the top by Horizon M-1 (Figure 5.17). The areal extent of the upper boundary is found throughout the entire domain of the seismic survey. The plan form of Horizon M-1 is seen to consist of two main regions (Figure 5.17). In the eastern part of Figure 5.17 a topographic high is noted, which trends northwest to southeast. The western part is seen to consists of an elongated topographic low that trends north - south (Figure 5.17). The thickness distribution of Unit U-3 as seen in Figure (5.10) ranges from about 50 msec TWT to 500 msec TWT (55 m to 550 m). The thinnest region of Unit U-3 occurs as an elongated area that is coincident with the structural highs (crestal region of the Thrust Block and the Nohoch Nose; Figure 5.10). Towards the west it thickens considerably, conversely towards the east, northeast it only exhibits subtle increase in thickness. The internal stratal architecture of Unit U-3 as seen in Figure (5.12) exhibits a combination of parallel and convergent onlap. The approximate angle of the convergent stratal configuration is very shallow (< 1°; Figure 5.18).

5.4.2.4 Unit U-4

Unit U-4 is defined to the base by Horizon M-3 and to the top by Horizon SF. The upper boundary consists of a planar and continuous surface. The thickness of Unit

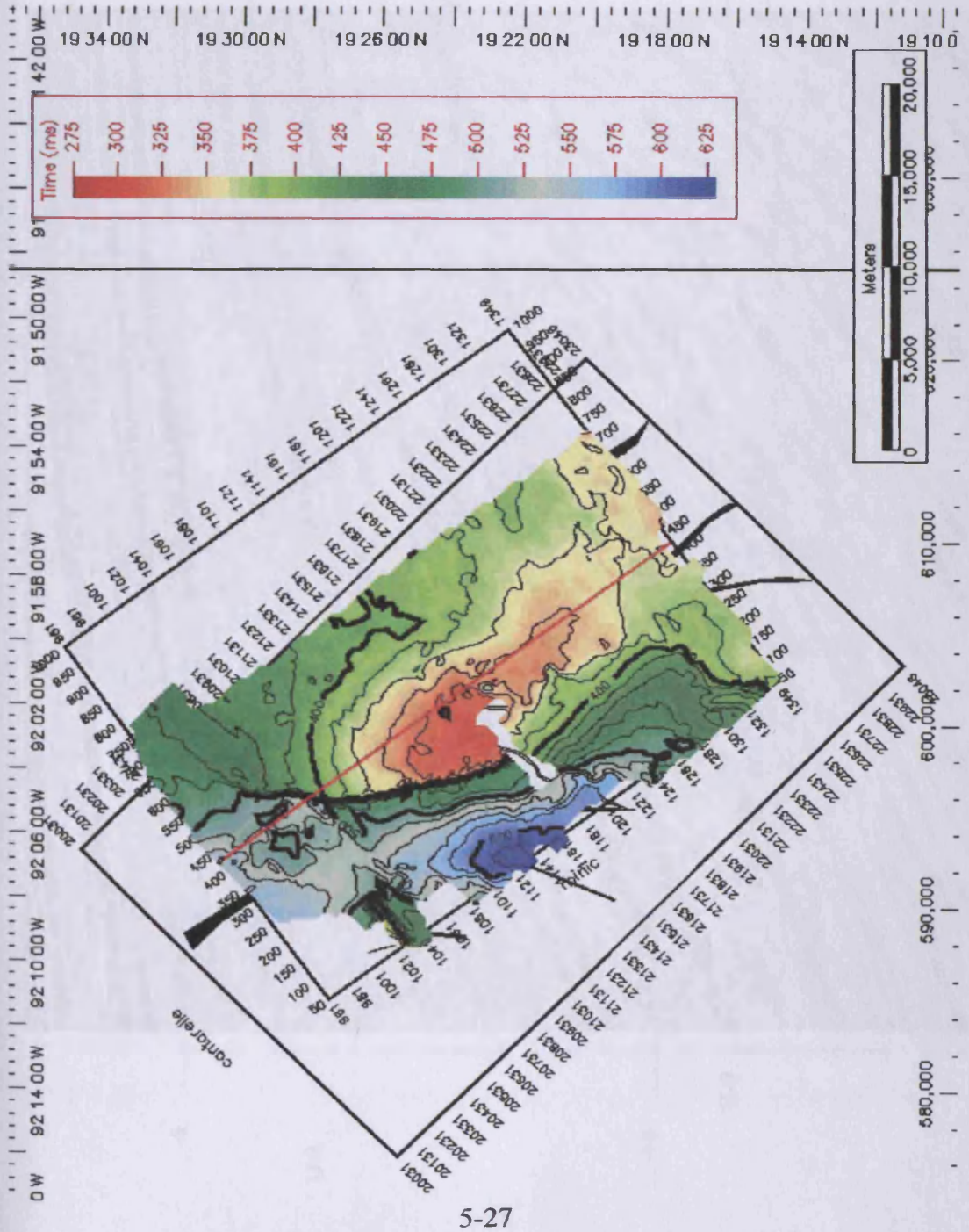

Figure 5.17
Structural map for the M1
Horizon in msec TWT.

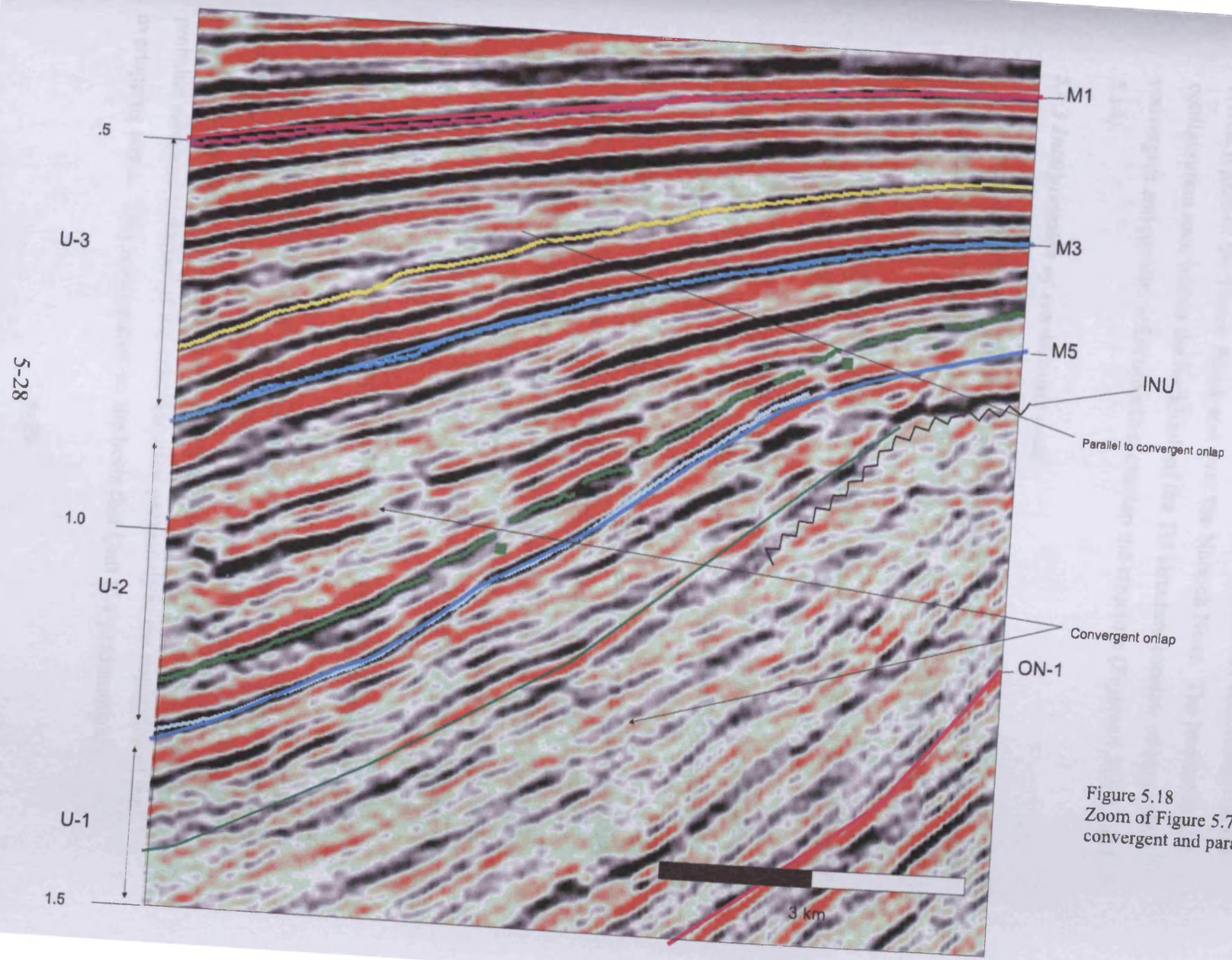

Figure 5.18
Zoom of Figure 5.7. Note the convergent and parallel onlap.

U-4 ranges from 500 to 150 msec TWT (550 m to 165 m; Figure 5.11). Within the western region of the thickness map, the thickness reduces significantly towards the crest of the structure. Conversely, subtle thickness reduction is noted in the eastern region of the map shown in Figure 5.11. The gross morphology of this Unit is very similar to Unit U-3, appearing mainly tabular whose thickness condenses over the crestal region of the Thrust Block and over the Nohoch Nose. The internal stratal configuration seen within the backlimb of the TB structure consists of very subtle convergent and parallel reflections that overlap the structure (Figures 5.1, 5.12 and 5.14).

5.4.3 Interpretation of syn-tectonic units

The most important observations undertaken from the syn-tectonic interval are summarised in the following points, which form the basis for the interpretation of the syn-tectonic units.

1. The gross morphology of the syn-tectonic unit observed within the backlimb of the TB consists of a wedge shape.

2. The internal stratal configuration observed within the syn-tectonic units within the backlimb of the structure consists of a combination of reflections that onlap and overlap the structure.

3. The internal stratal configuration is convergent and parallel. Convergent onlap mainly occurs within the lowermost Units U-1 and U-2 and markedly in Unit U-1.

4. Unit U-1 exhibits the most significant thickness reduction from the base of the backlimb towards the crestal region and the basal part of the unit passes laterally over the crest of the structure as the INU, where truncation of pre-tectonic reflections is observed.

5. All of the units at some stage overlap the structure. Most significantly the uppermost units.

Based on the above observations it is interpreted that the Thrust Block achieved most of its structural growth and fold amplification during the deposition of Units U-1 and U-2. Most significantly during deposition of Unit U-1 (Figure 5.19), in which probable subaerial exposure of the crest occurred previously to the deposition of the overlapping strata. This is suggested on the basis that Unit U-1 predominantly

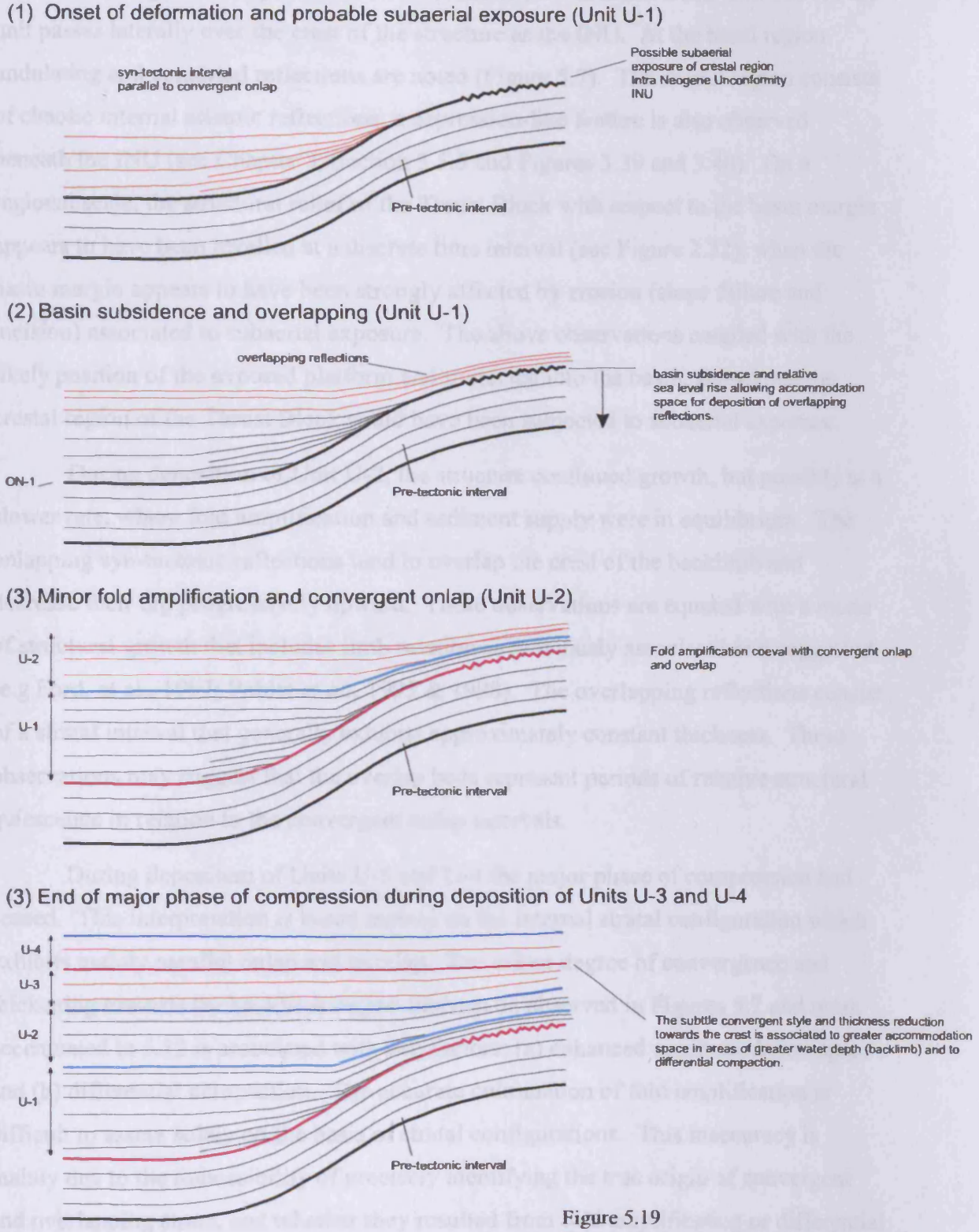

Figure 5.19
Schematic drawing illustrating the growth of the Cantarell Thrust Block based on syn-tectonic stratal styles supported with structural crestal relieves. The structural history for the main phase of compression is divided into three main stages 1 to 3. Where most of the fold amplification occurred during the deposition of Units U-1 and U-2, note graph.

exhibits convergence onlap, and thickness reduction towards the crest. The base of the unit passes laterally over the crest of the structure as the INU. At the basal region undulating and contorted reflections are noted (Figure 5.7). The crestal region consists of chaotic internal seismic reflections, a depression-like feature is also observed beneath the INU (see Chapter 3, Section 3.5.5 and Figures 3.39 and 3.40). On a regional scale, the structural relief of the Thrust Block with respect to the basin margin appears to have been levelled at a discrete time interval (see Figure 2.32), when the basin margin appears to have been strongly affected by erosion (slope failure and incision) associated to subaerial exposure. The above observations coupled with the likely position of the exposed platform and projected into the basin, shows that the crestal region of the Thrust Block could have been subjected to subaerial exposure.

During deposition of Unit U-2, the structure continued growth, but possibly at a slower rate, where fold amplification and sediment supply were in equilibrium. The onlapping syn-tectonic reflections tend to overlap the crest of the backlimb and decrease their dip progressively upward. These observations are equated with a mode of structural growth that includes limb rotation as previously associated and suggested (e.g Ford, et al., 1997; Poblet *et al.*, 1995 & 1998). The overlapping reflections consist of a stratal interval that generally exhibits approximately constant thickness. These observations may suggest that the overlap beds represent periods of relative structural quiescence in relation to the convergent onlap intervals.

During deposition of Units U-3 and U-4 the major phase of compression had ceased. This interpretation is based mainly on the internal stratal configuration which exhibits mainly parallel onlap and overlap. The minor degree of convergence and thickening towards the backlimb region that can be observed in Figures 5.7 and more accentuated in 5.12 is associated with two factors: (a) enhanced accommodation space and (b) differential compaction. The accurate culmination of fold amplification is difficult to assess solely on the basis of stratal configurations. This inaccuracy is mainly due to the impossibility of precisely identifying the true origin of convergent and overlapping strata, and whether they resulted from fold amplification or differential compaction respectively. Although, the approach undertaken here is considered to result in a close approximation.

5.5 Structural growth based on crestal relief

5.5.1 Analysis criteria and limiting factors

The technique employed to estimate the structural growth of the Cantarell Thrust Block based on the structural crestal relief is similar to the one described by Masaferro et al. (1999, 2002). This method consists on calculating the structural crestal relief of the various horizons defined (ON-1, M-5, M-3, M-1 and SF). The crestal relief is defined as the elevation between the crest and the "regional datum" of a given horizon (Figure 5.20). Where the regional datum is considered as the elevation at which the given horizon is near horizontal and did not experienced structural uplift (McClay, 1992). The regional datum here assumed consists of the lowermost depth observed from the gridded maps of the seismic horizons (ON-1, M5, M-3 and M-1; Figures 5.15, 5.16 and 5.17).

Crestal relief as calculated on two seismic profiles oriented north –south (Figures 5.20 and 5.21) and from the gridded maps of the various seismic horizons (Figures 5.15, 5.16, and 5.17). Tables 5.1 to 5.3 present the crestal structural relief calculations.

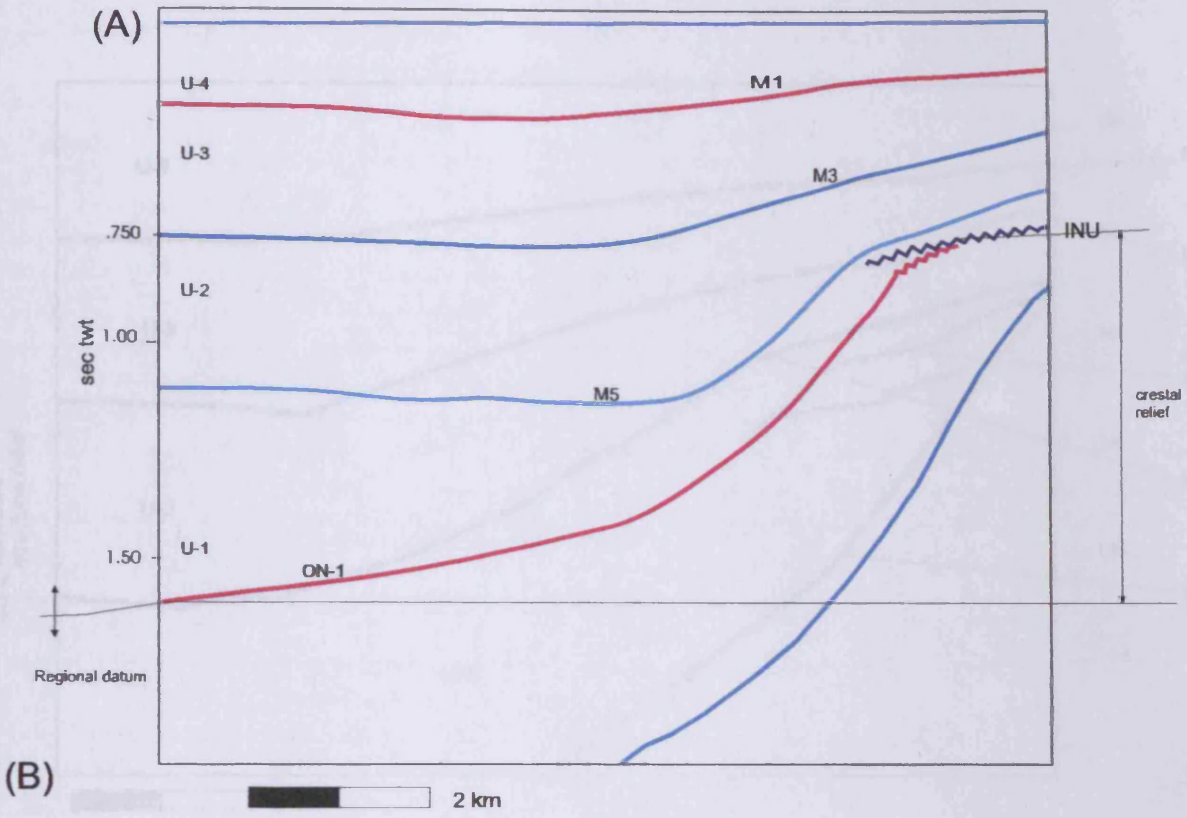

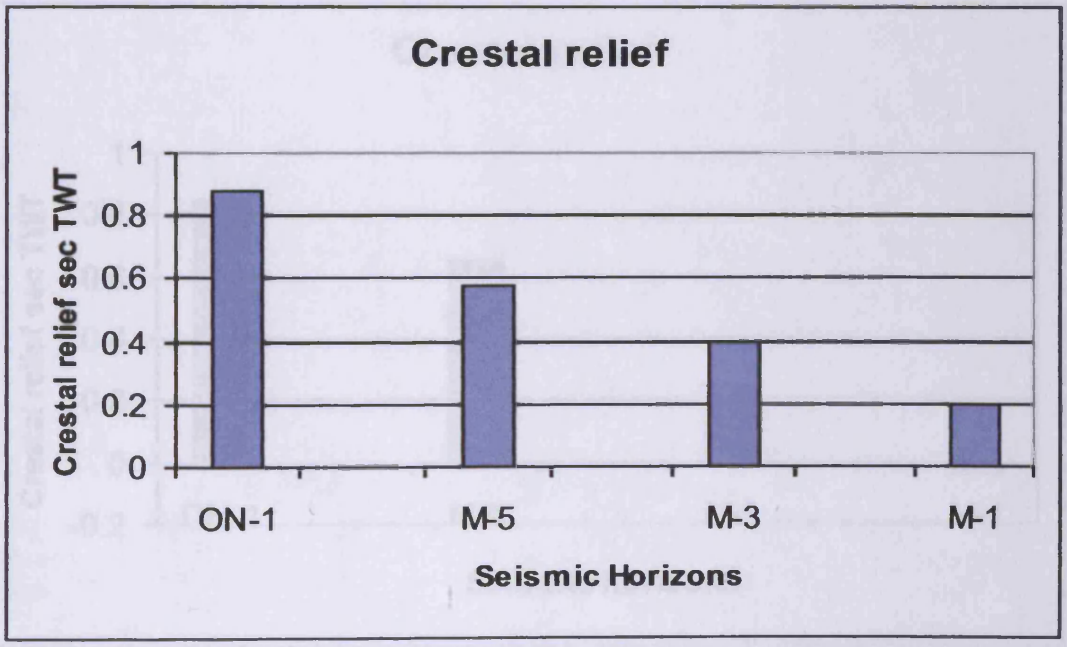

Figure 5.20
(A) Schematic drawing of seismic section shown in Figure 5.6. (B) Graph representing the crestal relief calculated at each seismic horizon. (See Table 5.1).

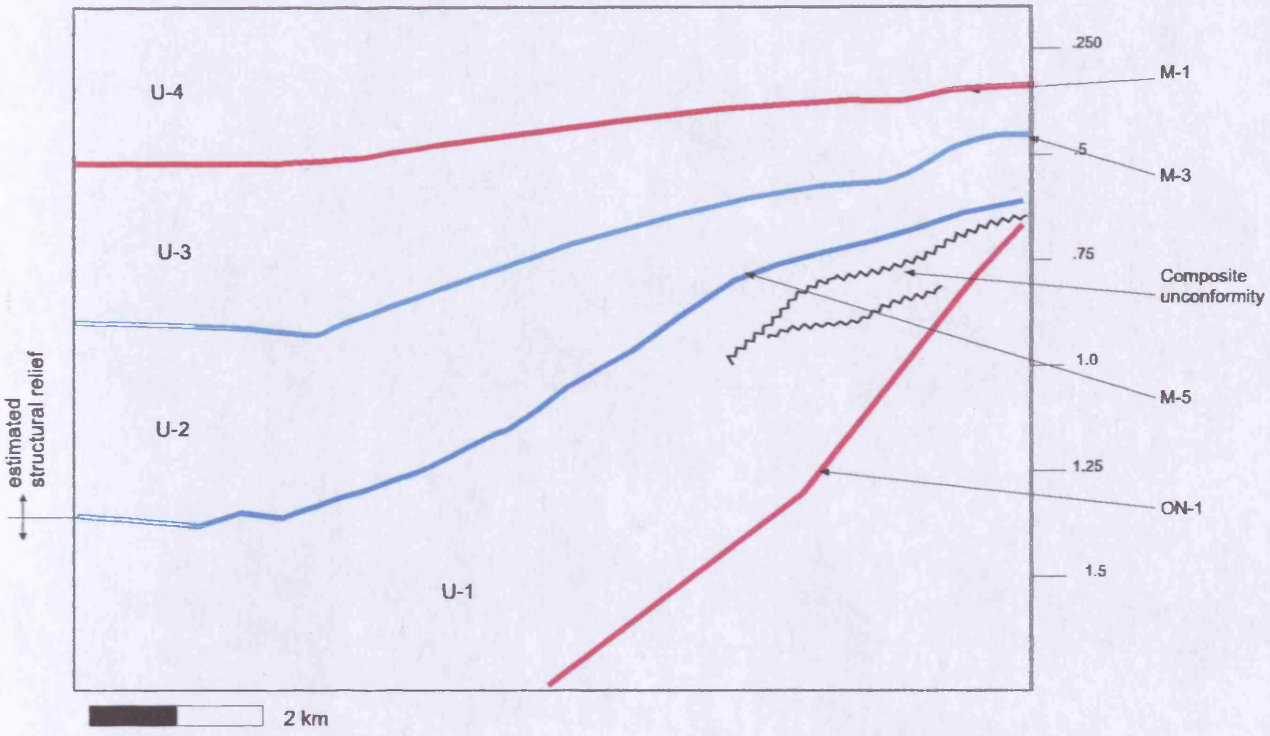

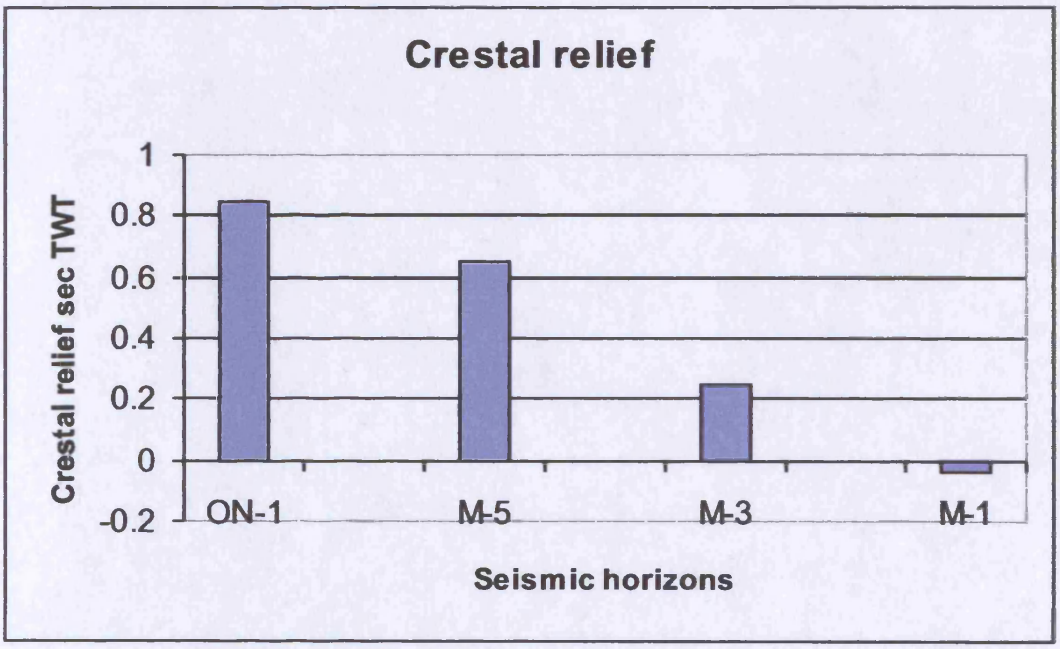

Figure 5.21
(A) Schematic drawing of seismic profile (see Figure 5.12), showing the different seismic horizons interpreted within the syn-tectonic interval. (B) Calculated crestal relief at various seismic horizons, and relative uplift for each unit shown in sec TWT and metres, an average interval velocity of 2200 m/sec was employed to depth convert (See Table 5.2, for calculated values).

Crestal relieves for seismic profile of Figure 5.6						
Seismic Horizon	unit	Crestal elevation sec twt	Base level sec twt	Crestal Relief	Crestal Relief metres Variable interval velocity	Int Velocity employed
ON-1		0.8	*1.65*	0.85	1870	2200 m/sec
	U-1			0		
M-5		0.65	1.3	0.65	1300	2000 m/sec
	U-2			0		
M-3		0.5	0.75	0.25	500	2000 m/sec
	U-3			0		
M-1		0.4	0.36	-0.04	-72	1800 m/sec
	U-4					
SF						

1.65 = estimated from interpolated map of seismic horizon ON-1

Table 5.1 Calculated crestal structural relief of seismic section shown in Figure 5.7.

Crestal relieves for seismic profile of Figure 5.7						
Seismic Horizon	unit	Crestal elevation sec twt	Base level sec twt	Crestal Relief	Crestal Relief metres Variable interval velocity	Int Velocity used
ON-1		0.72	*1.6*	0.88	1936	2200 m/sec
	U-1			0		
M-5		0.625	1.2	0.575	1150	2000 m/sec
	U-2			0		
M-3		0.4	0.8	0.4	800	2000 m/sec
	U-3			0		
M-1		0.35	0.55	0.2	360	1800 m/sec
	U-4					
SF						

1.65 = estimated value from interpolated map

Table 5.2 Crestal structural relief calculated of seismic section shown in Figure 5.6

Crestal relieves calculated of gridded maps						
Seismic Horizon	unit	Crestal elevation sec twt	Base level sec twt	Crestal Relief	Crestal Relief metres Variable interval velocity	Int Velocity used
ON-1		0.75	1.6	0.85	1870	2200 m/sec
	U-1			0		
M-5		0.625	1.25	0.625	1250	2000 m/sec
	U-2			0		
M-3		0.55	1	0.45	900	2000 m/sec
	U-3			0		
M-1		0.35	0.48	0.13	234	1800 m/sec

Table 5.3 Crestal structural relief calculated of various seismic horizons

The following assumptions are made and their influence that these may have in the interpretation of crestal relief are as follows:

(1) Each of the above seismic horizons represents a geological time line. The relative time intervals are given by the name of the units. For example the time context at which Unit U-1 was deposited is simply referred to as time interval U-1. This is due to the lack of biostratigraphic data that would allow more precise time constraints. Although from Figure 5.7 the well stratigraphic markers of wells C-2207 and C-2239 show that the syn-tectonic interval post dates the Middle Miocene.

(2) Sedimentation rates are not taken into consideration again due to the lack of biostratigraphic data. Different sedimentation rates have major implications in the development of the syn-tectonic units. For example, if sedimentation rates were greater at a given time of deposition the resultant geometry of the syn-tectonic interval would be different if considered the same geologic period under lower sedimentation rates (see Section 5.3.1). Based on regional seismic reflection configurations documented in Chapter 2 (Transect 5)and previously described (see Section 5.4.1) it is suggested that sediment supply was unidirectional (north to northwest), and probably fluctuated as part of the autocyclic processes involved in progradation (Schlager, 1993).

(3) No decompaction was undertaken for the syn-tectonic interval because no porosity data is available for the syn-tectonic units. Decompaction can be calculated assuming that porosity decreases with depth at a rate *c*, which depends on the lithology and the volume of rock grains (Angevine *et al.*, 1990). However, it is noted that the effects of compaction can result in significant thickness reduction and act differently in response to the specific lithologic medium. It has been noted that carbonate sediments usually consolidate quickly due to rapid cementation (Ebreli *et al.*, 1997). Cemented carbonates exhibit very little compaction (Anselmetti, 1994). Compaction exerted over depositional slopes may result in apparent enhanced dips when compared to their original decompacted configuration, resulting in an apparent development of crestal relief.

The results achieved using the analysis of structural crestal relief may include some inherited uncertainties derived from the lack of stratal decompaction, errors related to the occurrence of a palaeo-depositional slopes, errors related to possible tectonic thickness variations during fold uplift and errors in the geological interpretation of the

seismic profiles. Because most of these errors are difficult to quantify exactly, error ranges associated with the crestal structural relief are considered to be of the order 10 % of each value quoted (Poblet & Hardy, 1995).

5.5.2 Crestal relief of syn-tectonic units and interpretation

The analysis of structural crestal relief at the different interpreted seismic horizons (Tables 5.1 to 5.3 and Figures 5.20 and 5.21) provide evidence to suggest that just after horizon ON-1 had been deposited and during the deposition of Unit U-1 most of the structural development occurred. Horizon M-5 exhibits a significant decrease in the crestal relief interpreted as a decrease in fold amplification. The crestal relief of the overlying horizons are reduced as these become shallower. The trend observed in the graphs of Figures 5.20 and 5.21 suggests a diminishing of fold amplification with time, considering that each of the interpreted seismic horizons become younger vertically upwards. Importantly this interpretation is in agreement with the observations derived from the internal stratal configurations which will be discussed in greater detail in the following section.

5.6 Discussion: Syn-tectonic sedimentation and structural development

5.6.1 Syn-tectonic sedimentation and crestal relief

The interpretations derived from the observations of the internal seismic configurations and the crestal relief suggest similar scenarios. From the observations derived of the internal stratal configurations (see Section 5.4.2) most of the structural growth is interpreted to have occurred during the deposition of Unit U-1. This interpretation is further supported with the evidence provided by the crestal structural relief of Horizon ON-1. The following series of events illustrate the kinematic history of the thrust-related fold based on the analysis of stratal configurations and structural crestal relief.

(1) During the initial stages of deposition of Unit U-1 fold amplification initiated to a point that crestal region was subaerial (see Section 5.4.3).

(2) Intense basin subsidence or relative sea level rise must be considered as possible explanations for the occurrence of overlapping reflections occurring at the uppermost interval of Unit U-1 (see Section 5.4.2).

(3) During deposition of Unit U-2 fold amplification and sediment supply were in tune as evidence by the occurrence of convergent onlap, although the degree of onlap coupled with the diminished crestal relief of Horizon M-3 provides evidence to suggest that fold amplification was very subtle by the time of deposition of Horizon M-3.

(4) The internal stratal configuration observed mainly parallel with minor convergent onlap and overlapping (see Section 5.4.2) within Unit U-3 and the structural crestal relief bounding this unit suggests that fold amplification had culminated. The convergent onlap noted and the thinning against and over the crest of the structure is suggested to be the result of (i) enhanced sedimentation in areas of greater accommodation space and (ii) differential compaction.

5.6.2 Inferences on fold kinematics and timing

Three mechanisms for fold development were earlier discussed in Chapter 4 as viable for the development of the Thrust Block. As previously described these consists of: (1) fault-bend folding, (Suppe, 1983) (2) faulted detachment fold, (Mitra, 2002) and (3) fault-propagation folding (Suppe and Medwedeff, 1990). The geometry of the syn-tectonic strata can provide insights into the various stages of structural development.

The current geometry of the Thrust Block is consistent with a fault-bend fold (Suppe, 1983), this is not to say that the structure could have developed initially as a detachment fold that was subsequently faulted and displaced. The observed geometry of the syn-tectonic strata (convergent onlap) provides evidence to suggest that the structural development involves limb rotation. The structure as described in Chapter 4, in particular the relationship of the beheaded Nohoch Nose with respect to the Thrust Block argues for a series of events that involves: (1) folding followed by (2) faulting and (3) subsequent displacement of the fold structure. Limb rotation, faulting and displacement of the fold can be associated to a fault-bend folding model. Following are two main aspects based from the syn-tectonic stratal configurations coupled with the crestal relief observations that argues for a fault-bend folding model:

(1) A contrasting syn-tectonic stratal architecture is observed between the backlimb and the forelimb of the structure (see Figures 4.34 and 4.41 to 4.43). This

style has been previously linked to fault-bend and fault-propagation folds (Suppe *et al.*, 1992; Hardy & Poblet 1995; Hardy *et al.*, 1996).

(2) The southern dip orientation of the Cantarell Thrust, and the flat-ramp-flat geometry that exhibits a shallower ramp (see Section 4.4.1), together with the asymmetry of the syn-tectonic stratal architecture are compatible with a thrust bend fold (Suppe, 1983).

To constraint the timing of deformation in the surveyed area the following aspects are considered: (1) Stratigraphic markers of wells C-2207 and C-2239 located at the backlimb (Figure 5.7) exhibit Middle Miocene (M.M.) markers within the pre-tectonic interval just beneath the ON-1 horizon which is interpreted to mark the onset of structural deformation of the main compressive phase; (2) This observation agrees with the model proposed by Pemex. However, due to the lack of accurate and detailed biostratigraphic data, no constraints can be proposed on sedimentation rates which in turn may allow for a more precise time constraint on the kinematics of thrusting and folding. Based on the syn-tectonic stratal configuration in Figure 5.19 a time versus structural growth is provided.

5.7 Conclusions

Based on the above interpretation of the observations, the most important concluding remarks are:

(1) The analysis of syn-tectonic strata of the Thrust Block situated within the Cantarell area provided important insights on the kinematics of the development of the thrust and fold.

(2) Limited well data suggests that fold amplification within the surveyed area postdates the Middle Miocene.

(3) The syn-tectonic strata consist of a wedge that thickens basinwards and thins against the crest of the structure.

(4) The syn-tectonic stratal geometry consists predominantly of convergent onlap to parallel onlap that in some cases overlap the crest of the structure.

(5) Crestal relief calculations suggested that the structure developed most significantly during the deposition of Unit U-1, and decreased its rate of amplification over time. Such observations coincide with the interpretation of the syn-tectonic strata.

Chapter 6

Implications for the Upper Cretaceous calcareous breccias of Cantarell

6.1 Introduction

The aim of this thesis has been to provide a comprehensive geologic interpretation of the Cantarell area based on a detailed analysis of seismic data supported with key well data. This thesis (1) defines the basinal context in which the Cantarell area is situated (see Chapter 2), (2) defines the stratigraphic framework and the seismic stratigraphic character observed within the Cantarell area (see Chapter 3), and (3) defines the structural framework of the Cantarell area (see Chapter 4 and 5). In this Chapter the implications of the previous observations, with specific emphasis on the impact the structural evolution had on the reservoir interval hosted within the Upper Calcareous breccias are discussed.

In Chapters 2 and 3 evidence was provided that allowed the environmental interpretation of the Cantarell area as a moderate-deep basinal setting during the late Mesozoic and early Cenozoic. During the late Mesozoic (Upper Jurassic to Middle Cretaceous) the sedimentation style was dominated by carbonate deposition, and the Cantarell area was possibly situated in a mid to outer ramp setting. This interpretation is founded on seismic observations (see Chapter 2, Section 2.3) and core descriptions (see Appendix 4) as presented in Pemex completion log reports. The model for the Upper Cretaceous calcareous breccias that will be presented in this Chapter thesis partially conflicts with the previous models (Viniegra-Osorio, 1981; Grajales, 2000 and Horbury, 2001). One of the aims of this Chapter is to discuss the previous models by analysing them under the light of information derived from this thesis.

Chapters 4 and 5 presents evidence indicating that the present day structure of the Cantarell area resulted from a complex history of structural deformation. Three main phases of deformation were defined based on seismic observations (see Chapters 4 and 5). These include: early extension, compression and late extension. From the

seismic observations it was noted that the compressive event modified to a large extent the Cantarell area to a point that the preceding extensional phase of deformation is completely overprinted and very difficult to image. Although the compressive event postdates the initial deposition of the Upper Cretaceous breccias by some 30 – 40 Ma the overall structural framework was modified, and most importantly the internal reservoir intervals were also modified by this deformation.

The Upper Cretaceous calcareous breccias as described today by Pemex consists of a unit with a thickness up to 300 m (Grajales-Nishimura et al., 2000), that is found widely distributed throughout the Campeche Basin (see Figures 2.20 and 2.21). This unit occurs up to the Cretaceous – Tertiary boundary. Indeed, as seen from core photographs (see Appendix 4), the Late Cretaceous boundary zone not only encompasses sedimentary type breccias (polymictic) but also monomictic and crackle type breccias. Up to now, some authors (Grajales-Nishimura, 2000; Viniegra-Osorio, 1981) have suggested the Upper Cretaceous calcareous breccias resulted from a single geologic event and that was associated with a single geologic process. In the following sections three different geologic models are summarised and evaluated: (1) talus derived, (2) impact-derived, and (3) subaerial developed.

In summary the aims of this Chapter are:

- To review and evaluate the previous models for the Upper Cretaceous calcareous breccias under the light of the seismic observations derived in this thesis.
- To present a model for the Upper Cretaceous calcareous breccias.
- To present the influencing factors that the structural development had over the reservoir intervals.

6.2 Talus derived breccia model

As previously presented in Chapter 2, Section 2.2.4.3, Viniegra-Osorio(1981) interprets the Upper Cretaceous calcareous breccia interval as a talus deposit derived from the Yucatan Platform. The source for these deposits are described by Viniegra-Osorio (1981) was derived from the Yucatan Platform to the east of the Cantarell area. Their emplacement was triggered by both a relative sea-level drop, which exposed the platform margin, and tilting of the Yucatan Platform as a result of tectonism that occurred during the Late Cretaceous south of the Cantarell area in the Sierra de Chiapas (see Figure 2.1). As described earlier in Chapter 2 (see Section 2.2.4.2, Figure 2.21), to the south of the Cantarell area, during the Late Cretaceous the Artesa and Mundo Nuevo localities, the platform margin was experiencing relative uplift and tilting as a result of structuring (Horbury, 2003). This process shed carbonate clasts and mass flow units onto the slope and basin as a breccia type facies. From the above, the calcareous breccias that occur in the Campeche Basin and Cantarell were interpreted by Viniegra-Osorio (1981) to have resulted from a relative sea-level drop which most likely was triggered by tectonism.

6.2.1 Evaluation of talus derived model

Deposition of reworked carbonate material in slope settings, including sediment gravity flows and talus deposits have been the subject of numerous studies. These investigations have focused on the descriptions and interpretations of depositional processes and speculated on the triggering mechanisms responsible for the initiation of sediment gravity flows and sedimentation along slopes. Triggering mechanisms include relative sea level changes, tectonic seismicity, platform oversteepening, differential compaction and impacts of meteorites (Drzewiecki and Simo, 2002). Variations in the geometry and lithological assemblages along slope reflect changes that occur on the platform margin and shelf. In addition of providing information about the depositional history of the platform margin and upper slope, carbonate breccias, mega-breccias and conglomerates deposited along slope have been considered as important indicators of relative low sea level (Haq et al., 1987; Sarg, 1988). However, Jacquin et al., (1991) suggested that major volumetric mega-breccias can also result from platform –margin collapse. Influencing factors that have an effect on slope

instability are divided into endogenic processes that are intrinsically linked to the depositional system such as rate of sedimentation, relative sea-level change and depositional slope angle and exogenic processes which are independent of the depositional setting such as seismicity and storms. Whereas endogenic triggers may be occur in a predictable, cyclical way, exogenic triggers being completely random in occurrence, generally produce an irregular pattern of resedimentation (Spence and Tucker, 1997). In Section 6.2.1.3 analogue depositional settings are presented that may serve as comparison for the Cantarell area.

6.2.1.1 Carbonate slope

The geometry of the slope within the Cantarell area during the Cretaceous as seen from the 2-D seismic lines (see Enclosures 2 to 4) consists of a shallow dipping, concave upward slope that becomes steeper with slope height near the platform margin (see Chapter 2, Section 2.3.4.1 and Enclosure 2 to 4). In this thesis, it has been suggested that during the late Cretaceous two end-member types of slopes could be considered (Figure 6.1) as possible configurations for the basin margin. These slope settings are based on the basin architecture seen in Enclosures 2 to 4, and consist of: (1) onlapping slopes and (2) a bypass slope. Onlapping slopes are characterised by deposition of margin-derived sediment and pelagic carbonate across the entire slope, interbedded with margin-derived breccias that onlap the middle and lower slope. (2) Bypass slopes are characterised by an absence of any sedimentation on the upper slope. These types of slopes occur on both oversteepened upper slopes and along erosional scarps (Drewiecki and Simo, 2002). The occurrence of the subangular clasts that make up the calcareous breccia interval could be used to argue for either a scarp dominated margin or steeply-fronted margin. Normal faults are interpreted to have existed at the platform base in Enclosure 3 (see Figure 2.25), although, based on the seismic character the occurrence of the fault is not conclusive. Similar depositional settings have been recognised to occur in other basins of the world (see Section 6.2.1.3, for analogues). The hypothesis of the breccia as a talus deposit, therefore based on the recognition of a slope configuration consistent with a large scale mass wasting.

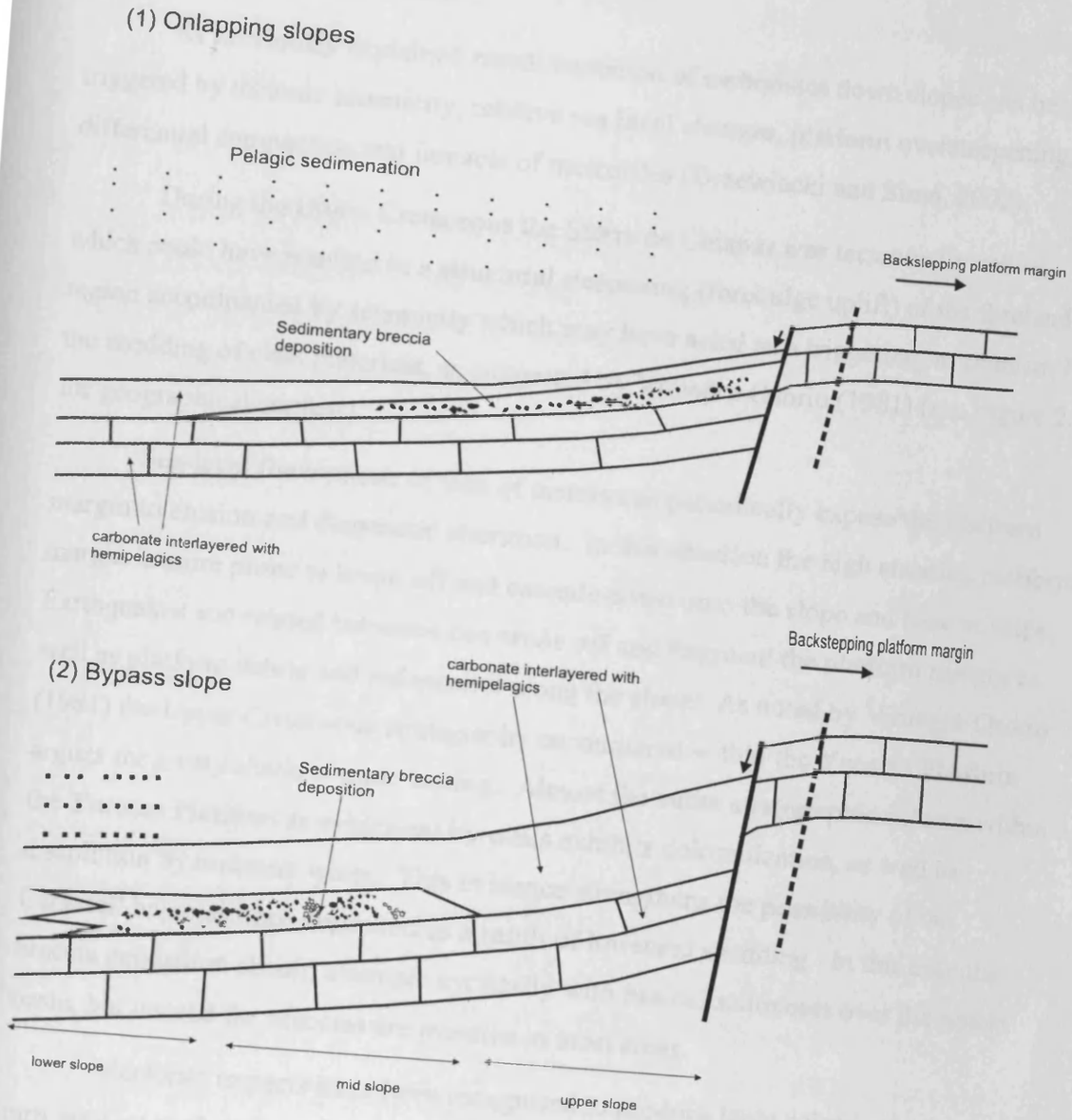

Figure 6.1
Sketches representing slope types associated to the basin margin architecture as seen within the Cantarell area.

6.2.1.2 Triggering mechanisms

As previously explained resedimentation of carbonates down slopes can be triggered by tectonic seismicity, relative sea level changes, platform oversteepening, differential compaction and impacts of meteorites (Drzewiecki and Simó, 2002).

During the Upper Cretaceous the Sierra de Chiapas was tectonically active, which could have resulted in a structural steepening (forebulge uplift) of the foreland region accompanied by seismicity which may have acted as a triggering mechanism for the shedding of clast materials, as suggested by Viniegra-Osorio (1981) (see Figure 2.1, for geographical context).

Sea-level fluctuations of tens of meters can periodically expose the platform margin to erosion and diagenetic alteration. In this situation the high standing platform margin is more prone to break off and cascade down onto the slope and base of slope. Earthquakes and related tsunamis can erode off and fragment the platform margin as well as platform debris and redeposit it along the slope. As noted by Viniegra-Osorio (1981) the Upper Cretaceous stratigraphy encountered within the Yucatan Platform argues for a very shallow water setting. Almost the entire stratigraphic column within the Yucatan Platform as evidenced by wells exhibits dolomitization, as well as dissolution by meteoric water. This evidence strengthens the possibility of the Cantarell breccias been deposited as a result of lowstand shedding. In this case the breccia deposition should alternate cyclically with basinal sediments over the whole basin, but instead the breccias are massive in most areas.

Meteorite impacts have been recognised to produce large seismic shocks that in turn may act as the triggering mechanism that could collapse platform margins and redeposit them along slope (Spence and Tucker, 1997 for list of breccias derived from seismic shocks). However, the only difference between a gravity deposit triggered by a meteorite impact or an earthquake is the occurrence of various melt particles and possible enrichment of iridium in the deposit triggered by a meteorite impact (Dypvik and Jansa, 2003). From the reported 300 m thick interval of Upper Cretaceous calcareous breccia with little finer material that fines upwards, and an overlying interval that contains particles that are associated to the Chicxulub meteorite impact, Grajales-Nishimura et al. (2000) have suggested that the breccia unit found within the

Campeche Basin and in the Cantarell area was triggered by a seismic shock related to the Chicxulub meteorite impact. See Section 6.4 for a detailed discussion of the meteorite impact model.

6.2.1.3 Analogue models

In this section a number of geologic models regarded as analogues from different basins are reviewed and compared with the Upper Cretaceous breccias found within the Campeche Basin and study area. The platform to basin architecture, triggering mechanisms, the dimensions and internal character of the breccia deposits are reviewed and compared (Table 6.1).

Poza Rica Trend, Mexico

Large slope apron deposits occur in the Mid Cretaceous of Mexico. During Mid Cretaceous times a shelf margin extended around the Gulf of Mexico region (Figure 6.2; Enos, 1993). Intrashelf basins occurred with steep margins with relief of c. 1 km. Atolls developed on the shelf such as the Golden Lane Atoll (Figure 6.2). The slope angles ranged from 20° to 43° and the slope deposits are as much as 1380 m thick. The platform margins were fringed by rudist banks which shed vast quantities of material that developed the slope apron deposits (Figure 6.3). The aprons were 15km wide and were composed of breccias and skeletal grainstones. Outcrops located to the west of the main reservoir units exhibit a coarsening-up trend that overlies a basinal peloidal-skeletal wackestones and lithoclast-skeletal packstone unit that hosts an olistolith of 1 km x .5 km .95 m. The apron itself passed from muddy to coarser and cleaner trubidites, to debris flows with margin and slope debris, and is capped by coarse, nearly whole rudists clasts as the platform margin prograded over the apron (Figure 6.3; Enos and Stephens, 1993).

The triggering mechanisms for the deposition of breccias along slope have been interpreted as due to the lowering of sea-level where erosion and collapse of the platform margin occurred during lowstands (Enos and Stephens, 1993). This mechanism is similar to the triggering mechanism for the Cantarell calcareous breccias as suggested by Viniegra-Osorio (1981).

Analogue name and location	Platform – Basin and slope architecture	Breccia deposit dimensions	Internal character	Interpreted triggering mechanisms
South Pyrenean Eocene carbonate megabreccias, Spain (SPECM), (Payros et al., 1999). A number of SPECM units deposited in the foreland basin, derived from a carbonate-platform system hosted by the basin passive margin.	Platform margin consisted of a shallow-water setting. The dip of the slope was approximately 6°.	Variations in size of the breccia deposits were observed. The larges breccia deposits exhibits a lateral extent parallel to platform margin of 130 km with a thickness of 200 m and a volume of 200 km^3. The smallest breccia deposit consists of 3 km wide parallel to margin, and a thickness of 3 to 24 m.	SPECM consist of (1) immature, homogeneous debrite in the proximal part, (2) a differentiated bipartite debrite and turbidite in the middle part; and (3) an incomplete base –missing debrite overlain by turbidite, or a turbidite alone in the distal part.	Deposited from partial platform margin collapse. The instability of the platform margin was triggered by phases of structural steepening (forebulge uplift) coupled with high-magnitude earthquakes and the combination of relative sea-level fall.
Poza Rica Field Mexico (Enos, 1977).	Slope apron deposit during the Mid Cretaceous. Platform margin had a 1 km of relief. Slope angles varied from 20 -43 %.	Thickness of about 1380 m consisting of interlayered finer sediments with breccia intervals. 15 km wide aprons.	The breccias are composed of breccias and skeletal packstone, which enclose an olistolith of 1 km x .5 km x .95 m. The apron passes form muddy to coarser and cleaner turbidites.	Depositional oversteepening and wave erosion.
The Upper Cretaceous carbonates of the Gargano-Murge region, southern Italy (Borgomano, 2000).	Platform margin juxtaposed to the deeper marine carbonates by the intermediary of a faulted scarp.	Breccia like facies vary in size from: Mattinata Formation (750 m thick) base-of-slope breccias and grainstones. Monte San Angelo Formation (10-200 m thick) carbonate breccias alternating with thin mudstones layers rich in pelagic foraminifera.	Interbedded deep-water pelagic mudstones with large volumes of rudist bioclasts. Some of these large bioclastic intervals have been transported 15 km from their source into the most distal part of the base-of-slope domain. Debris-flows and grain-flow deposits are dominant in the more proximal zone and consists of massive unsorted grain-supported units.	Tectonism and seismicity in a backsteeping platform margin setting.
Late Cretaceous south-central Pyrenees, Spain (Drzewiecki, 2002)	Platform margin juxtaposed to the deeper marine carbonates by the intermediary of a faulted scarp. Debris-flows originated at the platform margin that bypassed the upper slope and were deposited on the lower slope as polymicitc, clast-supported, matrix-rich megabreccias.	The megabreccias form channelized and sheet-lobe bodies with erosional basal surfaces. Submarine slide and slump deposits commonly grade laterally downslope into slope-derived megaconglomerates.	Matrix-poor, margin-derived megabreccias form a thick talus pile at the base of scarp.	Triggered by syndepositional seismic activity and upslope migration of instability and erosion.

Table 6.1
Table documenting breccia-like deposits from different localities.

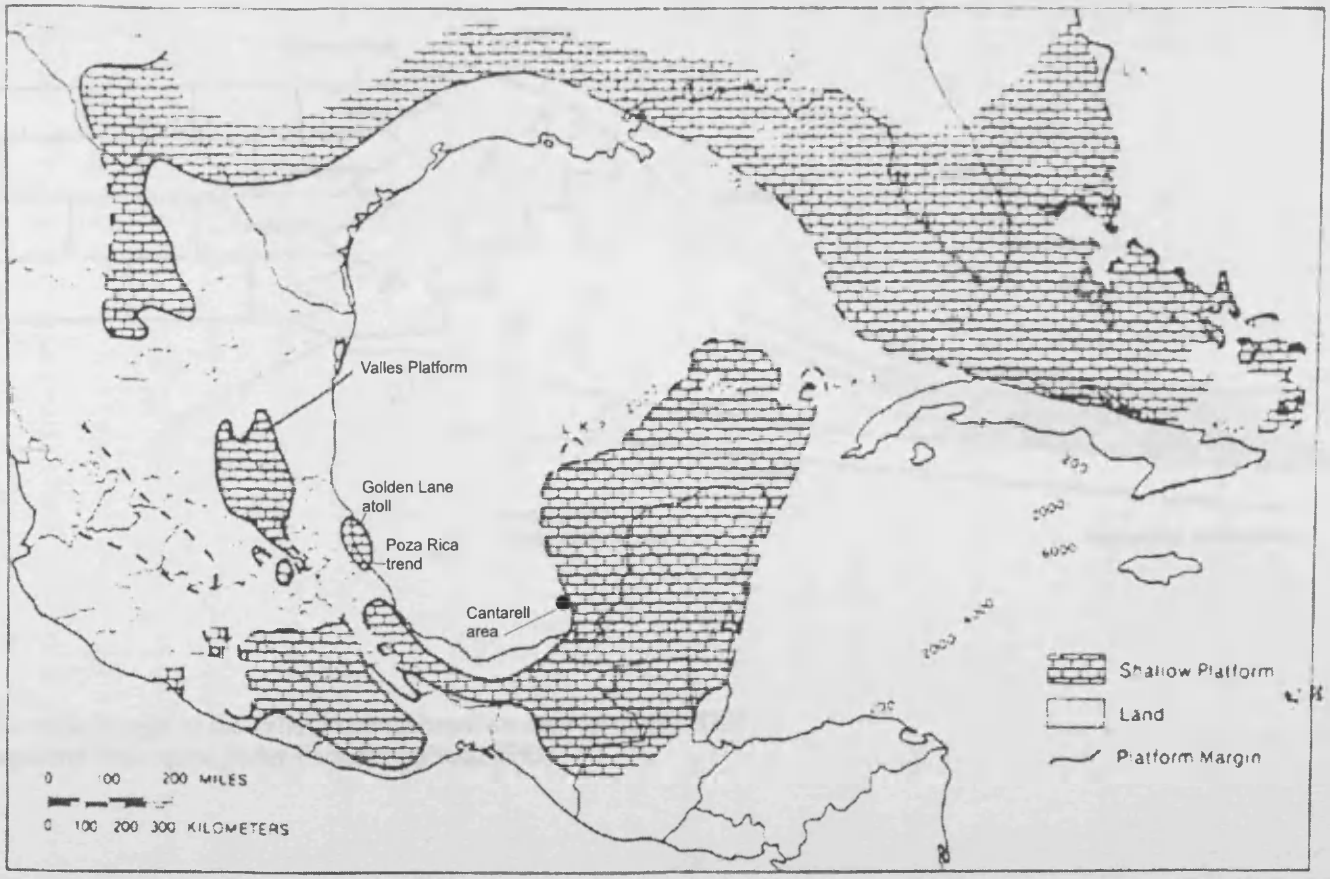

Figure 6.2
Mid Cretaceous shelf margin trends around the Gulf of Mexico and southern Atlantic coast.
After Enos, 1988.

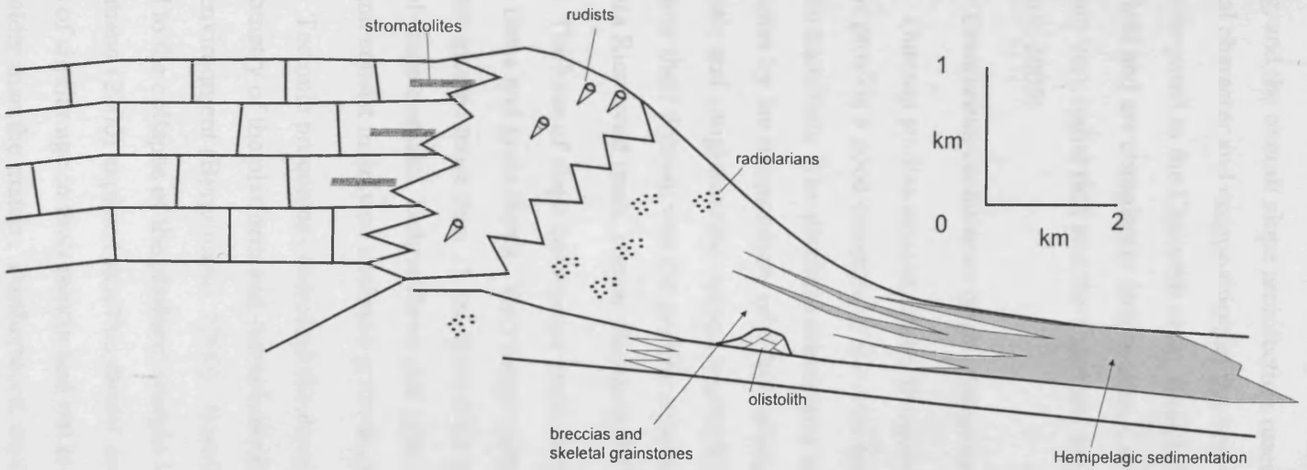

Figure 6.3
Schematic profile of the margin of the Valles Platform based on outcrop studies. This represents a prograding slope apron (After Enos & Stephens, 1993).

The margin architecture of the Poza Rica trend is similar to the basin margin profile seen in Enclosures 2 to 4. Even though the Poza Rica trend is situated in an intrashelf setting, and the overall slope architecture resemble the Cantarell area. However the internal character and composition of the breccias are very different from the Poza Rica trend compared to the Cantarell area. Skeletal grainstones are very typical of the Poza Rica field and are completely absent from Cantarell. Also the breccias at Poza Rica trend are very rudist rich and the Cantarell breccias are not in general (Pers. Comm. Horbury, 2005).

Upper Cretaceous carbonates of the Gargano - Murge region, southern Italy

Outcrop studies carried out by Borgomano (2000) in the Gargano-Murge regions provide a good example of the architecture and the processes of the platform-to-basin transition. The platform carbonates are juxtaposed to the deeper marine carbonates by the intermediary of a faulted scarp. The base of slope is characterised by bioclastic and conglomeratic aprons interbedded with pelagic mudstones (Figure 6.4). The outer shelf domain was the prolific source of rudist bioclastic aprons similarly to the Poza Rica trend (pers. comm. Horbury, 2005).

The base of slope carbonates were mainly deposited by turbidity currents, debris flows and grain flows. Very large volumes of rudist bioclasts appear to have been transported more than 15 km from their source into the most distal part of the base-of-slope domain. Debris flows and grain flows are more dominant to the proximal zone and consist mainly of unsorted grain supported units.

Tectonic processes controlled the development of an interpreted faulted edge, the geometry of the platform and the sedimentation of platform blocks in the base of slope environment (Borgomano, 2000). Bosellini (1993) argued that the breccias are related to the collapse of the platform margin in relation to sea level drops. However Borgomano (2000) explains that this model could only explain the breccia formed by blocks of similar age to their matrix and not to breccias that are dominated by blocks much older than the matrix. Furthermore, no major eustatic variations of Late Cretaceous age, and especially only with significant falls in sea level, have been identified in the Gargano-Murge area. Therefore periodic footwall uplift could have

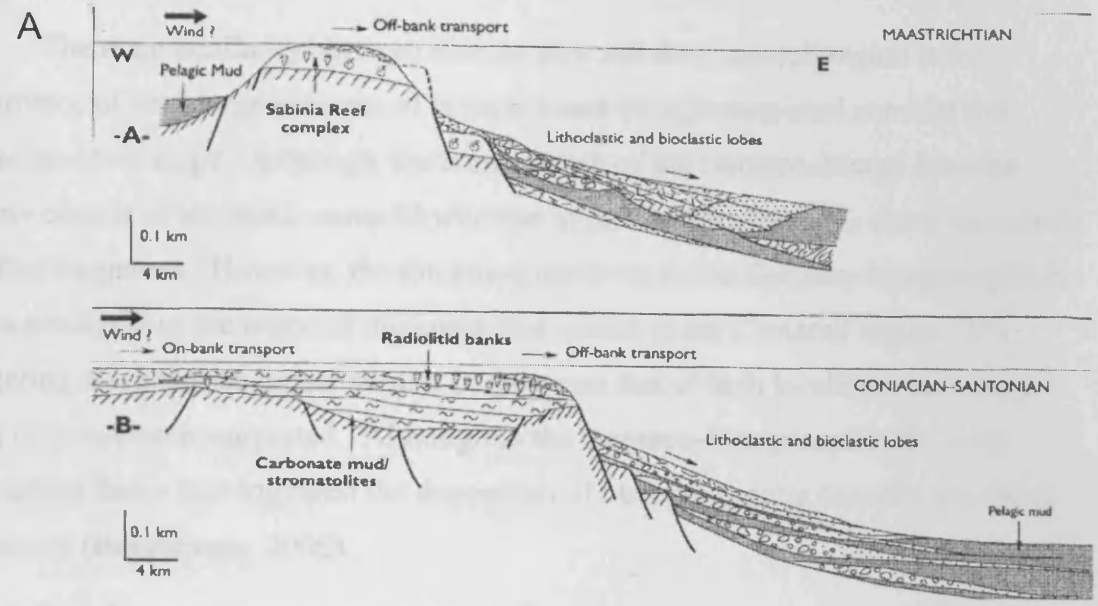

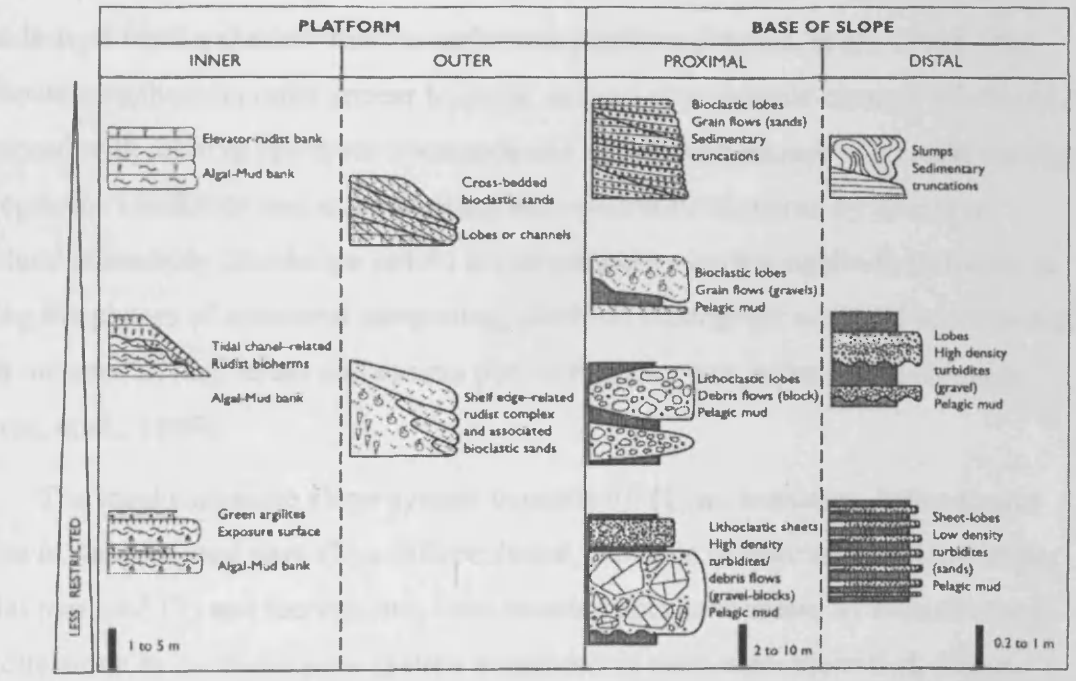

Figure 6.4
(A) Stratigraphic cross section of the platform to basin transition at the Maastrichtian and Coniacian-Santonian periods, Gargano-Murge region. (B) Summary of the main processes and environment of deposition in the Upper Cretaceous, Gargano-Murge region (After Borgomano, 2000).

been the mechanism that controlled resedimentation of older platform blocks (Borgomano, 2000).

The main similarity between this locality and the Cantarell region is the occurrence of very large volumes of breccia clasts being transported considerable distances down slope. Although, the composition of the Gargano-Murge breccias mainly consist of bioclastic material whereas in the Cantarell area the clasts are mainly lithified fragments. However, the thickness observed in the Gargano-Murge region is much smaller than the reported thickness that occurs in the Cantarell region. The triggering mechanisms appear similar in the sense that at both localities relative sea-level drop has been suggested. Although in the Gargano-Murge region, the main controlling factor that triggered the deposition of massive breccia deposits was likely seismicity (Borgomano, 2000).

South Pyrenean carbonate megabreccias, Spain

The South Pyrenean Foreland Basin contains numerous units of Eocene resedimented carbonate megabreccias intercalated with siliciclastic turbidites which were derived from a shallow marine carbonate platform (Payros, et al., 1999). The carbonate megabreccia units appear to occur as time-stratigraphic clusters which can be correlated with relative sea-level lowstands and linked with phases of tectonic activity. The episodic instability and mass wasting were probably triggered by phases of structural steepening (forebulge uplift) accompanied by high-magnitude earthquakes. During the phases of structural steepening, platform emergence occurred accompanied by an increase in load stress and excess pore-water pressure in the carbonate ramp (Payros, et al., 1999).

The ideal carbonate slope system consists of: (1) an immature, homogenous debrite in the proximal part; (2) a differentiated, bipartite debrite and turbidite in the medial part; and (3) and incomplete, base-missing debrite overlain by turbidite, or a turbidite alone in the distal part. Seven megabreccia units were identified, whose thickness ranged from 12 m to190 m; the areal distribution also ranged from 3 km to 135 km in length parallel to the platform margin. The megabreccia units have been correlated a distance of over 20 km in a basinwards direction, corresponding almost entirely to the total length of the Jaca and Pamplona basins.

Late Cretaceous breccias of the south-central Pyrenees of Spain

Cenomanian through Coniacian strata near the town of Sopeira in the south-central Pyrenees consists of variety of autochthonous and allochthonous carbonate slope lithologies. These successions shed light on the platform margin to basin evolution. Drsewiecki (2002) describes the slope facies and associates them to various depositional mechanisms for carbonate megabreccias. In particular, he addresses the relationship between the composition of slope deposits, the evolution of the platform margin, and the tectonic factors that control this evolution.

Based on an exhaustive literature review of breccia deposits along slopes, Drsewiecki (2002) defined three main types of mega conglomerates and mega breccias. The same types were identified in the Upper Cretaceous successions of the south-central Pyrenees. These types consist of:

(Type 1) conglomerate/breccias with clasts derived exclusively from the slope or other deep water environments. These can be matrix or clast supported and are usually interpreted to be deposited from debris flows, similarly as Type 2. Type 1 breccias typically form sheet-like deposits restricted to the slope and basin.

(Type 2) conglomerates/breccias with clasts derived from shallow (shelf and margin) environment mixed with clasts and/or matrix from deep slope environments.

(Type 3) matrix-poor conglomerates/breccias derived almost exclusively from shallow-water settings. These are always clast- supported, and are interpreted to result from rock fall, avalanches, and debris falls. These breccias are deposited from debris-flows that result from catastrophic collapse of the margin. They have chanelized bases and incorporate slope material during transport. The breccias originate from erosion of a steep, cemented margin scarp and essentially form a talus pile at the foot of that scarp.

Polymictic, clast-supported, matrix-rich megabreccias were deposited along the middle and lower slope, although dominantly along the lower slope (Drsewiecki, and Simo, 2002). These mega breccia deposits are up to 50 m thick and 600 m wide, and have been found to have been deposited along the entire slope before they lost momentum and stopped at the break of gradient in the toe-of-slope environment.

6.2.1.4 Synthesis

As noted from the above analogues for the breccias seen within and adjacent to Cantarell share some similarities with the breccias observed and described in the previous localities. In all the localities various types of breccia facies occur and most of the bulk volume of the breccias is found along the middle and lower slope. The areal extent of the breccia deposits varies between all localities. Although in most localities breccia deposits have been noted to occur several kilometres from the source.

The main difference of the calcareous breccias of the Cantarell compared to the other analogues is the gross thickness. This is reported to be in excess of 300 m as a single breccia unit. However in the Cantarell it is strongly emphasized that in all of the analysed well reports there is not a single continuous core sample along the suggested 300 m thick breccia interval. Instead this interval has been sampled intermittently mainly due to the poor core recovery and the costs of attempting to core a continuous interval of 300 m. Therefore the reported gross thickness and alleged fining-upward internal character of the breccias (Grajales-Nishimura, 2000), is based on a synthetic section.

The slope architecture at the Campeche Basin appears to be the most extensive of the previous examples. A platform to basin relief of about 1 km and an width of approximately > 20 km is calculated for the Cantarell slope, whereas at the south-central Pyrenees locality the vertical relief is < 1 km and the slope measured < 20 km in length. Furthermore, the dimension of the Yucatan Platform carbonate factory exceeded considerably the carbonate factory of the previous analogues. From this dimensions, it is possible to speculate that the Yucatan carbonate factory was productive enough to have shed off the vast amounts of calcareous material into the slope and basinal setting.

A very important point that was noted from the previous examples is that the triggering factors associated to the deposition of breccia-like deposits consist mainly of: (1) seismicity, and (2) lowering of the sea-level. In all of the above examples the breccia deposits are intercalated with finer hemipelagic sediments, but not in Cantarell area. Internally all of the breccia deposits exhibit variations in clast size and clast to matrix ratios.

6.3 Impact model

The impact model for the Upper Cretaceous calcareous breccia suggests that they were deposited as a result of massive platform margin collapse which was triggered by the seismic shock associated with the Chicxulub meteorite impact (Grajales-Nishimura et al., 2000). This model is based on stratigraphic and mineralogical studies of the Cretaceous-Tertiary boundary level studied offshore and onshore. Grajales-Nishimura et al. (2000) indicate that the Upper Cretaceous calcareous breccia and overlying dolomitized layer found in several wells of the Campeche Basin contain typical Chicxulub impact products such as shocked quartz, plagioclase and altered glass.

In their model the Upper Cretaceous in the Campeche Basin has been described as consisting of four units. From the base upwards these are: Unit 1 an undolomitized or dolomitized hemipelagic limestone; Unit 2 a 300 m thick dolomitized limestone breccia that corresponds to the most productive reservoir interval; Unit 3 is ± 30 m thick reworked dolomitised layer with breccia lenses that corresponds to the upper seal of the reservoir. Within it is a bed composed of clay minerals, containing a thin layer of silt-sized fragments of feldspar, quartz and pristine glass fragments together with rounded fragments of a greenish clay mineral that have been interpreted as smectite. Unit 4 consists of homogeneous Palaeocene laminated marls. These four units were correlated over 500 km to the south of the Campeche Basin located in the Chiapas Tabasco regions of southern Mexico (see Chapter 2, Figure 2.1). At the Guayal section (17° 32' 6.15" N, 92° 36' 15.1" W) a similar lithologic arrangement was observed: hemipelagic limestone overlain by ± 40 m thick, thinning-upward limestone breccia that was overlain by a 11 m thick reworked layer with localised breccia lenses (Grajales-Nishimura, et al., 2000).

The lithologic and biostratigraphic similarities and the distribution of impact material found within Unit 3 allowed Grajales-Nishimura (2001) to suggest the following sequence of events that took place within few minutes or hours after the impact: (1) carbonate platform collapse due to seismicity, which resulted in the deposition of the lower breccia unit; (2) deposition of ejecta layer with impact minerals; (3) reworking of and mixing of the deposited ejecta layer by tsunami waves. This last

mechanism led to the deposition of localised lenses of breccia (Grajales-Nishimura, 2000).

6.3.1 Evaluation of the impact model

Two main points regarding the impact model are discussed. (1) The first argument relates to the internal character of the breccias and the gross thickness of this deposit. (2) The second point considers the areal distribution of the calcareous breccias and the seismic observations that are documented in Chapter 2.

It is suggested that the subdivision scheme that is proposed for the calcareous breccias in the Campeche Basin is unrealistic in that it is over idealised. It has been noted that the Upper Cretaceous calcareous breccias exhibit a much wider variation in textures (see Chapter 3, Section3.4.3.3). Certainly a fining upward trend can be seen in some cores, but the scale at which this occurs is very difficult to estimate because there is not a continuous core data set that allows the full vertical examination of the breccia interval. This is due to the poor core recovery percentages that exist for this unit. From this it cannot be said with any certainty that the breccia interval is one single event deposit. For example in well C-418D core 1, in an interval of 8 m, an upwards-fining trend is noted, clasts of 1 mm to 1 cm occur at the upper part of the core whereas at the base of the core the clasts are of 2 mm to 8 cm. Furthermore the clasts are subrounded and moderately sorted (see Appendix 4). If the breccias consists of a single deposit and as evidenced from core 1, well C-418D, the clast size increases over a vertical range of 8 m, then what size would the clasts have to be at the basal most part of the breccia deposit ?.

The second point that argues against the impact model as the single mechanism is the homogeneously widespread distribution of the calcareous breccias found throughout the Campeche Basin (see Figure 2.20 and 2.21). It is difficult to envisage that the whole platform margin collapsed as a result of a single seismic shock triggered by the meteorite impact. Instead, it is speculated that a platform margin collapse associated to the meteorite impact would result in an irregular distribution of breccia deposits derived from zones of the platform margin that were the most prone to instability. The catastrophic margin collapse model that invokes entire collapse of the platform margin is too general if we are to take into consideration that platform

margins exhibit irregularities in their morphology and their intrinsic factors that both influence, to a large extent, the platform margin stability.

However, it is important to note that the areal extent and the thickness of the calcareous breccias exceeds any other breccia successions known in the geological record. One example that may serve as analogous to the possible platform margin collapse as earlier suggested is the Montagnais impact crater in eastern Canada (Jansa, 1993). At this site, in a morphological context based on a bathymetric map, the shelf edge seward from the Montagnais Crater shows a large semi-circular re-entrant where the slope is gentler than in the surrounding area which is accompanied by a sedimentary bulge at the toe-of-slope (Dypvik, 2003). These features have been interpreted to be associated to the collapse of the shelf edge triggered by the impact-generated shock waves. However, this hypothesis has not been tested as no wells have penetrated the deep basin of the Montagnais structure. Seismic data across the Montagnais structure shows that the crater rim is missing at the shelf edge, together with all Upper Cretaceous strata down to the top of the Lower Cretaceous carbonate platform (Figure 6.5). An important point to consider is that the possible margin collapse interpreted at the Montagnais Crater, as shown in Figure 6.5 is only 10 km away from the impact crater, whereas the breccias associated with the Chicxulub meteorite impact have been interpreted to extend as far as 300 km from the crater (Grajales-Nishimura, 2000). It is unfortunate that there is no clear evidence established that allows the visualization of the relative areal distribution and internal character of a platform margin collapse associated with meteorite impacts. In summary, the main component of the impact model is that the very large shock wave produced by the impact destabilised a long section of the platform margin and it collapsed in a single event to produce the 300 m breccia unit.

6.4 Subaerial Model

Horbury (2001) proposed an alternative model for the Upper Cretaceous calcareous breccias. His model is based on detailed analysis of well log data (mainly gamma and corrected gamma ray logs) from the hangingwall block of the Cantarell area. Some of the well logs were calibrated with core data. This analysis resulted in the construction of a litho-facies framework. Mapping over the structure of simple API

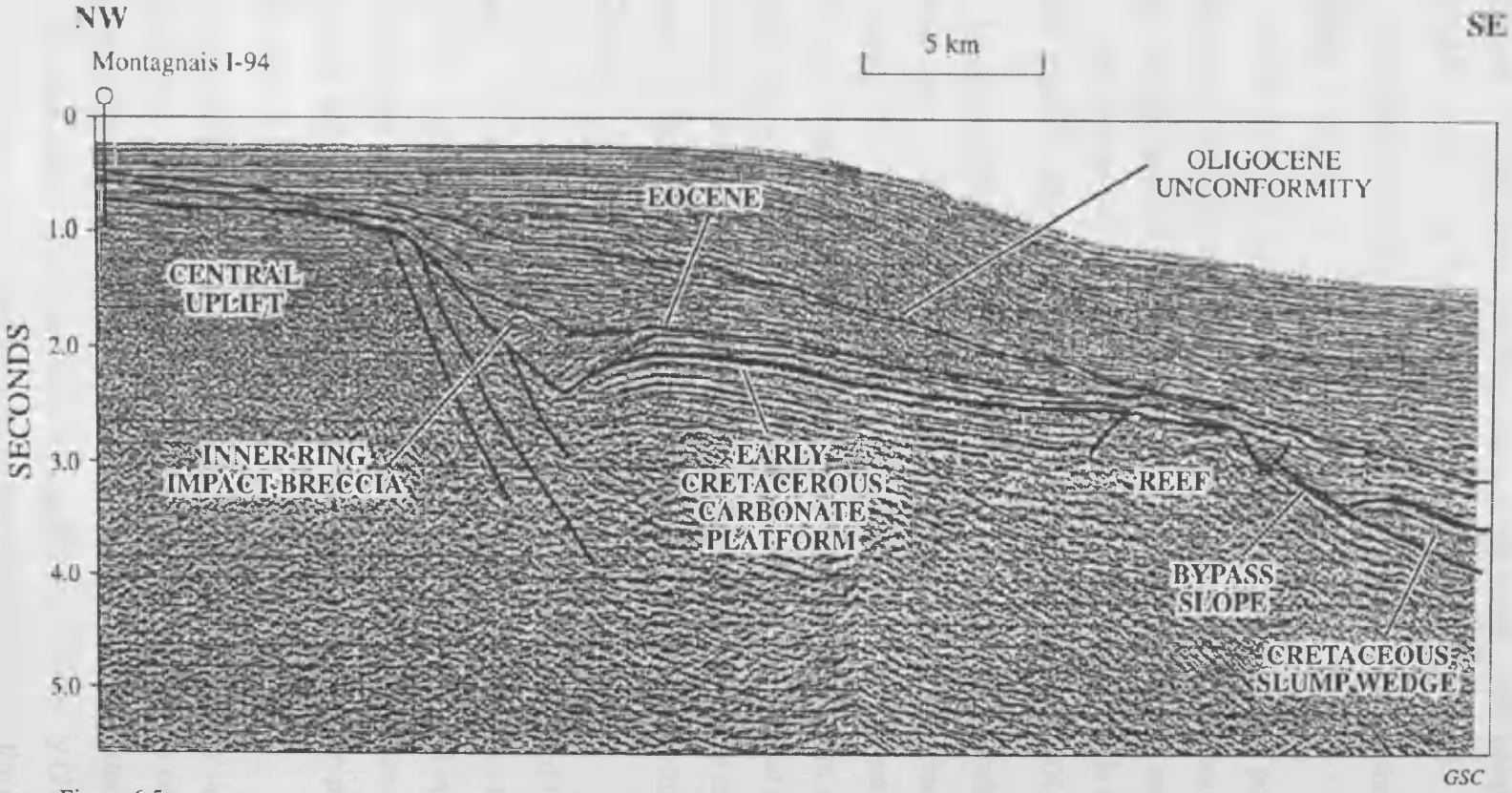

Figure 6.5
Seismic profile oriented form the central peak of the Montagnais impact crater toward the shelf edge and deep North Atlantic ocean basin, southern Canada. Note that the outer rim is interpreted to be missing as well as all Late Cretaceous sedimentary succession as a result of the outer continental margin collapse. After Dypvik, 2003.

gamma cutoffs (of 12.5 and 25 API) revealed an areal distribution that can be interpreted as a low-gamma platform margin type system located in the centre of the field, with high-gamma (high-U) platform interior facies to the north and a second high-gamma (high-K) slope / basinal facies to the south. This interpretation is supported by some of the facies noted from core data (Figure 6.6).

Horbury (2001) proposed a stratigraphic division scheme for the Upper Cretaceous:

The uppermost interval (units KS10 and KS20) consist of polymicitc conglomerates (see Chapter 3, Section 3.4.3.3, Appendix 4). Isopach maps of this interval indicate that there is a patchy distribution in the northern sector of the field. However, this is not the case towards the south where considerable thinning is observed, possibly due to erosion/or non deposition (Horbury, 2001).

Underlying the polymicitc conglomerates, unit KS 30, consists of high API and very spiky log character, often with upwards-decreasing API cycles, locally with low API marker beds. This is almost always the highest API unit found throughout the northern and central part of the field and is interpreted to represent a restricted platform carbonate setting. Core data from this interval exhibit textures that can be interpreted as karstic (see Chapter 3, Appendix 6) and a fracture arrangement that can also be interpreted to be indicative of cave collapse systems associated with karstic settings (see Chapter 3, Appendix 6) (Horbury, 2001).

The underlying units (KS40 to KS70) comprise the bulk of the lower gamma carbonate intervals. Isopachs indicate that this interval thickens to the south. From the isopach map and at the top of the unit, a sharp deflection is noted in the well logs, and an unconformity is interpreted. From the isopach map palaeohighs in the north and centre of the field are interpreted. These units are interpreted to represent mainly a platform setting (Horbury, 2001).

The basal most unit KS80 is seen to consist of a generally upwards decreasing API cycle. The character of this unit is usually spiky, and can be correlated locally within the southern part of the field, however it cannot be correlated with confidence across the entire field. Based on the well log character, Horbury (2001) suggests that much of the Middle Cretaceous appears to have been eroded in the central and

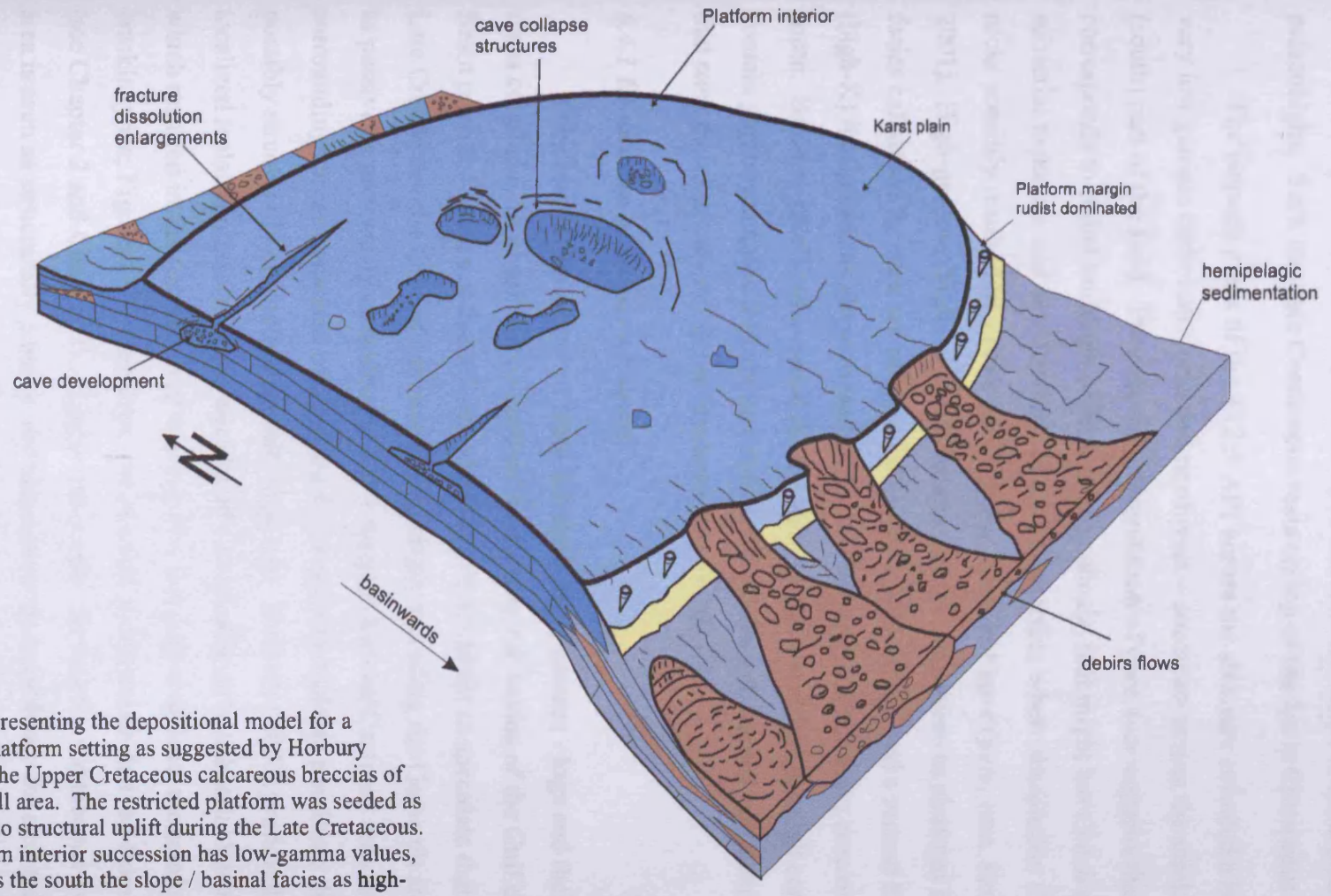

Figure 6.6
Cartoon representing the depositional model for a restricted platform setting as suggested by Horbury (2001) for the Upper Cretaceous calcareous breccias of the Cantarell area. The restricted platform was seeded as a response to structural uplift during the Late Cretaceous. The platform interior succession has low-gamma values, and towards the south the slope / basinal facies as high-gamma (high-K). The platform region was subject to periods of subaerial exposure which resulted in development of karstic features. Modified from Scholle, 1995.

northwestern parts of the field, and the Late Cretaceous onlaps or thins onto the palaeohighs. Such that late Cretaceous rests on top of the Early Cretaceous or older.

The isopach maps of the <12.5 API across the structure revealed a belt of local very low gamma carbonates oriented northwest – southeast across the southwestern – (south) part of the field. Provisional interpretation of core data suggests that this region corresponds to rudist buildups or high energy shoals, that might have been subjected to subaerial exposure and development of a karstic terrain where dissolution of carbonate rocks possibly resulted in a cave network and some collapse (pers. com. Horbury, 2001). High-gamma (high-U) facies interpreted to correspond to platform interior facies calibrated by core are present to the north of the field, and a second high-gamma (high-K) interpreted as slope to basinal facies and well calibrated by core occurs to the south. Horbury (2001) also noted that in this (high-K) southern area, all cored intervals contain globotruncanids that are associated with slope and basinal sedimentation, and that such facies are absent in the northern part of the field.

6.4.1 Evaluation of subaerial model

The observations derived from the analysis of gamma - logs and their isopach maps coupled with observations derived from other sub basins of the Gulf of Mexico Basin provided evidence that allowed Horbury et al (2003) to speculate that during the Late Cretaceous the Gulf of Mexico basin margin including the Cantarell area was not as passive as previously considered. They suggest that the Cantarell area and surroundings areas consisted of a setting dominated by isolated platforms that were possibly structurally controlled by salt diapirism. Horbury (2003) proposed that localized isolated platform areas were uplifted and subject to subaerial karstification which resulted in the formation of breccia-like facies (polymictic, monomictic and crackle types; Figure 6.6). However, the seismic observations derived from this thesis (see Chapter 2 and Chapter 3), suggest otherwise. During the Cretaceous the Cantarell area is seen as structurally passive and there is no clear evidence for structural uplift and development of minibasins. Furthermore, on a more regional scale the Cantarell area is now seen to be situated in a base of slope setting (see Enclosures 2 to 4, Chapter 2, Section 2.3.4).

A point to consider however, is the areal extent of the 3D seismic data used in this study may not be extensive enough to image the occurrence of the minibasin setting as suggested by Horbury (2001). Secondly, the structural development that occurred during the Neogene has altered significantly the signature of the Late Cretaceous depositional setting, which may have been overprinted. However, the Western and Eastern Platforms (see Chapter 4, Section 4.2.1) exhibit almost undeformed successions, which allow to argue for a passive structural domain during the Late Cretaceous time.

If structural uplift took place during the Late Cretaceous as suggested by Horbury (2001), this would have had to be less than the vertical resolution of the seismic data, because no evidence of structural uplift (onlap) is seen in the seismic data (see Chapter 3, Sections 3.5.3.2 and 3.6). In such a case, the structural relief would have to have been less than 100 to 170 m. Instead, parallel and concordant seismic reflections are seen in the Cretaceous interval. Although, the observations in this thesis agree with Horbury (2001) in that there is a general thinning of the Cretaceous towards the north (see Chapter 3 Figure 3.35).

6.5 Proposed model: a polyphase model

6.5.1 Introduction

The model here presented for the Upper Cretaceous calcareous breccias is based on a critical review of the previous models in the light of new evidence derived from this study. As previously documented, various internal breccia facies have been observed (see Appendix 4). Their origins have been interpreted to correspond to different geological processes, subaerial versus talus-derived. However, in the previous models presented above, the structural evolution and associated processes of the Cantarell area were not taken into consideration. In this thesis it has been demonstrated that the structural evolution of the area modified to a large extent the Cantarell reservoir package (see Chapter 4). Based on key observations it is suggested that during the compressive event that occurred during the Neogene, the originally deposited breccia underwent significant modifications at the macro and micro scale. These elements will be discussed in this section which forms the central element of the proposed model.

6.5.2 Supportive evidence

The supportive evidence for the proposed model as summarised from previous Chapters is presented below. The evidence is divided into well scale and seismic scale.

The most important observations derived from core data and well completion logs for the Upper Cretaceous calcareous breccias are summarised as follows:

1. Various types of breccia facies have been recognised within the Upper Cretaceous interval: Polymicitc conglomerates, polymicitc breccias, monomyctic breccias and crackle breccias (see Chapter 3, Section 3.4.3.3).
2. The porosity within this interval consist of vugular, fractured and matrix porosity (see Chapter 3, Section 3.4.3.3).
3. Some of characteristics noted from core data can be associated to karstic processes (see Section 6.2.3).
4. Core recovery percentages are significantly reduced towards the forelimb and the crestal regions (see Chapter 3, Section 3.4.3.3).

From the seismic analysis the following observations are summarised:

5. During the compressional event a structural relief greater than 1000 m was developed. As this occurred the structural highs were subject to wave base erosion and very probably to subaerial exposure (see Chapter 2, Section 2.3.4.3, Figure 2.32).
6. During the exposure of the crestal region of the Cantarell area, faults that are noted from the seismic data appear to vertically connect the erosional surface with deeper structural levels, as suggested by the truncation of the faults against the INU (see Chapter 3, Section 3.5.5).
7. The seismic character along the crest exhibits highly discontinuous seismic reflections. Although variations in the degree of continuity occur laterally and vertically, generally the seismic reflections become relatively more continuous with depth (see Chapter 4, Section 4.4.2.2).

6.5.3 Proposed model

Based on key observations of this thesis and a review of relevant literature it is suggested that the Upper Cretaceous calcareous breccias underwent various significant geological processes that have altered them as we see them today. A polyphase model is herein suggested to consist of three main stages (Figure 6.7).

6.5.3.1 Stage 1

It is interpreted that during the Late Cretaceous, the Cantarell area was situated in a base-of-slope to mid slope setting in which sedimentation occurred as debris flows, rock avalanches and slumps which were sourced mainly from the platform margin that was situated approximately 16 km to the east (see Enclosures 2 to 4, and Figure 6.8). Minor breccia intervals found at lower stratigraphic levels (Mid Cretaceous and Kimmeridgian) provide compelling evidence to suggest that deposition of debris-flows along the Cantarell area was a process well established since the Kimmeridigan (see Chapter 2, Section 2.23, and Appendix 4). However, during the Late Cretaceous this process was significantly enhanced as suggested by the apparent thickness of the breccia interval. Grajales-Nishimura (2000) reports this as being 300 m, whilst Cantú-Chapa and Landeros-Flores (2001) report it as consisting of up to 260 m that thins gradually towards the south-west where it becomes absent. The dimension of this platform margin derived succession as reported (Grajales-Nishimura, 2000; Cantú-Chapa and Landeros-Flores, 2001) exceeds any other breccia succession known in the geological record (see Table 6.1 and Section 6.2.1.3). From these observations the possibility is taken into consideration that the unusual thick deposit of Upper Cretaceous breccias were enhanced by the seismic shock delivered by the Chicxulub meteorite impact, which resulted at least in the collapse of portions of the platform margin. This hypothesis is strengthened when considering the volume of calcareous breccia that occurs at the Upper Cretaceous interval (see Figures 2.20 and 2.21). However, it is also stressed that the basin margin architecture during the Late Cretaceous provided the key factors that allowed the cyclic deposition of avalanches, debris flows and slumps along the base-of-slope.

Internally, some of the breccia clasts exhibit fractures that are only hosted within the clasts and do not appear to propagate towards the matrix. These have been

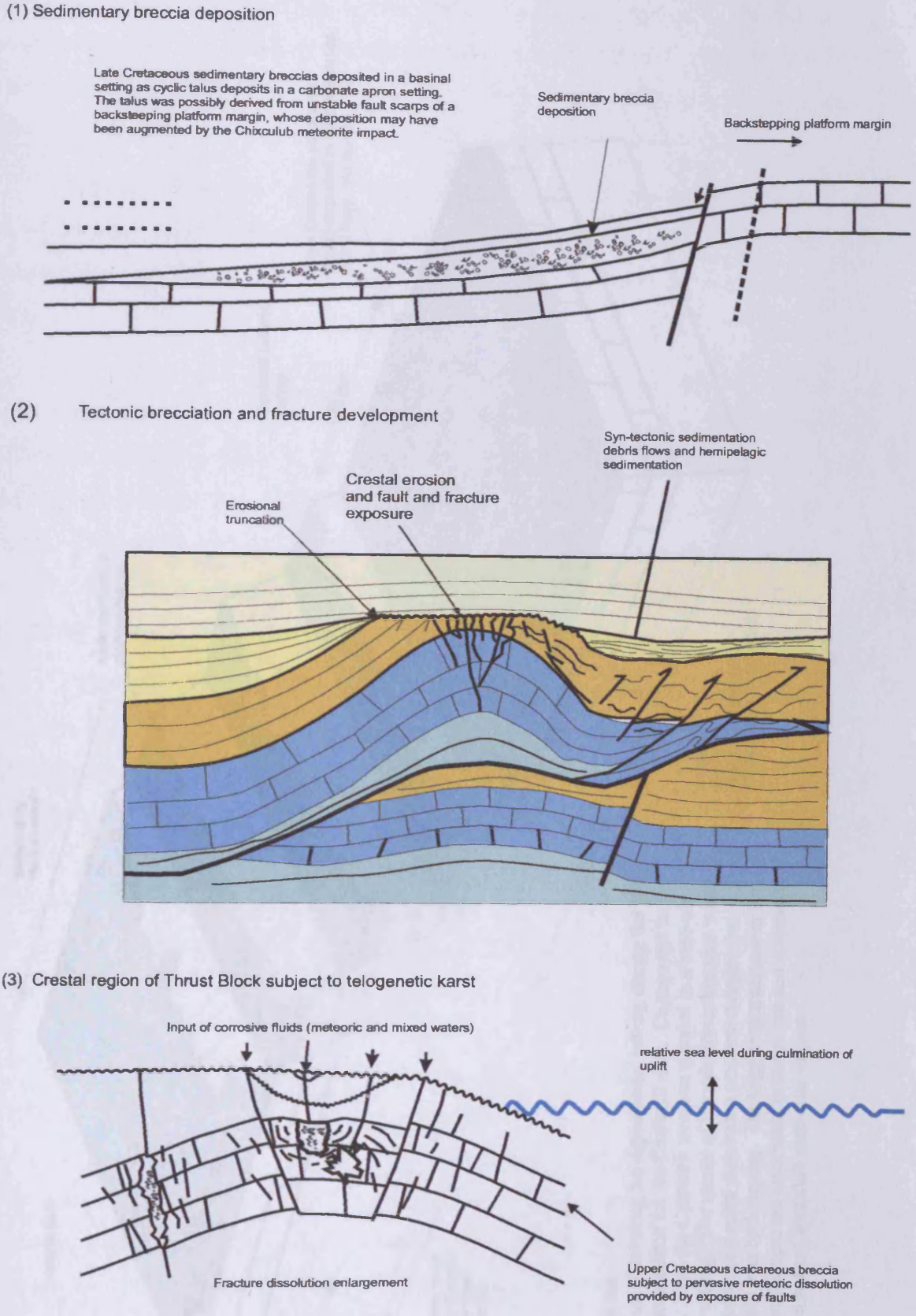

Figure 6.7

Cartoons illustrating the various stages that the Upper Cretaceous calcareous breccias were subject to. (1) Initial deposition of the calcareous breccias in a base-of-slope setting, (2) tectonic brecciation and fracture development as a result of the compressional event, and (3) development of karstic features derived from telogenetic karst associated to the uplift and subaerial exposure of the crestal region.

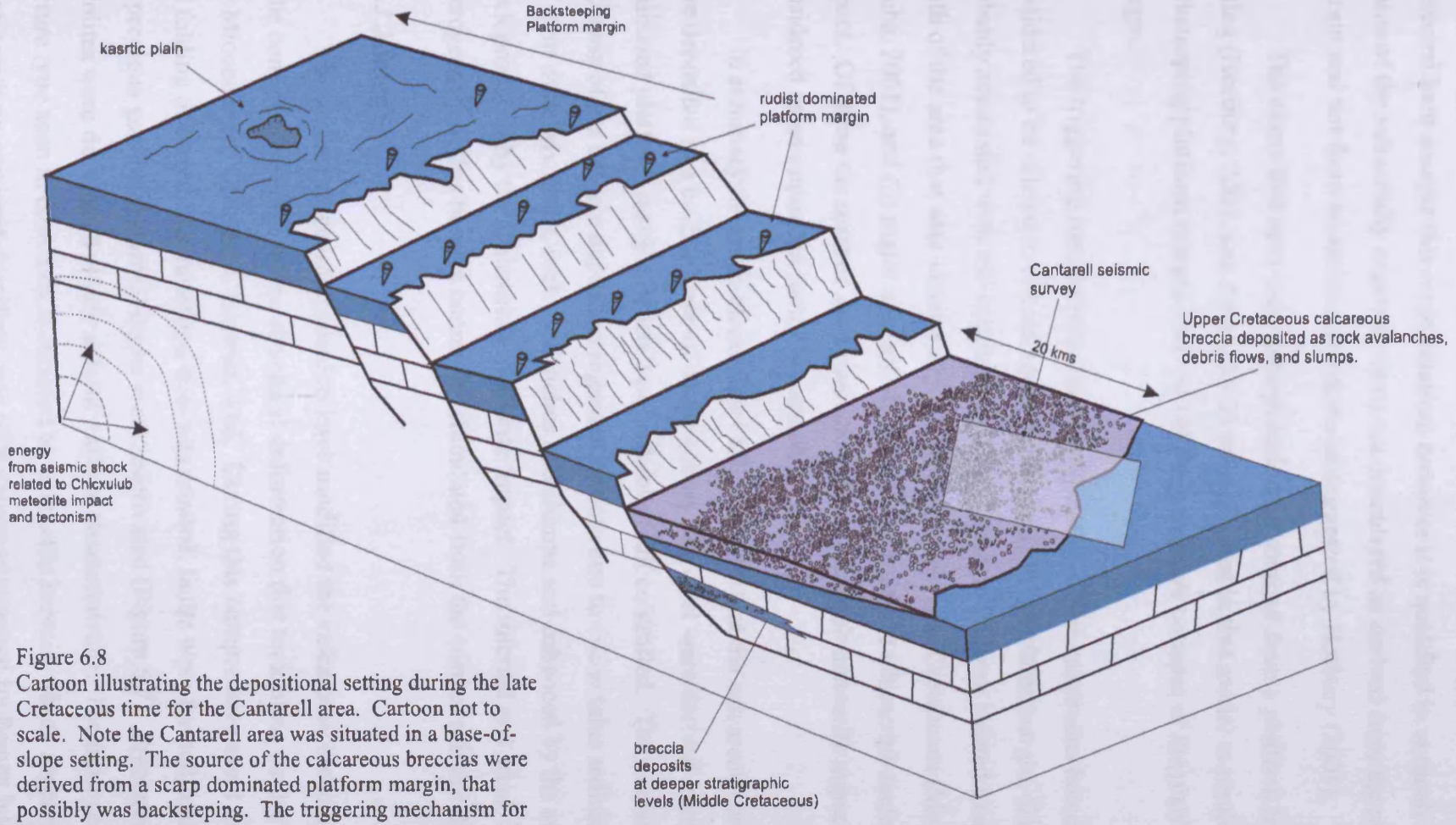

Figure 6.8
Cartoon illustrating the depositional setting during the late Cretaceous time for the Cantarell area. Cartoon not to scale. Note the Cantarell area was situated in a base-of-slope setting. The source of the calcareous breccias were derived from a scarp dominated platform margin, that possibly was backsteping. The triggering mechanism for margin collapse are associated to tectonism and seismicity related to the Chicxulub meteorite impact.

interpreted by Horbury (2001) as representative of subaerial exposure. The model presented here accepts this interpretation, however it is qualified in as much as the source of the subaerially exposed clasts are considered as derived from the platform margin and not from an isolated platform as suggested by Horbury (2001).

The clasts that have been interpreted to be sourced from a platform interior setting (Horbury, 2001, see Appendix 2) are explained in this model to result from (i) a backsteeping platform margin and / or (ii) from massive collapse of the platform margin.

The triggering mechanisms for the deposition of the calcareous breccias are considered to be related to (1) subaerial exposure of the platform margin, (2) seismicity probably associated with the structuring of the Sierra de Chiapas located towards the south of the area that was structurally active during the Late Cretaceous (Meneses-Rocha, 2001), and (3) major seismic shock derived from the Chicxulub meteorite impact. Of these the seismic shock associated to Chicxulub meteorite impact is considered as an important factor to consider.

In summary the main elements of this stage are that the calcareous breccias were deposited in a basinal base-of-slope setting, the clast were derived from a scarp dominated platform margin which was probably fault controlled. The overwhelming thickness of the breccia deposit is regarded as both due to cyclic talus sedimentation in the form of debris flows, rock avalanches and slumps and enhanced by the seismic shock produced by the Chicxulub meteorite impact. The internal and areal heterogeneity of this breccia cannot be elucidated from the current seismic data set.

6.5.3.2 Stage 2

The second stage interpreted to have modified the calcareous breccias is related to the compressive stage of the structural deformation that took place during the mid to late Miocene (see Chapter 4, Section, 4.6). During this compressive event thrusting and folding occurred, the structural trap was created, faults were formed, and some of the previous generated normal faults were reactivated (Figure 6.7). Fractures and stylolites were developed which exhibit various characteristics. The most common fracture type seen in core data is referred to as crackle breccia, which appears mainly as chaotic with no apparent dominant sets of fractures as reported by Pemex internal

reports (2000). However, it is suggested that the inability to identify defined fracture sets is related to the poor core recovery, where no continuous core samples have been obtained, and the fact that no oriented cores are available that would allow a better characterisation of fracture sets from core data.

Seismic observations reveal that faults in the hangingwall have a dominant north-west to northerly strike. The forelimb region as well as the crestal region exhibits the most seismically discontinuous character that is interpreted to be associated with faulting, and in turn gives a provisional index of fracture intensity. The provisional fracture intensity index needs to be calibrated against well data, either core and / or image logs. Along the forelimb the discontinuous seismic reflections appear mainly oriented north – south, as revealed from seismic sections that are oriented west-east (see Chapter 4, Section, 4.4.2.3).

In summary the main elements of this stage are that the calcareous breccias that were deposited during the Late Cretaceous underwent significant structural alteration during the compressive event (Early Miocene to Mid Miocene). This structural event overprinted the calcareous breccia interval with sets of fractures and faults. Seismic observations suggest that the Western and Eastern Fault corridors are the most structurally disrupted. Within the hangingwall, the crestal and forelimb regions exhibit significantly disrupted seismic reflections that are provisionally interpreted as a qualitative index of fracturing. Within the forelimb and crestal regions the discontinuous seismic character changes laterally, which has been interpreted as indicators that the fracture density changes laterally as well. From these observations three principal regions are suggested along the crest (see Figure 4.12 from Chapter 4, Section 4.4.2.2, and Figure 4.40). In a generalised manner, the seismic reflections become more continuous with depth at about .25 to .5 msec twt beneath the INU. However there are significant exceptions especially at the central part of the crest (see Figure 4.39, from Chapter 4, Section 4.4.2.2.).

6.5.3.3 Stage 3

During the compressive structural development (Early Miocene to Mid Miocene), uplift of the entire Thrust Block occurred. It is estimated that a structural relief of about 1000 m was developed as the result of this structuring (see Chapter 2, Section 2.3.4.3, Figure 2.32). Associated to the structural development the Intra Neogene Unconformity (INU) developed. This erosional surface is accentuated across the crestal region of the Thrust Block (see Chapter 3 and 4). Based on a regional correlation of the Cantarell structure with respect to the platform margin at the time of structuring, it is suggested that the crestal region of the structure was situated in a domain where possible subaerial exposure occurred (see Chapter 2, Section 2.3.4.3, Figure 2.32). Erosional truncation is widely observed at the crestal region and the faults appear truncated by the INU. Along the crestal region highly to moderately discontinuous seismic reflections occur just beneath the INU. Overlying the INU continuous seismic reflections are generally seen (see Chapter 3, Section 3.5.5, Figures 3.39 and 3.40, and Chapter 4, Section 4.2.2.2, Figures 4.39 and 4.40). Beneath the INU, a near rectangular depression feature is present that is bounded to the east and west by faults that appear almost vertical (see Chapter 3, Section 3.5.5.4, Figures 3.39 and 3.40). These faults propagate above the INU, and minor sagging configuration overlies the rectangular depression.

The core recovery along the crestal region is the poorest and total loss of drilling fluid has been recorded in most wells that are situated at the crest of the structure (pers. comm. Ortuno-Maldonado, 2001).

The above observations allow to suggest that the near rectangular depression-like feature consists of a collapse structure, and morphologically resembles Poljes (Ford, 1989). Poljes are defined by Gams (1978) as large, flat floored, with steeply marginal slopes that have a karstic drainage system (Figure 6.9). Their development is directly linked to the local water table as the corrosive agent. The interpreted collapse feature seen at the crest of the structure may have undergone similar karstic process to Poljes (Ford, 1989). However, the dissolution process that occurred within the Cantarell area, most likely occurred underground (Figure 6.10). Meteoric fluids are envisaged to have penetrated the hangingwall block through the faults, and mixed with

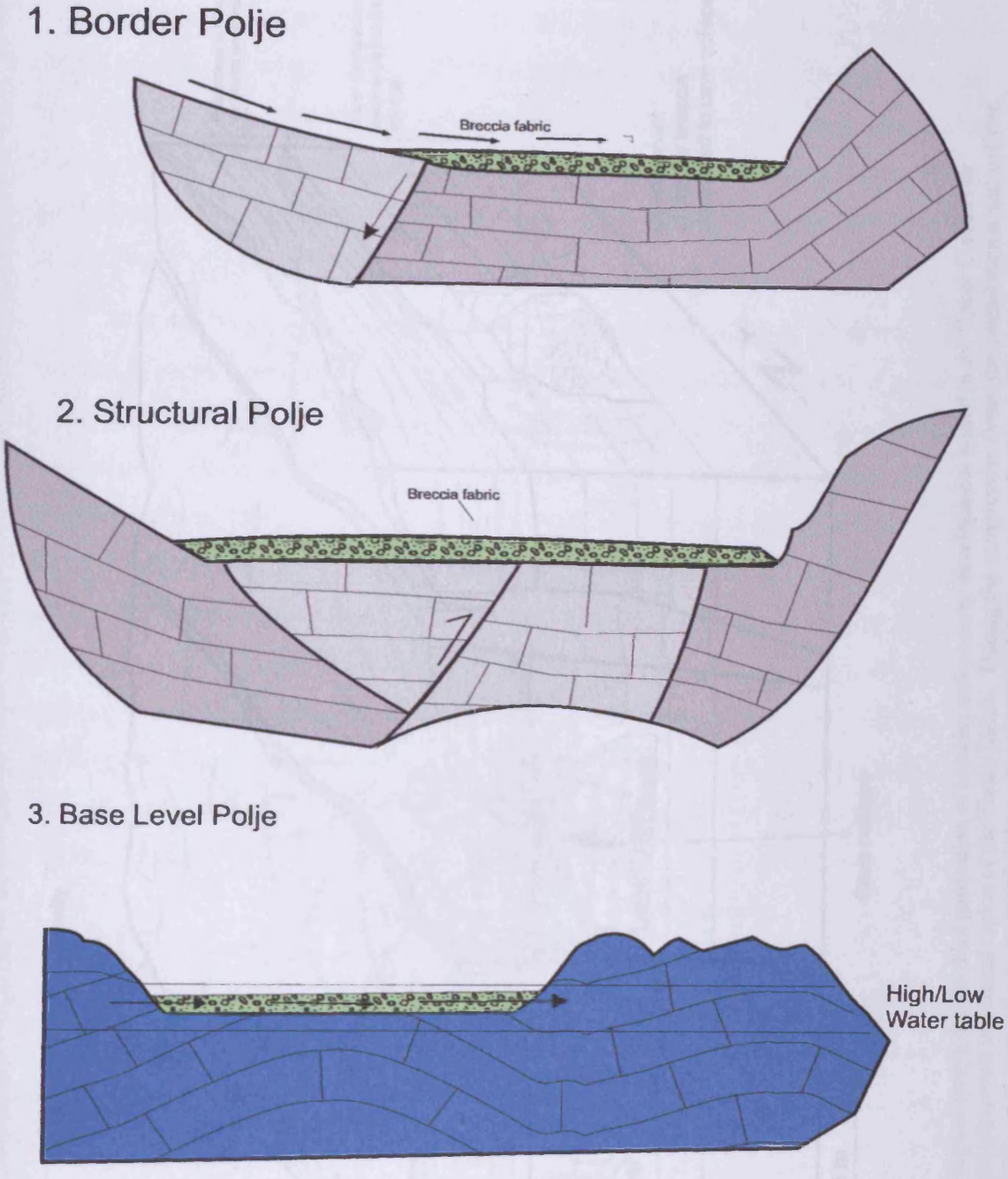

Figure 6.9
Basic types of Poljes modified from Ford, 1989. Defined as morphological features that occur within structural highs with a flat floor, closed basin with steeply marginal slopes, and have a karstic drainage system subject to meteoric water.

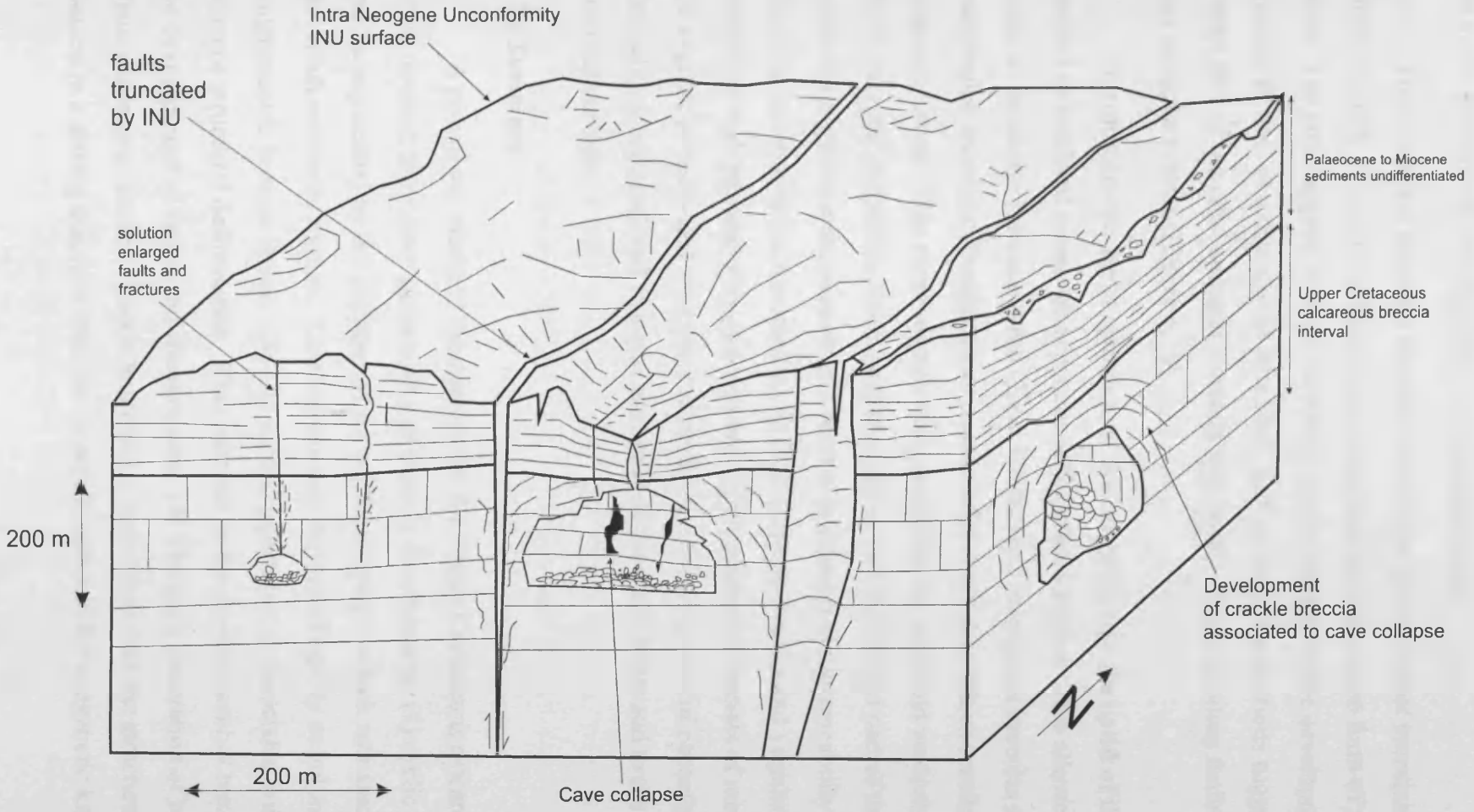

Figure 6.10
Cartoon illustrating the geological setting for the third generation of breccias and porosity development hosted in the Upper Cretaceous calcareous breccias. Cartoon represents the crestal region of the Thrust Block. During the compressive event, the crestal region was uplifted and subaerially exposed. Faults were exposed which provided the vertical permeability for meteoric fluids to infiltrate into deeper stratigraphic levels. (Modified from Loucks and Handford, 1992). Dissolution of the preexisting calcareous breccias resulted in the development of vugular porosity at various scales (macroscopic to seismic scale) as evidenced by core photos and seismic sections. Some fractures and faults were subject to solution enlargement.

the hosting fluids which resulted in dissolution of carbonate rocks. This would have led to the widespread development of telogenetic karst.

This proposed scenario resulted in the third generation of breccias. Cretation of karstic textures occurred, as formation of vugular porosity in the form of vugs and caves. The latter appear to have collapsed which resulted in the development of crackle breccias as well as monomyctic breccias. Key seismic observations suggest that the central part of the crest situated between two north – south trending faults consist of a cave collapse system (Figure 6.10)

In summary the main elements of this stage are that the uplift of the structure resulted in localised subaerial exposure of the crestal region. This allowed meteoric waters to penetrate the uncovered Upper Cretaceous calcareous breccias and lower stratigraphic intervals through the exposed faults at the INU which resulted in telogenetic karst. This event significantly modified the areal and vertical arrangement of the reservoir properties. This model suggests that the central part of the crestal region has high fracture porosity and vertical and horizontal permeability; the eastern part of the crestal region has medium to high fracture density and vugular porosity, and medium to high permeability; the western region probably consists of medium fracture and vugular porosity and medium permeability. Enhancement of porosity and permeability are predicted to occur proximal to the main faults and to the INU erosional surface.

6.5.4 Summary

A polyphase model is interpreted for the Upper Cretaceous calcareous breccias which resulted from three generations of breccia development: (1) cyclic talus derived breccia augmented by the collapse of the platform margin which was associated with Chicxulub meteorite impact. This breccia was deposited mainly as polymicitic and conglomeratic breccia facies. (2) The second generation is associated with the Neogene structural deformation. This resulted in the development of tectonic breccias and development of faults and fracture sets. (3) The third generation of breccias (mainly monomyctic and crackle breccias) is associated with the structural uplift which resulted in a setting that provided the required elements for telogenetic karst to develop.

6.5.5 Alternative speculative scenarios

In some reservoirs vugular porosity and palaeo- cave system development can also form as (1) hydrothermal karst (Smith, 2004) and (2) burial dissolution karst (Wright, 2002) also referred to as mesogenetic dissolution (Mazullo and Harris, 1992).

Dolomitization and leaching of carbonates occurs in many diagenetic environments. One that has historically been under-appreciated is the fault-controlled hydrothermal regime. In this regime, hydrothermal fluids that result in dolomitization following the same migration pathways and are trapped by the same seals as other fluids that result in leaching or diagenesis, or emplace hydrocarbons. Furthermore, these hydrothermal fluids move up the faults and fractures at times when the faults are active until they reach an overlying seal. At that point, the fluids are forced laterally into permeable zones. Thus, facies and fabrics matter - fluids are preferentially displaced into these more porous and permeable rocks (Smith, 2004). Not all of this process is positive for the reservoir properties. These migrating fluids also can bring with them fluids from which minerals precipitate in the voids created by dolomitization, thus reducing the new porosity and permeability. Late stage porosity-reducing minerals found associated with hydrothermal dolomites are anhydrite, sulfides, calcite, chert, chalcedony, kaolinite and other clays. Many of these have been observed in the Trenton-Black River reservoirs, along with breccias, vugs, cemented fractures, celestite, saddle dolomite and matrix dolomite. Porosity in these reservoirs is mainly vuggy and fracture porosity which is hosted within breccia intervals (Smith, 2004).

The geologic evolution of the Cantarell area provides the necessary factors for hydrothermal dissolution to have occurred: deep rooted faults being active during the compressive event and during the latest extensional event. It is speculated here that during the structural episode the faults acted as migration paths for hydrothermal fluids that resulted in diagenesis and dissolution of the host rock medium. However as noted by Smith (2004) hydrothermal karst generally have a mineralogical signature that should allow the identification of this process.

Karst associated with degradation of hydrocarbons results from the corrosive brines that are liberated as the hydrocarbon migrates into the reservoir rock. This

mechanism of burial dissolution (Wright, 2002) is also referred to as mesogenetic dissolution (Mazullo and Harris, 1992). Herein, burial dissolution is considered to occur below the zone of penetration of undersaturated meteoric waters (Wright, 2002). The processes that can cause this type of burial dissolution are related to the thermal degradation of hydrocarbons which is a natural process of hydrocarbon maturation, and to thermochemical reduction of sulphates. Corrosion can also be accounted for by mixing of different fluids. Thermal degradation of organic matter when hydrocarbons are produced releases methane, CO_2, H_2S, and organic acids. In the presence of sulphate ions the methane further breaks down to produce aggressive and corrosive solvents. The chemical processes can occur at the front of migrating hydrocarbons, dissolving the host rock thus creating secondary porosity in the form of vugs, fault widening and cave structures that may collapse. Further degradation of hydrocarbons at higher temperatures can lead to further release of CO_2, H_2S, methane and pyrobitumen. These products may further contribute to porosity development in the overlying gas cap, whereas pyrobitumen acts to decrease porosity (Moore, 2001).

Thermochemical sulphate reduction (TSR), usually takes place in temperature ranging 100-400 C. Biogenic sulphate reduction occurs at lower temperatures, < 80 C. These processes take place relatively rapidly, and produce sulphide, and bicarbonate that can contribute to cementation and CO_2. Porosity can be created in the deeper subsurface by dissolution of carbonate rocks resulted from the oxidation of hydrogen sulphide. This process has been termed "sulphuric acid oil filed karst" by Hill (1995). Alternatively the mixing of fluids with different H_2S concentrations can lead to corrosion.

Thermal degradation of hydrocarbons and thermochemical sulphate reduction are possible mechanisms for the formation of vugular porosity and cave collapse structures observed within the Thrust Block of the Cantarell area. However, the accurate identification of this process is beyond the scope of this study. Based on key observations carried out in this study, the following points are presented:

If vugular porosity is related to hydrocarbon maturation why is it that the vugular and cave collapse features are observed near the crest of the structure, when the source rock is located about 1500 m below this area. No major vugular porosity is observed near the source rock. On the contrary, the vugular and collapse structures are

located towards the crest of the Thrust Block and internally the reservoir contains a gas cap area that is saturated with CO_2, H_2S, methane and pyrobitumen products that may contribute to dissolution enlargement of pre-existing pores and fractures and creation of new pore systems.

The stresses involved in the deformation and uplift processes changed the internal fluid equilibrium and hydrostatic gradient (water and hydrocarbons). This change in fluid equilibrium and hydrostatic gradient may have resulted in the release of aggressive sulphides contained within the hydrocarbons and the possible migration of these could have dissolved carbonate and dolomite rocks; this process have been investigated and explained previously (Petukhov, 2001).

From the seismic data analysis and the integration of key well core descriptions it is not possible to discriminate the origin of the karst observed as a result of sub-aerial or deep burial karst. As discussed earlier both scenarios can be associated with the interpretation of karst. However, the evidence provided in this thesis argues for karst being mainly telogenetic in origin (see Stage 3). The accurate discrimination of these processes needs to be investigated from a geochemical and core analysis perspective (see Conclusions and future research, Chapter 7).

6.6 Conclusions

The Cantarell area hosts a world-class petroleum system. The most productive reservoir interval is hosted in Upper Cretaceous calcareous breccias. Key observations derived from this study and coupled with a critical review of previous models of the Upper Cretaceous calcareous breccias suggest a new model that explains some of the geologic complexities encountered within the Cantarell area. This model may help explain the scale of the reservoir and the significant spatial complexities of the reservoir properties.

Chapter 7

Conclusions and future research

7.1 Conclusions

The detailed analysis of 3D and 2D seismic data combined with key well information allowed the identification of various important geological processes that operated during the deposition and later alteration of the Cantarell Field. The seismic observations allowed documentation, in detail, of the stratigraphic and structural framework of the Field. The most relevant and general conclusions of this PhD project are summarised below. For detailed conclusions refer to the conclusions that are presented at the end of each Chapter.

1. The Cantarell area evolved from a mid ramp setting during the Late Jurassic (Kimmeridigan) to a base-of-slope setting with a scarp-dominated platform margin by the end of the Cretaceous. During the Tertiary the sedimentation style switched from a carbonate-dominated to a clastic-dominated setting. Major progradation of the continental shelf is observed during the Mid Miocene to Recent.

2. Three main phases of structural deformation were identified, these being: (1) early extension, (2) compression, and (3) late extension. The early compression was related to the initial opening of the Gulf of Mexico; the compressive event took place during the Miocene (Mid to Late). It was during this episode that the impressive thrust structure developed in conjunction with the Western Fault Corridor, Eastern Fault Corridor, Western Platform and Eastern Platform (structural elements defined in this PhD research). Structural uplift in the order of 1000 m of the thrust structure occurred. The late extension episode occurred during the Pliocene to Recent. In structural terms these three events have resulted in the reactivation of some structural features. Most extensively the within the Western Fault Corridor. The Cantarell structure is unique, it consist of a narrow thrust (8 km) with a measured displacement of 12 km and a

structural relief of over 1200 m, which is 500 m higher than the structures that are located nearby.

3. The Cantarell Field has undergone various geological processes that have modified significantly the reservoir plumbing system, these being: faulting and fracturing, and mesogenetic karst (see Chapter 6). These processes can answer some of the unique geological characteristics that have been observed within the Cantarell Field, such as the thick breccia deposit occurring at the Upper Cretaceous interval, and the structural morphology.
4. The breccias that occur at the Upper Cretaceous interval exhibit unique dimensions (300 m thick and widely distributed among the Campeche Basin). However, it is suggested here that this breccias are the result of at least three generations of breccia development which resulted from different geological processes occurring at different geological times.

7.2 Future Work

As in most cases the accuracy of any proposed geological model is sensitive to the integration and comparison with other data that either enhances the initial model or modifies the proposed hypothesis. By integrating new data to the current model the exploration/production model will be enhanced which will allow to understand better the plumbing system of the reservoir. Specific future research that is recommended includes:

(1) Further seismic mapping is necessary in areas adjacent to the Cantarell area, to provide an accurate picture of the structural trends. This will enhance the understanding of the kinematics of the region as a whole, and will allow assessing the current structural model herein proposed.

(2) To provide an accurate picture of the Cretaceous platform margin and to discern the possibility of whether the platform margin underwent massive collapse or platform margin bascksteepening; to achieve this continuous 3D seismic mapping is required over the entire platform margin.

(3) Detailed core analysis needs to be undertaken to understand the internal character of the Upper Cretaceous breccias, which will in turn provide insights into the

processes that occurred at the platform margin and along the slope. It should provide evidence on whether the breccias were deposited in a single event, or as a result of various events.

(4) Geochemical analysis will allow us to decipher the depth at which the karstic processes took place and to underpin the source of the corrosive brines, whether meteoric or hydrothermally derived. For a detailed methodology on how this analysis can be done see Wang (2000).

(5) A detailed analysis of FMI image logs will allow us to characterise and define fracture sets occurring among the reservoir units. This will provide a greater understanding of the plumbing system of the reservoir, and permit the assessment of the suggestions been proposed in Chapter 6 about the distribution of the reservoir properties.

8. CITED REFFERENCES

Ambrose, W. A., Wawrzyniec, T. F., Fouad, K., Talukdar, S. C., Jones, R. H., Jennette, D. C., Holtz, M. H., Sakurai, S., Dutton, S. P., Dunlap, D. B., Guevara, E. H., Meneses-Rocha, J., Lugo, J., Aguilera, L., Berlanga, J., Miranda, L., Ruiz-Morales, J., Rojas, R., Solis, H. 2003. Geologic framework of upper Miocene and Pliocene gas plays of the Macuspana Basin, Southeastern Mexico. American Association of Petroleum Geologists, Bulletin, 87, 1411-1435.

Angeles-Aquino, F., Cantu-Chapa, A. 2001. Subsurface Upper Jurassic Stratigraphy in the Campeche Shelf, Gulf of Mexico. In: C. Batolini, R. T. Buffler, A. Cantu-Chapa (eds). The Western Gulf of Mexico Basin: Tectonics, sedimentary basins, and petroleum systems. American Association of Petroleum Geologists, Memoir 75, 183-216.

Angeles-Aquino, F. J., Reyes-Nuñez, J. M., Quezada-Muñeton, Meneses-Rocha, J. J., 1994. Tectonic Evolution, Structural Styles, and Oil Habitat in the Sonda de Campeche, Mexico. American Association of Petroleum Geologists, Bulletin and Forty-fourth annual convention of the Gulf Coast Association of Geological Societies, Forty-first annual convention of the Gulf Coast Section of the Society of Economic Paleontologists and Mineralogists. 78, 9, 1448-1449.

Angevine, C. L., Heller, P. L., Paola, C. 1990. Quantitative sedimentary basin modelling. American Association of Petroleum Geologists. Course Note Series, 32.

Anselmetti, F. S. 1994. Sonic Velocity in Carbonate Rocks. In: I. Palaz, K. Marfut (eds). Carbonate Seismology. Geophysical Developments Series No 6. Society of Exploration Geophysicists, 53-74.

Bally, A., Garcia-Molina, G. 1994. Structural Styles in the Sureste Basins, Mexico. American Association of Petroleum Geologists, annual convention 4; 31.

Barnes, P. M. 1996. Active folding of Pleistocene unconformities on the edge of the Australian-Pacific plate boundary zone, offshore North Canterbury New Zealand. Tectonics 15, 540-623.

Berberian, M., Qorashi, M. 1994. Co-seismic fault-related folding during the South Golbaf earthquake of Novemeber 20, 1989, in southeast Iran. Geology, 22, 531-534.

Bernal, A., Hardy, S. 2002. Syn-tectonic sedimentation associated with three-dimensional fault-bend fold structures: a numerical approach. Journal of Structural Geology, 24, 609-635.

Bloch, R. B., Von, Huene, R., Hart, P. E., Wentworth, C. M. 1993. Style and magnitude of tectonic shortening normal to the San Andreas fault across Pyramid Hills and Kettlemand Hills South Dome California. Geological Society of America Bulletin, 105, 464-478.

Borgomano, J. R. 2000. The Upper Cretaceous carbonates of the Gargano-Murge region, southern Italy: A model of platform-to-basin transition. American Association of Petroleum Geologists, Bulletin, 84, 1561-1588.

Bossellini, A.1993. Sequence stratigraphy in carbonates successions: some Italian examples (abs.): OTC 7107, Offshore Technological Conference Houston, 249 – 255.

Brown, L. F., Fisher, W. L. 1977. Seismic stratigraphic interpretation of depositional systems: examples from Brazilian Rift and pull apart basins. In: C. E. Payton (eds). Seismic stratigraphy; applications to hydrocarbon exploration. American Association of Petroleum Geologists, Memoir 26, 213-248.

Buffler, R. 1985. Distribution of crust and early history, Gulf of Mexico basin. Gulf Coast Association of Geological Societies Transactions 35, 333-344.

Buffler, R., 1991. Seismic stratigraphy of the deep Gulf of Mexico basin and adjacent margins. In: A. Salvador (eds). The Gulf of Mexico Basin. Geological Society of America, 353-387.

Buttler, R. W. H., Lickorish, W H. 1997. Using high-resolution stratigraphy to date fold and thrust activity: examples from the Neogene of south-central Sicily. Journal of the Geological Society, London, 154, 633-643.

Camargo-Zanoguera, A. 1980. Aplicación de la gravimetría y magnetometría a la explaración petrolera de las plataformas continentales mexicanas. Boletin de la Asociacion Mexicana de Geologos Petroleros 37, 25-34.

Cantu-Chapa, A. 1992. The Jurassic Huasteca Series in the subsurface of Poza Rica, Eastern Mexico. Journal of Petroleum Geology, 15, 259-282.

Cantu-Chapa, A. 1994. Informe bioestratigráfico. IPN, ESIA, Sección de Estudios de Postgrado e Investigación de Geología. Mexico, D. F.

Cantu-Chapa, A. Landeros-Flores, R. 2001. The Cretaceous-Paleocene Boundary in the Subsurface Campeche shelf, Southern Gulf of Mexico. In: C. Batolini, R. T. Buffler, A. Cantu-Chapa (eds). The Western Gulf of Mexico Basin: Tectonics, sedimentary basins, and petroleum systems. American Association of Petroleum Geologists, Memoir 75, 389-395.

Cartwright, J. A. 1989. The kinematics of inversion in the Danish Central Graben. In: M. Cooper, G. D. Williams (eds). Inversion Tectonics. Geological Society, London, Special Publication, 44, 153-175.

Cartwright, J. A. Trudgill, B. 1994. Relay-ramp forms and normal-fault linkages, Canyonlands National Park, Utah. Geological Society of America Bulletin, 106, 1143 – 1157.

Carrillo-Bravo, J. 1980. Paleocañones Terciarios de la Planicie costera del Golfo de México. Asociación Mexicana de Geólogos Petroleros, n. 32, pp. 27-55.

Christie-Blick, N., Biddle, K. T. 1985. Deformation and basin formation along strile-slip faults. In: K. T. Biddle, N. Christie-Blick (eds). Strile-slip deformation, basin formation and sedimentation. Society of economoic paleontologists and mineralogists, Special Publication No. 37, 1-34.

Cramez, C., Jackson, M. P. A. 2000. Superposed deformation stranddling the continental-oceanic transition in deep-water Angola. Marine and Petroleum Geology, 17, 1095-1109.

Crowell, J. C. 1959. Problems of fault nomenclature. American Association of Petroleum Geologists Bulletin, 43, 2653-2674.

DeCelles, P.G., Gray, M. B., Ridgway, K. D., Cole, R. B., Srivastava, P., Pequera, N., Pivnik, D. A. 1991. Kinematic history of a foreland uplift from Palaeocene synorogenic conglomerate. Beartooth Range Wyoming and Montana. Geological Society of America Bulletin, 103, 1458-1475.

Dengo, G., Bohnenberger, O. 1969. Structural development of northern Central America. In A.R. McBirney (ed). Tectonic Relations of Northern Central America and the Western Caribbean -- The Bonacca Expedition. American Association of Petroleum Geologists, Memoir 11, 203-220.

Dewey, J. F. 1975. Finite plate models: some implications for the evolution of rock masses at continental margins. American Scientific Journal. 275, (A), 260-284.

Diegel, F.A., Karlo, J. F., Schuster, D.C., Shoup, R.C., Tauvers, P.R. 1995. Cenozoic Structural Evolution and Tectono-Stratigraphic Framework of the Northern Gulf Coast Continental Margin. In: M.P.A. Jackson, D.G Roberts, S. Snelson (eds). Salt Tectonics: a global perspective. Association of American Petroleum Geologists, Memoir 65, pp. 109-151.

Droxel, A. W., Schlager, W. 1985. Glacial vs interglacial sedimentation rates and turbidity frequency in the Bahamas. Geology 13, 799-802.

Drzewiecki, P., A., Simo, A., J. 2002. Depositional processes, triggering mechanisms and sediment composition of carbonate gravity flow deposits: examples from the Late Cretaceous of the south-central Pyrenees, Spain. Sedimentary Geology, 146, 155-189.

Duval, B., Cramez, C., Jackson, M. P. A. 1992. Raft Tectonics in the Kwanza Basin, Angola. Marine and Petroleum Geology 9, 389-404.

Dypvik, H., Jansa F. L. 2003. Sedimentary signatures and processes during marine bolide impacts: a review. Sedimentary Geology, 161, 309-337.

Ebereli, G., Swart, P. Malone, M. 1997. Proceedings ODP Leg 166. Initial Reports.

Enos, P., Stephens, B. P. 1993. Mid-Cretaceous basin margin carbonates. Sedimentology 40, 539-556.

Enos, P. 1988. Evolution of pore space in the Poza Rica trend (Mid-Cretaceous), Mexico. Sedimentology. 35; 2, 287-325.

Ewing, T., Lopez-Flores, R. 1991. Principal structural features, Gulf of Mexico Basin. In: A. Salvador (eds). The Gulf of Mexico Basin. In the collection: The geology of North America. American Geological Society, map.

Faugeres, J. C., Stow, D. A. V., Imbert, P., Viana, A. 1999. Seismic features diagnostic of contourite drifts. Marine Geology 163, 1-38.

Faust, J., M. 1990. Seismic stratigraphy of the mid-Cretaceous unconformtiy (MCU) in the central Gulf of Mexico basin. Geophysics 55, 7, 868-884.

Ford, P. W., Williams P. 1989. Karst geomorphology and hydrology. Ed. Boston Unwin Hyman, 428-430.

Ford, M., Williams, E. A., Artoni, A., Verges, J., Hardy, S. 1997. Progressive evolution of a fault-related fold pair from growth strata geometries, Sant Llorec de Morunys SE Pyrenees. Journal of Structural Geology, 19, 413-442.

Galloway, W. E. 1991. Cenozoic. In: A. Salvador (eds). The Gulf of Mexico Basin. in the collection: Geology of North America, The Geological Society of America.

García-Hernández, J., Soriano-Mercado, E. 2000. Estudio de caracterización inicial de los yacimientos Cretácico superior y jurásico superior del campo Lum. Ciudad del Carmen Campeche, Pemex, inedito.

GEODAS databases: http://www.ngdc.noaa.gov/mgg/gdas/gd_sys.html

Gonzalez-G., R., Cruz, P. 1994. A new petroleum system in offshore Campeche, Mexico. 1st joint AAPG/AMGP Research Conference. Geological Aspects of Petroleum Systems.

Grajales-Nishimura, M., Cedillo-Pardo, E., Rosales-Dominguez, C., Moran-Zenteno, D. J., Alvarez, W., Claeys, P., Ruiz-Morales, J., Garcia-Hernandez, J., Padilla-Avila, P., Sanchez-Rios, A. 2000. Chicxulub impact the origin of reservoir and seal facies in the southeastern Mexico oil fields. Geology 28, 4, 307-310.

Gregory, A. R. 1977. Aspects of rock physics from laboratory and log data that are important to seismic interpretation. In: C. E., Payton (eds). Seismic stratigraphy-applications to hydrocarbon exploration: American Association of Petroleum Geologists, Memoir, 26, 15-46.

Guzman-Vega M. A., Mello M. R. 1999. Origins of Oil in the Sureste Basin, Mexico. American Association of Petroleum Geologists, Bulletin 83, 7, 1068-1095.

Harding, T. P. 1990. Identification of Wrench Faults Using Subsurface Structural Data: Criteria and Pitfalls. American Association of Petroleum Geologists, Bulletin, 74, 10, 1590-1609.

Hill, C. A. 1995. H_2S- related porosity and sulphuric acid oil filed karst. In: D. A. Budd, A. H. Saller, P. M. Harris (eds). Unconformities and porosity in carbonate strata. American Association of Petroleum Geologists, Memoir 63, 301-306.

Holl, J. E., Anastasio, D. J. 1993. Paleomagnetically derived folding rates, southern Pyrenees Spain. Geology 21, 271-274.

Horbury, A., D. 2000. Report detailing the Carbonate Sequence Stratigraphy and Reservoir Geology of the Cantarell Field. Ciudad del Carmen, Campeche, PEMEX.

Horbury, A., D., Stephen, H., Gonzalez-P., F., Rodriguez-F., Reyes, A., Ortiz, P., Martinez-M., Quintanilla-R., G. 2002. The western margin of the Gulf of Mexico in the late Mesozoic and Tertiary: less passive than previously imagined. (In press) American Association of Petroleum Geologists.

International Western Atlas, 1996. Caracterizacion de Yacimientos del Campo Akal.

Jackson, M. P. A., Cramez, C., Mohriak, W. U. 1998. Salt tectonics provinces across the continental-oceanic boundary in the Lower Congo and Campos Basin on the South Atlantic margins (Exnteded abstracts). In: Mello, M.R., Yilmaz, P. O. (eds). Extended abstracts volume: AAPG International Conference Exhibition: Rio de Janeiro, 40 – 41.

Kelson, K. I., Simpson, G. D., VanArsdale, R. B., Haraden, C. C., Lettis, W. T. 1996. Multiple late Holocene earthquake along the Rellfoot Fault, central New Madrid seismic zone. Journal of Geophysical Research. 101, 6151-6170.

Kendall, C. G. St. C., Schlager, W. 1989. Carbonates and relative changes in sea-level. In: M.B. Cita W.B.F. Ryan (eds). Carbonate Platforms of the Passive-Type Continental Margins, Present and Past. Marine Geology, 44, 181-212.

Klinger, R. E., Rockwell, T. K. 1989. Flexural-slip folding along the eastern elmore ranch fault in the superstition hills earthquake sequence of November, 1987. Bull. Seismol. Soc. Am. 79, 297-303.

Koyi, H., Aasen, O. J., Nybakken, S., Hogstad, K., Torudbakken, B. 1992. Determining geometry of salt diapirs by depth modeling of seismic velocity pull-up. Oil and Gas Journal, v. 90, n. 40, pp. 97-100.

Landeros-Flores R., Medina, L. 1993. Apendices Paleontológicos de los Pozos: Taratunich-1B, Chuck- 101, Ku-407, Kambul-1 Mukuy-1, Ixtoc-18, Abkatun-5, Cantarell-2239, Zinic-1, Pol-79. Departamento de Paleontología , Superintendencia de Exploración, Zona Marina, Petroleos Mexicanos Inédito.

Limon, M. 1996. A new petroleum system in offshore Campeche, Mexico. In: American Association of Petroleum Geologists International Conference and Exhibition Abstracts. Bulletin, 80; 8, 1307.

Lin, J., Stein, R. S. 1989. Coseismic folding, earthquake recurrence, and the 1987 source mechanism at Whitter Narrows, Los Angeles Basin, California. Journal of Geophysical Research, 94, 9614-9632.

Magoon, L., B., Travis, L. 2001. Pimienta-Tamabra (!) - A Giant Supercharged Petroleum System in the Southern Gulf of Mexico, Onshore and Offshore Mexico. In C. Bartolini, R. T. Buffler, A. Cantu-Chapa (eds). The western Gulf of Mexico Basin: Tectonics, sedimentary basins, and petroleum systems. America Association of Petroleum Geologists, Memoir 75, 397-420.

Mansfield, C., Cartwright, J. A. 2001. Fault growth by linkage: observations and implications analogue models. Journal of Structural Geology, 23, 745 – 763.

Marcuda, D. B. Jr. 1997. Carbonate Seismic Facies Analysis. In: I. Palaz K. J. Marfut (eds). Carbonate Seismology. Geophysical Development Series, No. 6. Society of Exploration Geophysicists, 95-120.

Marion, D, Juzba, D. 1997. Acoustic properties of carbonate rocks: Use in quantitative interpretation of sonic and seismic measurements. In: I. Palaz K. J. Marfut (eds). Carbonate Seismology. Geophysical Development Series, No. 6. Society of Exploration Geophysicists, 75-94.

Maritn, R.G. 1980. Distribution of salt structures in the Gulf of Mexico: U.S. Geological Survey Miscellaneous Filed Studies Map MF-1213 2 plates, 8 p.

Marton, L. G., Buffler, R. T. 1999. Jurassic-Early Cretaceous Tectono-Paleogeographic Evolution of the Southeastern Gulf of Mexico Basin. In: P. Mann (eds). Caribbean Basins. In the collection: Sedimentary Basins of the World. 4, 63-91.

Marton, L. G., Tari, G.C., Lehman, C.T. 2000. Evolution of the Angolan passive margin, West Africa, with emphasis on post-salt structural styles. American Geophysical Union, Geophysiscal Monograph Series 115, 129 – 149.

Masaferro J. L., Bulnes, M., Poblet, J., Ebreli, G. P. 2002. Episodic folding inferred from syntectonic carbonate sedimentation: the Santaren anticline, Bahamas foreland. Sedimentary Geology, 146, pp. 11-24.

McClay, K. 1992. Glossary of thrust tectonics terms. In: McClay, K. (ed). Thrust Tectonics. Chapman Hall, London, 419-433.

McFarlan, J., Silvio-Meneses, L. 1991. Lower Cretaceous. In: A. Salvador (eds). The Gulf of Mexico Basin. In the collection: The Geology of North America. The Geological Society of America.

McNeeley, M. 1973. Biostratigrahy of the Mesozoic and Paleogene pelagic sediments of the Campeche Embankment. Initial reports of the Deep Sea Drilling Project. J. L. Worzel. Washington, D. C., U.S. Government Printing Office. 10: 679-695.

Mazullo, S. J., Harris, P. M. 1992. Mesogenetic dissolution: its role in porosity development in carbonate reservoirs. American Association of Petroleum Geologists, 76, 607-620.

Medwedeff, D. A. 1989. Growth fold-bend folding at Southeast Lost Hills, San Joaquin Valley, California. American Association of Petroleum Geologists Bulletin, 73, 54-67.

Mello, M. R. 1993. The habitat of petroleum in the Brazilian marginal basins; a paleoenvironmental and biological marker approach. In: AAPG/ SVG international congress/ exhibition; abstracts. American Association of Petroleum Geologists, Bulletin, 77, 2, 334.

Meneses-Rocha, J. 2001. Tectonic evolution of the Ixtapa graben, an example of a strike-slip basin in southeastern Mexico: Implications for regional petroleum systems. In: C. Batolini, R. T. Buffler, A. Cantu-Chapa (eds). The Western Gulf of Mexico Basin: Tectonics, sedimentary basins, and petroleum systems. American Association of Petroleum Geologists, Memoir 75, 183-218.

Meyerhoff, A. A. 1980. Future petroleum provinces of the Gulf of Mexico region. In: S. D. Meyers, W. Van-Wie, D. G. Bebout, M. Nault (eds). Transaction of the 30th annual meeting and the Twenty-seventh annual meeting of the Gulf Coast Section of the Soceite of Economic Paleontologists and Mineralogists. Transactions-Gulf Coast Asssociation of Geological Societies, 30 , 175.

Miranda-C., E. 2000 Contribución al estudio sobre el origen y distribución de las brechas Cretácicas del area Reforma-Comalcalco-Sen, inedit.

Mitchum, R., M., Jr., Vail, P. R. Sangree, J. B. 1977b. Seismic stratigraphy and global changes of sea level part 6: seismic stratigraphic interpretation procedure. In: Seismic stratigraphy- applications to hydrocarbon exploration (ed. by C. E. Payton). American Association of Petroleum Geologists, Memoir: 26, 117-133.

Mitra, S. 2002. Structural models of faulted detachment folds. American Association of Petroleum Geologists, 86, 9 1673-1694.

Molnar, P., Brown, E. T., Burchfiel, B. C., Deng, Q., Feng, X., Li, J., Raisbeck, G., Shi, J., Wu, Z., Yiou, F., You, H. 1994. Quaternary climate change and the formation of river terraces across growing anticlines on the northern flank of the Tien Chan, China. Journal of Geology 102, 583-602.

Montgomery, S. L. 1996. Cotton Valley lime pinnacle reef play: Branton Field. American Association of Petroleum Geologists, 80, 5, 617-629.

Moore, C. H. 2001. Carbonate Reservoirs: Porosity Evolution and Diagenesis in a Sequence Stratigraphic Framework, Elsevier, Amsterdam, p. 444.

Moran-Zenteno, D. J. 1994. Geology of the Mexican Republic. Geological Society Publishers, Studies 39, 1st English edition.

Morley, C. K., Nelson, R. A., Patton, T. L., Munn, S.G. 1990. Transfer zones in the East African Rift system and their relevance to hydrocarbon exploration in rifts. American Association of Petroleum Geologist, Bulletin, 74, 8, 1234-1253.

Morton, G. R. Cantarell, The Second Largest Oil Field in the World Is Dying. Internet reference: http://home.entouch.net/dmd/cantarell.htm

Mullins, H. T. 1985. Deep-water carbonates along the Blake-Bahamas boundary. SEPM core Workshop 6, 461-489.

Murillo-Alvarado, J. A., Figueroa-Correa, G. 2004. Tertiary tectonic evolution model in Cantarell, Ku, Maloob Zaap Fields, Campeche Bay. Abstracts, American Association Petroleum Geologists International conference, Cancun, Mexico.

Müller, R. D. Smith, W. H. 1993. Deformation of the oceanic crust between the North American and South American plates. Journal of Geophysical Research. 98, 8275-8291.

Nicol, A., Alloway, B., Tonkin, P. 1994. Rates of deformation, uplift, and landscape development associated with active folding in the Waipara area of north Canterbury New Zealand. Tectonics, 13, 1327-1344.

Ortuno-M., E. 1999. Titoniano formación productora de hidrocarburos en la Sonda de Campeche. Ingeneria Petrolera 39: 29-36.

Palaz, I. Marfut, K. J. 1997. Carbonate Seismology: An overview. In: I. Palaz K. J. Marfut (eds). Carbonate Seismology. Geophysical Development Series, No. 6. Society of Exploration Geophysicists, 1-8.

Pacheco-Gutierrez, A., C. 2002. Deformación Transpresiva Miocenica y El Desarrollo de Sistemas de Fracturas en la Porción Nororiental de la Sonda de Campeche. Tesis de Maestria, Ciencias de la Tierra. México DF, UNAM.

Pardo, G. 1975. Geology of Cuba. In: A. E. M. Nairim, F. G. Stehli (eds). The Gulf of Mexico and Caribbean. In the collection: The Ocean Basins and Margins, 553-615.

Peacock, D.C. P., Sanderson, D. J. 1991. Displacements, segments linkage and relay ramps in normal fault zones. Journal of Structural Geology, 13, 721-733.

Perez-C., G. A. 1992. Geologic evolution of the Burgos Basin, northeastern Mexico. Houston, Rice University.

Pemex, 1998. Internal well report C-418-D.

Pemex, 1998. Reporte interno, descripcion de pozo C-91.

Pemex, 1999. Reporte interno, descripcion de pozo C-2239.

Pemex, 1999. Reporte interno, descripcion de pozo C-2095.

Pemex, 1999. Reporte interno, descripcion de pozo C-3001.

Pemex, 1999. Reporte interno, descripcion de pozo C-1065D.

Pemex, 1980. Reporte interno, descripcion de pozo Chac-1.

Pemex, 1980. Reporte interno, descripcion de pozo Chac-2.

Peterson, J. A. 1983. Petroleum geology and resources of southeastern Mexico, northern Guatemala, and Belize: U.S. Geological Survey, Circular, 760, 44.

Phillip, H., Rogozhin, E., Cisternas, A., Bousquet, J. C., Borisov, G., Karakhanian, A. 1992. The Armenian earthquake of 1988 December 7: faulting and folding neotectonics and paleoseismicity. Geophysical Journal International, 110, pp. 141-158.

Pindell, J. L. a. D., J. F. 1982. Permo-Triassic reconstruction of western Pangea and the evolution of the Gulf of Mexico/Caribbean region. Tectonics, 1, 179-212.

Pindell, J. L. 1985. Alleghenian reconstruction and subsequente evolution of the Gulf of Mexico, Bahamas, and proto-Caribbean. Tectonics, 4, 1-39.

Pindell, J. L. K., Kenan, L., Barret, S. L. 2000. Kinematic Evolution of the Gulf of Mexico and Caribbean. American Association of Petroleum Geologists, Explorer, 21, 14-17.

Poblet, J., Hardy, S. 1995. Reverse modelling of detachment folds; application to the Pico de Aguila anticline in the South Central Pyrennes (Spain). Journal of Structural Geology, 17, 1707-1724.

Poblet, J., Munoz, J. A., Trave, A., Serra-Kiel, J. 1998. Quantifying the kinematics of detachment folds using three-dimensional geometry: application to the Mediano anticline (Pyrenees, Spain). Geological Society of America Bulletin, 110, 111-125.

Poblet, J. Hardy, S., 1995. Reverse modeling of detachment folds: application to the Pico de Aguila anticline in the South Central Pyrenees (Spain). Journal of Structural Geology, 17, 1707-1724.

Ramirez-Cruz, L. C., Mendoza-Amuchastegui, J., del Valle-Garcia, R., Gomez-Ruiz, P. 1996. Mapping salt structure and subsalt imaging in Campeche Bay Mexico, using seismic inversion, modeling and prestack attributes. In: Society of Exploration Geophysicists, 66th annual international meeting; technical program, expanded abstracts with authors' biographies. SEG Annual Meeting Expanded Technical Program Abstracts with Biographies. 66; 588-591.

Ricoy, J., U. 1989. Tertiary terrigenous depositional systems of the Mexican Isthmus basins. PhD. Thesis, Earth Sciences, The University of Texas at Austin, 145.

Rivas, A. 2002. Structural Model of the Chiapas-Tabasco Area (Southeast Mexico). Internet reference: http://www.cgg.com/proserv/reservoir/papers/rivas.html

Rockwell, T. K., Keller, E. A., Dembroff, G. R. 1988. Quaternary rate of folding of the Ventura Avenue anticline, western Traverse Ranges, southern California. Geological Society of America Bulletin, 100, 850-858.

Rowan, M. G, Linares, R. 2000. Fold-evolution matrices and axial-surface analysis of fault-bend folds; application to the Medina Anticline, Eastern Cordillera, Colombia. American Association of Petroleum Geologists, Bulletin, 84, 6, 742-764.

Salazar-Medina, G. 2001. Tertiary zonation based on planktonic foraminifera from the marine region of Campeche, Mexico. In: C. Batolini, R. T. Buffler, A. Cantu-Chapa (eds). The Western Gulf of Mexico Basin: Tectonics, sedimentary basins, and petroleum systems. American Association of Petroleum Geologists, Memoir 75, 397-420.

Salvador, A. 1987. Late Triassic -Jurassic paleogeorgaphy and origin of the Gulf of Mexico Basin. American Association of Petroleum Geologists, 71, 419-451.

Sangree, J., B., Widmier, J. M. 1979. Interpretation of Depositional Facies from Seismic Data. Journal of Geophysics, 44, 2, 131-160.

Sanchez-M, R. 1979. Geologia petrolera de la Sierra de Chiapas. Boletin de la Asociacion Mexicana de Geologos Petroleros, 31, 67-97.

Santiago, J., Baro, A. 1992. Mexico's giant fields, 1978-1988 decade. In: M. T. Halbouty (eds). Giant oil and gas fields of the decade 1978-1988. American Association of Petroleum Geologists, Memoir, 54, 73-99.

Sawyer, D. S., Buffler, R. T., Pilger, R. H. 1991. The crust under the Gulf of Mexico Basin. In: A. Salvador, The Gulf of Mexico Basin. In the collection: The Geology of North America. Geological Society of America, 53-72.

Schlager, W., Reijmer, J. J.G., Droxler, A. 1994. Highstand shedding of carbonate platforms. Journal Sedimentary Research, 64, 270-281.

Schlager, W. 1993. Accommodation and supply; a dual control on stratigraphic sequences. In: S. Cloetingh, W. Sassi, F. Horvarth, C. Puidgefabregas (eds). Basin analysis and dynamics of sedimentary basin evolution. Sedimentary Geology, 86, 1-2, 111-136.

Schneider, C. L., Hummon, D., Yeats, R. S., Huftile, G. L. 1996. Structural evolution of the northern Los Angeles basin, California, based on growth strata. Tectonics, 15, 341-355.

Sedlock, R. L., Ortega-Gutierrez, F., Speed, R. L. 1993. Tectonostratigraphic terranes and tectonic evloution of Mexico. Special Paper, Geological Society of America, 278, Boulder Colorado.

Sharp, R. V. 1967. San Jacinto fault zone in the Peninsular Ranges of southern California. Geological Society of America, Bulletin, 78, 705-730.

Shaub, F. 1987. The Catoche Tongue; an example of Mesozoic rift and subsidence episodes in the Gulf of Mexico. Nineteenth annual offshore technology, Proceedings - Offshore Technology Conference.

Shaw, J. H., Suppe, J., 1994. Active faulting and growth folding in the eastern Santa Barbara Channel California earthquake. Geological Society of America Bulletin, 106, 607-626.

Sheriff, R. E. 1977. Limitations on resolution of seismic reflections and geologic detail derivable from them. In: C. E. Payton (eds). Seismic stratigraphy; applications to hydrocarbon exploration. American Association of Petroleum Geolgists, Memoir, 26, 3-14.

Smith, 2004. Understanding the Trenton Black River reservoir. Internet reference: http://www.pttc.org.solutions.sol_2004/534.htm.

Sohl, N., Martinez, R. E., Salmeron-Urena, P., Soto-Jaramillo, F. 1991. Upper Cretaceous. In: A. Salvador (eds). The Geology of North America. In the collection: The geology of North America. Geological Society of America, 205-244.

Stein, R. S., King, G. C. P. 1984. Seismic potential revealed by surface folding: 1983 Coalinga, California earthquake. Science 224, 869-872.

Stewart, S. A., Coward, M.P. 1995. Synthesis of salt tectonics in the southern North Sea, UK. Marine and Petroleum Geology, 12, 5, 457-475.

Soriano, E. 2003. Personal Communication.

Spathopoulos, F. 1996. An insight on salt tectonics in the Angola Basin, South Atlantic. In: G. I., Alsop, D. J. Blundell, I. Davison, (eds). Salt Tectonics. Geological Society, London, Special Publication, 100, 153-174.

Sylvester, A. G., Smith, R. R., 1976. Tectonic transpression and basement-controlled deformation in the San Andres fault zone, Salton trough, California: American Association of Petroleum Geologists, Bulletin, 60, 2081-2102.

Suppe, J., 1983. Geometry and kinematics of fault-bend folding. American Journal of Science. 283, 684-721.

Suppe, J., Medwedeeff, D. 1990. Geometry and kinematics of fault propagation folding. Eclogae Geologicae Helvetiae, 83, 409-454.

Suppe, J., Chou, G., Hook, S., 1991. Rates of folding and faulting determined from growth strata. In: K. McClay (eds). Thrust Tectonics, Chapman and Hall, London, 105-121.

Suppe, J., Sabat, F., Muno, J. A., Poblet, J., Roca, E., Verges, J. 1997. Bed by bed fold growth by kink-band migration: Sant Llorenc de Morunys, eastern Pyrenees. Journal of Structural Geology, 19, 443-461.

Viniegra-Osorio, F. 1981. Great Carbonate Bank of Yucatan, southern Mexico. Journal of Petroleum Geology 3, 247-276.

Turner, R.E. 1999. Inputs and outputs of the Gulf of Mexico. In: H. Kumpf, K. Steidinger, K. Sherman (eds). The Gulf of Mexico large marine ecosystem; assessment, sustainability and management. Blackwell Science, Inc., 704 .

Vail, P. R., Mitchum, R.M., Thompson, S., III (1977b) Seismic stratigraphy and global changes of sea-level, part 3: relative changes of sea level from coastal onlap. In: C. E. Payton (eds). Seismic stratigraphy – Applications to hydrocarbon exploration. American Association of Petroleum Geologists, Memoir 26, 63-82.

Verges, J., Burbank, D. W., Meigs, A., 1996. Unfolding: an inverse approach to fold kinematics. Geology, 24, 175-178.

Wang, Z. 1997. Seismic properties of carbonate rocks. In: I. Palaz, K. Marfut (eds). Carbonate Seismology. Geophysical Developments Series No 6. Society of Exploration Geophysicists, 29-52.

Weimer, P. Buffler R.T. 1992. Structural geology and evolution of the Mississippi Fan fold belt, deep Gulf of Mexico. American Association of Petroleum Geologists Bulletin, 76, 225-251.

Wilcox, R. E., Harding, T. P., Seely, D. R. 1973. Basic wrench tectonics. American Association of Petroleum Geologists Bulletin, 57, 74-96.

Wilson, J. L. 1990. Basement structural controls on Mesozoic carbonate facies in northeastern Mexico a review. In: M. E. Tucker, J. L. Wilson, P. D. Crevello, J. R. Sarg, R. J. Fred (eds). Carbonate platforms, facies, sequences and evolution. Special Publication of the International Association of Sedimentologists, 9, 235-255.

Winker, C. D., Buffler, R. 1988. Paleogeographic Evolution of Early Deep-Water Gulf of Mexico and Margins, Jurassic to Middle Cretaceous (Comanchean). American Association of Petroleum Geologists, Bulletin, 72, 3, 318-346.

Wright, V. P. 2002. Dissolution and porosity development in carbonates. In: F. Gabrovsek (eds). Evolution of karst; from prekarst to cessation; proceedings. Zalozba ZRC, Slovenia, 13-30.

Yielding, G., Jackson, J. A., King , G. C. P., Sinval, H., Vita-Finzi, C., Wood, R. M. 1981. Relations between surface deformation, fault geometry, seismicity and rupture characteristics during the El Asnan (Algeria) earthquake of 10 October 1980. Earth and Planetary Scientific Letters, 56, 287-304.

Zoetemeijer, R., Cloeting, S., Sassi, W., Roure, F., 1993. Modelling of piggy-back-basin stratigraphy: record of tectonic evolution. Tectonophysics, 226, 253-269.

Platfrom	wellname	vertical	strucutral block
R 2239	2257	N	hangingwall
	2279	N	hangingwall
	2257D	N	hangingwall
	2078D	N	hangingwall
	2076D	N	hangingwall
	2078A	N	hangingwall
	2076	N	hangingwall
	2094D	N	hangingwall
	2058	N	hangingwall
	2054	N	hangingwall
	2074D	N	hangingwall
	2074	N	hangingwall
	2084	N	hangingwall
FO	285	N	hangingwall
	227D	N	hangingwall
	245D	N	hangingwall
	207D	N	hangingwall
	247D	N	hangingwall
	28D	N	hangingwall
	49D	N	hangingwall
	249	N	hangingwall
	48D	N	hangingwall
	269	N	hangingwall
	269D	N	hangingwall
G 66	68	N	hangingwall
	68D	N	hangingwall
	46D	N	hangingwall
	46	N	hangingwall
	44D	N	hangingwall
	24D	N	hangingwall
	44	N	hangingwall
	42H	N	hangingwall
	42	N	hangingwall
	2H	N	hangingwall
	64	N	hangingwall
	4062	N	hangingwall
	4064	N	hangingwall
	22H	N	hangingwall
	2096	N	hangingwall
	2098	N	hangingwall
	86D	N	hangingwall
	289	N	hangingwall
GP 468	469	N	hangingwall
	446	N	hangingwall
	468D	N	hangingwall
H	2071D	N	hangingwall
	2072D	N	hangingwall
	84	N	hangingwall
	81D	N	hangingwall
	62	N	hangingwall
	43	N	hangingwall
	63	N	hangingwall
	83	N	hangingwall
	81	N	hangingwall
	2091D	N	hangingwall
	2092D	N	hangingwall
	2092	N	hangingwall
	2072	N	hangingwall
	2094	N	hangingwall
NB 20	2001	N	EASTERN
	2051	N	CORRIDOR

Structural Elements:
WFC. = Western Fault Corridor
WP. = Western Platfrom
EP. = Eastern Platform
EFC.= Eastern Fault Corridor

Platfrom	wellname	vertical	strucutral block
2011 11D	2053	N	
	2031	N	
	2032	N	
NC 2095	2093	N	EASTERN
	2052	N	CORRIDOR
	2071	N	
	2073	N	
C 1	3	N	hangingwall
	11	N	hangingwall
	22	N	hangingwall
E 51	93	N	hangingwall
	95	N	hangingwall
	11D	N	hangingwall
	31	N	hangingwall
CI	CI47	N	hangingwall
	CI49	N	hangingwall
	CI69	N	hangingwall
	CI87	N	hangingwall
	CI85	N	hangingwall
7 - 7A	25	N	hangingwall
	5	N	hangingwall
	15	N	hangingwall
	17	N	hangingwall
	19D	N	hangingwall
	138	N	hangingwall
	9D	N	hangingwall
	9	N	hangingwall
	27	N	hangingwall
	25	N	hangingwall
	317	N	hangingwall
	17D	N	hangingwall
D 57	178	N	hangingwall
	75	N	hangingwall
	55H	N	hangingwall
	33H	N	hangingwall
	79	N	hangingwall
	57D	N	hangingwall
	50	N	hangingwall
	59	N	hangingwall
	79D	N	hangingwall
	178	N	hangingwall
DB 99D	3089D	N	hangingwall
	3089	N	hangingwall
	73D	N	hangingwall
O 219	436	N	hangingwall
	36D	N	hangingwall
	16	N	hangingwall
	209	N	hangingwall
	427	N	hangingwall
	409	N	hangingwall
L	1046D	N	hangingwall
	3046	N	hangingwall
	3024	N	hangingwall
	1024D	N	hangingwall
	3026N	N	hangingwall
	1021	N	hangingwall
	3044	N	hangingwall
	1084D	N	hangingwall

Structural Elements:
WFC. = Western Fault Corridor
WP. = Western Platfrom
EP. = Eastern Platform
EFC.= Eastern Fault Corridor

Platfrom	wellname	vertical	strucutral block
KL 1006	3008	N	hangingwall
	1016	N	hangingwall
	3006	N	hangingwall
TM 300 1	3002	N	hangingwall
	3002D	N	hangingwall
M	1023D	N	hangingwall
	3025	N	hangingwall
	1042D	N	hangingwall
	3023	N	hangingwall
	1043D	N	hangingwall
	3023D	N	hangingwall
B 1069	308	N	hangingwall
	1067	N	hangingwall
	1047D	N	hangingwall
	3047D	N	hangingwall
	1049	N	hangingwall
	1029	N	hangingwall
	3029	N	hangingwall
	3049	N	hangingwall
	1128	N	hangingwall
	148	N	hangingwall
	3069	N	hangingwall
	3067D	N	hangingwall
	3085	N	hangingwall
	1085D	N	hangingwall
SINGLES	1013	VERT	hangingwall
	1015	VERT	hangingwall
	1027	VERT	hangingwall
	418D	N	hangingwall
	2001	VERT	EFC
	2003	VERT	EFC
	2013	VERT	EFC
	2033	VERT	EFC
	2035	VERT	EFC
	2055	VERT	EFC
	2037	VERT	EFC
	2067	VERT	EFC
	2067D	VERT	EFC
	2075	VERT	EFC
	2075D	VERT	EFC
	2097	VERT	EFC
	2095	VERT	EFC
	CH1	VERT	EP.
	CH2	VERT	EP.
	CH-3	VERT	EP.
	2196D	VERT	EP.
	2194	VERT	EP.
	2192	VERT	EP.
	182	VERT	EP.
	184	VERT	EP.
	K1267	VERT	WFC.
	K1247	VERT	WFC.
	K1	VERT	WFC.
	WAK-1	VERT	WFC.
	IXT-1	VERT	WP.
	IXT-18	VERT	WP.
	KU-401	VERT	WP.
	KU-89	VERT	WP.
	POK-1	VERT	EP.
	TAK-1	VERT	EP.
	TAK-101	VERT	EFC

Structural Elements:
WFC. = Western Fault Corridor
WP. = Western Platfrom
EP. = Eastern Platform
EFC.= Eastern Fault Corridor

LOG CODE	Well name	start	end	index unit	max value	min value	unit	description
DRHO	C-1024D	773.111	3519.97	m	0.394	-0.014	g/cm3	Bulk Density Correction
GR	C-1024D	773.111	3519.97	m	302.814	8.1404	gAPI	Gamma Ray
GR	C-1024D	3172.82	3516.02	m	280.226	17.072	gAPI	Gamma Ray
GR	C-1024D	3158.79	3519.98	m	302.814	16.1597	gAPI	Gamma Ray
ILD	C-1024D	773.111	3519.97	m	1535.33	-0.951	ohm.m	Induction Deep Resistivity
LLD	C-1024D	773.111	3519.97	m	99999	2.192	ohm.m	Laterolog Deep Resistivity
LLD	C-1024D	3158.79	3519.98	m	100000	6.40E-10	ohm.m	Laterolog Deep Resistivity
LLS	C-1024D	773.111	3519.97	m	26776.4	1.566	ohm.m	Laterolog Shallow Resistivity
LLS	C-1024D	3158.79	3519.98	m	100000	7.57E-10	ohm.m	Laterolog Shallow Resistivity
MSFL	C-1024D	773.111	3519.97	m	4987.4	1.202	ohm.m	Micro-spherically-focused Resistivity
NPHI	C-1024D	773.111	3519.97	m	38.534	-0.557	m3/m3	Thermal Neutron Porosity (original Ratio Method) in Selected Lithology
NPHI	C-1024D	3158.79	3519.98	m	0.385337	-0.00556716	m3/m3	Thermal Neutron Porosity (original Ratio Method) in Selected Lithology
PEF	C-1024D	773.111	3519.97	m	4.964	2.743		Photoelectric Factor
RHOB	C-1024D	773.111	3519.97	m	2.855	1.789	g/cm3	Bulk Density
SP	C-1024D	3158.79	3519.98	m	57.8875	-134	mV	Spontaneous Potential
CGR	C-1025	3262.73	3511.91	m	180.301	-16.2346	gAPI	Gamma Ray Contribution from Thorium and Potassium
CGR	C-1025	752.5	3519.88	m	111.106	-7.7698	gAPI	Gamma Ray Contribution from Thorium and Potassium
DRHO	C-1025	752.5	3519.88	m	0.3578	-1.2268	g/cm3	Bulk Density Correction
DT	C-1025	752.5	3519.88	m	111.682	0	us/ft	Delta-T (also called Slowness or Interval Transit Time)
GR	C-1025	752.5	3519.88	m	180.017	3.5497	gAPI	Gamma Ray
GR	C-1025	3219.3	3510.38	m	128.681	5.45473	gAPI	Gamma Ray
GR	C-1025	3184.91	3510.53	m	125.383	5.76868	gAPI	Gamma Ray
ILD	C-1025	752.5	3519.88	m	2000	0.568	ohm.m	Induction Deep Resistivity
LLD	C-1025	752.5	3519.88	m	98478.2	0.0394	ohm.m	Laterolog Deep Resistivity
LLD	C-1025	3262.73	3511.91	m	100000	0.0276782	ohm.m	Laterolog Deep Resistivity
LLS	C-1025	3262.73	3511.91	m	100000	4.69E-09	ohm.m	Laterolog Shallow Resistivity
LLS	C-1025	752.5	3519.88	m	89832	0	ohm.m	Laterolog Shallow Resistivity
MSFC	C-1025	3262.73	3512.01	m	1893.33	0.0443483	ohm.m	Borehole-Corrected MSFL
MSFL	C-1025	3262.73	3512.01	m	2000	0.0861824	ohm.m	Micro-spherically-focused Resistivity
MSFL	C-1025	752.5	3519.88	m	2000	0.0961	ohm.m	Micro-spherically-focused Resistivity
NPHI	C-1025	752.5	3519.88	m	87.8472	0.6843	m3/m3	Thermal Neutron Porosity (original Ratio Method) in Selected Lithology
PEF	C-1025	752.5	3519.88	m	8.5042	0		Photoelectric Factor
POTA	C-1025	3262.73	3511.91	m	0.0585049	-0.000486192	%	Potassium Concentration
POTA	C-1025	752.5	3519.88	m	0.0489	-0.0148	%	Potassium Concentration
RHOB	C-1025	752.5	3519.88	m	3.063	1.2393	g/cm3	Bulk Density
SP	C-1025	3262.73	3511.91	m	15.125	-229.25	mV	Spontaneous Potential
THOR	C-1025	3262.73	3511.91	m	17.1431	-5.3102	ppm	Thorium Concentration
THOR	C-1025	752.5	3519.88	m	26.0853	-1.9125	ppm	Thorium Concentration
URAN	C-1025	3262.73	3511.91	m	11.5318	-2.99426	ppm	Uranium Concentration
URAN	C-1025	752.5	3519.88	m	16.0771	-0.4639	ppm	Uranium Concentration
CGR	C-3026-P	780.62	3489.99	m	186.804	0	gAPI	Gamma Ray Contribution from Thorium and Potassium
DRHO	C-3026-P	780.62	3489.99	m	0.351	-4.298	g/cm3	Bulk Density Correction
GR	C-3026-P	780.62	3489.99	m	335.921	13.4593	gAPI	Gamma Ray
ILD	C-3026-P	780.62	3489.99	m	2000	0.5521	ohm.m	Induction Deep Resistivity
LLD	C-3026-P	780.62	3489.99	m	40000	1.255	ohm.m	Laterolog Deep Resistivity
LLS	C-3026-P	780.62	3489.99	m	3113.89	0.025	ohm.m	Laterolog Shallow Resistivity
MSFL	C-3026-P	780.62	3489.99	m	1012.55	0.1	ohm.m	Micro-spherically-focused Resistivity
NPHI	C-3026-P	780.62	3489.99	m	61.5745	-0.506	m3/m3	Thermal Neutron Porosity (original Ratio Method) in Selected Lithology
PEF	C-3026-P	780.62	3489.99	m	11.211	2.2536		Photoelectric Factor
POTA	C-3026-P	780.62	3489.99	m	34.85	0.398	%	Potassium Concentration
RHOB	C-3026-P	780.62	3489.99	m	2.7947	-0.242	g/cm3	Bulk Density
SP	C-3026-P	780.62	3489.99	m	94	81.161	mV	Spontaneous Potential
URAN	C-3026-P	780.62	3489.99	m	39.764	0.117	ppm	Uranium Concentration
CGR	C-3066	621.006	2590.62	m	193.772	-4.028	gAPI	Gamma Ray Contribution from Thorium and Potassium
DRHO	C-3066	621.006	2590.62	m	1.263	-0.121	g/cm3	Bulk Density Correction
DT	C-3066	621.006	2590.62	m	137.764	0	us/ft	Delta-T (also called Slowness or Interval Transit Time)
GR	C-3066	621.006	2590.62	m	177.316	0	gAPI	Gamma Ray
ILD	C-3066	621.006	2590.62	m	1950	0.3214	ohm.m	Induction Deep Resistivity
LLD	C-3066	621.006	2590.62	m	100000	1.2863	ohm.m	Laterolog Deep Resistivity
LLS	C-3066	621.006	2590.62	m	12500.5	1.1038	ohm.m	Laterolog Shallow Resistivity
MSFL	C-3066	621.006	2590.62	m	3151.84	0.03	ohm.m	Micro-spherically-focused Resistivity
NPHI	C-3066	621.006	2590.62	m	46.9	-99925	m3/m3	Thermal Neutron Porosity (original Ratio Method) in Selected Lithology
PEF	C-3066	621.006	2590.62	m	10	0.95		Photoelectric Factor
POTA	C-3066	621.006	2590.62	m	0.035	-0.045	%	Potassium Concentration
RHOB	C-3066	621.006	2590.62	m	4.32	0	g/cm3	Bulk Density
SP	C-3066	621.006	2590.62	m	70.5582	-213.75	mV	Spontaneous Potential
THOR	C-3066	621.006	2590.62	m	64.687	-1.333	ppm	Thorium Concentration
URAN	C-3066	621.006	2590.62	m	13.173	-12.782	ppm	Uranium Concentration
GR	Cant-0016	2541.5	1846.25	m	139.683	2.906	gAPI	Gamma Ray
GR	Cant-0016	2541.5	1846.25	m	139.683	2.906	gAPI	Gamma Ray
RHOB	Cant-0016	2541.5	1846.25	m	2.9	2	g/cm3	Bulk Density
RHOB	Cant-0016	2541.5	1846.25	m	2.9	2	g/cm3	Bulk Density
CALI	Cant-1	146.305	1242.06	m	18.565	12.077	in	Caliper

Appendix 2 Wel logs

LOG CODE	Well name	start	end	index unit	max value	min value	unit	description
DRHO	Cant-1	146.305	1242.06	m	0.132	-0.093	g/cm3	Bulk Density Correction
DT	Cant-1	146.305	1242.06	m	106.97	47.82	us/ft	Delta-T (also called Slowness or Interval Transit Time)
GR	Cant-1	146.305	1242.06	m	87.582	11.42	gAPI	Gamma Ray
ILD	Cant-1	146.305	1242.06	m	93.591	0.444	ohm.m	Induction Deep Resistivity
NPHI	Cant-1	146.305	1242.06	m	44.875	0	m3/m3	Thermal Neutron Porosity (original Ratio Method) in Selected Lithology
RHOB	Cant-1	146.305	1242.06	m	2.696	689.138	g/cm3	Bulk Density
SP	Cant-1	146.305	1242.06	m	126.883	12.613	mV	Spontaneous Potential
GR	Cant-1005	526.695	2713.64	m	132.514	4.457	gAPI	Gamma Ray
ILD	Cant-1005	526.695	2713.64	m	3.189	0.513	ohm.m	Induction Deep Resistivity
LLD	Cant-1005	526.695	2713.64	m	61104.7	5.881	ohm.m	Laterolog Deep Resistivity
LLS	Cant-1005	526.695	2713.64	m	72878.2	3.801	ohm.m	Laterolog Shallow Resistivity
MSFL	Cant-1005	526.695	2713.64	m	1941.44	0.124	ohm.m	Micro-spherically-focused Resistivity
SP	Cant-1005	526.695	2713.64	m	37.801	-348.766	mV	Spontaneous Potential
CALI	Cant-1006	164.643	2985.26	m	23.474	10.209	in	Caliper
CGR	Cant-1006	164.643	2985.26	m	49.313	-54.606	gAPI	Gamma Ray Contribution from Thorium and Potassium
DRHO	Cant-1006	164.643	2985.26	m	0.397	-1.457	g/cm3	Bulk Density Correction
DT	Cant-1006	164.643	2985.26	m	172.329	40.812	us/ft	Delta-T (also called Slowness or Interval Transit Time)
GR	Cant-1006	164.643	2985.26	m	114.801	3.3876	gAPI	Gamma Ray
ILD	Cant-1006	164.643	2985.26	m	2000	0.444	ohm.m	Induction Deep Resistivity
LLD	Cant-1006	164.643	2985.26	m	100000	0.038	ohm.m	Laterolog Deep Resistivity
LLS	Cant-1006	164.643	2985.26	m	100000	0.009	ohm.m	Laterolog Shallow Resistivity
MSFL	Cant-1006	164.643	2985.26	m	2000	0.325	ohm.m	Micro-spherically-focused Resistivity
NPHI	Cant-1006	164.643	2985.26	m	62.895	-2.499	m3/m3	Thermal Neutron Porosity (original Ratio Method) in Selected Lithology
PEF	Cant-1006	164.643	2985.26	m	102.095	-0.438		Photoelectric Factor
POTA	Cant-1006	164.643	2985.26	m	0.026	-0.032	%	Potassium Concentration
RHOB	Cant-1006	164.643	2985.26	m	3.002	0.121	g/cm3	Bulk Density
SP	Cant-1006	164.643	2985.26	m	125.187	-869.907	mV	Spontaneous Potential
THOR	Cant-1006	164.643	2985.26	m	4.364	-1.919	ppm	Thorium Concentration
URAN	Cant-1006	164.643	2985.26	m	13.963	0.482	ppm	Uranium Concentration
CALI	Cant-1014-P	1791.16	3647.69	m	22.674	1.928	in	Caliper
CGR	Cant-1014-P	1791.16	3647.69	m	75.971	-9.921	gAPI	Gamma Ray Contribution from Thorium and Potassium
DRHO	Cant-1014-P	1791.16	3647.69	m	0.512	-3.2424	g/cm3	Bulk Density Correction
GR	Cant-1014-P	1791.16	3647.69	m	187.915	5.6135	gAPI	Gamma Ray
LLD	Cant-1014-P	1791.16	3647.69	m	40000	0	ohm.m	Laterolog Deep Resistivity
LLS	Cant-1014-P	1791.16	3647.69	m	10678.9	0	ohm.m	Laterolog Shallow Resistivity
NPHI	Cant-1014-P	1791.16	3647.69	m	110.537	0	m3/m3	Thermal Neutron Porosity (original Ratio Method) in Selected Lithology
PEF	Cant-1014-P	1791.16	3647.69	m	11229.5	-65111.3		Photoelectric Factor
POTA	Cant-1014-P	1791.16	3647.69	m	0.025	-0.005	%	Potassium Concentration
RHOB	Cant-1014-P	1791.16	3647.69	m	4.8077	-1.5438	g/cm3	Bulk Density
THOR	Cant-1014-P	1791.16	3647.69	m	11.424	-7.518	ppm	Thorium Concentration
URAN	Cant-1014-P	1791.16	3647.69	m	19.361	-0.689	ppm	Uranium Concentration
CALI	Cant-1022	2200.44	4205.62	m	22.609	0	in	Caliper
DRHO	Cant-1022	2200.44	4205.62	m	0.296	-1.21	g/cm3	Bulk Density Correction
DT	Cant-1022	2200.44	4205.62	m	179.812	40	us/ft	Delta-T (also called Slowness or Interval Transit Time)
GR	Cant-1022	4205.62	2200.13	m	133.312	0	gAPI	Gamma Ray
GR	Cant-1022	4205.73	2200.13	m	131.893	0	gAPI	Gamma Ray
ILD	Cant-1022	2200.44	4205.62	m	2000	0.2	ohm.m	Induction Deep Resistivity
LLD	Cant-1022	2200.44	4205.62	m	4847.74	0	ohm.m	Laterolog Deep Resistivity
LLS	Cant-1022	2200.44	4205.62	m	14786	0	ohm.m	Laterolog Shallow Resistivity
MSFL	Cant-1022	2200.44	4205.62	m	1737.5	0	ohm.m	Micro-spherically-focused Resistivity
NPHI	Cant-1022	2200.44	4205.62	m	49.129	-15	m3/m3	Thermal Neutron Porosity (original Ratio Method) in Selected Lithology
PEF	Cant-1022	2200.44	4205.62	m	2270.5	0		Photoelectric Factor
RHOB	Cant-1022	2200.44	4205.62	m	2.889	0	g/cm3	Bulk Density
DT	Cant-1035	4565.39	2950.24	m	129.435	40	us/ft	Delta-T (also called Slowness or Interval Transit Time)
DT	Cant-1035	4565.39	2950.24	m	950	0	us/ft	Delta-T (also called Slowness or Interval Transit Time)
GR	Cant-1035	4565.39	2950.24	m	106.562	0	gAPI	Gamma Ray
RHOB	Cant-1035	4565.39	2950.24	m	0	0	g/cm3	Bulk Density
RHOB	Cant-1035	4565.49	2950.24	m	2.91908	1.73119	g/cm3	Bulk Density
RHOB	Cant-1035	4565.39	2950.24	m	2.933	1.731	g/cm3	Bulk Density
GR	Cant-1042D	3170.5	800.24	m	244.485	4.007	gAPI	Gamma Ray
RHOB	Cant-1042D	3168.67	2103.58	m	5.427	-999.99	g/cm3	Bulk Density
CALI	Cant-1065D	765.2	3197.2	m	24.7164	8.266	in	Caliper
CGR	Cant-1065D	765.2	3197.2	m	135.152	-4.5354	gAPI	Gamma Ray Contribution from Thorium and Potassium
DRHO	Cant-1065D	765.2	3197.2	m	2.311	-1.1037	g/cm3	Bulk Density Correction
DT	Cant-1065D	765.2	3197.2	m	182.145	10.8492	us/ft	Delta-T (also called Slowness or Interval Transit Time)
GR	Cant-1065D	765.2	3197.2	m	174.839	0	gAPI	Gamma Ray
ILD	Cant-1065D	765.2	3197.2	m	18.1509	0.4194	ohm.m	Induction Deep Resistivity
LLD	Cant-1065D	765.2	3197.2	m	98811.3	0.0649	ohm.m	Laterolog Deep Resistivity
LLS	Cant-1065D	765.2	3197.2	m	76087.5	0.104	ohm.m	Laterolog Shallow Resistivity
MSFL	Cant-1065D	765.2	3197.2	m	2000.5	0.2053	ohm.m	Micro-spherically-focused Resistivity
NPHI	Cant-1065D	765.2	3197.2	m	63.8613	-99025	m3/m3	Thermal Neutron Porosity (original Ratio Method) in Selected Lithology
PEF	Cant-1065D	765.2	3197.2	m	1000.25	1.1468		Photoelectric Factor
POTA	Cant-1065D	765.2	3197.2	m	0.045	-0.002	%	Potassium Concentration

Appendix 2 Wel logs

LOG CODE	Well name	start	end	index unit	max value	min value	unit	description
RHOB	Cant-1086D	766.2	3197.2	m	4.1445	1.0776	g/cm3	Bulk Density
SP	Cant-1086D	766.2	3197.2	m	245.202	-467.12	mV	Spontaneous Potential
THOR	Cant-1086D	766.2	3197.2	m	18.23	-2.0358	ppm	Thorium Concentration
URAN	Cant-1086D	766.2	3197.2	m	8.2015	-0.859	ppm	Uranium Concentration
CALI	Cant-1089	119.786	3137.92	m	23.064	2.088	in	Caliper
DRHO	Cant-1089	119.786	3137.92	m	0.276	-0.213	g/cm3	Bulk Density Correction
DT	Cant-1089	119.786	3137.92	m	232.8	1.247	us/ft	Delta-T (also called Slowness or Interval Transit Time)
GR	Cant-1089	119.786	3137.92	m	207.875	4.001	gAPI	Gamma Ray
GR	Cant-1089	3128.57	119.227	m	207.875	4.001	gAPI	Gamma Ray
ILD	Cant-1089	119.786	3137.92	m	18.806	0.541	ohm.m	Induction Deep Resistivity
LLD	Cant-1089	119.786	3137.92	m	11945.5	2.22	ohm.m	Laterolog Deep Resistivity
LLS	Cant-1089	119.786	3137.92	m	1268.84	2.15	ohm.m	Laterolog Shallow Resistivity
MSFL	Cant-1089	119.786	3137.92	m	1982.66	0.229	ohm.m	Micro-spherically-focused Resistivity
NPHI	Cant-1089	119.786	3137.92	m	58.985	0.119	m3/m3	Thermal Neutron Porosity (original Ratio Method) in Selected Lithology
PEF	Cant-1089	119.786	3137.92	m	92.999	0.885		Photoelectric Factor
RHOB	Cant-1089	2543.6	868.727	m	2.808	1.075	g/cm3	Bulk Density
RHOB	Cant-1089	2543.53	868.727	m	2.808	1.0758	g/cm3	Bulk Density
RHOB	Cant-1089	119.786	3137.92	m	2.94	0.851	g/cm3	Bulk Density
SP	Cant-1089	119.786	3137.92	m	200.312	-240.672	mV	Spontaneous Potential
GR	Cant-1091	2296.18	1225.22	m	810	0	gAPI	Gamma Ray
RHOB	Cant-1091	2296.18	1225.22	m	2.947	1.331	g/cm3	Bulk Density
CALI	Cant-1128	839.125	4131.25	m	24.9821	1.689	in	Caliper
CGR	Cant-1128	839.125	4131.25	m	68.651	1.7619	gAPI	Gamma Ray Contribution from Thorium and Potassium
DRHO	Cant-1128	839.125	4131.25	m	0.3094	-3.2407	g/cm3	Bulk Density Correction
DT	Cant-1128	839.125	4131.25	m	246.722	43.8681	us/ft	Delta-T (also called Slowness or Interval Transit Time)
GR	Cant-1128	839.125	4131.25	m	192.491	7.0507	gAPI	Gamma Ray
ILD	Cant-1128	839.125	4131.25	m	18067	0.3792	ohm.m	Induction Deep Resistivity
LLD	Cant-1128	839.125	4131.25	m	13150.1	0	ohm.m	Laterolog Deep Resistivity
LLS	Cant-1128	839.125	4131.25	m	3201.1	0	ohm.m	Laterolog Shallow Resistivity
MSFL	Cant-1128	839.125	4131.25	m	19488	0	ohm.m	Micro-spherically-focused Resistivity
NPHI	Cant-1128	839.125	4131.25	m	79.7	0.4303	m3/m3	Thermal Neutron Porosity (original Ratio Method) in Selected Lithology
PEF	Cant-1128	839.125	4131.25	m	38.2595	-102.18		Photoelectric Factor
POTA	Cant-1128	839.125	4131.25	m	3.5798	0.0512	%	Potassium Concentration
RHOB	Cant-1128	839.125	4131.25	m	2.8039	-0.0797	g/cm3	Bulk Density
SP	Cant-1128	839.125	4131.25	m	308.39	-801.358	mV	Spontaneous Potential
THOR	Cant-1128	839.125	4131.25	m	9.089	0.272	ppm	Thorium Concentration
URAN	Cant-1128	839.125	4131.25	m	8.6545	0.105	ppm	Uranium Concentration
CALI	Cant-162	120.396	4146.8	m	21.844	-168.896	in	Caliper
DRHO	Cant-162	120.396	4146.8	m	0.327	-1.326	g/cm3	Bulk Density Correction
DT	Cant-162	120.396	4146.8	m	683.952	-100.864	us/ft	Delta-T (also called Slowness or Interval Transit Time)
GR	Cant-162	120.396	4146.8	m	203.104	0	gAPI	Gamma Ray
ILD	Cant-162	120.396	4146.8	m	2000	0.295	ohm.m	Induction Deep Resistivity
LLD	Cant-162	120.396	4146.8	m	1338.9	0.169	ohm.m	Laterolog Deep Resistivity
LLS	Cant-162	120.396	4146.8	m	1029.41	0.15	ohm.m	Laterolog Shallow Resistivity
MSFL	Cant-162	120.396	4146.8	m	2000	0.2	ohm.m	Micro-spherically-focused Resistivity
NPHI	Cant-162	120.396	4146.8	m	64.864	-181.36	m3/m3	Thermal Neutron Porosity (original Ratio Method) in Selected Lithology
PEF	Cant-162	120.396	4146.8	m	2444.88	-168.896		Photoelectric Factor
RHOB	Cant-162	120.396	4146.8	m	2.89	0.486	g/cm3	Bulk Density
DT	Cant-1A	1341.05	994.181	m	148.427	40.519	us/ft	Delta-T (also called Slowness or Interval Transit Time)
GR	Cant-1A	1341.05	994.181	m	99.891	1.035	gAPI	Gamma Ray
RHOB	Cant-1A	1341.05	994.181	m	2.671	2.055	g/cm3	Bulk Density
CALI	Cant-2011	138.074	3449.73	m	19	-409.805	in	Caliper
DT	Cant-2011	138.074	3449.73	m	140	-386.209	us/ft	Delta-T (also called Slowness or Interval Transit Time)
GR	Cant-2011	138.074	3449.73	m	109.001	-799.4	gAPI	Gamma Ray
ILD	Cant-2011	138.074	3449.73	m	89837.5	0.015	ohm.m	Induction Deep Resistivity
LLD	Cant-2011	138.074	3449.73	m	57048.8	0.71	ohm.m	Laterolog Deep Resistivity
LLS	Cant-2011	138.074	3449.73	m	1937.28	0.2	ohm.m	Laterolog Shallow Resistivity
NPHI	Cant-2011	138.074	3449.73	m	63.399	-14.356	m3/m3	Thermal Neutron Porosity (original Ratio Method) in Selected Lithology
RHOB	Cant-2011	138.074	3449.73	m	2.89	-408.864	g/cm3	Bulk Density
SP	Cant-2011	138.074	3449.73	m	86.825	-102.501	mV	Spontaneous Potential
CALI	Cant-2011D	350.52	2334.16	m	19.114	-804.724	in	Caliper
DRHO	Cant-2011D	350.52	2334.16	m	0.251	-800.392	g/cm3	Bulk Density Correction
DT	Cant-2011D	350.52	2334.16	m	110.54	-785.297	us/ft	Delta-T (also called Slowness or Interval Transit Time)
GR	Cant-2011D	2332.08	350	m	570	0	gAPI	Gamma Ray
GR	Cant-2011D	350.52	2334.16	m	119.639	-785.297	gAPI	Gamma Ray
ILD	Cant-2011D	350.52	2334.16	m	20.287	0.19	ohm.m	Induction Deep Resistivity
LLD	Cant-2011D	350.52	2334.16	m	950.099	0.001	ohm.m	Laterolog Deep Resistivity
LLS	Cant-2011D	350.52	2334.16	m	978.4	0.001	ohm.m	Laterolog Shallow Resistivity
MSFL	Cant-2011D	350.52	2334.16	m	878.52	0.767	ohm.m	Micro-spherically-focused Resistivity
NPHI	Cant-2011D	350.52	2334.16	m	51.8931	5.007	m3/m3	Thermal Neutron Porosity (original Ratio Method) in Selected Lithology
RHOB	Cant-2011D	350.52	2334.16	m	2.951	-804.724	g/cm3	Bulk Density
RHOB	Cant-2011D	3181.06	1174.05	m	2.951	1.825	g/cm3	Bulk Density
CALI	Cant-2033	413.613	3184.74	m	15.138	-747.439	in	Caliper

Appendix 2 Wel logs

LOG CODE	Well name	start	end	Index unit	max value	min value	unit	description
DRHO	Cant-3033	413.813	3184.74	m	0.39	-747.09	g/cm3	Bulk Density Correction
DT	Cant-3033	413.813	3184.74	m	194.286	0	us/ft	Delta-T (also called Slowness or Interval Transit Time)
GR	Cant-3033	413.813	3184.74	m	117.401	-0.15	gAPI	Gamma Ray
ILD	Cant-3033	413.813	3184.74	m	8.528	0.2	ohm.m	Induction Deep Resistivity
LLD	Cant-3033	413.813	3184.74	m	1560.46	0.2	ohm.m	Laterolog Deep Resistivity
LLS	Cant-3033	413.813	3184.74	m	1667.69	0.2	ohm.m	Laterolog Shallow Resistivity
MSFL	Cant-3033	413.813	3184.74	m	31669.4	0.415	ohm.m	Micro-spherically-focused Resistivity
NPHI	Cant-3033	413.813	3184.74	m	44.084	0.679	m3/m3	Thermal Neutron Porosity (original Ratio Method) in Selected Lithology
RHOB	Cant-3033	413.813	3184.74	m	2.897	-747.09	g/cm3	Bulk Density
SP	Cant-3033	413.813	3184.74	m	109.45	0	mV	Spontaneous Potential
CALI	Cant-2058	501.09	3599.89	m	10.568	-250.814	in	Caliper
DT	Cant-2058	501.09	3599.89	m	140	-414.444	us/ft	Delta-T (also called Slowness or Interval Transit Time)
GR	Cant-2058	501.09	3599.89	m	108	5.558	gAPI	Gamma Ray
ILD	Cant-2058	501.09	3599.89	m	5.565	0.2	ohm.m	Induction Deep Resistivity
LLD	Cant-2058	501.09	3599.89	m	54500	0.15	ohm.m	Laterolog Deep Resistivity
LLS	Cant-2058	501.09	3599.89	m	16298.3	0.168	ohm.m	Laterolog Shallow Resistivity
MSFL	Cant-2058	501.09	3599.89	m	4093.93	0.168	ohm.m	Micro-spherically-focused Resistivity
NPHI	Cant-2058	501.09	3599.89	m	45	-1.333	m3/m3	Thermal Neutron Porosity (original Ratio Method) in Selected Lithology
RHOB	Cant-2058	501.09	3599.89	m	2.922	-206.367	g/cm3	Bulk Density
SP	Cant-2058	501.09	3599.89	m	59.994	-989.322	mV	Spontaneous Potential
CALI	Cant-2079	126.49	4079.44	m	17.398	5.985	in	Caliper
CGR	Cant-2079	126.49	4079.44	m	126.706	-621.22	gAPI	Gamma Ray Contribution from Thorium and Potassium
DRHO	Cant-2079	126.49	4079.44	m	0.484	-0.971	g/cm3	Bulk Density Correction
DT	Cant-2079	126.49	4079.44	m	103.853	-206.248	us/ft	Delta-T (also called Slowness or Interval Transit Time)
GR	Cant-2079	126.49	4079.44	m	166.059	0.117	gAPI	Gamma Ray
ILD	Cant-2079	126.49	4079.44	m	320.596	-193.971	ohm.m	Induction Deep Resistivity
LLD	Cant-2079	126.49	4079.44	m	13727.4	3.09	ohm.m	Laterolog Deep Resistivity
LLS	Cant-2079	126.49	4079.44	m	4973.62	2.314	ohm.m	Laterolog Shallow Resistivity
MSFL	Cant-2079	126.49	4079.44	m	1726.25	0.313	ohm.m	Micro-spherically-focused Resistivity
NPHI	Cant-2079	126.49	4079.44	m	57.506	-0.179	m3/m3	Thermal Neutron Porosity (original Ratio Method) in Selected Lithology
PEF	Cant-2079	126.49	4079.44	m	7.489	0.988		Photoelectric Factor
POTA	Cant-2079	126.49	4079.44	m	0.049	-616.831	%	Potassium Concentration
RHOB	Cant-2079	126.49	4079.44	m	2.986	0	g/cm3	Bulk Density
SP	Cant-2079	126.49	4079.44	m	120.154	-113.731	mV	Spontaneous Potential
THOR	Cant-2079	126.49	4079.44	m	20.003	-616.831	ppm	Thorium Concentration
URAN	Cant-2079	126.49	4079.44	m	25.052	-616.831	ppm	Uranium Concentration
CALI	Cant-2095	69.7986	3693.26	m	20.15	-750.639	in	Caliper
DT	Cant-2095	69.7986	3693.26	m	159.535	-740.478	us/ft	Delta-T (also called Slowness or Interval Transit Time)
GR	Cant-2095	69.7986	3693.26	m	143.257	-750.738	gAPI	Gamma Ray
ILD	Cant-2095	69.7986	3693.26	m	17960.1	0.156	ohm.m	Induction Deep Resistivity
LLD	Cant-2095	69.7986	3693.26	m	16778.4	0.77	ohm.m	Laterolog Deep Resistivity
LLS	Cant-2095	69.7986	3693.26	m	1602.32	1.389	ohm.m	Laterolog Shallow Resistivity
NPHI	Cant-2095	69.7986	3693.26	m	69.958	-754.37	m3/m3	Thermal Neutron Porosity (original Ratio Method) in Selected Lithology
RHOB	Cant-2095	69.7986	3693.26	m	2.995	-750.153	g/cm3	Bulk Density
SP	Cant-2095	69.7986	3693.26	m	193.121	69.985	mV	Spontaneous Potential
GR	Cant-219	3048	501.091	m	101.111	-999.99	gAPI	Gamma Ray
RHOB	Cant-219	2672.18	1850.2	m	7.55	-999.99	g/cm3	Bulk Density
DT	Cant-2207	1492.49	28	m	200	45.565	us/ft	Delta-T (also called Slowness or Interval Transit Time)
GR	Cant-2207	3500.92	391.135	m	141.717	0.2	gAPI	Gamma Ray
RHOB	Cant-2207	3500.94	391.135	m	2.82829	1.47215	g/cm3	Bulk Density
RHOB	Cant-2207	3500.92	391.135	m	2.841	1.466	g/cm3	Bulk Density
CALI	Cant-2236	200.862	4757.62	m	22.434	2.201	in	Caliper
CGR	Cant-2236	200.862	4757.62	m	98.4	-1.738	gAPI	Gamma Ray Contribution from Thorium and Potassium
DRHO	Cant-2236	200.862	4757.62	m	0.387	-0.173	g/cm3	Bulk Density Correction
DT	Cant-2236	200.862	4757.62	m	139.712	13.744	us/ft	Delta-T (also called Slowness or Interval Transit Time)
GR	Cant-2236	200.862	4757.62	m	247.875	6.67	gAPI	Gamma Ray
ILD	Cant-2236	200.862	4757.62	m	5.52	0.2	ohm.m	Induction Deep Resistivity
LLD	Cant-2236	200.862	4757.62	m	57770	0.2	ohm.m	Laterolog Deep Resistivity
LLS	Cant-2236	200.862	4757.62	m	60868.1	0.2	ohm.m	Laterolog Shallow Resistivity
MSFL	Cant-2236	200.862	4757.62	m	2113.76	0.177	ohm.m	Micro-spherically-focused Resistivity
NPHI	Cant-2236	200.862	4757.62	m	53.601	-7	m3/m3	Thermal Neutron Porosity (original Ratio Method) in Selected Lithology
POTA	Cant-2236	200.862	4757.62	m	0.2	0	%	Potassium Concentration
RHOB	Cant-2236	200.862	4757.62	m	2.908	1.516	g/cm3	Bulk Density
THOR	Cant-2236	200.862	4757.62	m	11.808	-0.292	ppm	Thorium Concentration
URAN	Cant-2236	200.862	4757.62	m	10.186	-0.142	ppm	Uranium Concentration
GR	Cant-2275A	3153.94	2542.11	m	76.259	-81.663	gAPI	Gamma Ray
RHOB	Cant-2275A	3153.94	2542.11	m	3.446	0.68	g/cm3	Bulk Density
GR	Cant-267	2908.78	2040.25	m	98.886	13.333	gAPI	Gamma Ray
RHOB	Cant-267	2908.71	2040.25	m	141.111	40	g/cm3	Bulk Density
CALI	Cant-3001	200	3380	m	22.2922	0	in	Caliper
CGR	Cant-3001	200	3380	m	121.886	-4.4857	gAPI	Gamma Ray Contribution from Thorium and Potassium
DRHO	Cant-3001	200	3380	m	0.251	-1.1594	g/cm3	Bulk Density Correction
DT	Cant-3001	200	3380	m	138.215	-677.999	us/ft	Delta-T (also called Slowness or Interval Transit Time)

Appendix 2 Wel logs

LOG CODE	Well name	start	end	Index unit	max value	min value	unit	description
GR	Cant-3001	2218.94	2934.77	m	262.297	16.7883	gAPI	Gamma Ray
GR	Cant-3001	200	3380	m	262.836	0	gAPI	Gamma Ray
GR	Cant-3001	2217.42	2935.07	m	261.419	15.1987	gAPI	Gamma Ray
ILD	Cant-3001	200	3380	m	2000	0	ohm.m	Induction Deep Resistivity
LLD	Cant-3001	200	3380	m	40104	0.0973	ohm.m	Laterolog Deep Resistivity
LLS	Cant-3001	200	3380	m	33960.1	0.1536	ohm.m	Laterolog Shallow Resistivity
MSFL	Cant-3001	200	3380	m	1987.72	0.4879	ohm.m	Micro-spherically-focused Resistivity
NPHI	Cant-3001	200	3380	m	1291.87	0	m3/m3	Thermal Neutron Porosity (original Ratio Method) in Selected Lithology
PEF	Cant-3001	200	3380	m	970.639	0.3156		Photoelectric Factor
POTA	Cant-3001	200	3380	m	0.0492	-0.002	%	Potassium Concentration
RHOB	Cant-3001	200	3380	m	2.9232	0	g/cm3	Bulk Density
SP	Cant-3001	200	3380	m	1228.66	-1234.36	mV	Spontaneous Potential
THOR	Cant-3001	200	3380	m	15.06	-0.8478	ppm	Thorium Concentration
URAN	Cant-3001	200	3380	m	24.8732	-1.1475	ppm	Uranium Concentration
CALI	Cant-3068	99.875	4701.38	m	25.6875	3.498	in	Caliper
CGR	Cant-3068	99.875	4701.38	m	174.798	1.5945	gAPI	Gamma Ray Contribution from Thorium and Potassium
DRHO	Cant-3068	99.875	4701.38	m	0.369	-999.45	g/cm3	Bulk Density Correction
DT	Cant-3068	99.875	4701.38	m	303.972	38.1367	us/ft	Delta-T (also called Slowness or Interval Transit Time)
GR	Cant-3068	99.875	4701.38	m	363.234	0.6108	gAPI	Gamma Ray
ILD	Cant-3068	99.875	4701.38	m	10761.2	0.004	ohm.m	Induction Deep Resistivity
LLD	Cant-3068	99.875	4701.38	m	41898.8	-1.1177	ohm.m	Laterolog Deep Resistivity
LLS	Cant-3068	99.875	4701.38	m	36948.9	-0.396	ohm.m	Laterolog Shallow Resistivity
MSFL	Cant-3068	99.875	4701.38	m	828.157	-0.4555	ohm.m	Micro-spherically-focused Resistivity
NPHI	Cant-3068	99.875	4701.38	m	106.354	-.99825	m3/m3	Thermal Neutron Porosity (original Ratio Method) in Selected Lithology
PEF	Cant-3068	99.875	4701.38	m	20.2286	-456.235		Photoelectric Factor
POTA	Cant-3068	99.875	4701.38	m	8.4795	-1.3774	%	Potassium Concentration
RHOB	Cant-3068	99.8706	4701.34	m	338.318	-0.0221834	g/cm3	Bulk Density
RHOB	Cant-3068	99.8706	4701.38	m	380.675	-0.0239168	g/cm3	Bulk Density
RHOB	Cant-3068	99.875	4701.38	m	163353	-1.6377	g/cm3	Bulk Density
SP	Cant-3068	99.875	4701.38	m	98.308	-169.133	mV	Spontaneous Potential
THOR	Cant-3068	99.875	4701.38	m	18.1492	0.0444	ppm	Thorium Concentration
URAN	Cant-3068	99.875	4701.38	m	38.3242	-1.4497	ppm	Uranium Concentration
CALI	Cant-418-D	684.363	5548.06	m	27.641	1.275	in	Caliper
CGR	Cant-418-D	684.363	5548.06	m	3231.11	-2.673	gAPI	Gamma Ray Contribution from Thorium and Potassium
DRHO	Cant-418-D	684.363	5548.06	m	0.443	-1.186	g/cm3	Bulk Density Correction
DT	Cant-418-D	684.363	5548.06	m	366.556	-49.43	us/ft	Delta-T (also called Slowness or Interval Transit Time)
GR	Cant-418-D	684.363	5548.06	m	196.501	3.7385	gAPI	Gamma Ray
ILD	Cant-418-D	684.363	5548.06	m	22132.4	0.3739	ohm.m	Induction Deep Resistivity
LLD	Cant-418-D	684.363	5548.06	m	39688.4	0	ohm.m	Laterolog Deep Resistivity
LLS	Cant-418-D	684.363	5548.06	m	1644.99	0	ohm.m	Laterolog Shallow Resistivity
MSFL	Cant-418-D	684.363	5548.06	m	2000.5	0.132	ohm.m	Micro-spherically-focused Resistivity
NPHI	Cant-418-D	684.363	5548.06	m	79.2168	-1.575	m3/m3	Thermal Neutron Porosity (original Ratio Method) in Selected Lithology
PEF	Cant-418-D	684.363	5548.06	m	39.8517	1.251		Photoelectric Factor
POTA	Cant-418-D	684.363	5548.06	m	18.1	-40.3815	%	Potassium Concentration
RHOB	Cant-418-D	684.363	5548.06	m	2.9906	0.832	g/cm3	Bulk Density
SP	Cant-418-D	684.363	5548.06	m	133.264	-411.825	mV	Spontaneous Potential
THOR	Cant-418-D	684.363	5548.06	m	1039.38	-1.892	ppm	Thorium Concentration
URAN	Cant-418-D	684.363	5548.06	m	21.5585	-278.361	ppm	Uranium Concentration
CALI	Cant-43	495.608	2766.67	m	16	-855.09	in	Caliper
DT	Cant-43	495.608	2766.67	m	140	-986.342	us/ft	Delta-T (also called Slowness or Interval Transit Time)
GR	Cant-43	495.608	2766.67	m	143.785	-982.035	gAPI	Gamma Ray
ILD	Cant-43	495.608	2766.67	m	2000.5	0.299	ohm.m	Induction Deep Resistivity
LLD	Cant-43	495.608	2766.67	m	50213.2	0.2	ohm.m	Laterolog Deep Resistivity
LLS	Cant-43	495.608	2766.67	m	1375.89	0.201	ohm.m	Laterolog Shallow Resistivity
NPHI	Cant-43	495.608	2766.67	m	58.252	-983.73	m3/m3	Thermal Neutron Porosity (original Ratio Method) in Selected Lithology
PEF	Cant-43	495.608	2766.67	m	6.127	-982.781		Photoelectric Factor
RHOB	Cant-43	495.608	2766.67	m	2.966	-982.802	g/cm3	Bulk Density
SP	Cant-43	495.608	2766.67	m	0.333	-986.828	mV	Spontaneous Potential
CALI	Cant-468	162	2800.96	m	26.734	7.787	in	Caliper
CGR	Cant-468	162	2800.96	m	83.2577	0.5895	gAPI	Gamma Ray Contribution from Thorium and Potassium
DRHO	Cant-468	162	2800.96	m	0.4751	-1.7091	g/cm3	Bulk Density Correction
DT	Cant-468	162	2800.96	m	340.286	42.3336	us/ft	Delta-T (also called Slowness or Interval Transit Time)
GR	Cant-468	162	2800.96	m	132.825	6.0343	gAPI	Gamma Ray
ILD	Cant-468	162	2800.96	m	8.105	0.52	ohm.m	Induction Deep Resistivity
LLD	Cant-468	162	2800.96	m	40000	2.2365	ohm.m	Laterolog Deep Resistivity
LLS	Cant-468	162	2800.96	m	7663.89	0.3928	ohm.m	Laterolog Shallow Resistivity
MSFL	Cant-468	162	2800.96	m	20000	0.1	ohm.m	Micro-spherically-focused Resistivity
NPHI	Cant-468	162	2800.96	m	80.7702	-0.2219	m3/m3	Thermal Neutron Porosity (original Ratio Method) in Selected Lithology
PEF	Cant-468	162	2800.96	m	11004	0.8873		Photoelectric Factor
POTA	Cant-468	162	2800.96	m	3.8512	0.01	%	Potassium Concentration
RHOB	Cant-468	162	2800.96	m	2.885	1.0253	g/cm3	Bulk Density
SP	Cant-468	162	2800.96	m	2013.5	-1083.5	mV	Spontaneous Potential
THOR	Cant-468	162	2800.96	m	11.3631	0.0852	ppm	Thorium Concentration

Appendix 2 Wel logs

LOG CODE	Well name	start	end	Index unit	max value	min value	unit	description
URAN	Cant-6B	162	2800.86	m	8.6308	0.0303	ppm	Uranium Concentration
CALI	Cant-51	170.961	2219.86	m	17.243	2.211	in	Caliper
DRHO	Cant-51	170.961	2219.86	m	0.25	-248.825	g/cm3	Bulk Density Correction
DT	Cant-51	170.961	2219.86	m	202.786	63.586	us/ft	Delta-T (also called Slowness or Interval Transit Time)
GR	Cant-51	170.961	2219.86	m	101	-248.963	gAPI	Gamma Ray
GR	Cant-51	2221.96	1015.06	m	101	-0.66	gAPI	Gamma Ray
ILD	Cant-51	170.961	2219.86	m	43.781	0.197	ohm.m	Induction Deep Resistivity
NPHI	Cant-51	170.961	2219.86	m	80.192	-280.225	m3/m3	Thermal Neutron Porosity (original Ratio Method) in Selected Lithology
RHOB	Cant-51	170.961	2219.86	m	3	1.903	g/cm3	Bulk Density
RHOB	Cant-51	2221.95	1015.06	m	40	40	g/cm3	Bulk Density
SP	Cant-51	170.961	2219.86	m	244.227	0	mV	Spontaneous Potential
CALI	Cant-57	68.5791	2704.79	m	15.589	-281.377	in	Caliper
CALI	Cant-57	122.5	1682.38	m	18.1493	-250.414	in	Caliper
DRHO	Cant-57	68.5791	2704.79	m	0.351	-0.115	g/cm3	Bulk Density Correction
DRHO	Cant-57	122.5	1682.38	m	0.1796	-250.414	g/cm3	Bulk Density Correction
DT	Cant-57	68.5791	2704.79	m	193.713	-236.383	us/ft	Delta-T (also called Slowness or Interval Transit Time)
DT	Cant-57	122.5	1682.38	m	201.884	-220.439	us/ft	Delta-T (also called Slowness or Interval Transit Time)
GR	Cant-57	122.5	1682.38	m	100	-250.312	gAPI	Gamma Ray
GR	Cant-57	68.5791	2704.79	m	114.454	-334.836	gAPI	Gamma Ray
ILD	Cant-57	68.5791	2704.79	m	474.236	0.015	ohm.m	Induction Deep Resistivity
ILD	Cant-57	122.5	1682.38	m	19.202	0	ohm.m	Induction Deep Resistivity
LLD	Cant-57	68.5791	2704.79	m	32837.1	0.2	ohm.m	Laterolog Deep Resistivity
LLS	Cant-57	68.5791	2704.79	m	2253.92	0.348	ohm.m	Laterolog Shallow Resistivity
MSFL	Cant-57	68.5791	2704.79	m	8680.26	0.2	ohm.m	Micro-spherically-focused Resistivity
NPHI	Cant-57	122.5	1682.38	m	80.8677	-261.655	m3/m3	Thermal Neutron Porosity (original Ratio Method) in Selected Lithology
NPHI	Cant-57	68.5791	2704.79	m	65.234	-291.253	m3/m3	Thermal Neutron Porosity (original Ratio Method) in Selected Lithology
RHOB	Cant-57	68.5791	2704.79	m	3.047	-373.356	g/cm3	Bulk Density
RHOB	Cant-57	122.5	1682.38	m	2.7601	-248.953	g/cm3	Bulk Density
SP	Cant-57	68.5791	2704.79	m	165.424	-329.76	mV	Spontaneous Potential
SP	Cant-57	122.5	1682.38	m	69.7327	-250.414	mV	Spontaneous Potential
DT	Cant-6	1987.22	146.5	m	234.137	40	us/ft	Delta-T (also called Slowness or Interval Transit Time)
GR	Cant-6	1987.22	146.5	m	126.721	0	gAPI	Gamma Ray
RHOB	Cant-6	1987.22	146.5	m	2.848	1.945	g/cm3	Bulk Density
DT	Cant-66	2139.47	1709.92	m	187.911	-999.99	us/ft	Delta-T (also called Slowness or Interval Transit Time)
GR	Cant-66	2139.47	1089.76	m	147.311	-999.99	gAPI	Gamma Ray
RHOB	Cant-66	2139.47	1707.49	m	2.887	-999.99	g/cm3	Bulk Density
CALI	Cant-66A	117.042	3005.63	m	9.381	-250.413	in	Caliper
DT	Cant-66A	117.042	3005.63	m	205.555	-249.812	us/ft	Delta-T (also called Slowness or Interval Transit Time)
GR	Cant-66A	117.042	3005.63	m	174.972	-251.562	gAPI	Gamma Ray
ILD	Cant-66A	117.042	3005.63	m	549.412	0.196	ohm.m	Induction Deep Resistivity
LLD	Cant-66A	117.042	3005.63	m	105633	0.1	ohm.m	Laterolog Deep Resistivity
LLS	Cant-66A	117.042	3005.63	m	98012.7	0.047	ohm.m	Laterolog Shallow Resistivity
MSFL	Cant-66A	117.042	3005.63	m	36205.8	0.1	ohm.m	Micro-spherically-focused Resistivity
NPHI	Cant-66A	117.042	3005.63	m	83.027	-263.377	m3/m3	Thermal Neutron Porosity (original Ratio Method) in Selected Lithology
RHOB	Cant-66A	117.042	3005.63	m	2.834	-250.103	g/cm3	Bulk Density
SP	Cant-66A	117.042	3005.63	m	163.303	-310.126	mV	Spontaneous Potential
CALI	Cant-6A	140.36	2560.17	m	16.3544	-113.91	in	Caliper
DRHO	Cant-6A	140.36	2560.17	m	0.222	-0.052	g/cm3	Bulk Density Correction
DT	Cant-6A	140.36	2560.17	m	211.173	0	us/ft	Delta-T (also called Slowness or Interval Transit Time)
GR	Cant-6A	140.36	2560.17	m	106.483	0	gAPI	Gamma Ray
ILD	Cant-6A	140.36	2560.17	m	13.0379	0.2	ohm.m	Induction Deep Resistivity
LLD	Cant-6A	140.36	2560.17	m	39361.4	3.8485	ohm.m	Laterolog Deep Resistivity
LLS	Cant-6A	140.36	2560.17	m	59723	5.4225	ohm.m	Laterolog Shallow Resistivity
MSFL	Cant-6A	140.36	2560.17	m	2000	0.5274	ohm.m	Micro-spherically-focused Resistivity
NPHI	Cant-6A	140.36	2560.17	m	49.9	1.6	m3/m3	Thermal Neutron Porosity (original Ratio Method) in Selected Lithology
PEF	Cant-6A	140.36	2560.17	m	4.875	0.004		Photoelectric Factor
RHOB	Cant-6A	140.36	2560.17	m	2.858	-123.812	g/cm3	Bulk Density
SP	Cant-6A	140.36	2560.17	m	151.273	-139.063	mV	Spontaneous Potential
CALI	Cant-7A	117.957	2284.05	m	13.9	-602.837	in	Caliper
DRHO	Cant-7A	117.957	2284.05	m	0.26	-0.238	g/cm3	Bulk Density Correction
DT	Cant-7A	117.957	2284.05	m	198	-773.77	us/ft	Delta-T (also called Slowness or Interval Transit Time)
GR	Cant-7A	117.957	2284.05	m	103.982	-586.989	gAPI	Gamma Ray
ILD	Cant-7A	117.957	2284.05	m	493084	0.2	ohm.m	Induction Deep Resistivity
LLD	Cant-7A	117.957	2284.05	m	12619.1	0.173	ohm.m	Laterolog Deep Resistivity
LLS	Cant-7A	117.957	2284.05	m	1049.76	0.168	ohm.m	Laterolog Shallow Resistivity
MSFL	Cant-7A	117.957	2284.05	m	1628.1	0.173	ohm.m	Micro-spherically-focused Resistivity
NPHI	Cant-7A	117.957	2284.05	m	52.2	-966.737	m3/m3	Thermal Neutron Porosity (original Ratio Method) in Selected Lithology
RHOB	Cant-7A	117.957	2284.05	m	2.987	-758.336	g/cm3	Bulk Density
SP	Cant-7A	117.957	2284.05	m	145	-578.155	mV	Spontaneous Potential
CALI	Cant-82A	497.718	2904.24	m	21.9618	5.9805	in	Caliper
DRHO	Cant-82A	497.718	2904.24	m	0.5242	-0.0518	g/cm3	Bulk Density Correction
DT	Cant-82A	2902.84	2847	m	68.797	33.793	us/ft	Delta-T (also called Slowness or Interval Transit Time)
DT	Cant-82A	497.718	2904.24	m	67.234	33.864	us/ft	Delta-T (also called Slowness or Interval Transit Time)

Appendix 2 Wel logs

LOG CODE	Well name	start	end	index unit	max value	min value	unit	description
GR	Cant-82A	497.718	2904.24	m	186.98	6.2326	gAPI	Gamma Ray
GR	Cant-82A	2902.94	1819.89	m	182.062	-76.348	gAPI	Gamma Ray
ILD	Cant-82A	497.718	2904.24	m	22.7262	0.433	ohm.m	Induction Deep Resistivity
LLD	Cant-82A	497.718	2904.24	m	70681.9	1.8187	ohm.m	Laterolog Deep Resistivity
LLS	Cant-82A	497.718	2904.24	m	74752.2	1.8291	ohm.m	Laterolog Shallow Resistivity
MSFL	Cant-82A	497.718	2904.24	m	2000.89	0.484	ohm.m	Micro-spherically-focused Resistivity
NPHI	Cant-82A	497.718	2904.24	m	63.821	0.0297	m3/m3	Thermal Neutron Porosity (original Ratio Method) in Selected Lithology
PEF	Cant-82A	497.718	2904.24	m	5.7867	-0.7768		Photoelectric Factor
RHOB	Cant-82A	497.718	2904.24	m	3.6881	0.9307	g/cm3	Bulk Density
RHOB	Cant-82A	2902.94	1819.89	m	3.748	0.923	g/cm3	Bulk Density
SP	Cant-82A	497.718	2904.24	m	116.542	-999.255	mV	Spontaneous Potential
CALI	Cant-91	447.142	3367.74	m	18.19	-748.037	in	Caliper
CGR	Cant-91	447.142	3367.74	m	97.713	-250.212	gAPI	Gamma Ray Contribution from Thorium and Potassium
DRHO	Cant-91	447.142	3367.74	m	0.321	-0.607	g/cm3	Bulk Density Correction
DT	Cant-91	447.142	3367.74	m	130.027	-218.147	us/ft	Delta-T (also called Slowness or Interval Transit Time)
GR	Cant-91	447.142	3367.74	m	205.781	-827.187	gAPI	Gamma Ray
ILD	Cant-91	447.142	3367.74	m	2000	-248.061	ohm.m	Induction Deep Resistivity
LLD	Cant-91	447.142	3367.74	m	51890.3	0.169	ohm.m	Laterolog Deep Resistivity
LLS	Cant-91	447.142	3367.74	m	46088.9	0.119	ohm.m	Laterolog Shallow Resistivity
MSFL	Cant-91	447.142	3367.74	m	2000.89	0.169	ohm.m	Micro-spherically-focused Resistivity
NPHI	Cant-91	447.142	3367.74	m	55.347	-259.485	m3/m3	Thermal Neutron Porosity (original Ratio Method) in Selected Lithology
PEF	Cant-91	447.142	3367.74	m	3065.67	-410.707		Photoelectric Factor
POTA	Cant-91	447.142	3367.74	m	3.061	-250.212	%	Potassium Concentration
RHOB	Cant-91	447.142	3367.74	m	3.537	-246.745	g/cm3	Bulk Density
THOR	Cant-91	447.142	3367.74	m	11.859	-250.212	ppm	Thorium Concentration
URAN	Cant-91	447.142	3367.74	m	7.704	-250.062	ppm	Uranium Concentration
CALI	Cant-93	466.343	2571.6	m	23.338	-82.536	in	Caliper
DRHO	Cant-93	466.343	2571.6	m	0.647	-82.766	g/cm3	Bulk Density Correction
GR	Cant-93	466.343	2571.6	m	201.111	0	gAPI	Gamma Ray
ILD	Cant-93	466.343	2571.6	m	20	0.2	ohm.m	Induction Deep Resistivity
LLD	Cant-93	466.343	2571.6	m	3169.79	0.191	ohm.m	Laterolog Deep Resistivity
LLS	Cant-93	466.343	2571.6	m	477.318	0.192	ohm.m	Laterolog Shallow Resistivity
NPHI	Cant-93	466.343	2571.6	m	45	-80.117	m3/m3	Thermal Neutron Porosity (original Ratio Method) in Selected Lithology
PEF	Cant-93	466.343	2571.6	m	280.012	-225.514		Photoelectric Factor
RHOB	Cant-93	466.343	2571.6	m	3.644	-80.747	g/cm3	Bulk Density
GR	Cant-94	1289.31	799.56	m	57.513	-999.99	gAPI	Gamma Ray
CALI	Cant-94A	122.5	1682.38	m	18.1493	-250.414	in	Caliper
DRHO	Cant-94A	122.5	1682.38	m	0.1798	-250.414	g/cm3	Bulk Density Correction
DT	Cant-94A	1692.98	1073.27	m	195.99	0	us/ft	Delta-T (also called Slowness or Interval Transit Time)
DT	Cant-94A	122.5	1682.38	m	201.684	-220.439	us/ft	Delta-T (also called Slowness or Interval Transit Time)
GR	Cant-94A	1692.98	1073.27	m	100	0	gAPI	Gamma Ray
GR	Cant-94A	122.5	1682.38	m	100	-250.312	gAPI	Gamma Ray
ILD	Cant-94A	122.5	1682.38	m	19.202	0	ohm.m	Induction Deep Resistivity
NPHI	Cant-94A	122.5	1682.38	m	80.6977	-261.655	m3/m3	Thermal Neutron Porosity (original Ratio Method) in Selected Lithology
RHOB	Cant-94A	1692.98	1073.27	m	1.95	1.95	g/cm3	Bulk Density
RHOB	Cant-94A	122.5	1682.38	m	2.7801	-248.953	g/cm3	Bulk Density
SP	Cant-94A	122.5	1682.38	m	69.7327	-250.414	mV	Spontaneous Potential
CALI	Cant-95	547.06	2611.44	m	16.0487	0	in	Caliper
DRHO	Cant-95	547.06	2611.44	m	35.5152	-0.242	g/cm3	Bulk Density Correction
GR	Cant-95	547.06	2611.44	m	127.042	3.926	gAPI	Gamma Ray
ILD	Cant-95	547.06	2611.44	m	27.6938	-882.046	ohm.m	Induction Deep Resistivity
LLD	Cant-95	547.06	2611.44	m	9084.83	0	ohm.m	Laterolog Deep Resistivity
LLS	Cant-95	547.06	2611.44	m	2714.49	0	ohm.m	Laterolog Shallow Resistivity
MSFL	Cant-95	547.06	2611.44	m	2550.26	0	ohm.m	Micro-spherically-focused Resistivity
NPHI	Cant-95	547.06	2611.44	m	36.772	-8.5735	m3/m3	Thermal Neutron Porosity (original Ratio Method) in Selected Lithology
RHOB	Cant-95	547.06	2611.44	m	2.7998	0	g/cm3	Bulk Density
CALI	Cant-99D	134.788	3144.69	m	24.263	5.523	in	Caliper
CGR	Cant-99D	134.788	3144.69	m	372.412	-449.057	gAPI	Gamma Ray Contribution from Thorium and Potassium
DRHO	Cant-99D	134.788	3144.69	m	0.5	-1.873	g/cm3	Bulk Density Correction
DT	Cant-99D	134.788	3144.69	m	256.65	-998.008	us/ft	Delta-T (also called Slowness or Interval Transit Time)
GR	Cant-99D	134.788	3144.69	m	623.104	10.662	gAPI	Gamma Ray
ILD	Cant-99D	134.788	3144.69	m	133.314	0.041	ohm.m	Induction Deep Resistivity
LLD	Cant-99D	134.788	3144.69	m	40000	0.479	ohm.m	Laterolog Deep Resistivity
LLS	Cant-99D	134.788	3144.69	m	40000	0.464	ohm.m	Laterolog Shallow Resistivity
MSFL	Cant-99D	134.788	3144.69	m	20000	0.1	ohm.m	Micro-spherically-focused Resistivity
NPHI	Cant-99D	134.788	3144.69	m	110.537	2.442	m3/m3	Thermal Neutron Porosity (original Ratio Method) in Selected Lithology
PEF	Cant-99D	134.788	3144.69	m	26.358	-840.707		Photoelectric Factor
POTA	Cant-99D	134.788	3144.69	m	22.754	0.021	%	Potassium Concentration
RHOB	Cant-99D	134.788	3144.69	m	3.788	0.188	g/cm3	Bulk Density
SP	Cant-99D	134.788	3144.69	m	91.72	-154.912	mV	Spontaneous Potential
THOR	Cant-99D	134.788	3144.69	m	16.281	0.128	ppm	Thorium Concentration
URAN	Cant-99D	134.788	3144.69	m	34.154	-482.597	ppm	Uranium Concentration
GR	Cant-CI47	800.705	1333.49	m	86.937	18.594	gAPI	Gamma Ray

Appendix 2 Wel logs

LOG CODE	Well name	start	end	index unit	max value	min value	unit	description
ILD	Cant-CI47	800.706	1333.49	m	2000	0.362	ohm.m	Induction Deep Resistivity
SP	Cant-CI47	800.706	1333.49	m	1366.5	-788.75	mV	Spontaneous Potential
CALI	Cant-CI49	402.125	1445	m	22.8878	0	in	Caliper
DRHO	Cant-CI49	402.125	1445	m	0.2049	0	g/cm3	Bulk Density Correction
DT	Cant-CI49	402.125	1445	m	363.841	-340.384	us/ft	Delta-T (also called Slowness or Interval Transit Time)
GR	Cant-CI49	402.125	1445	m	75.8691	0	gAPI	Gamma Ray
ILD	Cant-CI49	402.125	1445	m	48.8883	0	ohm.m	Induction Deep Resistivity
NPHI	Cant-CI49	402.125	1445	m	105.859	-8.2	m3/m3	Thermal Neutron Porosity (original Ratio Method) in Selected Lithology
PEF	Cant-CI49	402.125	1445	m	10.958	0		Photoelectric Factor
RHOB	Cant-CI49	402.125	1445	m	2.4503	0	g/cm3	Bulk Density
SP	Cant-CI49	402.125	1445	m	334.504	-552.018	mV	Spontaneous Potential
GR	Cant-CI85	816.25	1482	m	131.766	16.1593	gAPI	Gamma Ray
ILD	Cant-CI85	816.25	1482	m	17.5833	0.3801	ohm.m	Induction Deep Resistivity
SP	Cant-CI85	816.25	1482	m	278.018	-972.223	mV	Spontaneous Potential
CALI	Chac-1	4858.07	2475.58	m	13.89	-999.99	in	Caliper
DT	Chac-1	4940.79	2475.58	m	132.201	15.3973	us/ft	Delta-T (also called Slowness or Interval Transit Time)
DT	Chac-1	4940.81	2475.58	m	132.208	15.397	us/ft	Delta-T (also called Slowness or Interval Transit Time)
DT	Chac-1	4940.79	2475.58	m	132.201	15.3973	us/ft	Delta-T (also called Slowness or Interval Transit Time)
GR	Chac-1	4940.96	498.957	m	197.73	-999.99	gAPI	Gamma Ray
GR	Chac-1	4940.81	498.957	m	197.86	-999.99	gAPI	Gamma Ray
RHOB	Chac-1	3899	3652.34	m	2.87	-802.543	g/cm3	Bulk Density
DT	Chac-2	4533.11	1431.57	m	174.879	43.933	us/ft	Delta-T (also called Slowness or Interval Transit Time)
GR	Chac-2	4533.17	1431.57	m	131.189	0	gAPI	Gamma Ray
GR	Chac-2	4533.11	1431.57	m	135.916	0	gAPI	Gamma Ray
RHOB	Chac-2	4533.11	1431.57	m	2.863	1.941	g/cm3	Bulk Density
RHOB	Chac-2	4533.17	1431.57	m	2.85889	1.94118	g/cm3	Bulk Density
CALI	IXTOC-1	186.842	3539.34	m	43.354	5.872	in	Caliper
DT	IXTOC-1	186.842	3539.34	m	101.667	-555.831	us/ft	Delta-T (also called Slowness or Interval Transit Time)
GR	IXTOC-1	186.842	3539.34	m	108.803	-626.82	gAPI	Gamma Ray
NPHI	IXTOC-1	186.842	3539.34	m	56.942	-555.497	m3/m3	Thermal Neutron Porosity (original Ratio Method) in Selected Lithology
SP	IXTOC-1	186.842	3539.34	m	67.194	-817.723	mV	Spontaneous Potential
CALI	IXTOC-16	146.913	4576.57	m	14.5	-876.451	in	Caliper
CALI	IXTOC-16	4576.57	3512.21	m	14.5	-876.451	in	Caliper
CGR	IXTOC-16	146.913	4576.57	m	90.356	-803.696	gAPI	Gamma Ray Contribution from Thorium and Potassium
DRHO	IXTOC-16	146.913	4576.57	m	0.404	-0.788	g/cm3	Bulk Density Correction
DT	IXTOC-16	146.913	4576.57	m	214.139	40	us/ft	Delta-T (also called Slowness or Interval Transit Time)
DT	IXTOC-16	4576.57	142.914	m	214.139	40	us/ft	Delta-T (also called Slowness or Interval Transit Time)
GR	IXTOC-16	4576.57	650.748	m	174.5	-999.99	gAPI	Gamma Ray
GR	IXTOC-16	146.913	4576.57	m	174.559	0	gAPI	Gamma Ray
ILD	IXTOC-16	146.913	4576.57	m	4.36	0.188	ohm.m	Induction Deep Resistivity
LLD	IXTOC-16	146.913	4576.57	m	849	0.105	ohm.m	Laterolog Deep Resistivity
LLS	IXTOC-16	146.913	4576.57	m	2400	0.168	ohm.m	Laterolog Shallow Resistivity
MSFL	IXTOC-16	146.913	4576.57	m	49600	0.188	ohm.m	Micro-spherically-focused Resistivity
NPHI	IXTOC-16	146.913	4576.57	m	55	-15	m3/m3	Thermal Neutron Porosity (original Ratio Method) in Selected Lithology
POTA	IXTOC-16	146.913	4576.57	m	4.283	-0.07	%	Potassium Concentration
RHOB	IXTOC-16	146.913	4576.57	m	2.94	0.984	g/cm3	Bulk Density
RHOB	IXTOC-16	4576.57	650.748	m	2.94	0.984	g/cm3	Bulk Density
RHOB	IXTOC-16	4576.55	650.748	m	2.93561	0.984474	g/cm3	Bulk Density
SP	IXTOC-16	146.913	4576.57	m	-1.305	-214	mV	Spontaneous Potential
THOR	IXTOC-16	146.913	4576.57	m	10.031	-0.346	ppm	Thorium Concentration
URAN	IXTOC-16	146.913	4576.57	m	10.816	-0.194	ppm	Uranium Concentration
DT	K-1247	3819.52	2971.28	m	391.266	156.381	us/ft	Delta-T (also called Slowness or Interval Transit Time)
DT	K-1247	4099.86	200.074	m	892.257	-1623.86	us/ft	Delta-T (also called Slowness or Interval Transit Time)
DT	K-1247	4099.86	200.074	m	892.257	-1623.86	us/ft	Delta-T (also called Slowness or Interval Transit Time)
GR	K-1247	4108.09	200.074	m	618.495	0.001	gAPI	Gamma Ray
GR	K-1247	4108.09	200.074	m	618.495	0.001	gAPI	Gamma Ray
RHOB	K-1247	4108.09	200.074	m	2.977	-0.12	g/cm3	Bulk Density
RHOB	K-1247	4108.09	200.074	m	2.977	-0.12	g/cm3	Bulk Density
DT	KU-401	3887.61	470.916	m	241.26	-18.383	us/ft	Delta-T (also called Slowness or Interval Transit Time)
DT	KU-401	3868.92	470.916	m	241.26	-18.383	us/ft	Delta-T (also called Slowness or Interval Transit Time)
GR	KU-401	4196.18	470.916	m	201.468	4.086	gAPI	Gamma Ray
RHOB	KU-401	4187.04	1800.45	m	3.465	1.75	g/cm3	Bulk Density
DT	KU-89	3477.84	1500	m	151.209	44.15	us/ft	Delta-T (also called Slowness or Interval Transit Time)
DT	KU-89	3477.84	1500	m	151.209	44.15	us/ft	Delta-T (also called Slowness or Interval Transit Time)
GR	KU-89	3483.64	151.867	m	216	12.914	gAPI	Gamma Ray
GR	KU-89	3483.64	151.867	m	216	12.914	gAPI	Gamma Ray
RHOB	KU-89	3477.84	1500	m	2.898	1.582	g/cm3	Bulk Density
DT	Kutz-1	3425.79	1929.16	m	149.375	48.25	us/ft	Delta-T (also called Slowness or Interval Transit Time)
GR	Kutz-1	3425.79	1929.16	m	116.223	10.989	gAPI	Gamma Ray
RHOB	Kutz-1	3425.79	1929.16	m	3.427	1.767	g/cm3	Bulk Density
DT	Tak-101	4343.74	202.49	m	169.423	-999.99	us/ft	Delta-T (also called Slowness or Interval Transit Time)
GR	Tak-101	4344.72	189.079	m	244.718	-999.99	gAPI	Gamma Ray

Appendix 2 Wel logs

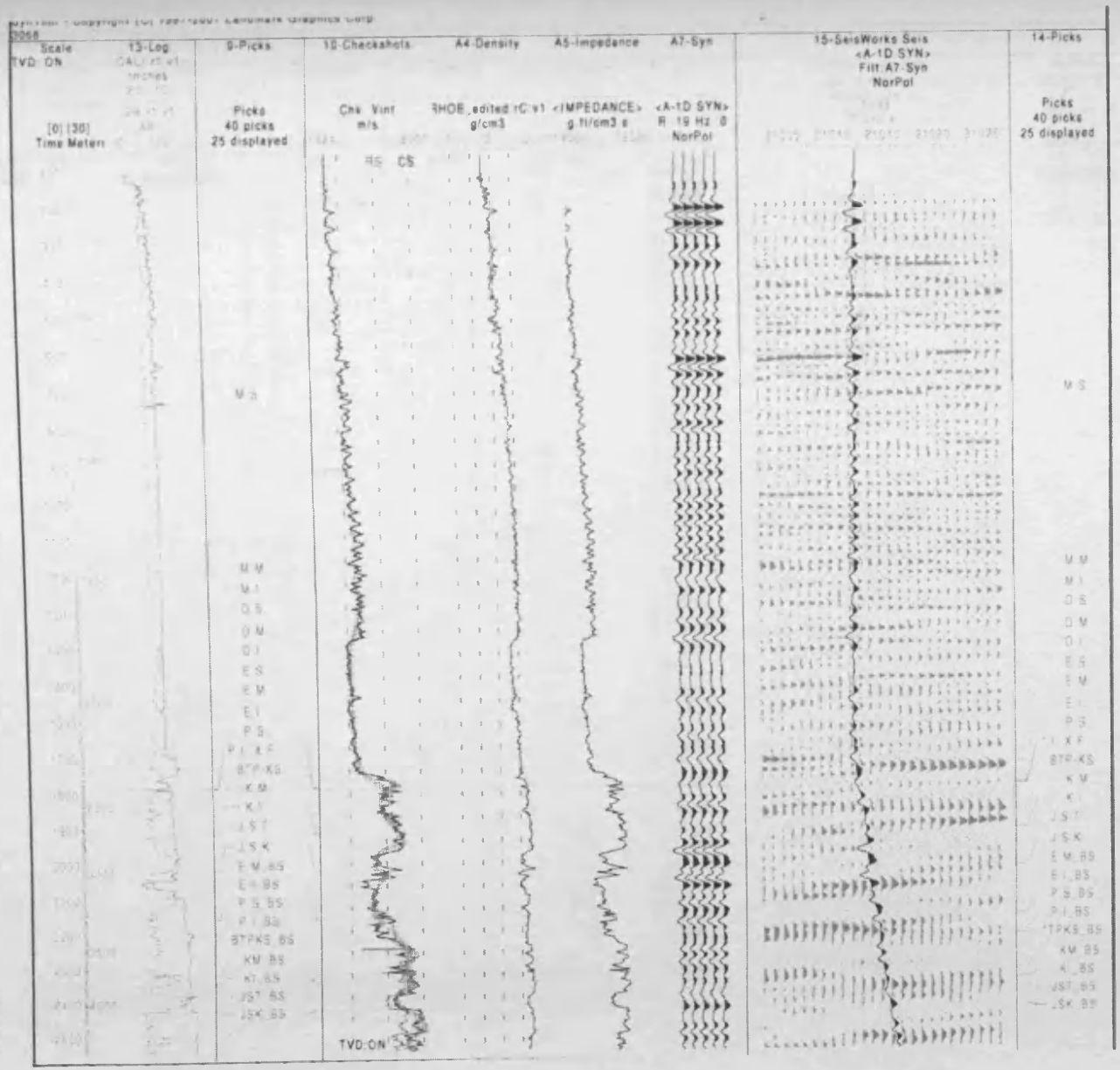

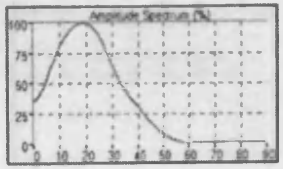

M.M. Mid-Miocene
M.I. Early Miocene
O.S. Late Oligocene
O.M. Mid-Oligocene
O.I. Early Oligocene
E.S. Late Eocene
E.M. Mid-Eocene
E.I. Early Eocene
P.S. Late Palaeocene
BTP-KS Upper Cretaceous
K.M. Mid-Cretaceous
K.I. Early Cretaceous
J.S.T. Late Tithonian
J.S.K. Late Kimmeridgian
E.M_BS Mid-Eocene footwall block
E.I.-BS Early Eocene footwall block
BTPKS_BS Upper Cretaceous footwall block
KM_BS Mid-Cretaceous footwall block
KI_BS Early Cretaceous footwall block
JST_BS Late Tithonian footwall block
JSK_BS Late Kimmeridgian footwall block

Synthetic for well C-3068

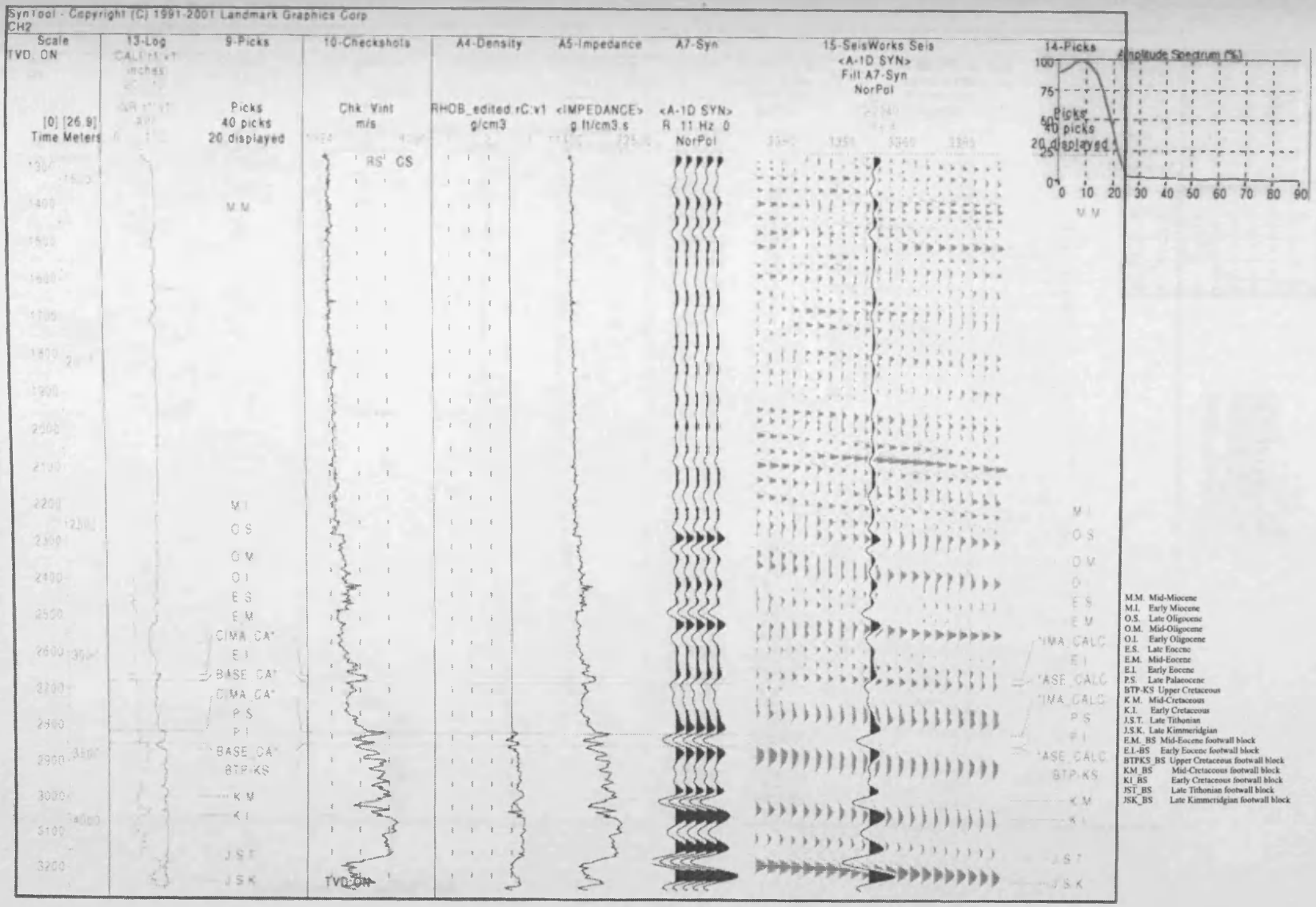

Synthetic for well Chac-2

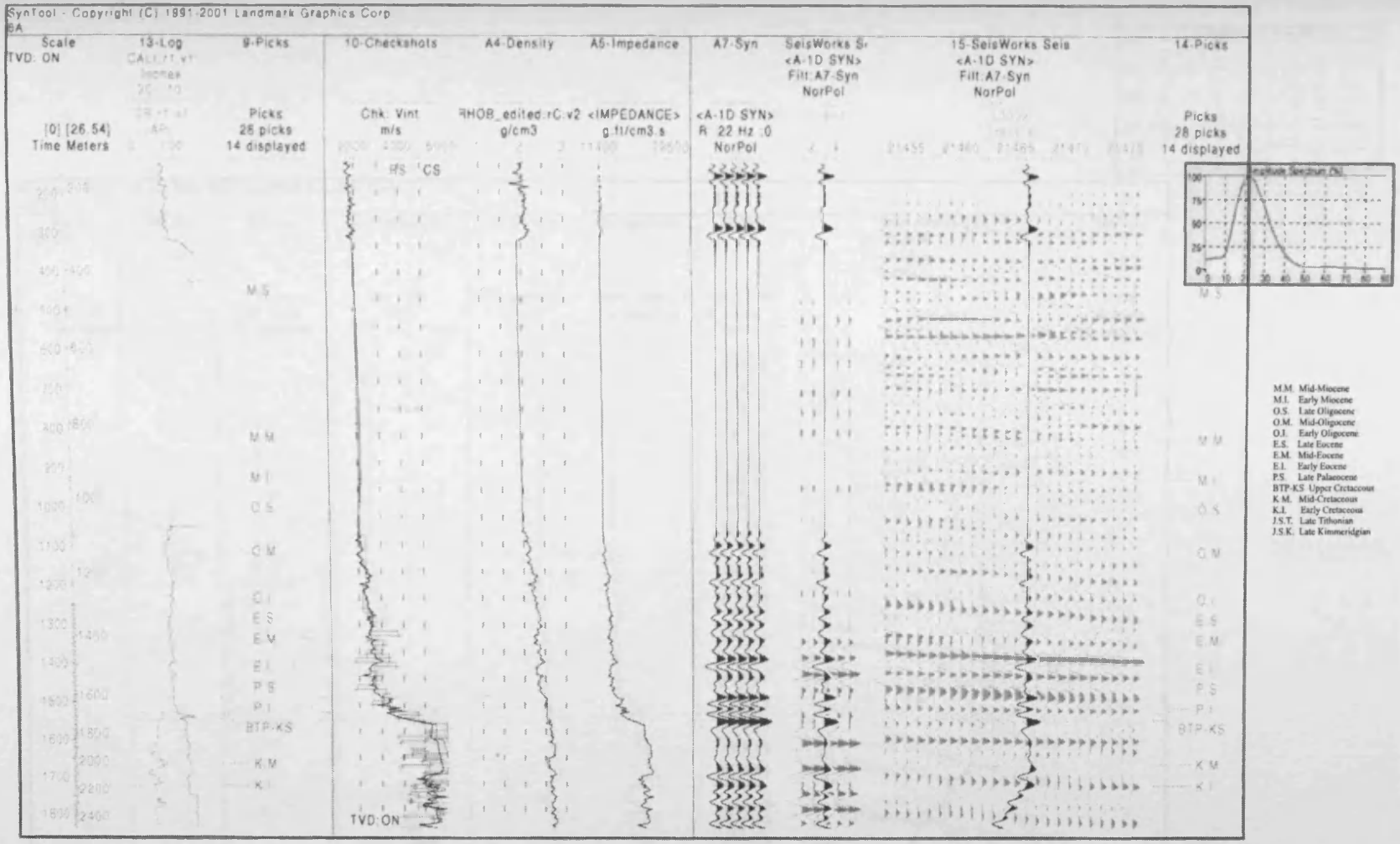

M.M. Mid-Miocene
M.I. Early Miocene
O.S. Late Oligocene
O.M. Mid-Oligocene
O.I. Early Oligocene
E.S. Late Eocene
E.M. Mid-Eocene
E.I. Early Eocene
P.S. Late Palaeocene
BTP-KS Upper Cretaceous
K.M. Mid-Cretaceous
K.I. Early Cretaceous
J.S.T. Late Tithonian
J.S.K. Late Kimmeridgian

Synthetic for well C-6A

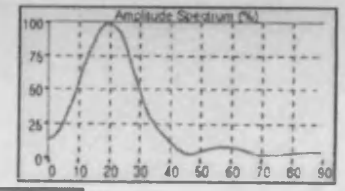

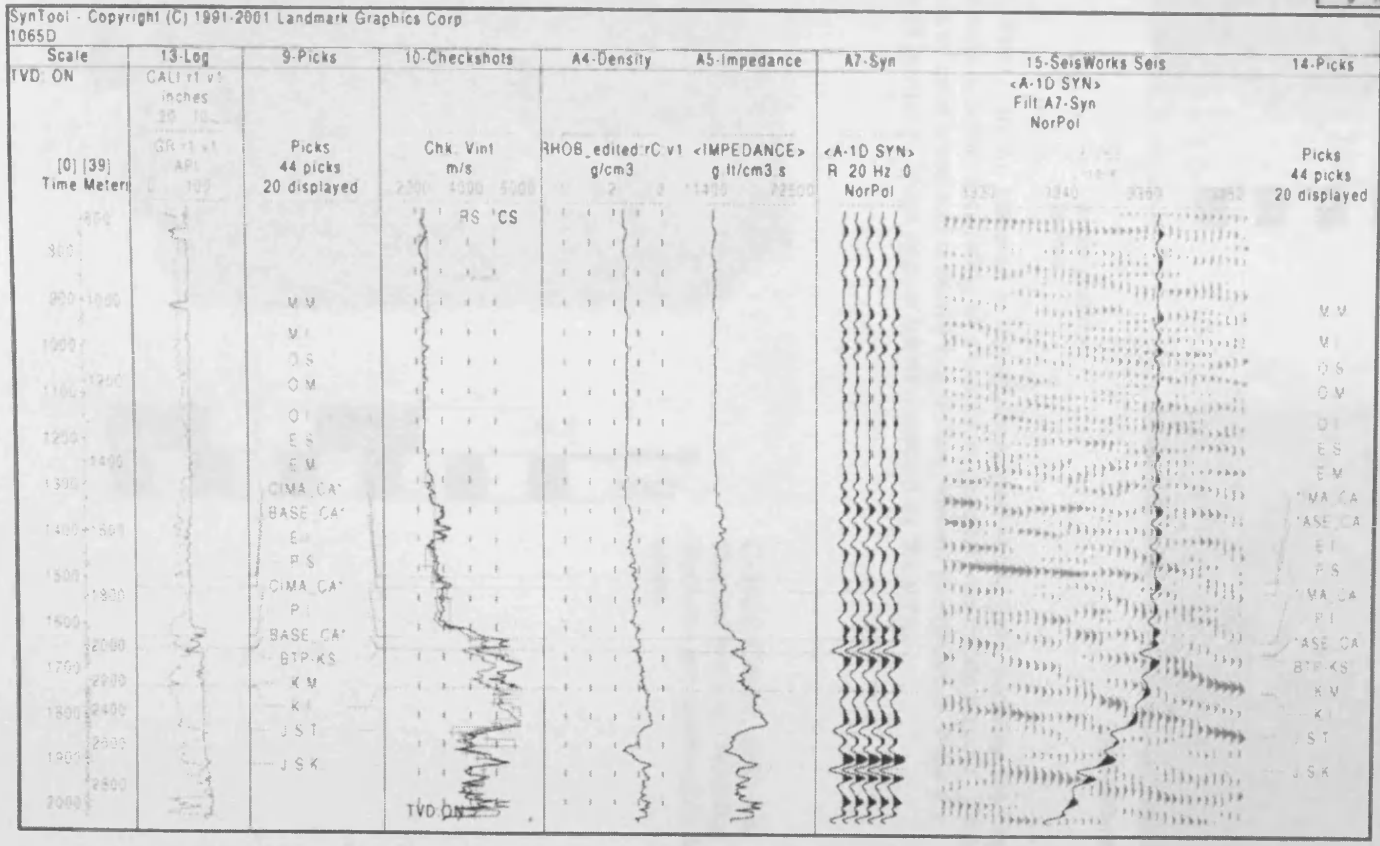

M.M. Mid-Miocene
M.I. Early Miocene
O.S. Late Oligocene
O.M. Mid-Oligocene
O.I. Early Oligocene
E.S. Late Eocene
E.M. Mid-Eocene
E.I. Early Eocene
P.S. Late Palaeocene
BTP-KS Upper Cretaceous
K.M. Mid-Cretaceous
K.I. Early Cretaceous
J.S.T. Late Tithonian
J.S.K. Late Kimmeridgian
*IMA_CA Top of calcarenites
*ASE_CA Base of calcarenites

Synthetic of well C-1065D

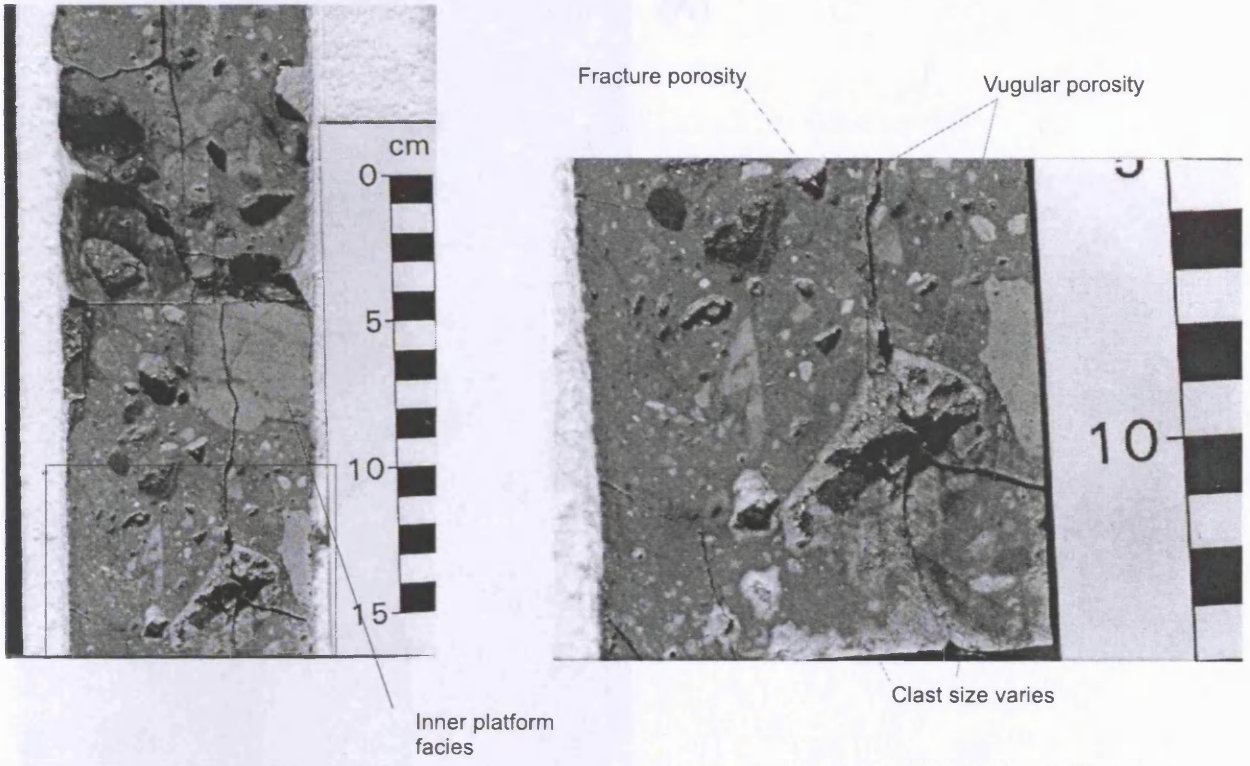

C-2092D, Core 1, 2392-2401m. Located in the southern part of the field, showing the Upper Cretaceous calcareous breccias consisting of a matrix supported polymicitc breccia. Note the wide variations of calst sizes and textures suggesting various provenances. Note the vugular and fracture porosity. Vugs appear interconnected by fractures.

C-3026, Core 1, 4081.4 m. Detrital breccia. Note that fractures are restricted to the clasts.

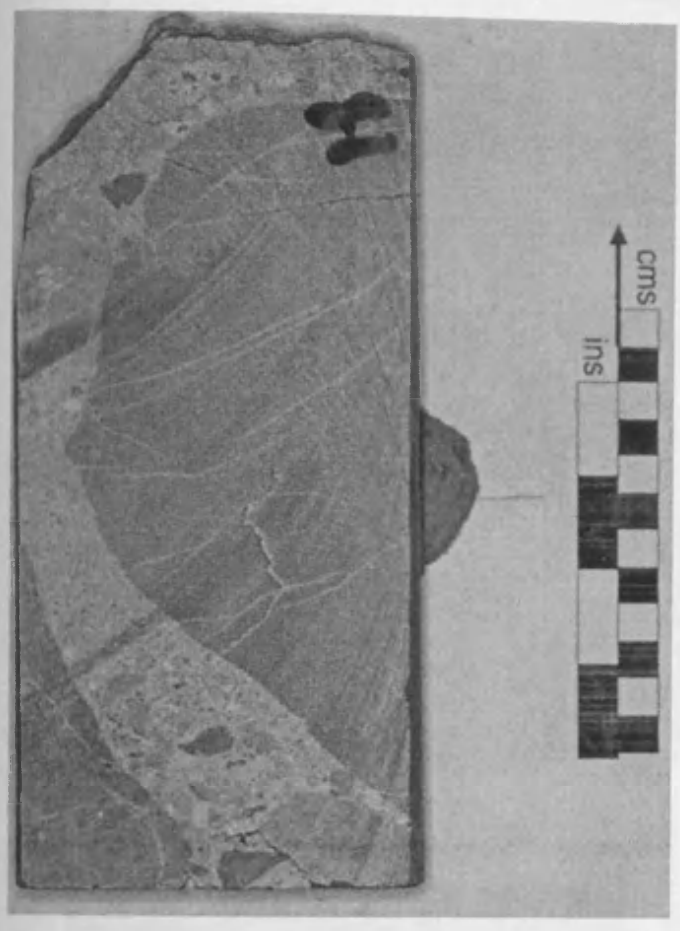

C-3045D, core ; (A) 4203.50 m unvarnished surface and (B) 4204 m, varnished surface. Note the Boulder-sized clast with granule-sized matrix

C-3045D, core 1, 4201.60 m
Possible calcrete

C-3045D, core 1, 4203.00 m,
Fractured clasts with ornate margins and graunled-sized matrix. Note clast variability.

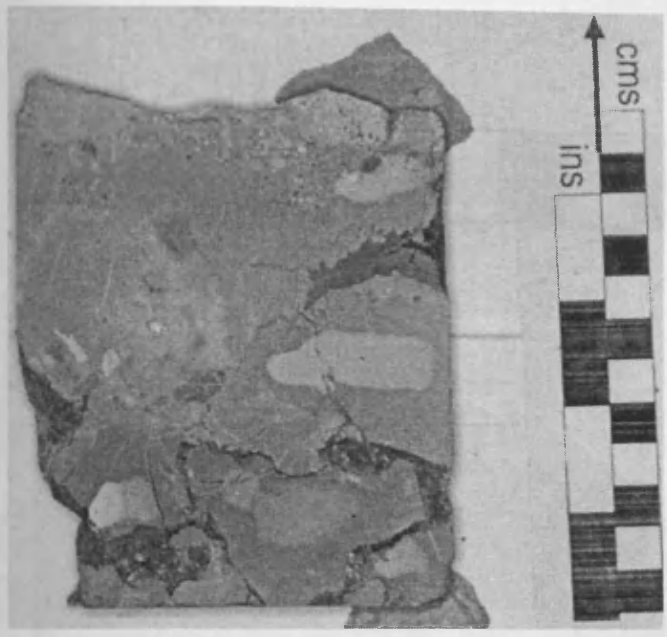

C-3045D, core 1, 4200.30 m
Fenestral dolomite clasts in conglomerate with grainstone matrix.

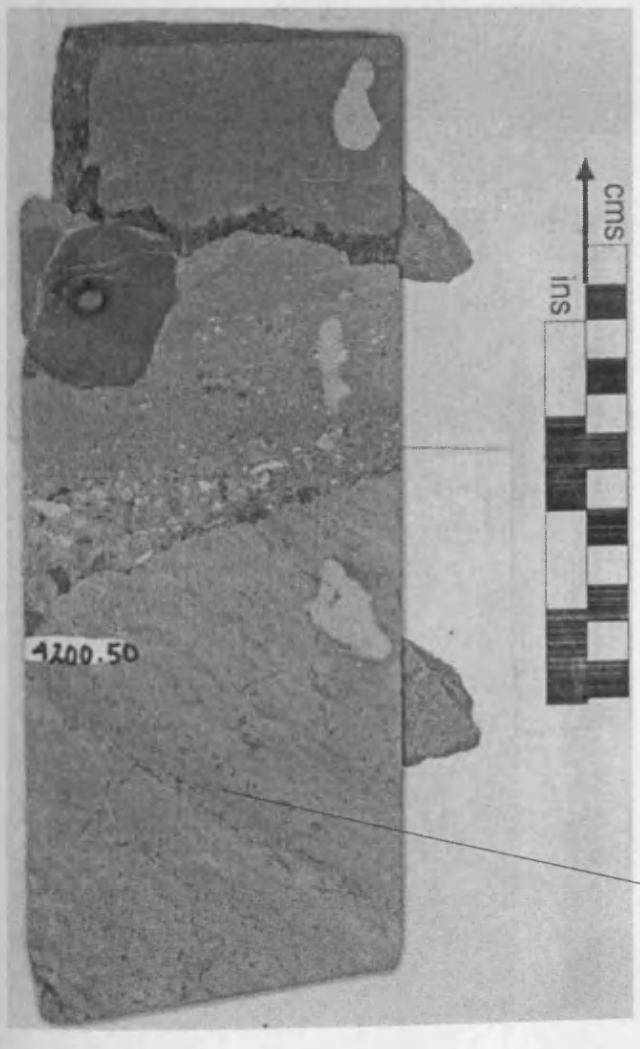

C-3045D, core 1, 4200.5 m
Note the boulder sized clast at the base exhibiting fenestral porosity. At its top an interval exhibitng a fining upwards trend which is overlain by larger clasts.

Fenestral porosity, and texture suggests an internal platform provenance

Well C-1128, core 1, 4010 - 1013 m. in the norhern part of the field, showing detail of polymict conglomerate but from a slice

oil stained fracture plane

C-42H, core 1, in the southern part of the field. Polymicitc conglomerate showing detail of core fragment as with oil stained fracture .

C-86D, core 1, 2276.75-2282.1 m

C-86D, core 1, 2276.75-2282.1 m. Located on the southern part of the field.

Upper Cretaceous interval. Deepwater micrite (pale) with microporosity (oil stained) at the top of a cycle, overlain by microstylolitic dark argillaceous wackestone. A phase of fracturing coincides with the cycle boundary. Note strongly developed open fractures in the clean beds, and erosional bed tops. Fractures appear to be tectonic.

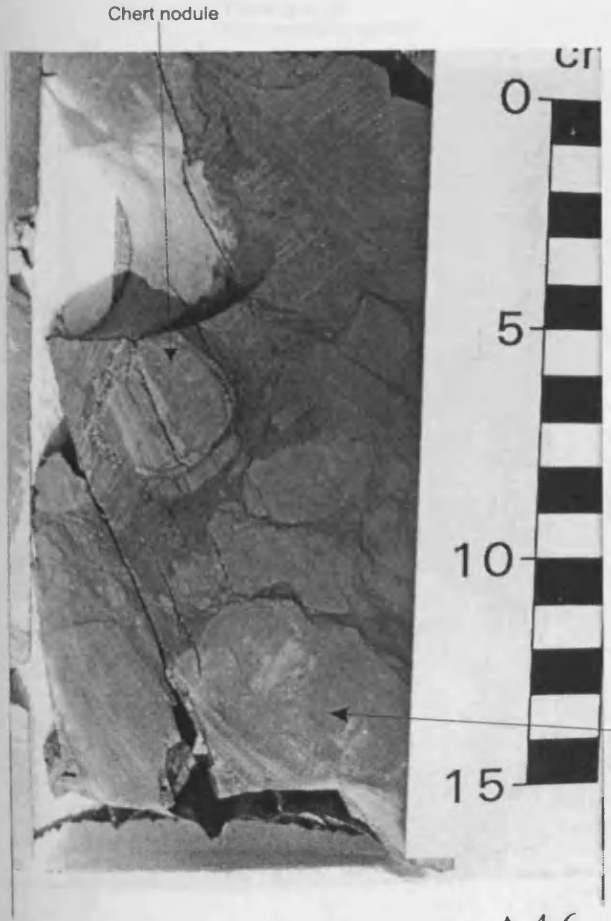

C-86D, core 1, 2276.75-2282.1 m. Located on the southern part of the field. Upper Cretaceous interval. Dark chert cemented nodules, overprint a nodular texture. Note the clasts at the base of the core.

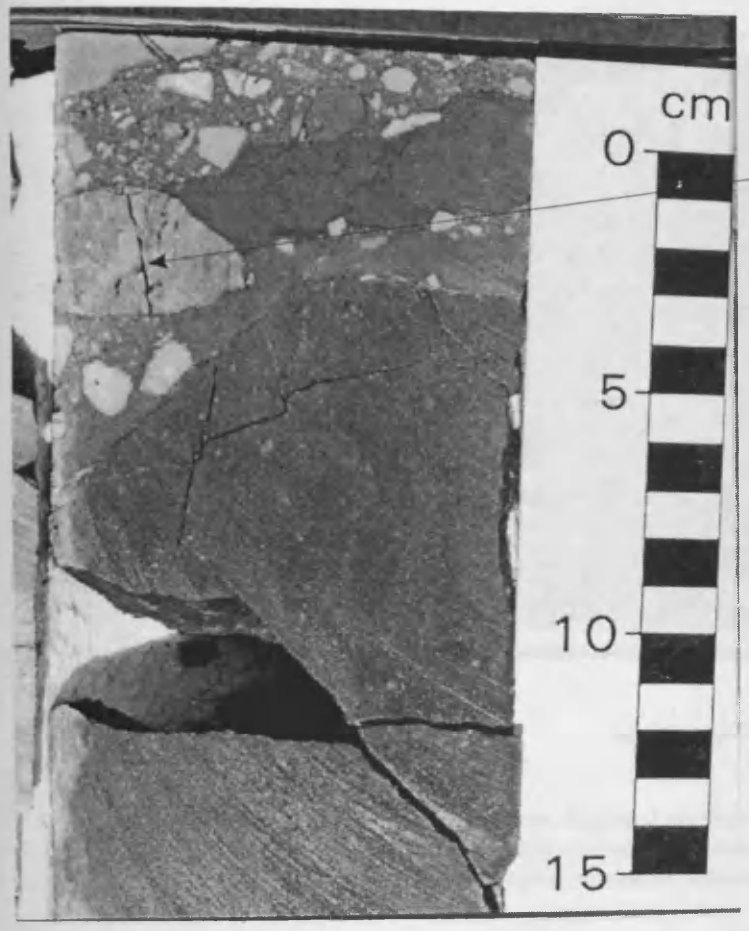

C-86D, core 2, 2456.57-2470.5 m. Located on the southern part of the field. Basal part of the Upper Cretaceous calcareous breccias. Note the polymicitc breccia appears mixed with hemipelagic sediments and overlies an interval of hemipelagic sediments. Some fractures are seen to be restricted to the clasts.

C-86D, core 2, 2456.57-2470.5 m. Located on the southern part of the field. Basal part of the Upper Cretaceous calcareous breccias, consisting of a breccia interval overlaying hemipelagic sediments. Note the calcite healed fractures.

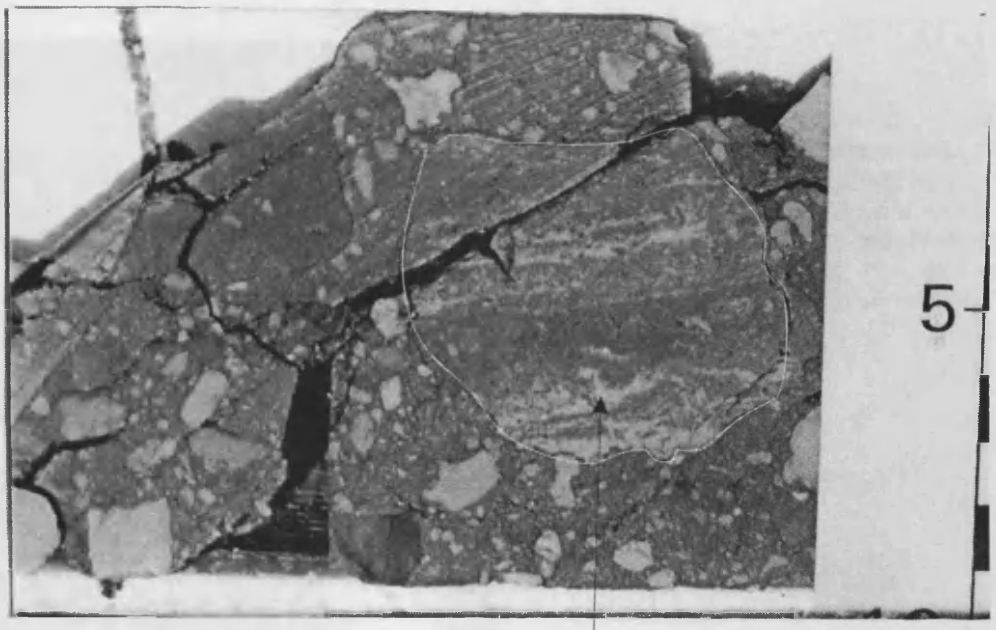

C-86D, core 2, 2456.57-2470.5 m. Located on the southern part of the field. Basal part of the Upper Cretaceous calcareous breccias. Polymict conglomerate, with well-developed laminated fenestral/reefal-textured clasts.

C-86D, core 2, 2456.57-2470.5 m. Located on the southern part of the field. Basal part of the Upper Cretaceous calcareous breccias. Detail of a large clast, of reddish-grey colour; internal texture is uncertain but could be biostromal.

C-86D, core 2, 2456.57-2470.5 m. Located on the southern part of the field. Basal part of the Upper Cretaceous calcareous breccias. Rudist fragments (?radiolitids) are present in the large clast, with matrix and smaller clasts visible above.

C-86D, core 2, 2456.57-2470.5 m. Located on the southern part of the field. Basal part of the Upper Cretaceous calcareous breccias. Detail of previous photo showing the rudist fragments in more detail.

Core photos of the Mid-Cretaceous interval

C-2092, core 2, 2646.19-2652.9 m from the southern part of the field. Middle Cretaceous showing mixed breccia with hemipelagic sediments. Note the dissolution clasts.

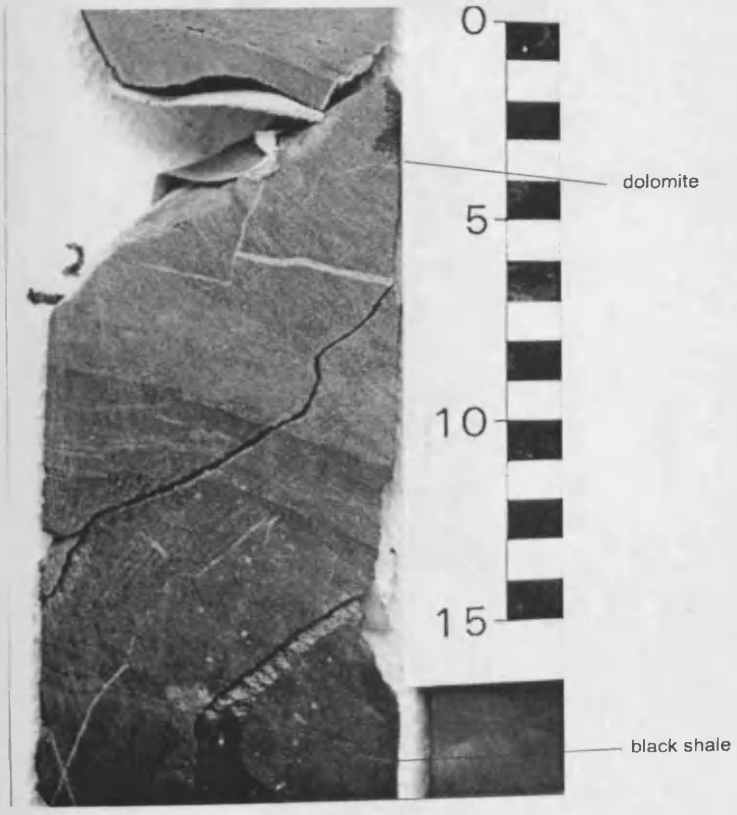

C-48D, core 4, 2950-2959.59 m.
From the southern part of the field.
Middle Cretaceous dolomite interbedded with bathyal shale and mudstone.

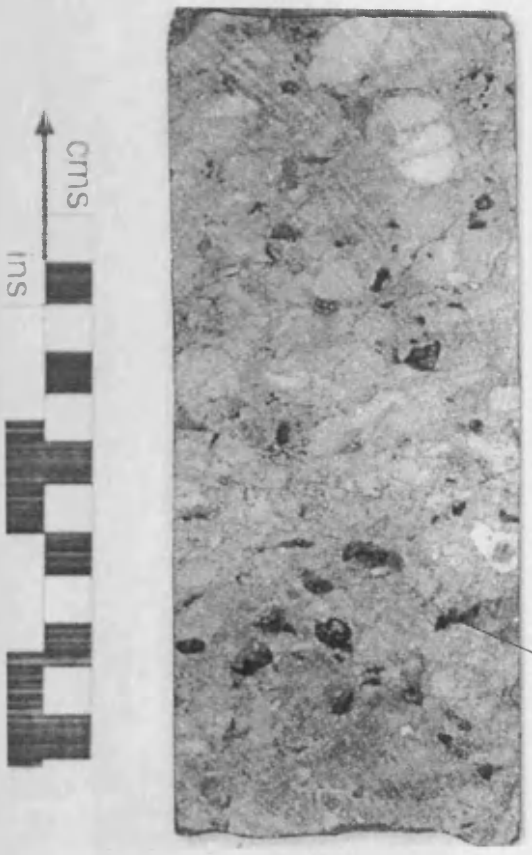

C-3068, core 13, 3646 m.
Situated at the northern part of the field. Middle Cretaceous consiting of a polymictic conglomerate withe vuggy porosity.

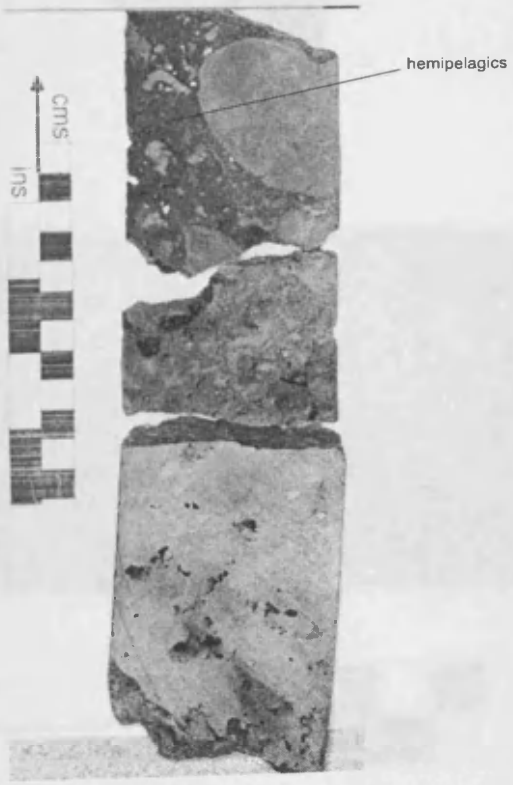

C-3068, core 14, 3718 m.
Situated at the northern part of the field. Middle Cretaceous consisting of a polymictic conglomerate intercalated with hemipelagic sediments with vuggy porosity.
Note the finning upwards trend of the clasts.

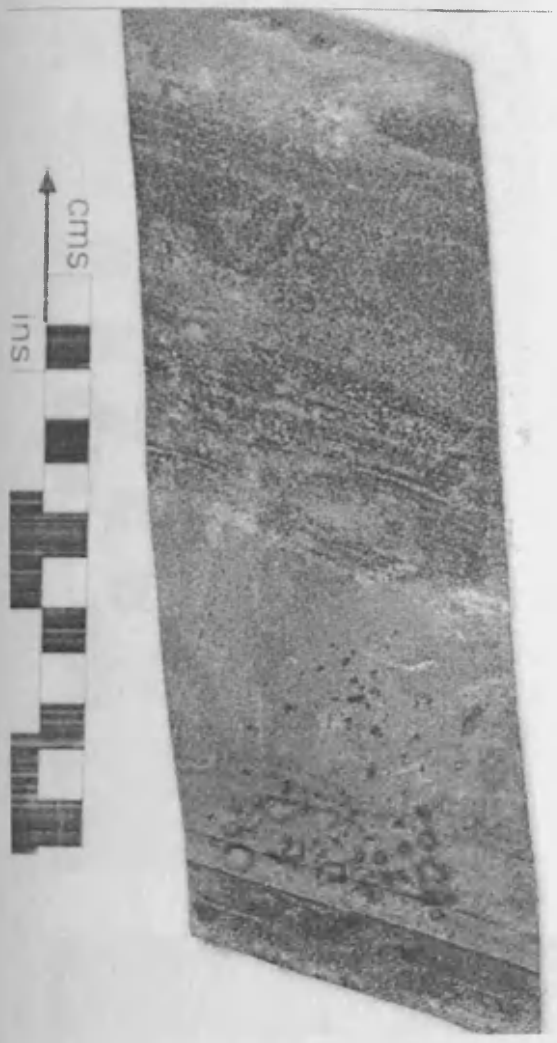

C-3068, Core 14, 3723.20 m
Middle Cretaceous. Doloarenite / Silite

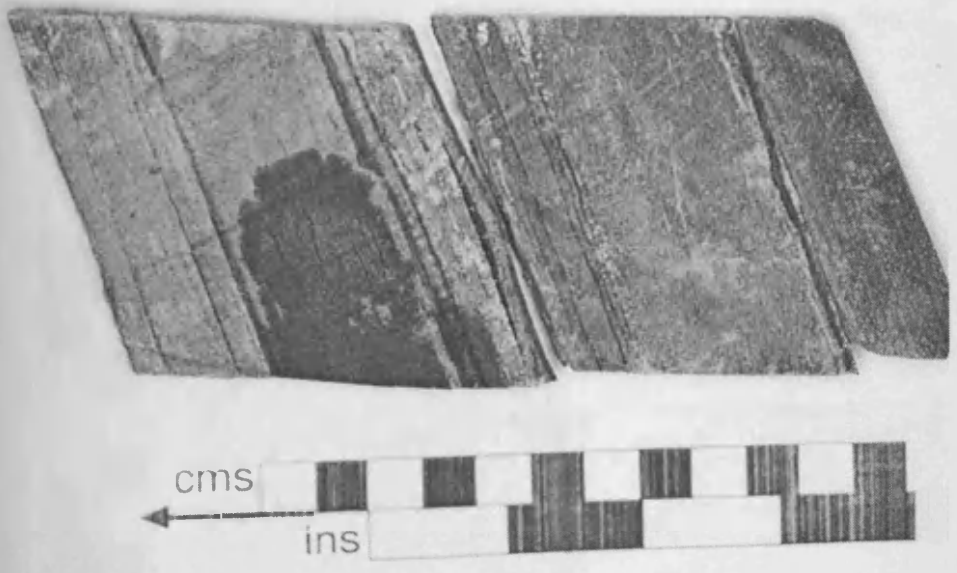

C-3068, Core 14, 3723.6 m. Located in the northern part of the field in the footwall block. Middle Cretaceous. Pyritic shale.

C-3068, Core 15, 3790.8 m, located in the footwall block of the structure in the northern part of the field.
At the base of the core a conglomerite breccia is note, overlain by hemipelagic sediments.

C-3068, Core 15, 3791.20 m, located in the footwall block of the structure in the northern part of the field.
Core exhibits a mud supported breccia that is interpreted as a debris flow.

C-418D hangingwall block
Early Cretaceous

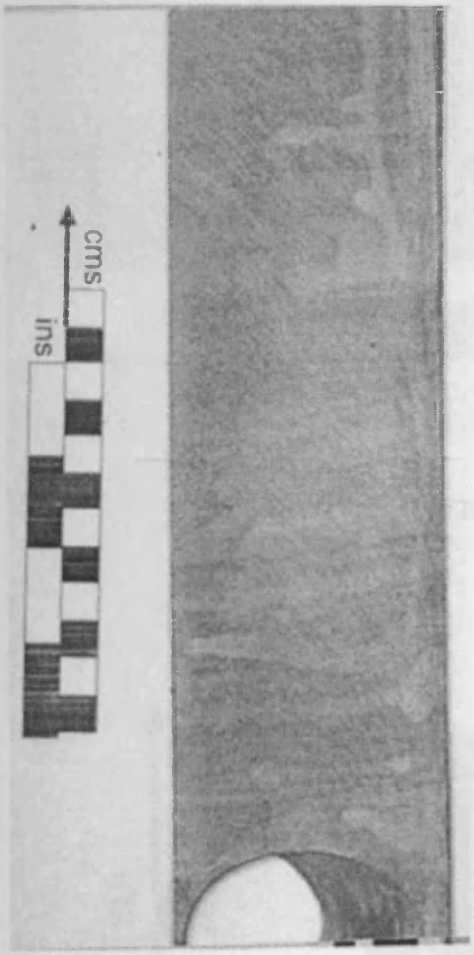

C-418D, Core 4, 5207.50 m
Lower Cretaceous. Winnowed layers in dolowackestone

C-418D, Core 5, 5208.00 m
Lower Cretaceous. Relict fractures in dolowackestone.

C-418D, Core 5, 5210.5 m.
Lower Cretaceous. Conjugate fractures with relict porosity.

C-418D, Core 5, 5211.75 m.
Lower Cretaceous,
Dolowackestone showing
Chondrite burrows.

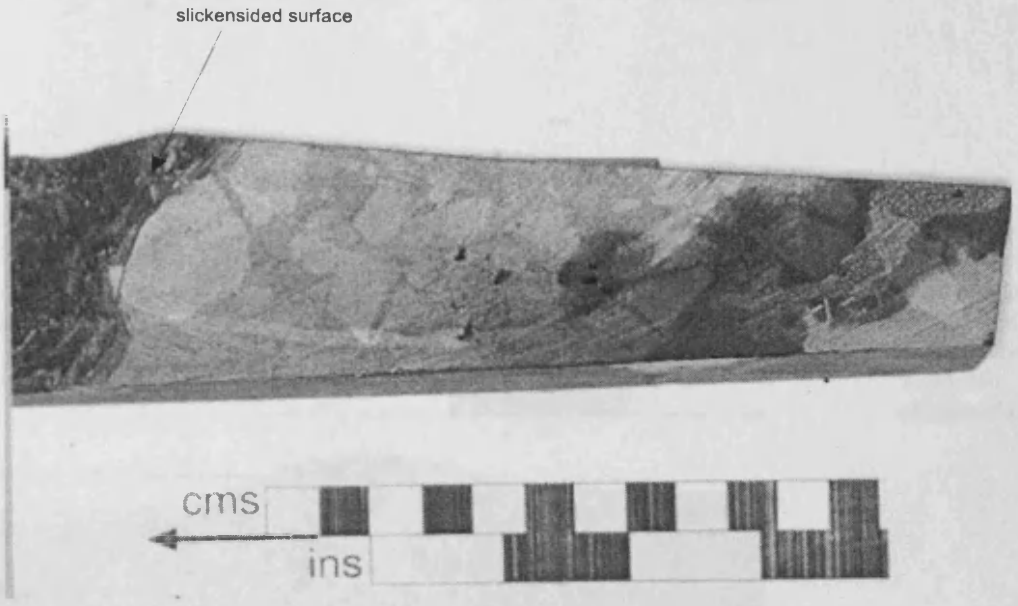

C-418D, Core 5, 5212.0 m.
Lower Cretaceous. Dolowackestone showing clasts that have been dolomitized. Note slicknsided surface.

Core photos for the Tithonian

C-3068 from the footwall block

C-3068, Core 16, 3896.20 m. Located in the footwall block of the structure. Tithonian. Slickensides on oblique clay seam.

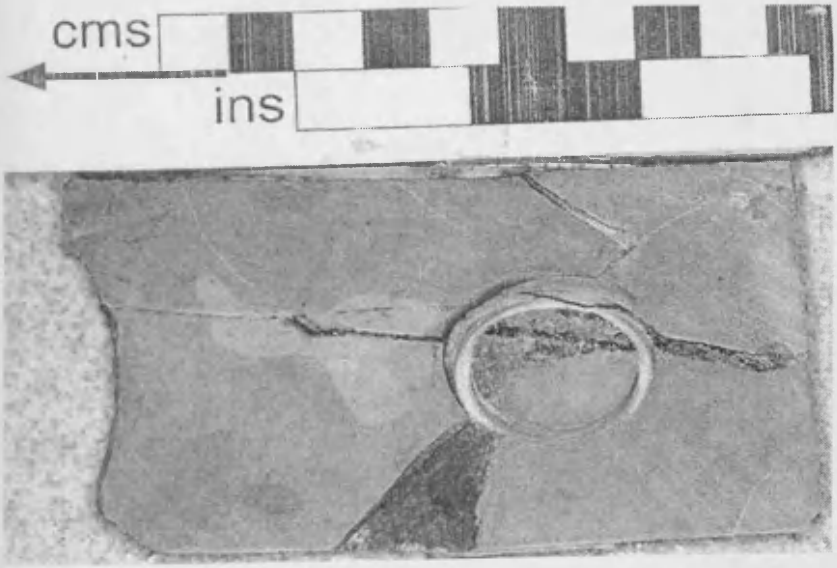

C-3068, Core 16, 3897.6 m. Located in the footwall of the structure at the northern region of the field. Tithonian. Argillaceous dolomite. Note that also polymicitc conglomerates occur at this stratigraphic level. Note the anastomosing fracture within.

Core photos for the Kimmeridgian stratigraphic interval

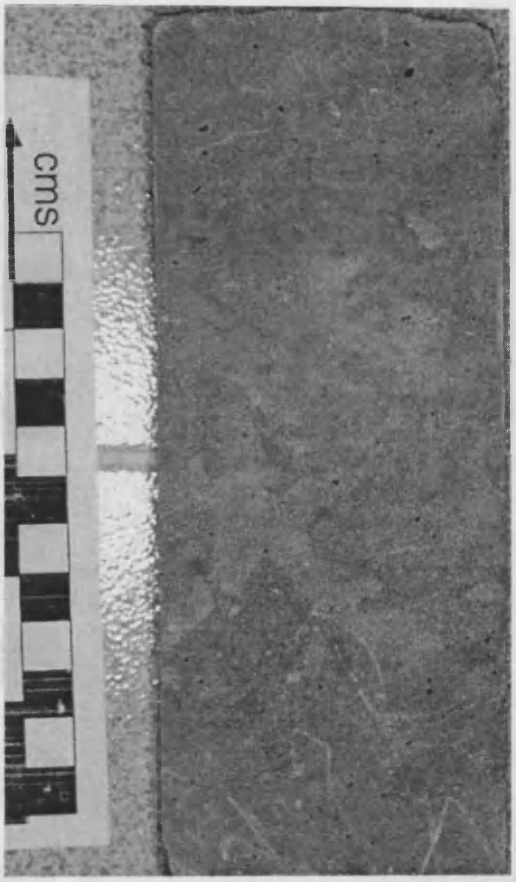

Chac-1, Core 10, 4197.50 m.
Kimmeridgian exhibiting a
massive dolowackestone.

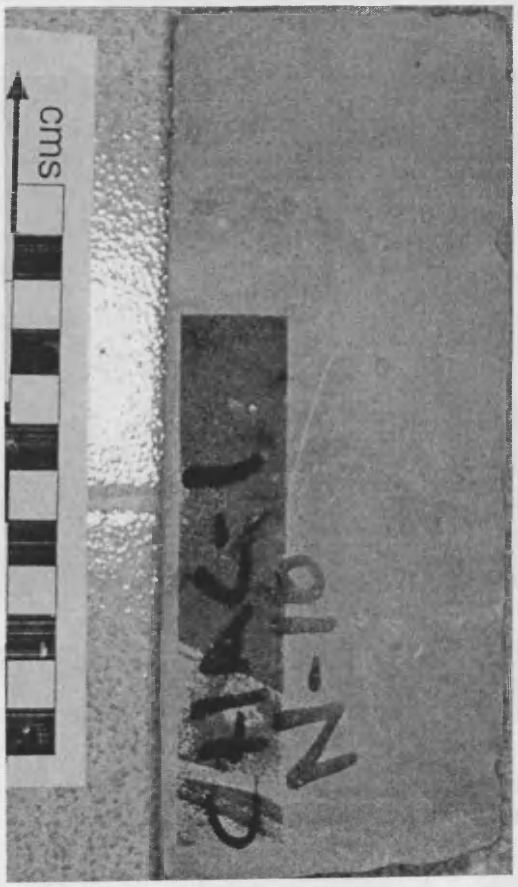

Chac-1, Core 10, 4195.50 m.
Kimmeridgian exhibiting a
massive dolowackestone.

Chac-1, C-3, 4233.50 m. Located at the Eastern Platform.
Kimmeridgian. Anhydrite nodule in mottled dolomudstone.

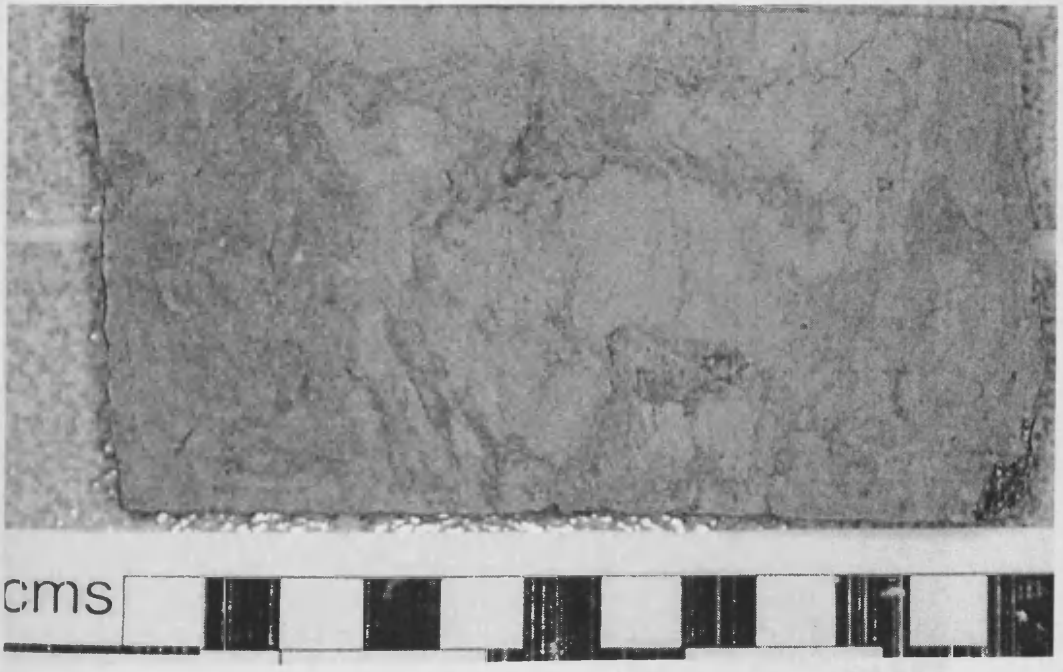

Chac-1, Core 12, 4357.2 m. Located in the Eastern Platform.
Kimmeridgian. Bioturbated dolowackestone.

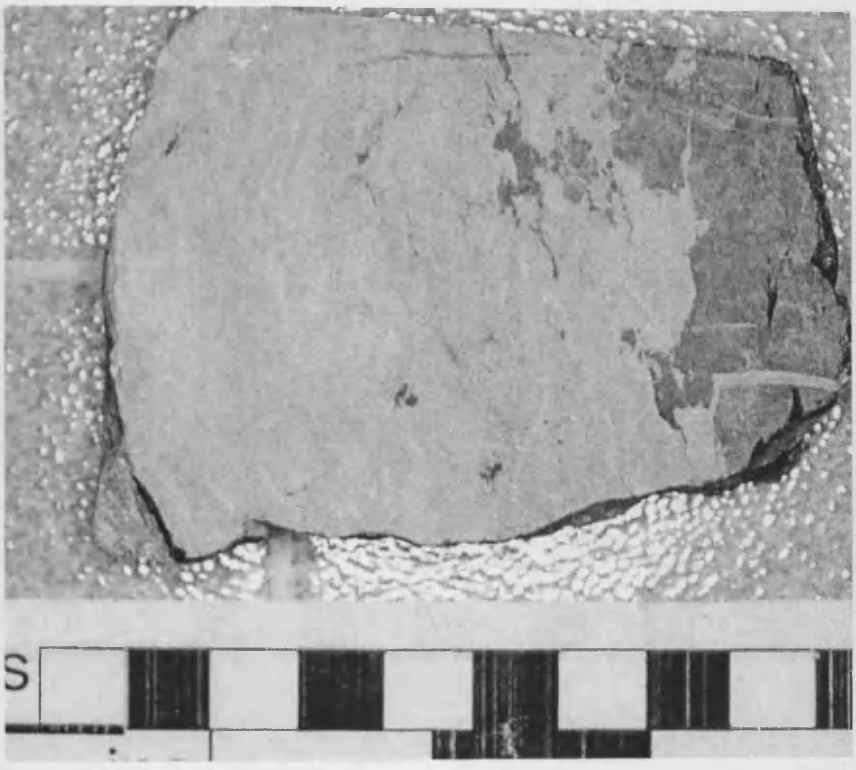

Chac-1, Core 11, 4235.80 m. Located in the Eastern Platform. Kimmeridgian. Anhydrite nodule in dolomudstone.

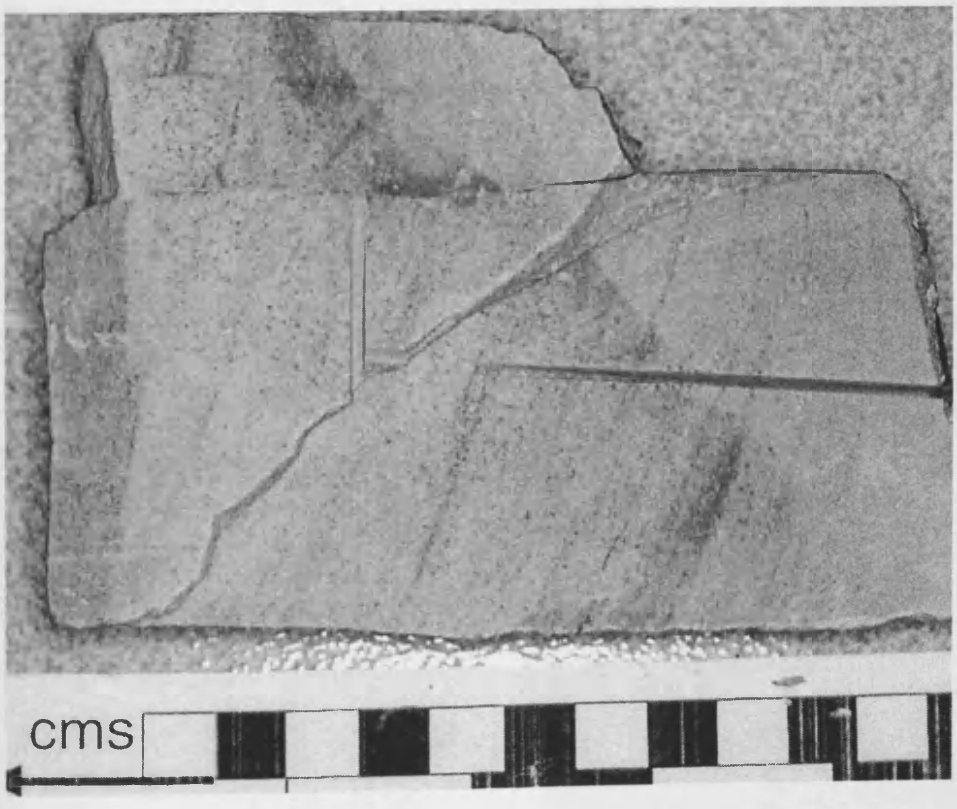

Chac-2, Core 15, 4473.70 m. Located in the Eastern Platform. Kimmeridgian. Cross-bedded sandstone.

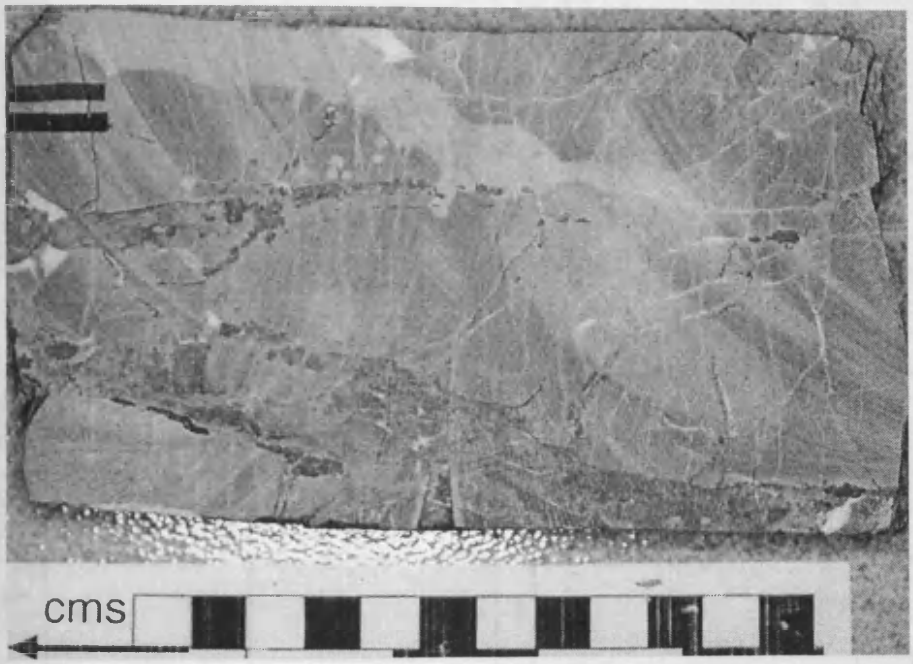

Chac-2, Core, 15, 4474.9 m. Located in the Eastern Platform. Kimmeridgian. Dolowackestone fractured and infilled by anhydrite.

Data / Wells	Biostrat report	Core description	Well Logs	Well driller report	Check Shots	Vertical	Reached hangingwall	Comments
C-3001		N1 (2393-2408) (KS breccia) (Milliolids)(Triloculina sp., Sigmoilopsis sp.) (sedimentray breccia, clasts) (P); N2 (2650-2668) (fauna not observed due to dolomitization) (dolomite, intercalations of bituminous matter, intense microfracturing, vugs, lower part sedimentray breccia dolomitized, fragments elongated and subangular 1-9cm, oil impregnated) (P); N3 (2850-2858.35) (JT) (fauna not observed due to dolomitization) (mesodolomite, laminar in portions) (P); N4 (3170-3179) (JK) (molluscs, forams) (dolomite ooids, disseminated pyrite, wackstone bioclastic, fractures) (P); N5 (3179-3188) (JK) (gastropods, echinoderms spines and plates, mollusc valves, bryozoans, algae dacycladaceas, algae codiaceas) (wackestone pisolithic, dolomitized, benthonitic).	y		Y	Y		Pictures
C-418D	yes	N1 (4517-4525) (KS breccia) (fossils not observed) (sedimentary breccia rounded to subraouded clasts dolomitized) (P); N2 (4600-4604) (KS possible base of breccia) (forams benthonic, ostracods and fragments of molluscs) (packstone dolomitized and fractured) (P), N3 (4846-4854.6) (Campanian-Maastrichtian) (Miliolids, algae dacicladaceas, ostracods, Globotrucanita stuartiformis, Globotruncana Ipparente, Contusotruncana plummerae, Contusotruncana fornicata) (conglomerate that grades to wackstone packsone argillaceous) (P), N4 (4961-4967) (KS by correlation) (fauna not observed due to dolomitization) (Conglomeratic breccia strongly dolomitized) (P); N5 (5207-5216) (KI by correlation) (fauna not observed due to dolomitization) (dolomite micro to mesocrytalline) (P)	yes	Y	Y		Y	
C-3025	yes	yes	yes					Missing well location
C-3067	yes	yes	yes					Missing well location
C-49	yes	yes	yes					Missing well location
C-99D	yes	N1 (2023-2032) (Unkn-No planktonic fossils, Codiaceas, fragments of Algae Mesophyllum sp., Milliolids, plates and spines of echinoderms Lenticulina sp., Benthonics biserales) (P); N3 (2100-2107.8) (KS-breccia) (fossils not observed due to Dolom.) (P); N4 (2233-2237), (KS breccia) (fossils not observed) (P); N4C (2238-2242.3) (KS breccia) (fossils not observed) (P); N6 (2480-2492) (KM by correlation) (fossils not observed) (intensly fractured dolomite microcrystalline) (P); N7 (2540-2554) (KI by correlation) (fossils not observed) (intesively fractured dolomitized mudstone) (P); N8 (2808-2815) (JT well log correlation) (fossils not observed) (argillaceous sandstone alternated with dolomite and shales) (P); N9 (2840-2847.4) (JT) (fossils not observed) (sandstone intercalated with bituminous shale) (P); N11 (3080-3089) (JK by well log correlation) (calcareous shale minor fractures) (P); N12 (3115-3124) (JK by well log correlation) (fossils not observed) (shale calcareous and benthonic) (P);	yes		Y			
C-1042	yes	yes	yes					
C-1065D	yes	N1)1955-1957.4) (1963.4-1965) (1976-1978) (Palaeo Sup.) (miliolids, amphisteginidos, Globorotalia velasconsis) (Alternations of packsotne with hemipelagic shale and sedimentary breccia) (P); N2 (2150-2157) (2159-2167.5) (KS breccia by correlation and lithological association) (seimantary breccia) (P); N3 (2380-2385) (KI by correlation) (fauna not observed) (dolomite fractured appeareance monomyctic breccia tectonic??); N10 (2959-2968) (JK by correlation and lithological association) (Benthonitic shale, slightly calcareous) (P)	yes					
C-3067	yes	yes	yes					Not in data set provided by Pemex
C-4062	yes	yes	yes					
C-8D	Y	N-1 (2940-2947): (JT) (Crassicolaria sp., Crassicolaria massutiniana, Calpionella alpina, Calpionella elliptica, fish remainnings) (Mudstone-Wackstone shaly, abundant quartz grains 20-69 micras, laminar) (P)		N	N	N		Well not loaded

Appendix 5
Completion logs synthesis

Data / Wells	Biostrat report	Core description	Well Logs	Well driller report	Check Shots	Vertical	Reached hangingwall	Comments
C-24D	Y	N4 (3280-3291): KI by correlation (fauna not observed) (mesocrystalline dolomite argillaceous in portions, thin horizons of shale, apparent sedimentray dip) (P); N5 (3422-3431): JT (radiolarians, Saccocomas sp., molluscs, fish, and ammonites) (wackestone, argillaceous, bituminous, grains of quartz, abundant organic matter, fractured, dissmeinated pyrite (P)						Core photos are representative for Jurassic fossils
C-26D	Y	N1 (500-509) (Mio-Tp) (Globigerinoides obliqus extremus, Glia. Miocenic, Glia. Humerosa humerosa, Globigerinoides ruber) (sandy calcareous shale abundant molluscs remains and sporadic quartz grains subrounded) (P)						
C-48D	Y	N1 (2735-2746) (KS) (globotrunanita calcarata, globotrunca bulloides, contusotruncana fronicata globotruncana sp., parasigalia sp., miliolids) (mudsonte-wackestone of bioclasts and intraclasts slightly argillaceous, laminar, apparent sedimentary dip) (NP); N2 (2828-2832) (KM) (fauna not observed due to dolomitization) (mesodolomite laminar) (NP); N3 (2940-2949) (Unkn) (fossils not observed due to dolomitization) (mesodolmite with a brecciated aspect, horizons of sedimentary breccia with subrounded clasts 1-3 cm. (P)						bad picture quality
C-49D	N-V-Dolo	N-1 (2666-2672) KM by correlation (no fossils observed due to dolomitization) (microdolomite laminar) (P)						
C-49	Y	N1 (537-546) (Mio-Tp) (planktonic: Globigernioides obliqus extremus, G. Trilobus trilobus, G. Trilobus immaturus, G. trilobus sacculiferus, Neogloboquadrina dutertrei, G. ruber, Globorotalia menardii; benthnics bulimina marginata, Astacolus vaughani, Cribroephidium advenum, astacolus cristi, textularia mayori; macrofauna: gastropods, and bivalves) (wackestone benthonic in portions sandy, to mudstone-wackestone benthonic, intraclasts and bioclasts) (P); N2 (555-562) (Mio-Tp) (planktonics: idem) (biozone bulimina marginata, astacolus vaughani, criboelphidium advenum, astacolus cristi, textulaira mayori) (wackestone benthonic, in portions sandy, apparent sedimentary dip) (P)						Core has good representative pictures; well deviation not loeaded only surface position.
C-68D	N-V-Dolo	N1 (2439-2447) (KI) (NP)						
C-86D	Y	N1 (2276-2285) (KS Maastrichtiano - Campaniano Pseudotextularia sp., Lenticulina sp., Miliolids, Gastropods & Ostracods, (NP); N2 (2456-2470) Campanian-Santonian: Miliolids, Globotruncana bulloides, Globigerinelloides sp., Globotruncanita sp., Rosita caliciformis (P); N3 (2828-2835) (Unkn-Not-Visible)						Good photo examples of sedimentary breccia occurring within the top Cretaceous; well not loaded, only surface location.
C-182	Y	N1 (3222-3229) (Eo_med) (Biozone Globorotalia lehneri) (shale to grainstone) (P)						Good photo example for the Eocene
C-207D	Y	N1 (2317-2326) (Eo_med) (by correlation) (Miliolids: Triloculina sp., Simoilopsis sp., Quinquelculina coraline) (P)	DT, GR, ILD, ILM	N	NOT GOOD	N	N	well sits at the backlimb of Akal south of C-418D; Ckshots are not good
C-245D	Y	N1 (2175-2184) (Eo_med) (Lepifocyclina sp., Miliolids, Nummulites sp, Rotalids, Textularidos) (P); N2 (2184-2193) (Eo_med) (Lepidocyclina antillea, Amphistegina parvula, Nummolites, Miliolids, Rotalidos, Globigerina sp.) (P) (Interp: platform exterior)	N	N	N	N	N	Very good photos representative of Mid Eocene
C-468		N3 (2030-2034.4) (KS breccia by correlation) (upper portion microdolomite & lower portion sedimentary polymictic breccia (fauna not observed due to dolomitization) (P); N4 (2170-2179.7) (KM Albian) (in matrix: calcisphaerula innominata, stomiosphaera sp., Bishopella alata; in clasts: miliolids (sigmoilopsis sp., Triloculina sp.) and spines of echinoderms) (Grainstone to packstone) (P); N5 (2250-2255) (KM by correlation) (fossils not observed) (mesodolomite laminar intensivelly fractured) (P); N6 (2275-2284) (KM by correlation) (fossils not observed due to dolomitization) (P); (N7 (2560-2572) (KM by well log correlation) (fossils not observed) (micro to mesodolomite, intercalations of .5 cms of anhydrite with algae, fractured) (P); N8 (2730-2737) & (2737-2746) (KI by well log correlation) (fossils not observed) (micro to mesodolomite, intesivelly fractured, detrital flows and lithoclasts) (P)						Very good photos representative of the Cretaceous successions, good quality images.
C-487	Y	N1 (3240-3247) (KM Albian) (Calcisphaerula innominata, Stomiosphaera sp., Pithonella sp., Globigerinelloides sp., Globigerinelloides sp., Globotuncanita subspinosa, Globotuncana sp.) (Wackstone-Packsotnes with lithoclasts and bioclasts; Limesotne bioturbated partilly dolomitized) (P); N2 (3380-3389) (KI by correlation) (fossil not observed) (dolomite, mesocrystalline texture) (P)						Good pictures of Upper Cretaceous; Not loaded.

Appendix 5
Completion logs synthesis

Data / Wells	Biostrat report	Core description	Well Logs	Well driller report	Check Shots	Vertical	Reached hangingwall	Comments
C-1006		N3 (2837-2846) (KI by correlation) (fauna not observed) (micro to meso dolomite intesivelly fractured) (P), N3C (2846-2855.5) (fauna not observed) (NP); N4 (2872-3027) (KI by correlation) (fauna not observed due to dolomitization) (micro to mesodolomite laminar, exoclasts, fractured) (P)						
C-1024D		N1 (3280-3289) (KS breccia) (in clasts benthonics bivalved, miliolids (Sigmoilopsis sp., Quinoquelocullina sp., probable Chubbina sp.) (Sedimentary breccia, angular to subangular clasts, intensivelly fractured chaotically, vuggy); N1C (3290-3294) (KS breccia by correlation and texture) (Sedimentary breccia, calsts angular to subangular of mudstone to argillaceous mudsotne, to wakcstone paskstone) (P); N						
C-1025D		N1 (3072-3082) (JT) (Saccocoma sp., Lombardina angulata, Eothrix alpina) (Mudsotne-wackstone biogenic, laminar, abundant detrital quartz silt size) (P), N2 (3191-3200) (JK by correlation) (fauna not observed) (Meso macro dolomite pathces of quartzitic sandstone) (P); N3 (3435-3443) (JK by correlation) (fauna not observed) (meso to macro dolomite) (P); N4 (3443-3452) (JK by correlation) (fauna not observed) (meso to macro dolomite with anhydrite nodules) (P good!)						Not loaded
C-1042D	N-V-Dolo	N1 (2772-2774) (Ks breccia by correlation and lithological association) (fauna not observed) (sedimentary breccia dolomitized compacted, angular clasts 1-65 mm, mudstone, matrix constitutes 20 %) (P); N2 (2958-2959) and (2960-2961) (KM by correlation) (fauna not observed) (dolomite microcrystalline, intercalated withthin horizons of compact shale) (P);						
C-1046D	N-V-Dolo	N2 (2987-2991) (KS breccia) (fauna not observed) (dolomite intesly dolomitized and fractured, resembles a monomyctic breccia tectonic??)						Tectonic breccia in N1 and 2
C-1086	N-V-Dolo	N1 (2985-2995) (JK by correlation against C-1065 N7 and lithological association) (fauna not observed) (micorcrystalline dolomite, ooids pelloids and oncoloids, pyrite crystals, anhydrite) (P); N2 (3100-3108) (JK by correlation and lithological association with C-1065 N10) (fauna not observed) (benthonitic shale, calcareous, dolomitized and sandy) (P)						Not loaded
C-1088	N-V-Dolo	N1 (2945-2954) (JK) (fossils not observed) (microcrystalline dolomite, agrillaceous patches of subangular quartz arenites, vugs sealed with dolomite) (P);						Not loaded
C-2052		N1 (3188-3192) (KS breccia by correlation and lithological correlation) (seimentary breccia polymictic, fragments subraounded to angular .1 to 5 cm., vuggy) (NP)						
C-2074D		N2 (3605-3607) (KS breccia by correlation and lithological association) (sedimentary breccia, cream colour, sporadic fragments of chert and anhydrite) (NP)						Not loaded
C-2092D		N2 (2646-2647) (KS breccia by correlation) (fauna not observed) (sedimentary breccia, clasts angular to subangular 1 tp 5 cm., dolomitized, stylolites) (P)						Not loaded
C-2196D		N1 (3655-3661.3) (Eoc_Lower-Med) (G. aragonensis, Gna. Broedermanni, H. aragonensis, Gna. Bullbrooki, G. lehneri, Gna. Soldadoensis soldadoensis; T. topilensis, Melonis pompiloides; Biozone G. aragonensis) (calcareous shale, betonithic, semihard, apparent sedimentary dip, laminar and bioturbation traces) (interpretation submarine channels and fans) (P)						pictures Eocene; deviation survey and ck shot survey needed
C-2295D		N1 (2748-2753) (KS breccia) (in clasts Miliolids (Quinqueloculina sp., Sigmolinita sp., Glomospira sp) (sedimentary breccia, clasts angular to subangular, 1-7 cm.) (P)						good pictures of sedimentary breccia

KS breccia = Upper Cretaceous calcareous breccia

KM = Mid-Cretaceous

KI = Early Cretaceous

JT = Jurassic Tithonoian

JK = Jurassic Kimmeridgian

P= picture

NP = No Picture

Appendix 5
Completion logs synthesis